

(1714)  
NASA Conference Publication 2468



# Atmospheric Turbulence Relative to Aviation, Missile, and Space Programs

(NASA-CP-2468) ATMOSPHERIC TURBULENCE  
RELATIVE TO AVIATION, MISSILE, AND SPACE  
PROGRAMS (NASA) 257 p Avail: NTIS HC  
A12/HF A01

CSCI 04B

N87-22341

--THRU--

N87-22355

Unclass

H1/47 0068073

*Proceedings of a workshop held at  
Langley Research Center  
Hampton, Virginia  
April 2-4, 1986*

**NASA**



NASA Conference Publication 2468

# Atmospheric Turbulence Relative to Aviation, Missile, and Space Programs

*Edited by*  
Dennis W. Camp and Walter Frost  
*FWG Associates, Incorporated*  
*Tullahoma, Tennessee*

Proceedings of a workshop sponsored by the  
National Aeronautics and Space Administration  
and the Department of Defense, and held at  
Langley Research Center  
Hampton, Virginia  
April 2-4, 1986



National Aeronautics  
and Space Administration

Scientific and Technical  
Information Branch

1987

## PREFACE

A portion of NASA's aviation safety activities has involved obtaining a clearer understanding of weather-related phenomena. Atmospheric turbulence has always been of concern, not only for aircraft but also for missile and space programs as well.

In 1984, Richard Tobiason of the NASA Headquarters Office of Aeronautics and Space Technology (OAST) began urging that a workshop be conducted on the topic of atmospheric turbulence. This topic involves so many interrelated specialities (designers, operators, forecasters, modelers, flight measurement experimenters, regulator (design criteria) and statistical analysts) that a sharing of information and improved communication in general appeared to deserve special attention. Accordingly, FWG Associates was given responsibility for conducting a workshop, which was jointly sponsored by NASA and the Department of Defense.

The primary goals of the workshop were to assess the state of knowledge in the various discipline areas and identify efforts needed to alleviate weaknesses. Attendees were assigned to committees, and after interaction with other committees, their viewpoints were compiled; these viewpoints are included in the proceedings as committee summary reports. Dr. Walter Frost, Mr. Dennis W. Camp, and Mrs. Barbara Smith are to be commended for their work in planning and conducting the workshop.

Harold N. Murrow  
Conference Coordinator

**PRECEDING PAGE BLANK NOT FILMED**

## CONTENTS

PREFACE	iii
EXECUTIVE SUMMARY . . . . .	1
WORKSHOP PARTICIPANTS . . . . .	6
INTRODUCTION AND WELCOME	
Jerry C. South and Harold N. Murrow . . . . .	7
INVITED PAPERS	
<i>Comments on the Problem of Turbulence in Aviation</i> James C. McLean, Jr., National Transportation Safety Board, Washington, D.C. . . . .	11
<i>DoD (USAF) Turbulence Accidents and Incidents</i> Douglas Miller, USAF Inspection and Safety Center, Norton AFB, California . . . . .	17
<i>New Generation Aircraft Design Problems Relative to Turbulence</i> <i>Stability, Aeroelastic Loads, and Gust Alleviation</i> Richard M. Heimbaugh, Douglas Aircraft Co., Long Beach, California . . . . .	27
<i>Tactical Missile Turbulence Problems</i> Richard E. Dickson, U.S. Army Missile Command, Redstone Arsenal, Alabama . . . . .	47
<i>Remote Versus In Situ Turbulence Measurements</i> Walter Frost, FWG Associates, Inc., Tullahoma, Tennessee . . . . .	53
<i>Measurements of Atmospheric Turbulence</i> Harold N. Murrow, NASA Langley Research Center, Hampton, Virginia . . . . .	73
<i>Turbulence as Observed by Concurrent Measurements Made at NSSL</i> <i>Using Weather Radar, Doppler Radar, Doppler Lidar, and Aircraft</i> Jean T. Lee, National Severe Storms Laboratory, Norman, Oklahoma . . . . .	93
<i>CAT-Generating Mechanisms</i> Morton G. Wurtele, UCLA, Los Angeles, California . . . . .	111
<i>Physical Mechanisms of Heat, Momentum, and Turbulence Fluxes</i> John S. Theon, NASA Headquarters, Washington, D.C. . . . .	127
<i>Turbulence Forecasting</i> C. L. Chandler, Delta Air Lines, Atlanta, Georgia . . . . .	137



<i>Transport Models for Numerical Forecast</i> Stephen D. Burk, Naval Environmental Prediction Research Facility, Monterey, California . . . . .	155
<i>Example on How to Model and Simulate Turbulence for Flight Simulators</i> John C. Houbolt, NASA Langley Research Center, Hampton, Virginia . . . . .	159
<i>Implementation of Turbulence Models Into Simulators</i> Robert L. Ireland, United Airlines Flight Center, Denver, Colorado . . . . .	179
<i>The Status of Military Specifications with Regard to Atmospheric Turbulence</i> David J. Moorhouse, USAF, Wright-Aeronautical Laboratories, Wright- Patterson AFB, Ohio, and Robert K. Heffley, Manudyne Systems Inc., Los Altos, California . . . . .	181
<b>COMMITTEE SUMMARY REPORTS</b>	
Design Committee: David O'Keefe, Chairman . . . . .	201
Operations Committee: John J. Pappas, Chairman . . . . .	205
Remote Sensing Committee: Gary P. Ellrod, Chairman . . . . .	211
Simulation Committee: Robert L. Ireland, Chairman . . . . .	215
Measuring Committee: Robert A. McClatchey, Chairman . . . . .	219
Modeling Committee: Robert K. Heffley, Chairman . . . . .	223
Predicting Committee: John L. Keller, Chairman . . . . .	239
Understanding Committee: Rodney Wingrove, Chairman . . . . .	243
<b>CLOSING REMARKS</b>	
Walter Frost . . . . .	249
Harold N. Murrow . . . . .	250
<b>ATTENDEES</b> . . . . .	251

## EXECUTIVE SUMMARY

The purpose of the workshop was to bring together various disciplines of the aviation, missile, and space programs involved in predicting, measuring, modeling, and understanding the processes of atmospheric turbulence. Working committees re-examined the current state of knowledge, identified present and future needs, and documented and prioritized integrated and cooperative research programs. The details of the overall workshop are fully documented in the proceedings.

The workshop was sponsored by NASA and DoD and conducted by FWG Associates, Inc. The workshop was held at Langley Research Center, Hampton, Virginia, April 2-4, 1986. Issues addressed by an interdisciplinary group of professionals were: common user requirements, common existing research facilities, as well as new facility requirements, current status of our knowledge of turbulence processes, forecasting and prediction techniques, computational algorithms, measurement capabilities, potential future instrumentation, and design criteria.

Invited papers provided an overview on the current status of turbulence modeling theories, measurement techniques, and operational and design needs. The papers are documented in the proceedings.

The results of the committee working sessions and interactive discussions are summarized in Tables 1 through 4. Recommendations as related to user needs and research areas are tabulated under the broader areas of operations, design, simulation, and space needs. Detailed descriptions of the research needs and suggestions as to agencies responsible for the research areas are given in the committee summary reports.

**TABLE 1**

**OPERATIONS**

1. Establish a clear definition of operational objectives for understanding turbulence.
2. Standardize turbulence terminology and reporting procedures.

**UNDERSTANDING**

1. Prepare a survey to assess the state-of-the-art on the turbulence:
  - a) Frequency of occurrence
  - b) Duration
  - c) Spatial/temporal distribution
2. Establish high-altitude turbulence data and understanding.
3. Assemble a comprehensive sensor system to provide cost-effective flight research.
4. Support development of high-resolution CFD research models.
5. Industry agencies and sectors of the industry should work together to develop and disseminate a standard that clearly encompasses all aspects of aircraft turbulence.

**MODELING**

1. New parameterization models should be investigated.
2. Models should establish more direct contact with the remote sensing community.
3. The lidar community should define and present their needs to modeling community.

**MEASURING**

1. Develop measurement techniques to distinguish gravity waves from turbulent fluctuations.
2. Develop turbulence avoidance techniques:
  - a) Aircraft measurement
  - b) Ground-based measurement
  - c) Prediction
  - d) Current on-board information
3. Refine techniques for detecting turbulence using VAS sounding data.
4. Investigate methods of direct sensing of turbulence from ground-based lidar and radar for long-range implementation.
5. Document present state of knowledge on the use of profilers for monitoring turbulence aloft.

**PREDICTING**

1. Focus on various pieces of turbulence problem for numerical prediction since current grid resolution will not allow mesoscale effects to be operationally computed:
  - a) Mountain waves
  - b) Convection
  - c) EEC
2. Use existing forecast fields to provide higher resolution through the development of adaptive nesting techniques.
3. Verify and identify most effective forecast techniques.
4. Research presently used rules of thumb forecasting and develop valid and standard techniques and publish the results for use on space platform.
5. Continue the development of filters for use on space platform.
6. Determine if aircraft, VAS, or profiler data will improve numerical models.
7. Continue the development of equipment and algorithms for accessing and determining turbulence encounters from flight recorder data.
8. Establish a centrally located automated PIREPS assimilation center.
9. Train users and operators to interpret turbulence data from WSRAD radars.



# TABLE 2

## DESIGN

1. Re-assess TAC 78-55:
  - a) Turbulence prediction techniques
  - b) Design approach
  - c) Airflow measurement prediction

## UNDERSTANDING

1. Analyze and establish a national repository of turbulence data:
  - a) Establish current data base
  - b) Establish as needed
  - c) Analyze as needed
  - d) Develop a catalog
2. Determine benefits of effects on the increased life span of aircraft due to improved clear-air turbulence forecasts and/or warning and avoidance systems.
3. Develop detailed flow visualization and/or measurements of unsteady atmospheric phenomena.
4. Calculate the evolution of three-dimensional vortices and their effects on flow near the ground plane.
5. Investigate (research and measure) the response of aircraft with multi-surface control systems during turbulence penetration.

## MODELING

## MEASURING

1. Develop turbulence measurement techniques for altitudes greater than 20 km.
2. Develop a "one-stop" meter which permits easy visual reading and repeat capability.
3. Expand research, development, and validation in the area of avoidance and awareness.

## PREDICTING

ORIGINAL PAGE IS  
OF POOR QUALITY

**TABLE 3**

**SIMULATION**

1. Review current MIL-STD models for structural, flying qualities, and flight control applications.
2. Provide explicit guidance on how to implement turbulence models.

**UNDERSTANDING**

1. Generate data for modeling the probability density function of turbulence.
2. Analytically investigate the effect on time averaging due to multi-passes (i.e., time, rain, etc.).
3. Verify physical and wind tunnel turbulence models of superimposing gusts on wind tunnel turbulence (i.e., gusts on turbulence).
4. Systematically investigate and determine the various effects of gusts of turbulence (i.e., etc.) which can be predicted by gusts and their relative level of importance.
5. Study the necessity of a three-dimensional wing shear/turbulence model for existing applications.
6. Develop an understanding of the most important types of wing shear/turbulence near airports and/or topographic features.

**MODELING**

1. Investigate the general Monte Carlo turbulence simulation problems and consider potential coupling with CFD models.
2. Develop models of anisotropic turbulence associated with various forms of wind shear (particularly microbursts).
3. Develop suitable turbulence models for rotary wing design and simulation.
4. Develop realistic turbulence models below:
  - a) Wind shear
  - b) Gusts
  - c) See above
  - d) Other local scales

**MEASURING**

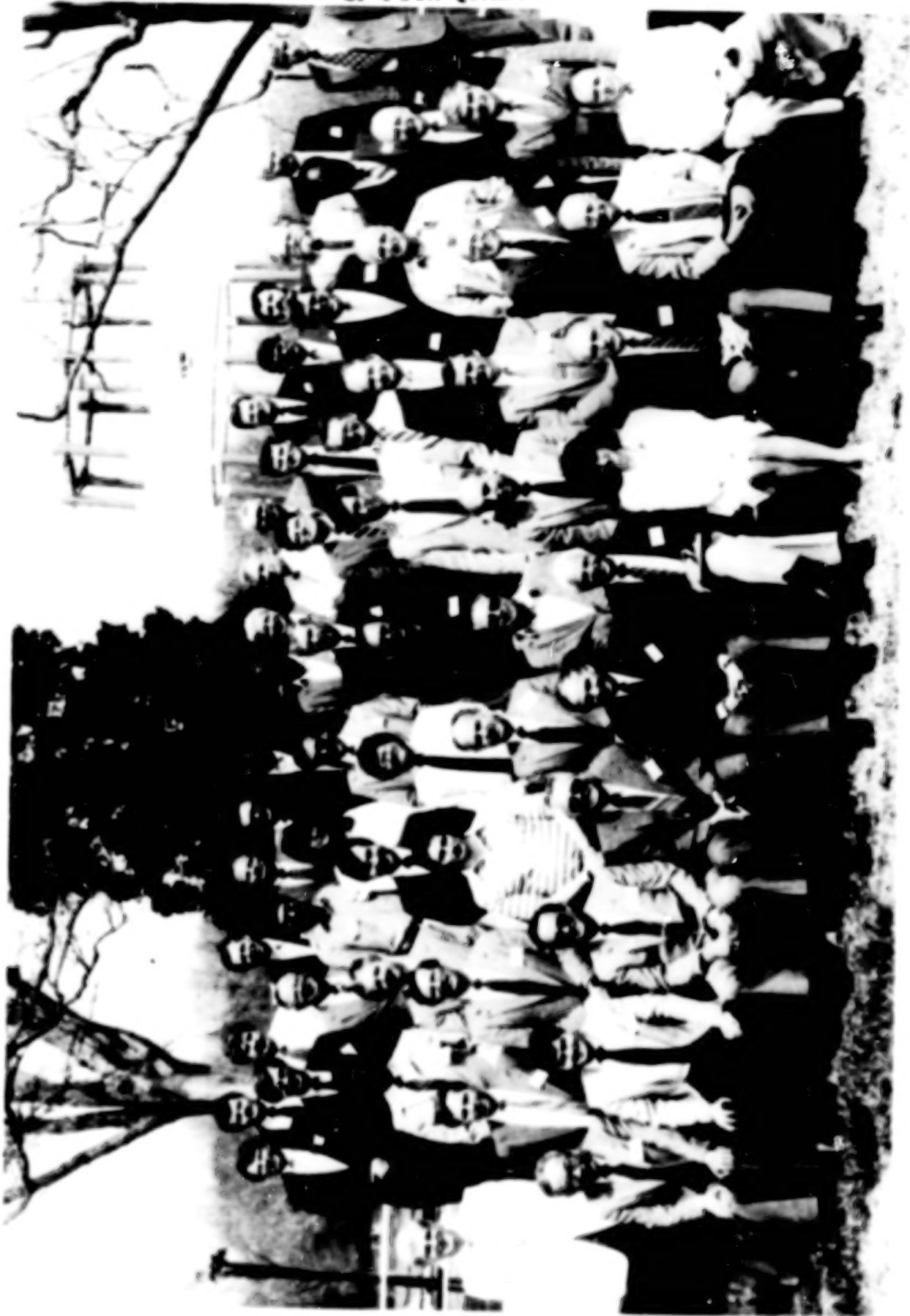
**PREDICTING**

# TABLE 4

SPACE				
UNDERSTANDING	MODELING	MEASURING	PREDICTING	
		1. Develop remote sensing capability of measuring density at 70 to 120 km.		



ORIGINAL PAGE IS  
OF POOR QUALITY



**WORKSHOP PARTICIPANTS**

## INTRODUCTION AND WELCOME

Jerry C. South  
NASA Langley Research Center  
Hampton, Virginia

It is my pleasure to welcome all of you to NASA Langley Research Center. We're very happy to co-host this workshop with the DoD. I was involved in my research days in a group that included atmospheric turbulence research and that's where I got to know Harold Murrow originally.

We host many workshops during the year, and if there is anything that we can do to make your stay more productive and comfortable, please let us know. Harold is the administrative chairman and can take care of any of your needs. If you have any questions or if you have some extra time and would like to have a tour of some of the facilities at Langley, Hal can probably arrange that, too. I'll get out of the way. I know your objective is transferring a lot of information and trying to look at research needs for the future, so get to it and have a good couple of days.

Harold N. Murrow  
NASA Langley Research Center  
Hampton, Virginia

As most of you know, atmospheric turbulence has always been of concern to the aerospace community and will continue to be. The very first NACA report\* was on that subject. There are so many interrelated facets that, one to two years ago, several people thought that it would be profitable to try to bring together people with differing perspectives on the subject in a workshop arrangement. Probably the biggest initiator of that was Dick Tobiason, who was at NASA Headquarters, OAST, at that time. Later, further support was offered by John Theon, OSSA, and Captain Ed Harrison with the Secretary of Defense. So we, along with John Houbolt here at Langley and Dennis Camp at Marshall met with Walt Frost and formed an organizing committee which led to this workshop. We certainly appreciate the support, and we certainly hope that this will be profitable to everyone here.

\*Wilson, E. B.: Theory of an Airplane Encountering Gusts. NACA Report 1, Part 2, 1915.

INVITED PAPERS

PRECEDING PAGE BLANK NOT FILMED

PRECEDING PAGE BLANK NOT FILMED



N87  
22342  
UNCLAS

## COMMENTS ON THE PROBLEM OF TURBULENCE IN AVIATION

James C. McLean, Jr.  
National Transportation Safety Board  
Washington, D.C.

Since there has been aviation there has been a turbulence problem. The earliest aviators recognized several potentially turbulent situations such as strong low-level winds across rough terrain, convective turbulence due to solar heating and instability. They also had a great respect for the damaging turbulence associated with thunderstorms. Much of this knowledge was based on experience. It was not until the 1940's that much of the problem underwent scientific scrutiny. The Thunderstorm Project described the dynamics of the airmass thunderstorm, but as we now know, it did not address many of the ancillary characteristics that thunderstorms can generate. In the late 1950's the mountain wave was investigated and described.

With the advent of high-altitude jet aircraft in the 1950's, it was commonly thought that flight would be above all troublesome weather. The Air Force and, shortly thereafter, the airlines learned this was not so. A type of turbulence called CAT (Clear-Air Turbulence) reared its head and extended sharp claws. In February 1966 the joint military-civilian National Committee for Clear-Air Turbulence was established. This action, in part, led to a period of intensive research to both describe the phenomenon and to accurately forecast it.

In 1977, the downburst associated with thunderstorms was first described, and since that time there have been intensive efforts to identify the onset of this phenomenon and to give pilots a timely warning of the hazard.

In spite of all the efforts to improve the forecasting and detection of turbulence, the problem is still with us. Excerpts from the statistics of the most recent period of accident records compiled by the National Transportation Safety Board (NTSB) may give some insight into the magnitude of the problem.

Table 1 enumerates the accidents that occurred during the period from 1982 through 1984, the latest period that NTSB has complete records. It gives the total number of accidents for the three-year period for large commercial carriers--both scheduled and non-scheduled--operating under FAR Part 121, the commuter and air taxis operating under FAR Part 135, and general aviation, which includes corporate aircraft, operating under FAR Part 91. These accidents have, in turn, been subdivided into fatal and nonfatal accidents and subtotaled as weather-involved and, more specifically, as turbulence-involved accidents. The weather-involved accidents are accidents in which weather is listed as a cause or factor. Other casual factors such as those attributable to pilot actions or maintenance problems may have been assigned to the same accident.

More indicative of the magnitude of the weather hazard is Table 2 which gives the weather accidents as percentages of the total number of accidents

and the turbulence-associated accidents as a percentage both of the total number of accidents and a percentage of weather-involved accidents. Most significant in these numbers is that the odds that an accident involving a large commercial carrier being in a weather accident are greater than for either the commuter and air taxi operations or for general aviation. This is probably due, at least in part, to the fact that the aircraft operated under FAR Part 121 are most sophisticated and more likely to have redundant systems than the smaller aircraft, and hence are less likely to suffer from catastrophic mechanical failure. Additionally, the pilots, as a group, have more experience and are less likely to become involved in situations attributable to operational errors. But based upon their scheduled operation, they do encounter all varieties of weather situations.

It is noteworthy that in all three operational categories, weather is a factor in a higher percentage of fatal accidents than it is in accidents overall, and in the case of FAR Part 121 operations, over half of all the fatal accidents are weather involved and they account for almost all of the fatalities. The common thread in this particular data sample is snow and/or ice, which was a factor in four of the five fatal accidents. Engine ice and ice and snow on the wings were major factors in the Air Florida accident in Washington, D.C., in January 1982 which killed 78 people. During the same month, two people were killed when a World Airways DC-10 ran off the runway into Boston harbor due to ice and snow on the runway. The other accidents were a Republic Airlines Convair 580 which ran into a snowbank in Brainerd, Minnesota, on January 9, 1983. A propeller disintegrated, fatally injuring a passenger. The other involved an Ozark Air Lines DC-9 which collided with a snow sweeper in Sioux Falls, South Dakota, on December 20, 1983, killing the sweeper operator. The fatal accident that was not involved with snow and/or ice was the wind shear encounter by Pan American Flight 759 on takeoff from New Orleans International Airport on July 9, 1982, which caused 153 fatalities.

Turbulence accounts for 24 percent of the accidents involving large commercial carriers and 54 percent (over half) of the weather-involved accidents. Fortunately during the 1982 through 1984 time period, there were no fatalities caused by turbulence encounters. This is not unique to the period. There have been no fatal accidents involving large commercial aircraft directly attributable to turbulence since the crash of a Braniff Airways Lockheed Electra on May 3, 1968, in which 85 people were killed. In this case, the aircraft suffered structural failure recovering from an unusual attitude induced by a thunderstorm. There have been two fatal turbulence accidents since that time: a Fairchild F-27 in December 1968 and a Lockheed Hercules in May 1974. In both cases, the structural failure was attributed to fatigue or pre-existing cracks in the airframe. This is not to imply that turbulence is not a hazard. During the 1982 to 1984 time period, there were 81 injuries in FAR Part 121 operations, 24 of them listed as serious. This represents both considerable pain and suffering to those involved and a significant financial liability to the airlines. Those generally at greatest hazard by turbulence are flight attendants who often continue cabin services when the seat belt sign is on and are injured both by being thrown about the aircraft's interior and by service equipment, such as food and drink carts and galley equipment. An additional problem is the large amount of loose luggage

and other objects that are carried aboard airliners and improperly stowed. These objects often become missiles in severe turbulence.

In the categories operating under FAR Parts 135 and 91, the turbulence accidents only account for 2 percent of the total accidents and 6 and 7 percent of the weather-related accidents, respectively. The difference between the smaller commuter, air taxi, and general aviation aircraft and the larger commercial carriers is that turbulence-related accidents with the smaller aircraft are much more likely to be fatal. The reason for the lower percentage of turbulence accidents is readily explainable. In the smaller aircraft, the passengers and crew remain strapped in and there are generally not the loose and potentially hazardous objects in the passenger spaces. Consequently, the turbulence--so long as control of the aircraft is maintained--is a discomfort. The serious problem is when control is not maintained. The large majority of fatal turbulence encounters are a result of the pilot losing control of the aircraft due to extreme accelerations or disorientation and either colliding with the ground while out of control or by overstressing the aircraft during an attempted recovery from an unusual attitude which results in an in-flight breakup of the aircraft.

The NTSB has investigated several turbulence accidents and has made recommendations to improve the system in those instances where the Board believed that changes in procedures might serve to alleviate the problem to some degree. Unfortunately, the NTSB does not have the resources to investigate all turbulence encounters. It is limited to investigating those classified as accidents by the Board's definition, which means that there was serious injury to passengers or crew members or sufficient damage to the aircraft that its airworthiness was affected. The following paragraphs are synopses of some of the accidents investigated by the NTSB which are examples of the problems associated with turbulence.

On May 19, 1980, a Gates Learjet Model 25D was enroute from West Palm Beach to New Orleans on J-58. The aircraft reached its cruise altitude of 43,000 feet just prior to reaching Clovia Intersection, about 104 miles west of Sarasota. Shortly after the pilot had reported leveling off the controller at the Jacksonville Center, monitoring the frequency used by the Learjet, heard an unusual staccato sound followed about 18 seconds later by a report from the co-pilot, "Can't get it up...it's in a spin." About 33 seconds after the first staccato sounds, radio and radar contact with the aircraft were lost. Floating debris was found in the water in the vicinity of Clovia Intersection, but the two pilots were missing and presumed to have been killed. There were no passengers on board.

Another Learjet was following about 16 minutes behind the accident aircraft at the same altitude. In the vicinity of Clovia Intersection the pilot reported that he encountered the most severe turbulence he had ever encountered in a Learjet.

An analysis of the weather conditions in the vicinity of the accident showed an upper front or vertical discontinuity at the approximate altitude where the aircraft encountered the turbulence. This discontinuity appeared on the sounding of Bootheville, Louisiana, and Appalachicola and Tampa Bay,



Florida, the three stations nearest to the accident. Additionally, there were strong vertical and horizontal wind shears in the vicinity of the discontinuity.

It was determined that this upper front was most likely the cause of the turbulence that led to the accident. The NTSB believed that the indicators of potential CAT may have been available prior to the accident and recommended that the National Oceanic and Atmospheric Administration (NOAA):

Define the relationship between clear-air turbulence and upper fronts as analyzed by soundings and develop forecasting techniques to utilize the information to improve clear-air turbulence forecasts.

A CAT encounter by a United Airlines DC-10 over Morton, Wyoming, caused serious injuries to seven people and minor injuries to 19 others as well as causing damage to the aircraft, mostly to the interior from objects tossed about the aircraft.

A study of the weather data available showed that conditions were approaching those conducive to mountain wave development, but of several systems used to forecast the onset of a mountain wave only one would have forecast it and then only based upon the hourly data recorded about 2 minutes prior to the accident. Analysis also showed that there was a discontinuity below the tropopause with 10 kts of wind shear across it recorded at one sounding station. The conclusion was that the turbulence was caused by a combination of an incipient mountain wave and wind shear through an atmospheric discontinuity. It was also concluded that there were no known forecasting systems that would have predicted the turbulence.

There have been two accidents caused by turbulence that have been associated with strong upper level winds in the vicinity of intruding thunderstorms. These are the accidents involving a United Airlines DC-10 near Hannibal, Missouri, on April 3, 1981, and an Air Canada L-1011 about 60 miles south of Wilmington, North Carolina, over the Atlantic Ocean on November 24, 1983. In the United Airlines accident there were eight serious injuries, and in the Air Canada accident there were five serious injuries.

In both cases there were developed or developing thunderstorms in the vicinity of the jet stream, and the aircraft encountered the turbulence several miles downwind of the thunderstorm cell. The United pilot reported being in cirrus clouds, probably an anvil cloud. There have been several studies of these accidents with efforts to describe the atmospheric mechanics. Hopefully, these will lead to a better understanding of the phenomenon. In any event, the area downwind of a thunderstorm in a jet stream regime should be considered potentially turbulent. This is not a new idea. The Air Force has preached this gospel for many years and at least one airline recommends aircraft avoid thunderstorms downwind by at least one mile for every knot of wind speed at flight altitude.

As a result of its investigation of these two accidents, the NTSB recommended that NOAA:



Advise its weather forecasters to be alert for situations where there is a jet stream or strong upper level winds in association with lines of developing or developed thunderstorms which may produce an area of severe clear-air turbulence, and to issue appropriate warnings of this potential turbulence to pilots through area forecasts, SIGMET's, or other appropriate means of communication.

In spite of years of efforts, the problem is not solved and will probably never have a complete solution but improvements can be made. Instrumentation is being improved in quantum jumps and with this improvement will come better observations, a better understanding of the dynamics of turbulence, and in turn better forecasts with a better understanding of turbulence will come improved training helping pilots to recognize some turbulent situations and avoid them. This will help but will not be the total cure. The scale of some turbulence is too small for accurate forecasts. Here the answer may be on-board detectors that will give pilots a warning of turbulence ahead.

However, the problem is approached, the efforts of many scientists and engineers will be needed to help bring increased safety and comfort to those not always so-friendly skies.

TABLE 1. U.S. Civil Aviation Aircraft Accident Totals for the Time Period 1982 to 1984.

	Total accidents	Fatal accidents	Fatalities	Weather accidents	Fatal weather accidents	Weather fatalities	Turbulence accidents	Fatal turbulence accidents	Turbulence fatalities
FAR Part 121 large commercial	62	9	253	28	5	235	15	0	0
FAR Part 135 commuter and air taxi	485	96	260	154	43	106	9	5	17
FAR Part 91 general aviation	9,302	1,688	3,377	2,593	717	1,561	198	94	237

TABLE 2. U.S. Civil Aviation Weather Accident Percentages for the Time Period 1982 to 1984.

	Weather accidents, percent of all accidents	Fatal weather accidents, percent of all fatal accidents	Weather fatalities, percent of all fatalities	Turbulence accidents, percent of all accidents	Fatal turbulence accidents, percent of all fatal accidents	Turbulence fatalities, percent of all fatalities	Turbulence accidents, percent of all weather accidents	Fatal turbulence accidents, percent of all fatal weather accidents	Turbulence fatalities, percent of all weather fatalities
FAR Part 121 large commercial	45	56	93	24	0	0	54	0	0
FAR Part 135 commuter and air taxi	32	45	41	2	5	7	6	12	16
FAR part 91 general aviation	28	42	46	2	8	6	7	13	15

N87  
22343  
UNCLAS

DoD (USAF) TURBULENCE ACCIDENTS AND INCIDENTS

Douglas Miller  
USAF Inspection and Safety Center  
Norton AFB, California

This presentation is a summary of Air Force turbulence-related mishaps for the last ten years of Air Force mishaps from a perspective of where we have been, where we are now, and where we are going. In addition to accounts of major mishaps, a summary of what actions were taken to preclude future similar mishaps will be presented. Also, a discussion of some of the things being done now and being planned for the future to prevent turbulence-related mishaps will be presented.

Before presenting this summary, a short explanation of how mishaps are classified is in order. The mishaps to be discussed in detail fall into a Class A category. Class A mishaps are defined as a mishap resulting in:

1. Total cost of \$500,000 or more for injury, occupational illness, and property damage, or
2. A fatality, or permanent total disability, or
3. Destruction of, or damage beyond economical repair to, an Air Force aircraft.

The DoD as a whole uses pretty much this same system.

The definition of our Class B mishap category is a mishap resulting in:

1. Total cost of \$100,000 or more, but less than \$500,000, for injury, occupational illness, and property damage, or
2. A permanent partial disability, or
3. Hospitalization of five or more personnel.

Do not pay much attention to the Class B parameters since none of the Air Force turbulence-related mishaps fell into this category.

The definition of our Class C mishap category is a mishap resulting in:

1. Total damage which costs \$10,000 or more, but less than \$100,000
2. Any injury or occupational illness which results in a lost workday case involving days away from work (i.e., 8 hours or greater), or
3. A mishap which does not meet the criteria above, but which Chapters 5 through 9 require reporting.

Until January 1, 1986, the dollar limits for Class C damage ranged from \$1000 to \$100,000 (the Air Force just recently raised the lower limit to \$10,000).

To give a perspective on the size of flight operations during this study, in 1985 the Air Force has possessed 9,927 active aircraft and flew 3,488,000 flight hours since 1976.

Table 1 shows the total numbers of Classes A, B, and C mishaps we have experienced in the last ten years as well as the number of turbulence-related mishaps which we have experienced by mishap category. From a statistical point of view, a very small percentage of our mishaps are turbulence related. However, as shown in Table 2, there is a problem that the Air Force has taken seriously from actions taken in our Air Force turbulence-related Class A mishaps.

TABLE 1. Total Air Force Class A, B, and C Mishaps and Turbulence-Related Mishaps from 1976 to 1985.

<u>CLASS A</u>	<u>CLASS B</u>	<u>CLASS C</u>
782	931	36,729
TURBULENCE RELATED:		
<u>CLASS A</u>	<u>CLASS B</u>	<u>CLASS C</u>
5	0	17

The first turbulence-related Class A mishap in my study occurred when one of our transport aircraft flew into or near a thunderstorm. The aircraft had departed home base with weather radar problems. The radar set was repaired prior to departure but failed again during the flight. Arriving near their destination, they found that there was significant weather between their position and their destination base. Civil air traffic control (ATC) advised them of a temporary radar failure, and that there was pretty solid cover between them and their destination. Ironically, military radar was tracking them and the Air Force possesses radar pictures of the weather conditions and aircraft for this flight. The controller stated, "There's no way I can get you around it." The aircrew indicated that they were in visual meteorological conditions (VMC) and would visually circumnavigate the thunderstorms. Two minutes later, the aircraft failed to respond to a transponder change. The aircraft broke apart in flight, went out of control, and crashed. Crew members and passengers perished in the crash. The aircraft had flown close to thunderstorm cells and, as a result, encountered extreme turbulence which failed the #4 pylon and right wing.

A lot of action was generated by this mishap. For example, the weather radar which had been experiencing a lot of reliability and maintainability problems was replaced with a much better and more reliable system. The Air Force came out with much more specific guidance on thunderstorm avoidance in our basic flight rules. Finally, there was a call for increased research in the area of severe weather avoidance.

A Multiagency Conference on Severe Convective Storms and Their Hazards to Aviation was held on February 16 and 17, 1977. A number of agencies were represented at this conference: National Weather Service, Environmental Research Labs, National Severe Storms Lab, National Severe Storms Forecast Center, FAA, NTSB, NASA, Lockheed, University of Chicago, and Air Force Inspection and Safety Center.

Some of the recommendations that came out of the conference are given in Table 3. With regards to the first recommendation, a number of studies have been conducted on thunderstorms by the National Severe Storms Lab and other agencies. For the second, the Air Force has acquired films on thunderstorm avoidance and other training aids. The third recommendation was covered in our corrective action. The fourth, a test program was established to see if full-time weather expertise would be useful at Kansas City Air Route Traffic Control Center. Flight simulation techniques have been developed for low-level wind shear and are used in Air Force cargo aircraft flight simulator programs. The last recommendation was covered in our corrective action.

The second major mishap occurred when a trainer aircraft penetrated a thunderstorm at high altitude. The mishap pilot accepted a routing from air traffic control which had more severe weather than what had been forecast for this flight planned route. When the pilot entered significant weather, he reported it to ATC. The controller offered the pilot a 180° turn as there were cells in all quadrants. The pilot received clearance to climb (even though the aircraft was already out of its engine operating envelope). At flight level 464, still in the cell, both engines flamed out. The aircraft traveled 5.4 nautical miles from its last radar painted position to its point of impact in 2 minutes 9 seconds. It was hypothesized that severe turbulence within the storm contributed to spatial disorientation and a delayed decision to eject. The aircraft did not have an on-board weather radar. The mishap pilot had significant flight experience, including being a graduate of Air Force Test Pilot School, but let his good judgment get side-tracked by intense motivation to get to his destination. There were no weather-related corrective actions taken as a result of this mishap.

Our third Class A mishap occurred in 1985 when a forward air controller (FAC) aircraft, encountered turbulence and downdrafts associated with a mountain wave phenomena. Mountain wave had not been forecast prior to the mishap flight. A pilot report of severe turbulence was issued by a helicopter after the mishap aircraft was airborne, but the information was not relayed to the mishap pilot. It was determined that the mishap aircraft got into an area of downdrafts which exceeded the aircraft's capability to climb to avoid terrain. Search for the crash site was hampered by severe turbulence in the area.



As a result of this mishap, a warning was put in the aircraft flight manual that in even moderate turbulence vertical gust velocities could exceed the aircraft's climb capabilities.

Less than two months later, another FAC aircraft was lost when it penetrated severe weather as it attempted to return to base during a weather recall. The mishap pilot whose visual routes of escape had been closed off by weather moving in from all directions decided to climb to 5,000 feet in instrument meteorological conditions (IMC) so that he could be radar vectored around the severe weather. During his IMC climb, he encountered a severe updraft which he interpreted as an attitude indicator failure. He then made a right descending turn to get back into visual (VMC) conditions. The mishap pilot then failed to reduce his high-power setting and the aircraft entered a nose-low, high-speed descent. The left wing failed at approximately 2,500 feet AGL due to high speed and turbulence. The aircraft entered a left uncontrollable roll and was completely destroyed on impact, fatally injuring the pilot.

Actions and suggestions coming from this mishap were similar to those of the other FAC aircraft mishaps. A warning regarding the dangers of flying low to medium performance aircraft in the vicinity of severe updrafts or downdrafts were recommended for Air Force Manual 51-12, "Weather for Aircrew," as well as a similar warning for the aircraft flight manual.

Finally, in our last turbulence-related mishap a transport aircraft was performing a medical evacuation mission into a remote site. Crosswinds on this approach were high requiring occasional full use of cross controls. A turbulent downdraft destabilized the aircraft a quarter mile from the runway. As this was a one-way site, one that requires that you fly your approach in one direction and your departure in the opposite direction--due to rising terrain in three quadrants--and they were already past the commit point (the point past which go-around is improbable), the pilot was committed to land. The aircraft touched down in a left drift and continued to drift left until it departed the runway. The aircraft sustained significant damage. There were no weather-related corrective actions taken as a result of this mishap. This concludes the look at our Class A turbulence-related mishaps.

Table 4 summarizes the last ten years of Class C turbulence-related mishaps. A Class C mishap is any damage that is between \$1000 and \$100,000. I will not go into detail on these mishaps unless someone has a particular question. Copies of our Class C investigations are not retained except for a brief narrative summary which is put into our computer. If the summary mentioned that turbulence was forecast, this was noted as a yes or no; if it was not mentioned, unknown (UNK) was noted. Also, if the airspeeds and altitudes at which the turbulence was encountered were contained in the summary, this is noted on the charts.

In reviewing the Class C mishaps, two major trends were noticed. First, that most of these mishaps occurred in large aircraft and second that most turbulence-related injuries were sustained by unrestrained occupants. In talking with fighter aircraft action officers (by the way, I am the C-130 action officer), their comment was that high-performance aircraft are not



usually adversely affected by turbulence. Fighter aircraft are built for high "G" loading, and when they do hit turbulence, crew members are always well restrained.

I believe the reason we have a very good record in the area of turbulence-related mishaps is that our aircrews maintain a high level of awareness of severe weather. It is a frequent topic in our safety magazines, it is covered in pilot training, annual instrument refresher training, and aircrew briefings from our Air Weather Service people. Another factor is that good weather forecasting keeps us away from severe weather and turbulence.

Some areas where I see improvement for the future in turbulence avoidance includes better aircraft and ground-based weather radar. NEXRAD, which should come on line in the early 1990's, will have a turbulence algorithm. For improved forecasting, the Air Weather Service has recently completed a geophysical requirement for future turbulence research (defining Air Force and Army future forecasting needs). It is presently under review at Air Force Geophysics Labs. Dr. Dale Meyer from Air Weather Service, who was at this conference, is involved in this effort and has told me that he would be glad to give any of you who are interested in this geophysical requirement an overview of the project.

**QUESTION:** Dave O'Keefe (Lockheed). I noticed in your Class C you had an F105 where the vertical stabilizer broke apart or suffered damage due to turbulence. Was there any indication that there was a fatigue problem or there were corrosion problems? Were there any investigations as to why that stabilizer broke apart?

**ANSWER:** No, we do not retain copies of our Class C investigations. All I had to go on was a computer short summary. There were no indications at all of structural fatigue. The F105 is an old airplane, but it seems that if there had been indications, they would have been mentioned in our findings and they weren't.

**QUESTION:** Capt. Ed Harrison (The Pentagon). As the C130 action officer you should be well equipped to answer this one. I noticed the Air Force uses C130's for hurricane and typhoon reconnaissance. I was just curious as to their weather-related safety record. They are flying directly into the jaws of danger. Do they have a significant experience with turbulence-related incidents?

**ANSWER:** That is a good question. I know of one C130 mishap of a weather C130 flying into a typhoon in the Pacific in 1974. They never found the airplane so they were never able to determine what exactly caused the failure of the aircraft.

**QUESTION:** Mike Tomlinson (Air Weather Service). In your listing of the factors that you think are involved in a relatively good safety record, a factor that I didn't see that I think should be there is the need for pretty tight operational rules that specify when certain levels of turbulence are forecast. Do you think that is a significant factor, and because you're not

out there when the forecast calls for severe turbulence, are you less likely to be exposed to those conditions and have resulting accidents?

**ANSWER:** Yes, you are. I guess I did fail to mention that as a result of that 1976 C141 accident, they did come up with very specific guidance on thunderstorm avoidance. And that has, unfortunately, been relaxed since that time. For a while the Air Force as a whole had a regulation telling you how far you had to stay away from thunderstorms. You had to be 20 miles downwind or 10 miles upwind, I don't remember the exact parameters. After that, the fighter community wanted different limitations. That parameter still exists in military airlift command supplement to 60-16, the general flight rules, but it is not in the Air Force regulation itself. But you're right. It is very true that we do have a lot of operating restrictions that keep us out of severe weather.

**COMMENT:** Dale Meyer (HQ Air Weather Service). As was pointed out, I will be glad to discuss our perspective of Air Force and Army requirements.

**QUESTION:** George Treviño (Michigan Tech). Will photocopies of all these slides and presentations be made available to the participants?

**ANSWER:** To answer your question on my briefing in particular, there are parts of it in which I went into specifics, such as places and types of aircraft, and they are "For Official Use Only." What I'm going to do is give to the workshop organization all of my briefing which is not restricted and present a summary that won't name the specific aircraft.

**QUESTION:** Al Bedard (NOAA). You have a criteria for classifying the strength of turbulence which I believe dealt with the G forces, if I read that slide correctly. Is that widely accepted by the defense community or is that your own internal classification?

**ANSWER:** That is something I think AWS would be better at answering. I think Dr. Meyer can probably answer that better than I can.

**ANSWER:** Dale Meyer (HQ Air Weather Service). We do have a procedure that was developed by the Air Force Wright Aeronautical Laboratories in 1981 that uses gust loading to classify all Air Force aircraft into four categories. We use that information operationally in tailoring our forecasts and interpreting PIREPS. I don't have the details with me but I have access to them.

TABLE 2. Air Force Turbulence-Related Class A Mishaps.

---

TRANSPORT AIRCRAFT IN-FLIGHT BREAKUP; NEAR THUNDERSTORM
TRAINER AIRCRAFT CONTROL LOSS; IN THUNDERSTORM
FORWARD AIR CONTROLLER (FAC) COLLISION WITH THE GROUND DURING MOUNTAIN WAVE ENCOUNTER
FAC AIRCRAFT IN-FLIGHT BREAKUP IN THUNDERSTORM UPDRAFTS AND TURBULENCE
TRANSPORT AIRCRAFT RUNWAY DEPARTURE AFTER APPROACH DESTABILIZED BY TURBULENT DOWNDRAFT

---

TABLE 3. Multiagency Conference on Severe Convective Storms and Their Hazards to Aviation.

---

RECOMMENDATIONS

- THE NEED FOR BASIC RESEARCH INTO THE LOCATION, DURATION, AND INTENSITY OF TURBULENCE IN THE VICINITY OF THUNDERSTORMS
  - NEW AIRCREW TRAINING AIDS
  - BETTER GROUND-BASED AND AIRBORNE-WEATHER RADAR
  - ASSIGNING FULL-TIME WEATHER EXPERTISE IN THE AIR TRAFFIC CONTROL SYSTEM
  - DEVELOP FLIGHT SIMULATION TECHNIQUES WITH REGARD TO LOW-LEVEL WIND SHEAR
  - REVIEW AND STRENGTHEN REGULATIONS AND CRITERIA WITH REGARD TO PENETRATING HAZARDOUS WEATHER
-

TABLE 4. Class C Turbulence-Related Mishaps.

	<u>WAS TURBULENCE FORECAST</u>	<u>ALTITUDE/AIRSPEED</u>	<u>DAMAGE</u>
<u>1976</u>			
T-39A	NO	FL410/220 KIAS	ENGINE FLAMEOUT
EC-135J	UNK	FL310	CAT CAUSES OSCILLATIONS/FAILURE OF TRAILING WIRE ANTENNA
<u>1977</u>			
C-130B	UNK	FL110	CHAIN BOX LATCHES FAIL WHEN A/C ENCOUNTERS SEVERE TURBULENCE IN CLOUD
B-52G	YES/MOD	HIGH ALT/300 KIAS	SEVERE TURB THROWS CREW VIOLENTLY ABOUT
T-38A	UNK	FL210/300 KIAS	DAMAGE TO LEADING EDGES OF BOTH WINGS AND VERT STABILIZER WHEN AIRCRAFT ENTERED AREA OF HEAVY RAIN AND MODERATE TO SEVERE TURBULENCE
<u>1978</u>			
B-52G	YES	TRAFFIC PATTERN/	DAMAGE TO FLAPS WHEN A/C ENCOUNTERED MODERATE TURBULENCE IN RAINSHOWERS
<u>1979</u>			
C-130H	NO	LOW ALT	LOADMASTER BREAKS LEG WHEN A/C ENCOUNTERS SEVERE CAT
B-52H	YES	UNK	MODERATE TURBULENCE CAUSED DAMAGE TO BOMB DOORS, WHILE OPEN
EC-135H	UNK	FL330	TRAILING WIRE ANTENNA SEPARATES DUE TO CAT
<u>1980</u>			
C-130A	UNK	1000 AGL/125 KIAS	LOADMASTER BREAKS WRIST WHEN A/C ENCOUNTERS CAT
C-130B	NO	UNKNOWN	CREW CHIEF INJURES BACK WHEN A/C ENCOUNTERS MODERATE CAT
<u>1981</u>			
C-130A	UNK	FL180/240 KIAS	TWO CREWMEMBERS INJURED WHEN A/C ENCOUNTERS A SEVERE DOWNDRAFT

TABLE 4. (concluded).

	<u>WAS TURBULENCE FORECAST</u>	<u>ALTITUDE/AIRSPEED</u>	<u>DAMAGE</u>
<u>1981</u>			
F-105D	UNK	1000 FT AGL/ 500 KIAS	PART OF VERTICAL STABILIZER LOST WHEN A/C ENCOUNTERED SEVERE TURBULENCE EN ROUTE TO RANGE
C-130H	NO	FL160	TWO CREWMEMBERS INJURED WHEN A/C ENCOUNTERS ABRUPT SEVERE CAT
<u>1982</u>			
KC-135	YES	3000 MSL	PASSENGER INJURED WHEN A/C ENTERS AREA OF HEAVY WEATHER AND SEVERE TURBULENCE
<u>1985</u>			
KC-135A	UNK	FL220	A/C SUSTAINS CRACKS IN ALL FORWARD ENGINE MOUNTS WHEN A/C ENCOUNTERS SEVERE TURBU- LENCE
C-130B	YES	LOW LEVEL	FIVE AIRCREW SUSTAIN INJURIES WHEN A/C ENCOUNTERS MOUNTAIN WAVE

N87  
22344  
UNCLAS



NEW GENERATION AIRCRAFT DESIGN PROBLEMS RELATIVE TO  
TURBULENCE STABILITY, AEROELASTIC LOADS,  
AND GUST ALLEVIATION

Richard M. Heimbaugh  
Douglas Aircraft Co.  
Long Beach, California

Figure 1 schematically illustrates past history, present status, and future of discrete gusts. Etkin [1] notes that the actual first discrete gust analysis was done in 1915 [2] where the equations and physical concepts related to gust response were derived. In the early 1930's the idea of using an aircraft as a measuring device based on a sharp-edged gust formula was initiated [3]. In the 1930's and 1940's, discrete gust data were collected and analyzed [4]. The present widely used mass parameter gust formula was published in the 1954 timeframe and subsequently resulted in the CAR-4B requirement for gusts [5]. Later the British introduced the idea of tuning a one minus cosine (1-cos) gust [6].

Figure 2 schematically illustrates a secondary line of development. In the early 1930's efforts were started to investigate the idea of gust gradients, and the importance of gradients was recognized. In fact, during this era, a dimensional analysis study showed that gust intensities are related to the cube root of the wavelength [7]. More recently, in the late 1960's, there was a probability analysis which showed that gust gradients and intensities are related and that the cube root type law is valid [8]. Finally, there was a survey that investigated the derived gust velocities of modern jet airplanes [9].

Figures 2 and 3 show there are basically two approaches to the gust analysis: discrete and spectral density. The roles of these two approaches to gust analyses will be discussed later in this presentation. In the early 1930's, von Karman derived the present spectral density characterization of the atmosphere [10], and the idea of using PSD (power spectral density) methods applied to gust analysis was introduced in the early 50's [11]. Again, a period of collecting and analyzing data and refining the approach followed in the 50's and 60's. The result was the FAA Report No. ADS-53 in 1966, which was the first serious attempt at trying to come up with a design criteria for sizing airplane structure based on the PSD gust [12]. Subsequently in 1980, the FAA Appendix G was introduced which requires PSD gust analysis [13]. Some other significant milestones are shown at the bottom of Figure 3. In a paper by Firebaugh [14] an analysis of data was presented which illustrated different conclusions in terms of what some of the gust parameters should be. Also, in the early 1970's the government (DoD) issued a MIL-008861A requirement for PSD type analysis [15].

The present discrete criteria (Figure 4) used by the FAA is based on the mass parameter gust derived in the 1950's [12]. It is a 1-degree-of-freedom analysis which is based on the airplane flying through an idealized 1-cosine gust that is 25 mean aerodynamic chords long. That type of analysis does not



lend itself to a close-loop method such as would be done for gust alleviating systems or even if it were desired to analyze the effect of SCAS (Stability Control Augmentation System) systems. The criteria specifies design gust velocities based on the data derived in the 1930's and 1940's and, therefore, does not reflect the experience of modern aircraft.

The problem with discrete gust analysis is that it does not really address the question of gradients. Realistic gust gradients are needed if it is desired to evaluate the effects of short-period and dutch roll stability and how the stability of the airplane relates to the airplane response in gust (see Figure 5). Realistic gradients are needed to evaluate the effect of gusts in exciting vibration modes. Finally, realistic gradients are also needed for evaluating close-loop systems or load-alleviating systems. The steeper the gradients through which the airplane flies, the harder it is to design load-alleviating systems that are effective. So, to get a good prediction or analysis, you need to have realistic gradients; that is the main problem with the discrete gust formula.

As shown in Figure 6, the British recognized [6] some of the problems summarized in Figure 5, and in the early 1960's came up with this idea of tuning. In Reference 6 it was stated that realistically the airplane not only plunges but also pitches and it is also known that vibration modes can be excited. The British indicated that these types of parameters should be included in the analysis. At that time, they did not know what the gradients of the gust should be; thus, they required a survey of all possible gradients. Effectively, they were saying that all gradients are equally likely and it is necessary to tune an airplane to find the worst one. The design gust levels, however, were the same design gust velocities that were used by the mass parameter formula and the criteria as originally stated only mentions vertical gust; for some reason no mention of lateral gust was made. The wording of the criteria along with some additional information suggests that the British believe that the main driver in terms of determining the structural gust load should be the discrete gust. The PSD gust is considered secondary and they require it but only as a guide.

Again, the problem is that you do not have realistic gradients. There has been an analysis [10] which indicates that the gradients are, in fact, dependent on the gust intensity and the larger the gust intensity the smaller the gradients as shown in Figure 7. Another problem is that the design gust velocities were not recalibrated to reflect the significant changes in the analysis that the British required. They proposed [8] the original design velocities that were derived based on a simple mass formula parameter, which did not account for vibration modes and pitching of the airplane; they then applied those velocities to the new analysis. An additional problem is that the criteria need to be recalibrated based on the new analysis method.

In terms of the PSD gust, the basic criteria are based on the von Karman spectra which are defined in Figure 8. In this figure,  $L$  is the scale of turbulence and  $\Omega$  refers to spatial frequency in radians per foot. If the airplane is flying through the turbulence at a particular speed, it can be related to a spectrum defined relative to frequency in Hz. The analysis is a linear one in which the gust varies only in a streamwise direction. The

design parameters were developed with a somewhat different philosophy than was used for the discrete gusts. Discrete gust velocities were based on a probability approach where some level of turbulence was chosen such that an encounter was experienced every so many million miles as a basis for the design velocities. The PSD criteria were backed out based on the philosophy of providing equivalent strength to successful airplanes flying in the 1960's. Finally, the present criteria are also characterized by the fact that the various certifying agencies specify different parameters for many of the design parameters. The basic approach is the same but different agencies vary some of the details. Some of these details are significant.

In Figure 9, the PSD analyses are illustrated by two approaches: (1) a mission approach and (2) a design envelope approach. The mission approach seeks to represent the operational characteristics of the airplane in terms of how it is flown, what altitudes and speeds it is flown, what payloads, fuel loadings, and so forth. The design envelope approach is similar to the way other types of loads are computed in that you specify extreme conditions in terms of flying at speeds and altitudes that correspond to the limits of the flight envelope, investigating extreme payloads and fuel loadings, etc. There are various schools of thought within the community in terms of which approach is most desirable, and, in fact, there is a reluctance to really rely on any single approach. The feeling being perhaps that no single approach completely addresses all of the problems related to gust analysis. Presently, both approaches are used. One agency, the military, requires a mission approach; the FAA, however, allows only the use of a design envelope approach.

Presently, there is a question of whether to use discrete or PSD analysis to determine gust design loads. An illustration of these two is presented in Figure 10. The British tend to feel that discrete analysis should be the main thrust. However, the original ADS-53, perhaps reflecting a prejudice in the people who worked on it, indicated that PSD analysis should be the primary means for determining design gust loads [12]. Presently, there is not a specific detailed criteria in terms of how to certify active load-alleviating systems; however, there is an Advisory Circular that is very specific.

Presently, particularly with the FAA [13], both discrete and PSD analyses are required (Figure 11). The discrete mass parameter gust analysis by itself is not adequate since it does not account for dynamic effects. The shaded areas of Figure 11 indicate the parts of the airplane that are likely to be sensitive to dynamic effects. The engine pylons and perhaps wing tips are sensitive to exciting vibration modes which are not predicted by the mass parameter method. The tail is sensitive to dutch roll stability, which again is not accounted for in the mass parameter formula. Finally, the PSD approach has important applications in terms of supporting fatigue and damage tolerance analysis.

The PSD approach is basically a linear approach for analyzing active systems. The problem with approach is how to represent nonlinearities. Figure 12 indicates that you have a control system command and an actual control surface motion which are not necessarily linearly related to the command. An important parameter in PSD mission analysis is the zero crossing

of the mean ( $N_0$ ). The calculation of  $N_0$  involves calculating the spectra of the rate of change of acceleration. A dot indicates a derivative of acceleration. With the streamwise gust model that we have today, the integral of the acceleration rate does not converge. You can get any value you want for  $N_0$  depending on what you choose for the limits of integration.

As mentioned earlier, the vertical tail is particularly sensitive to dutch roll stability (see Figure 13). Modern transports generally have low dutch roll damping and as the damping approaches zero the PSD analysis will predict higher and higher loads on the vertical tail because the analysis assumes resonance at each solution frequency. Therefore, very large vertical tail loads are possible if you have a very low damped dutch roll mode and further assume no pilot interaction in terms of artificially supplying damping and also assume no yaw damper control system.

Historically, as shown in Figure 14, most of the data and criteria is based on using the airplane as a measuring device. The early discrete gust criteria is based on obtaining VG data recorded while flying through turbulence and analyzing that data by using the discrete gust formula. Based on that analysis, deducing what must be the gust velocities that the airplane experienced can be obtained. Then based on that data, coming up with a criteria in terms of design gust values that envelope all the experience or at least the likely experience is possible. The significance here is if it is desired to go the reverse way and re-create extreme acceleration data from the criteria and to change the analysis, it is not possible to get back the original acceleration data. The point to be made is that the criteria and the analysis are tied together and you really should not modify one without modifying the other. The same principle applies for the PSD approach where you are flying through random turbulence. The criteria is derived based on backing out the required design parameters such that the PSD analysis will predict loads consistent with the known strength of successful airplanes. Assume you wish to go the reverse direction using existing criteria but to do something to improve the analysis, if you were to analyze the original airplanes that the criteria was based on, different conclusions would be obtained. One might conclude that the reference airplanes were under-strength or over-strength. Thus, the need to relate the criteria and the analysis is realized. If there is some significant improvement to be made in the analysis, that improvement needs to be related to the criteria.

The basic goal of the criteria is to successfully extrapolate the experience of past airplanes. Illustrated in Figure 15 are old airplanes that are considered to be satisfactory from the structural point of view, are economically viable, and now you have some new airplane which needs to have the same characteristics. The new airplane should be structurally safe and economically viable. The analysis and the criteria primarily are ways of extrapolating the successful experience of old airplanes to new airplanes. The important question is how well the analysis and criteria predict the relative characteristics between the old and new so that significant changes are accounted for in the new design relative to the old design.

Generally, the criteria need to be integrated with modern analysis (Figure 16). Modern analysis refers to a method that accounts for dutch roll



and short-period stability, and vibration modes along with the need to define realistic gust gradients. If those changes are made, then the design criteria should be reviewed in terms of what should be the design gust levels and also perhaps incorporate any experience we have with modern aircraft along with historic data from the 1930's and 1940's.

The main message is the need for standardization of approach and consensus in terms of what the approach should be (Figure 17). Some think PSD by itself is sufficient for determining design gust loads. There are other schools of thought that suggest if you have a realistic discrete gust approach, you do not need PSD gust for determining design loads. Is there something unique that the PSD gust analysis offers that is not part of the discrete gust analysis? Variations in the way mission and design envelope approaches to PSD gust are treated in criteria should be resolved.

There are various data, proposals, and interpretations of data in terms of how the scale of turbulence varies with altitude (Figure 18). Another question concerns the calculation of the zero crossing count, which is important in the mission analysis. As discussed earlier, the integral of the acceleration rate spectra does not converge; thus, we need to have a criteria that defines what the cutoff frequency is so that everyone is consistent. Another issue which is left up to the individual is whether one should analyze vertical gusts and lateral gusts independently or whether they should be combined.

Should there be some minimum standards concerning mission segments when the mission PSD approach is used (Figure 19)? In the extreme case you could define the mission as a single segment altitude, speed, and weight configuration. Or you could have many segments. Is there some minimum standards that could be imposed? Since the structures and controls disciplines are separate, there tends to evolve a separate description of the atmosphere that is used by controls engineers in terms of how they evaluate control system performance in turbulence versus the criteria the structural engineer uses in sizing the structure.

Shown on the top of Figure 20 is the formula that is used in the mission analysis for computing the crossings with positive slope of any load level  $L$ . As shown, it is a function of the  $N_0$  mentioned earlier.  $P_1$  and  $P_2$  are the proportion of time in storm and non-storm turbulence, and  $b_1$  and  $b_2$  relate to the intensity of the storm and non-storm turbulence. If you change values for the scale of turbulence or cutoff frequency, the  $P$ 's and  $b$ 's should be recalibrated. This is true because the  $P$ 's and  $b$ 's were backed out to match flight experience, so the analysis and data are related. If the  $P$ 's and  $b$ 's are changed, you could conceivably come up with a different exceedance curve as indicated by the solid and dashed lines. The philosophy in the past has been to set the design crossing level ( $N_{DL}$ ) to be consistent with known levels of limit load. The limit load is a known number that corresponds to the known strength of a previous airplane that has been successful. Now what would happen if you change the analysis to reflect a different exceedance curve? You should back out a different  $N_{DL}$  as opposed to saying that the crossing exceedance relationship is different and therefore the design load level is now  $x$  percent bigger.

Relative to future airplanes that are going to be flying at higher altitudes than present aircraft: Probably we need to think about what should be the gust criteria at altitudes above 50,000 feet (Figure 21). The other question relates to the streamwise gust model. A lot of information indicates that at least at low altitudes the scale of turbulence is relatively small so that three-dimensional effects may be important at low altitudes.  $b/L$  is the span to scale of turbulence rates. There is perhaps some value for that parameter where you could say that three-dimensional effects are important and other values where three-dimensional effects can be neglected.

#### References

1. Etkin, B.: Turbulent Wind and Its Effect on Flight. *Journal of Aircraft*, 18(5), May 1981.
2. Wilson, E. B.: Theory of an Airplane Encountering Gusts. NACA Report 1, Part 2, 1915.
3. Rhode, R.; and Lundquist, E.: Preliminary Study of Applied Load Factors in Bumpy Air. NACA TN 374, 1931.
4. Pratt, K. G.; and Walker, W. G.: A Revised Gust-Load Formula and a Re-Evaluation V-G Data taken on Civil Transport Airplanes from 1933 to 1950. NACA Report 1206, 1954.
5. Civil Air Regulations, Civil Aeronautic Manual 4b, Transport Categories Amendment 4b-3, adopted Feb. 7, 1956.
6. British Civil Airworthiness Requirements Appendix to Chapter D3-3-Gust Loads, revised Dec. 1, 1964.
7. Rhode, R.: Gust Loads on Airplanes. *SAE Journal*, 40(3), Mar. 1937.
8. Jones, J. G.: A Theory for Extreme Gust Loads on an Aircraft Based on the Representation of the Atmosphere as a Self-Similar Intermittent Random Process. RAE Technical Report 68030, 1968.
9. Zalovcik, J. A.; Jewel, J. W., Jr.; and Morris, G. J.: Comparison of VGH Data from Wide-Body and Narrow-Body Long-Haul Turbine-Powered Transports. NASA TN-D-8481, 1977.
10. von Karman, T.: The Fundamentals of the Statistical Theory of Turbulence. *Journal of Aeronautical Science*, (4):131-138, 1937.
11. Liepmann, H. W.: On the Application of Statistical Concepts to the Buffetting Problem. *Journal of Aeronautical Sciences*, 19(12), 1952.
12. Hoblit, F. M.; et al.: Development of a Power Spectral Gust Design Procedure for Civil Aircraft. Technical Report FAA-ADS-53, Jan. 1966.
13. Federal Airworthiness Regulations, Part 25, Appendix G, added 1980.

14. Firebaugh, J. M.: Evaluations of a Spectral Gust Model Using VGH and V-G Flight Data. *Journal of Aircraft*, 4(6), 1967.
15. Military Specification MIL-A-008861A. Airplane Strength and Rigidity Flight Loads, revised Mar. 1971.

QUESTION: Warren Campbell (BDM Corporation). One thing that you didn't address was what importance you place on the shape of your probability density distributions. I noticed that when you showed that exceedance curve, part of that exceedance curve was based on the assumption of the Gaussian distribution.

ANSWER: That is true.

CAMPBELL: Do you have any feel for the importance of probability distributions?

ANSWER: I guess I don't. As long as the distribution which, in turn, relates to that exceedance curve is a tool to back out the design values not an end in itself, I don't think it is terribly important but I don't really know.

CAMPBELL: One other question. When you design an aircraft, pardon my ignorance, do you consider fatigue in the PSD part.

ANSWER: Yes.

QUESTION: Bob Heffley (Manudyne Systems). From the standpoint of the designer, can you comment on how the pilot in the loop needs to be accounted for and what the implications are on the analysis methods that you describe, i.e., for both the discrete gust and power spectral density.

ANSWER: I guess in terms of the pilot the implications center on how he would respond to turbulence and how he would interact with it. Presently, the analysis generally doesn't account for that. You either do an open loop analysis in which you assume the pilot has no interaction at all or a closed loop analysis which again assumes the pilot isn't doing anything but the active system is doing all the feedback. I know in the controls area there are various pilot models that attempt to simulate delays and gains to represent the pilot as if he were a control law. I am not sure if there is a universal agreement as to what is a good pilot model. I guess it could be included if it could be represented as a control law, but right now they're not.

QUESTION: John Houbolt (NASA Langley). Richard, that was a nice rundown. I'd like to make this observation though. I wish I had a half hour to get up and give a follow-up talk to what you just said and place a lot of your notions in a little bit different context and from a little bit different perspective. There are a number of things that could be slanted differently than what you have done there. Let me just mention two of them. One of them is the power spectral density approach. You can do everything with that that you can do with the discrete gust approach but more and in a much rational

way. So you can cover everything that the discrete gust approach has in it automatically in the power spectral density approach. And now the second thing I'd like to comment on is your comments on  $N_0$ , the zero crossing problem. If you do it right there is no problem getting  $N_0$  correctly. It will converge very nicely and very rapidly. The reason I mention this is that this is one of the problems that we have at a conference of this sort. It's a heck of a time to disseminate certain pieces of information. Ten years ago I told people how to calculate  $N_0$  in a proper way. That still hasn't gotten around the community and there is a reason for that. There is probably only one person in this audience, namely you, that is familiar with the  $N_0$  problem and it is a difficult problem of getting this information around to the various people, because there is very little interest in it, but indeed if you do it properly, there is no problem whatsoever in calculating  $N_0$ . I think the sort of thing we need to take up in this conference is how do we get some of this information out of the group in a better way than we have presently been doing. This is an observation, not a question.

**QUESTION:** Jack Ehernberger (NASA Ames). Can you amplify briefly on your comment for a future requirement of more data characteristics above 50,000. Is that related to a specific inadequacy of previous data sets or some new unique design concepts?

**ANSWER:** Yes, I would think in terms of the discrete gust, the design gust velocities are functions of altitude and, as I remember, the discrete gust is only defined in military and civil regulations up to 50,000 feet. At the cruise speed, it is 50 ft/sec, up to 20,000 feet, and then it linearly reduces to some value at 50,000 feet. I'm raising the question that above 50,000 feet what do you do? Should structural analysts continue to allow it to linearly reduce to zero or assume a different function? I was thinking of what I had seen in the news about some of these hypersonic airplanes that are going to be flying at the edge of the atmosphere.



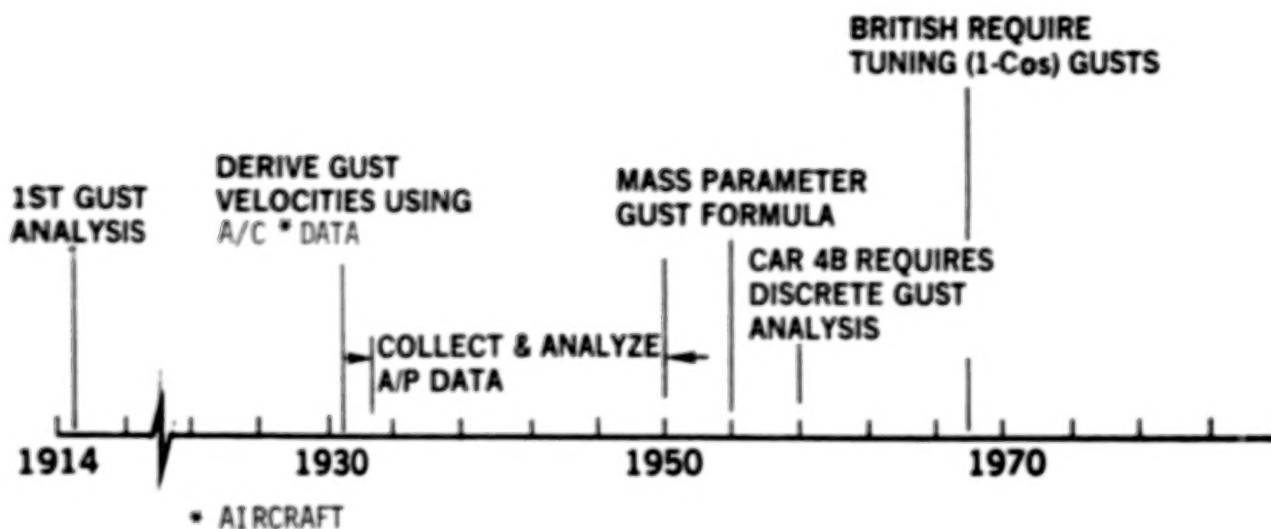


Figure 1. Development history of discrete-type gust description.

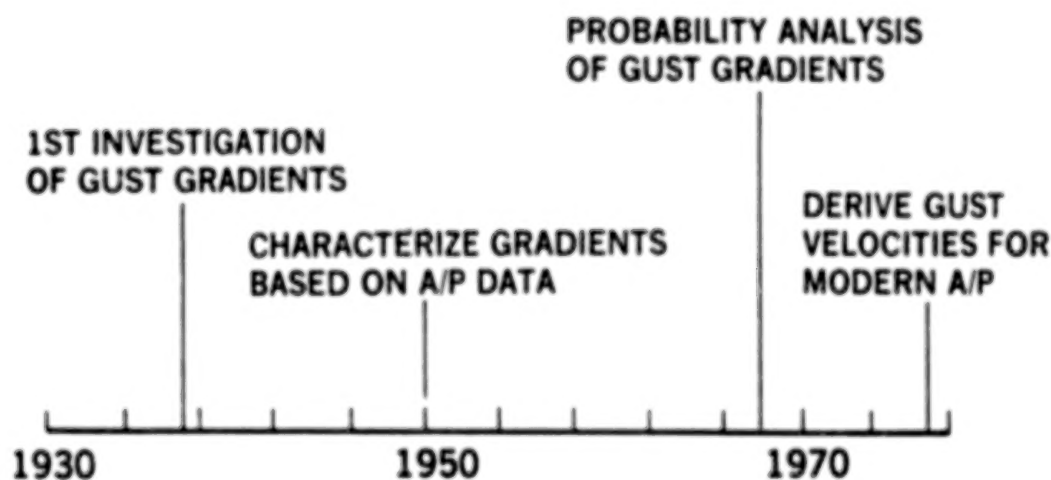


Figure 2. Time frame for gust gradient analysis development.

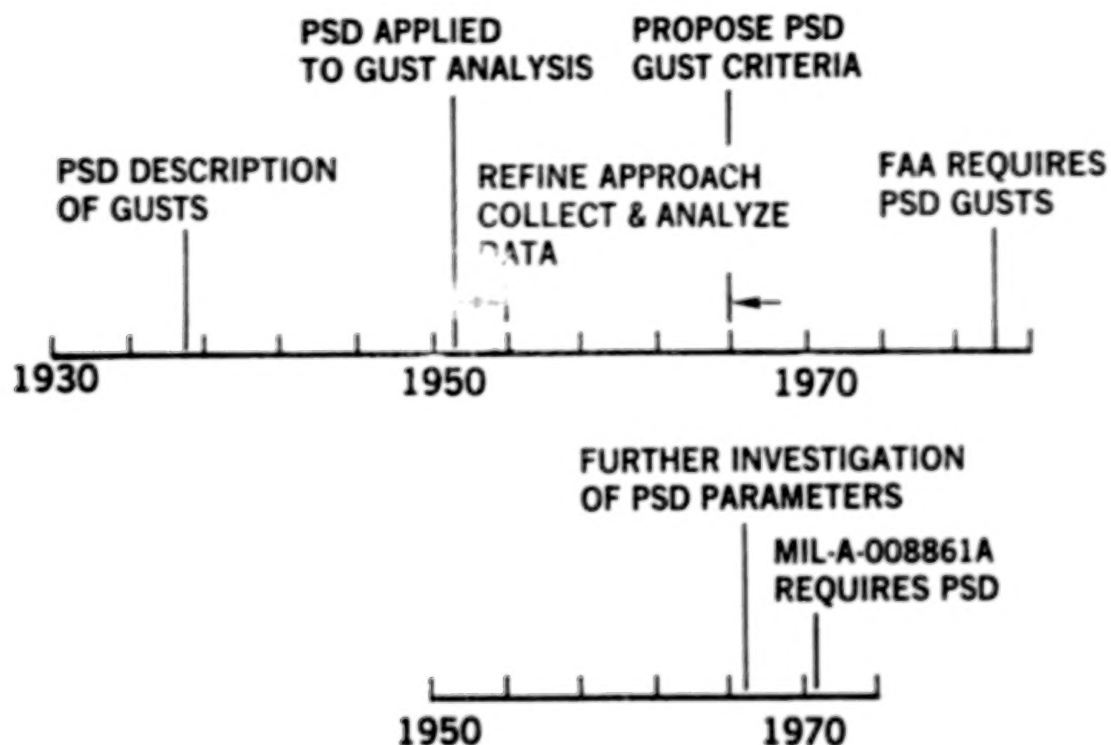
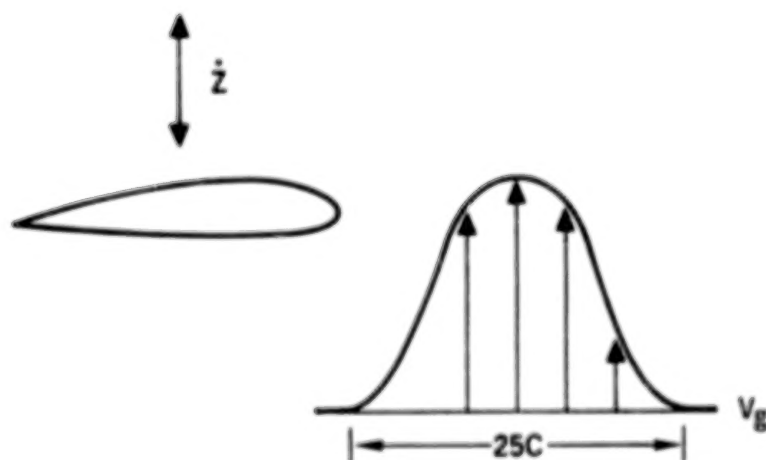


Figure 3. PSD gust history.



- BASED ON 1 DOF ANALYSIS
- BASED ON METHODOLOGY AND DATA 30-50 YEARS OLD
- DOES NOT PERMIT CLOSED-LOOP ANALYSIS
- DOES NOT REFLECT MODERN AIRCRAFT

Figure 4. Discrete gust--present criteria.

## REALISTIC GUST GRADIENTS

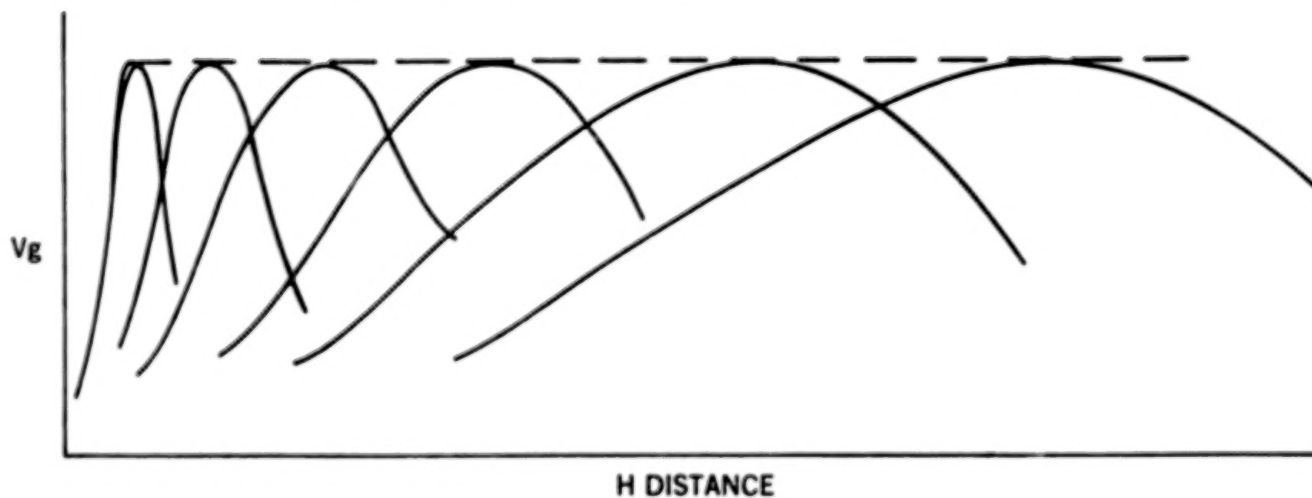
NEEDED TO EVALUATE A/P STABILITY

NEEDED TO EVALUATE VIBRATION MODES

NEEDED TO EVALUATE GLA SYSTEMS

Figure 5. Discrete gust--problems.

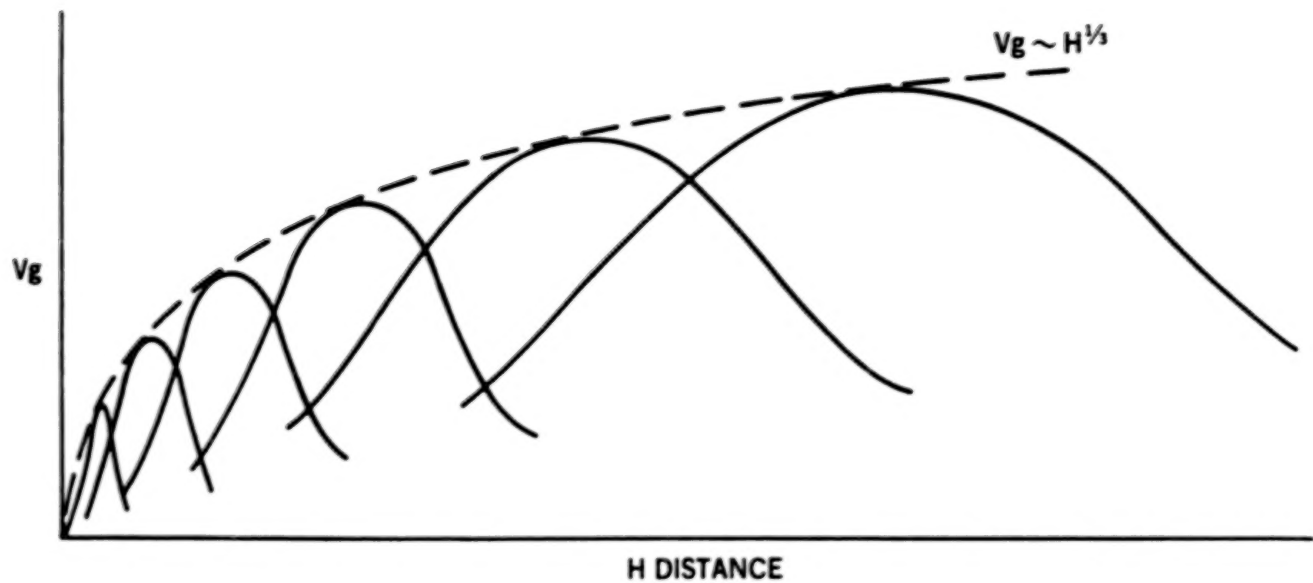
- REQUIRE MODERN METHODS TO "TUNE"  $1 - \cos$  GUSTS



- USES MASS PARAMETER DERIVED GUST VELOCITIES
- "TUNING" SPECIFIED ONLY FOR VERTICAL GUSTS
- PSD GUSTS REQUIRED AS "GUIDE"

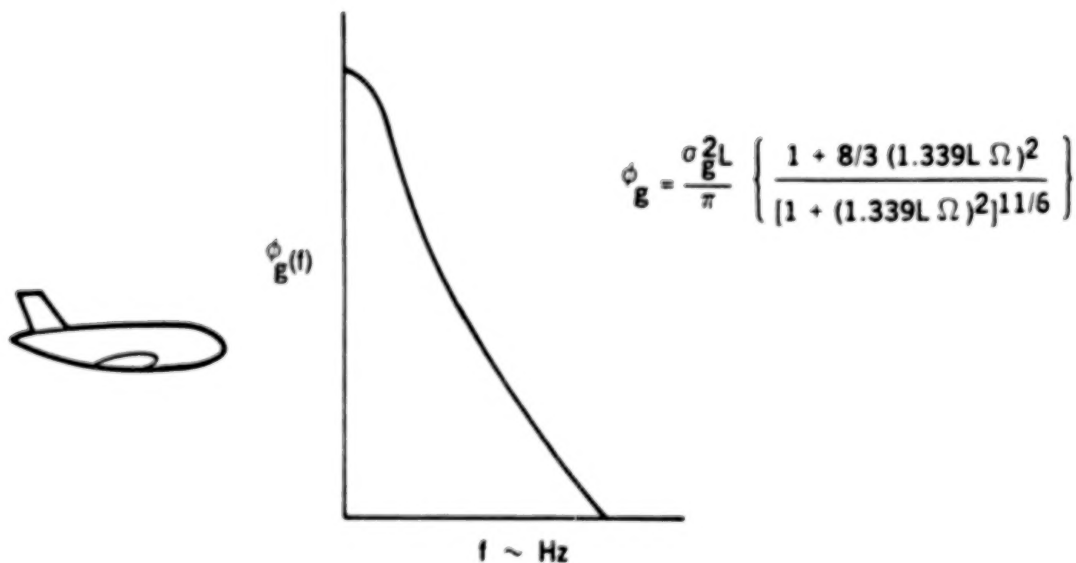
Figure 6. British discrete gust--present.

- "TUNING" DOES NOT PRODUCE REALISTIC GRADIENTS



- DESIGN VELOCITIES WERE NOT RECALIBRATED

Figure 7. British discrete gust--problems.



- LINEAR ANALYSIS OF STREAMWISE GUSTS
- STRENGTH EQUIVALENT TO 1960s AIRCRAFT
- VARIETY OF GUST CHARACTERIZATIONS

Figure 8. PSD gust--present criteria.

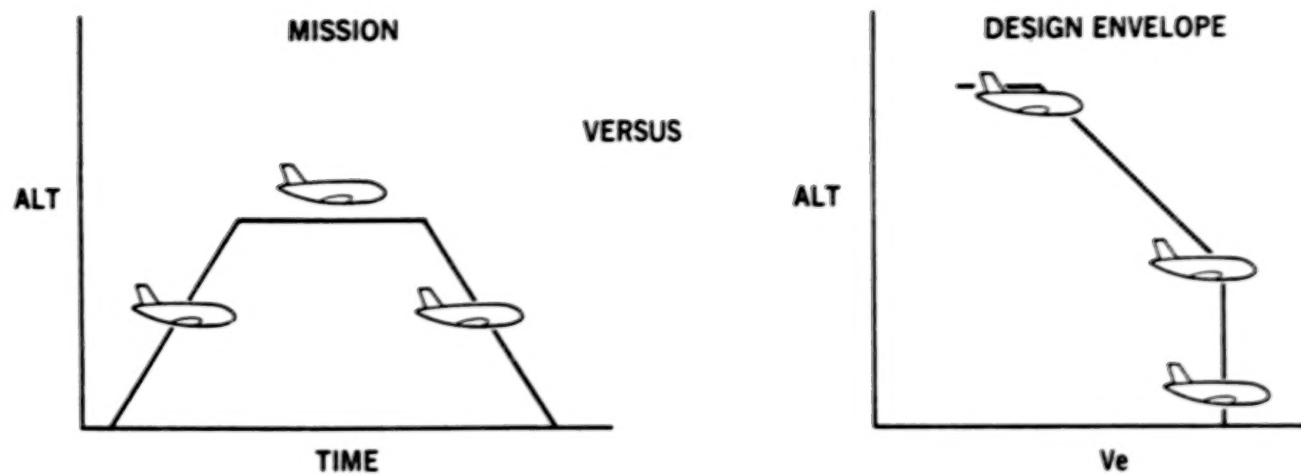
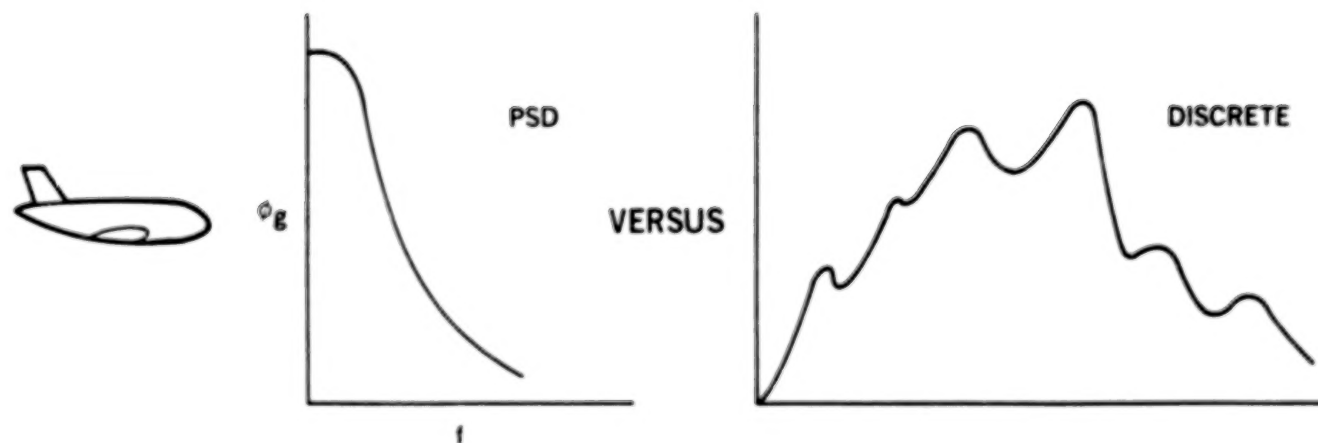


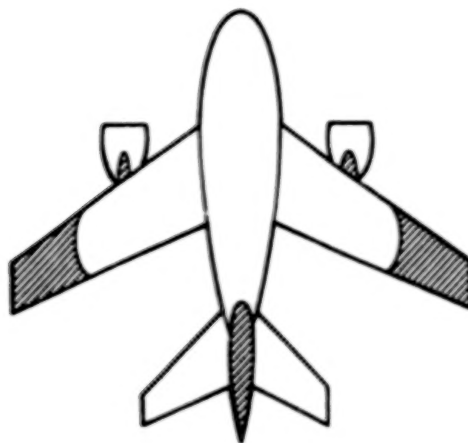
Figure 9. PSD gust--present criteria.



• FAA ADVISORY CIRCULAR ON ACTIVE CONTROLS FOR LOAD ALLEVIATION

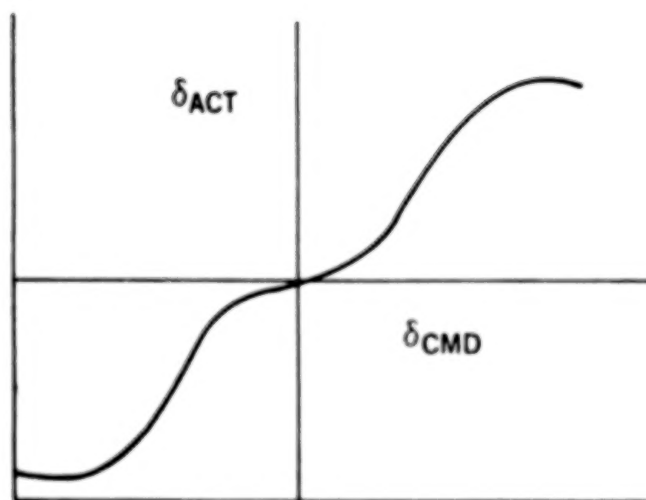
Figure 10. PSD gust--present criteria.

- BOTH DISCRETE AND PSD REQUIRED

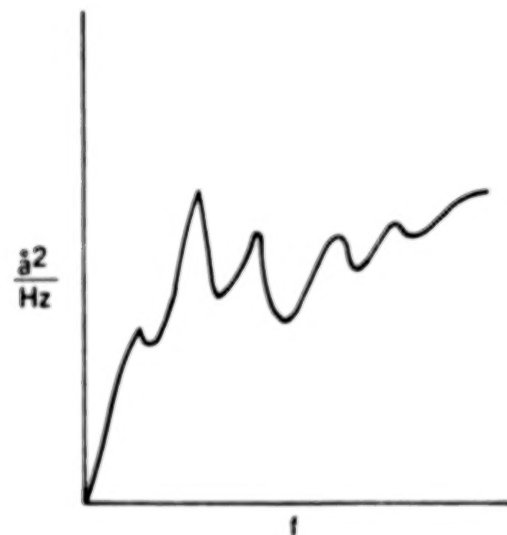


- MASS PARAMETER GUSTS CANNOT REPRESENT A/P STABILITY AND VIBRATION MODES
- PSD IMPORTANT PART OF FATIGUE-DTA

Figure 11. Gust criteria--present.



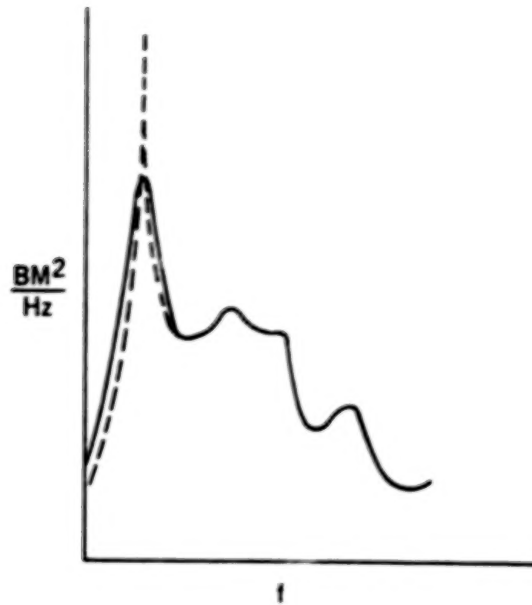
- REPRESENTATIONS OF CONTROL SYSTEM NONLINEARITIES



- INTEGRATION FOR ACCELERATION  $N_0$  DOES NOT CONVERGE

Figure 12. PSD--problems.





• PSD LOADS  $\rightarrow \infty$  AS  $\xi_{DR} \rightarrow 0$

Figure 13. PSD--problems.

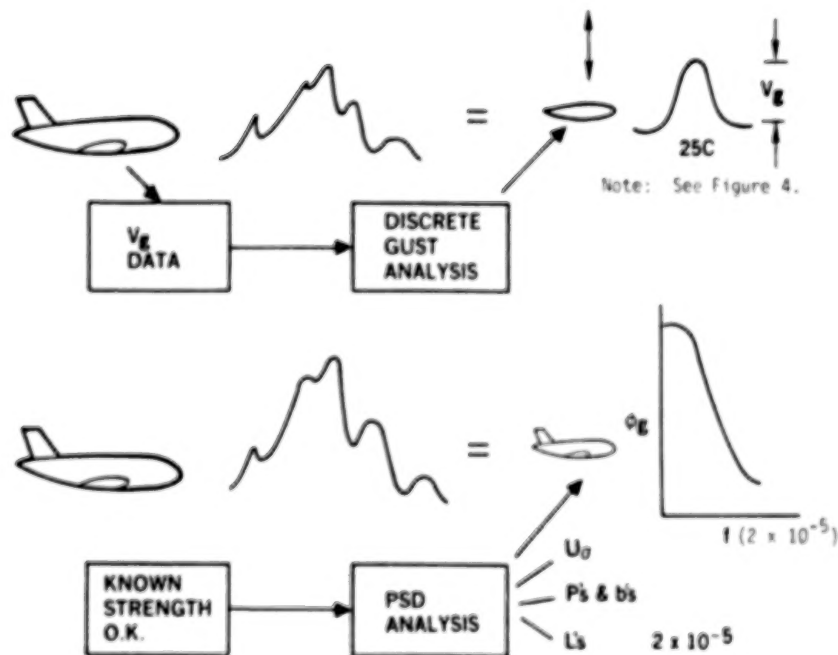
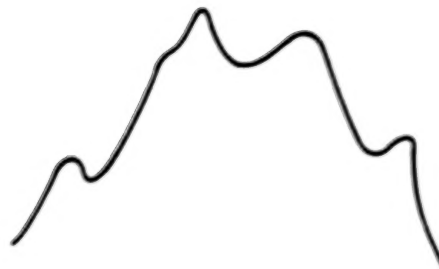


Figure 14. Criteria--background.



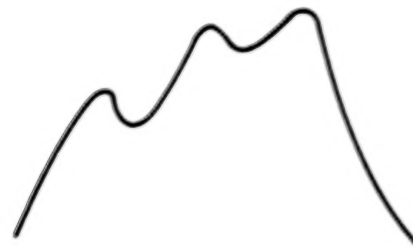
OLD



O.K.



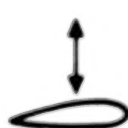
NEW



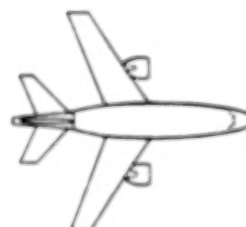
?

- ANALYSIS/CRITERIA USED TO ASSURE EQUIVALENT LEVEL OF SAFETY
- RELATIVE CHARACTERISTICS ARE PREDICTED

Figure 15. Criteria--philosophy.



- INTEGRATE DISCRETE GUST CRITERIA WITH MODERN ANALYSIS
- DEFINE REALISTIC GRADIENTS
- RECALIBRATE DESIGN GUST LEVELS



- ACCOUNT FOR DATA ON MODERN AIRCRAFT

Figure 16. Discrete gust--future.

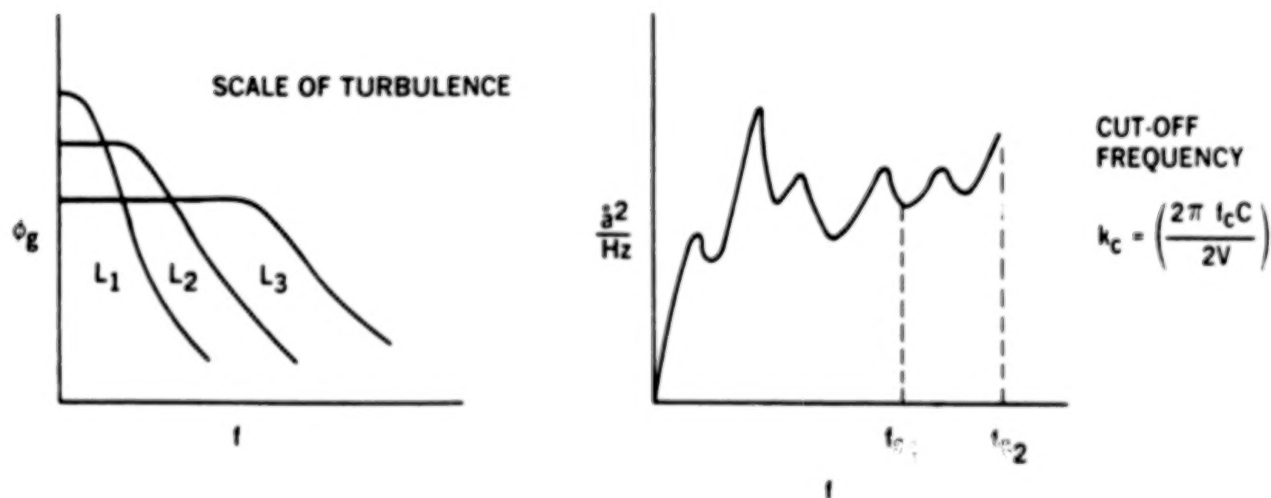


### CONSENSUS AND STANDARDIZATION



- PSD GUST FOR DETERMINING DESIGN LOADS?
- MISSION VERSUS DESIGN ENVELOPE?

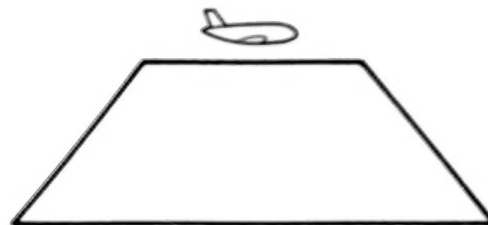
Figure 17. PSD gust--future.



- ISOLATED OR COMBINED VERTICAL-LATERAL GUSTS

Figure 18. PSD gust--standardization.

- MINIMUM STANDARDS FOR MISSION ANALYSIS



OR ?



- SAME TURBULENCE FOR CONTROL AND STRUCTURAL ANALYSES

Figure 19. PSD gust--standardization.

$$N_{DL} = p_1 N_0 e^{-\left(\frac{L \cdot L_1 G}{\bar{A} b_1}\right)} + p_2 N_0 e^{-\left(\frac{L \cdot L_1 G}{\bar{A} b_2}\right)}$$

- RECALIBRATE p's AND b's
- RECALIBRATE DESIGN ENVELOPE DESIGN VELOCITIES
- RECALIBRATE  $N_{DL}$

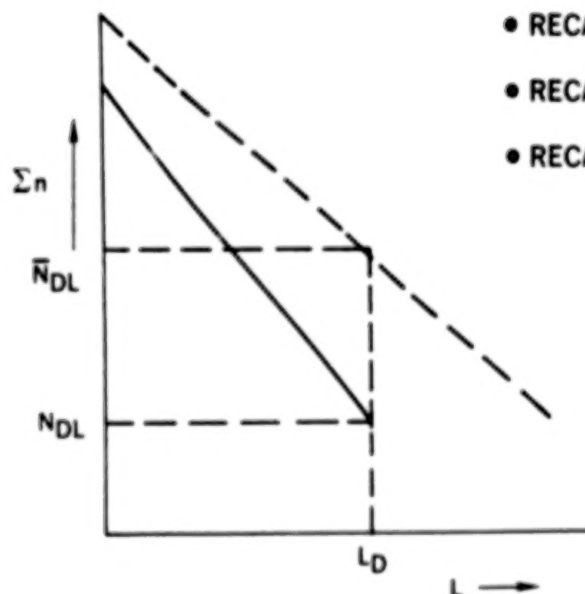


Figure 20. PSD gust--recalibration.

**DESCRIBE GUST CHARACTERISTICS ABOVE 50,000 FT**

**ADEQUACY OF STREAMWISE GUST MODEL  
FOR LOW ALTITUDES**

**(b/L) WHERE 3-D EFFECTS BECOME IMPORTANT**

Figure 21. Future--general.

N87  
22345  
UNCLAS



## TACTICAL MISSILE TURBULENCE PROBLEMS

Richard E. Dickson  
U.S. Army Missile Command  
Redstone Arsenal, Alabama

1. INTRODUCTION

Recently, the Missile Command acquired two new project offices: Remotely Piloted Vehicles (AQUILA) and Unmanned Aerial Vehicles. Usually, missile and rockets do not bank to turn so we are playing catch-up on winged vehicles.

Our usual bill of fare consists of free flight rockets and guided missiles. They range from direct fire systems to tactical ballistic missiles, with air defense thrown in for good measure.

Add to the above smart and dumb submunitions, and it is readily apparent that our interest is from the surface to the exoatmosphere. Of particular interest is atmospheric turbulence in the atmospheric boundary layer, since this affects both the launch and terminal phase of flight, and the total flight for direct fire systems.

2. ROCKET ARTILLERY BOOST WIND PROBLEMS

Rocket artillery, being unguided, is unable to correct for the effects of winds after launch. Cannon artillery is boosted in the tube, while rocket artillery is boosted outside the tube. When a rocket comes out of the launch tube it is moving rather slowly. Any crosswind will cause an aerodynamically stable rocket to cock into the crosswind; then the propulsion will drive the rocket upwind. All the wind has to do is turn the rocket; the propulsion does the rest. Most of this effect occurs in the rocket's first yaw wavelength, about 20 to 200 m, depending on the rocket's characteristics.

One technique to reduce this effect is to reduce the aerodynamic stability by delaying the opening of the fins till the rocket is going faster. Since neutrally stable rockets also have their problems, the time delay is chosen to trade off various error sources.

3. MEAN WIND CORRECTION

With tube artillery, a forward observer may adjust the fire onto the target. This is not practical for rocket artillery since the targets are deep in the enemy's territory. The Swiss company Contraves has developed the FIELDGUARD fire directing radar which is used by the Federal Republic of Germany (FRG) with their 110 m Light Artillery Rocket System (LARS).

The FIELDGUARD radar tracks three registration rounds to the target area and adjusts fire like a forward observer. Due to the time of flight of the

rocket to the target, the FIELDGUARD can only reduce the effect of mean winds during boost and coast. Coast wind effects and wind effects after burnout are the same for rocket and cannon artillery.

#### 4. TURBULENT BOOST WIND CORRECTION

The effects of turbulence during the first yaw wavelength are not corrected by FIELDGUARD. It has been proposed [1] that each round be tracked over the first yaw wavelength and this information then be used to correct the aiming of the next round. This is referred to as the Dynamically Aimed Free Flight Rocket (DAFFR) concept.

The coast wind effects could have already been determined by FIELDGUARD, or a MET message could be used as is done with tube artillery.

Of course, the ability of the DAFFR scheme to reduce the effects of turbulence during boost depends upon the correlation of turbulence over time [2,3] and the time between rounds.

The turbulence intensity which is a function of surface roughness can be quite large near the earth's surface. Cannon cockers like to fire from the tree line for concealment. The failure to consider surface roughness in the selection of rocket artillery launch sites could adversely affect system performance, particularly if that performance was determined in a benign turbulence environment. White Sands Missile Range could be considered a rather benign turbulence environment when compared with forested, mountainous, or urban regions of Europe.

#### 5. THE DAFFR WIND FILTER

Assuming the longitudinal wind,  $u$ , is the sum of the mean wind,  $\bar{u}$ , and the turbulent wind,  $u'$ , one has [2]:

$$u(t) = \bar{u} + u'(t)$$

The turbulent wind is related to its value at some previous time by [2]:

$$u'(t + \tau) = \rho(\tau) u'(t) + u''(t + \tau)$$

where  $\rho$  is the correlation coefficient for a time delay,  $\tau$ , and  $u''$  is the random component of the turbulence. The variance of the random component is defined by the relationship [2]:

$$\sigma^2(u'') = \sigma^2(u')[1 - \rho^2(\tau)]$$

so that the turbulent energy is conserved with time.

With this wind model, it was possible to develop a discrete recursive filter, Figure 1. First, a discrete Kalman filter was developed and then the Kalman filter gains were simplified to a set of suboptimal gains (Figure 1).

The gain for the mean,  $1/n$ , should be quite familiar. The gain for turbulence,  $(1 - 1/n)$ , is reduced by epsilon to take into consideration the effects of the random component of the turbulence and measurement noise. Since the rocket is being used to sense the wind, its randomness constitutes measurement noise.

## 6. THE DAFFR TEST

The DAFFR concept, with a FIELDGUARD on loan from FRG, was demonstrated at Eglin Air Force Base, Florida, in the spring of 1983 and 1984.

Two equipment problems were encountered. The first was ionization in the rocket exhaust plume that attenuated the DAFFR radar signal to such an extent that tracking had to be delayed until after burnout. No tracking data were available during the first yaw wavelength. The second and more severe problem was the slowness of the "surplus" launcher drives to re-aim. The time between rounds was approximately 6 seconds while 2 to 3 seconds was desired.

Even at 6 seconds between rounds, some improvement (10 percent) was noted. More importantly, that improvement was in good agreement with the preflight prediction for a 6-second delay. It is hoped that with 2 or 3 seconds between rounds, a reduction of turbulence boost effects of 50 percent could be achieved.

An interesting adjunct to the test was Lockheed's Active Infrared Measurement (AIM), a laser Doppler velocimeter. Though used during the DAFFR test as range instrumentation to measure boost winds, Lockheed contends the AIM could be used to measure the wind prior to the launch of each round and correct aim based upon those measurements. There is no one best answer.

## 7. ROCKET WAKE TURBULENCE PROBLEMS

During boost, the exhaust plume forces the airflow around the rocket away from the rear of the rocket. This reduces the aerodynamic effectiveness of fins placed at the rear, thus reducing the stability.

Another problem of interest is wake interference. Following rockets cut across the exhaust plume of leading rockets if they are too close in space and time. The effect decays quite rapidly (in seconds) but it does limit how close together rockets may be fired. During the DAFFR test, Lockheed's AIM did sense the wake and its decay. The effect is not well understood.

## 8. CONCLUSIONS

Of course, many of the turbulence problems of rockets and missiles are common to those of aircraft, such as structural loading and control system design. This discussion has been primarily about a problem peculiar to free flight rockets, which has not been solved at this time.

Besides the correlation of turbulence over time, the correlation over space is also of interest. What relationship do measurements of wind at the launcher have to winds in front of the launcher? What effect does turbulence have on the impact angle of dumb submunitions?

Each new system will have new turbulence problems associated with it.

#### REFERENCES

1. McCorkle, Jr., W. C.; and Lilly, J. A.: An Adjusted Fire Technique for a Highly Accurate Free Flight Rocket Artillery System, U.S. Army Missile Command Technical Report RD-74-13, Redstone Arsenal, Ala., June 1974.
2. Hanna, S. R.: Some Statistics of Lagrangian and Eulerian Wind Fluctuations, *Journal of Applied Meteorology*, 18:518-525, April 1979.
3. Frost, W.; Long, B. H.; and Turner, R. E.: Engineering Handbook on the Atmospheric Environmental Guidelines for Use in Wind Turbine Generator Development, NASA TP-1359, Dec. 1978.

**QUESTION:** Warren Campbell (BDM Corporation). Can you tell me what the minimum range of the AIM Doppler lidar is? What is your first range gate?

**ANSWER:** I think the minimum range was just a few meters off the launcher, but I'd have to check. The range went out to 700 but we had lots of measurements in close and spread them out in a geometric progression because we were interested in the close-in effects. We kept doubling where the gates were as we went out. The first range gate was at 10 m.

**CAMPBELL:** I have just one comment: I don't know how you will ever get around the problems you have with trees. Of course, the fetch downstream where the internal boundary layer is developing is felt a long way downstream and that depends on where you are.

**DICKSON:** I have seen some work where it was as much as 400 m. One of my suggestions was that we get lawnmowers and chainsaws and go upwind and clear everything out. I might add one other thing, since you mentioned the LDV, we did see missile wake turbulence effects with the LDV. Of course, the AIM was using a conical scan and a Fast Fourier Transform. The missile wake turbulence just blew the AIM off the air, but when we went back to the raw data we could see the missile wake turbulence and its decay. We weren't instrumented or looking for it, but it was definitely there, and I see LDV's as tools for examining missile wake turbulence in addition to turbulence around airports and other things.

**QUESTION:** Bob Heffley (Manudyne Systems). I have one quick comment. There is an Army ECOM report circa 1966 (TR-ECOM-6019) which describes boundary layer profiles below tree lines and various kinds of vegetation. This was based on both wind tunnel and full scale measurements.

STATE:

$$\begin{pmatrix} \bar{U} \\ U' \end{pmatrix}_n = \begin{pmatrix} 1 & 0 \\ 0 & \rho \end{pmatrix} \begin{pmatrix} \bar{U} \\ U' \end{pmatrix}_{n-1} + \begin{pmatrix} 0 \\ U'' \end{pmatrix}_n, \quad U''_n \sim N(0, q), \quad q = \sigma_U^2 (1 - \rho^2)$$

OBSERVATION:

$$Z_n = \begin{pmatrix} 1 & 1 \end{pmatrix} \begin{pmatrix} \bar{U} \\ U' \end{pmatrix}_n + V_n = U_n + V_n, \quad V_n \sim N(0, r)$$

PREDICTION:

$$E(U)_n^- = \begin{pmatrix} 1 & 1 \end{pmatrix} E \begin{pmatrix} \bar{U} \\ U' \end{pmatrix}_n^- = \begin{pmatrix} 1 & 1 \end{pmatrix} \begin{pmatrix} 1 & 0 \\ 0 & \rho \end{pmatrix} E \begin{pmatrix} \bar{U} \\ U' \end{pmatrix}_{n-1}^+$$

FILTER:

$$E \begin{pmatrix} \bar{U} \\ U' \end{pmatrix}_n^+ = E \begin{pmatrix} \bar{U} \\ U' \end{pmatrix}_n^- + \begin{pmatrix} \frac{1}{n} \\ (1 - \frac{1}{n})\epsilon \end{pmatrix} [Z_n - E(U)_n^-]$$

$$\epsilon \approx \frac{q}{q+r}$$

Figure 1. Discrete recursive filter.

N87  
22346  
UNCLAS



## REMOTE VERSUS IN SITU TURBULENCE MEASUREMENTS

Walter Frost  
FWG Associates, Inc.  
Tullahoma, Tennessee

Comparisons of in situ wind and turbulence measurements made with the NASA B-57 instrumented aircraft and those remotely made with both radar and lidar systems are presented. Turbulence measurements with a lidar or radar system as compared with those from an aircraft are the principal themes. However, some discussion of mean wind speed and direction measurements is presented.

First, the principle of measuring turbulence with Doppler lidar and radar is briefly and conceptually described. The comparisons with aircraft measurements are then discussed. Two studies in particular are addressed: One uses the JAWS Doppler radar data and the other uses data gathered both with the NASA Marshall Space Flight Center (NASA/MSFC) and the NOAA Wave Propagation Laboratory (NOAA/WPL) ground-based lidars. Finally, some conclusions and recommendations are made.

Figure 1 illustrates conceptually how Doppler radars and lidars measure winds. A pulse of microwave energy is transmitted into the atmosphere. The beam of energy spreads out in a conical manner. The transmitted signal is scattered back to a receiver by raindrops or, in clear air, by aerosols, bugs, or other materials which scatter back the signal. The signal is then recorded and processed. The volume element in space which the radar probes is conical in shape. It gets bigger as it moves out. The length of the volume element for a pulsed radar or lidar system is equal to the speed of sound,  $c$ , times the pulse duration,  $\tau$ , divided by 2. Each volume element is called a range gate. There are several range gates that extend outward in space until the transmitted signal is too weak for further radiation to be scattered to the receiver. Typically  $\tau$  is 1  $\mu$ s, and with the speed of light being 300,000 m/s the range gate length is 150 m long. The length varies based on the system capabilities, and for lidars it is often 300 m long. Therefore, it is quite a long volume in space that the system interrogates. The lateral spread of the beam,  $d$ , depends on the divergence angle,  $\theta$ , and the distance from the transmitter. The diameter of the volume element is thus variable becoming larger further from the transmitter. For radar the spread rate may be on the order of 17 m/km.

The signal scattered back to the receiver is from those particles which are within the volume element. The particles are assumed to move in equilibrium with the air and thus at the mean wind speed. Of course, due to turbulence and wind shear across the volume element, the particles will also be relative to one another.

The radar system signal processor records the Doppler frequency shift due to the velocity component of the particles away from or toward the receiver. The Doppler frequency is then related to each individual particle motion by the relationship  $f_d = -2v_{r1}/\lambda$  where  $v_{r1}$  is the velocity component of

the  $i$ th particle along the direction of the beam (i.e., the radial velocity component). The mean wind is essentially the average of the sum of all these motions. The subscript  $r$  in Figure 1 denotes the radial component either toward or away from the radar.

The processed signal of the Doppler frequency shift due to each particle is idealized as having a Gaussian shape. Thus, the signal represents a frequency spectrum. If the majority of the particles are moving with the mean air motion, then the most energy is scattered at the value of the mean Doppler shift frequency,  $f_d$  (see Figure 1). The mean frequency shift is then correlated with the mean velocity. Due to the fact that the particles are also moving randomly relative to one another because of the turbulence and other air motions, there is a spreading of the energy associated with the  $f_d$ . Thus, different amounts of energy are associated with different frequencies depending on how the particles are moving relative to each other. If you assume the signal is Gaussianly distributed, then a standard deviation (called the pulse standard deviation),  $\sigma_p$  (see Figure 1), can be defined and, in principle, is a measure of the chaotic motion due to turbulence within the volume element being sampled. Thus, the standard deviation of the Gaussian distribution or the spectral width of the return signal should be a measure of the atmospheric turbulence.

A pulsed lidar works on the same principle. A typical Doppler frequency shift spectrum from a lidar is shown in Figure 2. In practice, the signal does not have the nice Gaussian distribution that is assumed and generally several pulse signals are averaged to get meaningful results. If the pulse repetition is 100 cycles/sec and ten pulse returns are averaged, a 10 millisecond average measure of the wind is obtained.

Thus, with a radar or lidar measurement you are averaging the wind both spatially and with time which could be 0.5 to 2 seconds depending on how many pulses are averaged to obtain a good strong return. The beam spreading of a lidar is much smaller than that of a radar. The lidar signal at most spreads about 1 m for the range achievable. In effect, the spatial volume sensed by a lidar can be considered as a pencil line approximately 100 to 300 m long.

The spreading or spectral width of the time average signal for the lidar is also a measure of turbulence, i.e., the pulse standard deviation,  $\sigma_p$ . In turn, a time history of 0.5 to 2 seconds averaged wind speeds can be plotted from the lidar data as illustrated in Figure 2. From this time history, a standard deviation of the wind,  $\sigma_w$ , can be computed by conventional techniques. Thus, two standard deviations will be discussed; one is  $\sigma_p$  which represents the second moment or spectral width of the Doppler frequency lidar signal distribution and the other one is  $\sigma_w$  which is calculated as illustrated by the equation in Figure 2. Both measurements remember are turbulence averages over a relatively large spatial region in space due to the volume resolution of the radar or lidar.

Figure 3 is a sketch (approximately to scale) of a typical volume element that is 5 km from the transmitter at which point the volume element is 150 m long and 85 m in diameter. The size of a B-57 type aircraft relative to volume element is illustrated. The radar volume element overwhelmingly

engulfs the entire aircraft. In turn, the lidar beam is more like a line through space, 300 m long.

To compare the aircraft measurement of turbulence, which is effectively a point measurement, with Doppler radar or lidar, you must fly along the beam and compare the data measured in each range gate with that measured by the aircraft while it is in or next to that portion of the beam (see Figure 4). The aircraft measurement is essentially the turbulence measured point by point along a line of flight. The different sampling volumes cause some problems in interpreting what turbulence is actually being compared. The aircraft turbulence intensity will, in general, be small because we compare measurements only for the period of time when the aircraft is "beside" the individual range gates. The time for an aircraft to travel the length of a range gate is about 1.5 to 2 seconds. Thus, when we compute the mean for each 1.5 to 2 second turbulence record, the mean is really turbulence itself. Turbulence intensities defined in this manner will be small compared to values computed typically from 45-minute to one-hour records normally reported in the literature.

In considering the pulse volume standard deviation, there are physical factors other than turbulence, which will cause the second moment of the Doppler signal frequency spectrum to broaden. Figure 4 lists four factors which cause spectral broadening. Various correction factors are also shown in the figure.

If there is a gradient in mean wind (i.e., wind shear) across the volume element, spectral broadening will occur. The magnitude of spectral broadening due to wind shear is estimated by the expression for  $\sigma_s$  in Figure 5.

There will be spectral broadening due to the fact that the radar is generally scanning. As the radar beam moves through space, spectral broadening occurs. Finally, there is spectral broadening from raindrops having different fall rates. The value of  $\sigma_t$  is of interest to our study. Therefore, it is necessary to correct the overall pulse spectral width,  $\sigma_p$ , by subtracting  $\sigma_s$ ,  $\sigma_a$ , and  $\sigma_d$ . The radar data have been corrected in this paper, but the lidar data have not. At the bottom of Figure 5 you can again see the definition of the wind standard deviation as contrasted to the pulse standard deviation at the top of the figure.

First, some of the comparisons of aircraft data with Doppler-radar-measured turbulence are presented. Second-moment data from JAWS are used. Three cases are considered. During the JAWS Project in Colorado, three Doppler radars were used to measure the wind field throughout a huge volume in space. The location of these volumes is shown in Figure 6. The volumes are typically 2 km high and their areal extent is as illustrated in the figure. For the July 14 case, the region indicated on the figure was probed with both the CP-2 and CP-4 radars located as shown. Velocities from two directions for an overlapping volume in space were available from this experiment. During the JAWS Project, the NASA B-57 aircraft was flown in the experiment region to gather data on gust gradient across the wing span, which is described in Murrow's paper [1]. Although we were principally gathering data relatively to gust gradients, the opportunity to use the data for comparisons with Doppler



radar turbulence measurements is a fringe benefit. Unfortunately, the only time flights actually coincided with the particular dual Doppler measurement was for the July 14 case. The problem we encountered in trying to operate the aircraft during the JAWS Project was that the JAWS experimental region encompassed Stapleton International Airport, Denver, Colorado. If there was any interesting weather like microbursts or thunderstorm activity, the aircraft was vectored out of that region because of traffic control problems. We, therefore, never really got the opportunity to fly repeatedly where the Doppler radar was probing a region that contained the aircraft flight path.

The July 14 case is the best data set available. For this case, three runs, Runs 23, 24, and 25, from Flight 6, as shown on Figure 7, were available where the aircraft flew through or close to the region the radar was scanning at that moment. Run 23 occurred slightly before the Doppler measurement was made. Run 24 corresponds exactly with the time the measurement was made. Run 25 also corresponds in time with the Doppler radar measurement but it is somewhat outside the radar volume element.

Characteristics of the flight path for Run 24, Flight 6, are shown in Figure 8. The flight occurred at approximately 6500 ft altitude which is about 500 to 600 ft above the terrain. The terrain was relatively uniform. The aircraft was flying in the direction indicated in the upper right-hand corner of the figure. A strong tailwind was encountered during this particular phase of the flight as shown by the arrows which represent one-second average horizontal wind vectors along the flight path during the run.

Figure 9 shows the results of the comparison of the turbulence measurements. The crosses are the second-moment data from the radar at each volume element or range gate. Strictly speaking, it is not exactly the value in each volume element. The data we used was provided to us by NCAR. The  $\sigma_p$  values were interpolated to a 200 m square grid system from the initial radial wind speed data. The zero's on the figure are the wind standard deviation,  $\sigma_w$ , which we calculated from the radar data from the formula given in Figure 7. The symbols \*, L, and V are longitudinal, lateral, and vertical (relative to the aircraft) turbulence standard deviations. The aircraft measurements, in general, correspond with the wind standard deviation values. Notice that the values are low compared with normally reported values. This is because each  $\sigma$  represents the standard deviation about a spatial mean for the 150 m section of wind corresponding to the range gate or volume element through which the airplane flies.

The pulse volume standard deviation,  $\sigma_p$ , is higher than the other values by at least a factor of 2. The reason for this is not fully understood at this time. If the standard deviation for the three velocity components are computed from the total time history (87 seconds) while the airplane flies the entire length of the flight path for the July 14 case (i.e., not just through each range gate) and if the square root of the turbulence kinetic energy is taken as an effective value of  $\sigma$ , good agreement with the radar pulse standard deviation is achieved. I am not sure as of yet how to interpret this. Jean Lee from NOAA/NSSL compares dissipation rates, which are a measure of turbulence kinetic energy with their Doppler radar second-moment measurements.

Figure 10 offers an explanation of possibly why there is a major difference between radar turbulence and aircraft-measured turbulence. When you measure turbulence with an aircraft, even if you go right through the radar volume element, you are basically making point measurements along a line, say path A in the figure. There is some mean wind speed along that line in space during the period required to fly the path. The aircraft turbulence intensity reported here is the fluctuations about that particular mean. If we flew through another part of the volume element, say along path B, you might see quite a different mean wind speed or distribution about that mean for the short period of time required to fly along the path. The second-moment data from the radar, on the other hand, is an effective total spatial average throughout the entire volume element. The radar measurement is representative of the turbulence within that volume element because it is a spatial measurement. If we had a long enough time record and Taylor's hypothesis is valid, the aircraft measurement should, in principle, give the same result. The time records we are working with, however, are very short and work needs to be done to learn how to handle non-stationary turbulence resulting from sampling over very short times or regions of space.

Next, the Doppler lidar turbulence measurements are addressed. Three studies have been carried out. The February 7 and 9 study is described here. This study was funded by NASA Goddard and carried out at Boulder, Colorado. Two things were of interest: (1) Measuring turbulence flux parameters relative to mountain-induced flows and (2) making comparisons with the NOAA/WPL ground-based lidar. Again, the NASA B-57 aircraft was used; the program was a joint effort between NASA Goddard (who provided the funds), NASA Langley (who reduced the data), NASA Dryden (who operated the aircraft), and NASA Marshall (who directed the program).

The flight patterns flown during the lidar comparison test are shown on Figure 11. The NOAA/WPL lidar was set up on Table Mountain. Interest was in turbulence due to winds blowing over the mountains and parallel to the mountains, respectively. The lidar beam was directed at approximately  $4.5^\circ$  elevation and  $200^\circ$  azimuth and an approach was made along this trajectory. The aircraft would then make a turn and at the same time the lidar beam was rotated to a  $290^\circ$  azimuth at the same  $4.5^\circ$  elevation. The aircraft would then climb out along that line of sight. Our intent was to make enough flights along each trajectory to do ensemble averaging. Turbulence in the boundary layer is not homogeneous, particularly over or in the vicinity of mountains. Several samples of turbulence corresponding to each range gate (roughly 300 m) was needed in order to analyze the data by ensemble averaging techniques. Roughly ten samples for each 300 m increment in space is needed. Ensemble statistical analysis can then be carried out with the data. That was the plan. However, Doppler lidar data of the time resolution needed was not recorded at corresponding times with flights as frequently as planned. Thus, we had a limited data set.

Figure 12 is a cross section in space of the lidar beam path relative to the terrain for the  $4.5^\circ$  elevation and  $290^\circ$  azimuth orientation. Each vertical line represents a range gate (300 m long). Data were taken at 0.5 seconds, i.e., pulsing 12 times per second and averaging six pulse returns. The vectors plotted along vertical lines are the time histories of 0.5-second

averaged wind speeds. The vector length represents the magnitude of the wind speed and time is plotted in the vertical direction. In this particular case, the wind was getting stronger with time. The arrowheads show that there is a reverse flow over this mountain which is interesting. The wind is blowing toward the left-hand side of the figure in the upper range gates and is blowing to the right-hand side in the lower range gates. The flow pattern corresponds to a wake region such as readily observed in laboratory studies. Mountain flows obviously have flow separation regions as can be seen in these data.

Tables 1 and 2 list the data sets analyzed. The plan was to obtain eight to ten runs along each lidar beam so we could do ensemble averaging. However, we only got six for February 7 and four for February 9. In principle, to do ensemble statistics these are not enough records. However, if that is all the data you have, then you try to do the best you can.

Figures 13 and 14 show results from the February 7 and February 9 data sets. Mean wind speed (average wind speed for the period of time the aircraft is in that 300 m volume element) is compared with the time history from the radar signal for that same period of time in the left-hand side figures. There's general agreement here which we think is very good. You cannot expect one to one agreement since it is impossible to fly the aircraft directly along the beam. Moreover, because of the presence of the mountains, which can block or shed the wind, not measuring the wind at exactly the same region in space can cause large differences. Note also that because of the short averaging times of 1.5 to 3 seconds, the reported wind speed, are in themselves low-frequency turbulence.

The difference between Doppler mean winds and aircraft mean winds was on the order of 2 m/s. There are several other factors besides terrain effects and large-scale turbulence that could contribute to these differences. The inertial navigation system has a Schuler drift. If you are on the high side of the Schuler oscillation you can easily be 2 m/s off in inertial velocity. Also, one of the problems we were having with the lidar during this test was the pulse transmission frequency was varying slightly which would give a velocity error relative to the reference frequency. The right-hand side of that figure shows the measured turbulence intensity. A "\*" designates aircraft-measured turbulence defined as previously described and a "+" designates the lidar spectral width turbulence. We did not take the wind shear out of the lidar data, and you will notice this right away. There is a very pronounced peak in the pulse volume data at corresponding positions of wind shear.

As with the radar data, the second moment data are roughly a factor of 2 greater than the aircraft data and the wind standard deviation data. I did not expect the lidar results to be a factor of 2 or 3 higher than the aircraft data because the beam from the lidar is at most 1 m thick in conical shape. Thus, the spatial volume sampled is small compared to the Doppler radar, which can have a sampling volume greater than 85 m in thickness. An explanation as to why the second-moment or spectral broadening of the lidar data are so much larger than the aircraft measurements is not presently clear.



Figure 15 shows turbulence spectra computed from the data. There is quite a bit of scatter in these data because of ensemble averaging of only a limited number of runs. The "\*" represents the turbulence spectrum calculated using the aircraft data. The open circles are the spectra computed from the lidar data. In general, these agree pretty much with one another over the region where they overlap. The lidar is actually 0.5-second averages. With 0.5-second data, the maximum frequency that can be resolved is 1 Hz. The lidar data then have a frequency range from 1 Hz to about 0.01 Hz whereas the aircraft data, where we were sampling 40 times per second, range from 20 Hz to about 0.04 Hz. Typically, the computed spectrum follow roughly a  $-5/3$  slope.

Preliminary conclusions are that lidar- and radar-measured winds generally agree with the aircraft-measured winds. Differences in agreement could be due to problems with comparing spatial and temporal data, Schuler drift in the INS system or to variation in the pulse transmission frequencies from the lidar system.

Not only does the magnitude of the winds agree reasonably well but also the profile shapes, in general, correspond. Other results from the NASA/MSFC lidar that are even better than these are available because at Marshall we made eight to ten runs with which we could carry out ensemble averaging. The results look quite a bit better. It is also concluded that the wind standard deviation turbulence intensity and aircraft standard deviations are in good agreement. This conclusion is based on the fact that the intensity is the correct order of magnitude and the spectrum overlap a  $-5/3$  slope and follow. Maybe good agreement is too strong, but they are in agreement.

The spectral width or second-moment data which come directly from the radar or lidar signal is about two or three times larger than the aircraft measurement for both the lidar and radar. The reasons may be due to the fact that the radar is looking at a very large volume and the turbulence is a spatial measurement whereas the airplane is sampling along a line in space. Study is required, however, to resolve this difference. The variation of the spatial width standard deviation with height is very similar to the wind standard deviation and aircraft standard deviation values.

Recommendations are to plan and carry out research to fully resolve the issue of turbulence measurements with lidar and radar to establish a physical understanding of the temporal and spatial resolution of the turbulence data measured. There needs to be work done, although I understand there is work being done by the USAF/Geophysics Lab and NOAA/NSSL, in developing algorithms for operationally predicting or forecasting turbulence. Finally, I see great hope for the use of Doppler radar and lidar in numerical forecasting. If the point is ever reached where turbulence flux models are incorporated into these computational techniques and they are updated periodically with measurements, as currently done for wind speed and direction, it would be very useful to develop a scanning method using the Doppler lidar or radar which would provide measured momentum flux and perhaps heat and mass flux, also. The flux models in the numerical codes could then be updated routinely with actual measurements.

## Reference

1. Murrow, Harold N.: Measurements of Atmospheric Turbulence, NASA CP-2468, pp. 73-92, 1987.

**COMMENT:** C. M. Tchen (City College of New York). It is found in atmospheric turbulence that the energy spectrum does not necessarily follow the Kolmogoroff  $-5/3$  law, but it is often modified into the  $-1$  law by wind shear. I noticed that your data in strong wind shear also show a milder slope than the  $-5/3$  slope. The  $-1$  spectrum can be broadened by the presence of rain or snow because of the added air-particle interaction. The recent turbulence measurements in the atmospheric surface layer in Scandinavian and the Russian laser measurements in atmospheric precipitation show this deviation from the Kolmogoroff law.

**FROST:** How were those measurements made?

**TCHEN:** The ORESUND Experiments 1985 by the northern European countries measured the atmospheric turbulence by means of a variety of instrumentations: hot-wire anemometers, cup anemometers, Doppler sodars, radiosonde microwave radiometers, and balloons. The Russian experiments measured the atmospheric turbulence in precipitation by means of laser intensity fluctuations.

**QUESTION:** Dave Emmitt (Simpson Weather Associates). Due to the length-to-diameter ratio of the lidar beam, at Marshall we tried to look at the difference in interpretation when we looked downwind versus crosswind with our beam and found there was some difference. You were looking at  $200^\circ$  and  $290^\circ$ . Did you detect any difference in trying to interpret data for those two directions?

**FROST:** We didn't look specifically at that problem but, if the effect was present, it was not obvious.

**QUESTION:** Bob McClatchey (AFGL). You didn't say much about clouds and precipitation in your comments. Lidar can't see through clouds and precipitation; radar has the hope of doing that. It wasn't obvious either whether the radars that were used in the Colorado experiment were looking at hydrometeors or whether they were looking at clear air and index of refraction changes. Can you comment on that, and whether in that context you conceive of a dual system involving both radar and lidar to really look at the whole regime? What's the maximum altitude range you can get with such ground-based systems.

**FROST:** There was no rain or clouds in any of our experiments. The radar returns for the data we looked at were clear-air returns. As you say, the radar does look through the clouds and the lidar will not. If there is any cloud cover, then your measurements are basically limited to the elevation of the cloud cover with the lidar system.

TABLE 1. Selected Runs of the February 7 Test.

B-57B Aircraft Data			NOAA Lidar Data		
Run No.	Azimuth Angle	Sampling Time (MST) Start to End	PRF (Hz)	Number of Pulse Average	Sampling Time (MST) Start to End
2	290	11:46:42-11:49:19	12	6	11:46:53-11:49:04
3	200	11:56:42-12:00:27	12	6	11:57:59-12:00:06
4	290	12:02:03-12:03:59	12	6	12:00:50-12:02:55
5	200	12:12:01-12:15:56	12	6	12:12:17-12:16:41
6	290	12:17:48-12:21:29	12	6	12:16:43-12:19:50
7	200	12:27:51-12:31:49	12	6	12:27:00-12:29:35

TABLE 2. Selected Runs of the February 9 Test.

B-57B Aircraft Data			NOAA Lidar Data		
Run No.	Azimuth Angle	Sampling Time (MST) Start to End	PRF (Hz)	Number of Pulse Average	Sampling Time (MST) Start to End
9	200	12:14:06-12:17:45	12	48	12:13:39-12:17:23
10	290	12:19:30-12:23:09	12	24	12:17:45-12:22:13
11	200	12:28:05-12:31:43	12	24	12:28:49-12:30:53
12	290	12:33:25-12:37:09	12	24	12:33:47-12:36:49

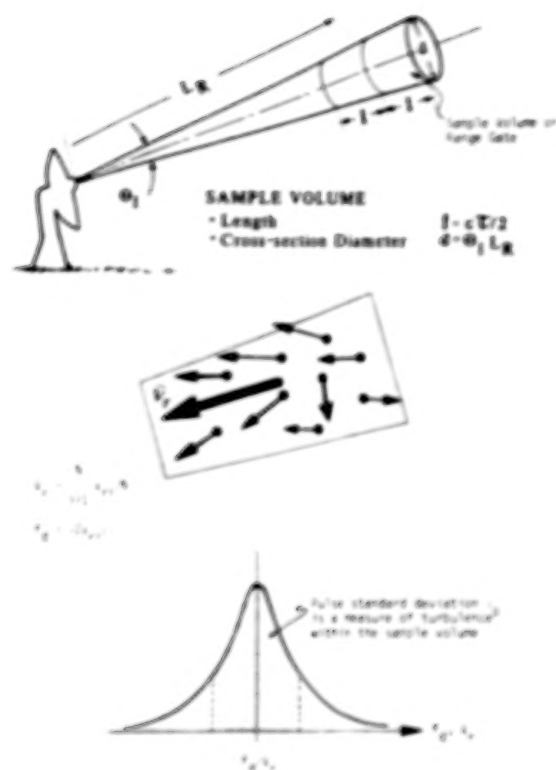
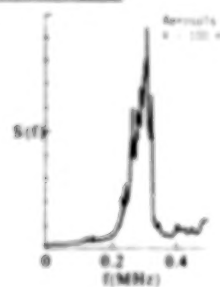


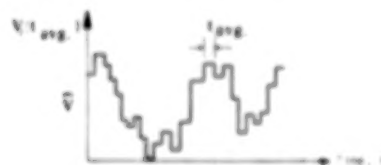
Figure 1. Doppler radar.

#### LIDAR SIGNAL SPECTRUM



SEVERAL SPECTRA ARE AVERAGED TO GIVE THE MEAN WIND SPEED AND SPECTRAL WIDTH. TYPICAL AVERAGING TIMES ARE 0.5 TO 2 SECONDS.

#### TIME HISTORY OF RADIAL VELOCITY



#### WIND STANDARD DEVIATION

$$\sigma = \sqrt{\frac{1}{N} \sum_{i=1}^N (V_i - V_{avg})^2}$$

Figure 2. Lidar signal.

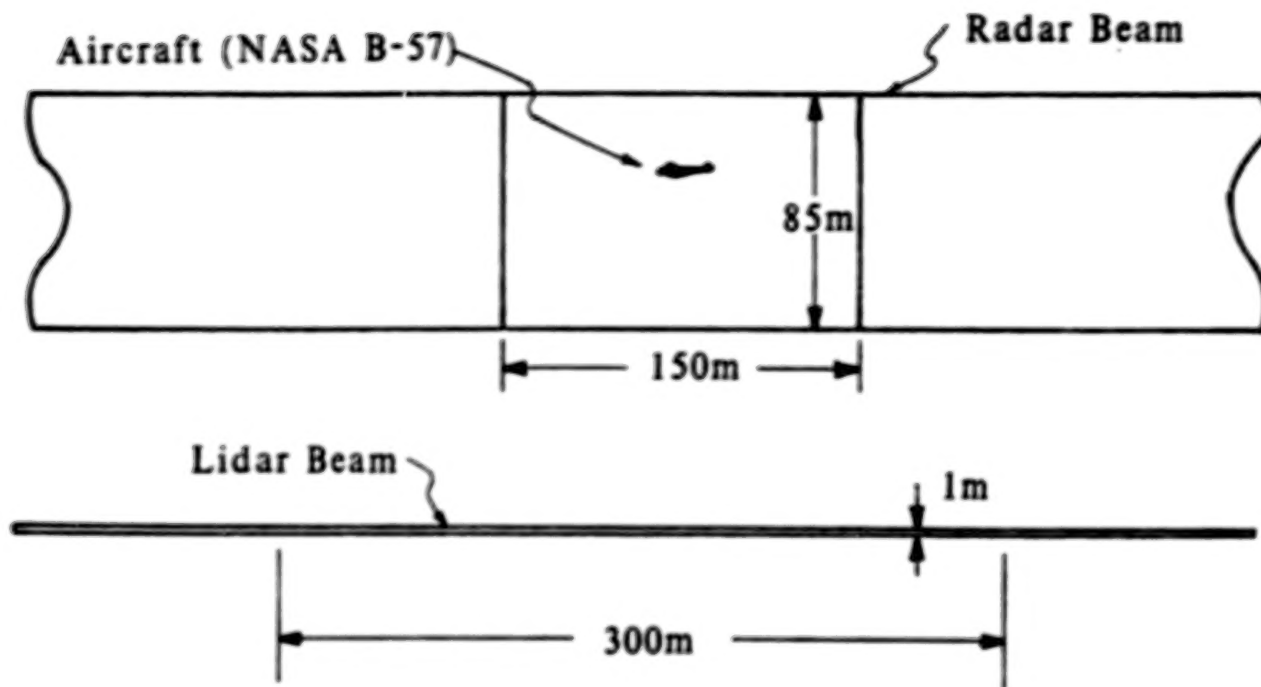


Figure 3. Sketch of relative sizes of aircraft, radar beam, and lidar beam. Scale 1 in = 50 m.

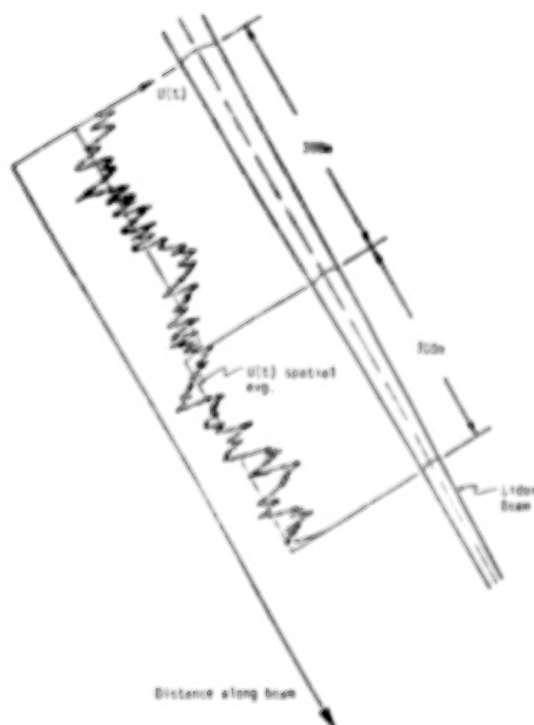


Figure 4. Aircraft measures turbulence along a line in space as compared to a lidar or radar which measures a spatial averaged turbulence in a conical volume element.

## PULSE SD

ORIGINAL PAGE IS  
OF POOR QUALITY

$$\sigma_p = (\sigma_s^2 + \sigma_t^2 + \sigma_a^2 + \sigma_d^2)^{1/2} \text{ in a pulse volume}$$

where

$\sigma_s$  = broadening due to radial wind shear

$$= [(c_r K_r)^2 + (R_0 \sigma_s K_s)^2 + (R_0 \sigma_s K_\theta)^2]^{1/2}$$

$\sigma_t$  = turbulence intensity

$\sigma_a$  = broadening due to antenna motion

$$= (\omega \lambda \cos \theta_e / 2\pi) \sqrt{\ln 2}$$

$\sigma_d$  = contribution of different speeds of fall for various sized drops

$$= \sigma_{d0} \sin \theta_e$$

$$\sigma_\theta^2 = \sigma_\phi^2 = \sigma_1 / (16 \ln 2)$$

$$\sigma_r^2 = (0.35 \text{ ct}/2)^2$$

## WIND SD

$$\sigma_w = \left( \frac{1}{N} \sum (V_r^2 - \bar{V}_r^2) \right)^{1/2} \text{ in a grid volume (200 m x 200 m x 200 m)}$$

Figure 5. Turbulence intensity.

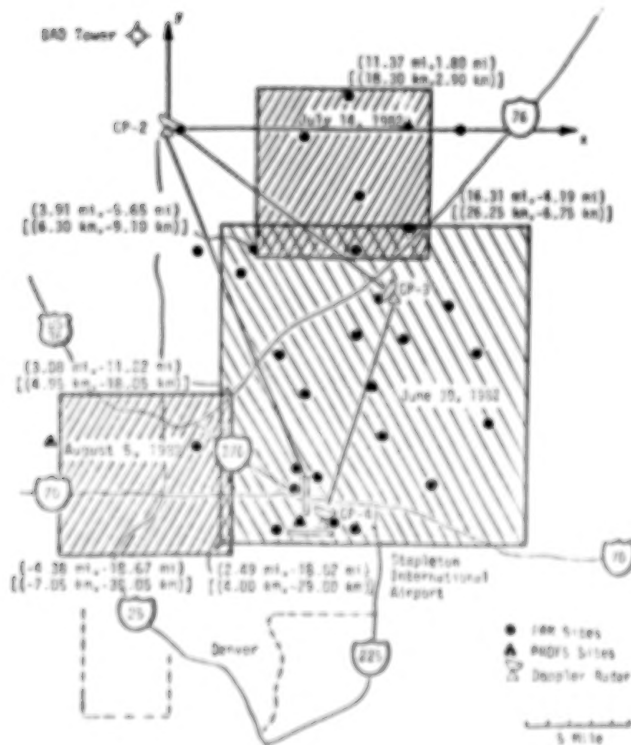


Figure 6. Location of spatial region for which JAWS data are available.



ORIGINAL PAGE IS  
OF POOR QUALITY

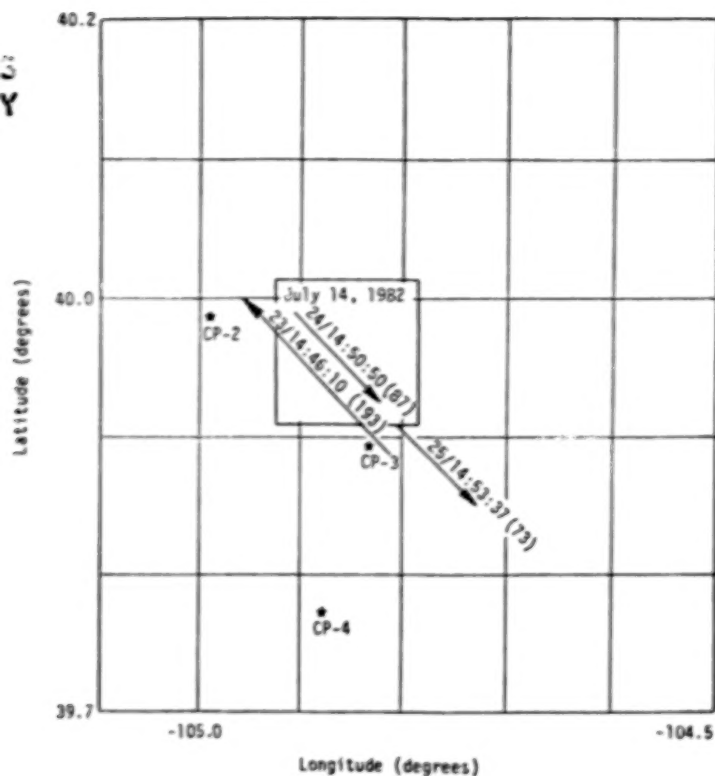


Figure 7. Relative positions of the JAWS July 14, 1982, microburst and the flight paths of Runs 23, 24, and 25 in Flight 6 of NASA B-57B aircraft.

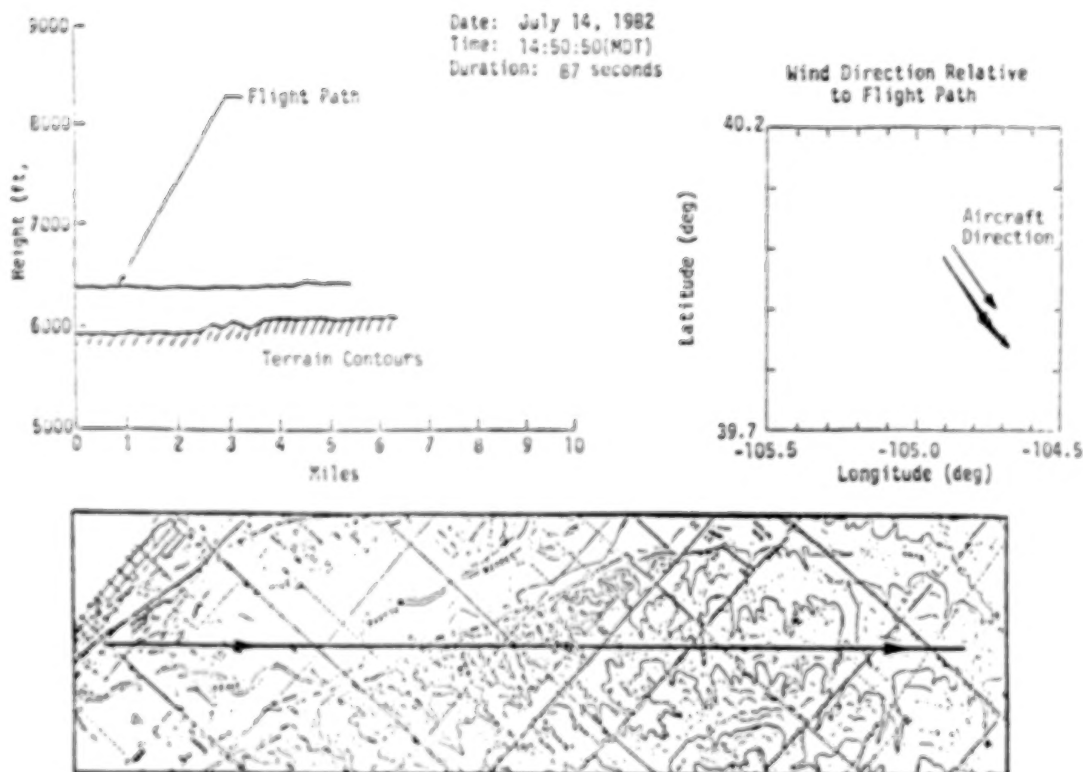


Figure 8. Flight path information: Flight 6, Run 24.

ORIGINAL PAGE IS  
OF POOR QUALITY

+ JAWS  $\sigma_t$  ;  $\sigma_w$  JAWS  $\sigma_w$   
\* Aircraft Longitudinal SD  
L Aircraft Lateral SD  
V Aircraft Vertical SD

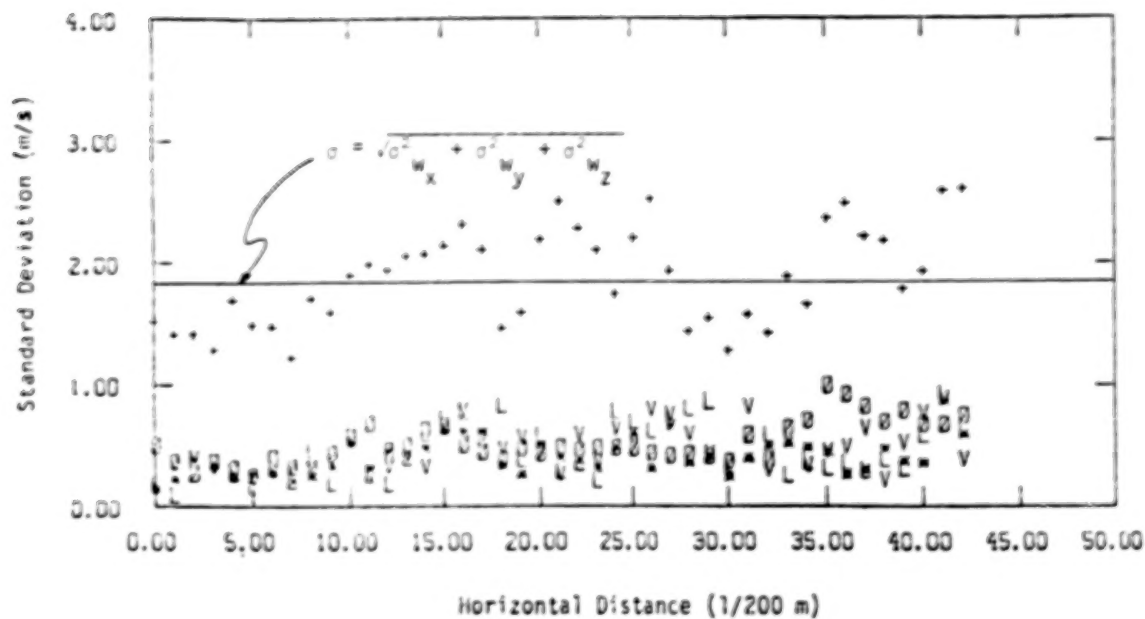


Figure 9. Comparison of  $\sigma_t$  with calculated turbulence intensities from NASA B-57B measurement (Run 24).

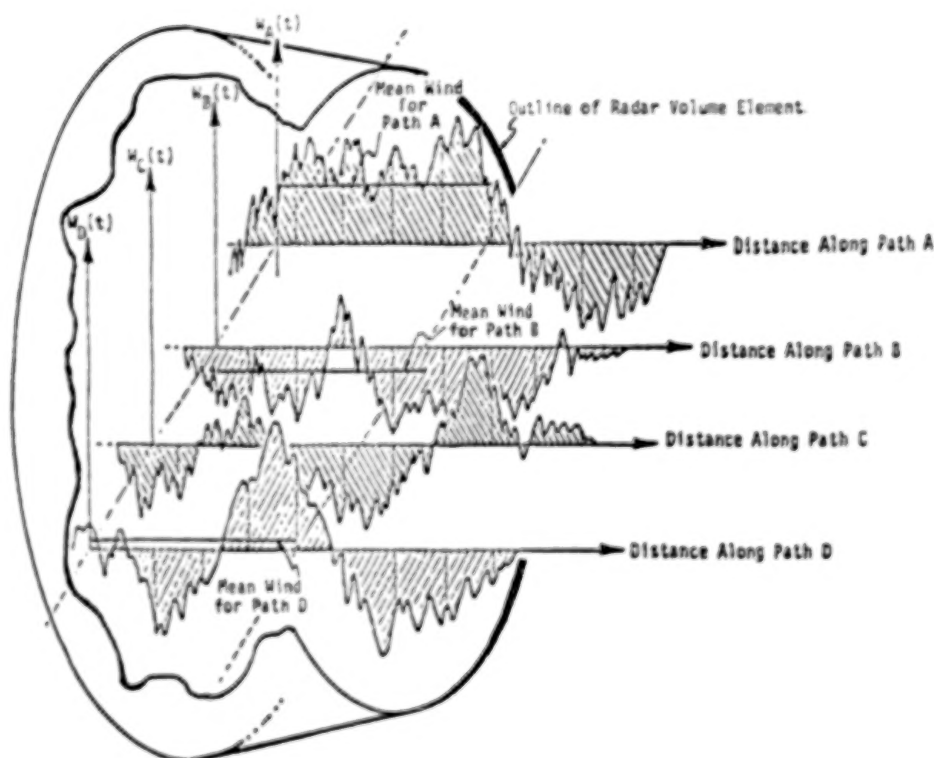


Figure 10. Schematic illustration of spatial extent of turbulence measurements from an aircraft and from a radar.

ORIGINAL PAGE IS  
OF POOR QUALITY

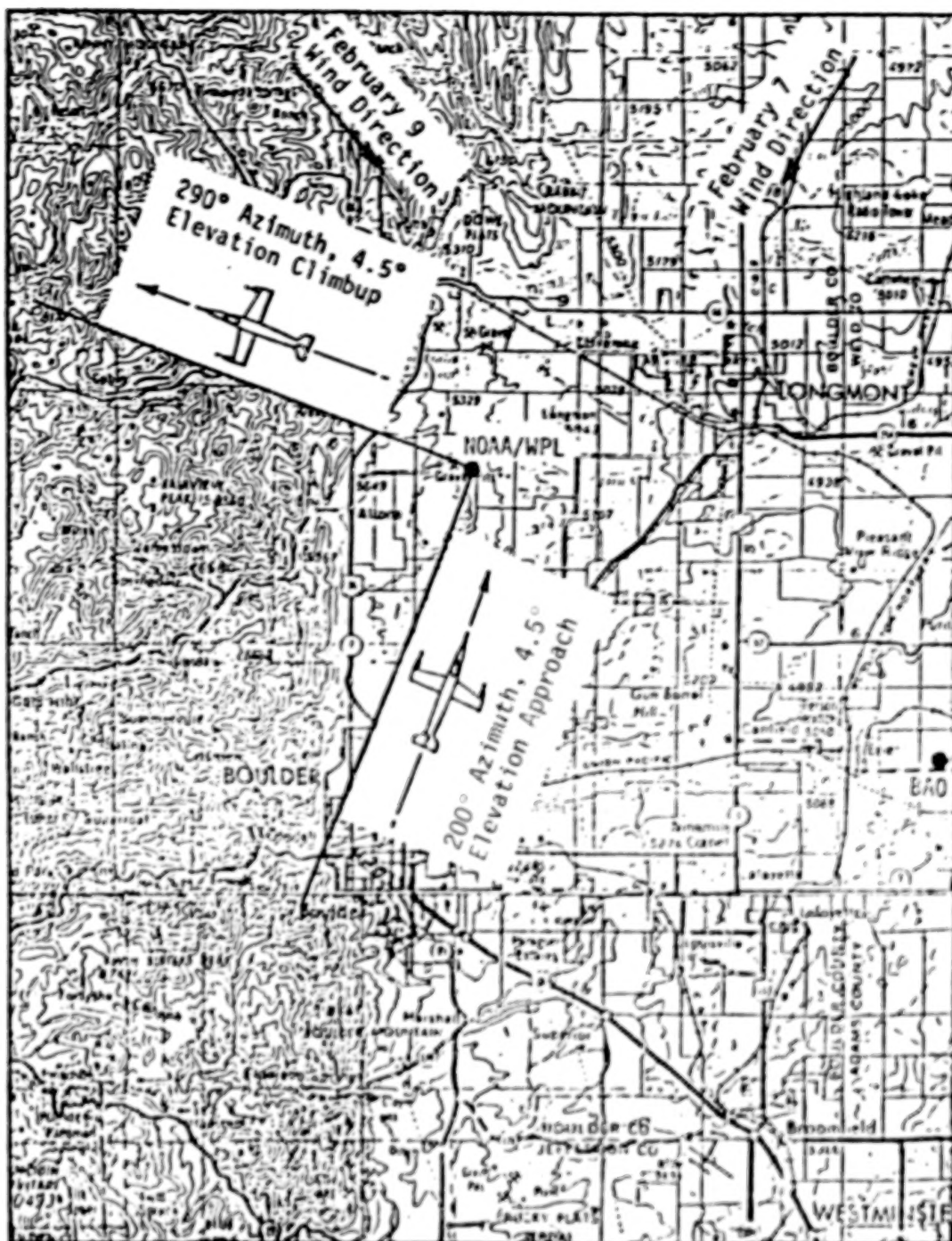


Figure 11. Flight paths relative to the lidar beam at 200° and 290° azimuth, respectively, at Boulder, Colorado, February 7 and 9, 1984.

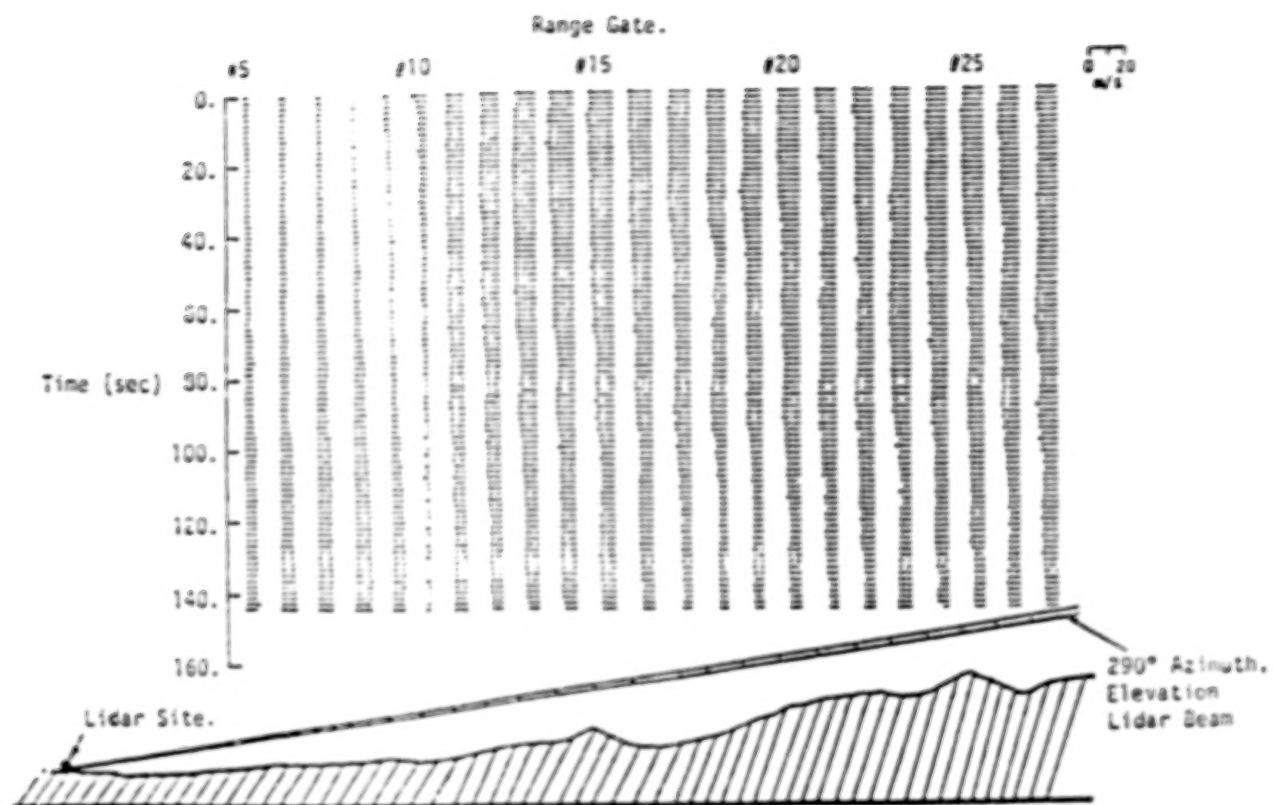


Figure 12. Time history of lidar-measured wind vector at 290° azimuth, 4.5° elevation relative to the terrain on February 9, 1984, Boulder, Colorado.

ORIGINAL PAGE IS  
OF POOR QUALITY

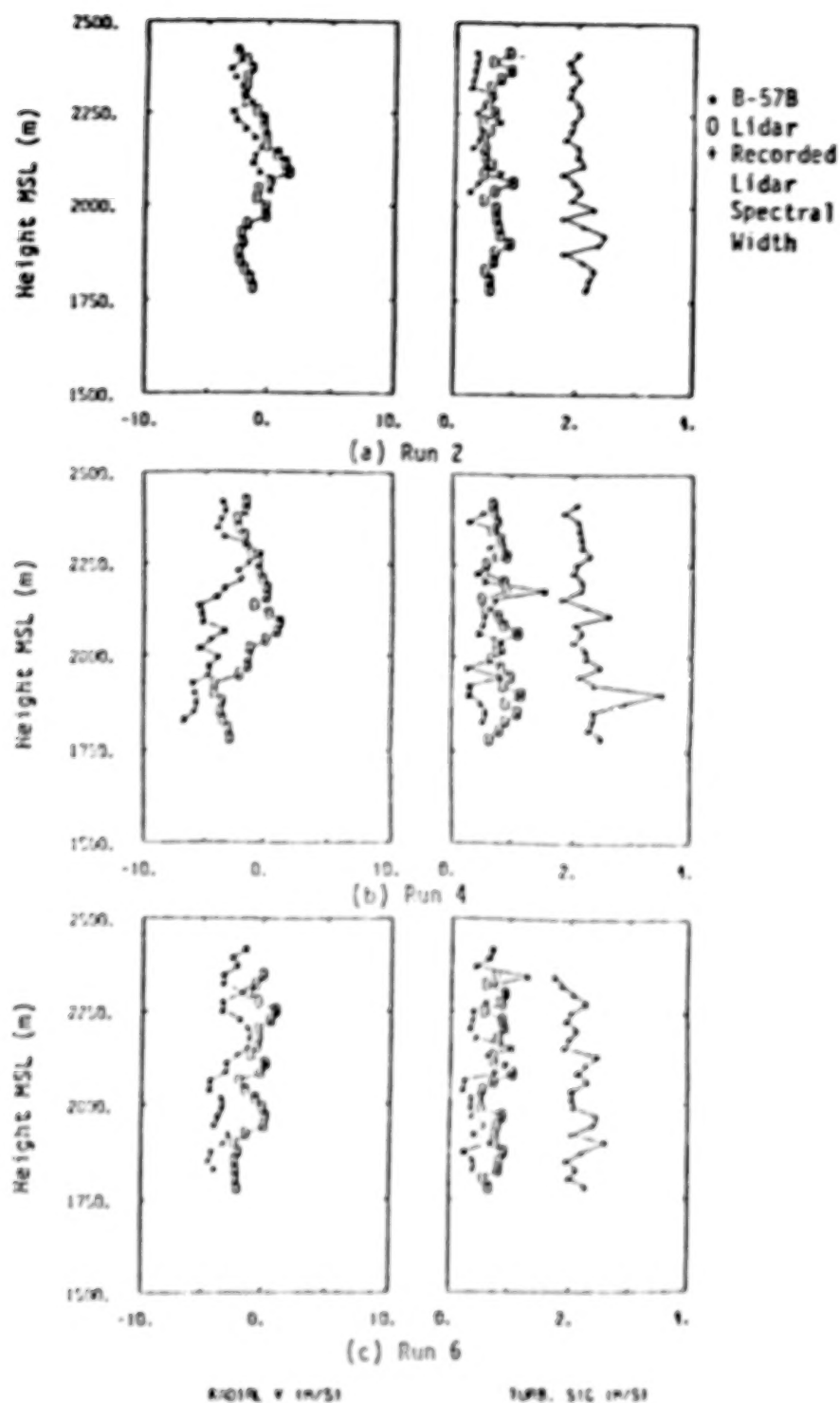


Figure 13. Comparison of radial mean wind velocity, calculated turbulence intensity, and lidar spectral width between aircraft measurement and lidar measurement on February 7, 1984 (280° azimuth).

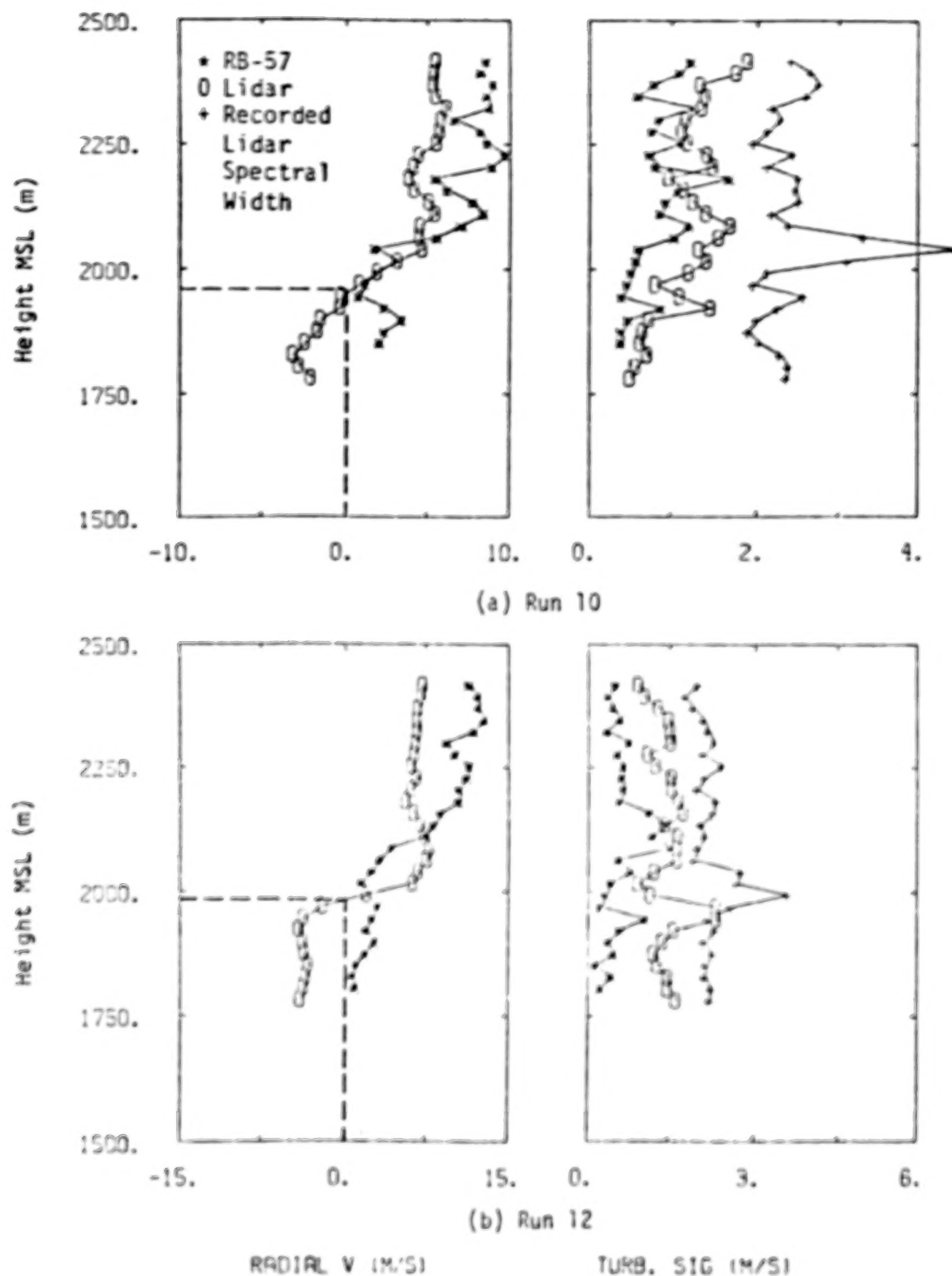


Figure 14. Comparison of radial mean wind velocity, calculated turbulence intensity, and lidar spectral width between aircraft measurement and lidar measurement on February 9, 1984 (290° azimuth).



ORIGINAL PAGE IS  
OF POOR QUALITY

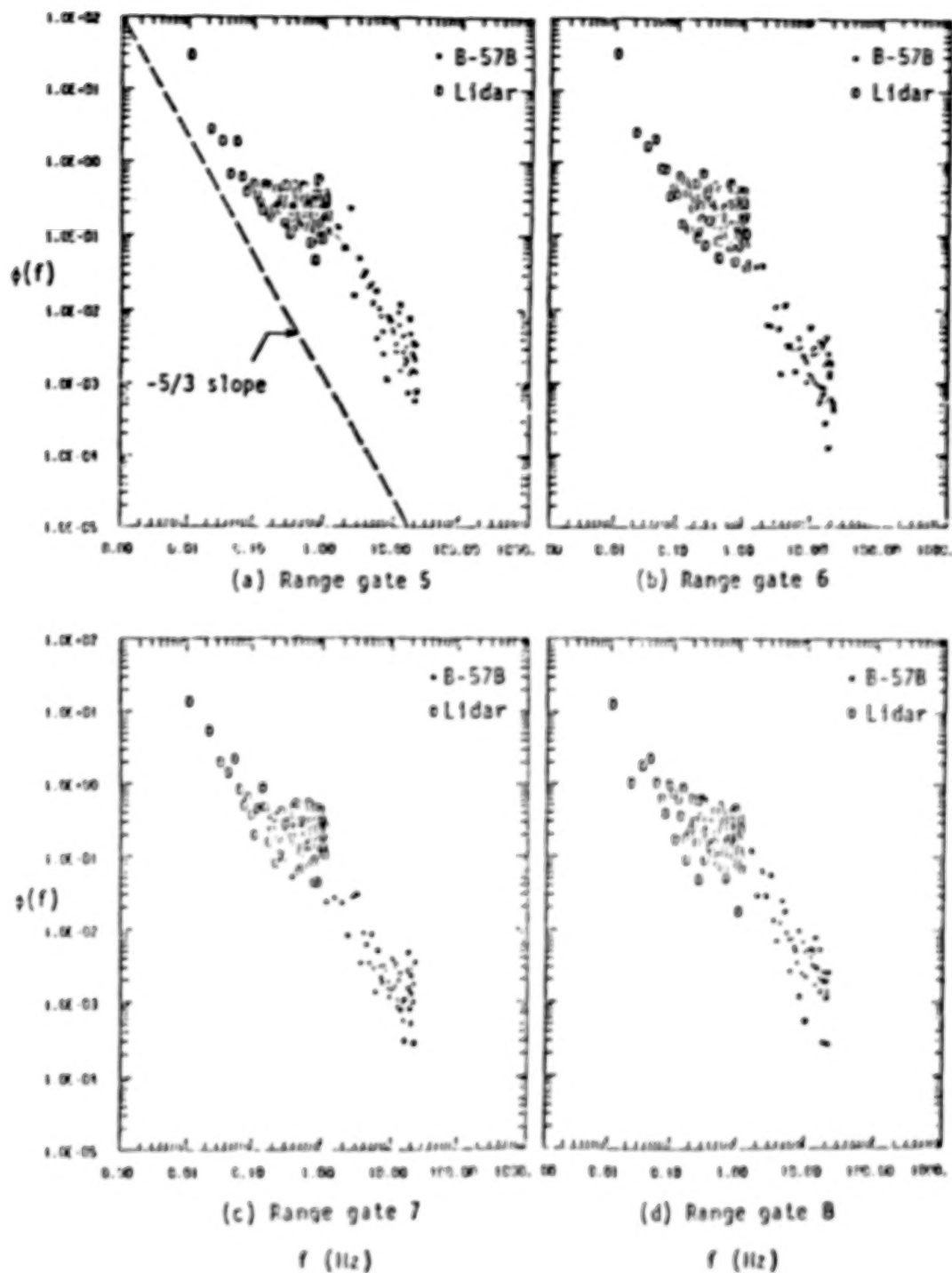


Figure 15. Computed radial turbulence spectra at 200° azimuth path.

N87

22347

UNCLAS

## MEASUREMENTS OF ATMOSPHERIC TURBULENCE

Harold N. Murrow  
NASA Langley Research Center  
Hampton, Virginia

This paper is intended to address various types of atmospheric turbulence measurements for the purpose of stimulating discussion during the interactive committee sessions of the workshop where measurement requirements relative to available data may be addressed. An outline of these various types of measurements is as follows:

1. Characterization studies
  - a. Integral scale value
  - b. Spanwise gradient
2. Encounter studies
  - a. Velocity, vertical acceleration in g's, and pressure altitude
  - b. Special encounters
3. Other
  - a. Ground-based measurement
  - b. Other in situ measurements
4. Summary

Some specific results of detailed characterization studies made at NASA Langley will be emphasized. References [1] through [13] are pertinent to these measurements and some modeling studies associated with them. Reference will be made to an existing program for measuring the spanwise gradient of gust velocity [14-17]. The most recent reports on statistics of turbulence encounters for various types of aircraft operations are summarized [18,19]. Special severe encounter studies [20] and reference to remote sensing [21] are also included. Wind shear is considered to be a special topic and is not covered here.

The objectives of the NASA Measurement of Atmospheric Turbulence (MAT) program are to obtain atmospheric turbulence power spectra and determine appropriate values of the integral scale length,  $L$ , for different meteorological conditions (jet stream, low altitude clear air, mountain waves, and near thunderstorms) over an altitude range from near sea level to about 65,000 feet. The same instrumentation system and data reduction procedure was to be utilized for all measurements. Very low frequency measurements were required since the emphasis was on the long wavelength portion of the power spectrum in order to estimate values of  $L$ .

The classical von Karman expression is given in Figure 1 and shows that two parameters are required to describe a power spectrum,  $\sigma$ , the intensity, and  $L$ , the scale of the turbulence sample. The family of curves shown is normalized with respect to intensity and shows how the location of the "knee" or flattening of the power spectrum changes with  $L$ . Some design

specifications designate that  $L = 2500$  ft be utilized if power spectral analysis techniques are to be used.

As shown in Figure 2, the gust characteristics of most contemporary aircraft are in a frequency range that knowledge of an appropriate  $L$  value is not needed; however, for large flexible supersonic aircraft, the principal response is at much lower frequencies. Thus, the aircraft response can be significantly different for the same intensity turbulence (note the log scales on the figure), and utilization of an appropriate  $L$  for design is important.

An instrumented B-57B Canberra aircraft was utilized as the sampling airplane. Samples of clear-air turbulence were obtained for conditions shown in Figure 3. While the instrumentation was later installed on a B-57F for higher altitude samplings, due to various difficulties, data sufficient for publication was not acquired.

The equations in Figure 4 show how the primary measurements made by balsa flow vanes and a sensitive airspeed device were corrected by use of instrumentation that measured aircraft motion to result in three components of gust velocity, longitudinal, lateral, and vertical with respect to the sampling aircraft.

Figures 5 through 8 give example true gust velocity time histories measured under different meteorological conditions. Four cases were selected by a research meteorologist as representing turbulence caused by low-altitude convective activity, mountain wave action, high-altitude wind shear, and so-called rotor action with sampling in the lee of rather sharp mountain peaks in the presence of strong wind. The convective case shown in Figure 5a resulted from a run extending for approximately 150 miles at 1000 ft altitude near the Virginia and North Carolina line and exhibits similar characteristics for all three components, and their  $\sigma$  values ranged from 3.78 to 4.41 ft/sec.

In Figure 5b the shape of the spectra for the convective case is reasonably close to the von Karman representation (shown by the solid lines superimposed on the data curves); however, in order to have a reasonable fit,  $L$  values of 1000, 2000, and 4000 ft appear appropriate for the vertical, lateral, and longitudinal components, respectively.

Time histories for the mountain wave case shown in Figure 6a are distinctively different in that major long wavelength content is obvious. At least three wave cycles are obvious in the 12-minute run for the vertical component--approximately one longer wave is noted on the horizontal components. The high-frequency content is variable in intensity and for this and other mountain wave samples it appears to intensify during positive swings in vertical gust velocity.

In Figure 6b the power spectra for the mountain wave case emphasize the observations noted on the time histories. High power is evident at long wavelengths and fitting a von Karman representation to the data is very difficult. It should also be noted that the higher frequency data exhibit the expected  $5/3$  slope, then tend to flatten, and then rise sharply in power at lower frequencies.

Observation of time histories shown in Figure 7a indicate that the wind shear case characteristics, in general, seem to fit between the convective and mountain wave cases with intensity varying gradually with time. It is known that this nonhomogeneous or nonstationary behavior will affect the "knee" of the corresponding power spectrum. An assessment of this effect will be shown later.

The power spectra for the wind shear case shown in Figure 7b indicate more power content in the horizontal components at low frequencies than the vertical component and less severe. The von Karman model can be made to fit reasonably well, especially for the vertical component. Appropriate integral scale values are in the range of 6000 ft for the horizontal components and 1000 ft for the vertical component.

The time histories for the rotor case shown in Figure 8a exhibit continual high-intensity, high-frequency turbulence and some long wavelength content is obviously included. The standard deviation,  $\sigma$ , for the vertical gust velocity component is 12.5 ft/sec--more than 50 percent greater than any other sample acquired. Acceleration increments of 1 g were equaled or exceeded 80 times in this traverse with maximum incremental accelerations of +2.2 g and -1.8 g.

The power spectra for the rotor case are shown in Figure 8b. It appears that an integral scale value of 6000 ft for the von Karman expression would approximate the spectra reasonably well.

Table 1 summarizes the four cases shown in Figures 5 through 8 with respect to altitude, length of run (in both time and miles), statistical degrees of freedom applicable for the power spectra, and values of standard deviation for the three gust velocity components.

The results of Figure 9 were obtained in an analytical study by Dr. William Mark of Bolt, Beranek, and Newman and provide "rule of thumb" guidance on the effects of intensity variation on the resulting power spectrum. Here,  $L_0$  is the spatial length of the sampling run for a linear increase and one half of the spatial length for an intensity burst, and  $L$  is the integral scale value of the turbulence. For the ratio of  $L_0/L$  greater than 10 to 13, the effect on the power spectrum is barely detectable whereas for ratios below 5 to 7 a strongly rounding effect will be present.

Figure 10 summarizes the approximate relative integral scale values for the four cases. Because the turbulence in the mountain wave case is not continuous, the use of power spectra for characterization is somewhat questionable.

The objectives of the sampling program with the additional probes at the wing tips are given on Figure 11. It is interesting to note that whereas the emphasis in the MAT program was on the low-frequency portion of the power spectrum, the emphasis here is at the higher frequencies.

The B-57B was again utilized as the sampling test bed. The aircraft was selected because of its rugged design, broad flight envelope, ease of flying, and availability (see Figure 12). The wing tip probes located 60 feet apart are mounted at locations designed to accept fuel pods.



Figure 13 (taken from Houbolt and Sen [14]) shows theoretical prediction of the cross-spectra for the same gust component a distance  $S$  apart, assuming homogeneous isotropic turbulence. The curves are for various ratios of  $S/L$  where  $L$  is the integral scale value. Note that for  $\sigma = S/L = 0$ , the curve would be a von Karman spectrum with a  $-5/3$  slope at higher frequencies. Flights are being made at low altitude where  $L$  is expected to be small and thus get an expected deviation from  $S/L = 0$ , and this region is appropriate since the spanwise effects are especially important for pilot workload in the terminal area.

Figure 14 shows some example time histories from the two wing tips and the centerline. While the general and long wavelength characteristics are similar, significant differences are evident in the mid and higher frequency region.

Figure 15a shows the auto-power spectra (APSD) for each wing tip with a fitted von Karman spectrum superimposed on the measured data. The  $L$  value from the fitted spectrum is used to provide the theoretical curve for cross-spectra (labeled CPSD) on Figure 15b. An example case of flight data is also shown. In this case the data deviate further from the prediction at the higher frequencies. The effects of filtering and data processing are presently under study.

Significant research and development efforts are under way in the remote sensing area. The use of Doppler radar and lidar (light detection and ranging) is encouraging. Some example data are shown in Figure 16 (from [21]) where power spectral estimates from ground-based lidar, in situ aircraft measurements, and tower measurements are shown. Lidar data are shown up to a frequency of 1 Hz; however, the agreement deteriorates above about 0.1 Hz. The authors of Reference [21] attribute this to a decrease in signal-to-noise ratio for the lidar data. The development and application of airborne units is expected to expand in the near future.

Figure 17 gives a summary of the NASA VG (velocity, vertical acceleration in g's) and VGH (velocity, vertical acceleration in g's, and pressure altitude) program. This program was a continuing effort to obtain pertinent statistical information on transport aircraft turbulence encounters. Recorders were installed on many aircraft over a 20-year period. From time history records of indicated airspeed, pressure altitude, and normal acceleration, peak values of derived gust velocity were determined. This program has been terminated, and the last report was published in 1977. A general aviation program was conducted in the 1960 to 1982 time period where various operation types were studied. Data were obtained for a total of 42,155 hours from 105 airplanes. Reporting is nearly complete.

The feasibility of utilizing data available from transport crash recorders to provide VGH-type information has been demonstrated and is outlined in Figure 18. In addition, an instrument has been developed that can record, store, and provide statistical data in a desired format. At the present time, there is no on-going activity in these areas.

Special analyses are being conducted of severe turbulence encounters utilizing data from on-board flight data recorders. A summary of these



analyses is given in Figure 19. The procedure, which is shown on Figure 20, involves applying measured inertial and air data to equations of motion with parametric values appropriate for the particular aircraft involved. The derived atmospheric disturbance data can then be installed on a simulator for study of response of various aircraft to that disturbance. Figure 20 gives a block diagram of the analysis procedure and lists cases of wide-body special severe encounters for which data are presently available.

Results to date for several high-altitude cases indicate that a strong shear layer has been destabilized either by storm passage or mountain waves. For these cases, the disturbance is not of continuous random nature but periodic large vortex flows.

To summarize the status of measurement of atmospheric turbulence, it appears that no new measurements for characterization of clear-air turbulence are being planned; however, measurements--perhaps with less severe requirements--are being made to support other atmospheric measurement programs. The VGH work is inactive; however, if funding were available, a new recorder could be utilized that would greatly simplify the process of converting the data to publication form. Remote sensing developments are expected to continue and results to date are encouraging. A better understanding of unexpected high-altitude encounters should result from incident studies utilizing on-board recorder information, and results from this, spanwise gradient measurements and others should lead to more realistic simulation work.

It is expected that turbulence measurements will continue to be made in the future to support further developments in forecasting, development of detection devices, and evaluate design techniques and the validation of gust alleviation systems.

## References

### **Measurement:**

1. Murrow, H. N.; and Rhyne, R. H.: The MAT Project--Atmospheric Turbulence Measurements with Emphasis on Long Wavelengths. Proceedings of the Sixth Conference on Aerospace and Aeronautical Meteorology of the American Meteorological Society, Nov. 1974, pp. 313-316.
2. Rhyne, R. H.; Murrow, H. N.; and Sidwell, K.: Atmospheric Turbulence Power Spectral Measurements to Long Wavelengths for Several Meteorological Conditions. Aircraft Safety and Operating Problems, NASA SP-416, 1976, pp. 271-286.
3. Murrow, H. N.; McCain, W. E.; and Rhyne, R. H.: Power Spectral Measurements of Clear-Air Turbulence to Long Wavelengths for Altitudes Up to 14000 Meters. NASA TP-1979, 1982.
4. Davis, R. E.; Champine, R. A.; and Ehernberger, L. J.: Meteorological and Operation Aspects of 46 Clear Air Turbulence Sampling Missions With an Instrumented B-57B Aircraft, Volume I--Program Summary. NASA TM-80044, 1979.

5. Waco, D. E.: Meteorological and Operational Aspects of 46 Clear Air Turbulence Sampling Missions With an Instrumented B-57B Aircraft, Volume II (Appendix C)--Turbulence Missions. NASA TM-80045, 1979.
6. Waco, D. E.: Mesoscale Wind and Temperature Fields Related to an Occurrence of Moderate Turbulence Measured in the Stratosphere Above Death Valley. *Mon. Weather Rev.*, 106(6):850-858, June 1978.

#### Modeling:

7. Reeves, P. M.; Campbell, G. S.; Ganzer, V. M.; and Joppa, R. G.: Development and Application of a Non-Gaussian Atmospheric Turbulence Model for Use in Flight Simulators. NASA CR-2451, Sept. 1974.
8. Sidwell, K.: A Mathematical Study of a Random Process Proposed as an Atmospheric Turbulence Model. NASA CR-145200, 1977.
9. Sidwell, K.: A Qualitative Assessment of a Random Process Proposed as Atmospheric Turbulence Model. NASA CR-145247, 1977.
10. Mark, W. D.; and Fischer, R. W.: Investigation of the Effects of Nonhomogeneous (or Nonstationary) Behavior on the Spectra of Atmospheric Turbulence. NASA CR-2745, 1976.
11. Mark, W. D.: Characterization of NonGaussian Atmospheric Turbulence for Prediction of Aircraft Response Statistics. NASA CR-2913, 1977.
12. Mark, W. D.; and Fischer, R. W.: Statistics of Some Atmospheric Turbulence Records Relevant to Aircraft Response Calculations. NASA CR-3464, 1981.
13. Mark, W. D.: Characterization, Parameter Estimation, and Aircraft Response Statistics of Atmospheric Turbulence. NASA CR-3463, 1981.

#### Spanwise Gradient:

14. Houbolt, C.; and Sen, A.: Cross-Spectral Functions Based on von Karman's Spectral Equation. NASA CR-2011, 1972.
15. Camp, D.; Campbell, W.; Frost, W.; Murrow, H.; and Painter, W.: NASA's B-57B Gust Gradient Program. *AIAA Journal of Aircraft*, 21(3):175-182, March 1984.
16. Campbell, W.; Camp, D. W.; and Frost, W.: An Analysis of Spanwise Gust Gradient Data. *Preprints: 9th Conference on Aerospace and Aeronautical Meteorology*, June 6-9, 1983, Omaha, Neb., p. 7.
17. Painter, W. D.; and Camp, D. W.: NASA B-57B Severe Storms Flight Program. NASA TM-B4921, 1983.

**VGH:**

18. Zalovcik, J. A.; Jewel, J. W., Jr.; and Morris, G. J.: Comparison of VGH Data from Wide-Body and Narrow-Body Long-Haul Turbine-Powered Transports. NASA TN D-8481, July 1977.
19. Jewel, J. W., Jr.: Tabulations of Recorded Gust and Maneuver Accelerations and Derived Gust Velocities for Airplanes in the NASA VGH General Aviation Program. NASA TM 84660, Sept. 1983.

**Special Encounters:**

20. Parks, E. K.; Wingrove, R. C.; Bach, R. E.; and Mehta, R. S.: Identification of Vortex-Induced Clear Air Turbulence Using Airline Flight Records. *AIAA Journal of Aircraft*, 22(2):124-129, Feb. 1985.

**Lidar:**

21. Frost, W.; Huang, K. H.; and Theon, J. S.: Comparison of Winds and Turbulence Measurement from Doppler Lidar and Instrumented Aircraft. Presented at the Third Topical Meeting on Coherent Laser Radar, Worcestershire, England, July 8-11, 1985.

**QUESTION:** George Treviño (Michigan Tech). I saw by your measurements that you had some different scale lengths for the longitudinal scales and the vertical scales (6000 ft versus 1000 ft). That to me would indicate a very strong anisotropy in the turbulence but yet you got some very good correlation with the theoretical isotropic von Karman spectra. How do explain that? Some of the data indicate a strong anisotropy but yet you do get correlation with an isotropic curve?

**ANSWER:** As I mentioned earlier, I think that comes about because of the very high power content at the very low frequencies which is down to where you have wind effects. The question is where does the turbulence end and the wind begin? The high power content can be seen in the horizontal components but not in the vertical components. That's true if you are talking about frequencies that go all the way down to those low values or out to those long wavelengths.

TABLE 1. Four Selected Cases.

Meteorological condition	Altitude, km (ft)	Run length		Statistical d. f. for power spectra	$\sigma_w'$ m/sec (ft/sec)	$\sigma_v'$ m/sec (ft/sec)	$\sigma_u'$ m/sec (ft/sec)
		min	km (miles)				
Convective	0.3 (1000)	19.1	148 (91.7)	45	1.15 (3.78)	1.18 (3.86)	1.35 (4.41)
Wind shear	13.0 (42600)	12.2	137 (85.1)	29	2.45 (8.05)	7.33 (24.04)	4.48 (14.70)
Rotor	3.9 (12800)	8.1	88.5 (55.0)	19	3.82 (12.52)	5.51 (18.09)	3.57 (11.73)
Mountain wave	14.3 (46800)	12.6	149 (92.4)	29	1.34 (4.41)	5.39 (17.69)	4.30 (14.11)

d. f. =  $f(\text{bandwidth, length})$

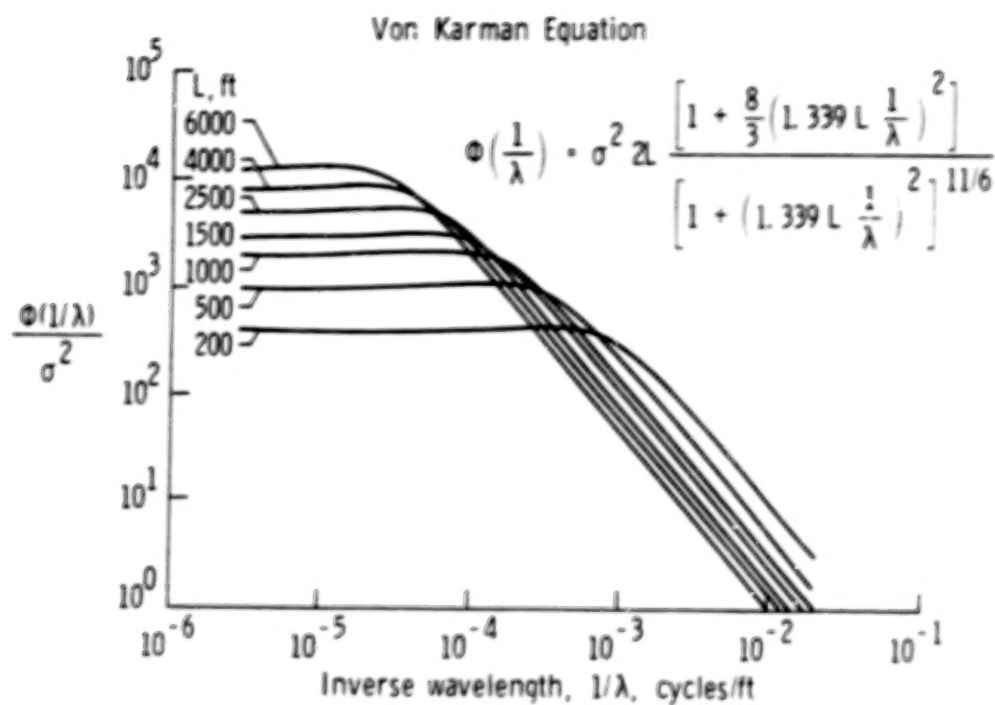


Figure 1. Theoretical transverse power spectra.

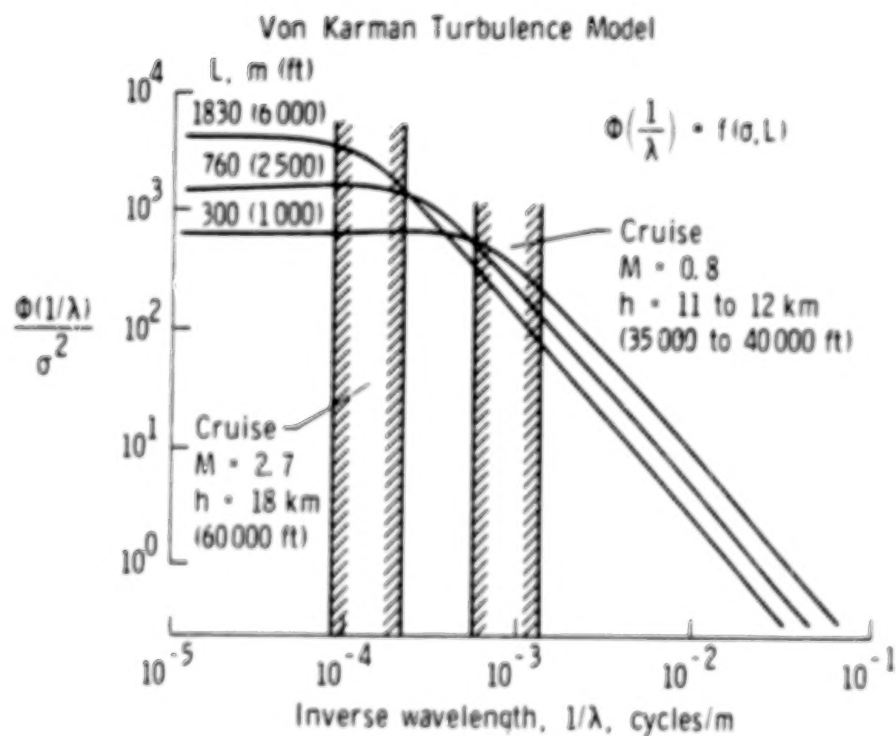


Figure 2. Theoretical power spectra.



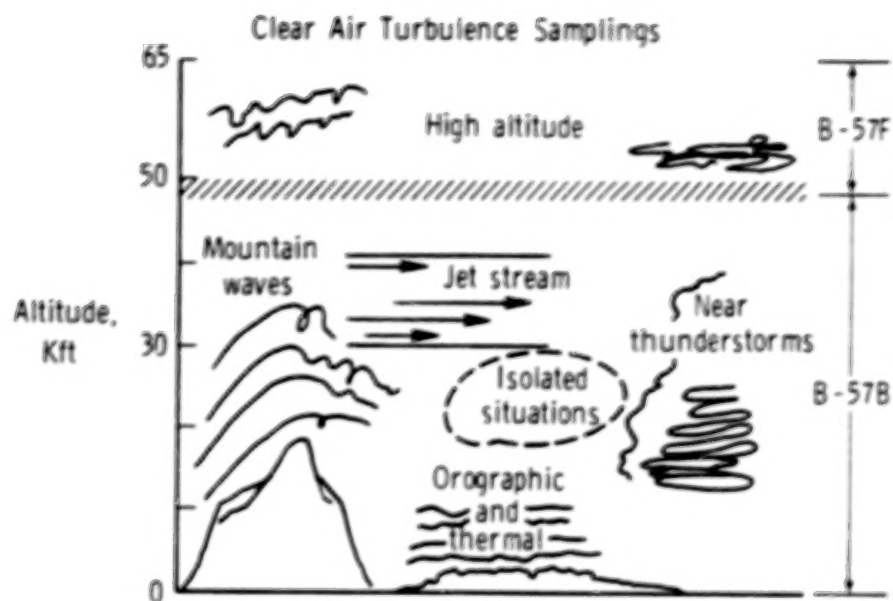
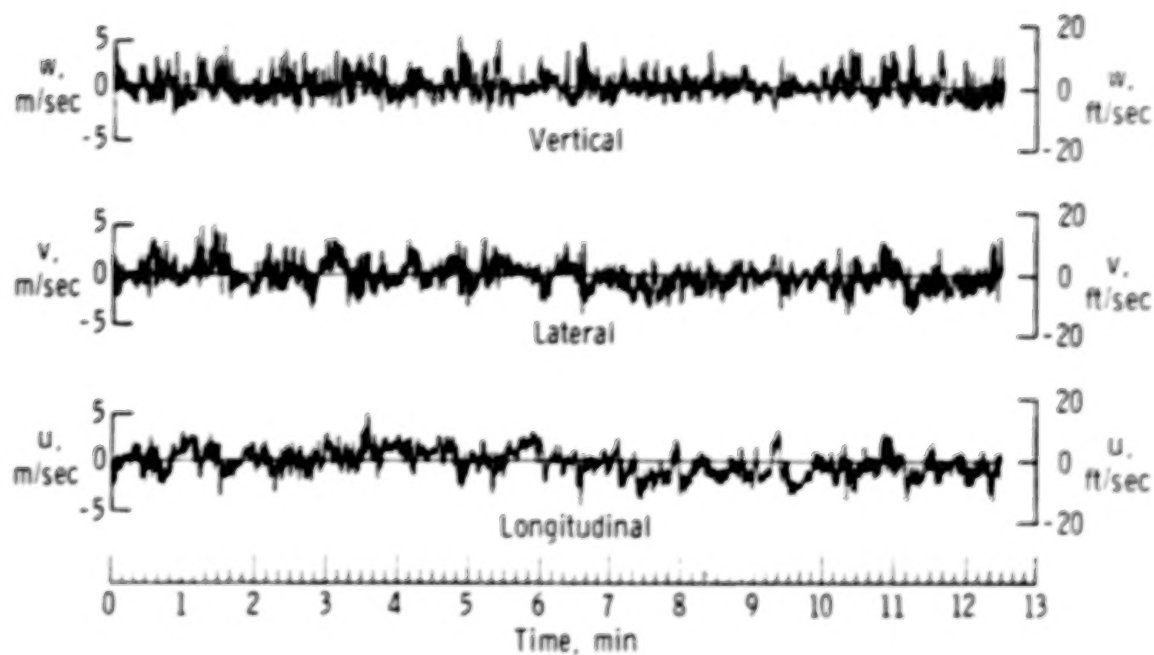


Figure 3. MAT project.

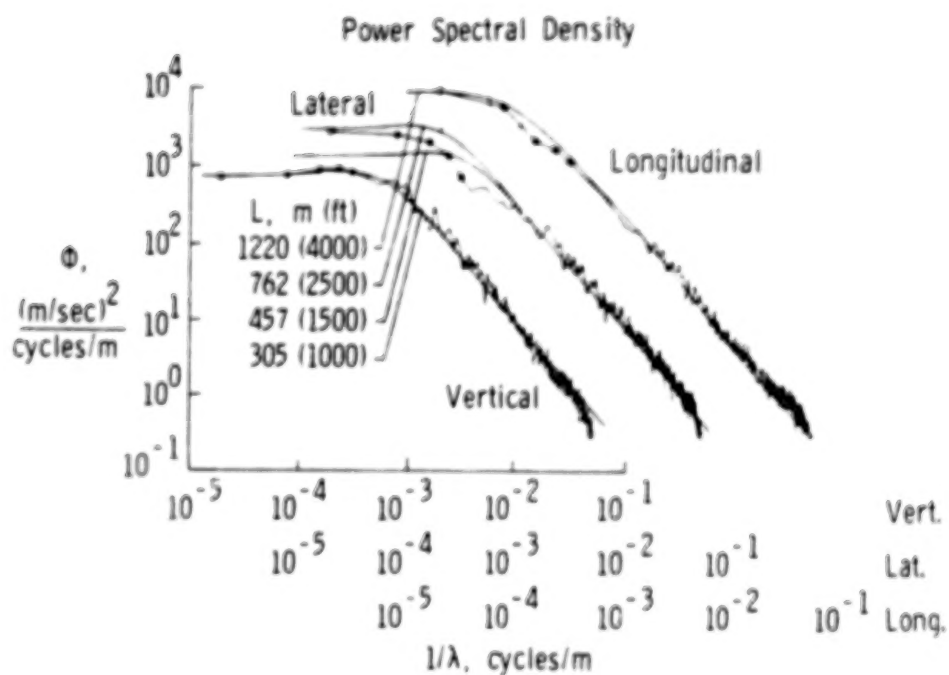
Gust velocity component	*	Primary measurement	+	Aircraft motion corrections
<u>Longitudinal</u>				
$u_g$	*	$[\Delta V]$	+	$[v_{ax} \sin \bar{\psi} + v_{ay} \cos \bar{\psi}]$
<u>Lateral</u>				
$v_g$	*	$[V\beta]$	+	$[-V\Delta\psi + v_{ax} \cos \bar{\psi} - v_{ay} \sin \bar{\psi} + l\dot{\psi} + V\alpha\phi]$
<u>Vertical</u>				
$w_g$	*	$[V\alpha]$	+	$[-V\theta + v_{az} + l\dot{\theta} - V\beta\phi]$

Figure 4. Equations for the determination of gust velocity component time histories.

# Turbulence Time History

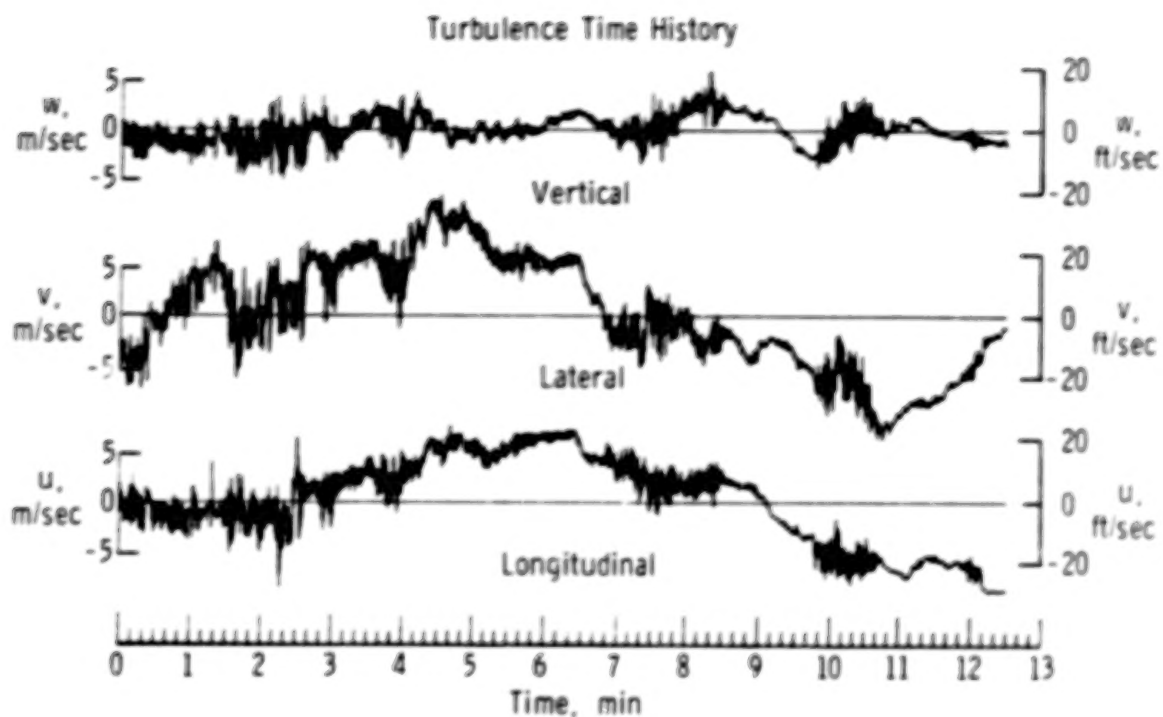


(a) Turbulence time history.

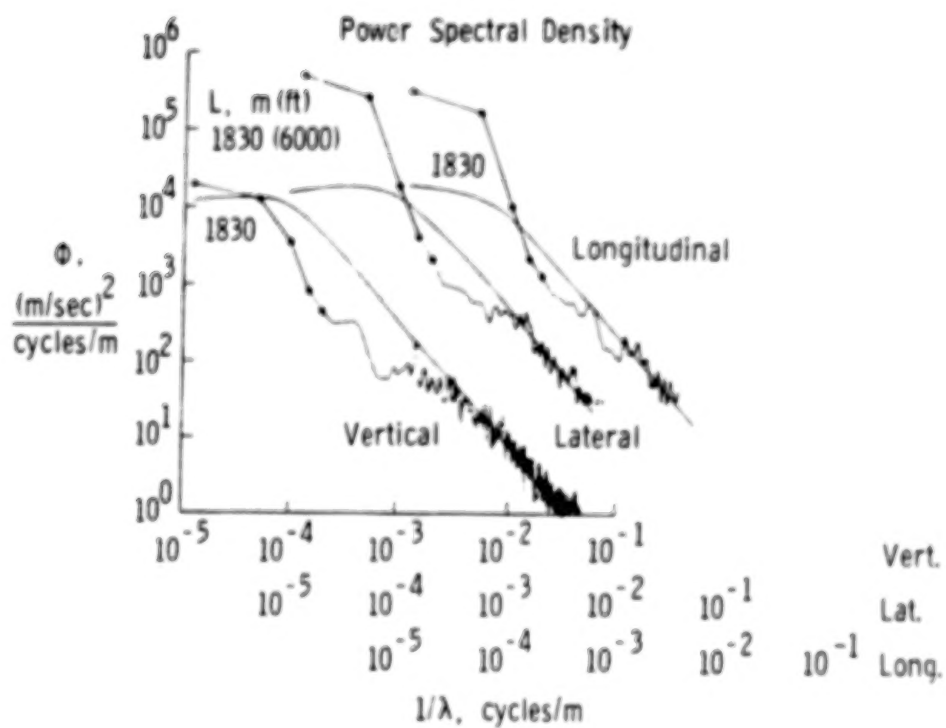


(b) Power spectral density.

Figure 5. Convective case.

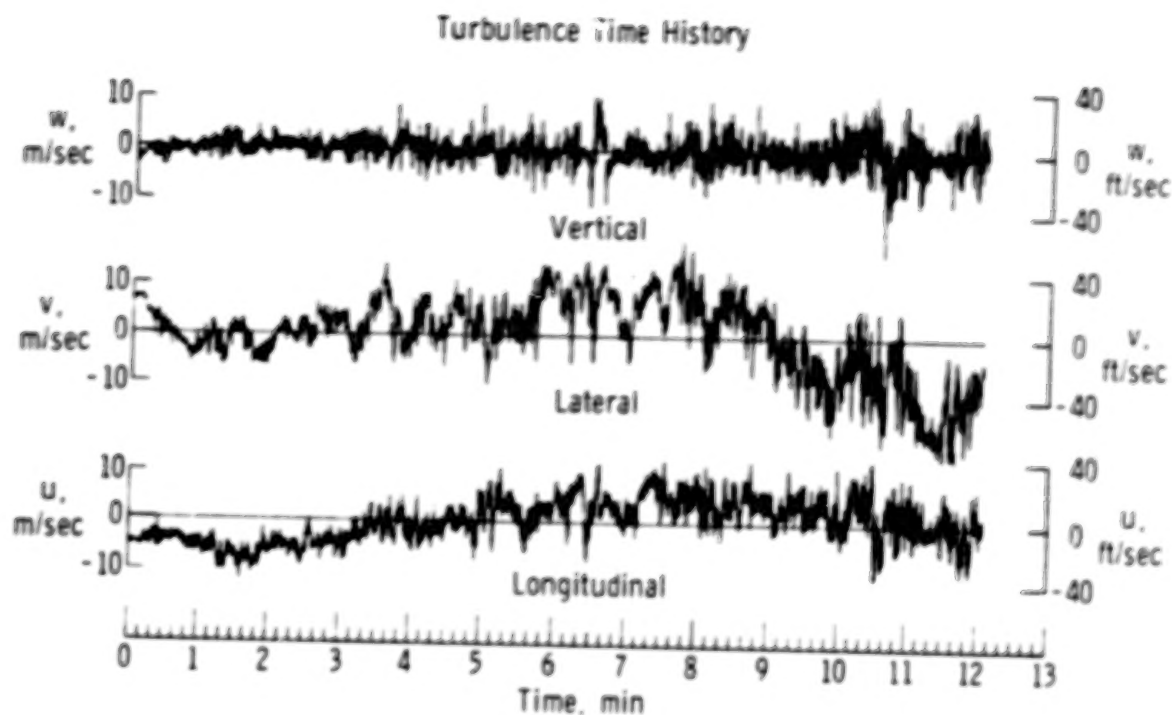


(a) Turbulence time history.

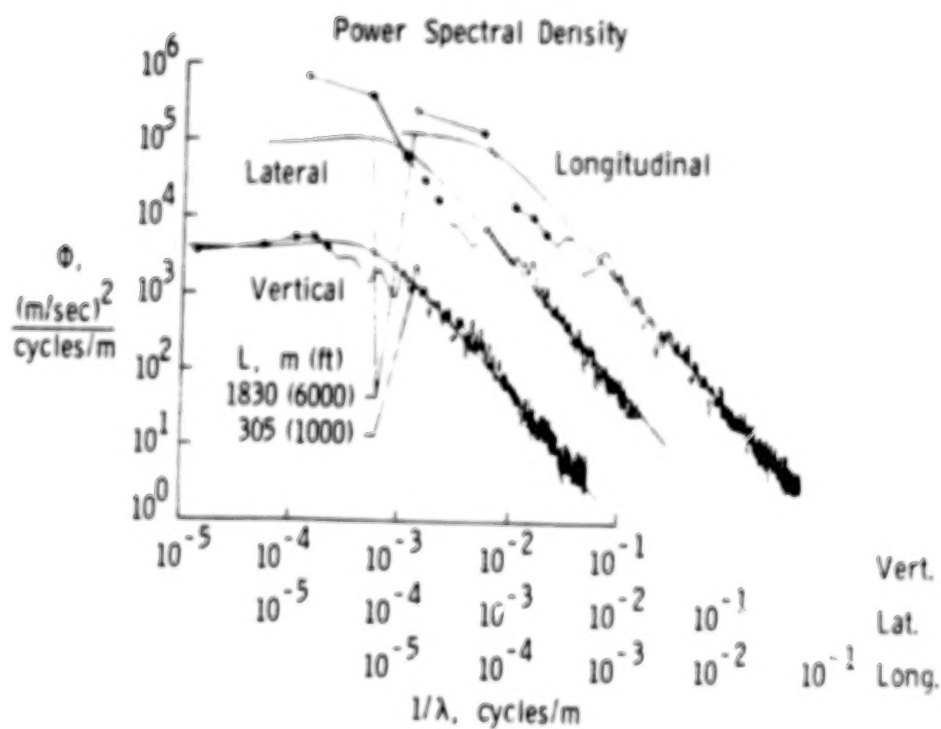


(b) Power spectral density.

Figure 6. Mountain wave case.

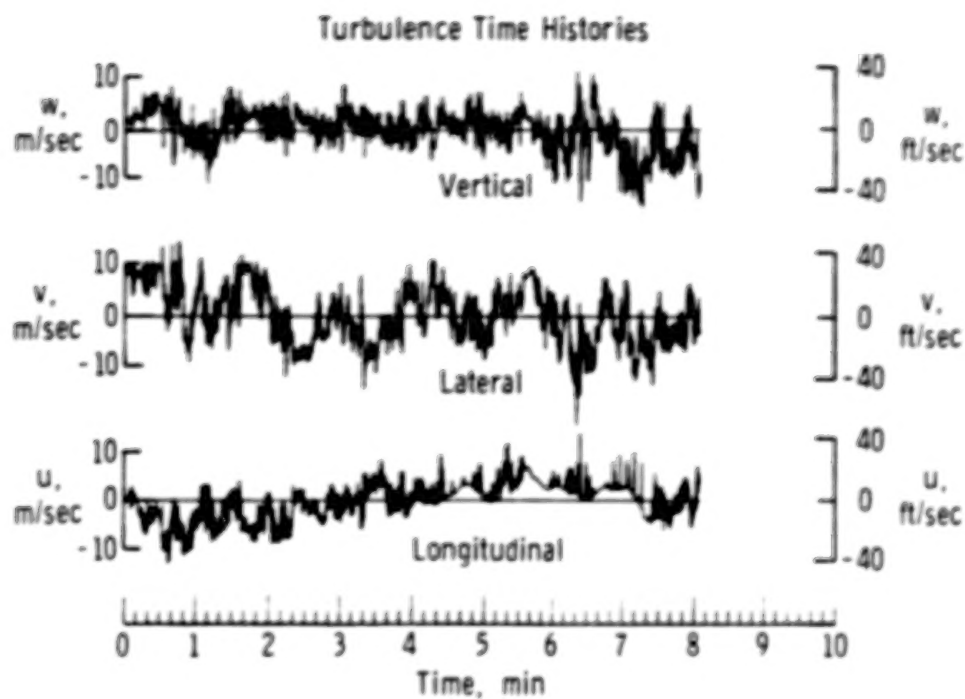


(a) Turbulence time history.

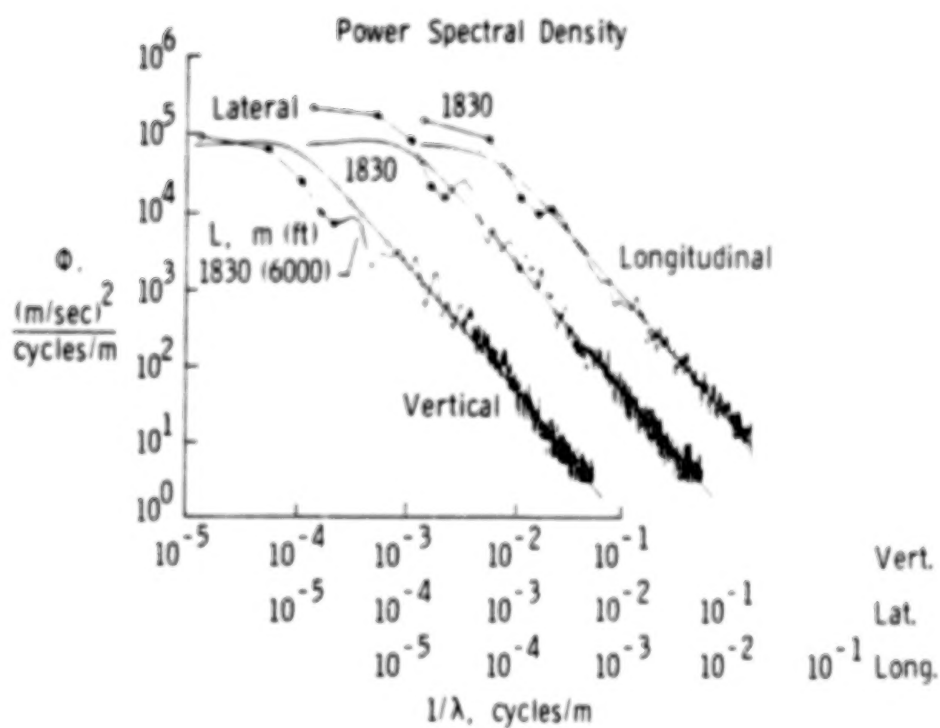


(b) Power spectral density.

Figure 7. High-altitude wind shear case.



(a) Turbulence time histories.



(b) Power spectral density.

Figure 8. Rotor case.

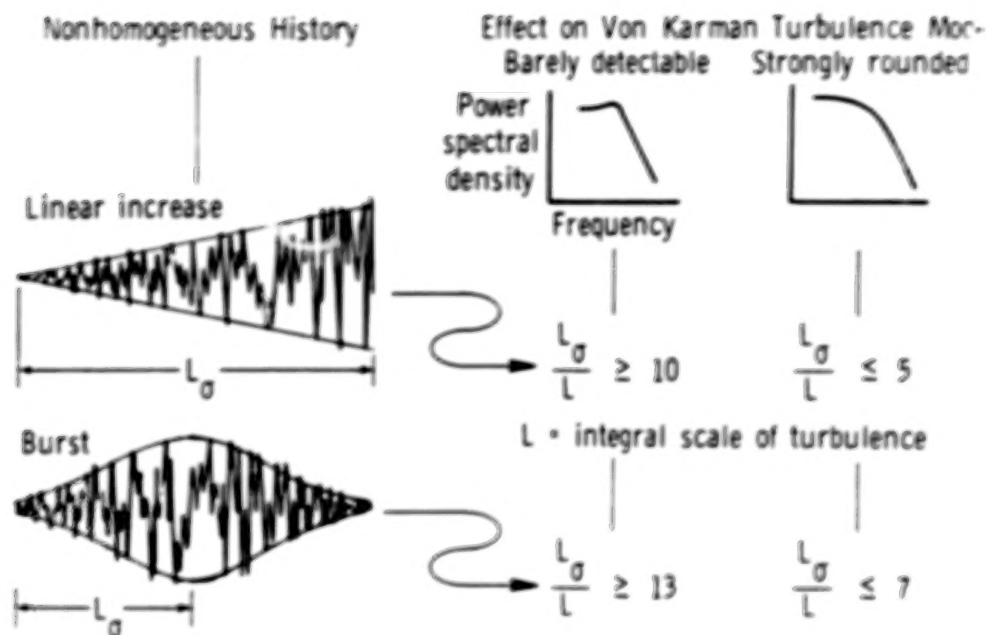


Figure 9. Effects of nonhomogeneous behavior on the power spectra of atmospheric turbulence.

- For wavelengths shorter than approx. 3000 ft, spectrum with  $-5/3$  slope is reasonable
- For wavelengths greater than 3000 ft, appropriate integral scale value is variable
- In general, vertical component  $L$  smaller than that for lateral and longitudinal components

$$L_{\text{vert}} \cong 1000 \text{ ft}$$

$$L_{\text{long, lat}} \cong 6000 \text{ ft}$$

- Mountain wave cases not continuous: spectral representation questionable

Figure 10. Assessment of integral scale value ( $L$ ).



Objective: Acquisition of in situ atmospheric turbulence data for correlation with analytical models, for use in simulations, and for comparison with data obtained from remote sensing techniques.

- Measure spanwise gust gradients applicable to terminal area operations
- Characterize wind shear, severe storm outflows and low altitude turbulence in utilitarian terms

Figure 11. Spanwise gradient (SPAN-MAT) research.

ORIGINAL PAGE IS  
OF POOR QUALITY



## TEST BED AIRPLANE

Figure 12. Test bed airplane.

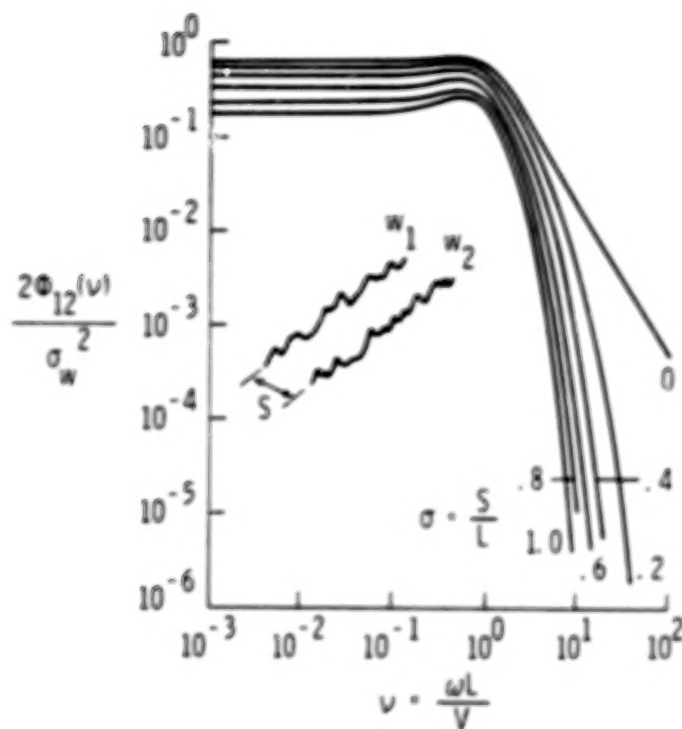


Figure 13. Cross-spectra for treatment of nonuniform spanwise gusts.

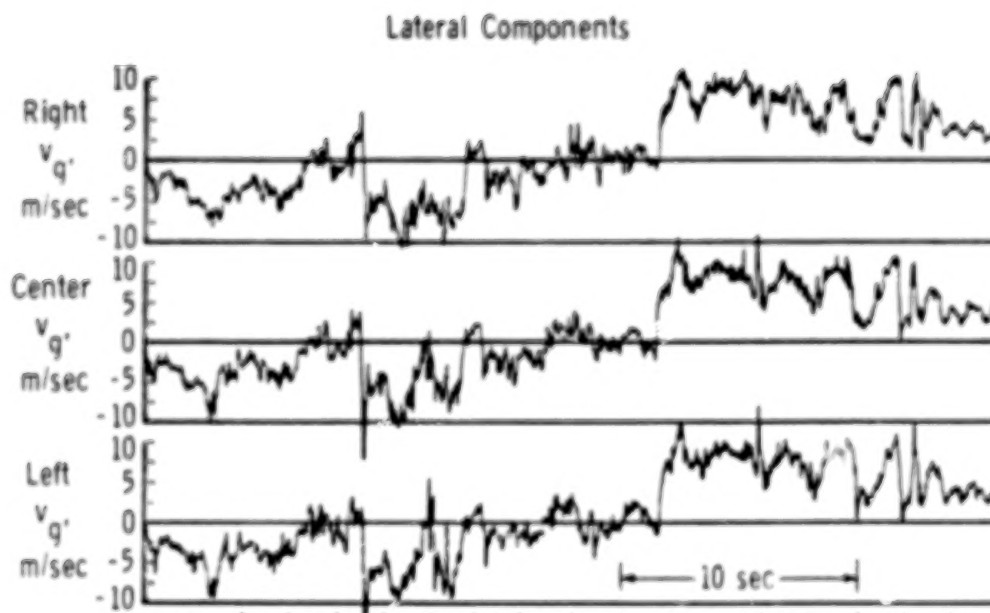


Figure 14.- SPAN-MAT gust velocity time histories.

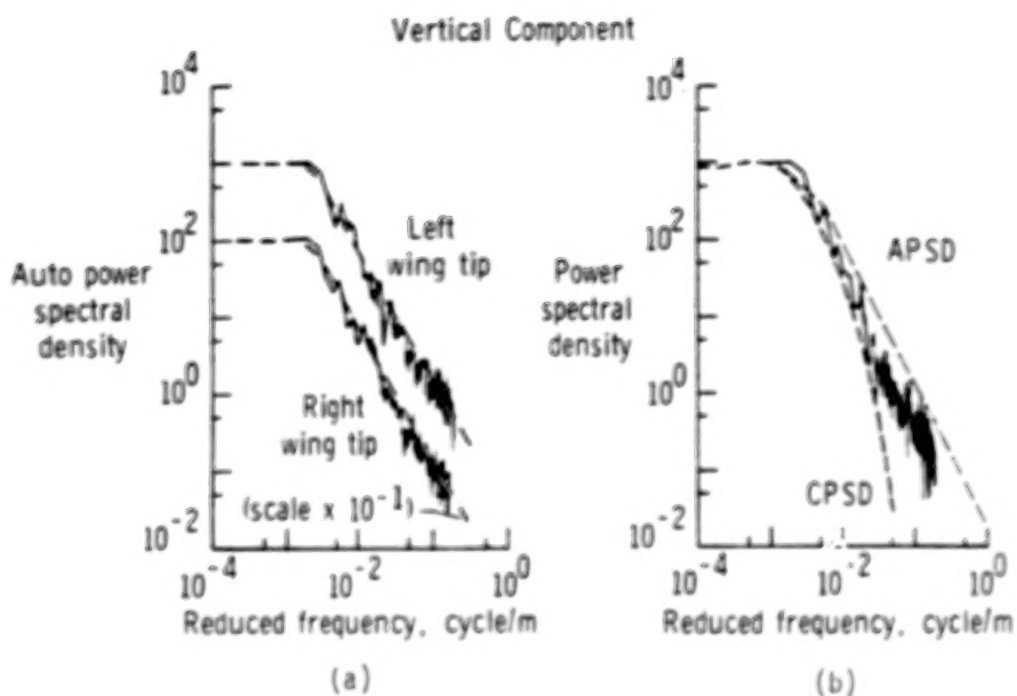


Figure 15. Gust velocity power spectra.

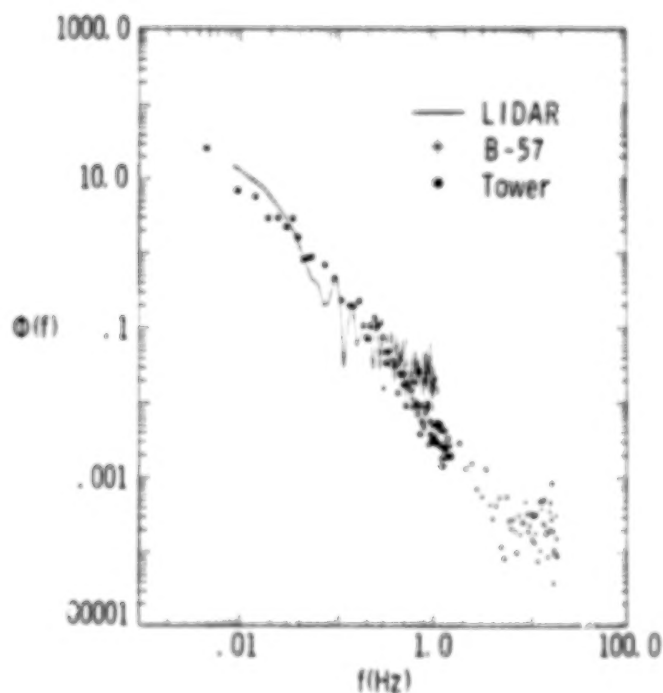


Figure 16. Comparison of ground-based and in situ measurements.

- On-board recorders provide time history records of indicated airspeed, pressure altitude, and normal acceleration
- Derived gust velocity,  $U_{DE}$ , computed for acceleration peaks
  - $U_{DE} = f(\text{normal accel., equivalent airspeed, lift curve slope, weight, wing area, and gust alleviation factor})$
- Recorders installed on numerous transport aircraft beginning in 1950's
  - Program terminated in early 1970's
  - Last report published 1977 on comparison of wide and narrow body long-haul turbine-powered transports
- General aviation program 1960-1982
  - Operation types included single- and twin-executive, personal, instructional, aerial applic., forest fighting, pipeline patrol, commercial fish-spotting, aerobatic, commuter, and float
  - Total of 42,155 hours of data collected from 105 airplanes

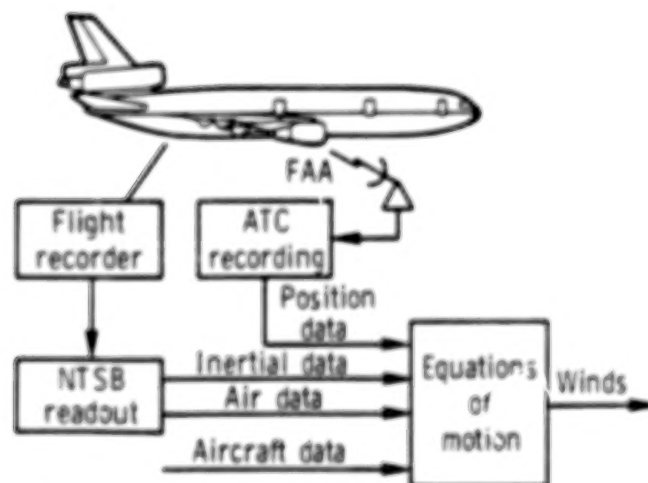
Figure 17. NASA VGH program.

- Feasibility of utilizing data available from transport crash recorders demonstrated
  - Data includes normal and lateral c.g. accel., indicated airspeed, pressure altitude, trailing edge flap and spoiler/drag brake position, and autopilot status
  - Data from wide body transports have been edited, processed and compiled (total of 2341 flights and 5067 hours flight time)
- Smart recorder
  - Instrument developed capable of recording, storing, and providing specified flight and ground data in desired format (statistical or time history)

Figure 18. Digital velocity, vertical acceleration in g's, and pressure altitude.

- Detailed analysis of encounters based on flight data recorders
  - Convert response data to atmospheric description
  - Correlation with meteorological phenomena
  - Establish model and install on simulator
  - Study response of different aircraft
- Study to date indicates that:
  - Strong shear layers destabilized by storm passage or mountain waves provide disturbance
  - Turbulence is not of random nature, but of periodic large vortex flow

Figure 19. Special clear-air turbulence encounters by commercial airliners.



- Eight cases available for analysis
  - All at altitudes between 33000 and 41000 ft
  - Occurrences in 1975, 1981, 1982, 1983(2) and 1985(3)
  - Locations from California to Greenland

Figure 20. Wide body airline accidents/incidents involving atmospheric disturbances at cruise altitudes.



N87  
22348  
UNCLAS

TURBULENCE AS OBSERVED BY CONCURRENT MEASUREMENTS MADE AT  
NSSL USING WEATHER RADAR, DOPPLER RADAR,  
DOPPLER LIDAR, AND AIRCRAFT

Jean T. Lee  
National Severe Storms Laboratory  
Norman, Oklahoma

ABSTRACT

As air traffic increases and aircraft capability increase as to range and operating altitude, the exposure to weather hazards increases. Turbulence and wind shears are two of the most important of these hazards that must be taken into account if safe flight operations are to be accomplished.

Beginning in the early 1960's, Project Rough Rider began thunderstorm investigations. This paper summarizes past and present efforts at the National Severe Storm Laboratory (NSSL) to measure these flight safety hazards and to describe the use of Doppler radar to detect and quantify these hazards. In particular, the evolution of the Doppler-measured radial velocity spectrum width and its applicability to the problem of safe flight is presented.

1. INTRODUCTION

Quantative data presentation and information assimilation are becoming increasingly important as Doppler radar evolves toward operational use by the weather services. Weather radar researchers have been faced with the development of techniques to identify and measure wind shear, vortices, and turbulence which constitute weather hazards to aviation. This paper summarizes past and present efforts at the NSSL in regards to weather hazards in convective cloud areas which can be encountered in aircraft operation.

2. BACKGROUND

Modern concepts of the internal structure of thunderstorms are developing mainly from multiple Doppler radar observations. Used in combinations of two or more, these radars now provide detailed portrayals of the precipitation-traced airflow in and beneath storm clouds and give new insights regarding the location of severe weather events. Furthermore, we can expect to see Doppler radar applications extended to include practical methods for measuring wind fields in optically clear air outside of storms for various altitudes [1]. The intensity of the radar return has been and still is used routinely by many to identify and track areas of heavy precipitation and hail (for examples see [2,3,4]), and operational tests have shown the great value of the radial velocity data in detecting mesocyclones and predicting tornadoes [5].

Thus, Doppler radar technology offers the unique opportunity to watch the complete development cycle of thunderstorms with a proven capability for

early detection of aviation hazards and other severe weather events, and a likely capability to anticipate the rapid intensification which precedes severity [6].

The rationale for developing new diagnostic procedures is that:

1. Warnings will depend on real-time detection of singular events which provide controllers with criteria for advising pilots where dangerous conditions exist, and
2. Forecasts of severe weather events will depend on pattern recognition techniques which will provide aviation meteorologists, pilots, and air traffic personnel with criteria for predicting the likelihood (and locations) of hazardous weather events for flight and control planning.

Computer software to produce both types of products quickly and accurately depend on research studies which: (1) Objectively define data requirements, and (2) establish relationships among reflectivity, radial mean velocity, and spectral width with known weather hazards. Although this has been done and tested for mesocyclones and tornadoes, and to some extent for heavy rain and hail, work remains to better define the boundaries for turbulence, dangerous shear, strong directional outflow (gust fronts), and microburst.

## 2. HISTORY

The thunderstorm project of 1946 and 1947 was the first systematic documentation of these hazards at flight levels below 25,000 ft. In the 1950's, United Air Lines conducted studies in conjunction with commercial flights over the midwestern United States. With the advent of commercial jet aircraft operations at altitudes to 40,000 ft and increased air traffic density, accidents, and incidents involving aircraft in the vicinity of thunderstorms it was determined that a greater understanding of the thunderstorm was required. While a simple detour of all convective storms is the easiest way to avoid the associated hazards, the economics of civil aviation operations and non-combat military flights require a minimum disruption of service while safety is not compromised. Since the early 1960's, a cooperative research program involving the Federal Aviation Administration (FAA), National Aeronautics and Space Administration (NASA), U.S. Air Force (USAF), National Research Council (NRC) of Canada, the Royal Aircraft Establishment (RAE) at Bedford, England, and NSSL of the National Oceanographic and Atmospheric Administration (NOAA) has been in operation in Oklahoma. From 1960 to 1982 aircraft made controlled flights into thunderstorms of varying intensities (Figure 1) in order to determine the distribution of the hazards and their possible correlation with observations made by indirect probes such as weather radar and later with Doppler weather radar and lidars. In fact, we now recognize that radar correctly used and interpreted provides the best method known to date to improve the safety of flight near thunderstorms.

### 3. TURBULENCE

In the pre-Doppler era, over 500 penetrations of thunderstorms were made above 20,000 ft and a representative sample was obtained. In a second phase following the completion of the first phase, aircraft flights were confined to lower altitudes to obtain a sufficient sample size.

All aircraft were instrumented to measure and record the time, duration, and magnitude of the turbulence encountered during flight as well as other pertinent flight parameters. From these readings, derived gust velocities were calculated. The derived gust velocities are proportional to the change in acceleration ( $\Delta N$ ). The aircraft were tracked by the radar at Norman, and the position of the aircraft and the thunderstorm echo displayed on a Plan Position Indicator (PPI) scope were photographically recorded (Figure 2).

It was found early in the flight program that reflectivities of  $10^5 \text{ mm}^6\text{m}^{-3}$  (50 dBZ) were often associated with 3/4-inch diameter hail or layers [7], sizes that cause damage to an aircraft. Therefore, areas of indicated hail were avoided, and it may be possible that the gust velocities in these areas ( $Z_e$  values  $\geq 10^5 \text{ mm}^6\text{m}^{-3}$ ) exceed those measured outside of the area. Figures 3 and 4 are graphs of the distance from the center of the storm core when encounters of turbulence having derived gust velocities equal to or greater than  $20 \text{ ft sec}^{-1}$  were recorded. Storms of greater intensity were associated with greater gust velocities and with greater distances of significant turbulence from storm centers [8]. If one considers the average diameter of a severe thunderstorm to be 10 to 15 miles--a radius of 5 to 7.5 miles--it is apparent that severe turbulence can be encountered even near the edge of the visible cloud.

I would like to quote one conclusion from a report\* by the National Research Council of Canada on flights conducted in Oklahoma:

The results of this experiment are considered extremely important from an operational standpoint. It has been shown that at lower levels around squall lines and thunderstorms the return from weather radar provides insufficient information for avoidance of moderate and often severe turbulence, unless the aircraft is maneuvered in such a way as to avoid all radar echo by well over five miles. The intensity of turbulence encountered at this distance lends support to the view that echoes should be avoided by at least 10 miles and possibly more.

This view of turbulence differs from that of hail; the latter is closely related to echo intensity in a particular area because hailstones are themselves strong radar targets. At this time in our research we think of a thunderstorm system as a cluster of cells. The maximum radar reflectivity of which is an indicator of overall storm intensity, with the overall intensity determining the probability of hazardous turbulence, and the location of hail specifically indicated by the strong echo centers.

The two sampling phases (high and low altitude) produced similar statistics (Figure 5) which can be interpreted as meaning that turbulence

\*G. K. Mather and D. S. Treddenick: Turbulence Measurements at Low Levels Around Squall Lines, National Research Council of Canada Aeronautical Report LR-515, 1969.



encounters vary little with altitude. These sample penetrations also showed that turbulence could be related to radar reflectivity only in the broadest sense and that such a measure as reflectivity gradient was not the answer and, in fact, could be very misleading.

The next major stride was made when Doppler radar was applied to observe meteorological phenomena. Doppler radar offers the highest potential for further defining turbulence because turbulence is known to be related kinematically to features that are best measured remotely with a Doppler radar.

#### 4. DOPPLER RADAR AND TURBULENCE

The NSSL staff began a series of experiments in 1973 using the Doppler radar in place of the conventional WSR-57 weather radar to study weather hazards to aviation. These joint experiments involved the USAF, FAA, NASA, Colorado State University, University of Oklahoma, and various NOAA components. Penetration aircraft (F-4-C, F-101, F-100, and F-106) suitably equipped to make in situ wind and turbulence measurements, were used simultaneously with the Doppler radar.

One of the first experiments used the Plan Shear Indicator (PSI) developed by the USAF Cambridge Research Laboratory (now known as the Air Force Geophysical Laboratory (AFGL)); this device graphically depicts radial shear [9] (Figure 6).

Moderate or severe turbulence was encountered in all cases when the PSI displayed shear along the aircraft flight path, but shear was not indicated with all turbulence encounters, and it appears from these cases that moderate or less turbulence (derived gust velocities ( $U_{de}$ )  $\leq 9.1 \text{ ms}^{-1}$ ) may escape detection by the PSI. This is not surprising since only the wind's radial component is measured by radar. Where severe turbulence ( $U_{de} > 9.1 \text{ ms}^{-1}$ ) repeatedly was encountered, the PSI showed transient shear areas along the flight path. Arc deformations apparently have an operational detectability threshold associated with wind shears  $\geq 1.5 \times 10^{-2} \text{ s}^{-1}$ .

In 1974, a second-generation radar real-time display was developed at NSSL. The three spectral moments were presented as a field of arrows shown by a minicomputer-graphic display terminal interfaced to the NSSL Doppler radar [10]. Arrow length is proportional to the logarithm of received power, arrow direction displacement from a horizontal position is proportional to velocity (similar to a speedometer indicator) and the arrowhead size to Doppler spectrum width (Figure 7).

Using the new display for real-time analysis, we directed USAF Aeronautical System Command F-4-C aircraft in a number of thunderstorm penetrations, and successfully located areas where the aircraft experienced turbulence. In post-analysis, the data were searched for significant correlations between turbulence, radar reflectivity, and velocity data. Figure 8 is a time history of aircraft-recorded turbulence and Doppler velocity spectrum width along the flight path. Note how well the turbulence

trend matches the trend in the spectrum width plot. A total of 45 such penetrations were analyzed; all show a similar relationship. During the 45 penetrations, there were 76 occurrences of moderate or greater turbulence. Ninety-five percent had spectrum widths of  $4.0 \text{ ms}^{-1}$  or greater [11]. There will be non-turbulent areas where the spectral width is large because the spectral width may be biased by wind shear and beam broadening [12]. However, in two tornadic storms studied, the cumulative probability for the spectrum width to be  $\geq 4 \text{ ms}^{-1}$  due to all factors is only about 30 percent [13]. For non-severe storms the probability is even less; thus, only a small portion of even a severe storm will have "false alarm" values.

In another set of experiments analyzed by Bohne [14], a correlation of 0.89 was obtained between the curves showing turbulence measured by aircraft and radar along a flight path. More importantly, for higher turbulence levels, which pose a greater flight hazard, the agreement between radar measurements and the turbulence actually experienced by the aircraft was nearly total. Other experiments have led to similar conclusions [15]. Judging from available information, it appears that a spectrum width threshold of  $4 \text{ ms}^{-1}$  may be associated with the onset of flight discomfort and  $6 \text{ ms}^{-1}$  with potential hazard. The Next Generation Radar (NEXRAD) is expected to estimate Doppler spectrum widths with an accuracy of  $1 \text{ ms}^{-1}$  down to a signal-to-noise ratio (SNR) of 5 dB [16]. For a radar of the NEXRAD type, this means that good estimates of spectrum width (turbulence) can be obtained out to the maximum range of 230 km even with very light precipitation, of the order of  $0.3 \text{ mm hr}^{-1}$ .

Aircraft penetration studies have further shown that extreme turbulence may occur as far as 20 nautical miles (36 km) from the edge of the radar contour of the center of severe thunderstorm clouds, and the FAA advises pilots to avoid all thunderstorms by a margin at least equal to this distance [17]. This is a safe procedure to follow in relatively uncrowded airspace. In airplanes with heavy traffic, however, it is desirable to keep detours to a minimum. NEXRAD can help in this content in two main ways. First, since it can accurately sense precipitation and turbulence, it can better define the boundaries of thunderstorms. Thus, uncertainties due to imprecise edge definition will be minimized. Second, unlike present operational weather and ATC radars which scan the azimuth with fixed antenna elevations, NEXRAD will scan its surrounding space at several elevation angles providing a three-dimensional picture of storms. Thus, flights well above the tops of thunderstorms may not have to be disturbed.

In addition, turbulence appears to be nearly isotropic and therefore independent of viewing angle. Figure 9 shows a comparison of the spectrum widths in a storm being observed by both Norman and Cimarron radars which are separated by more than 40 km. We have looked at several storms with four to six elevations per case and have found essentially the same result. This also tends to substantiate the findings of isotropicity in the turbulence data gathered during earlier penetration flights.

We have also looked at comparing Doppler-radar-measured turbulence with that measured by Doppler lidar and by a 444 m (1500 ft) instrumented KTVY-TV tower. Figure 10 shows the agreement in wind speed and direction and Figure



11 the comparison of the standard deviations (turbulence) of the horizontal velocity fluctuations [18]. The variances of the  $u$  and  $v$  components were computed for each lidar- and radar-estimated vector wind field and combined to find  $\sigma_T = (\sigma_u^2 + \sigma_v^2)^{1/2}$ , the standard deviation of the horizontal velocity fluctuations. The total variance is taken as being composed of the errors due to velocity estimates and that due to turbulence and small-scale flows. It can be seen that the horizontal velocity fluctuations measured by the three different systems is in remarkable agreement.

It also appears that turbulent areas in a storm are not randomly distributed (Figure 12). Figures 13 and 14 show how a NEXRAD algorithm of turbulence and a smoothing integration produces turbulent areas (volumes) which can be tracked in time and space thus making the output valuable for the aviation community.

Wind shear such as seen in gust fronts and downbursts are also amenable to Doppler radar use in their detection. However, there remains to be accomplished the numerical modeling of these features to determine if their formation, movement, and intensification (or decay) can be accurately predicted and this is the area in which NSSL is now engaged.

## 5. SUMMARY

Turbulence, wind shear, microburst, and hail are amenable to observation by Doppler radar. Techniques to obtain the information and present the probabilities of encounter in an effective manner is a goal of the NEXRAD system. Emphasis at NSSL has now shifted from aircraft in situ measurements to the corresponding remote sensor observation and the modeling of these hazards for use in the NEXRAD environment and in aircraft operations.

## 6. REFERENCES

1. Berger, M. I.; and Doviak, R. J.: An Analysis of the Clear Air Planetary Boundary Layer Wind Synthesized from NSSL's Dual Doppler Radar Data. NOAA Technical Memo. ERL NSSL-87, 1979, 55 pp.
2. Zittel, W. D.: Evaluation of a Remote Weather Radar Display, Vol. II Computer Applications for Storm Tracking and Warning. FAA Report No. FAA-RD-75-60, 1976, 114 pp.
3. Elvander, R. C.: An Evaluation of the Relative Performance of Three Weather Radar Echo Forecasting Techniques. *Preprints: 17th Radar Meteorology Conference*, Seattle, Washington, 1976. American Meteorological Society, pp. 526-532.
4. Bjerkaas, C. L.; and Donaldson, R. J.: Real Time Tornado Warning Utilizing Doppler Velocities from a Color Display. *Preprints: 18th Radar Meteorology Conference*, Atlanta, Ga., 1978. American Meteorological Society, pp. 449-452.

5. National Oceanographic and Atmospheric Administration (NOAA): Final Report on the Joint Doppler Operational Project (JDOP) 1976-1978. NOAA Technical Memo. ERL NSSL-87, 1979, 84 pp.
6. Lemon, L. R.: New Severe Thunderstorm Radar Identification Techniques and Warning Criteria: A Preliminary Report. NOAA Technical Memo. NWS NSSFC-1, 1977, 58 pp.
7. Foster, D. C.: Aviation Hail Problems. Technical Note 37, World Meteorological Organization, Geneva, Switzerland, 1961, 160 pp.
8. Lee, J. T.; and Carpenter, D.: 1973-1977 Rough Rider Turbulence-Radar Intensity Study, Final Report. FAA Report No. FAA-RD-78-115, 1979, 22 pp.
9. Armstrong, G.; and Donaldson, R., Jr.: Plan Shear Indicator for Real-Time Doppler Radar Identification of Hazardous Storm Winds. *Journal of Applied Meteorology*, 8:376-383, 1969.
10. Burgess, D. W.; Hennington, L.; Doviak, R. J.; and Ray, P. S.: Multimoment Doppler Display for Severe Storm Identification. *Journal of Applied Meteorology*, 15:1302-1306, 1976.
11. Lee, J. T.: Applications of Doppler Weather Radar to Turbulence Measurements Which Affect Aircraft. FAA Report No. FAA-RD-77-145, 1977, 45 pp.
12. Zrnic, D. S.: Spectral Moment Estimates from Correlated Pulse Pairs. *IEEE Transactions: Aerospace and Electronics Systems*, AES-13, 1977, pp. 344-354.
13. Doviak, R. J.; Sirmans, D.; Zrnic, D.; and Walker, G. B.: Considerations for Pulse-Doppler Radar Observations of Severe Thunderstorms. *Journal of Applied Meteorology*, 17:189-205, 1978.
14. Bohne, A. R.: Radar Detection of Turbulence in Precipitation Environments. *Journal of Atmospheric Sciences*, 39:1819, 1982.
15. Zrnic, D. S.; and Lee, J. T.: Pulsed Doppler Radar Detects Weather Hazards to Aviation. *Journal of Aircraft*, 19:183, Feb. 1982.
16. National Oceanographic and Atmospheric Administration (NOAA): "NEXRAD Technical Requirements" in NEXRAD Request for Proposal SA-82-TPB-0010. U.S. Dept. of Commerce, NOAA/NWS, Aug. 1981.
17. FAA Academy: Weather and Flying Safety--Chapter 6: Thunderstorms. Mike Monroney Aeronautical Center Training Guide, Nov. 1981.
18. Eilts, M. D.; Doviak, R. J.; and Sundara-Rajan, A.: Comparison of Winds, Waves, and Turbulence as Observed by Airborne Lidar, Ground-Based Radars, and Instrumented Towers. *Radio Science*, 19(6):1511-1522, Nov.-Dec. 1984.

**QUESTION:** Walter Frost (FWG Associates). I noticed in one of your plots that you compare intensities using  $\sigma_u^2 + \sigma_v^2$ . Do you always compare turbulence intensities in that fashion or do you ever compare individual radial components of turbulence intensities?

**ANSWER:** No we use various approaches. We compare individual radial components of the Doppler radar, lidar, and tower.

**FROST:** When you are comparing tower lidar and Doppler data for the NASA tests, how did you collocate those sigmas?

**LEE:** What we did was to place these data on a grid using the Taylor hypothesis to move the tower data downwind into a location being sampled by aircraft, Doppler lidar, and Doppler radar. We did some of the early experiments with the aircraft flying right down the Doppler radar radial in the vicinity of the tower. But we did not do the experiments that were done at Huntsville. Most of our data are located on a grid matrix (0.5 km size). Lidar measurements are approximately at 500 m spacing, the Doppler radar depth is 150 m, which was averaged to 0.5 km, and, of course, in range you have a spreading out of the beam so that we felt our grid size was obtained at 0.5 km grid both vertically and horizontally at about 40 km from NSSL. The comparisons were made using those grid values.

**QUESTION:** Mike Tomlinson (Air Weather Service). In putting together the information you have on precipitation and then adding the Doppler spectral width and turbulence, have you tried to correlate those locations with the lightning detection systems? There is some marketing going on that says lightning information can infer turbulence information. And I'm wondering if you had an opportunity to validate or invalidate that theory.

**ANSWER:** We were unable to determine the relationship between lightning and turbulence. All the research studies that have been conducted in our area and in other areas indicate that there is very little in the way of correlation. Similarly, the correlation of lightning and the severity of the storm is not apparent. We have had tornadic storms in which the lightning activity has been very light. We've had extremely heavy electrical activity in storms and have had no surface manifestations of any severe weather, neither heavy rain, hail, nor high winds. We are continuing research at NSSL. We do have the radars, we have three different lightning locating systems that we are working with, the LLP, the LPAT, and one which has a very high-frequency response so that we can actually watch the strokes develop. We are trying to find out where the lightning develops. Using the dual-Doppler system to monitor the storm buildup, we are attempting to find out what flow patterns cause the separation which then ends with a discharge. But right now we see no correlation; in fact, there almost seems to be a negative correlation between the activity and turbulence--if NASA's research is an indication of all systems. I have no reason to doubt that this is not true. When an aircraft flies where there is active lightning, its flight is relatively smooth. If it goes through another area where there is hardly any lightning, the aircraft may trigger the lightning.

**QUESTION:** Creighton Pendarvis (SimuFlite). I've enjoyed your presentation and found it most enlightening. I'm interested in your last statement that you are now able to keep an aircraft out of a hail shaft and also out of destructive turbulence. Is there any air traffic control (ATC) facility in this country at this time that you know that has the same capability?

**ANSWER:** No. The NEXRAD radar system is planned for the contract to be awarded in October 1986. Their prototype radar is to be installed at Norman by March 1987. The first production radar will come in the Oklahoma City area in 1988, and then by 1989 or 1990, other units will be distributed across the United States. The Doppler radars are coming; they will be installed. A main problem, of course, in the algorithm development and interpretation, is still going to be troublesome. I think there is still going to have to be a man in the loop.

**QUESTION:** C. M. Tchen (City College of New York). I am interested to know whether you see a difference in the spectral density without the rain and with the rain on the same site?

**ANSWER:** No, we do not see the difference in convective systems we have studied. In other words we do not see any affect of rain in the layers where data were obtained.

**TCHEN:** The theory on the two-phase turbulence where the droplets are suspended predicts a broadening of the  $k^{-1}$  spectral distribution by the precipitation in confirmation with the Russian laser experiments. Have you measured the spectral distributions in your experiments?

**LEE:** Yes. It may be that if we look specifically for that effect, we might find it.

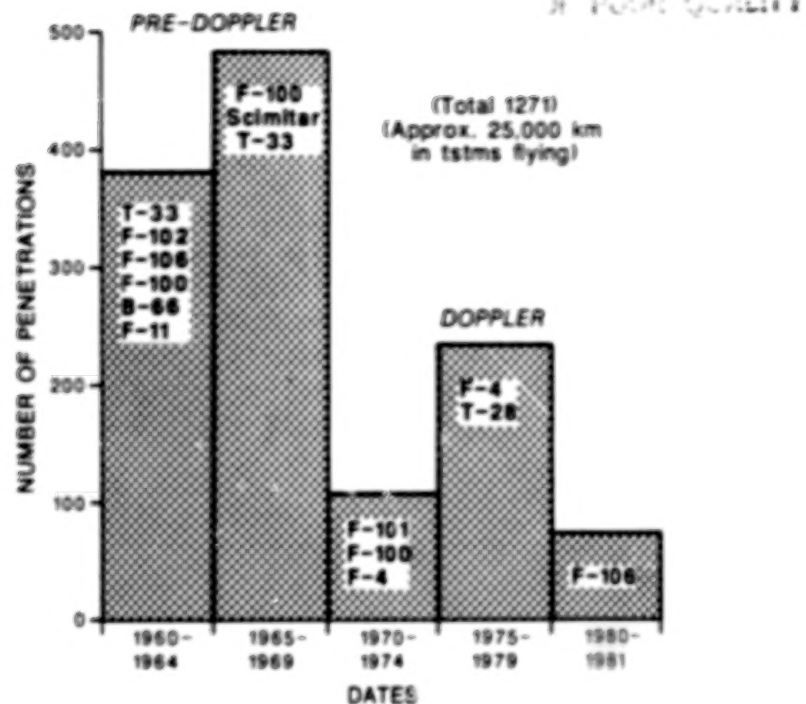


Figure 1. Number of thunderstorm penetrations made in Project Rough Rider 1960-1982 along with aircraft used in the data acquisition. Reduced numbers in 1970-1974 are results of no penetrations in 1970-1972 when emphasis was shifted to over thunderstorm flying using U-2 and RB-57F aircraft. In 1973 Doppler radar came into use and penetrations were once more initiated.

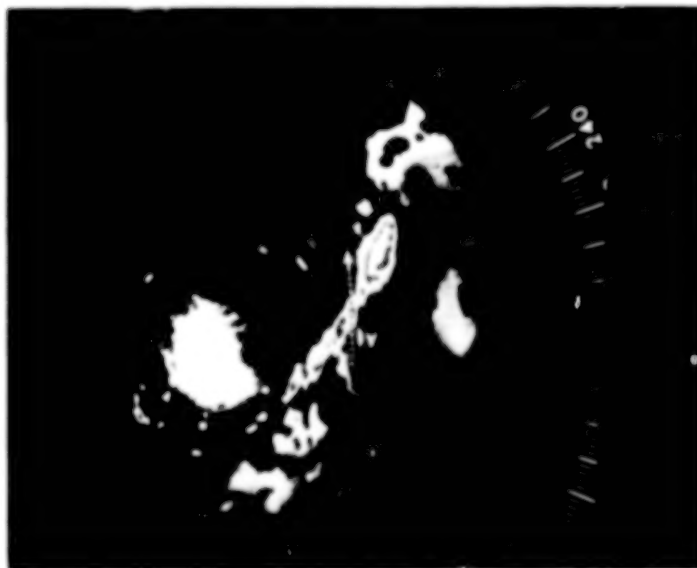


Figure 2. 16 June 1973 WSR-57 weather radar reflectivity iso-echo contour display with aircraft transponder beacons superimposed. Point "A" is the beacon return from the F-100 at 1357:25 CST; the dotted line indicates aircraft path. Range marks at 40 km intervals.



STORMS OF $Z_{e,max} = 10^3$		OCCURRENCE RELATIVE TO DISTANCE FROM STORM CORE (NM)						
WHEN $U_{10}$ EQUALS:	AND ALT IS:	TOTAL NUMBER OF OCCURRENCES = 170						
		0-5	6-10	11-15	16-20	21-25	26-30	30+
$\geq 20 < 35$ FT/SEC	10-19	27(7)	4(4)	5(3)	4(1)			
	20-29	72	25	2				
	30+	7(2)	6(2)	5(1)				
$\geq 35 < 50$ FT/SEC	10-19	1(1)						
	20-29	4(4)						
	30+	3(1)						
$\geq 50$ FT/SEC								
	10-19							
	20-29							
	30+							

NUMBER OF PENETRATIONS		
AT	20-34	13
10-19	35-49	4
(15)	50+	-
	20-34	28
20-29	35-49	4
(28)	50+	-
	25-34	5
30+	35-49	4
(5)	50+	-

Figure 3. Distance from storm core with maximum reflectivity of  $Z_e = 10^3$  to  $0.9 \times 10^3 \text{ mm}^6 \text{ m}^{-3}$  (30 dBZ). Turbulence is shown in three categories. Each turbulence category has penetrations divided into three altitude bands. The first indicates the number of separate occurrences while the number in parentheses indicates the number of penetrations. The occurrences are shown as a function of distance to core.



STORMS OF  $Z_{max} \geq 10^5$

WHEN  $U_{max}$  EQUALS:

OCCURRENCE RELATIVE TO DISTANCE FROM STORM CORE (NM)		TOTAL NUMBER OF OCCURRENCES = 343						
		ALTITUDE K FT.	0-5	6-10	11-15	16-20	21-25	26-30
$\geq 20 < 35$ FT/SEC	10-19				1 (1)			
	20-29	66 (7)	3 (2)	2 (1)	1 (1)			
	$\geq 30$	140 (13)	70 (12)	19 (5)	13 (1)			
$\geq 35 < 50$ FT/SEC	10-19				1 (1)			
	20-29	7 (2)						
	$\geq 30$	10 (4)	3 (1)	2 (2)				
$\geq 50$ FT/SEC	10-19							
	20-29	2 (2)						
	$\geq 30$	3 (2)	1 (1)					

NUMBER OF PENETRATIONS	
AT 10-19	20-35 +
(1)	20-35 11
20-29	35-50 3
(11)	50+ 2
	20-35 35
30+	35-50 7
(35)	50+ 3

Figure 4. Distance from storm core with maximum reflectivity of  $10^5 \text{ mm}^6 \text{m}^{-3}$  or more ( $\geq 50$  dBZ). Turbulence is shown in three categories. Each turbulence category has penetrations divided into three altitude bands. The first indicates the number of separate occurrences while the number in parentheses indicates the number of penetrations. The occurrences are shown as a function of distance to core.

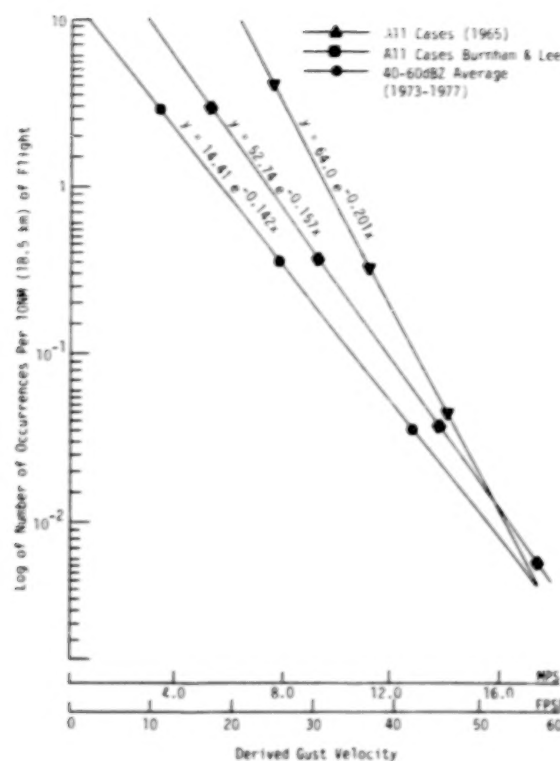


Figure 5. Frequency of turbulence encounters observed 1973-1977, as compared to observations made during the mid-1960's. Equations are exponential corresponding to the least-squares best fit for the data shown.

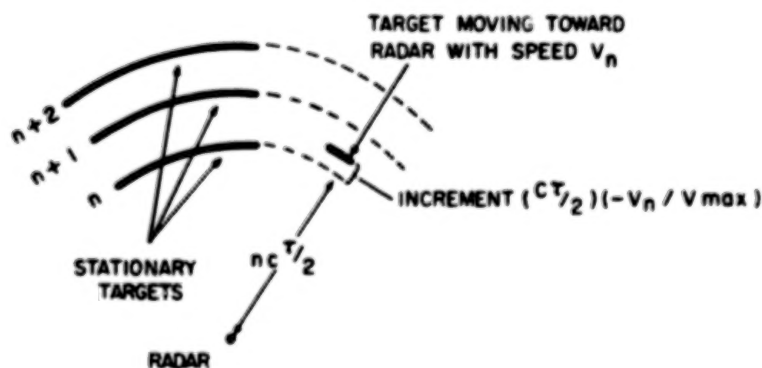


Figure 6. PSI display for stationary targets (left) and a moving target (right). The moving target is located at the same distance from the radar as the nearest stationary target ( $n$ ) but is displaced from it on the PSI display by an increment proportional to its velocity.

ORIGINAL PAGE IS  
OF POOR QUALITY

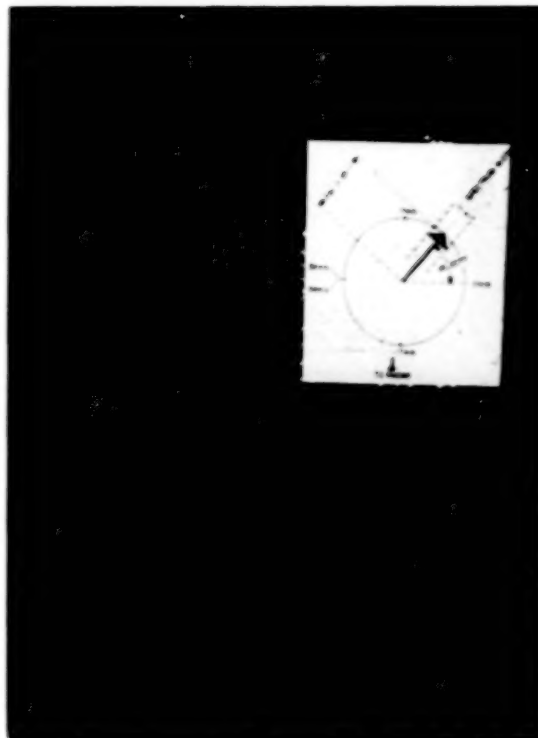


Figure 7. The multi-moment Doppler display of a mesocyclone. Each arrow contains information of the three principal Doppler spectrum moments for a resolution volume. For interpretation of arrows see insert in upper right corner (arrow length is proportional to received power, arrow direction to velocity and arrowhead size to Doppler spectrum width). Abscissa is azimuth and ordinate scale denotes range (km) from radar. Housekeeping information is at top of screen.

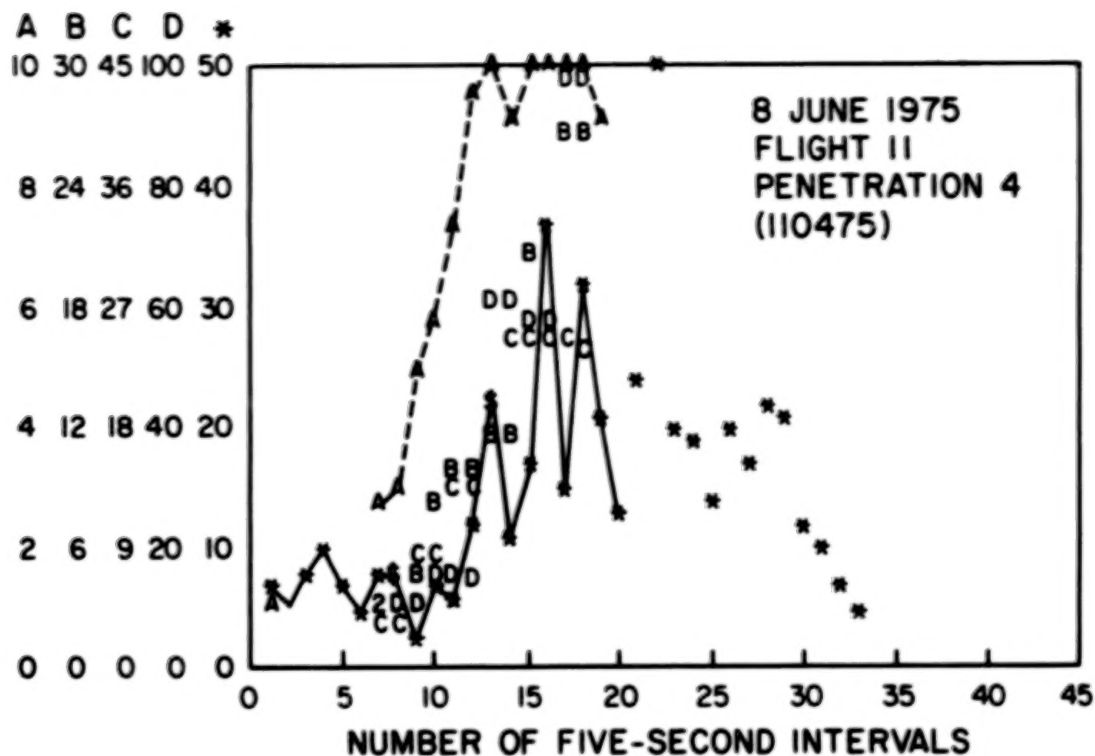


Figure 8. 8 June 1975 penetration number 4: Time (space) cross section for maximum values recorded for each five seconds of flight and corresponding Doppler radar data during penetration. Derived gust velocities in ft-l; spectrum width (A's) in ms-l; velocity gradient (B) in 1000 x s-l; Laplacian is "D." A number indicates the number of collocated data points. Dashed line connects values of spectrum width and solid line the derived gust velocities.

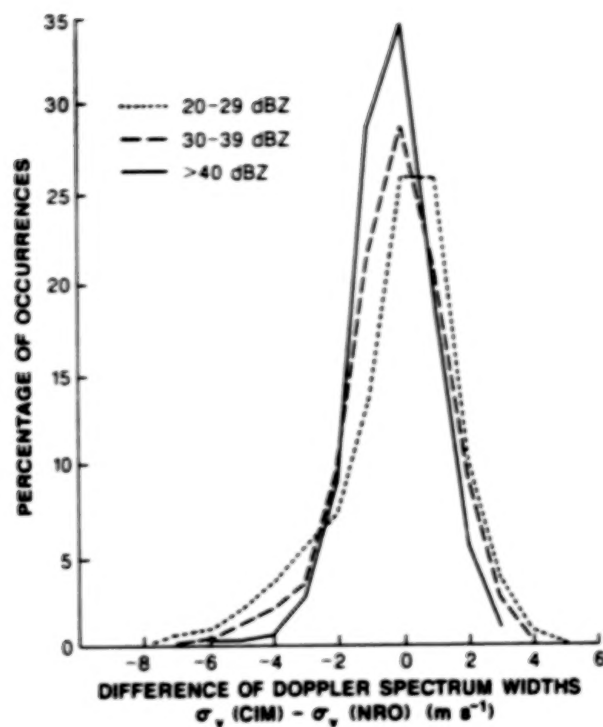
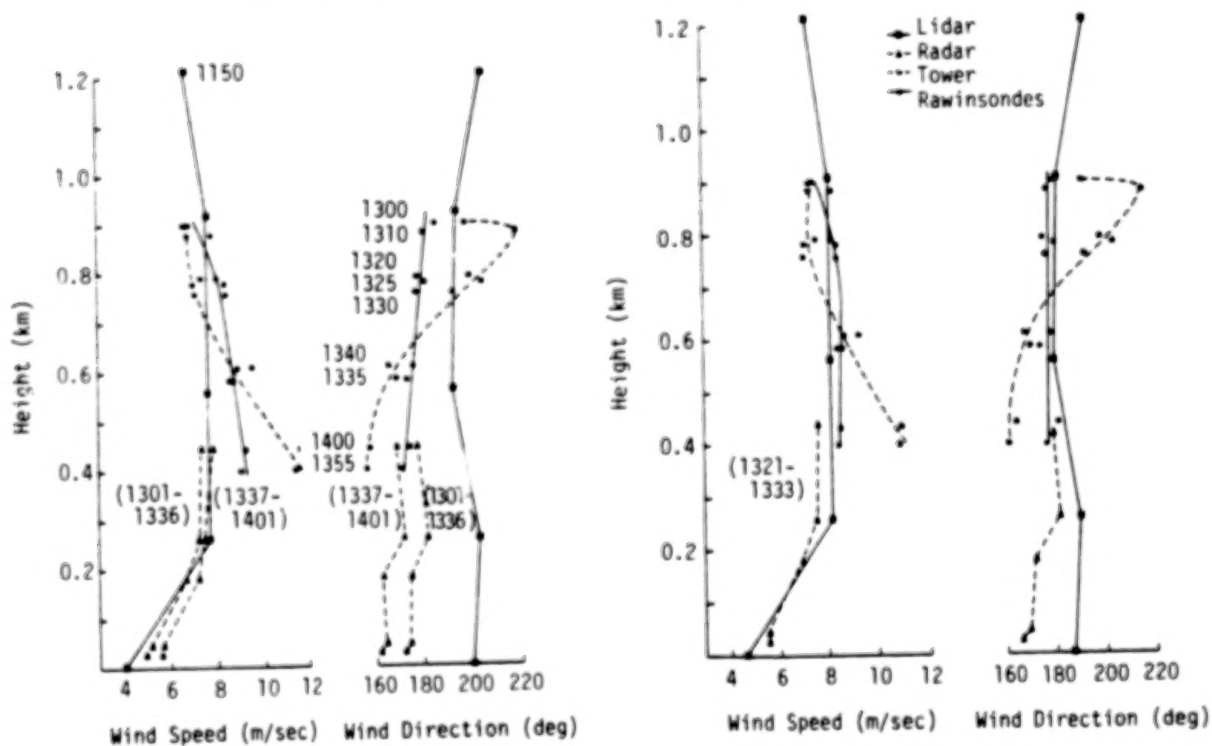


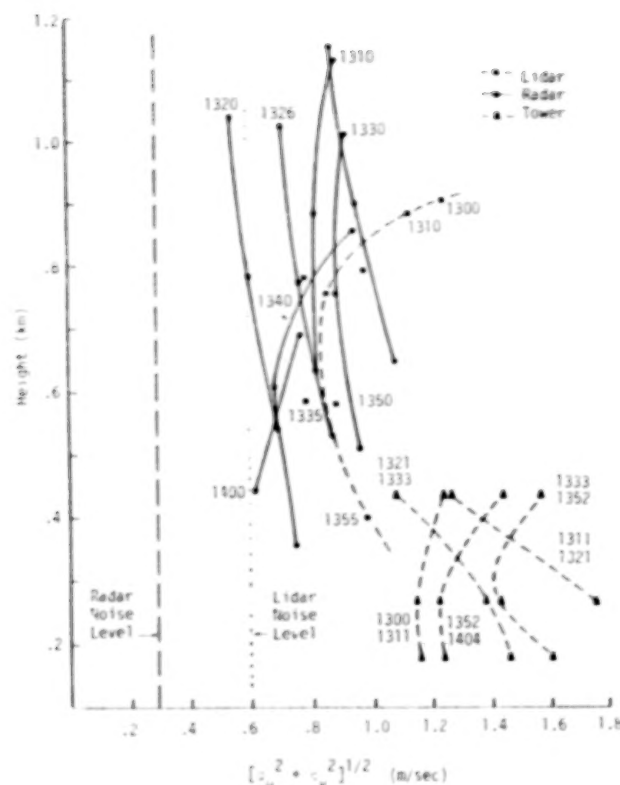
Figure 9. Comparison of spectrum widths obtained by two Doppler radars for various areas of reflectivity.



(a) Wind profiles measured by lidar, radar, tower, and rawinsondes

(b) Wind profiles measured by lidar, radar, tower, and rawinsondes adjusted to remove a time trend relative to 1330 CST. The tower profile was constructed from a 12-minute average of data from 1321-1333 CST.

Figure 10. Comparison of wind profiles.



ORIGINAL PAGE IS  
OF POOR QUALITY

Figure 11. Standard deviation of the horizontal velocity fluctuations from lidar, radar, and tower.

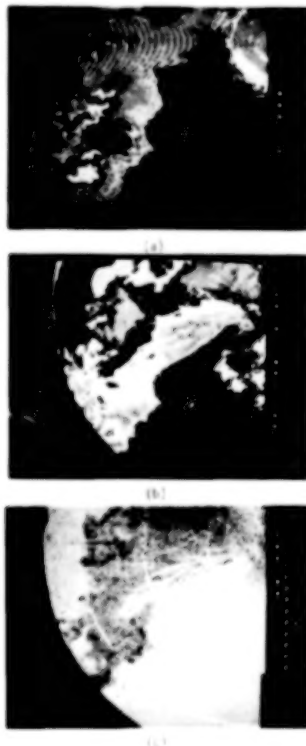


Figure 12. Doppler radar display of (a) reflectivity, (b) velocity, and (c) spectrum width of a storm south of NSSL. Note displacement of the position of areas of maximum reflectivity, maximum velocities, and maximum spectrum widths relative to each other.



ORIGINAL PAGE IS  
OF POOR QUALITY

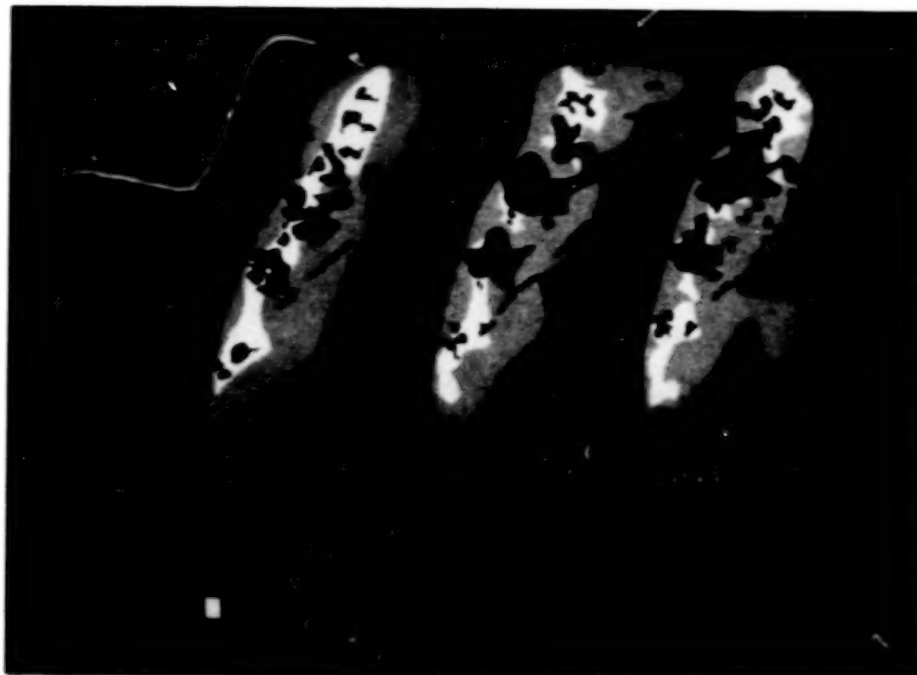


Figure 13. Storm hazard proposed NEXRAD display showing the use of a smoothing algorithm to delineate the hazard. Note time continuity of the hazards.

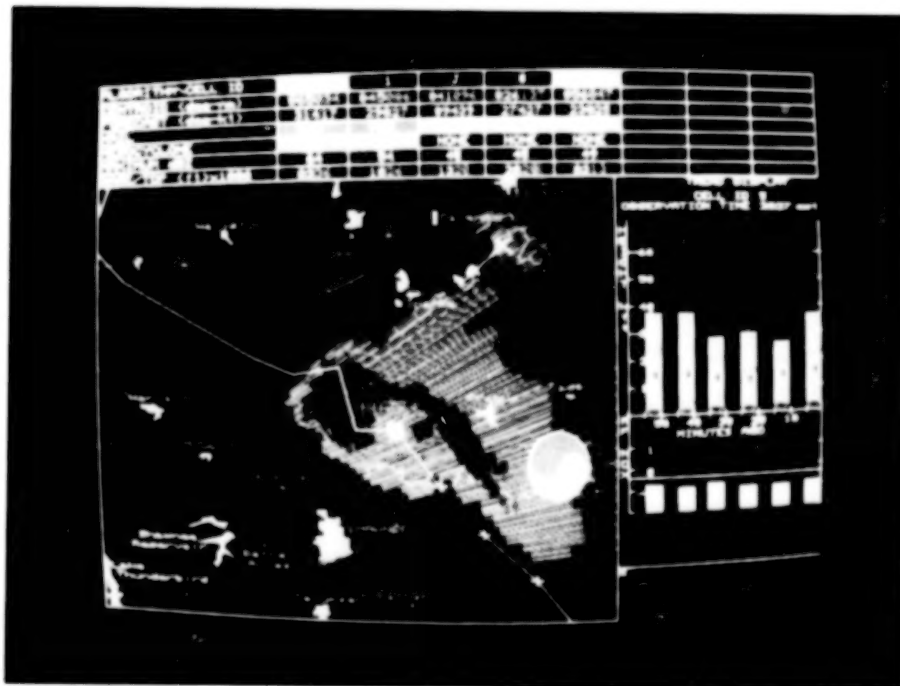


Figure 14. A second proposed type of NEXRAD display under development to provide pertinent information for a forecaster.

N87

22349

UNCLAS

## CAT-GENERATING MECHANISMS

Morton G. Wurtele  
UCLA  
Los Angeles, California

I'll begin with these three areas:

1. Development of instability configurations
2. The transition from unstable growth of these configurations into turbulence and a description of the nature of that turbulence
3. The question of decay of turbulence and one of the most controversial topics, the existence of what is called "fossil turbulence."

People involved in design and simulation want simple descriptions of turbulence that exists in the atmosphere and oceans, in these "clear-air" conditions. That description is not going to be forthcoming at this time. There are going to be all sorts of characteristics of these turbulent states. And, I might add, that it is amusing that the oceanographers have the advantage of us here. They are able to get in there and measure these things better than we can in the atmosphere now, when it comes to accurate measurements. And you want to keep your eye on what they are doing because a lot of the information that we gain is going to come from them.

As far as the existence of unstable configurations goes, of course, the vortex sheet has been known to be unstable for more than a century, but the first actual computation, beyond the simple fact of instability, was that of Rosenhead [1] in 1931 where he represented the vortex sheet as a sum of a lot of little vortices (Figure 1), each of which is acting on the others. And, of course, the vortex sheet is an equilibrium configuration until it is disturbed, and then the little vortices tend to move each other until it winds up in this familiar way. A lot of the literature refers to instability and/or wave breaking. These are very confusing terms really because this type of situation could conceivably be called a wave breaking. The next one (Figure 2) has totally different dynamics, namely, a wave on the surface of the ocean. Here is a laboratory wave breaking in the surface of water (Figure 2a). The dotted line is Longuet-Higgins' analytic solution to the problem [2]. Figure 2b is a picture from a surfing magazine which Longuet-Higgins picked up and fit his theoretical profile precisely to the pictured profile [3].

We are in a position to understand both of the mechanisms illustrated in Figure 2, even though they are quite different. The second one (Figure 2b) is so familiar, of course--the degeneration of that instability into a turbulent flow on the beach--that it may be surprising how little it has been studied. There are many pictures such as Figure 3 that depict the configuration of these roll-up type vortices in the atmosphere which have usually been visualized by cloud patterns [4]. This one is just off the coast of California. The atmosphere is known to have density differences like the water wave and vorticity in the basic flow like that studied by Rosenhead [1],

but in both of these cases the atmosphere has the variable continuously distributed, rather than concentrated either in a vortex sheet or an interface between the fluids of different densities. Attempts at simulation have been made in the laboratory. Figure 4 is an early example of the fact that, if one takes high resolution rather than the characteristic radiosonde resolution, one can identify layers of low Richardson number in an overall stable layer [5]. In this case, the resolution is only 400 m and the Richardson number varies over four orders of magnitude and, of course, it can go to infinity as the shear goes to zero. This has been well known. We do not know exactly how these fine layers come about, but we can expect to find them.

In the laboratory, wave breaking can be represented, for example, in the early work of Thorpe [6] a very clever device was used (Figure 5). This is the two fluid system here and that is tilted so that you can get a shearing across the interface and these little waves develop, break, mixing occurs, and they die down. Thorpe suggested that the K-H mechanism looked like this. Compared to Rosenhead's calculation, Thorpe's work is in an earlier stage because we are only looking qualitatively and not doing numerical work. In Figure 6 we have the development of a roll-up. Then the next step is pure arm-waving: the whole thing breaks down in some fashion. Quite recently, in 1983, McEwan [7], by use of a paddle, produced a breaking wave in the fluid and was able to measure the density gradient throughout. McEwan's figures are in color and so cannot be reproduced here, but Figure 7 presents an idealization of his results, which are as follows. The sequence of events is:

1. The rolling-up process produces an unstable density gradient, heavy fluid over light.
2. The breakdown of this convectively unstable region occurs on a much smaller scale, permitting irreversible diffusion of density and momentum.
3. This microstructure persists after the restoration of gross stability. The experiment shows that by this stage the motions are three-dimensional. This stage is relatively long-lasting, and is referred to by some authors (though not by McEwan) as "fossil turbulence."
4. Finally, the stratified structure is reformed, although with a slightly reduced mean density gradient in the mixed region.

This is one of the first demonstrations, even though quite recent, that the breakdown is essentially three-dimensional in character. The sequence of events is a little more clear than it was in Thorpe [6] but still not numerical. In other words, we still have not gotten in there yet and measured the character of the turbulent exchange which goes on between the breakdown of an unstable situation and the final decay of the turbulence.

We now turn to another current research approach, that of numerical simulation. This method has the great advantage of providing vast quantities of accurate data. But there are compensating disadvantages: turbulence is three-dimensional and involves a range of scales larger than non-turbulent flows; as a result, true turbulence simulation requires, at present, unconscionable amounts of time on the largest computers. Thus, it may be some

years before numerical simulation answers the questions concerning CAT that are being asked. However, progress is already evident.

In two articles, Klaassen and Peltier [8,9] have proceeded as follows. Beginning with an unstable K-H wave, they integrated numerically with a two-dimensional model. The expected roll-up occurs, bringing heavy fluid over light, but no breakdown takes place. Rather, the system oscillates, energy going back and forth between mean state and perturbation. Then, choosing a time in this development, which is of course highly nonlinear, they subject the given configuration to a three-dimensional linear stability analysis. The time development of the unstable wave is shown in Figure 8, the streamlines in the top panels and potential temperature in the bottom panels. The results of the stability analysis--which obviously requires extensive computation--are shown in Figure 9. The growth rate of the fundamental mode  $\omega_0$ , at its maximum value corresponds to a wavelength in the (longitudinal) y-direction of about one-fourth the depth of the shear layer. If this maximum growth rate of this mode is converted to dimensional values, it turns out to be approximately equal to  $N$ , the Brunt frequency, showing that the breakdown is convective in its dynamics.

People who are more operationally inclined may be very impatient with these results. Of course, if you have heavy fluid over light fluid you expect a gravitational instability to result! Nevertheless, these steps are necessary in arriving at something that operationally concerned people will want to see. This is as far as the Klaassen-Peltier model can go (since it is not a simulation in itself, but the three-dimensional stability analysis of a two-dimensional configuration derived from an earlier simulation). The next step will presumably be a full-scale simulation of the turbulent breakdown, with parameterization of eddies of less than a certain scale. This would be the beginning of a quantitative characterization of the turbulence.

I will now proceed to discuss some of my own work, numerical simulations of a very different kind: the flow of a stratified fluid--e.g., the atmosphere--over an obstacle. This can be an obstacle on the ground, or an obstacle at any elevation, of course. The terrain is a natural obstacle to conceive of, but a frontal surface aloft could be the source of the disturbance, or a cloud mass. We first take a simple linear analytic solution. The wind is increasing linearly with elevation and the Brunt frequency is constant. We consider a small disturbance (Figure 10a).  $Nh/U_0$  is the parameter which traditionally is taken to govern the linearity of the computation. If  $h$  is the height of the obstacle, the Brunt frequency is  $N$ , and the speed of the fluid at the level of which it encounters the obstacle is  $U_0$ . Here the ratio 0.1 suggests that it is a purely linear situation. And, therefore, the analytic solution is valid. The next figure will show the development of the Richardson number field from this particular streamline field (Figure 10b).

Here we have cells corresponding to the cells of the streamline field. In these cells, we have alternately Richardson number increases and decreases. You will notice there are more contour lines in the increase than in the decrease. In other words, the imposition of the gravity wave on the stable fluid increases the stability of the fluid more than it decreases the stability of the fluid. However, the fluid does have cells in which  $Ri$  decreases, and the next figure will show what happens when we increase the



magnitude of the disturbance. In Figure 11,  $Nh/U_0 = 3$ , and now we can no longer use the analytic solution; we have to use a simulation code. Again, simulation means starting the motion from scratch and allowing the atmosphere to flow over the obstacle. In Figure 11a the signal has only gone as far downstream as the first crest. We see the streamlines are no longer sinusoidal but are beginning to get nearly vertical at points. Figure 11b shows the density field. So here we do get, not surprisingly, regions of overturning. The point is: where the wave is trapped by the increasing velocity, by the shear itself, the situation is so stabilized by that trapping that the instability exists only in highly local regions at approximately the height of the disturbance. Nothing terribly exciting can happen. You can get a rotor cloud, but you cannot get the vast outbreaks of instability and clear-air turbulence that are characteristic of certain situations. These two figures have represented the type of thing that can develop when increases with height in the atmosphere, therefore, providing a reflecting or trapping mechanism. We now take a case, and this is one that has been studied more than any in which the wind is constant and the stability is constant. The analytic solution is by Miles and Huppert [10]. Figure 12 is a flow over an ellipse where  $Nh/U = 0.5$ , a reasonably linear situation. Here is our simulated solution of the same situation and this is a special simulation code. I do not know of any other simulation in atmospheric sciences in which an orthogonal grid is generated numerically in order for the disturbing boundary to be a coordinate surface. The computation is then done with this new grid preserving the character of the equations but with the new coordinate surface and then transferring back into the old  $x, z$  system so that the ellipse shows as an ellipse. You simply get waves in this linear case. However, if the disturbing obstacle is increased in elevation, we get the pattern of Figure 13, with one vertical streamline.  $Nh/U$  in this case is 0.93, the critical value for this ellipse. Here we have simulation reproducing that situation, and we do get that vertical streamline precisely. The second vertical streamline, or almost vertical streamline, has lost some of its energy because the energy is spreading out in two dimensions. But that is simulated less well because the time is not long enough for the energy to fully straighten up that streamline.

The fact is, of course, that in nature the wind is not constant with height and the Brunt frequency is not constant with height. Either increasing or decreasing wind is the rule. We will now go to the situation in which we get a decreasing wind. If you have a wind that is linearly decreasing, it will eventually go through zero. This gives what is called a critical level; it has been much studied, but less simulated; and it is a situation that is highly productive of a nonlinear type of reflection. We have studied that first by taking a simple sinusoidal disturbance. That is a monochromatic disturbance; but the reflection from the critical layer produces many higher frequencies.

In Figure 14, however, the disturbance generates all frequencies. The left-hand panel represents the stream function; the mean flow is seen to reverse directions at 10 km elevation, the critical level. Well below this, at  $z = 8$  km elevation, a reverse flow or rotor circulation is evident. The density field (right-hand panel) exhibits similarly a reverse density gradient. This would be a region of extreme turbulence. Note that almost no disturbance penetrates above the critical level.



However, it turns out that the existence of a critical level is not necessary to produce this type of nonlinear reflection. Figure 15 represents a similar result for a flow that decreases exponentially with elevation; in the diagrammed panels, the mean flow exceeds 10 m/s at all levels. The left-hand panel shows the total horizontal velocity. At elevations near 4 km, the oncoming flow of 25 to 30 m/s has reversed itself to -25 m/s just in the lee of the obstacle! The right-hand panel shows violent vertical updrafts and downdrafts of more than 14 m/s within the horizontal distance of a few kilometers. Again, a very turbulent region would result.

We conclude that the only thing necessary for the existence of a highly reflective and potentially turbulent situation is a reasonably deep layer of decreasing wind speed. (By decreasing I mean that it is lower at higher levels than at lower levels.) This is fairly characteristic of the stratosphere. So it suggests that the structure of the lowest stratosphere is often extremely pregnant as far as clear-air turbulence is concerned. The question is: Does the disturbance, which in these cases originates at the surface of the earth, actually propagate sufficiently into the stratosphere to produce this sort of turbulence? The answer is, sometimes it does and sometimes it does not. And it is surprising how little this question has been studied. It is what we in my group are devoting ourselves to now. To what extent does the flow structure in the troposphere plus the tropopause itself act as a barrier to gravity wave energy being propagated upward?

Figure 16 will show a situation in which this is the case. The simulation used the best data we could get from Jack Ehernberger and others upwind of the famous United Airlines episode over Hannibal in 1981 [11]. In this case, there was quite a bit of damage and injury inside the plane. We tried as best we could, but there is not any source of disturbance at the surface of the earth near Hannibal. But even if we exaggerated the profile of the terrain there, we could not propagate energy into the stratosphere. Nothing much happened. However, there was an enormous cumulonimbus cloud bank, which was really a very good two-dimensional obstacle to the flow at the time, and it extended to about 9 km. We assume the cloud bank to be the obstacle; and it was sufficient to produce this very large disturbance in the stratosphere. From about 11 km up we had rapidly decreasing wind speed. The hatched areas are areas of subcritical Richardson number. I believe the plane was flying at about 13,000 feet.

The two approaches I have outlined present, I think, the present position of our understanding. We understand how very stable atmospheric flows with large Richardson numbers can be rendered unstable. We understand the process of breakdown of this instability. We can watch the turbulence develop in the laboratory and distinguish between an active stage and a "fossil" stage. But we await detailed measurement and/or simulation of the turbulence.

I feel that this workshop was well conceived and should be repeated. Perhaps by the time of the next one, the scientists will be able to answer the questions asked by the engineers at this one.

#### References

1. Rosenhead, L.: The Formation of Vortices from a Surface of Discontinuity, *Proc. Roy. Soc. (London)*, A134:170-192, 1931.

2. Longuet-Higgins, M. S.: On the Overturning of Gravity Waves. *Proc. Roy. Soc. A*, 371:453-478, 1981.
3. Longuet-Higgins, M. S.: Parametric Solutions for Breaking Waves. *Journal of Fluid Mechanics*, 121:403-424, 1982.
4. Gossard, E. E.; and Strauch, R. G.: *Radar Observation of Clear Air and Clouds*. New York: Elsevier Science Publishing, 1983, 280 pp.
5. Woods, J. D.: On Richardson's Number and Criterion for Laminar-Turbulent-Laminar in the Ocean and Atmosphere. *Radio Science*, 4:1289-1298, 1969.
6. Thorpe, S. A.: Experiments on the Stability of Stratified Shear Flows. *Radio Science*, 4:1327-1331, 1969.
7. McEwan, A. D.: Stratified Mixing Through Internal Wavebreaking. *Journal of Fluid Mechanics*, 128:47-57, 1983.
8. Klaassen, G. P.; and Peltier, W. R.: The Evolution of Finite Amplitude Kelvin-Helmholtz Billows in Two Spatial Dimensions. *Journal of the Atmospheric Sciences*, 42:1321-1339, 1985.
9. Klaassen, G. P.; and Peltier, W. R.: Turbulent Onset in Kelvin-Helmholtz Billows. *Journal of Fluid Mechanics*, 155:1-36, 1985.
10. Miles, J. W.; and Huppert, H. E.: Lee Waves in a Stratified Fluid, Part 3. *Journal of Fluid Mechanics*, 35:481-496, 1969.
11. Parks, E. K.; Wingrove, R. C.; Bach, R. E.; and Mehta, R. S.: Identification of Vortex-Induced Clear Air Turbulence Using Airline Flight Records. *Journal of Aircraft*, 22:124-129, 1985.

**QUESTION:** David Walker (Lehigh University). Could you say something about your simulation. Is it an inviscid simulation? You don't have the no-slip condition on the surface in those calculations? Is that correct? In those obstacles, I would expect that you would get a structured kind of eddy shedding off those obstacles that I didn't see in those results.

**ANSWER:** This is a completely inviscid model.

**WALKER:** The comment I would make is we've done a number of experiments involving obstacles of that nature at Lehigh. What in fact you get is a structured kind of hairpin vortex shedding off those kinds of obstacles that penetrates after a while well up above the ground plane.

**WURTELE:** These are not intended to represent the flow in the immediate region of the obstacle at all. In order to do that we would have to simulate the whole atmospheric boundary layer and we haven't attempted to do that. Really these solutions are valid at distances from the obstacle. Particularly it's the vertical propagation we are concerned with here.

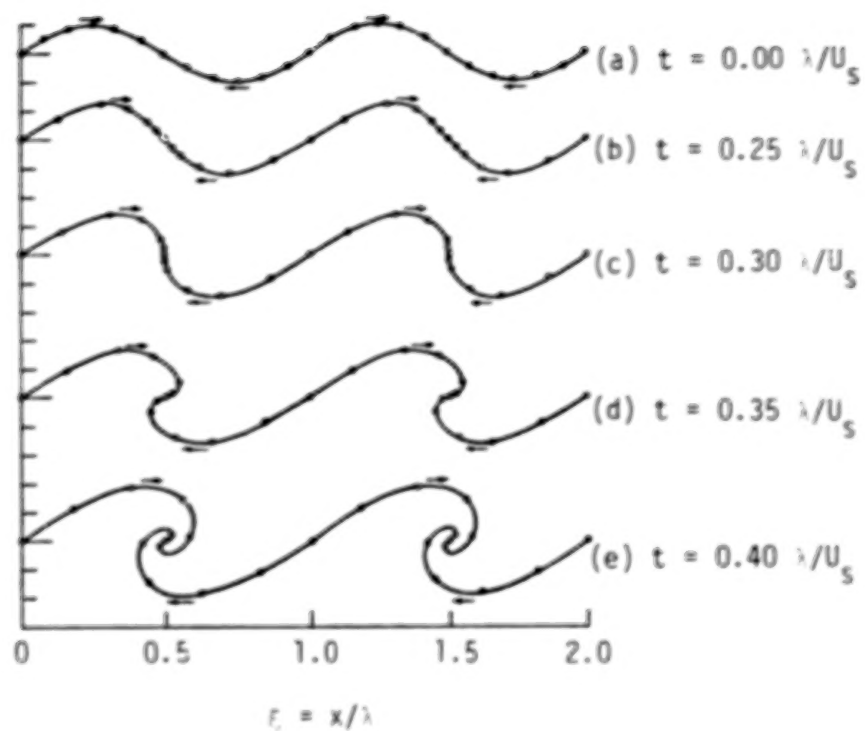
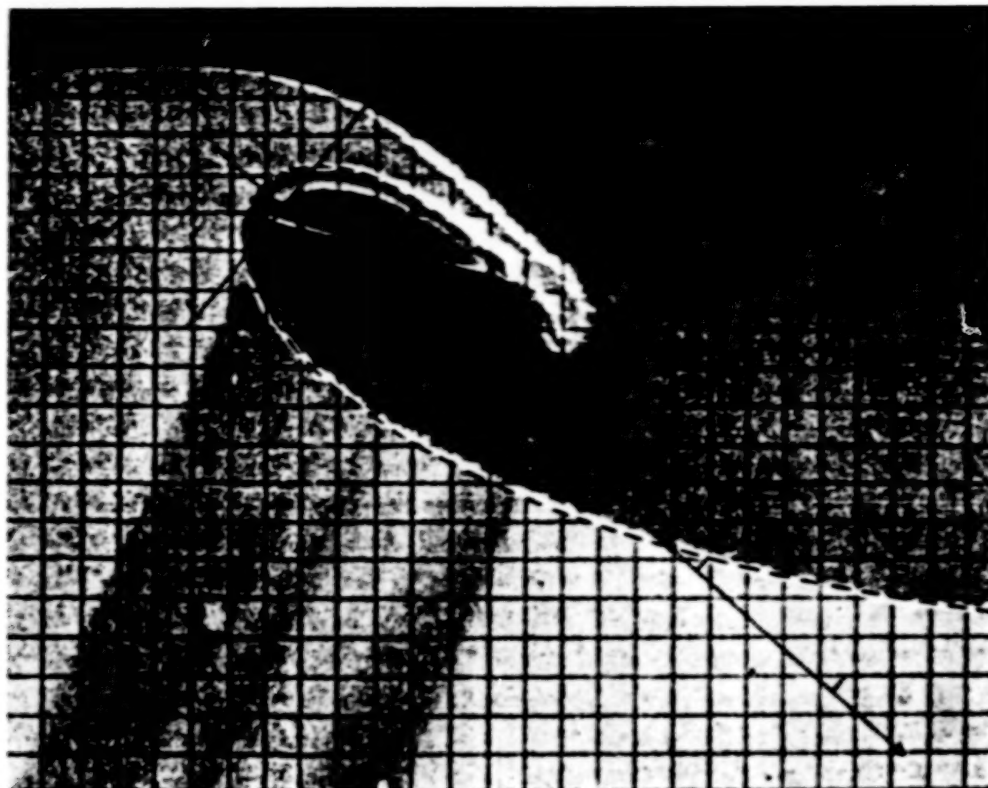
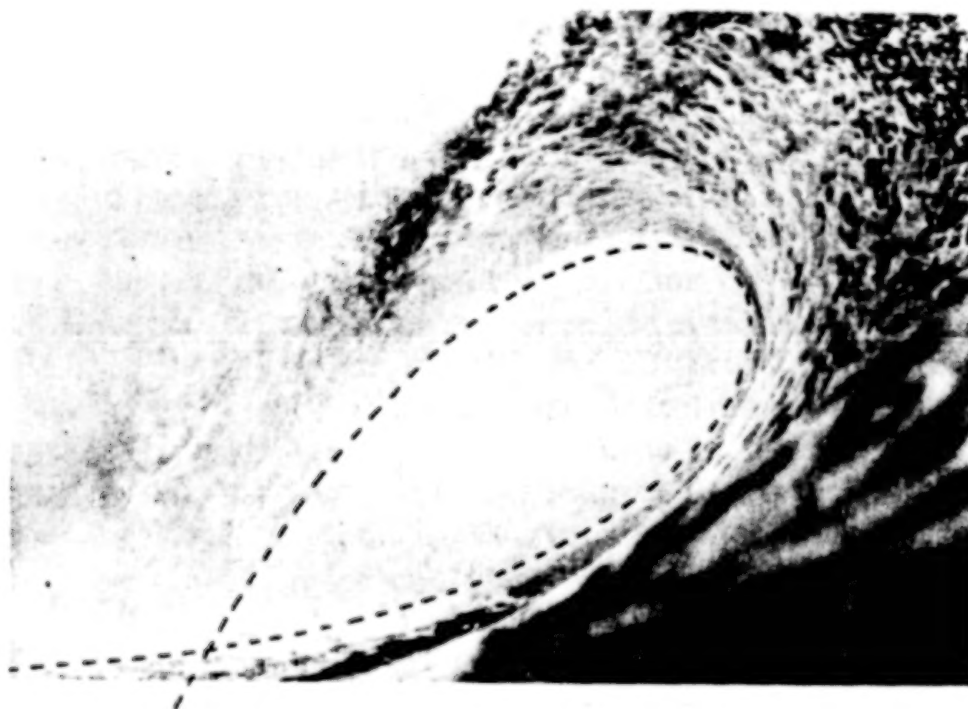


Figure 1. The rolling-up of a vortex sheet which has been given a small sinusoidal displacement [1].



(a) Laboratory wave breaking



(b) Longuet-Higgins [2]  $P_3$  solution superimposed on a breaking wave

Figure 2. Surface waves breaking, with analytic solutions of Longuet-Higgins [2,3] superimposed.

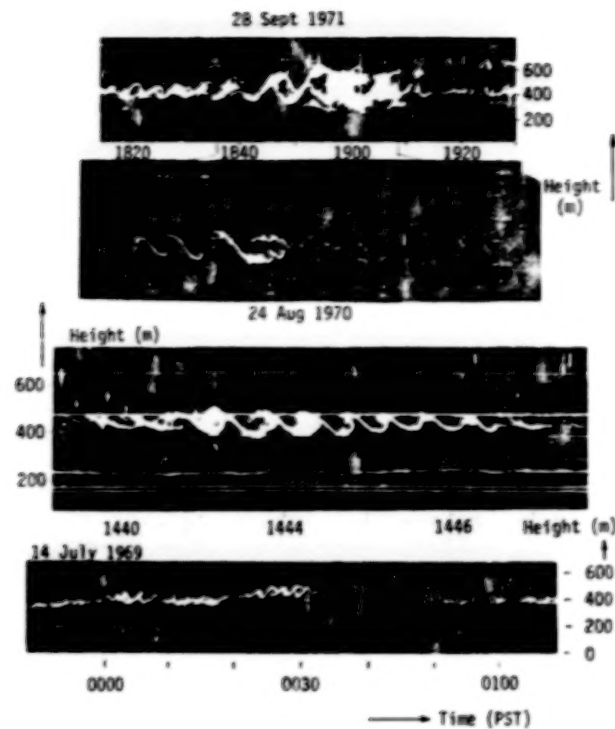
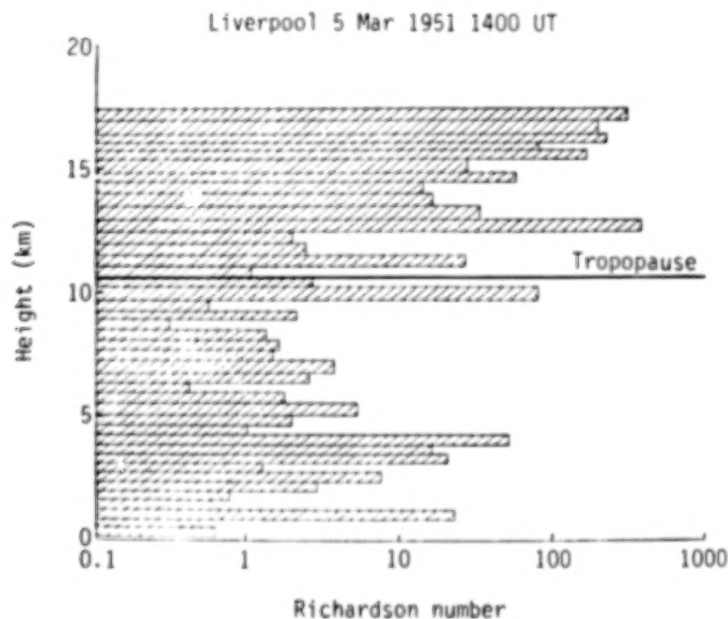
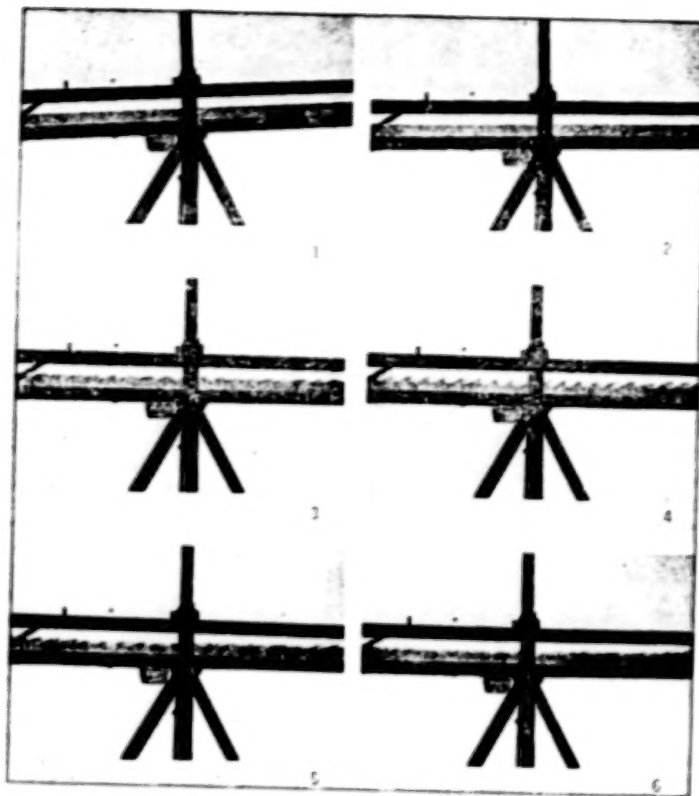


Figure 3. Kelvin-Helmholtz wave roll-up configurations as detected in the atmosphere by FM-CW radar [4].



A profile of gradient Richardson numbers in the atmosphere deduced from radiosonde wind and temperature data averaged over layers about 400 m thick.

Figure 4. High-resolution profile of Richardson number from Woods [5].



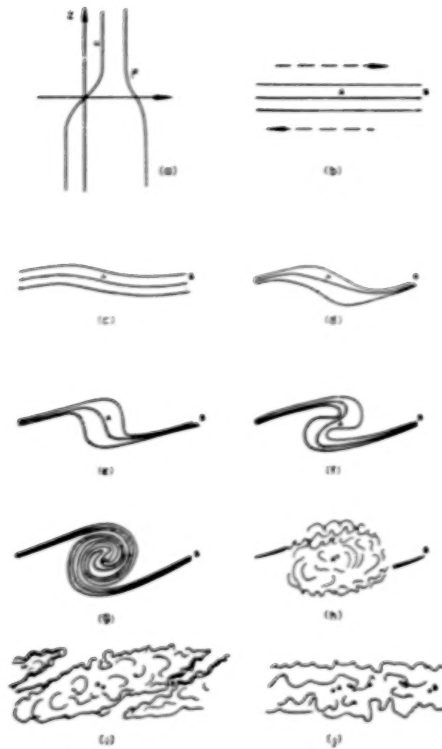
The growth of disturbances in a flow with  $J = 0.077 \pm 0.01$ . The time between each successive photograph is about 0.5 sec and the length of the scale is 45 cm.

Figure 5. Breaking of unstable Kelvin-Helmholtz waves in the laboratory [6].

ORIGINAL PAGE IS  
OF POOR QUALITY

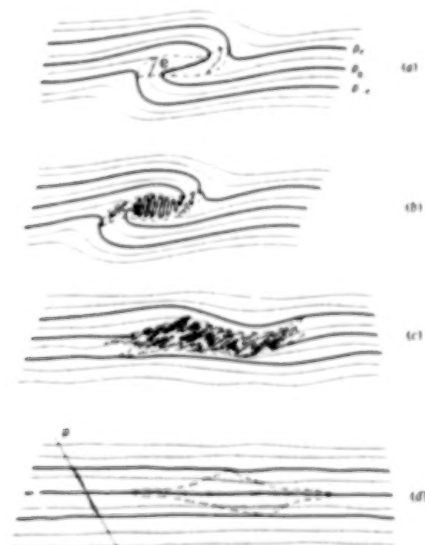


ORIGINAL PAGE IS  
OF POOR QUALITY



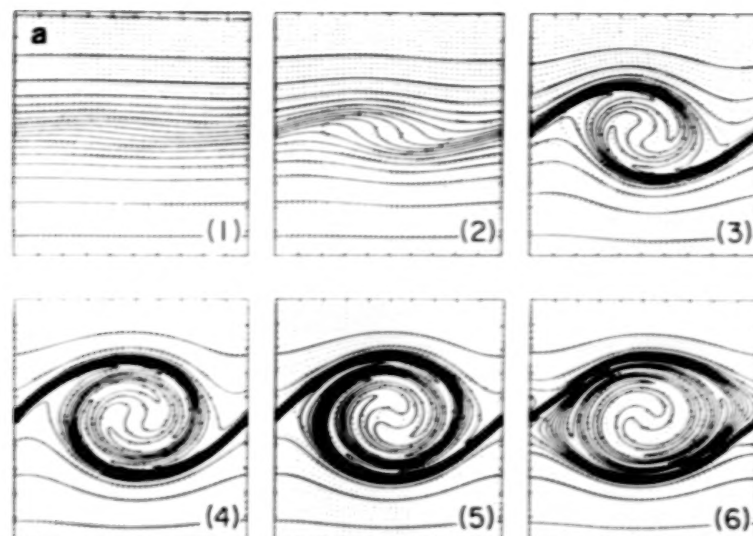
The growth of disturbances: (a) the density  $\rho$  and velocity  $u$  distributions; (b) the lines mark a fluid of constant density, points A and B are fixed, the arrows indicate the direction of flow; drawings (c) to (j) show the development of instability. The points A and B remain fixed, and the lines continue to mark a fluid of constant density.

Figure 6. Schematic of generation of turbulence from breaking of unstable Kelvin-Helmholtz waves [6].

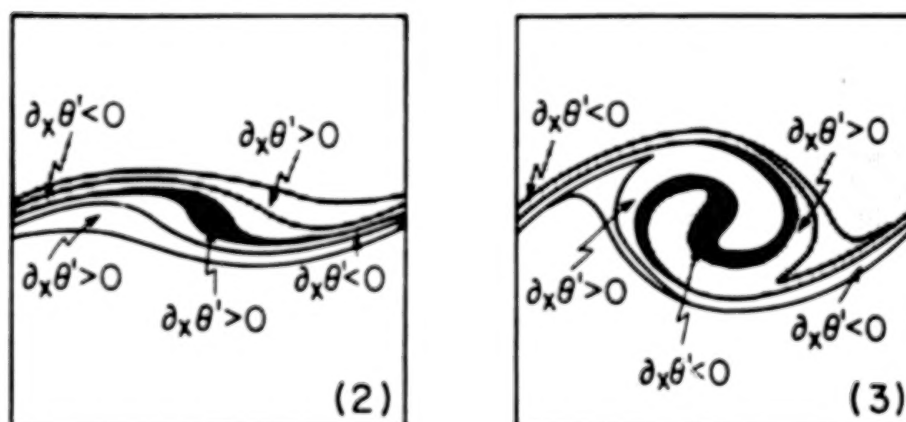


Idealization of a mixing event in a continuous stratification. (a) Overturning. (b) Development of interleaving microstructure. (c) Static stability is restored but microstructure is preserved. (d) Gravitation to an equilibrium has changed the surrounding density profile between extremum isopycnals. The distortion of the profile is exaggerated for clarity. The intermediate isopycnals (fourth and sixth from the top) are displaced upwards and downwards respectively from their original positions, representing a gain in stratification potential energy.

Figure 7. Schematic of generation and decay of turbulence from breaking of unstable K-H waves [7]. Stage (c) is sometimes called "fossil turbulence."

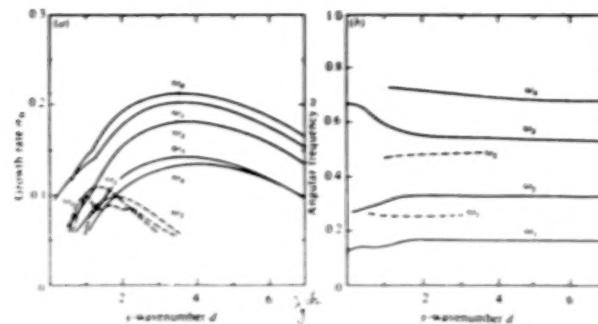


(a) Streamlines (dashed) have been overlaid on (a) the isentropes (solid), and (b) contours of the vorticity field (solid) illustrating evolution of the KH wave at  $Re = 500$ . Numerals 1-6 refer to key times. Contour intervals for the potential temperature field and streamfunction are all  $\Delta\theta$  and  $\Delta\psi$ , respectively. The contour intervals for the vorticity field are  $\Delta\zeta$  for (2) and  $2\Delta\zeta$  for the remainder.



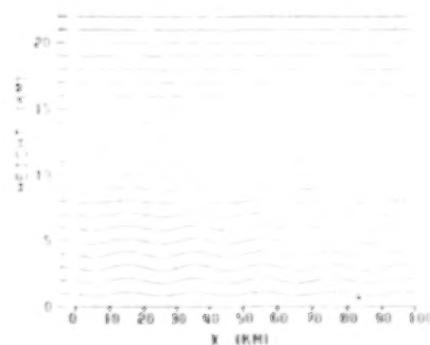
(b) Sketches of potential temperature field illustrating baroclinic sources and sinks of vorticity for a typical KH wave at key times (2) and (3) in the energy cycle. Median contour interval has been shaded darkly; regions with potential temperatures greater than the median value have been shaded lightly. Regions of baroclinic generation of vorticity ( $\partial_x \theta' > 0$ ) are found in the braids; regions of baroclinic destruction ( $\partial_x \theta' < 0$ ) are found at the right and left edges of the core.

Figure 8. Roll-up of unstable Kelvin-Helmholtz waves in simulation by Klaassen and Peltier [8]. Breakdown does not occur in two dimensions.

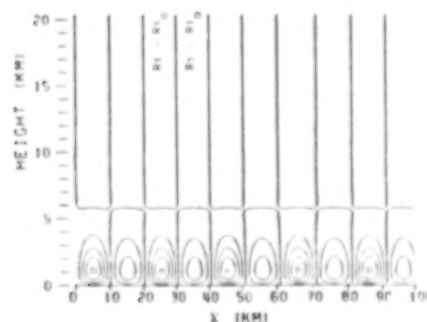


The growth rate  $\sigma_R$  and (b) angular frequency  $\omega$  as functions of the spanwise wavenumber  $d$  for various longitudinal ( $b = 0$ ) unstable modes of the  $Re = 500$  KH wave at the key time (5) in its energy cycle. The sequence of modes labeled  $\omega_0 \dots \omega_4$  (solid lines) is associated with the primary SAR, while that for the  $\omega_0' \dots \omega_2'$  modes (dashed lines) is associated with the secondary SAR. The truncation level used was the maximum  $N = 19$ .

Figure 9. Growth rate of three-dimensional perturbation of unstable configuration of Figure 8 [9].

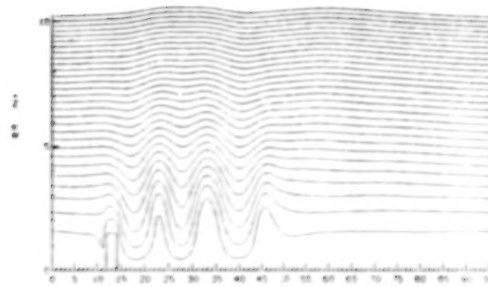


(a) Streamlines ( $Ri = 8$ ,  $Nh/U = 0.1$ ).

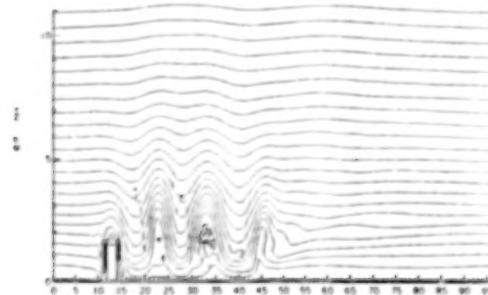


(b) Richardson number field perturbations (contours for quantity  $(Ri - Ri_0)/Ri_0$  at intervals of 0.05).

Figure 10. Stratified shearing flow over an obstacle (small disturbance of height  $h$ ) and corresponding perturbations of Richardson number field.



(a) Streamlines for flow of Figure 10a except that  $Nh/U = 3.0$



(b) Density field for flow of Figure 11a showing unstable regions

Figure 11. Streamlines and density field for flows.

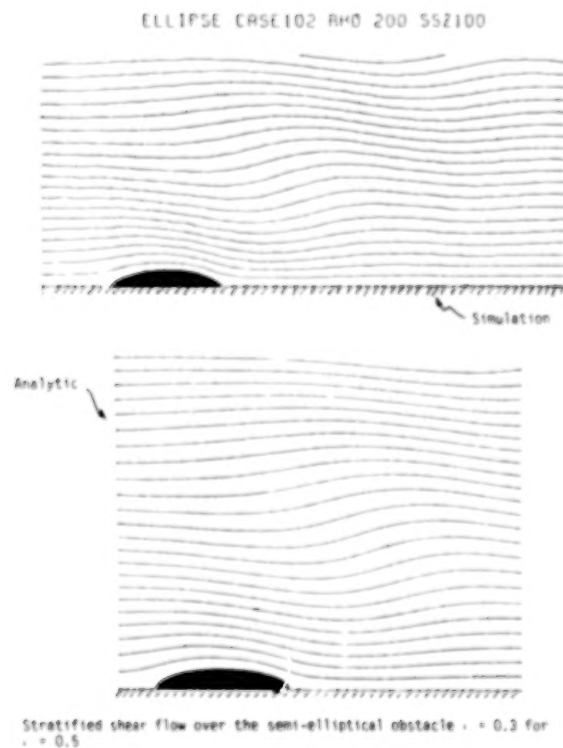


Figure 12. Flow over an ellipse of height  $h$  with  $Nh/U = 0.5$ . Upper panel: simulation. Lower panel: analytic [10].

ELLIPSE CASE105 RHO 200 SS2100

ORIGINAL PAGE IS  
OF POOR QUALITY

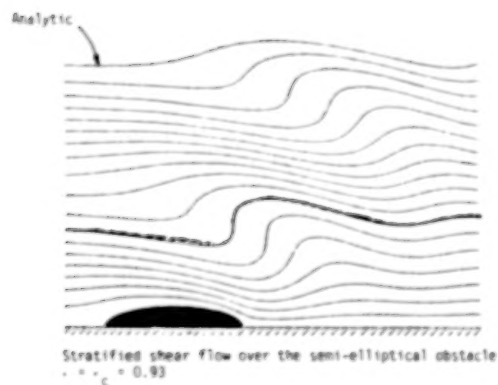
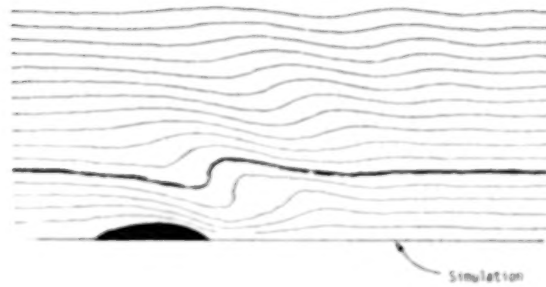


Figure 13. Same as Figure 12 but for  $Nh/U = 0.93$ . Unstable streamline is darkened. Upper panel: simulation. Lower panel: analytic [10].

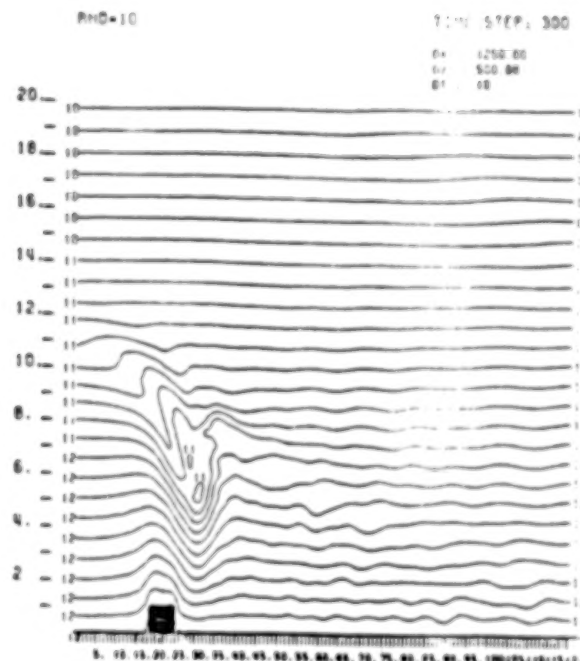
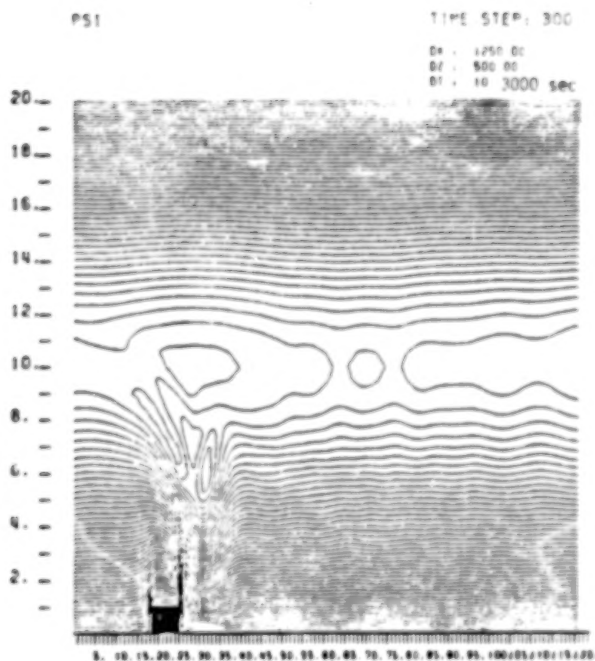


Figure 14. Stratified shear flow with critical level. Left-hand panel: streamlines. Right-hand panel: density.

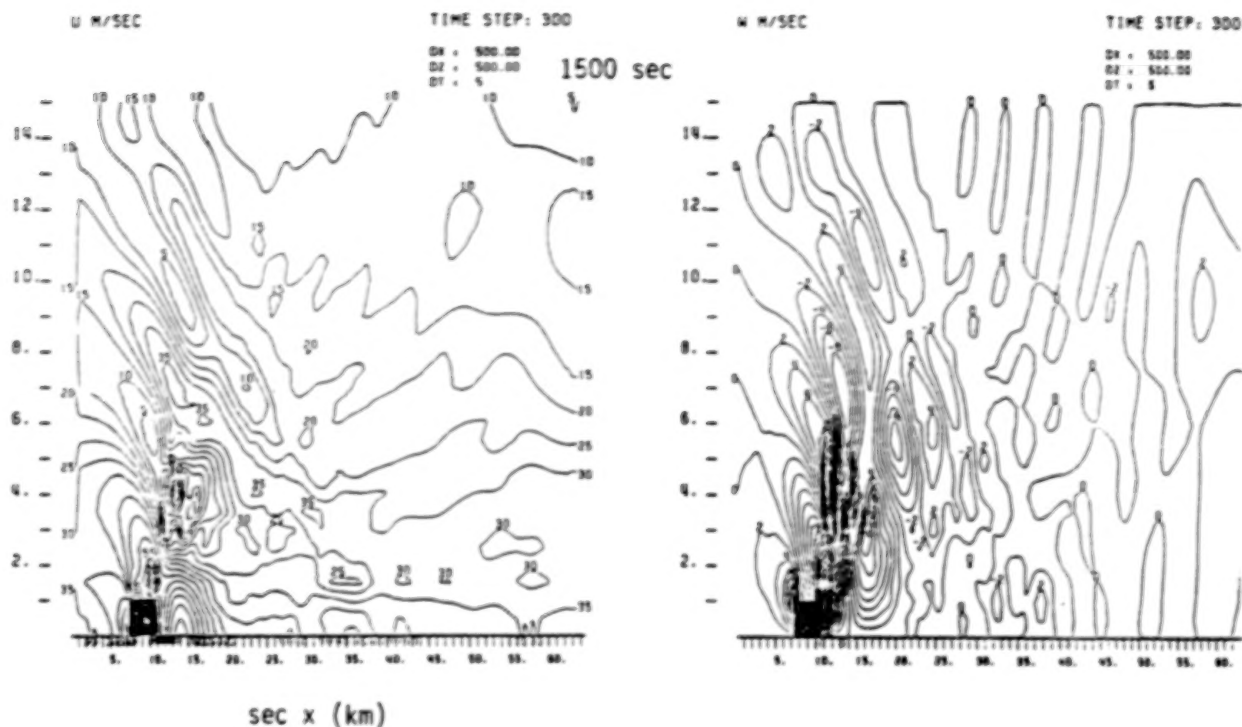
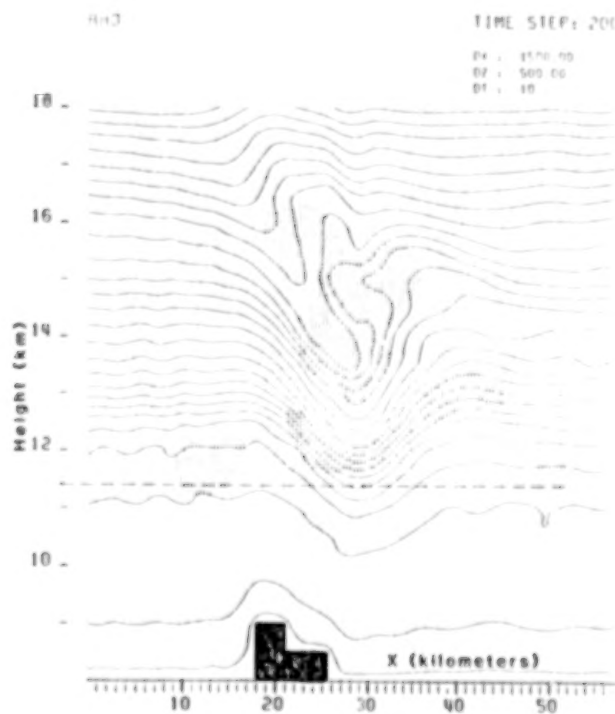


Figure 15. Stratified shear flow with exponentially decreasing speed. Left-hand panel: total horizontal velocity. Right-hand panel: vertical velocity.



ORIGINAL PAGE IS  
OF POOR QUALITY

Figure 16. Simulation of conditions under which CAT-encounter occurred. Regions of  $Ri < 1$  are hatched.



N87  
22350  
UNCLAS

## PHYSICAL MECHANISMS OF HEAT, MOMENTUM, AND TURBULENCE FLUXES

John S. Theon  
NASA Headquarters  
Washington, D.C.

This paper discusses, in a qualitative way, the physical mechanisms which generate fluxes of heat, momentum, and turbulence in the atmosphere. This material is presented to acquaint those people in attendance at the workshop who normally are involved in the aviation aspects of turbulence with the Earth science aspects of turbulence as important processes in the atmosphere.

To attempt to describe turbulent fluxes of heat, momentum, and moisture in precise mathematical detail becomes an intractable problem. It is burdened by an eighth order set of equations involving more variables than equations. It is a closure problem which requires complicated assumptions that are not necessarily always satisfied, variable boundary conditions, and sparse observational data. Therefore, we must approach the problem in a simplified manner to obtain any kind of solution involving the variables of shear, stress, and heat, moisture, and momentum fluxes. In general, the planetary boundary layer is small in comparison to the total depth of the atmosphere. Thus, in models which attempt to describe the entire atmosphere (for example, general circulation models), the planetary boundary layer can be ignored entirely because it does exert a fairly small influence over a short time scale. However, after about 12 hours or more, the dissipation processes in the planetary boundary layer become noticeable and when the model is applied to longer and longer forecast time periods of up to a week or ten days (as is now being done in Europe), then these effects must be included. They become very important in models describing the long-term behavior of the atmosphere, especially climate models.

There are other problems, of course, in which the inclusion of the planetary boundary layer is extremely important. Air pollution studies, air-sea exchanges, mesoscale models, and so on, must account for the planetary layer in very specific terms. Some of the physical mechanisms that are involved in generating fluxes are described in the following.

Figure 1 illustrates the scales of size and motion that are important in the generation of fluxes in the atmosphere (after Brown [1]). The top part of the figure shows the depth of the entire tropopause to be on the order of 10 to 20 km and the mixed layer depth about 1 km. An expanded view of the lowest kilometer shows this to be the level of the typical inversion (at 1 to 1.5 km), or the layer below which there is complete mixing with more or less stratified flow above. The important dimensions here in terms of roughness are of the order of 10 m high, but examination of the microscale in that layer involves concerns about such things as the trees, bushes, etc. Again, examination of an even smaller scale, perhaps the lowest 10 cm, which would normally be called a smooth surface on the planetary boundary layer scale, has within it roughness elements as well. These are very fine in detail and the turbulence they generate is also very small. Fortunately, it is not necessary

to describe the smallest scales in that succession to obtain some benefit from the processes of heat, momentum, and moisture exchange. It is now recognized that the biosphere has a very important role in exchanging moisture, heat, and momentum with the atmosphere.

Let us consider some of the physical mechanisms for this exchange. Figure 2 shows, conceptually, some of the mechanisms for the generation of atmospheric turbulence which effect the fluxes of heat, momentum, and moisture. Of course, one of the most obvious mechanisms is vertical wind shear, shown in Figure 2(a). When there is a shearing action of any kind, turbulence can occur if the shear is sufficiently strong. This is a means for converting the energy in the larger scale flow into turbulence kinetic energy, and it is a mechanism that can generate turbulence anywhere in the atmosphere. Frequently, it is near the ground because strong shears occur in flows near a fixed boundary.

Differential heating is also a very important turbulence generating mechanism. The surfaces of the Earth are not uniform. Forests absorb solar energy quite differently from the oceans, and the highly reflective areas in the desert have quite a different capability for absorbing solar energy. In terms of thermal properties, the ocean has great heat capacity and is relatively stable in surface temperature both day and night. The reason is that the energy is absorbed through a deeper layer. Also, the heat capacity of water is large and can be mixed to a depth which virtually guarantees that the temperature of the surface will not change very much during the diurnal heating cycle. On the other hand, particularly barren land surfaces have very little thermal capacity. They have very poor conduction to the subsurface layers, and so the surface temperature over land can vary enormously from day to night. As shown in Figure 2(b), such temperature differences can generate vertical motions, literally heating or boiling the air that is lying in contact with the hot surfaces to generate turbulence. Flying in an aircraft in the boundary layer on a bright, sunny day produces a choppy ride from this kind of effect.

Even when there is a uniform surface temperature, surface roughness can generate turbulent flow. Figure 2(c) illustrates a stratified, laminar flow encountering a rough underlying surface which generates turbulence. This is the same kind of mechanism that occurs when an aerodynamic surface with rivets or surface debris on it trips a laminar flow into a turbulent flow.

Professor Wurtele [2] mentioned waves in the atmosphere that are set up by obstacles to the flow. Certainly, gravity waves can be generated by a number of phenomena in the atmosphere. Such waves can reach a state where their amplitudes are sufficiently large and the shear and buoyancy forces acting on them are conducive to the generation of turbulence. Figure 2(d) shows that the wave can literally destroy itself in turbulence. Professor Wurtele showed an example of Kelvin-Helmholtz waves that do produce overturning in the atmosphere, thereby generating turbulence.

It has been known for a long time that when the horizontal gradient is sufficiently severe in jet streams, and particularly if there is curvature in

the flow, vortices can be shed to one side of the jet as illustrated in Figure 2(e). Such a phenomena is one cause of clear-air turbulence.

Differential advection often occurs in the midwest and southwest in the springtime. In such a case, a low-level flow from the south, which is quite warm and moisture laden, is overrun by a dry flow from the west across the Rockies, as illustrated in Figure 2(f). This situation can literally produce sufficient vertical instability so that there is natural overturning. Of course, when that happens, very severe turbulence occurs and the conditions are very conducive to producing thunderstorms and tornadoes.

The downburst is a phenomenon that in recent years has received a lot of attention. One type of downburst is thought to occur when a moist layer aloft drops precipitation through a fairly dry layer below it. The precipitation evaporates and in so doing cools the dry layer considerably. As shown in Figure 2(g), the resulting cold air is very dense, causing it to plunge downward rapidly toward the surface in a relatively confined region. This downburst generates turbulence as it shears through the horizontal flow on the way down, and when the plunging column of air hits the ground, it generates additional turbulence as well.

We heard yesterday how precipitation generates turbulence. This mechanism operates on a smaller scale, but hydrometeors falling through the air very definitely generate turbulence and alter the flow patterns that would otherwise occur in the vicinity of non-precipitating clouds. Figure 2(h) shows schematically the turbulence generated by falling precipitation.

Tropopause folds are a phenomenon which have been recognized for some years, but until recently no one believed that they occur as frequently as they do, nor was their role in transporting potential vorticity into the troposphere well understood previously. These folds generate turbulence because of the instability established when more buoyant stratospheric air is forced below heavier tropospheric air as shown schematically in Figure 2(i). Here, the air with higher potential temperature ( $\theta$ ) penetrates into the dense air below it in the fold and is then cut off. The instability thus generated is restored to more stable flow by turbulent processes.

We have already heard about the role of fronts in generating turbulence. Figure 2(j) shows a cold dome of air that has a reasonably coherent surface advancing into warmer, lighter air and actually stirring it up. Ahead of the front, squall lines or thunderstorms often develop. Thus, fronts are a source of turbulence and, though it is a moving mass of air, it could just as well be considered a solid obstacle that is moving along the surface generating turbulence ahead of it.

Orography is another important mechanism for generating turbulence, particularly in the boundary layer. Figure 2(k) shows the turbulence generated when flow crosses an orographic barrier. In this case, air is flowing over mountains, and a wake that contains considerable turbulence is generated right in the boundary layer. Rotor flows are generated in the wake at the top of the boundary layer, stirring additional turbulence themselves. There are gravity waves and mountain waves; gravity waves propagating away



from the mountain and mountain waves standing on the lee side of the mountain at higher levels. Graphic examples of such waves were given in Dr. Wurtele's paper [2].

There is a class of stirring actions in the atmosphere that literally consists of convective instabilities. Here I am talking about air that might initially be stable but if slightly disturbed, it becomes unstable. In Figure 2(1), convergence is shown which lifts a parcel from near the surface to its original level. If the parcel contains enough moisture, the moisture starts to condense, releasing latent heat. Of course, that energy makes the parcel more buoyant, raising it further. This lifting mechanism can generate a great deal of turbulence. Once the process starts, it can accelerate, becoming less stable, and eventually generating thunderstorms with violent weather activity.

All of these mechanisms are somewhat localized in space and time. If you look at the atmosphere as a whole, you would probably say that the atmosphere is largely stratified, and it is. But these important turbulence generating mechanisms are exceptions to that stratification which really make the system what it is, and they cannot be neglected. Turbulence creates the fluxes of heat, momentum, and moisture which account for virtually all the interactions between the surface and the rest of the atmosphere.

There are a number of ways that people have attempted to handle all of these exchanges in models. Time does not permit me to talk about all of them, but I am going to mention one that is in current use today. It was developed in 1972 by Deardorff [3]. His method relies on a bulk parameterization scheme as follows:

1. Deardorff begins by estimating the mean values of wind velocity, potential temperature, and moisture in the boundary layer from the estimated height of the boundary layer and the lowest grid levels of the model.
2. Then he estimates the mean vertical fluxes of momentum, heat, and moisture from the bulk Richardson number (based upon the differences between the mean values of the boundary layer and the surface values).
3. Next, he estimates the direction of the surface wind using the surface pressure gradient to refine the mean wind velocity in the bulk Richardson number. If needed, these steps are iterated.
4. Finally, he obtains the height of the boundary layer as a function of  $x, y, t + \Delta t$ , given the height as a function of  $x, y, t$  (from the prognostic equation in unstable cases and a simple relationship in stable cases). This step uses model velocities and surface fluxes from step 2 above.

If you go through all the equations, you will find that it is still simple compared to a detailed description of the real processes that are involved.

This parameterization of the boundary layer is used in a number of models. Figure 3 is a schematic of the way it is used in the Goddard Laboratory for an atmosphere fourth-order, primitive equation, general circulation model. In this particular case, Deardorff's parameterization is used and the fluxes at the surface, indicated by  $F_s$ , are equated to the mean fluxes in the mixed layer,  $F_m$ . Inclusion of these fluxes actually makes a difference in the results of the model. It is a simplified accounting for all the processes described in Figure 2.

In Figure 4, a schematic diagram of a newer model called the global integrated biosphere model (by Sellers et al. [4]) is shown. This model has just recently been developed. The diagram shows how the fluxes develop from the surface, the ground cover, and the tree canopy, particularly the moisture and heat fluxes. The portion of Figure 4 outlined at the top of the page is the Deardorff parameterization, which describes the bulk flux parameterization between the surface and the atmosphere, but, in addition, there is a more elaborate system for describing the fluxes from the canopy and the ground cover and from the soil. The cavities represent the stomata of the plants. The symbolic resistances represent the resistance to the transport of moisture, in this case, through the biota. It is a complicated process which is empirically determined and accounts for both heat and moisture exchanges. Although it makes the model more complicated, it actually does produce visible results. From this approach, the surface stresses are computed in the model. The surface stress varies considerably according to the vegetation, soil type, roughness, etc.

Differences have been generated in the atmospheric portion of the model because soil moisture and vegetation do affect the behavior of the atmosphere. Precipitation is more realistically simulated because of the moisture mixing which is related to the vegetation. Soil moisture makes an enormous difference in how the model actually responds by producing precipitation which we hope will be realistic. It really does make a difference, particularly in climate models.

To summarize, although the atmospheric flow is basically stratified, there are a number of very important exceptions. In qualitative terms, these exceptions to that stratification make a significant difference in the way the atmosphere behaves. These exceptions enhance turbulent exchange processes and these turbulent exchange processes ultimately modify the behavior of the atmosphere over a wide range of spatial and temporal scales. Finally, the present methods for parameterizing turbulence and the fluxes they generate use bulk approximations. The question is: Are these adequate and can we improve them?

#### References

1. Brown, R. A.: *Analytical Methods in Planetary Boundary-Layer Modelling*. New York: John Wiley & Sons, Inc., 1974, 148 pp.
2. Wurtele, M. G.: "CAT-Generating Mechanisms," *Proceedings: Workshop on Atmospheric Turbulence Relative to Aviation, Missile, and Space Programs*, pp. 111-126, NASA CP-2468, 1987.



3. Deardorff, J. W.: "Parameterization of the Planetary Boundary Layer for Use in General Circulation Models," *Monthly Weather Review*, 100:93-106, 1972.
4. Sellers, P. J.; Mintz, Y.; Sud, Y. C.; and Dalcher, A.: "A Simple Biosphere Model (SiB) for Use within General Circulation Models," *Journal of the Atmospheric Sciences*, 43(6):505-531, March 15, 1986.

**QUESTION:** Jack Ehernberger (NASA Ames). You've indicated the importance of turbulence processes to the atmosphere. Can you characterize or has it been examined to any extent, the degree which the interest from the atmospheric prediction standpoint in simulation depends on turbulence as the turbulence intensity increases. In other words, the aircraft audience probably begins to be interested in an RMS value of 0.5 m/s and generally everyone who flies is interested in 1 m/s. The extreme incidents and accidents probably happen at a range of 3 or 5 m/s RMS. That doesn't infer that the larger the RMS is the more important it is to the atmospheric circulation. Has a breakdown been made or might it be made? Does your interest increase with the severity of the turbulence?

**ANSWER:** I don't think I have come across any cases in which in large-scale modeling or climate modeling that is a consideration. Certainly, if people are trying to model mesoscale processes they might be very concerned with it, and there are local scale models and cloud scale models that might account for turbulence. I think, in general terms, that even the smaller processes which occur more frequently are of great importance because they occur on a very widespread basis. For example, by changing the roughness of the Saudia Arabian peninsula, we were able to show that the Indian monsoon flow could be considerably altered. There is a very small-scale process (we are talking about turbulent flows over sand). It is generally concluded that sand does not produce much in the way of turbulence, but alter the roughness in the model slightly and increased surface stress actually produces curvature in the flow that leaves Saudia Arabia, thus changing the very important monsoon that occurs over India. So, the answer to your question is: I think not. I would like to emphasize the areas of mutual interest and perhaps overlook the divergence of interests at this meeting. With that intent, we attempted to convene the two communities, aviation and earth sciences.

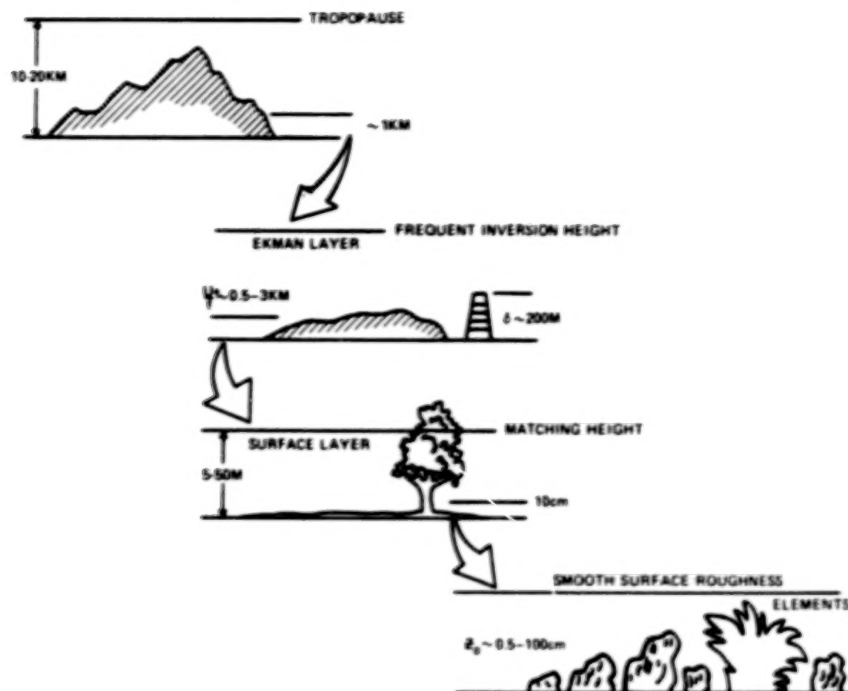


Figure 1. Turbulent scales of size and motion important to generation of fluxes (after Brown [1]).

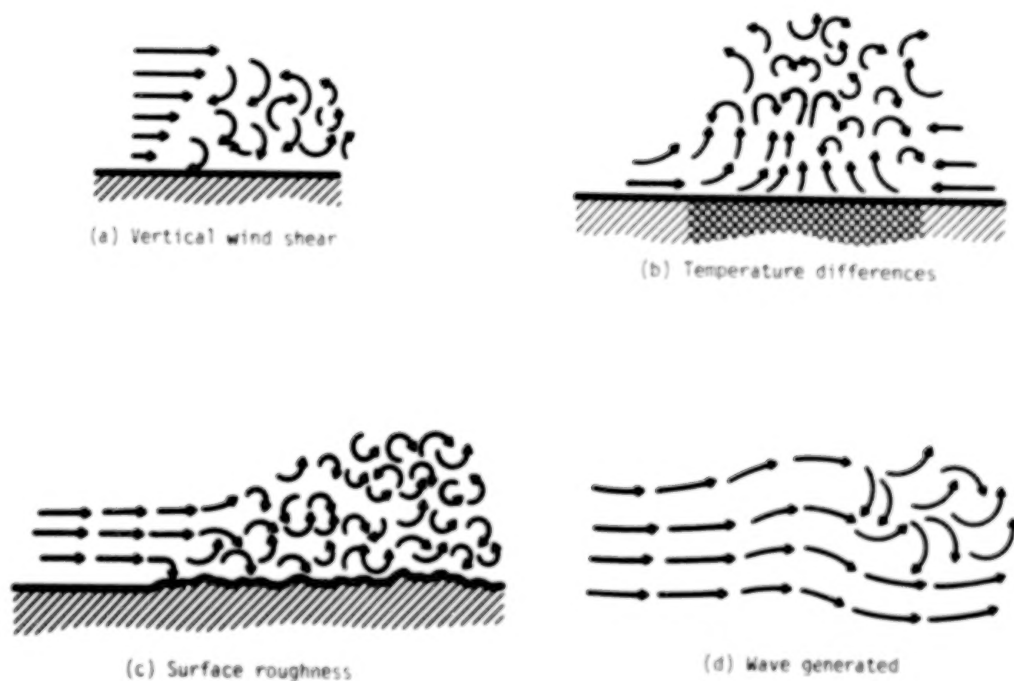


Figure 2. Conceptual illustration of mechanisms for generation of atmospheric turbulence.

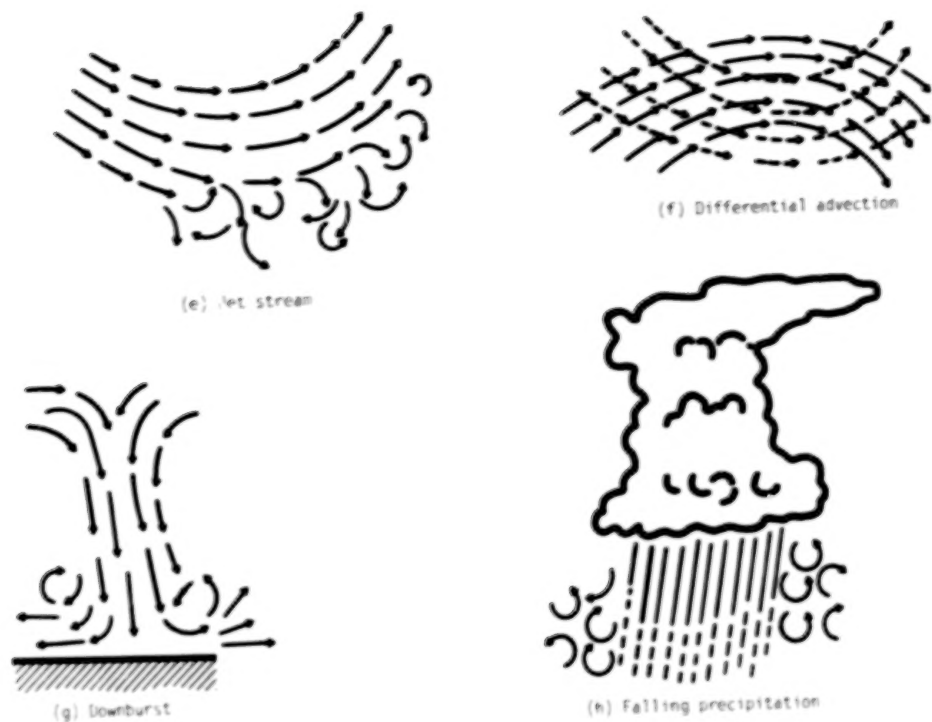


Figure 2. (continued).

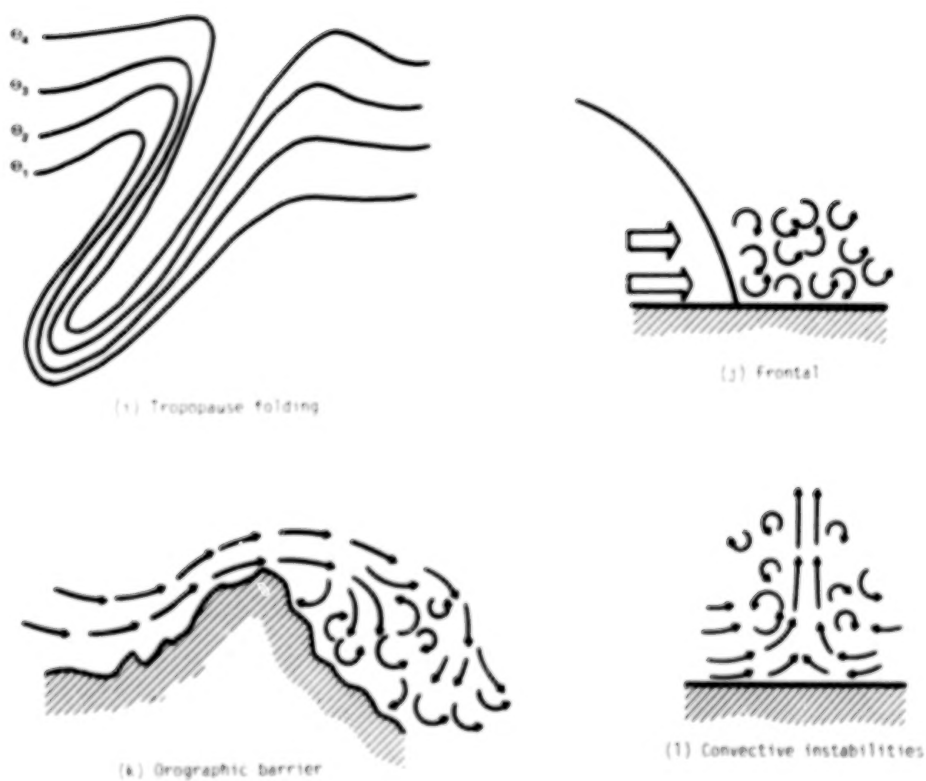


Figure 2. (concluded).

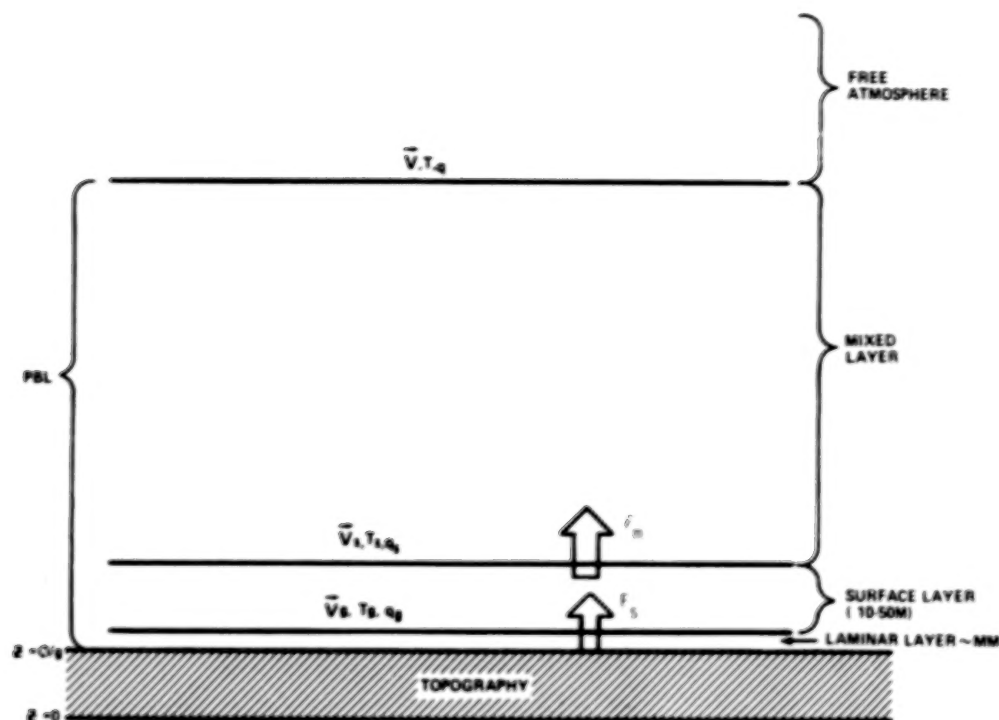


Figure 3. Schematic of parameterization model used by the Goddard Laboratory for Atmosphere.

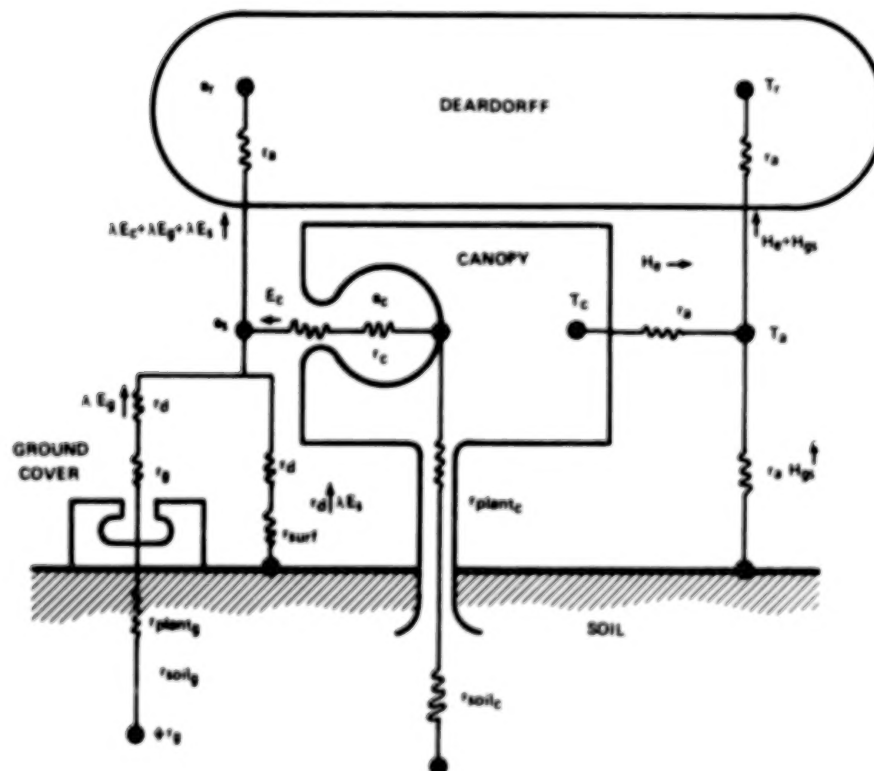


Figure 4. Global integrated biosphere model (by Sellers et al. [4]).

N87

22351

UNCLAS

## TURBULENCE FORECASTING

C. L. Chandler  
Delta Air Lines  
Atlanta, Georgia

In order to forecast turbulence, one needs to have an understanding of the cause of turbulence. Therefore, we shall attempt to show the atmospheric structure that often results when aircraft encounter moderate or greater turbulence. The following is based on thousands of hours of observations of flights over the past 39 years of aviation meteorology.

### 1. AIRMASS ANALYSIS

One of the best tools in analysis and forecasting turbulence is the frontal contour method of airmass analysis as perfected by the Canadians in the late 1940's and early 1950's.

In winter, on the average, one will find four major frontal zones (five airmasses) between about 20N and 50N latitude over the eastern United States. Figure 1 shows the mean position of the various surface fronts during an average winter. Large day-to-day variations often occur as well as mean year-to-year positions during the colder months. In summer, the Sub-Tropical surface front average position is just south of the Great Lakes and the upper air position is over the lakes. As before, there are large day-to-day variations in these positions. Figure 2 shows the same frontal positions but within the upper troposphere. Average temperatures are also shown at other MB (millibar) heights as well as mean heights/temperatures of the airmass tropopause.

We shall now look at vertical cross sections of the various frontal models and often associated wind maximums in winter. Figure 3 shows a typical model of the Arctic front with a wind maximum at about FL230\* or near the 400 MB level. Southward, we find the Maritime Arctic frontal zone (often called Sub-Arctic) with a wind maximum much stronger at about FL290-300 or near 300 MB. This is shown in Figure 4. The next southward frontal zone is the polar front as shown in Figure 5. We see an average wind maximum of about the same strength as the Maritime Arctic but a maximum wind level of near FL340-350 near 250 MB. The most southern frontal zone (except in rare cases) we call the Sub-Tropical frontal zone. The height of this maximum moves up to near FL390 at 200 MB. This frontal model is shown in Figure 6.

At the higher levels above about 400 MB, we occasionally see a frontal zone south of the Sub-Tropical front in the temperature range of near -34° to -35° C at the 300 MB level. It appears now and then in the tropical areas in winter and even over the United States during the warmer months. Likewise, we occasionally see frontal zones north of the Arctic front in very cold airmasses and we call this frontal zone the Super Arctic.

---

\*FL230 = Flight level of 23,000 feet above mean sea level.



## 2. FRONTAL TURBULENCE

All of the frontal zones shown on Figures 1 through 6 may contain turbulence to some degree. Above about 12,000 ft, most of the turbulence will be of the clear-air type (CAT) due to descending air within the frontal zones. Figure 7 shows all four of the major frontal zones and the area of frequent, moderate, or greater CAT. As the altitude increases toward the "Z layer" (level of non-horizontal temperature gradient), the CAT will decrease reaching a minimum at the Z layer. This altitude of the reversal of the thermal wind, located at the level of maximum wind speed, is a desired level to fly for smooth air (jet core). One has only horizontal wind shear rather than vertical and horizontal shear. The altitude for maximum turbulence seems to be at about two-thirds of the way from the surface front to the Z layer for each frontal model as shown in Figure 7. The colder the airmass, the lower the CAT zones within each frontal model. This is the reason that CAT is found at the lower altitudes in winter. Likewise, the lower latitudes result in the height of the CAT being found at higher altitudes within the frontal zones.

## 3. TROPOPAUSE TURBULENCE

Tropopause surfaces below about FL310 very seldom contain moderate or greater CAT. Cold airmasses north of the Maritime Arctic frontal zone result in sinking air. The resultant low tropopause does not contain enough of a temperature inversion and associated horizontal and vertical wind shear. Tropopause surfaces at and above about FL340 (250 MB) are the ones that often result in moderate or greater CAT within the ascending airmasses. Most CAT within tropopause surfaces will be found in temperatures colder than standard as well as temperature inversions, horizontal and vertical wind shear. Figure 8 shows various vertical temperature signatures through tropopause surfaces. Curves A and B seldom result in more than light CAT. Curves C and D often result in moderate or greater CAT at temperatures colder than standard if relative high wind speeds are present.

Figure 9 shows B, C, and D temperature curves across a typical frontal model and associated jetstream.

## 4. MOUNTAIN WAVES

The mountain wave is highly over-rated as a direct cause of clear-air turbulence. In fact, Delta Air Lines has been flying to the west coast for over 20 years from various cities east of the Rockies. We do not know of one case in which a Delta aircraft has encountered moderate or greater turbulence caused solely by a mountain wave when flying at altitudes above 25,000 feet. We have encountered turbulence many times over the mountains but the cause was determined to be upper front, tropopause, trough, or ridge lines when it was the CAT type. In some cases, the discontinuity was located within a wave condition and the turbulence within discontinuities may well be enhanced by mountain waves.

Figure 10 shows a mountain wave model with two frontal zones (three airmasses). As long as flights avoid the upper front and tropopause surfaces, flights are most always very smooth. In some cases, aircraft within the wave crest may well exceed the aircraft airframe speed limitations. In some of these cases, aerodynamic buffet may occur which no doubt results in often reported turbulence. Figure 11 shows that eastbound aircraft are more apt to experience this overspeed buffet due to the very sudden encounter due to high ground speeds. The example shows a 13-second difference between downwind versus upwind, which gives the headwind flight crews a much longer period in which to react to the ascending air.

## 5. CLOUD TURBULENCE

In this analysis, we will exempt all types of convective clouds except a few special cases of thunderstorms associated with widespread cirrus. As a general rule, cirrus results in only light turbulence in areas of relative light winds. Under moderate to strong winds, there is often found moderate turbulence near the cirrus tops and in this area there is a strong increase in wind speed near the cloud top. Most of the turbulence will be found within the last 1000 feet just before the top. This condition is shown in Figure 12. The cloud retards the horizontal wind flow (cloud drag) and as the top is approached, there is a sharp increase in wind speed as well as turbulence.

There is one condition that aircraft flying at higher levels encounter several times a year that result in passenger injuries. This is also shown in Figure 12 where the aircraft is flying on top in the clear. Below the cirrus, a thunderstorm has formed and the top has merged into the higher cirrus deck. The major updraft of the thunderstorm has created a bubble or ridge-row near the top of the cirrus deck. Flight crews often do not see this ridge-row or bubble and will just nick the top or pass through the wave effect just on top. In most cases, there is one sharp shock that results in a messy aircraft and/or injuries if seatbelts are not secured. To avoid this, weather radar tilt control tilted downward for the target should be used and then go either right or left of the target rather than the risk of flying the wave effect just on top.

## 6. TROUGHS AND RIDGES

Most always there will be some type of turbulence within trough lines. In most cases, it will be of short duration at any altitude and is more apt to be only light to moderate. Sloping trough lines seem to enhance the turbulence. Figures 13 and 14 show both a ridge line and trough line as it may appear on an upper air chart. In many cases, ridge lines give airborne aircraft many more problems than trough lines as often associated upper warm fronts, widespread cloud cover, and sharp cold air tropopause surfaces above the warmer airmasses below.

## 7. LOW-LEVEL CYCLONIC FRONTAL WAVES

Moderate to severe low-level turbulence is often caused during the cooler months by shallow, warm frontal cyclonic waves that may appear anywhere, but the severe cases favor the east coast of the United States as shown in Figure 15. Strong northeast surface winds with strong southwest winds above are only a few miles north and north-northeast of the center of the wave. Figure 16 shows a vertical cross section along the line AB as shown in Figure 15.

## 8. EXAMPLES OF FLOW PATTERNS THAT OFTEN RESULT IN MODERATE/SEVERE TURBULENCE

Figure 17 shows a very sharp upper warm front within a ridge line that most always will result in moderate to severe turbulence. Near the crest of the ridge line within the frontal zone, the warm front will produce the worst upper air turbulence within the tropopause than any other feature. Likewise, above the jet core and to the south toward the high pressure side, the cold tropopause will contain moderate to severe CAT in many cases.

Figure 18 shows a cold cut-off cold low with an upper jet front. The area north through northeast of the closed low is the area of frequent, moderate, or great CAT as we have two frontal zones, sharp trough line as well as cold sloping tropopause surface above the frontal zones. It is very important to fly the Z layer under this flow pattern or well above the tropopause. The lower levels in some cases may well prove to be relatively smooth. Figure 19 is a vertical cross section along the line AB which shows the areas of turbulence.

Figure 20 shows the position of the surface front and associated upper air position. The Coriolis effect comes into play as the cause of this type of turbulence, which in most cases will be only light but found at most all altitudes above about 15,000 feet. Cross contour flow is present above and near the surface position of the front.

## 9. FORECASTING TURBULENCE AT DELTA AIR LINES

In order to forecast turbulence, one has to have the proper analysis on large scale actual surface and upper air charts. Delta's actual upper air chart for 0000-1200 GMT contains computer-plotted data from 400, 300, 250, and 200 MB plus the height and temperature of the tropopause as well as maximum wind data. All this information is plotted on one large-scale chart and then the analysis is done by a Delta meteorologist. The actual charts also contain wind and temperature information from aircraft that has INS and ACARS equipment. This is hand plotted at present. Short-range forecasts are then made with the help of the Bracknell computer forecast of winds and temperatures at 12, 18, 24, and 30 hours from base data which also is plotted by computer at the same levels as the actual charts. Frontal analysis may be made on the forecast charts as on the actual with the corrected position of upper fronts and maximum wind. Both Suitland and Bracknell computers forecast the position of the maximum wind in error by about 60 miles too far on the

high-pressure side in warm fronts in ridge lines. Both, also, underforecast the maximum wind speed by 30 to 40 knots in the case of Suitland and 15 to 25 knots in the case of Bracknell. The decrease in wind speed on the low-pressure side of the maximum is also in error by both Suitland and Bracknell but Bracknell will show a tighter gradient on the low-pressure side as it should be. Figure 21 shows the actual for 1200 GMT on March 31, 1986, for the Pacific Northwest with Maritime and polar fronts.

Figure 22 is a sample Delta turbulence alert that Delta's meteorologists enter into the Delta flight planning system by grid numbers, and if an aircraft passes through the area, it will be picked up by the Delta computer weather system and be placed on board the flight (B20). The second alert is for thunderstorms (T21).

For Delta's international flights, a more detailed flight forecast is made for turbulence by the Delta meteorologists as shown below:

Delta 14/24 --- Lgt/Mdt CAT CLB FL 290-310 upper front --- Lgt CAT 40SW GVE FL330 trop temp rise --- Lgt CAT ACK trough FL350 --- Lgt/Mdt CAT FL370 50NE YYT trop temp drop --- Lgt 33W ridge line --- Lgt/Mdt CAT 30W CRK FL370 trop temp rise --- Lgt CAT DVR trough --- Lgt CAT descent FL290-280 trop --- Mdt CAT FL220-200 descent front.

Delta's meteorologists and flight dispatchers have access to company VHF for most of the route structure as well as HF for the international flights.

**QUESTION:** George Modica (AFGL). Do you have a large concern for tropopause folding type turbulence? And if so, what meteorological information do you look for?

**ANSWER:** We don't believe such turbulence really exists. In our practice at the Z layer, the "trop" is above it and the front is below it. If you want to extend that tropopause down into the top of the upper front, and you can do so, there is a lot of shear there. But if you go through at the Z layer horizontal, we hardly ever find any significant turbulence.

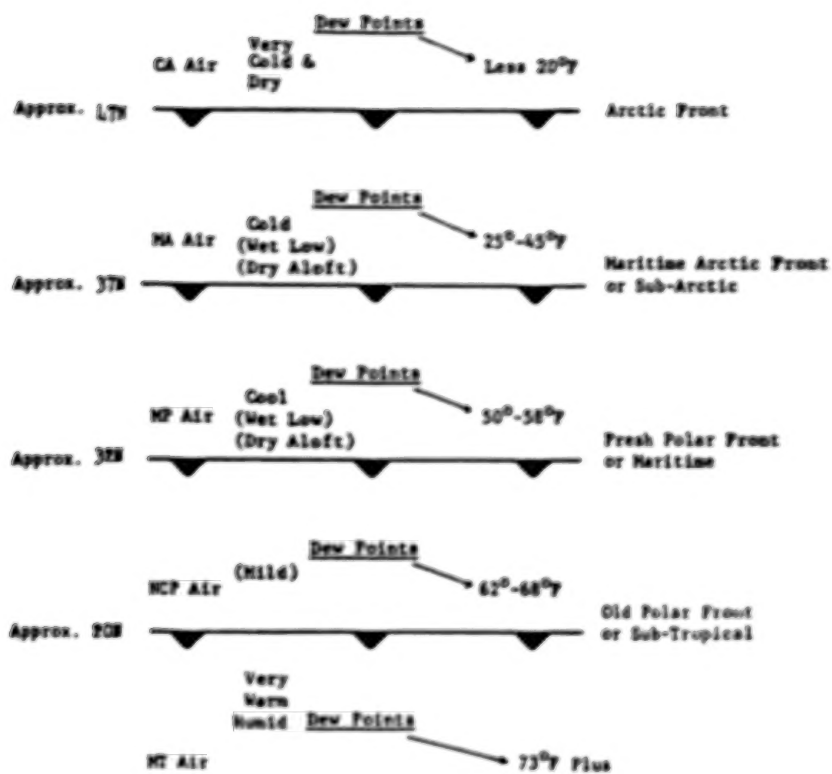


Figure 1. The mean position of the various surface fronts in the eastern United States during an average winter.



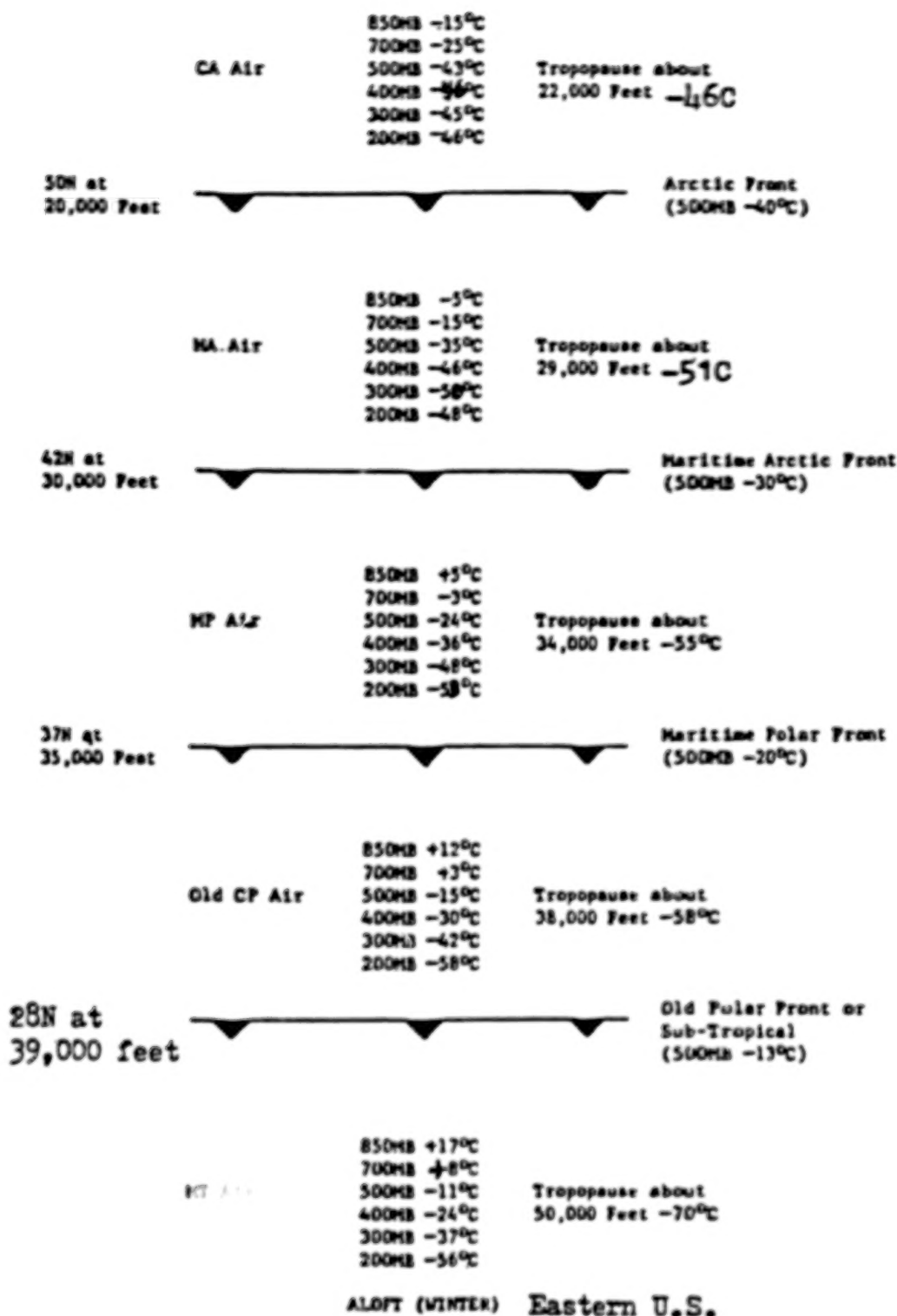


Figure 2. The mean position of the upper troposphere in the eastern United States during an average winter.



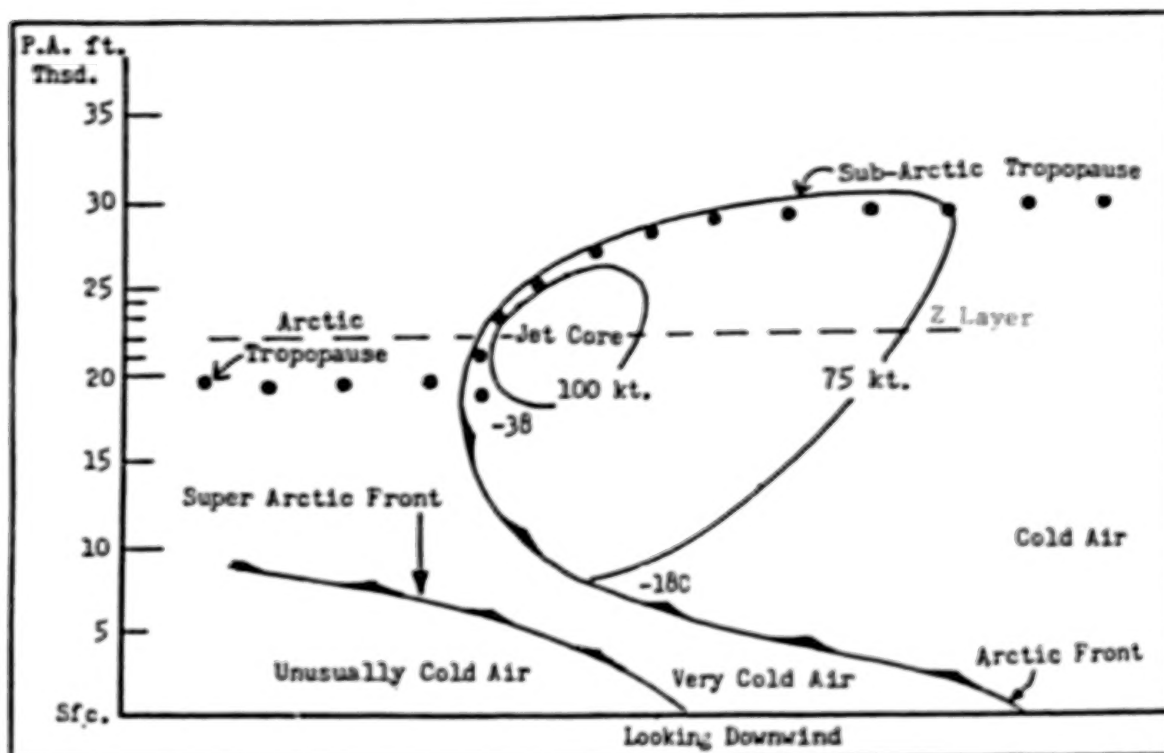


Figure 3. A typical model of the Arctic front with a wind maximum at about FL 230 or near the 400 MB level.

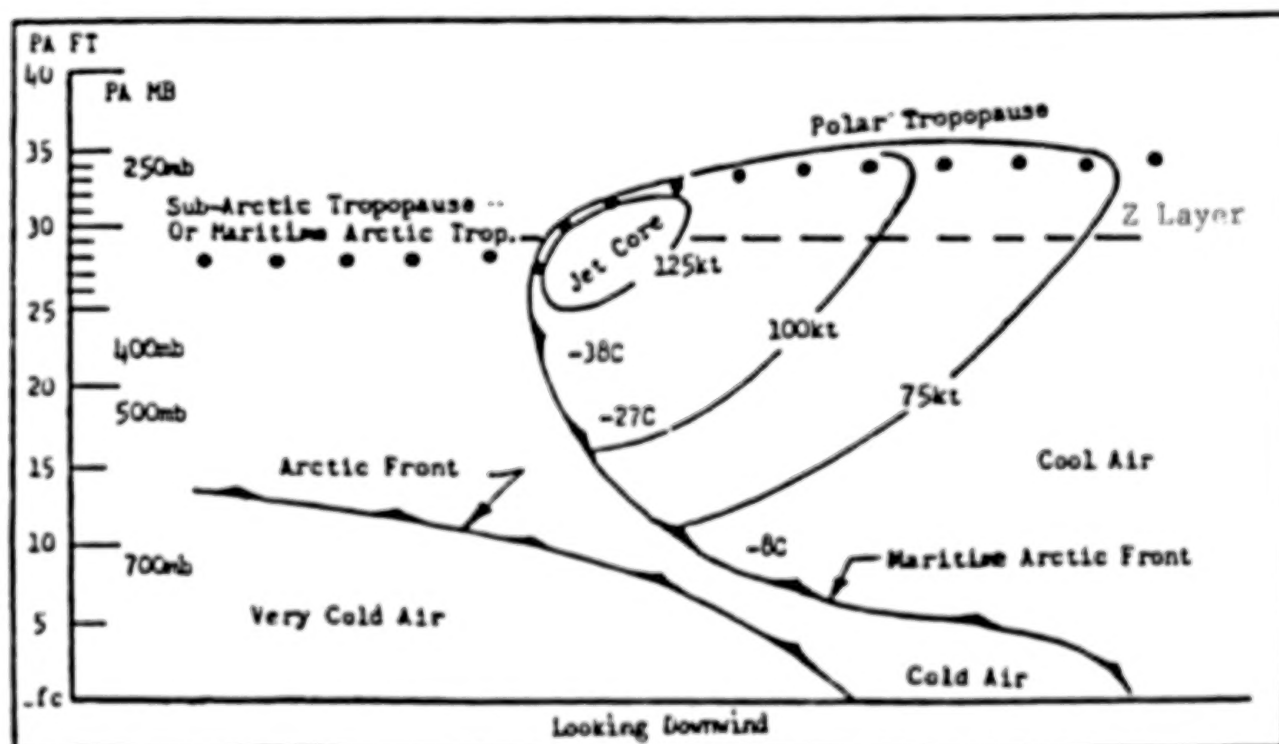


Figure 4. A typical model of the maritime Arctic frontal zone with a wind maximum at about FL290-300 or near 300 MB.

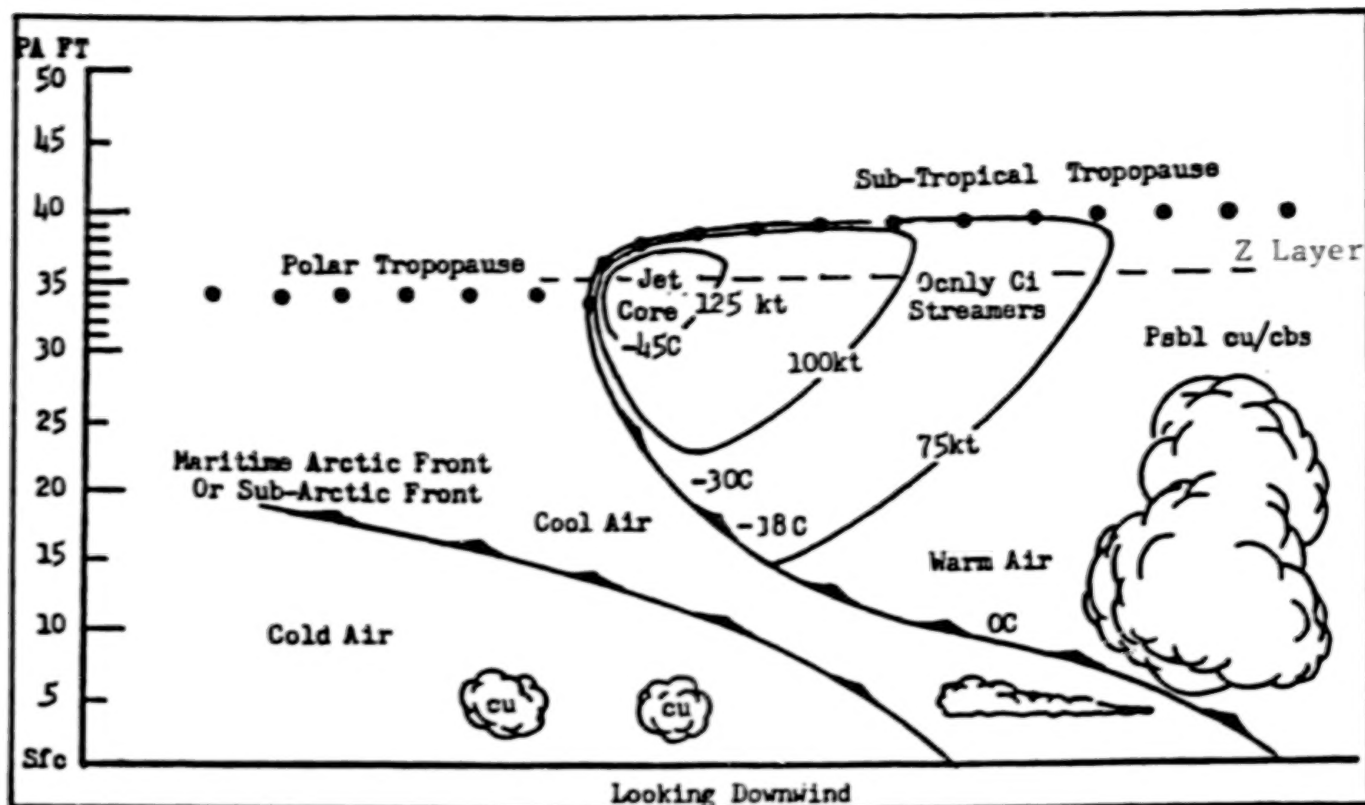


Figure 5. A typical model of the polar front with a maximum wind level of near FL340-350 at 250 MB.

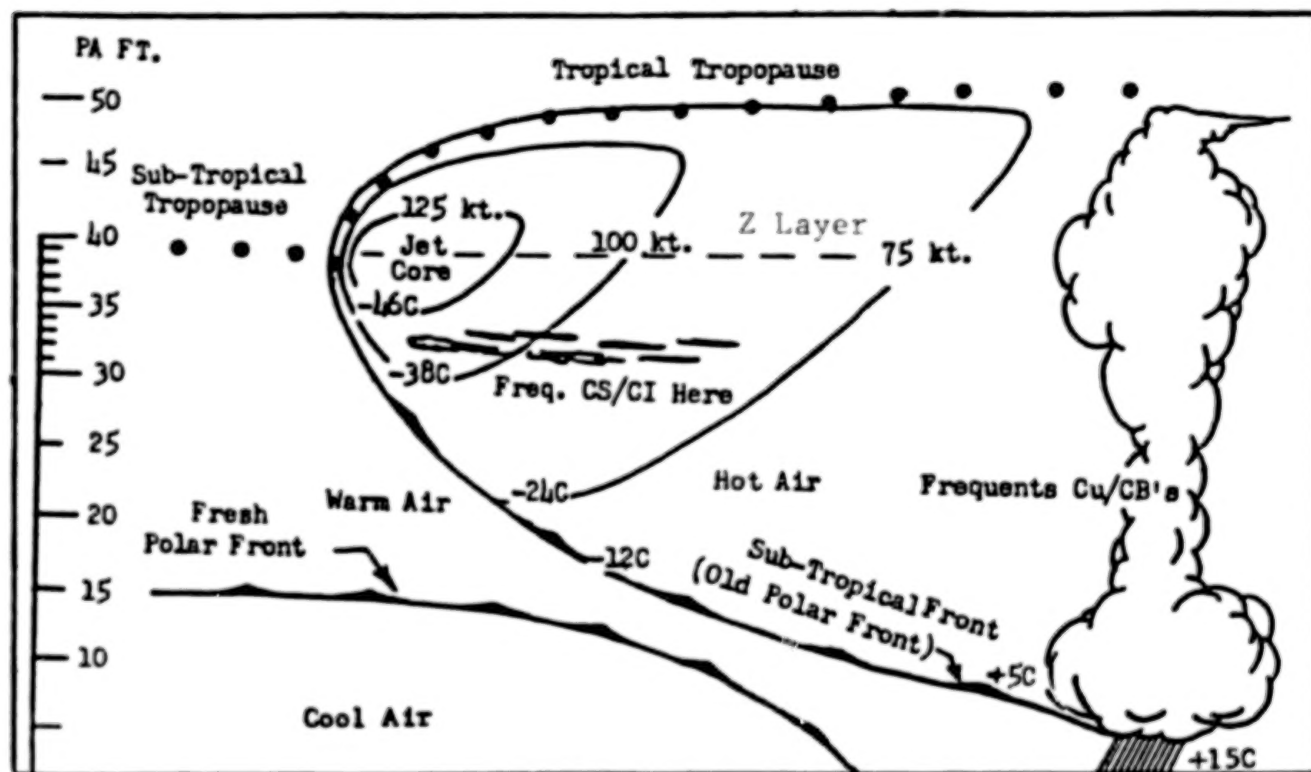


Figure 6. A typical model of the sub-tropical frontal zone with a wind maximum at about FL 390 at 200 MB.

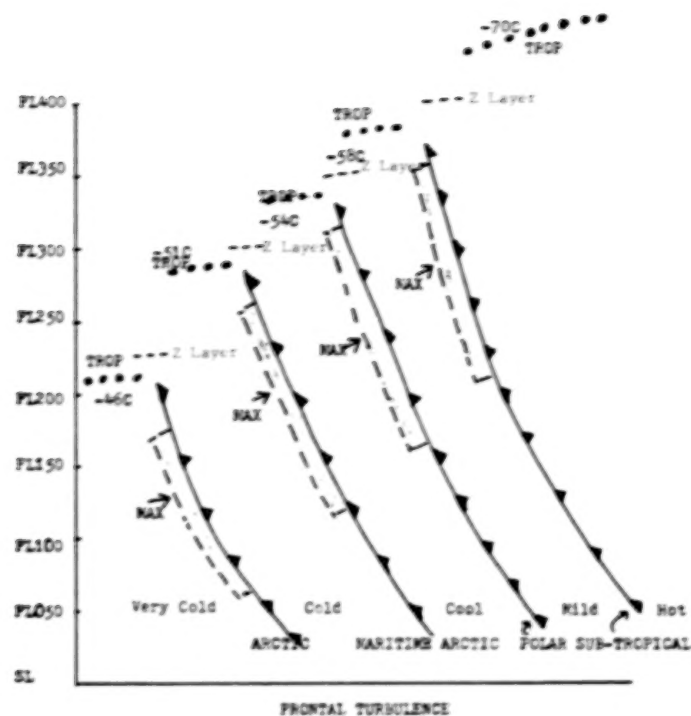


Figure 7. All four of the major frontal zones and the area of frequent, moderate, or great CAT.

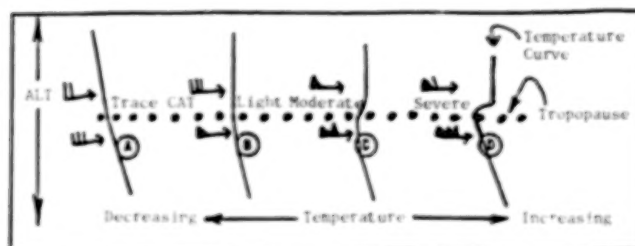


Figure 8. Various vertical temperature signatures through tropopause surfaces.

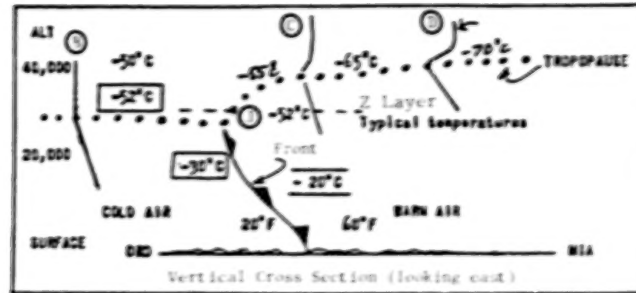


Figure 9. The B, C, and D temperature curves across a typical frontal model and associated jetstream.

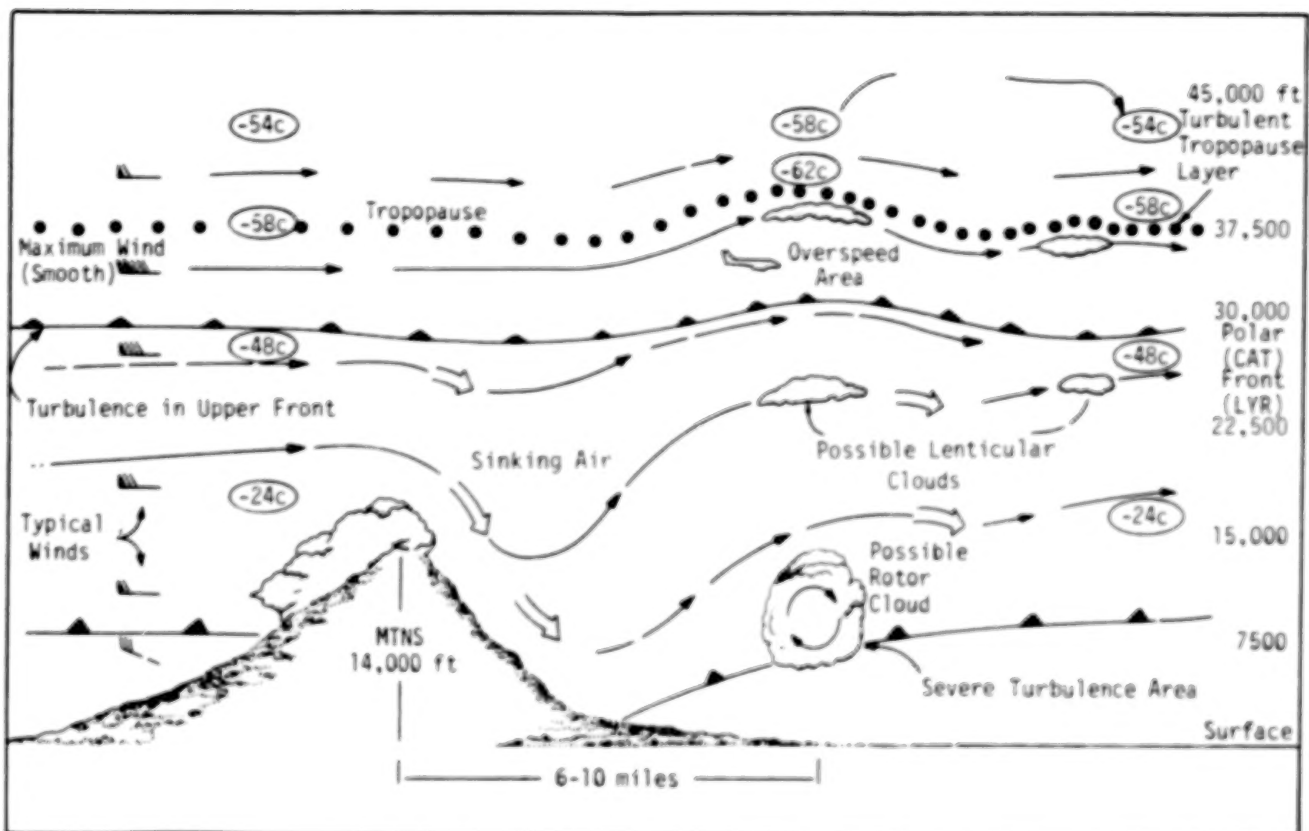


Figure 10. A classical model of a mountain wave.

Westbound GS 377 knots - Time in updraft 38.5 secs.

Eastbound GS 577 knots - Time in updraft 25.2 secs.

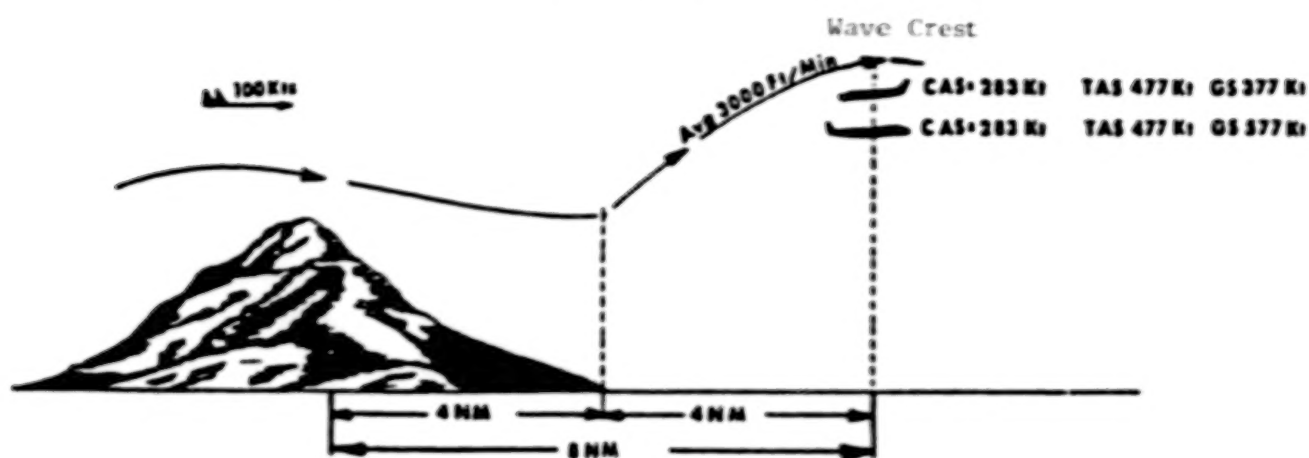


Figure 11. A typical wave with updraft.

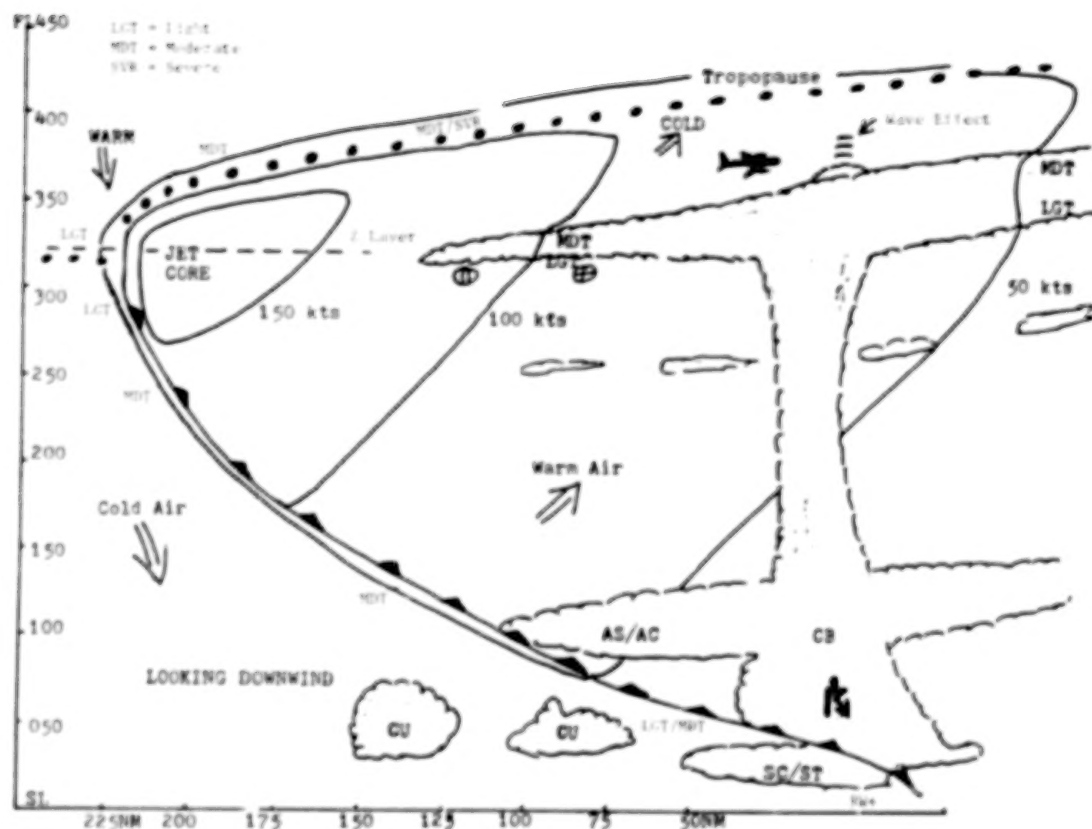


Figure 12. Cloud turbulence.

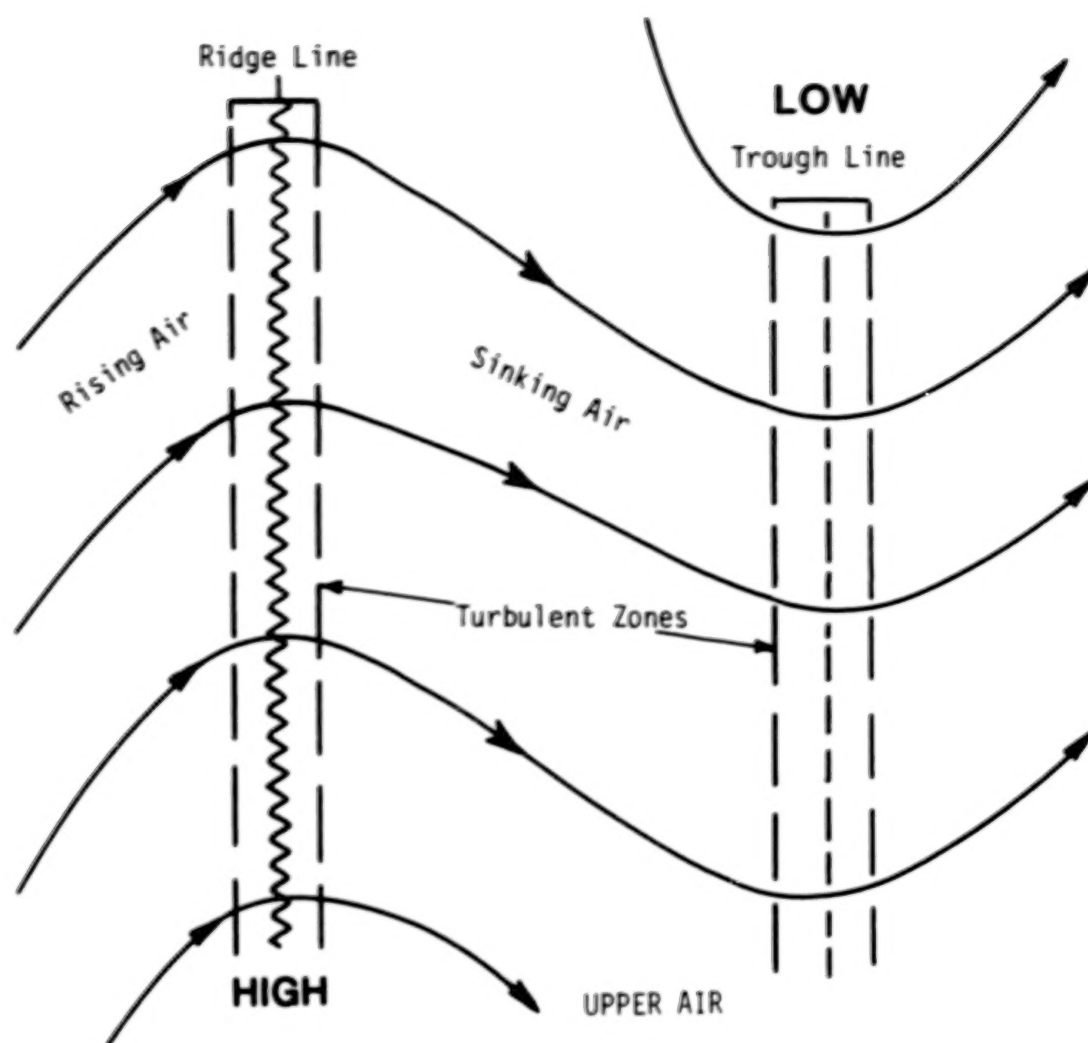


Figure 13. A ridge line as it may appear on an upper air chart.

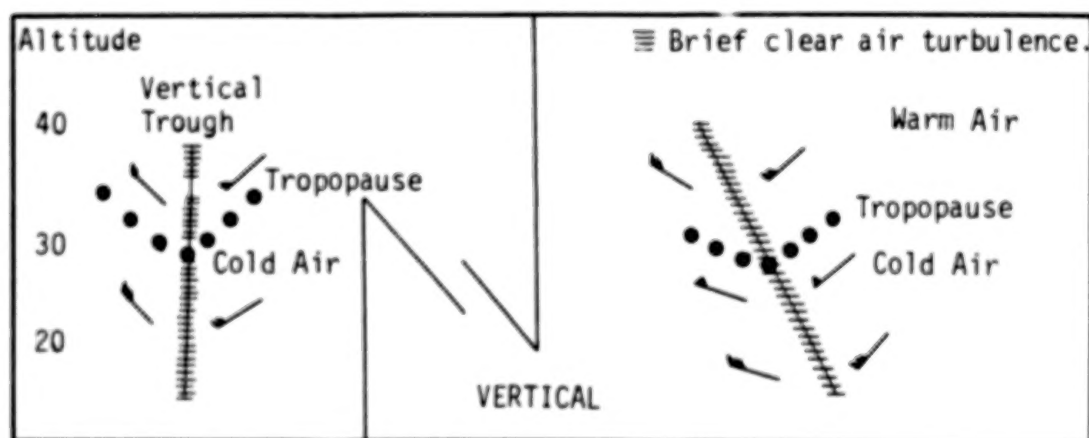


Figure 14. A trough line as it may appear on an upper air chart.



ORIGINAL PAGE IS  
OF POOR QUALITY

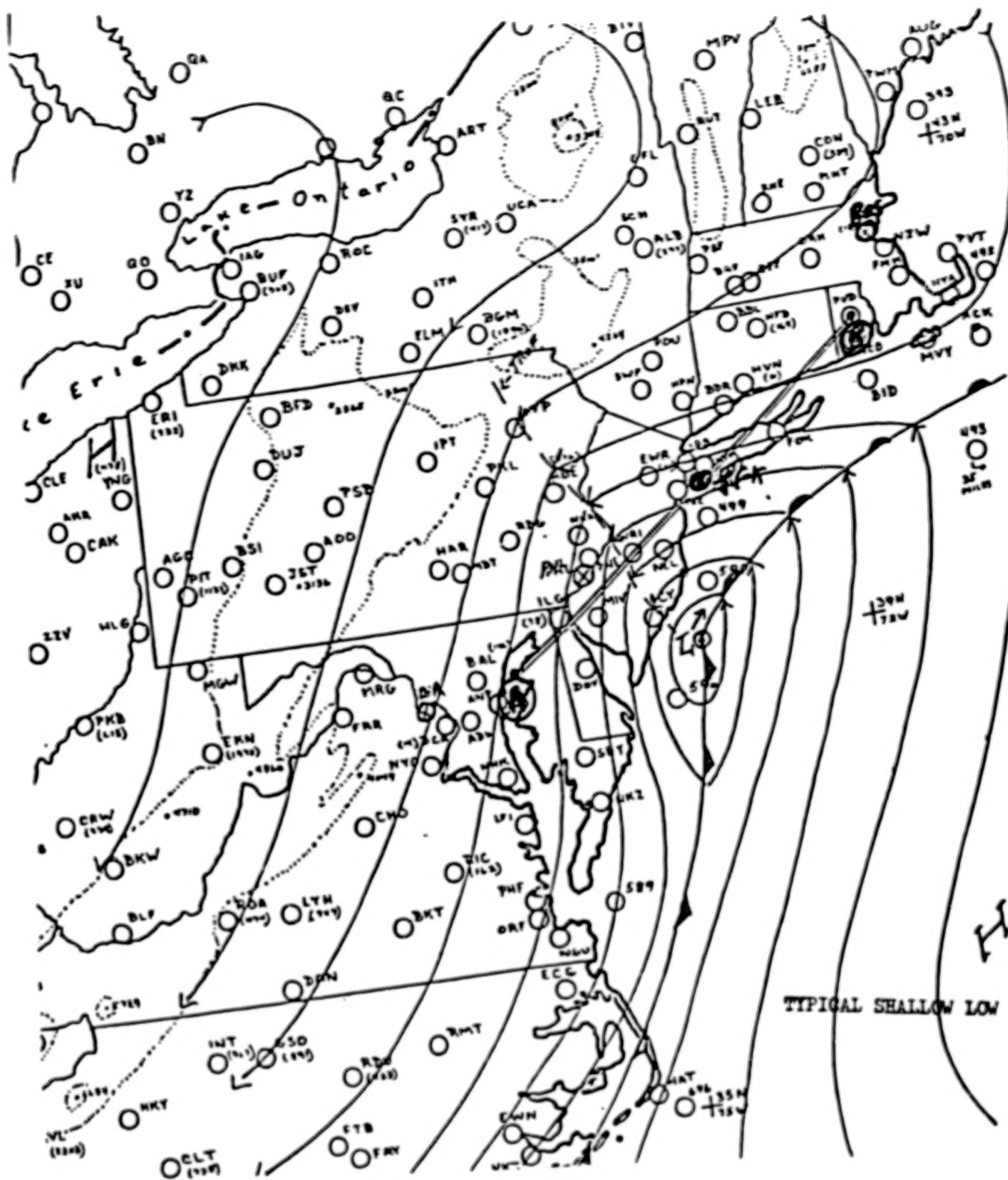
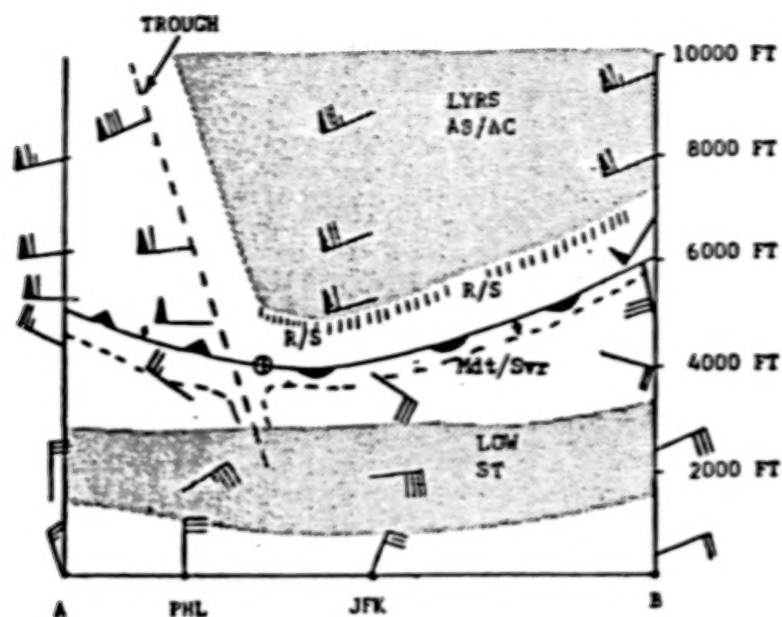


Figure 15. Severe cases of moderate to severe low-level turbulence in the east coast area of the United States.



Most of the turbulence would be found along the frontal zones (about 4000 ft at JFK and 6000 ft at B). Also, along the sloping trough line.

Figure 16. Vertical cross section along the line AB.

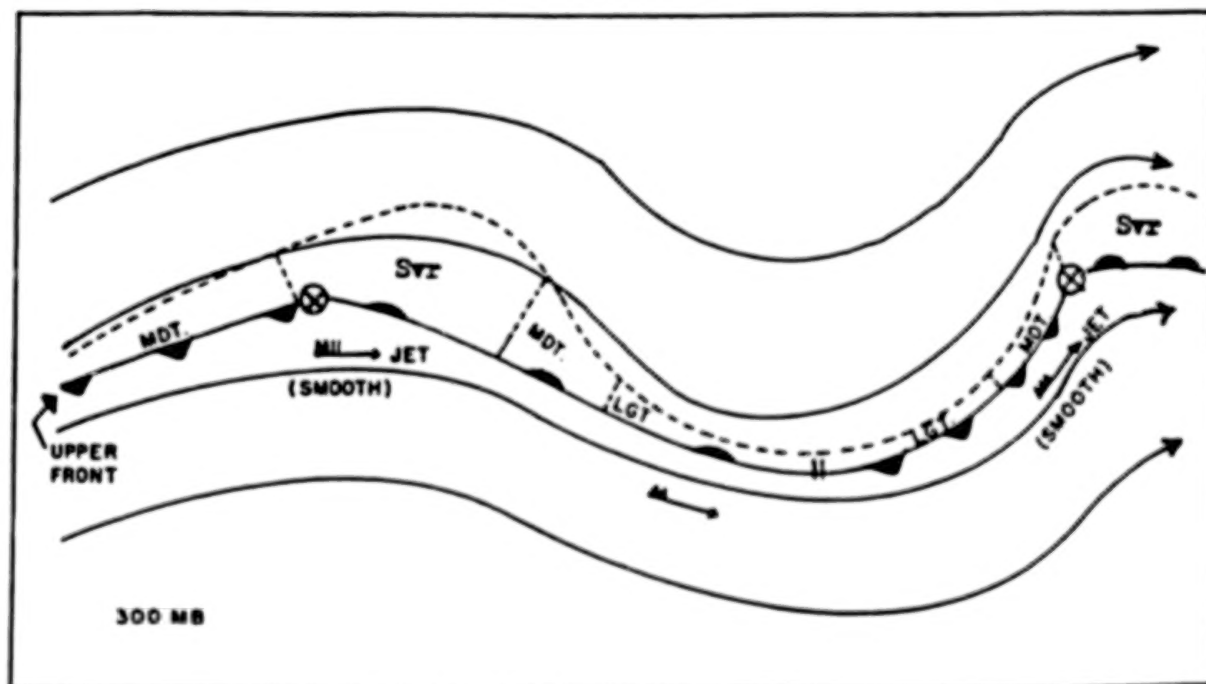


Figure 17. An illustration of a very sharp upper warm front within a ridge line that most always result in moderate to severe turbulence.

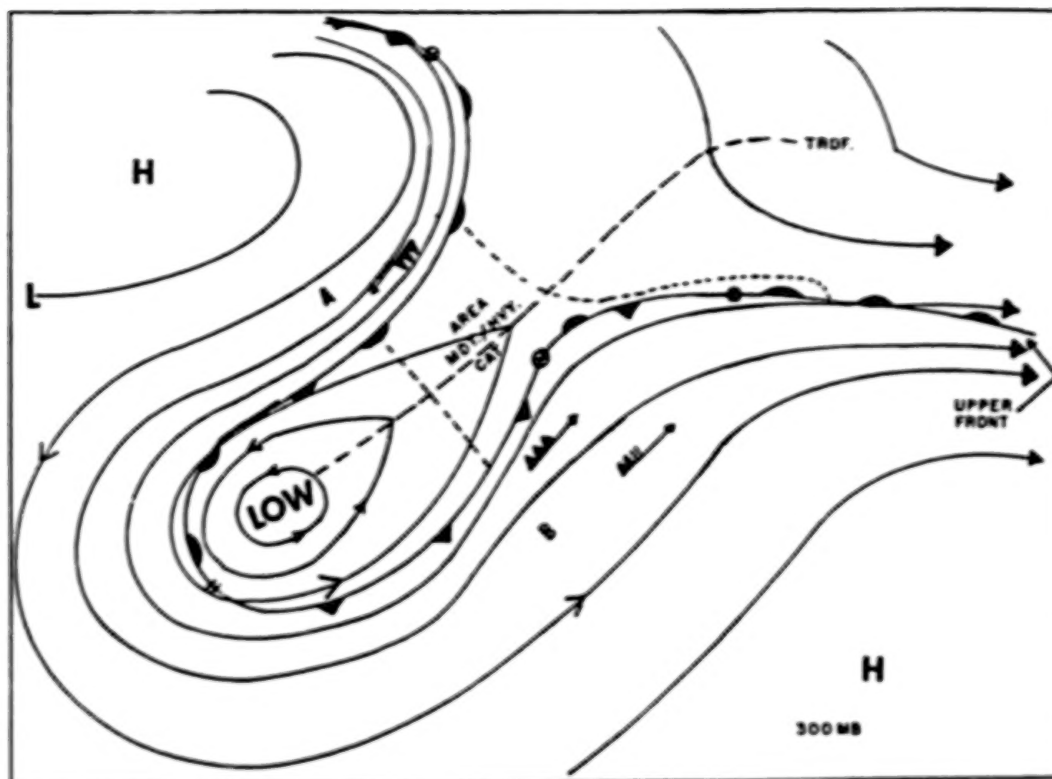


Figure 18. A cold cut-off cold low with an upper jet front.

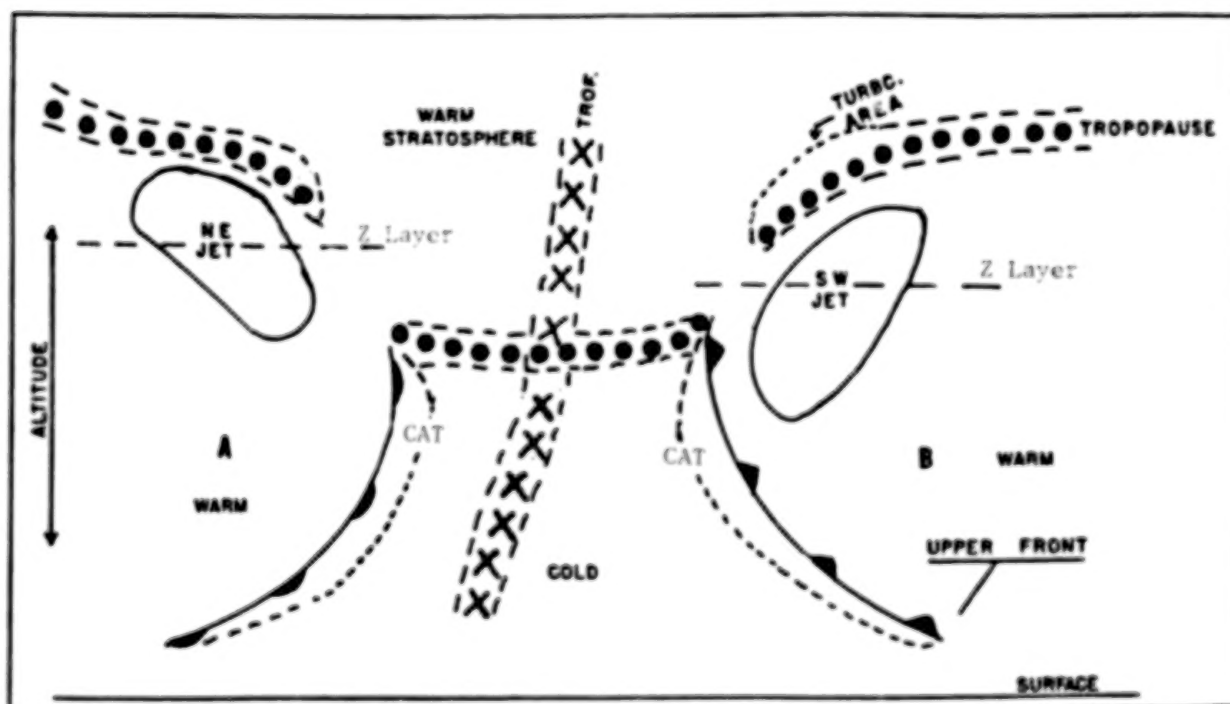


Figure 19. A vertical cross section along line AB which shows the areas of turbulence.

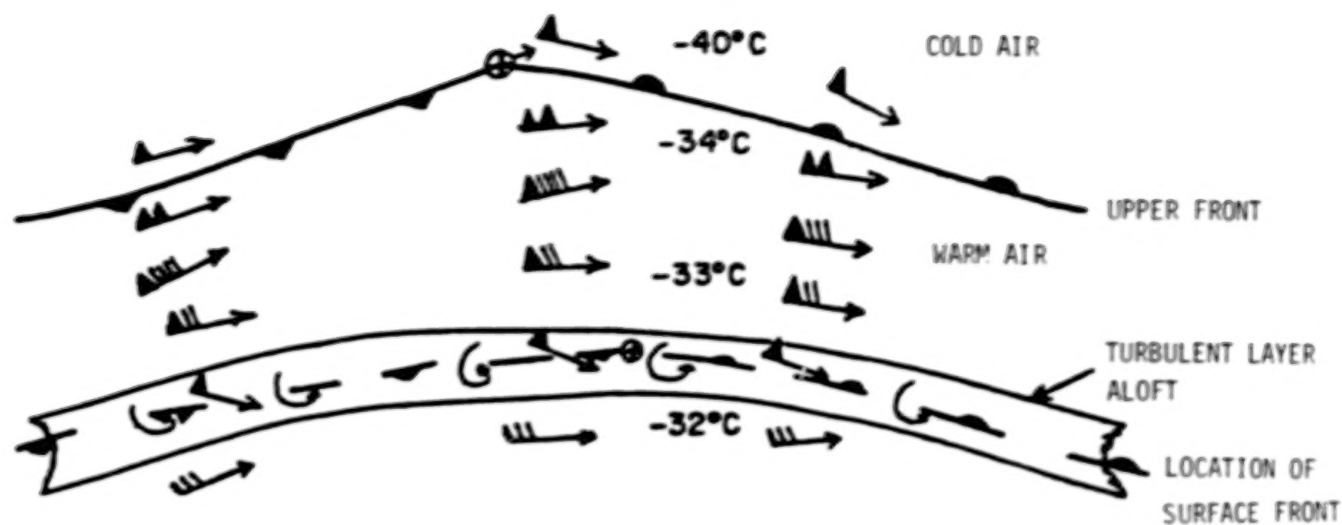


Figure 20. The position of the surface front and associated upper air position.

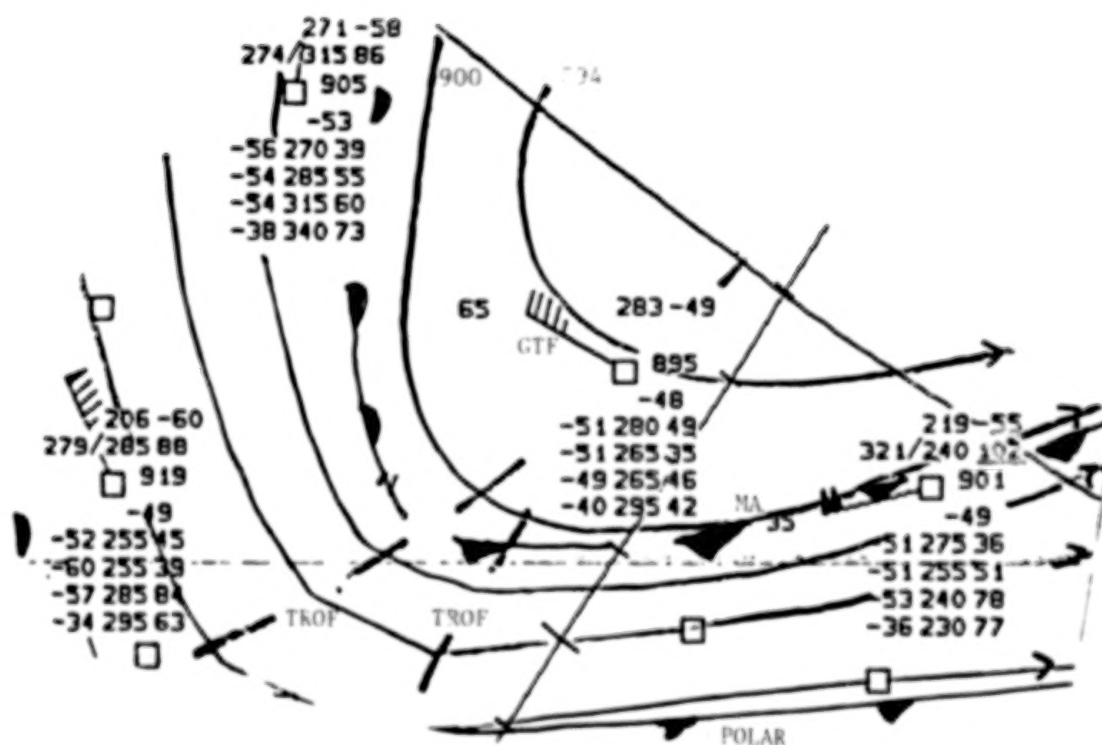


Figure 21. The actual for 1200Z on March 31, 1986, for the Pacific Northwest with maritime and polar fronts.

GBTA0000/29-0600/29B20/1552/1546/1545/1541/1544/1540/1187/1183/  
1186/1182/1185/1181/1184/1180\*

AT 29/0000Z AN UPPER FRNT AT FL320 EXTENDS FRM BIS SUX OMA  
MCI TUL TO DFW. SLOPING DOWN TO THE EAST..THE TROP AT FL360  
ABV THE FRNT SLOPES UP TO THE EAST....BY 29/0600Z THE FRNT AND  
TROP WILL BE ALONG A LINE FAR RWF IRW 80W LIT TXN GGG CLL.

LOOK FOR MOSTLY MDT TURBC THRU THE FRONTAL SLOPE FL180 UP TO  
FL260 AND LGT PSBL BRW MDT FL260 TO FL320..OCNL LGT TURBC THRU  
THE SLOPE OF THE TROP.

FL330 AND FL350 THE 2 LAYER SMOOTHEST WAY THRU..

A/C WEST BOUND BLO FL330 DESCEND AND ABV FL350 CLB FOR THE  
FASTEST OUT....A/C EAST BOUND BLO FL330 CLB AND ABV FL350  
DESCEND FOR FASTEST OUT..PATTON

GBTA0000/29-0600/29T21/1176/1181/1175/1180/1174/0823/0817\*

AT 29/0000Z AN AREA OF SCTD TRW COVERS MOST OF MISS ALA THE  
WESTERN FLA PANHANDLE AND WESTERN TENN..

A SCTD TO BRN LINE OF TRW EXTENDS FRM MEM TO JAN AND MCB  
TOPS IN THE LINE TO 400. THE CELLS ARE MOVING NE WHILE THE  
LINE IS MOVING EAST. AND BY 29/03Z WILL EXTEND FRM 95SW BNA TO  
MEI AND MSY TOPS NOW TO NEAR 470..BY 29/06Z THE LINE WILL EXTEND  
FRM BNA TO BHM CXL MOB..TOPS NOW DOWN TO 410..LINE TO CONTINUE  
EAST BEYOND FORECAST PERIOD.....PATTON

Figure 22. A sample Delta Air Lines turbulence alert that is entered  
into the flight planning system.

N87

22352

UNCLAS



## TRANSPORT MODELS FOR NUMERICAL FORECAST

Stephen D. Burk  
Naval Environmental Prediction Research Facility  
Monterey, California

The explosive growth of computing power, coupled with scientific and technological emphasis on the national scale, has led to significant major advances in operational numerical weather prediction (NWP) during the last two decades. There are about half a dozen major centers around the world running global NWP models operationally. Many more countries have operational hemispheric or limited-area models which provide weather forecasts. The global models typically have several hundred kilometer resolution, while the limited-area models usually have horizontal spacing of 50 to 100 km. Given the pace of burgeoning growth in this area, it seems warranted to occasionally take an overview of aspects of the field common to all modelers. In this note I take a brief look at the nature of subgrid scale turbulence transport parameterization, and some of the difficulties pertaining thereto, with particular emphasis on operational NWP models.

The Navier-Stokes equations describe the physics of atmospheric flow, and one might expect that it would be possible to numerically solve these equations in such a way as to yield near perfect depiction of all details of the flow, and hence, near perfect forecasts. It would be simply a matter of resolving all elements of the flow which have a significant impact on its evolution. While such direct simulations are possible for low Reynolds number flows, it can be demonstrated [1] that because of the wide range of scales of turbulent motion that are coupled nonlinearly, it would take roughly  $10^{20}$  grid points to directly compute the flow over a region 10 km on a side. This is clearly beyond the capability of any dimly envisioned future computer.

Instead of trying to resolve all important eddy scales, one necessarily must address a less ambitious goal of forecasting the evolution of averaged values of the meteorological relevant quantities. Typically in operational NWP models, this means forecasting the value of a variable within a grid volume that may be 100 km on a side horizontally, and 50 to 100 mb thick vertically. Clearly, this grid will not have sufficient resolution to describe many interesting phenomena. A powerful thunderstorm having a horizontal scale of 10 km will not be resolved by this grid, nor will the details of a sea breeze, or clear-air turbulence, etc. But if the model cannot resolve these phenomena, and if we are only attempting to define averages on quite a large scale, do we really have to concern ourselves with such subgrid scale processes? The answer is a definite yes. These features of the turbulent flow, even though they be subgrid to our model, still interact in a complex, nonlinear manner with flow on the resolved scale. Thus we are led to the problem of parameterization, which in essence is the science (and to some degree, art) of properly representing subgrid scale influences on the model's resolvable scale variables.

There exists considerable diversity in the techniques used for parameterizing transport processes within NWP models. The earliest form of

transport parameterization used in NWP models involved eddy-coefficient or K-theory. In K-theory the subgrid fluxes which one wishes to parameterize are assumed to be proportional to the local gradient of the relevant mean quantity. The proportionality factor is the eddy coefficient, K. The problem thus shifts from one of specifying unknown subgrid scale fluxes to that of defining "proper" eddy coefficients for the flow. In early treatments, the eddy coefficients generally were selected *a priori* according to some analytical function. Thus, to some extent one was determining the answer before beginning the integration. Current K-theory models often use eddy coefficients which depend in some manner on the stability of the flow (through deformation and buoyancy, or a bulk Richardson number, for example). Thus, the magnitude of K varies in time and space in a manner dependent on the evolution of the flow variables--a very desirable feature. Some weaknesses in K-theory, however, have led to the development of alternative approaches to transport modeling. For example, in convective situations where large eddies fill the atmospheric boundary layer (ABL) and are responsible for a significant fraction of the transport, the fluxes are not strongly related to the immediate local gradient. In fact, these eddies may transport heat counter to the local temperature gradient, which would imply nonphysical, negative eddy coefficients.

One of the alternate approaches to modeling transport processes within the atmospheric boundary layer takes advantage of the observation that often under convective situations the wind, potential temperature, and specific humidity are nearly constant with height from near the surface to near the boundary layer top--that is, these quantities are well-mixed within the convective ABL. Given such conditions, it is unnecessary to have many grid points in the vertical resolving the profiles, since their values within the mixed-layer can be defined by single mean values. It is, however, necessary to carefully define the fluxes at the top and base of the mixed-layer since these fluxes will determine how the mean values within the mixed-layer change with time. Since one does not have multiple grid points near the top of the ABL to help compute the entrainment flux in this type of complex, this is particularly true when the boundary layer contains clouds, because the presence of clouds has a major impact on turbulence, hence entrainment at ABL top. Thus, although initially attractive because of their apparent simplicity, the mixed-layer formulations can become complex and require considerable ingenuity to define entrainment fluxes in situations more complicated than the clear, convective ABL.

In R&D applications, second-order closure modeling has been widely used for parameterizing the transports due to turbulence. Second-order models, like K-theory models, require numerous grid points for their computations--making no *a priori* assumptions concerning the degree to which the ABL is well mixed. Unlike K-theory models, however, the fluxes are not assumed directly proportional to local mean gradients. Instead, dynamic equations for the fluxes are developed and added to the collection of model equations to be numerically integrated. A multiplicity of terms requiring closure arises from these new equations, and fundamental work in this area centers on improving and generalizing the closure expressions.

While the second-order models often permit greater realism in their description of ABL processes, a significant price must be paid in model complexity and computer time. (In a recent third-order closure calculation, Bougeault [2] was required to integrate 50 differential equations--this being feasible only because it was a one-dimensional model.) Currently, only substantial simplification will permit second-order modeling techniques to be incorporated into operational NWP models. It is possible, for example, to include a length scale equation and the turbulent kinetic energy equation in a NWP model to help in defining a generalized eddy coefficient, without carrying all of the second-moment differential equations.

Thus, the necessity for an operational NWP model to represent the atmosphere on a horizontal scale of many hundreds or even thousands of kilometers means that resolution of turbulence transport with the same detail as practiced in current R&D boundary layer models is impractical. However, transport parameterization in these NWP models, while necessarily somewhat crude, is still of great importance to the success of their forecasts. The important question here then becomes this:

How do we take the advances being made in turbulence modeling research with high-resolution models, and with observation programs that focus on the details of local ABL turbulence, and use them to the best advantage in developing the physical parameterizations required in coarser-scale NWP models?

It clearly requires more than "scaling-up" the closure assumptions used on the fine scale to the larger scale. For example, a transport parameterization used for describing turbulent fluxes in a detailed cloud model cannot be expected to also represent the situation when towering cumulus, embedded in an otherwise nearly laminar troposphere above the ABL, become entirely subgrid to the model. And, indeed, entirely different phenomenological approaches have been developed for representing cumulus effects in synoptic scale models. But where are the bounds defining the types of transport scheme appropriate to a given model simulation? Or, to pose the problem slightly differently, if we begin with a fine-resolution three-dimensional model and gradually increase the grid spacing in successive simulations of the same situation, how should we gradually alter the parameterization algorithms so as to continuously represent the flow in a realistic manner at each scale? The demand for increased skill in sub-synoptic and mesoscale NWP models requires that such questions be addressed in a serious, extensive manner.

#### References

1. Wyngaard, J.: Boundary-Layer Modeling in *Atmospheric Turbulence and Air Pollution Modeling* (Nieuwstadt, F. T. M.; and Van Dop, H., eds.), pp. 69-107, 1982.
2. Bougeault, P.: The Diurnal Cycle of the Marine Stratocumulus Layer: A Higher-Order Model Study, *Journal of the Atmospheric Sciences*, 42:2826-2843, 1985.

**QUESTION:** Warren Campbell (BDM Corporation). How do you calibrate the models that you use? Ordinarily when you start doing model equations you end up with a group of parameters and then you have to come up with solutions to those parameters. How do you go about actually making comparison with what's going on in the atmosphere in making those calibrations?

**ANSWER:** As far as the second-order closure models, most of that kind of thing is done first by using model calculations of laboratory flows to set the model constants. I have been working with the various versions of the Mellor and Yamada formulation, and they have a hierarchy of different order closure models. If you look at how they got the closure constants that are used, it traces back to laboratory flow simulations. So you don't have to change them for every new meteorological condition you are dealing with, which is a nice feature.

N87  
22353  
UNCLAS



EXAMPLE ON HOW TO MODEL AND SIMULATE TURBULENCE  
FOR FLIGHT SIMULATORS

John C. Houbolt  
NASA Langley Research Center  
Hampton, Virginia

There has been a lot of analytical development on gust response in the past several years, but evidently the material has not been disseminated very well.

Therefore, I would like to first discuss length scale,  $L$ ; using the spectrum differently; how  $\sigma$  and  $L$  form a combined parameter; why  $L$  is not important; and the exceedance number  $N_0$ .

Consider Figure 1 which deals with the scale of turbulence. Note that sometimes it is improper to derive an artificial or apparent value for turbulence length scale and then label it as the integral scale of turbulence. Suppose we have some data, as depicted in Figure 1, and then we curve fit an analytical function to the data. We do this specifically to deduce a value of  $L$  that makes the function fit the data. We should be very careful and not call this deduced value the integral scale of turbulence. Keep in mind that what we are doing is not only measuring the turbulence but also measuring the phenomenon that is causing the turbulence. The value of  $L$  may thus be misleading.

Figure 2 shows the power spectrum as obtained from measurements of turbulence and winds for very different intervals of sampling times ranging from 1 second to 1 minute, to an hour, to a day, to a week, to a month, to a year, and to five years. Just about all wavelengths of turbulence are possible in this representation of the turbulence spectra. If we fit a chosen function to the data, say a von Karman function, we might deduce a scale of turbulence on the order of 1000 miles. Thus, be very careful how you describe the scale of turbulence because it depends on the phenomenon and on the time interval of sampling. In the case of sampling over years, we are working with wavelengths that may be several thousand miles long.

For a number of years I have advocated that spectral functions should be looked at in a different way; that is, use the same spectrum function or functions that we have used before but interpret them differently. For example, we can rearrange the von Karman spectrum function so that it appears as shown in Figure 3. There is only a single line at the high frequencies. We combine both the severity and scale of turbulence to form a new parameter, designated as  $\sigma_1$  in the figure. Non-dimensionalizing the spectrum with this parameter results in all the curves condensing to the elegant form shown. Working with this modified form of the analytical function greatly simplifies the rest of the analysis.

For example, suppose we have made measurements in a patch of turbulent air and have deduced the power spectrum shown schematically in Figure 4. If



you make use of the function depicted in Figure 3, you can calculate automatically the combined parameter  $\sigma_w/L^{1/3}$  by the equation:

$$\frac{\sigma_w}{L^{1/3}} = [1.919 \Omega_1^{5/3} \phi_w(\Omega_1)]^{1/2} \quad (1)$$

This equation is obtained by simply going to the straight line portion of the curve, any place along it, and inserting the values of the abscissa,  $\Omega_1$ , and ordinate,  $\phi_w(\Omega_1)$ , into the equation. Do not try to separate the severity from the scale in any more detail. They are combined in the parameter,  $\sigma_1$ , and they should be used that way.

Let's also make an inference from this observation. For a given set of data,  $\sigma_w/L^{1/3}$  is a constant value. What does that infer? It infers the results shown in Figure 5.

From this figure we can, if indeed we want to, split it out and write  $\sigma_w$  as a function of  $L$ ; specifically,  $\sigma_w = CL^{1/3}$ . It is not surprising then that the British have come up with the notion that the turbulence severity tends to vary according to the third power of the gust gradient distance. Spectral theory predicts this behavior if  $L$  is equated to gust gradient distance  $H$  as is often supposed. But again, I remind you, although this behavior can be inferred, it is not necessary to separate  $\sigma_w$  from  $L$ ;  $\sigma_1$  should be used as a combined parameter.

When we use the combined parameter,  $\sigma_1$ , we find the output spectrum of the vertical acceleration for an airplane as a function of the reduced frequency appears as shown in Figure 6. The influence of scale shows up only in a minor way at the lefthand tails of the curves; the influence is inconsequential with respect to the overall acceleration that the airplane feels because the primary airplane response takes place out in the region of frequency where scale is completely out of the picture. This observation is true for all the airplanes I have examined so far. As an aside, we should keep in mind that at the very low frequencies where scale does have a minor effect, we are dealing with wavelengths where the pilot, the autopilot, or the navigation system is controlling the airplane. The question of turbulence scale is thus a moot point.

Some questions have arisen about the number of zero crossing values,  $N_0$ , particularly with regard to certain pertinent integrals which do not converge. However, if it is done right, there is no problem getting a meaningful value of  $N_0$ . The  $N_0$  integral will converge to a realistic value if the proper ingredients are included in the analysis. These are specifically the two functions shown in the middle of the equation on Figure 7. This equation depicts in simplified form the spectrum for the vertical acceleration of the center of gravity (c.g.). The first function on the right-hand side of the equation is a simplified form of the airplane transfer function. The last function represents the gust spectrum in simplified form. The second function takes into account gust penetration effects; notice the  $k^2$  falloff at high frequency. The third term takes into account the effects of spanwise variation in turbulence. This avoids the usual assumption that the gusts are

uniform in the spanwise direction. Observe how the effect of spanwise variation falls off inversely with  $k$  at the high frequency. Notice that the spanwise effects function also contains the aspect ratio  $A$ . When the two middle functions shown in Figure 7 are included, no problem is involved in determining the value of  $N_0$ .

Some simplified results for  $N_0$  that have been obtained will now be discussed. To start the discussion, it is noted that the study of a number of airplanes indicates that the reduced frequency  $k_0$  is related to the reduced short-period frequency by:

$$k_0 = 1.29 k_s^{0.6} \quad (2)$$

where

$$k_s = \omega_s \frac{c}{2V} \quad (3)$$

In turn, the zero crossing value follows:

$$N_0 = \frac{V}{\pi c} k_0 \quad (4)$$

Consider now the history of the gust loads analysis. If we consider the load on an airplane when it enters a sharp-edged gust such as shown in Figure 8, the load or lift on the airplane is given by:

$$L = \frac{a}{2} \rho S V^2 \frac{U}{V} \quad (5)$$

Equating this lift to an equivalent incremental acceleration gives:

$$\Delta n = \frac{L}{W} = \frac{a \rho S V}{2W} U \quad (6)$$

Note that the basic parameter which involves the combination of the variables  $a$ ,  $\rho$ ,  $s$ ,  $V$ , and  $W$  is an equation we have seen and used for years. Its continued use, however, has led us into a trap. Later I will show that by rearranging the form of the basic parameter, our results will be greatly simplified. This equation is a first cut at establishing the vertical acceleration the airplane will feel when entering a sharp edge gust. We recognize, however, that gust penetration effects, non-steady lift effects, and the vertical motion of the aircraft tend to alleviate the load. In the early years--the 1940's--we introduced an alleviation factor ( $K$ ) in the equation:

$$\Delta n = \frac{a \rho S V}{2W} K_g U \quad (7)$$

The factor was arbitrarily derived and was plotted as a function of the wing loading on the airplane as illustrated in Figure 9. We recognized, however, that the wing loading was not the right parameter to use when we started analyzing the acceleration in a more rational way, that is, when we began to include penetration effects, non-steady lift effects, and airplane motion effects.

When these various effects were taken into account the results shown in Figure 10 were obtained. The fundamental assumption leading to this figure is that the airplane is a point mass which moves in the vertical direction only; the gust was assumed uniform across the span. The incremental acceleration is noted to be of the same form as obtained for a sharp edge gust, except that a rationally derived alleviation factor,  $K_g$ , is introduced.  $K_g$  was found to be a function of the mass parameter  $\mu$ . The gust shape assumed was a one minus cosine with a gust gradient distance  $H$  of 10 to 12 chords.  $U$  was taken to be on the order of 50 fps. Actually, there is nothing magic in the choice of the one-cosine gust; it is arbitrary. A triangle or half sine wave would have served equally well.

Progressing historically, the power spectral techniques for analyzing the response of aircraft in turbulence began to be introduced. Some basic results obtained are shown in Figure 11. The equation for vertical acceleration:

$$\begin{aligned}\sigma_{\Delta n} &= \frac{\rho S V}{2W} K_g \sigma_w \\ &= \frac{V}{cg} \frac{K_g}{\mu} \sigma_w\end{aligned}\quad (8)$$

is found to be analogous to the discrete gust equation, except that the gust severity and acceleration values are now expressed in rms units. The alleviation factor  $K_g$  is also found to be a function of the mass parameter  $\mu$ , and in addition is found to depend on  $2L/c$ . This ratio  $L/c$  is analogous to the gust gradient distance in the discrete gust formulation. We should note that if the gust spectrum had been introduced as depicted in Figure 3 (i.e., as a function of  $\sigma_1$ ), then the various curves in Figure 11 would collapse to nearly a single curve.

When everything is put together in a simple rational way, the gust response equation for acceleration can be shown to collapse to the very simple result:

$$\Delta n = 1.5 \sqrt{\frac{0.13}{\alpha}} \quad (9)$$

However, Equation 9 is the complete equation for designing an airplane for gust penetrations;  $\alpha$  is the angle of attack of the airplane necessary to maintain level flight, where  $\alpha$  has the value at which  $C_L = 0$ . That is all there is. The equation automatically takes into account the altitude of the

airplane, the speed of the airplane, the weight, all the alleviation factors, everything. I believe this to be a profound equation. People should be aware of it and it should be introduced into the regulations. We must note, however, that we have not been able to change the regulations for 40 years so the chances of getting this equation into the regulations appear slim.

Note the inferences from the equation. If you run into turbulence, one of the first things you want to do is slow down a little. To slow down but maintain altitude you've got to increase  $\alpha$ . Increasing  $\alpha$  gives you smaller incremental accelerations. As I mentioned, this is a fascinating equation, and I hope we can make the aviation community aware that it exists.

I also have derived generalized equations for  $N_0$ . If we had started with the von Karman expression, the  $N_0$  value is simply given by:

$$N_0 = \frac{1.084}{\sqrt{c\alpha}} \quad (10)$$

Again, all flight conditions are taken into account in this equation. The only item determining  $N_0$  is  $\alpha$ . If we had started with the Dryden spectrum, the same form of the result is found but the constant is different:

$$N_0 = \frac{0.858}{\sqrt{c\alpha}} \quad (11)$$

Now consider the aspects of turbulence for simulator applications. There has been trouble in the past with the simulations of turbulence in flight simulators. This is primarily because only one component was used. There has been some attempt to alleviate this situation with added sophistication but overall this has not been realistic. Specifically, attempts have been made to include non-stationary turbulence such as a modulation times a stationary kind of random turbulence. But invariably when pilots fly the simulator they comment that "It does not seem realistic." It is not surprising that it does not seem realistic because the simulation is not very realistic. As I have mentioned on previous occasions, turbulence is three-dimensional in nature, and this must be taken into account.

For example, as shown in Figure 12 there are, in general, three forces and three moments due to turbulence. Not all these forces are important, not all the moments are important. There are three, in particular, that are significant. They are: (1) vertical force, (2) pitch moment, (3) rolling moment. In many cases, pitching and rolling moment have not been taken into account. We must look at the turbulence situation in a little more realistic fashion. We cannot have a rolling moment if we make the assumption that the turbulence is uniform in the spanwise direction. There is a spanwise gradient in the turbulence just like there is a variation in longitudinal direction of flight. When we take into account the spanwise gradient you will have rolling moments on an airplane. All pilots know this fact. During approach an airplane can suddenly be thrown into a 20 degree roll condition. So in simulation studies we should at least include the vertical force, pitch



moment, and roll moment because these are the important ones. In general we have not done so. The question is, how do we do that? The remainder of the presentation gives a quick insight as to how we can introduce the vertical force and the two important moments into simulation studies in a very realistic way.

Figure 13 introduces the notion of cross spectra. Along paths  $W_1$  and  $W_2$  we have different turbulence time histories. We have, in turn, differing cross spectra according to the separation distances that are involved. Let's take this into account in deriving the equations that produce the vertical force and the rolling moment.

Consider the vertical force as an example. We can simulate this very rationally in a simulator. The lift is given by:

$$L = \frac{a}{2} \rho S V^2 \frac{W}{V} \quad (12)$$

or

$$L = \frac{1}{2} \rho V^2 S C_L \quad (13)$$

where

$$C_L = a \frac{W}{V} \quad (14)$$

The actual form of the equation for  $L$  is much more complicated than shown, but if we considered the equation in complete form and took the Fourier transform of the lift coefficient you would arrive at the  $F_{CL}$  function:

$$F_{CL}(\omega) = \frac{a}{V} (P + iQ)(R + iS) F_W(\omega) \quad (15)$$

Because we have non-steady lift effects, we work with complex numbers in the frequency plane;  $(P + iQ)$  gives the in-phase and out-of-phase lift components that are due to gust penetration effects;  $(R + iS)$  is a similar kind of function but it occurs due to the spanwise variation in turbulence. It would take a week of lectures to present the complete derivation of  $(R + iS)$  but I'll indicate its basic nature as a final result. Finally, in Equation 15 we have  $F_W(\omega)$  the Fourier transform of the turbulence itself. From the Fourier transform we can readily deduce the power spectrum of the lift coefficient as:

$$\phi_{CL} = \frac{a^2}{V^2} (P^2 + Q^2)(R^2 + S^2) \phi_W \quad (16)$$

An indication of the nature of some of these functions is given in Figure 14. If we penetrated a sharp-edged gust, the lift would grow as sketched in the

upper part of the figure. Converting to the frequency plane, the  $(P^2 + Q^2)$  function as shown is obtained.

The function  $(R + iS)$  is the one term that comes about because of the explicit consideration of the spanwise variation in turbulence. It involves evaluating the integral:

$$R^2 + S^2 = 2 \int_0^2 \int_{-1}^{1-S} \frac{c(S+\eta)}{c_0} \frac{c(\eta)}{c_0} \phi_{12}(|S|, \omega) d\eta ds \quad (17)$$

where  $c$  is wing chord and  $\phi_{12}$  is the cross spectra. Evaluating the integral gives the function:  $1/(1 + 0.55AK)$ . A good approximation to this function is sketched in Figure 15.

For purposes of illustration, I have adapted:

$$\phi_w = \frac{\sigma_1^2 \left(\frac{2L}{c}\right)^2}{1 + \left(\frac{2L}{c} K\right)^2} \quad (18)$$

as the power spectrum of the input gust. I have introduced  $\sigma_1$ , the combined severity and scale parameter, and this makes all the spectra for  $c_L$  fall at the same points at high frequency.

Figure 16 shows the power spectrum of the lift coefficient as a function of reduced frequency. When all the functions are put together the equation:

$$\phi_{c_L} = \frac{a^2}{v^2} \sigma_1^2 \frac{2500}{1 + 4743k^2 + 45357k^4} \quad (19)$$

represents a quite accurate curve fit of the spectrum result. We now ask the question: Is there a differential equation which when considered could lead to this function? The answer is yes, and the equation is:

$$213 \left(\frac{c}{2v}\right)^2 \dot{c}_L + c_L = 50 \frac{a}{v} \sigma_1 W_n \quad (20)$$

This is a differential equation that would yield the spectrum given by Equation 19. If we wish, we can have coefficients in the equation vary during an approach according to the way the speed of the airplane is varying. The  $W_n$  on the right-hand side of the equation is white noise as obtained from a white noise generator; the equation automatically shapes the white noise to an appropriate turbulence spectrum. The approach for simulation is illustrated in Figure 17. Utilizing a white noise generator, feed the white noise into the analog of this differential equation. A time-varying  $c_L$  is generated which you input into the simulator, specifically to the equation for vertical



motion. A realistic simulation of vertical force on the airplane is thus obtained.

For rolling moment (see Figure 18), it is essential to take into account the spanwise variation in turbulence. The general equation for the spectrum of the rolling moment coefficient is:

$$\phi_{CM} = \frac{a^2}{16V^2} \frac{A^2}{A_0^2} I (P^2 + Q^2) \phi_w \quad (21)$$

where

$$A = \frac{b^2}{S} \quad \text{and} \quad A_0 = \frac{b}{C_0}$$

The nature of the integral  $I$  of Equation 21 is:

$$I = 2 \int_0^2 \int_{-1}^{1-S} \frac{c(S+\eta)}{C_0} \frac{c(\eta)}{C_0} (S+\eta)\eta \phi_{12}(151, \omega) d\eta ds \quad (22)$$

is shown in Figure 19.

The rolling moment integral is a little more complicated than the vertical force integral because we have to take moment arms into account. The very definite pronounced peak in Figure 19 is associated with wavelengths near the span of the aircraft. Indeed a very good approximation to the value of  $k$  at which this peak occurs at  $\pi/A$ . A very useful and simple approximation to  $I$  is:

$$I = \frac{5.57v}{7.84 + v^2} \times \frac{0.32 - 0.26\epsilon}{1 + 0.8\epsilon} \quad (23)$$

where

$$v = \frac{C}{2L} A \sqrt{1 + \left(\frac{2L}{C} k\right)^2} \quad (24)$$

Note that a different frequency argument than  $k$  alone is found.

Figure 20 shows the spectrum for rolling moment coefficient as a function of a reduced frequency. The equation:

$$\phi_{CM} = \frac{a^2}{16V^2} \frac{A^2}{A_0^2} \sigma_1^2 \frac{33.8}{1 + 685k^2 + 1473k^4} \quad (25)$$

fits that curve exceptionally well. There is a differential equation that can lead to this spectrum which we will discuss later.

Figure 21 is added here to show again the non-importance of  $L$ . The spectrum of the rolling moment coefficient is at the top of the figure. When we include the transfer function for the airplane,  $|H|^2$ , that is associated with roll dynamic behavior, you get the output spectrum for roll angle as shown at the bottom of the figure. The scale of turbulence is not important in the consideration because the predominant response is in the frequency range that is not influenced by the scale of turbulence.

The differential equation for the rolling moment coefficient is:

$$38 \left( \frac{C}{2V} \right)^2 \ddot{C}_M + 28 \frac{C}{2V} \dot{C}_M + C_M = \frac{a}{4V} \frac{A}{A_0} 5.81 W_n \quad (26)$$

Again, as in the case of the vertical force (see Figure 22), you have a white noise generator, you feed its output into the analog of the differential equation (Equation 26), and out comes the time varying moment coefficient; you input this to your simulator, specifically to the rolling equation of motion. The simulation of the rolling moment due to a turbulence encounter will then automatically be taken into account.

**QUESTION:** Hal Murrow (NASA Langley). Two points I would like to make. On the spectrum correction factor, I agree that there needs to be a correction. The point that is unclear is the magnitude of the correction and probably the biggest reason for this is the fact that in our instrumentation system for the B-57B we have some anti-aliasing filters. Their effect has to also be taken into account to determine the magnitude of the correction to apply. The second point I wanted to make is that we are talking about hypersonic airplanes nowadays, the Orient Express, that sort of thing. If you think of the primary response of the airplane as being in the short-period mode and calculate what that would be, it would go down to the very low frequencies or wavelengths. In these regions it would make a difference as to what is the value of  $L$ . I'm not convinced that  $L$  and  $\sigma$  are directly related in all cases.

**ANSWER:** That is something we will argue about in the future. You will not get down to those low frequencies with any airplane.

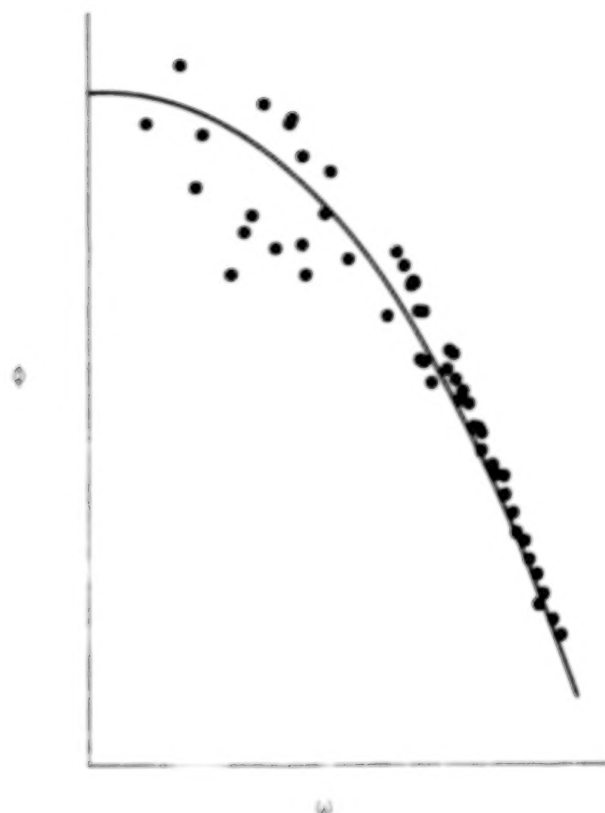


Figure 1. Curve fit of an analytical function to deduce a value for  $L$ .

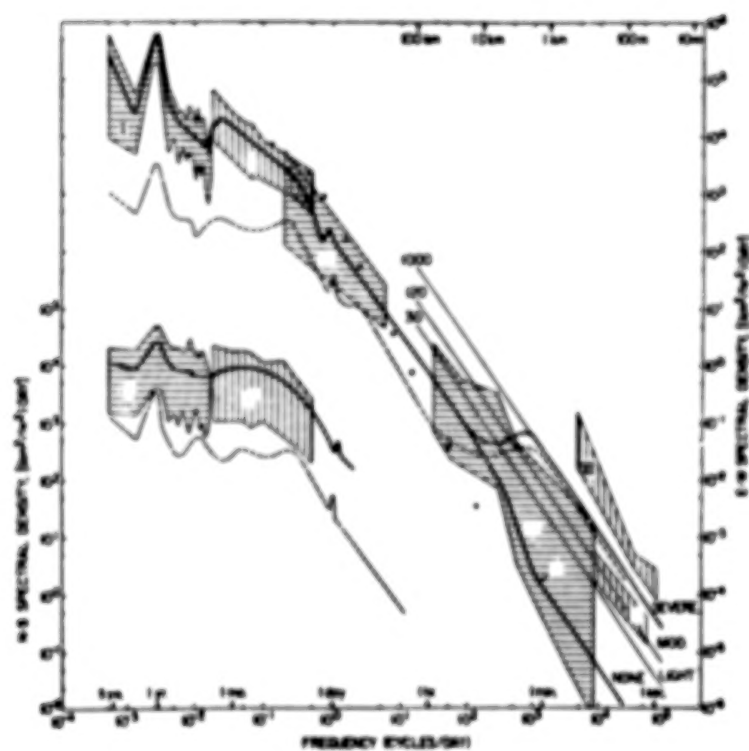


Figure 2. Power spectrum.

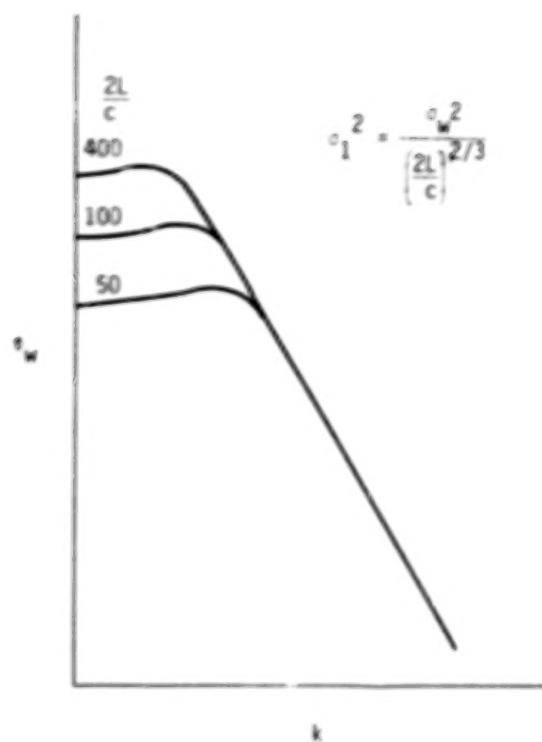


Figure 3. A von Karman spectrum.

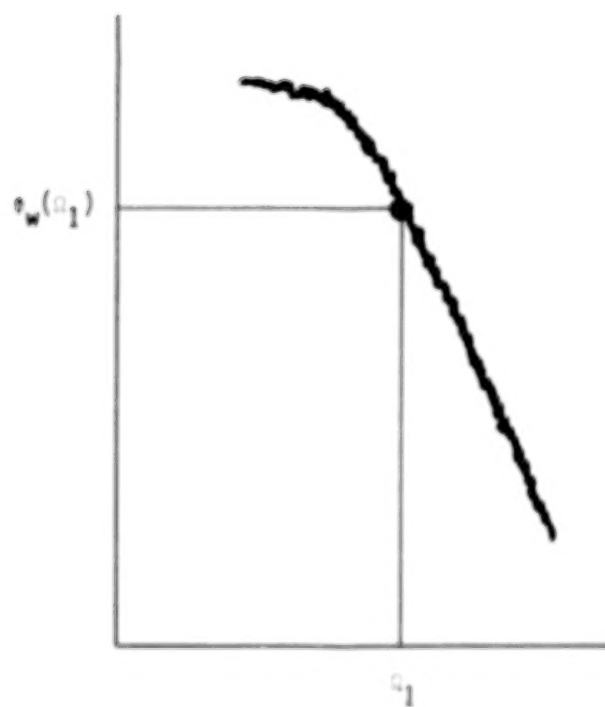


Figure 4. Example of a power spectrum for a patch of turbulent air.

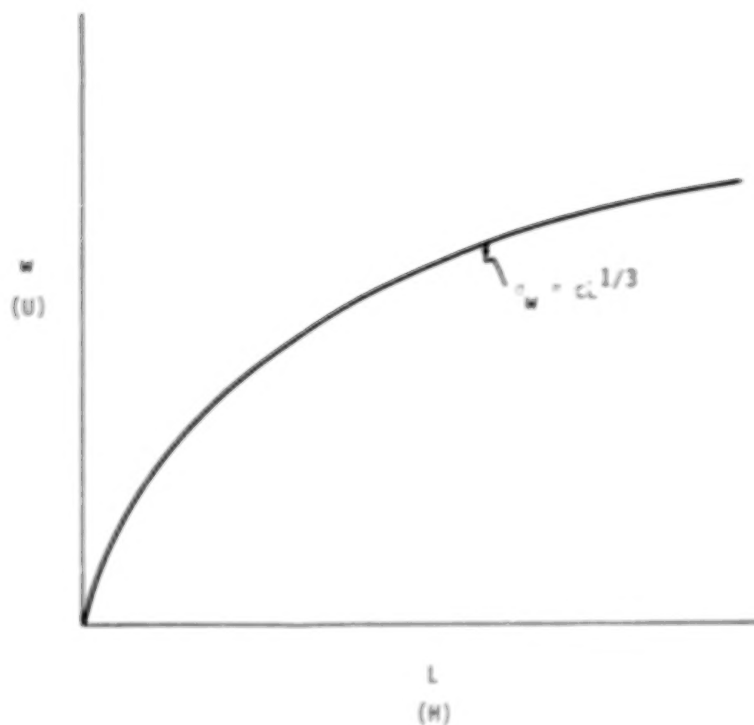


Figure 5. Influence from the relationship of  $\sigma_w$ ,  $L$ , and  $C$ ; namely,  $C = \sigma/L^{1/3}$ .

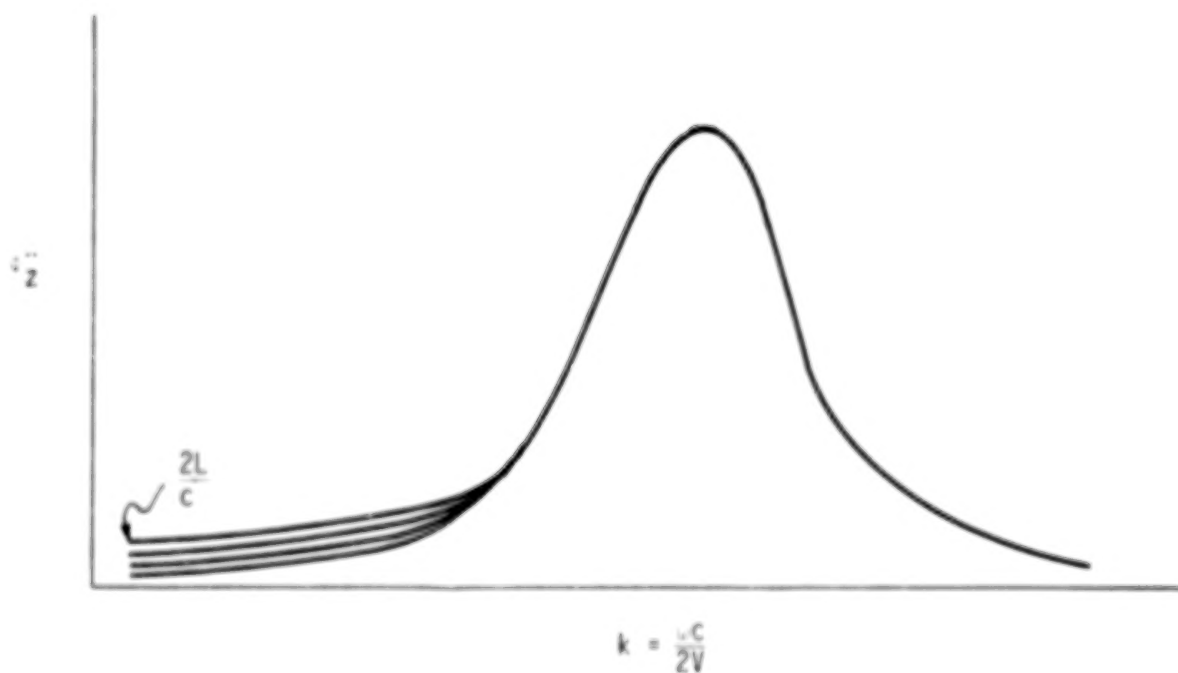


Figure 6. Example of an output spectrum for vertical acceleration of an airplane which illustrates the influence of the scale.

$$\ddot{\theta}_z = \frac{a_1 k^2}{1 + a_1 k^2} \times \frac{\beta^2}{\beta^2 + 1.5\pi k + \pi^2 M k^2} \times \frac{1}{1 + 0.55AK} \times \frac{\sigma_w^2}{1 + \left(\frac{2L}{c} k\right)^{5/3}}$$

Transfer Function

Gust Penetration Effects

Spanwise Effects

Gust Spectrum

Figure 7. Simplified form of the spectrum of vertical acceleration of the center of gravity.



Figure 8. Sharp edge gust.



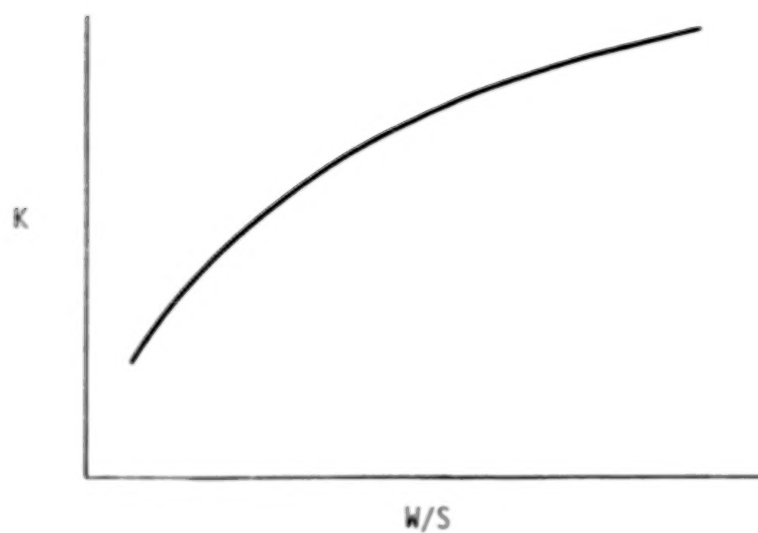


Figure 9. A 1940's version of the gust alleviation factor as a function of wing loading.

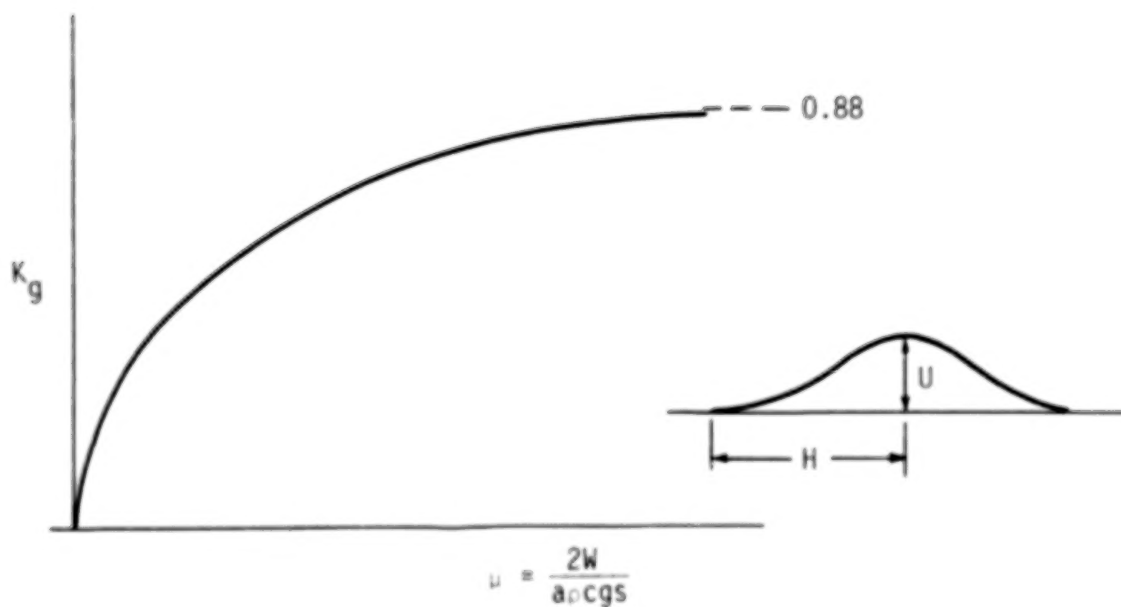


Figure 10. The gust alleviation factor as a function of mass parameter.

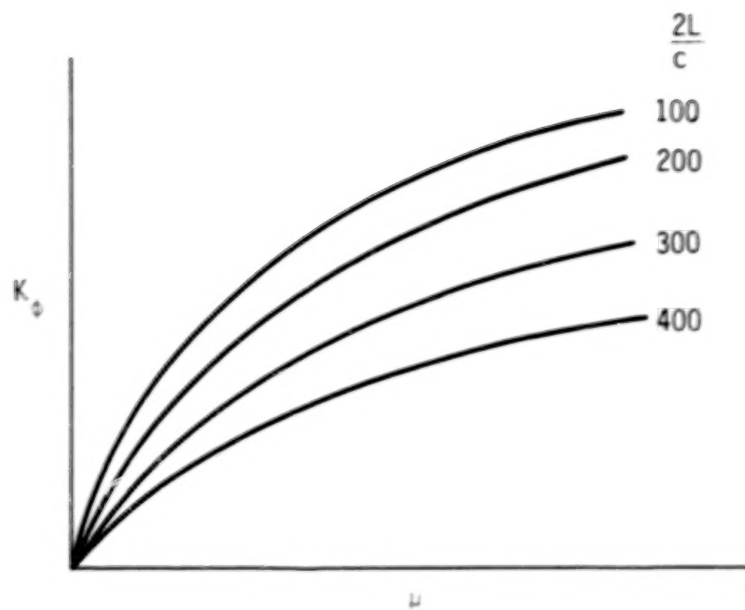


Figure 11. The gust alleviation factor as a function of the mass parameter as well as showing its dependence on gust gradient distance.

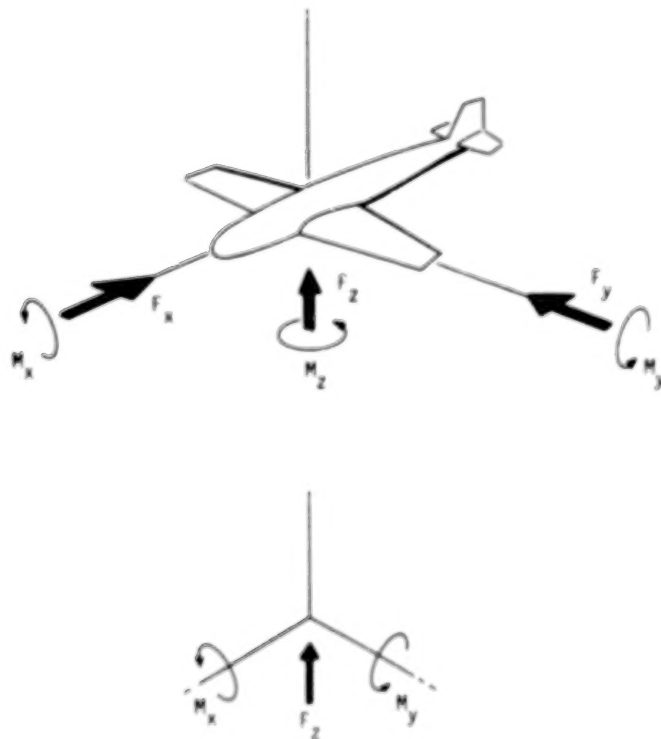


Figure 12. The forces and moments due to turbulence.

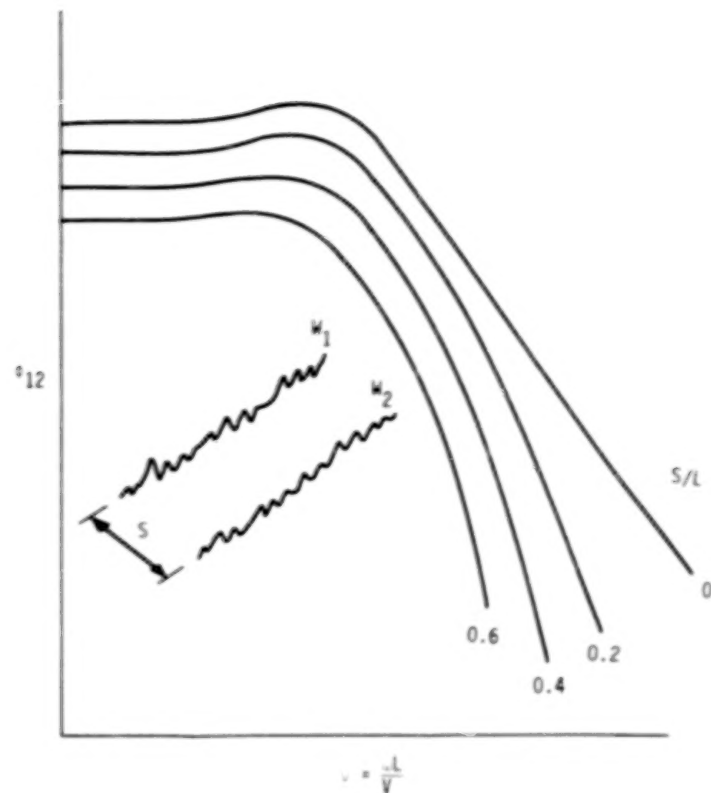
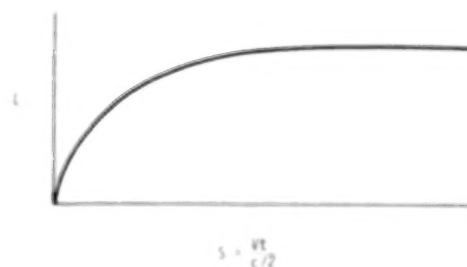
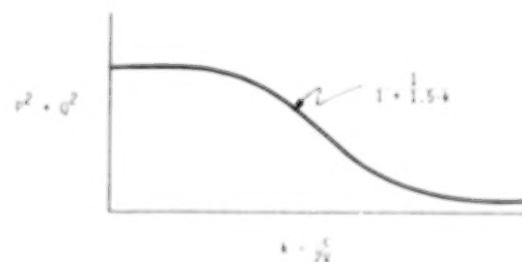


Figure 13. Illustrating the effect of separation distance on cross spectra.



(a) Time plane



(b) Frequency plane

Figure 14. Lift relationships as a function of time and frequency components.

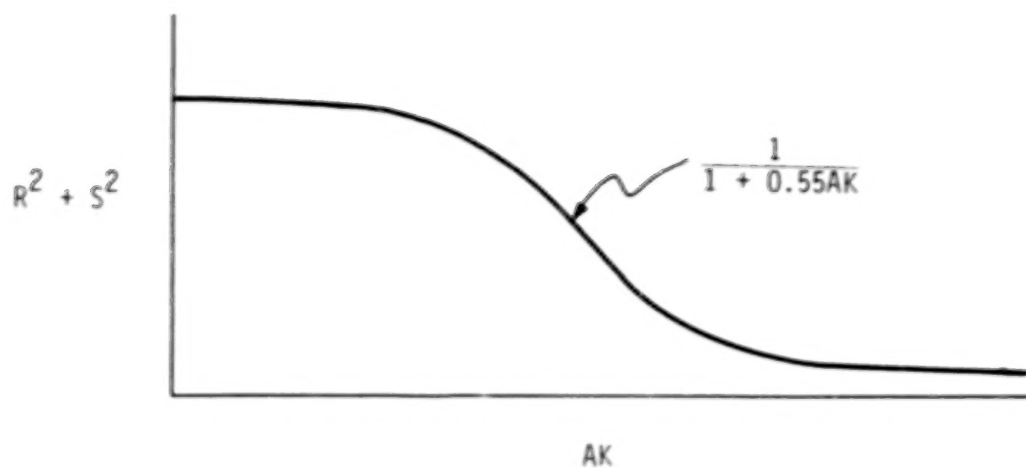


Figure 15. Spanwise variation effects with a consideration of cross spectra.

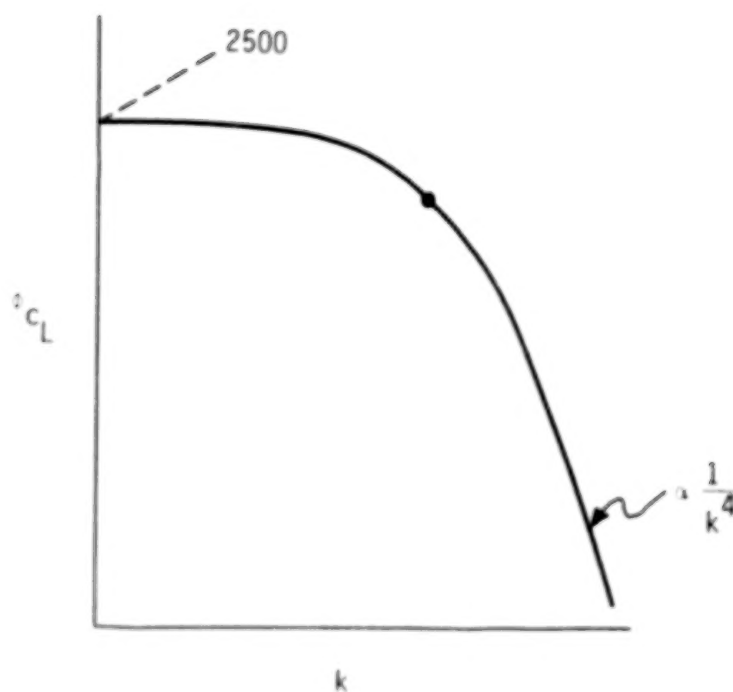


Figure 16. Power spectrum of the lift coefficient as a function of reduced frequency.

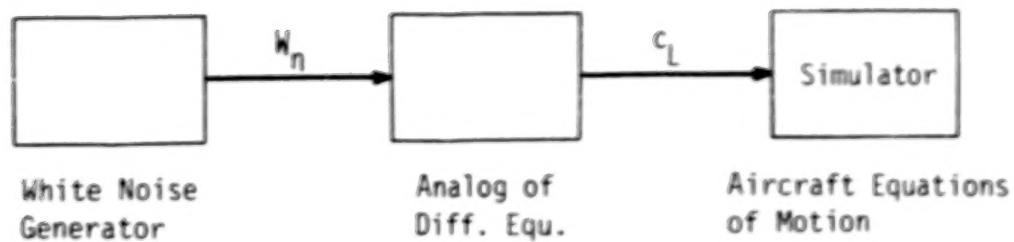


Figure 17. A realistic simulation approach.

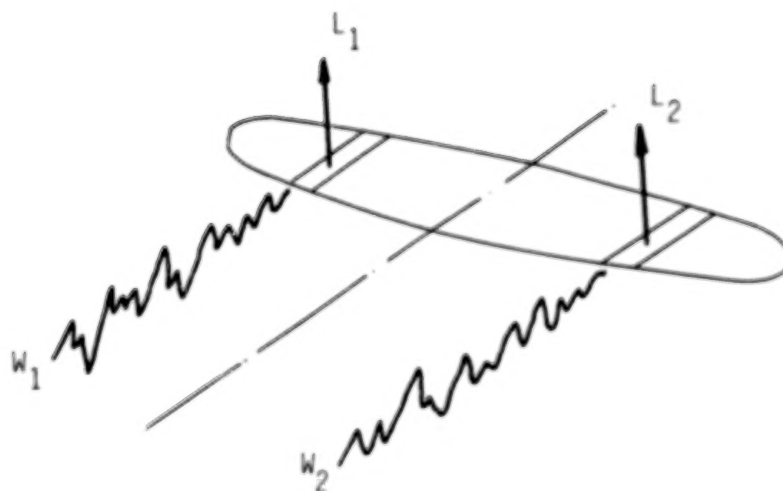


Figure 18. Spanwise variation in turbulence illustration.

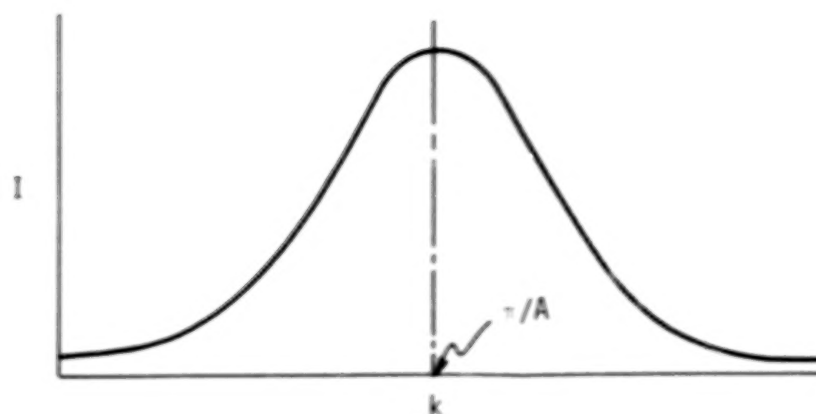


Figure 19. Rolling moment integral relationship to reduced frequency.

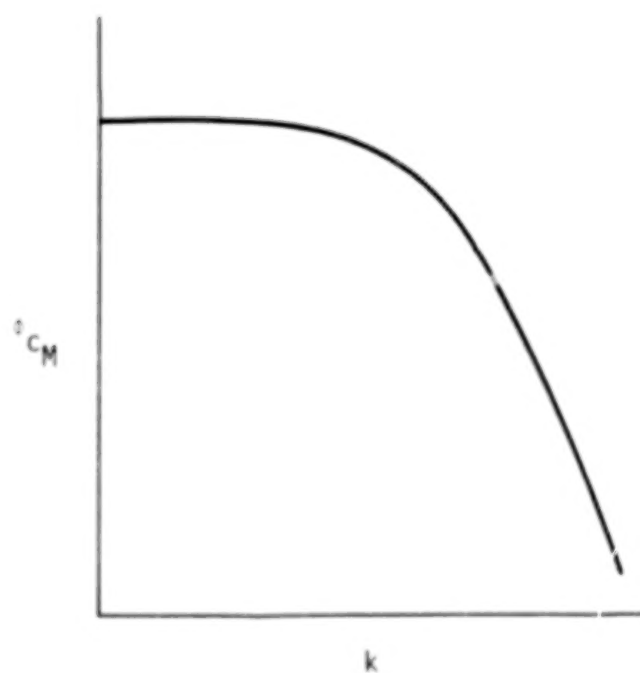


Figure 20. Rolling moment coefficient as a function of reduced frequency.



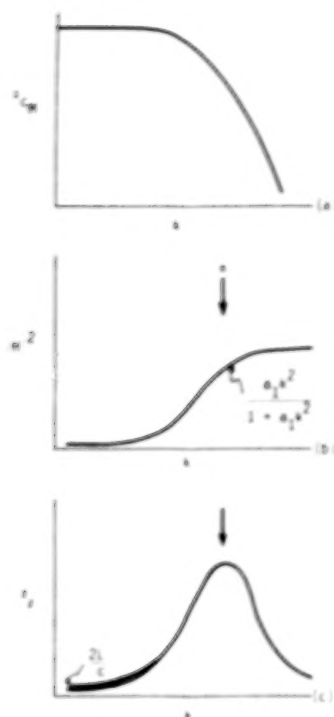


Figure 21. Output spectrum ( $\phi_\phi$ ) obtained from spectrum of rolling moment coefficient ( $\phi_{CM}$ ) by a consideration of the transfer function  $|H|^2$ , i.e.,  $\phi_\phi = |H|^2 \phi_{CM}$ .

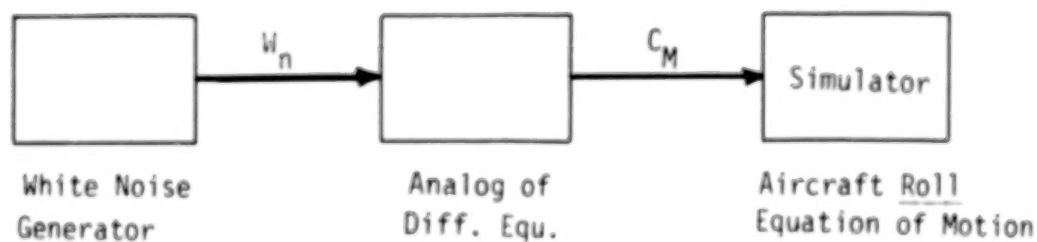


Figure 22. Roll behavior simulation.

N87  
22354  
UNCLAS

## IMPLEMENTATION OF TURBULENCE MODELS INTO SIMULATORS

Robert L. Ireland  
United Airlines Flight Center  
Denver, Colorado

In this paper, I discuss simulation of turbulence as it relates to the flight training environment. This is a remote discipline for many of you, and its requirements are significantly different from a research environment.

We find in flight training that an accurate depiction of the turbulence phenomenon is not a necessary end in itself. In fact, it is something that we do not often have the time or money to accomplish. Instead we are interested in a turbulence situation that feels good to the pilot, and perhaps what Dr. Houbolt was talking about was a very good description of where we need to go in that regard [1].

We consider all simulation enhancements in terms of training objectives. That is what we have to address, and we have a limited time to do it when a pilot that comes to the Training Center for only a three-day proficiency check each year. High-frequency sources of turbulence have to offer a distraction to the pilot. They should cause an oscillation of the instruments, and cause the simulator to move if it has a motion system. The exact scientific nature is really fairly unimportant. We do have some more specific training objectives, however, associated with the large magnitude large-scale turbulence that is often known as wind shear.

I will discuss the high-frequency turbulence issue first. We have several different examples of turbulence in the range of simulation at United Airlines at the present time. Our simulators range in age from 3 years to 25 years. Some of them merely put random white noise into the motion system, that is, of course, the most primitive. Some put random motion into the equations of motion and nothing else. There are two kinds of simulators that put the turbulence into the equations of motion. One type varies the period of the turbulence such that it does cause a disturbance of the instruments. It turns out to be pretty good. However, some newer simulators use white noise summed into the equations of motion but at the iteration rate of the simulator (30 Hz). As a result, nothing is seen in the instruments but the feel of the motion is good.

We do have two simulators in which we have implemented a more sophisticated approach. They are not limited to vertical turbulence but also incorporate pitch and roll moments. That, of course, is the best cost-effective depiction we have found. The tradeoff in implementation of turbulence in the flight training simulators comes with the interaction with the motion system. Motion systems are actually tuned so that gross maneuvers of the aircraft do not exceed the hardware limits. Consequently, in order to insert turbulence that feels adequate to the pilot, the levels are so high that they may be causing very undesirable effects in the aerodynamics. One thing that I am personally looking into at United at the present time is separately gaining the input of the turbulence to the motion system, so that a

lower level of turbulence--a realistic level of turbulence--will also produce a realistic level of motion.

With regard to wind shear, we started putting some different kinds of wind shear models into our simulators about three years ago associated with specific training objectives. We find it very important in the training environment, with more than 2000 crews passing through our simulators each year, that we have some consistency of the training product. Therefore, a microburst model which can be flown through many different ways becomes as much a hindrance as it is a benefit. While it may be a very realistic depiction of the microburst phenomenon, it nevertheless provides no two pilots with the same training experience because it can be flown through an infinite number of ways. Therefore, we have moved to simplified models based on microburst phenomena. For example, a slice through the JAWS data could be programmed into the simulator in a one-dimensional fashion. This would allow us to know that every pilot received exactly the same training experience while at the same time making sure that a level of technical realism is maintained.

In closing, one point that I would like to reference is something that is missing from our simulations right now. No appropriate level of high-frequency turbulence to go along with the microburst models has been defined. I understand that there is some work out on that now. One problem we have with our simple simulation models of wind shear is that the recognition for the pilot is not difficult at all because the airspeed suddenly begins moving and he knows immediately that he is in a wind shear. We would like to add to our wind shear simulations some appropriate levels of high-frequency turbulence to mask that and get the pilot used to what he might have to recognize in the real world.

#### Reference

1. Houbolt, J. C.: Example on How to Model and Simulate Turbulence for Flight Simulators, *Proceedings: Workshop on Atmospheric Turbulence Relative to Aviation, Missile, and Space Programs*, NASA CP-2468, 1987, pp. 159-178.

N87

22355

UNCLAS

## THE STATUS OF MILITARY SPECIFICATIONS WITH REGARD TO ATMOSPHERIC TURBULENCE

David J. Moorhouse  
USAF Wright Aeronautical Laboratories  
Wright-Patterson AFB, Ohio

Robert K. Heffley  
Manudyne Systems Inc.  
Los Altos, California

1. INTRODUCTION

Atmospheric turbulence models are included in a number of military specifications although there is no military specification devoted solely to atmospheric turbulence models, *per se*. Perhaps the closest example of one is Reference 1, a compilation of maximum gust values for design of ground equipment. Aircraft design specifications which contain gust or turbulence models do so for different purposes. One series addresses the vehicle structural design to ensure sufficient strength when penetrating gusts and turbulence in flight. The turbulence model is expressed in terms of probability of encountering certain levels of disturbance, and has not been revised since the 1960's. Reference 2 contains a turbulence model for use in flight control system design. Again this model has not changed in recent revisions of the specification. The main emphasis of study has been on the interaction of a pilot with his aircraft in various forms of disturbances. This is manifested in the flying qualities specification [3] which contains an extensive model of winds, wind shear, turbulence, and gusts for use in aircraft design and development. It is used in flight stability and control augmentation development and as a simulator model for aircraft design. The model was updated significantly in 1980 [3] and is being further refined in the change from a Specification to a Standard [4]. The remainder of this paper will concentrate on the development and application of the "flying qualities atmospheric disturbance model."

The evaluation of the effects of atmospheric disturbances on airplane flying qualities has been approached in a diverse number of ways. The large volume of literature is evidence of this. At the same time, we have little guidance for choosing among these alternatives when specifying or examining a given airplane design. It is far too easy to become bogged down in the ill-defined tradeoffs between Dryden and von Karman turbulence forms, the need for non-Gaussian or non-stationary characteristics, the debate over how and when to model wind shear effects, or whether shorter turbulence scale lengths are more realistic than longer ones. Airplane designers and simulator researchers continually face such questions, and while they may find answers suitable for one situation, the same questions can re-appear on a subsequent occasion.

The paper will first discuss the features of atmospheric disturbances that are significant to aircraft flying qualities. Next follows a survey of proposed models. Lastly, there is a discussion of the content and application



of the model contained in the current flying qualities specification and the forthcoming MIL-Standard.

## 2. FLYING QUALITIES NEEDS

It is appropriate first to define what is meant by flying qualities, in order to keep the whole discussion in perspective. One accepted definition is "those airplane characteristics which govern the ease or precision with which the pilot can accomplish the mission" [5]. Further, flying qualities are often "measured" by subjective pilot opinion according to the Cooper-Harper rating scale [5] wherein it is stated that flying qualities are tied to accomplishing a specific task. Due consideration of environmental conditions is, in turn, implied. An airplane can have characteristics that make the task of landing relatively easy in calm air. The same task becomes very demanding in strong turbulence or even impossible in a violent thunderstorm, even though the airplane characteristics may not have changed. Thus, due consideration of atmospheric disturbances is implicit in any analysis of flying qualities.

For the purposes of the Flying Qualities Specification, an engineering model of the atmosphere may be considered as the simplest or minimum acceptable model which correctly identifies the primary parameters of particular interest. This is in contrast to the objectives of basic research into meteorological phenomena or the physics of atmospheric dynamics. Reference 6 discusses this dichotomy in more detail, with some indication of how the model is built up of components. Each component either exercises a particular feature of the man/machine combination or adds a particular aspect of realism to the piloting task. Let us, therefore, devote a few paragraphs to an overview of atmospheric disturbance features which are involved in flying qualities matters.

## 3. ATMOSPHERIC DISTURBANCE FEATURES

Prior to discussing atmospheric disturbance modeling needs, let us quickly review some of the basic features of all such models realizing that each claims some kind of uniqueness with regard to the following features. We shall discuss the nature of the variations in properties, but in general they can be viewed in terms of their engineering convenience versus their physical correctness. For example, the well-known von Karman turbulence form yields more correct spectral characteristics, but it is not as easily realized computationally as the more approximate Dryden form. The same kind of tradeoff between convenience and correctness is a dominant theme in several other respects as we shall discuss under the following subheadings.

### 3.1 Determinism Versus Randomness

Atmospheric disturbance models first can be separated according to their degree of determinism or randomness. At some level, the dynamics of the earth's atmosphere must be deterministic, but at our degree of understanding they frequently appear random. While characteristics such as mean wind and wind shear are normally handled on a deterministic basis, turbulence is

usually modeled as a randomly occurring phenomenon. Nevertheless, wind velocity or wind shear can be just as well described in strictly probabilistic terms, and turbulence, conversely, can be described in wholly deterministic terms (as with gusts composed of summed sinusoids). In addition, random and deterministic models are often combined to suit the needs of a particular application [7,8]. Deterministic features are usually quantified directly using analytic functions or tables (e.g., mean wind respect to time or space). Random components, on the other hand, involve random variable sources having their own particular statistical properties of probability distribution and correlation. The differences are probably academic to a pilot, since either or both approaches can give a realistic mode; however, appropriate partition of model determinism versus randomness figures greatly in the success of any given application as we shall discuss shortly.

### 3.2 Probability Distribution

The probability distribution of gusts describes their range of amplitudes and frequency of occurrence. This can be quantified in terms of probability density, cumulative probability distribution, or a varying number of central moments (mean, variance, skewness, kurtosis, etc.). While the Gaussian distribution is mathematically convenient, several turbulence models having more correct non-Gaussian distributions have been developed in order to address the characteristics of patchiness and intermittency. Patchiness is frequently considered as corresponding to a proportionately higher rate of occurrence of very large magnitude gusts than found in a Gaussian distribution and is reflected by the higher order even central moments (fourth, sixth, etc.) [9]. Intermittency is the counterpart to patchiness when applied to gust velocity differences over a given time or space interval [10]. But the usefulness of these model features depends upon whether the specific application can accommodate a characteristic such as patchiness on a probabilistic basis. Pilots comment on the noticeable symmetry of the Gaussian distribution. Given only Gaussian-distribution turbulence, a perturbation is invariably followed by a correction so that he can allow the aircraft to fly "hands off." One way to look at this is that the time-average of the mean is comparatively short, even for manned simulations, which involve a limited duration time frame and a limited number of sample runs. Mathematically, the frequency of occurrence of the larger magnitude gusts is more in real life than in the Gaussian distribution. Models have been proposed to correct this discrepancy but those have the undesirable effect of increasing the variability from run to run.

### 3.3 Correlation

Correlation is the measure of the predictability of a gust component at some future time or point in space based on the knowledge of a current gust. Since the modeling of a random process such as turbulence consists of developing techniques for predicting the behavior of that process, it can be seen that correct duplication of the correlation can be important since these are measures of predictability. There are at least two ways of presenting correlation information, in the time or space domain (correlation functions) or in the frequency domain (spectral density functions).

The correlation function can be converted to the frequency-domain via a Fourier transformation resulting in the power spectral density function. A frequency domain representation is often useful because it permits comparison of the aircraft's spectral features with the spectral content of the turbulence. It is thereby possible to judge the degree to which the turbulence will affect the aircraft's motion, as described in Reference 11.

The two most common ways of describing gust correlation are the Dryden and von Karman power spectral density forms [3]. The correctness advantage of the von Karman form is not an issue unless the significant spectral content is centered in the microscale range about one decade or more above the integral scale break frequency. The microscale of turbulence is an indication of the distance of time separation over which gusts remain highly correlated, i.e., the initial subrange [12]. The von Karman turbulence involves a non-zero microscale--Dryden does not. The integral scale of turbulence is equal to the area under the normalized autocorrelation function and much larger than the microscale. Correct measurement of the integral scale depends on stationarity.

### 3.4 Dimensionality of Gust Field

A gust field can be described using various orders of dimensionality. The simplest is a one-dimensional-field model which involves just the three orthogonal velocity components taken at a single point (usually the aircraft center of gravity). The Taylor hypothesis (frozen field) can be applied, however, in order to approximate gust gradients with respect to the x-axis of the aircraft without increasing dimensionality. A two-dimensional field model is used to define a gust field in the aircraft x-y plane and can account for the size of the aircraft relative to gust scales. (A large aircraft relative to the gust scale attenuates gust gradient spectral power at high frequencies.) A two-dimensional field can lead to greatly increased mathematical complexity over a one-dimensional field [13], but some turbulence models simply define one-dimensional uniform velocity components and then add two-dimensional forms for gust gradients which contain aircraft size effects (as in Reference 3). These additional components are typically the first term in a Taylor expansion. More recent work [14] indicates that the correctness of these terms may be no better than ignoring them. A third dimension can be introduced in the form of an altitude-dependent wind shear [7,8], independent of the remainder of the model. Because of the inordinate increase in computational complexity, Reference 6 suggests that the gust gradient terms should be considered only if required by a specific piloting task.

### 3.5 Stationarity

A random gust is stationary if, for a collection of gust samples, the corresponding probability and correlation properties describe any additional gust sample which may be taken. Thus, stationarity implies an atmospheric disturbance having an invariant mean, variance, and correlation length (or time). There is no restriction on whether the probability distribution is Gaussian or not. In piloting terms, the effects are similar to the discussion of predictability that results from the probability distribution.



#### 4. EVALUATING ATMOSPHERIC DISTURBANCE MODEL NEEDS

Atmospheric modeling needs vary greatly with the specific application, even for a single given aircraft and flight condition. Some analysis procedures require only a simple one-dimensional turbulence model (e.g., Dryden) and a single gust component. At the other extreme, elaborate simulation can involve a fully defined two-dimensional, non-stationary turbulence field along with a spatially or time varying mean wind field (i.e., wind shear). It is the role of References 4 and 6 to offer guidance in evaluating such needs and selecting appropriate disturbance model options among the variety of modeling choices and identifying the appropriate method of demonstrating compliance.

Some ways of viewing the modeling needs of a user include:

1. How disturbance components enter the airframe force and moment equations.
2. Inner/outer loop structure hierarchy for mission/aircraft centered features.
3. The need for determinism versus randomness in the flying qualities application.

Based on our knowledge of the various stability derivatives and respective gust component intensities, we can estimate the relative effect of various gust terms in order to judge:

1. Axis cross coupling (e.g., longitudinal and lateral-directional forces and moments are likely to be fairly well decoupled).
2. Translation motion (e.g., force equations are mainly affected by gust velocity components alone).
3. Rotational motion (e.g., moment equations are affected by gust velocity, time derivative, and gradient components).

The loop structure hierarchy in mission/aircraft centered features provides us with another way of judging atmospheric disturbance model needs. Figure 1 shows a spectral comparison of mission/aircraft-centered features against atmospheric disturbance features. Although the spectral boundaries of each feature are admittedly more ill-defined than shown, we can nevertheless illustrate a point. That is, any mission/aircraft features which are to be analyzed require the significant atmospheric disturbance features acting within the same spectral range. Conversely, atmospheric disturbance features outside that spectral range are superfluous. Taking the argument to the extreme, navigation considerations are not likely to involve the microscale or even integral scale range of turbulence. Likewise, flexibility effects would not require inclusion of mean wind or wind shear features.

Continuing in a similar vein, the results obtained from exciting an airplane by atmospheric disturbances depend greatly upon how the airplane is

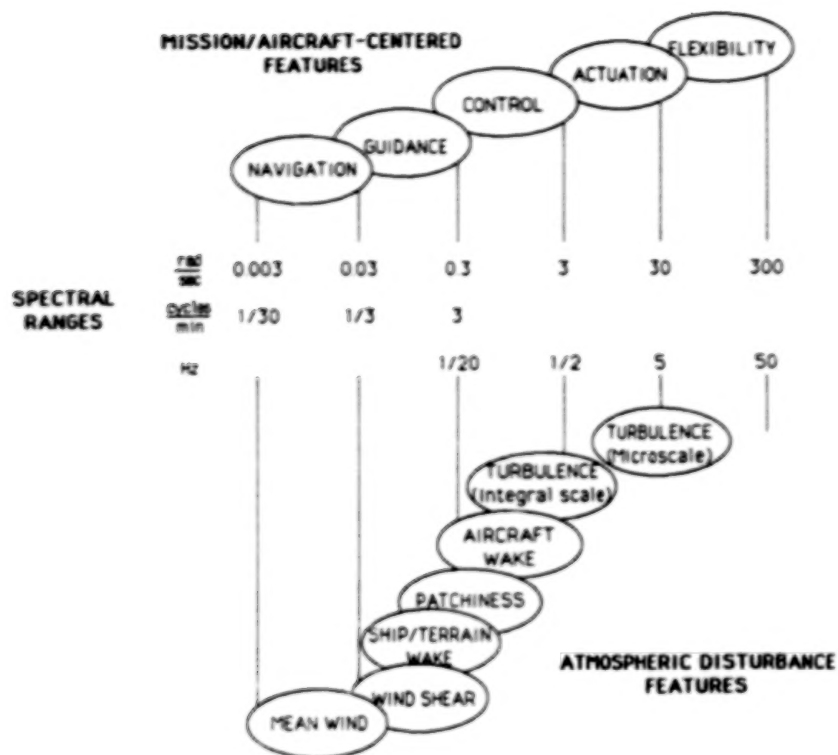


Figure 1. Spectral comparison of mission/aircraft-centered features against atmospheric disturbance features.

being operated, i.e., what the pilot is doing. The gust response can vary dramatically between hands-off operation and that involving tight regulation of attitudes and flight path. Frequently, the effects of wind shear are evaluated by measurement of the flight path excursion for a controls-fixed penetration of the shear. The phugoid is, of course, the dominant response mode in this case, and the result is a large-amplitude, undamped, roller-coaster-like flight path oscillation. But pilots do not characteristically operate hands-off in a wind shear environment. Rather, aircraft attitude is likely to be very well regulated by the pilot; hence, the flight path and airspeed modes would be exponentially decaying according to heave and speed damping stability derivatives ( $Z_w$  and  $X_u$ , respectively). Each of these two cases would lead one to vastly different conclusions regarding performance and identification of critical flying qualities parameters.

We need also to consider how determinism and randomness affect our choice of atmospheric disturbance models. Strict reliance upon a wholly random gust model for small-sample, short-term task evaluation is both impractical and improper. As investigators and evaluators, we desire to control disturbances well enough so that critical conditions and events can be staged especially in the case of manned simulation. This demands a fair degree of model determinism. On the other hand, pilot surprise and sensitivity to variation calls for a degree of randomness. Therefore, a compromise must be reached. This is an area which deserves to be addressed in a systematic way, but sometimes solutions must be based more upon experience than clear rationale.

## 5. PRACTICAL IMPLEMENTATION CONSIDERATIONS

The application of atmospheric disturbance models can involve a number of practical implementation problems--many associated with digital computer programming. One role of the Flying Qualities Handbook [4] will be to assist in answering some of the common implementation questions and to point out pitfalls frequently encountered. Some examples include:

1. Digital implementation of continuous spectral forms
2. Correct scaling of random noise sources
3. Evaluation of need for gradient components
4. Implementation of gust gradients, gust time derivatives, and gust transport lags.

Although these kinds of questions are based on fairly elementary mathematical or physical principles within the capacity of any practicing engineer, they are things which can nevertheless unnecessarily consume time and effort by flying qualities analysts. Table 1 illustrates some of the practical implementation matters addressed by the Flying Qualities Handbook [4].



TABLE 1. A List of Some Practical Implementation Topics from the Flying Qualities Handbook [4].

Implementation Item	Handbook Method	Comments
Digital implementation of continuous filter forms. Example: First-order Dryden form (applicable to u-gust or p-gust).	<p>Spectral form:</p> $\Phi_{uu} = \sigma_{u_g}^2 2L_u/\pi \cdot \frac{1}{1 + (L_u\Omega)^2}$ <p>Discrete realization:</p> $u_g = c_1 u_g + c_2 \eta$ <p>where</p> $c_1 = \begin{cases} \text{either } \exp(-aT) & (\text{z-transform}) \\ \text{or } (1-aT) & (\text{Euler integration}) \\ \text{or } \frac{2-aT}{2+aT} & (\text{Tustin transform}) \end{cases}$ $a = V/L_u$ <p>and</p> $c_2 = \sqrt{1-c_1^2} \frac{\sigma_{u_g}}{\sigma_\eta}$ <p>where <math>\eta</math> is a normally distributed random number with variance <math>\sigma_\eta^2</math>.</p>	This matter can be confusing because spectral forms are written in a number of ways (e. g., one-sided or two-sided, spatial or temporal frequency, or in terms of angular or cyclical frequency). Furthermore, white noise in the continuous domain must be converted to random numbers in the discrete domain.
Determination of p-gust level of importance.	<p>Criterion: p-gust is significant relative to v-gust if:</p> $\sqrt{\frac{b}{L_w}} \cdot  C_{lp}  >  C_{lv} $ <p>or</p> $\frac{2}{\sqrt{L_w b}} \cdot  L_p  >  L_v $ <p>where b is span and <math>L_w</math> is gust scale length.</p>	The p-gust can be an important disturbance component in the roll axis, especially if effective dihedral is small.
Determination of p-gust intensity.	<p>Holley-Bryson model:</p> $\sigma_{pg} = \frac{2.15 \sigma_{wg}}{\sqrt{b L_w (1+b/L_w)}}$ <p>MIL-F-8785C model:</p> $\sigma_{pg} = \sqrt[3]{\frac{0.95 \sigma_{wg}}{b^2 L_w}}$ <p>Approximate intensity averaged over several models:</p> $\sigma_{pg} = \sqrt{\frac{1.9 \sigma_{wg}}{b L_w}}$	If the p-gust component is considered important, one must determine the intensity in order to implement the gust filter. A specific easy-to-compute value for intensity is seldom available. Also the various p-gust model forms all have different ways of expressing model parameters.

## 6. A SURVEY OF EXISTING MODELS

A major task in the development of the Military Standard and Handbook was the review of existing atmospheric disturbance models and model forms. The objective was to examine how various models make the tradeoff between convenience and correctness and to search for strengths or deficiencies which could be important to a flying qualities investigator. Rather than arriving at a single most universal model to serve as the basis for the Military Standard, a variety of model forms appropriate for various applications were suggested. Table 2 lists some of the models which have been surveyed and offer some potential in flying qualities applications. For each table entry a few summary remarks are given along with a list of basic references.

## 7. THE CURRENT MILITARY SPECIFICATIONS FOR FLYING QUALITIES

Since our goal is discussion of the Flying Qualities Military Specifications, we should try to understand their weaknesses as well as their strengths. Prior to the existing specification, MIL-F-8785B presented a basic disturbance model consisting of turbulence and discrete gusts, but the requirements for its use were few in number and qualitative in nature. For the current version, the MIL-F-8785B model was extended and more explicit requirements were formulated. It is instructive to understand the background of this existing array of model components and how they are used in defining flying qualities requirements.

The effect of increasing disturbance intensity is typically an increase in pilot workload and/or a degradation in task performance. The effect on pilot rating is similar to a degradation in flying qualities from other causes. This consideration led heuristically to the specification of three disturbance intensities, which are qualitatively linked to the three levels of flying qualities. In attempting to formulate requirements for use of the models, it was proposed originally to incorporate the effects of disturbances into the levels of flying qualities. In the final version, "qualitative degrees of suitability" are defined to parallel the levels of flying qualities. A new section of the specification now contains requirements for use of the disturbance model. These are presented as a matrix of failure versus disturbance intensities for the different flight envelopes.

Both the von Karman and Dryden forms of the turbulence spectra are retained with specified intensities corresponding to probabilities of occurrence of  $10^{-1}$ ,  $10^{-3}$ , and  $10^{-5}$ . The "versine" (or 1-cosine) shape is retained for the discrete gust, except that only half a period is specified. In this way it can be used singly (e.g., representing a wind shear) or in pairs (as in the familiar discrete gust application) yielding more flexibility in application.

A completely new model is specified for low altitudes, with a more realistic variation of turbulence intensities and scale lengths with height above the ground. A mean wind having a logarithmic variation with height (planetary boundary layer) is specified. In order to account for the severe but less probable phenomena that cause difficulties close to the ground, a

TABLE 2. A Survey of Atmospheric Disturbance Models.

Model	Key Features	Sources*
Dryden turbulence	A convenient spectral form based on an exponential autocorrelation function for the axial component.	15
von Karman turbulence	A spectral form for which the autocorrelation function includes a finite microscale, thus the relative proportion of spectral power at high frequencies exceeds that of the Dryden.	16,17
Ornstein-Uhlenbeck turbulence	A spectral form with first-order longitudinal and transverse components.	18
Etkin one dimensional turbulence power spectra	The local turbulent velocity field is approximated by a truncated Taylor series which yields uniform and gradient components. High frequency spectral components eliminated on the basis of aircraft size. Based on Dryden form, but gradient spectra are non-realizable unless simplified.	13,19,20
Versine gust	A discrete gust waveform.	3
Lappe low-altitude turbulence model	Experimentally-obtained data of vertical gust spectra, mean wind speed, and lapse rate were used to develop a low-level turbulence model. The turbulence spectra are presented for different types of terrain, height, and meteorological conditions.	21
Multiple point source turbulence	A two-dimensional gust field generated from two or more noise sources having prescribed correlation functions and located sparwise or lengthwise on the vehicle.	22,23,24
Holley-Bryson random turbulence shaping filters	A matrix differential equation formulation of uniform and gradient components including aircraft size effects. Filter equation coefficients determined from least square fit to multi-point-source-derived correlation functions.	23
University of Washington non-Gaussian atmospheric turbulence model	Non-Gaussian model using modified Bessel functions to simulate the patchy characteristic of real-world turbulence. Spectral properties are Dryden and include gust gradients.	9,25

\*Source numbers refer to references cited at end of paper.

TABLE 2. (continued).

Model	Key Features	Sources
Delft University of Technology non-Gaussian structure of the simulated turbulent environment	Non-Gaussian model similar in form to the University of Washington model, but uses the Hilbert transform to model intermittency as well as patchiness. Includes University of Washington model features extended to approximate transverse turbulence velocities and gradients.	26
Royal Aeronautical Establishment model of non-Gaussian turbulence	Non-Gaussian turbulence model with a variable probability distribution function and a novel digital filtering technique to simulate intermittency. Spectral form approximately von Karman.	27,28,29
The Netherlands National Aerospace Laboratory model of non-Gaussian turbulence	Similar to the Royal Aeronautical Establishment model, but extended to include patchiness and gust gradient components and transverse velocities.	30, 31
University of Virginia turbulence model	Models patchiness by randomizing gust variance and integral scale length of basic Dryden turbulence.	32
Mil Standard turbulence model	First order difference equation implementation of turbulence filters based on 8785 Dryden turbulence and refitted rolling gust intensity.	4
Indian Institute of Science non-stationary turbulence model	Nonstationary turbulence is obtained over <u>finite</u> time-windows by modulating a Gaussian process with either a deterministic or random process. The result is patchy-like turbulence similar to the University of Washington model except the time-varying statistics of the turbulence are presented for the deterministic modulating functions.	18
FAA wind shear models	Three-dimensional wind profiles for several weather system types including fronts, thunderstorms, and boundary layer. The profiles are available in table form.	7,33
STI wind shear model	Time and space domain models of mean wind and wind shear (ramp wave forms) are combined with MIL-F-8785C Dryden turbulence to obtain the total atmospheric disturbance. The magnitudes of the mean wind and wind shear are evaluated in terms of the aircraft's acceleration capabilities.	8,34

TABLE 2. (continued).

Model	Key Features	Sources
Sinclair frontal surface wind shear model	A generic model of frontal surface wind shear derived from a reduced-order form of Navier-Stokes equations. Relatively simple to use and can match the overall characteristics of measured wind shears.	35,36
MIL-F-8785B atmospheric disturbance model	Intensities and scale lengths are functions of altitude and use either Dryden or von Karman spectral forms or a one minus cosine discrete gust. Also spectral descriptions of rotary gusts.	37,38
MIL-F-8785C atmospheric disturbance model	Same as 8785B with the addition of a logarithmic planetary boundary layer wind, a vector shear, and a Naval carrier airwake model.	3
ESDU atmospheric turbulence	Rather general, but contains comprehensive descriptive data for turbulence intensity, spectra, and probability density	39,40
Boeing atmospheric disturbance model turbulence	A comprehensive model of atmospheric disturbances that includes mean wind, wind shear, and random turbulence. Turbulence is Gaussian and uses linear filters that closely approximate the von Karman spectral form. Mean wind and turbulence intensity are functions of meteorological parameters.	41
Wasicko carrier airwake model	Includes mean wind profile, effect of ship motion, and turbulence.	42
Naval ship airwake model	Includes free air turbulence filters plus steady, periodic, and random components of airwake which are functions of time and space.	3, 43
Vought airwake model for DD-963 class ships	Combined random and deterministic wind components for free air and ship airwake regions. Based on wind tunnel flow measurements.	44
STI Wake vortex encounter model	A two-dimensional model of the flow-field due to the wake vortex of an aircraft is presented. The parameters of the flow-field model are weight, size, and speed of the vortex-generating aircraft, and distance and orientation of the vortex-encountering aircraft. Strip theory is used to model the aerodynamics of the vortex-encountering aircraft.	45

TABLE 2. (concluded).

Model	Key Features	Sources
Cambell and Stanborne wind shear and turbulence model	Spatial model based on joint airport weather studies (JAWS) microburst data. Permits calculation of aerodynamic loads over body of aircraft.	46
Zhu and Etkin microburst model	Generic spatial model of microburst velocity components based on potential flow singularity distribution involving only three adjustable parameters.	47



vector shear is specified--a change in wind direction over a certain change in height. This is used in lieu of a particular wind profile or set of profiles. It is believed that varying the orientation and height of the specified vector shear covers an adequate range of aircraft responses for the landing task.

The specification of vector shear has the appearance of an engineering artifact, i.e., a 90° change in wind direction over a given height. It is, however, based on the wind conditions that existed at the time of an actual aircraft accident [48]. The winds did not compromise aircraft performance and had no obvious indication of dangerous conditions--they formed an insidious contribution to the busy landing task. The use intended by MIL-F-8785C is to produce a complex but realistic task in piloted ground-based simulation. As the wind changes from crosswind to headwind, or vice versa, the pilot is continually controlling both longitudinal and lateral/directional axes. The six-degrees-of-freedom aspect of this control task is frequently missing in simulation.

Based on meetings with the Navy, it became apparent that their atmospheric disturbance requirements were driven by the carrier landing task. The carrier airwake represents a severe environment. The disturbance model of MIL-F-8785C was completed by adding a carrier airwake model supplied by Nave of NADC [43]. We know that a degradation in pilot rating is accepted relative to landing in calm air; however, we do not yet know how the severity compares with the other portions of the disturbance model.

It should be emphasized strongly that the intent is not to add a whole new dimension to all the existing requirements. In MIL-F-8785B, the guidance was to establish the flying qualities and probabilities associated with critical flight conditions and failures. For MIL-F-8785C, the intent is to limit the degradation in flying qualities due to atmospheric disturbances for the critical cases. With the requirements contained in separate sections, they can be easily modified, emphasized, or even deleted by the procuring activity according to the mission needs. Reference 6 supports the existing specification with more detail on the items discussed herein.

## 8. IMPLICATIONS FOR THE FORTHCOMING MILITARY STANDARD

The foregoing discussions have tended to dwell on practical aspects of atmospheric disturbance modeling in flying qualities applications. We have described the existing military specification, a variety of modeling topics, and a partial list of modeling alternatives. Regarding atmospheric disturbance models, again we should note that it would be difficult, if not unwise, to embody in a single model all of the features which have been addressed in the existing body of models. Furthermore, to the extent that this could be done, the resulting model would then become "overkill" for many applications. In addition, since the Standard is just that--a standard--it is not necessary to apply a high fidelity facsimile of the real-world environment (assuming that we could ever reach agreement on what the "real world" is). Rather, it is only necessary to apply something good enough to permit a judgment or comparison in each specific context addressed by the Standard. Our inclination is therefore to recommend individualized modeling approaches which

would be stylized for a particular application and which would draw upon the rich variety of existing models or modeling forms. This would be accomplished by setting forth an unquantified checklist of atmospheric disturbance properties in the Military Standard document. Specific qualification would then be made by the procuring agency on the basis of the application, vehicle type, mission, and expected environment. This would be done from consultation of the accompanying Handbook and recommended sources listed within. The same procedure could also be followed by the disturbance model user performing analysis or simulation not necessarily connected with aircraft procurement.

Flying qualities requirements set by the Military Standard must necessarily recognize the key role which atmospheric disturbances play in the piloting of an airplane. Hence, prescription of performance (amplitude of response) or workload (pilot opinion or other workload-related metrics) requirements must be made with an understanding of the combined pilot-vehicle disturbance system. This implies that more is needed than guidelines between, say, gust components and airframe aerodynamics. Due consideration must also be given to the piloting tasks and the effect that it has on modifying airplane dynamics and their sensitivity to atmospheric disturbances.

#### 9. REFERENCES

1. "Military Standard, Climatic Extremes for Military Extremes": MIL-STD-210B, Dec. 1973.
2. "Flight Control Systems--Design, Installation and Test of, Piloted Aircraft, General Specification for": MIL-F-9490D, June 1975.
3. "Flying Qualities of Piloted Airplanes": Military Specification, MIL-F-8785C, Nov. 5, 1980.
4. Hoh, R. H.; Mitchell, D. G.; Ashkenas, E. L.; Klein, R. H.; Heffley, R. K.; and Hodgkinson, J.: "Proposed MIL Standard and Handbook--Flying Qualities of Air Vehicles," AFWAL-TR-82-3081, Nov. 1982.
5. Cooper, G. E.; and R. P. Harper, Jr.: "The Use of Pilot Rating Scale in the Evaluation of Aircraft Handling Qualities," NASA TN D-5153, April 1969.
6. Moorhouse, D. J.; and Woodcock, R. J.: "Background Information and User Guide for MIL-F-8785C," AFWAL-TR-81-3109, July 1982.
7. Foy, W. H.; and Gartner, W. B.: "Piloted Flight Simulation Study of Low-Level Wind Shear, Phase 4," FAA-RD-79-84, March 1979.
8. Hoh, R. H.; and Jewell, W. F.: "Investigation of the Vulnerability of Powered Lift STOLs to Wind Shear," NASA CR-152064, Oct. 1976.
9. Reeves, P. M.; Campbell, G. S.; Ganzer, V. M.; and Joppa, R. G.: "Development and Application of a Non-Gaussian Atmospheric Turbulence Model for Use in Flight Simulators," NASA CR-2451, Sept. 1974.

10. van de Moeskijk, G. A., Jr.: "Non-Gaussian Structure of the Simulated Turbulent Environment in Piloted Flight Simulation," Delft University of Technology, Dept. of Aerospace Engineering, Memorandum M-304, April 1978.
11. Heffley, R. K.: "A Study of Key Features of Random Atmospheric Disturbance Models for the Approach Flight Phase," AIAA-77-1145, Aug. 1977.
12. Lumley, J. L.; and Panofsky, H. A.: The Structure of Atmospheric Turbulence. New York: Interscience Publishers, Inc., 1964.
13. Etkin, B.: "Theory of the Flight of Airplanes in Isotropic Turbulence--Review and Extension," AGARD Report 372, April 1961.
14. Etkin, B.: Dynamics of Atmospheric Flight. New York: John Wiley and Sons, Inc., 1972.
15. Dryden, H. L.: "A Review of the Statistical Theory of Turbulence," Turbulence--Classic Papers on Statistical Theory (S. K. Friedlander and L. Topper, eds.). New York: Interscience Publishers, Inc., 1961.
16. von Karman, T.: "Progress in the Statistical Theory of Turbulence," Turbulence--Classic Papers on Statistical Theory (S. K. Friedlander and L. Topper, eds.). New York: Interscience Publishers, Inc., 1961.
17. Houbolt, J. C.: "Atmospheric Turbulence," AIAA Journal, 11(4):421-437, April 1973.
18. Gaonkar, G. H.: "Review of Nonstationary Gust-Responses of Flight Vehicles," AIAA 80-0703, July 1980.
19. Etkin, B.: Dynamic of Flight. Stability and Control. New York: John Wiley and Sons, Inc., 1959.
20. Etkin, B.: "Theory of the Response of Airplanes to Random Atmospheric Turbulence," Journal of the Aero/Space Sciences, July 1959, pp. 409-420.
21. Lappe, U. O.: "Low-Altitude Turbulence Model for Estimating Gust Loads on Aircraft," Journal of Aircraft, 3(1), Jan.-Feb. 1966.
22. Etkin, B.: "The Turbulent Wind and Its Effect of Flight," AIAA-80-1836, Aug. 1980.
23. Holley, W. E.; and Bryson, A. E., Jr.: "Wind Modeling and Lateral Aircraft Control for Automatic Landing," Stanford University, Dept. of Aeronautics and Astronautics, SUDAAR No. 489, Jan. 1975.
24. Skelton, G. B.: "Investigation of the Effects of Gusts on V/STOL Craft in Transition and Hover," AFFDL-TR-68-85, 1968.
25. Reeves, P. M.: "A Non-Gaussian Turbulence Simulation," AFFDL-TR-69-67, Dec. 1969.

26. van de Moesdijk, G. A. J.: "Non-Gaussian Structure of the Simulated Turbulent Environment in Piloted Flight Simulation," Delft University of Technology, Dept. of Aerospace Engineering, Memorandum M-304, April 1978.
27. Tomlinson, B. N.: "Developments in the Simulation of Atmospheric Turbulence," Royal Aircraft Establishment, Technical Memorandum FS 46, Sept. 1975.
28. Jones, J. G.: "Modeling of Gusts and Wind Shear for Aircraft Assessment and Certification," Royal Aircraft Establishment, Paper prepared for CAARC Symposium on Operational Problems, India, Oct. 1976.
29. Jewell, W. F.; and Heffley, R. K.: "A Study of Key Features of the RAE Atmospheric Turbulence Model," NASA CR-152194, Oct. 1978.
30. Jansen, C. J.: "A Digital Turbulence Model for the NLR Moving-Base Flightsimulator, Part I," National Aerospace Laboratory, NLR Memorandum VS-77-024 U, Aug. 29, 1977.
31. Jansen, C. J.: "A Digital Turbulence Model for the NLR Moving-Base Flightsimulator, Part II," National Aerospace Laboratory, NLR Memorandum VS-77-025 U, Aug. 29, 1977.
32. Jacobson, I. D.; and Joshi, D. S.: "Investigation of the Influence of Simulated Turbulence on Handling Qualities," Journal of Aircraft, 14(3):272-275, March 1977.
33. Frost, W.; and Camp, D. W.: "Wind Shear Modeling for Aircraft Hazard Definition," FAA-RD-77-36, March 1977.
34. Heffley, R. K.; and Jewell, W. F.: "Study of a Safety Margin System for Powered-Lift STOL Aircraft," NASA CR-152139, May 1978.
35. Jewell, W. F.; Clement, W. F.; West, T. C.; and Sinclair, S. R. M.: "Powered-Lift Aircraft Handling Qualities in the Presence of Naturally-Occurring and Computer-Generated Atmospheric Disturbances," FAA-RD-79-59, May 1979.
36. Sinclair, S. R. M.; and West, T. C.: "Handling Qualities of a Simulated STOL Aircraft in Natural and Computer-Generated Turbulence and Shear," Piloted Aircraft Environment Simulation Techniques, AGARD-CP-249, Oct. 1978.
37. "Flying Qualities of Piloted Airplanes," Military Specification, MIL-F-8785B, Aug. 1969.
38. Chalk, C. R.; Neal, T. P.; Harris, T. M.; and Pritchard, F. E.: "Background Information and User Guide for MIL-F-8785B(ASG), Military Specification Flying Qualities of Piloted Airplanes," AFFDL-TR-69-72, Aug. 1969.



39. Anonymous: "Characteristics of Atmospheric Turbulence Near the Ground. Part III: Variations in Space and Time for Strong Winds (Neutral Atmosphere)," Engineering Sciences Data Unit Item No. 74031, London, England, Oct. 1974.
40. Anonymous: "Characteristics of Atmospheric Turbulence Near the Ground. Part III: Variations in Space and Time for Strong Winds (Neutral Atmospheres)," Engineering Sciences Data Unit Item No. 75001, London, England, July 1975.
41. Barr, N. M.; Gangsaas, D.; and Schaeffer, D. R.: "Wind Models for Flight Simulator Certification of Landing and Approach Guidance and Control Systems," FAA-RD-74-206, Dec. 1974.
42. Durand, T. S.: "Carrier Landing Analyses," Systems Technology, Inc., Technical Report No. 137-2, Feb. 1967.
43. Nave, R. L.: "Development and Analysis of a CVA and a 1052 Class Fast Frigate Air Wake Model," NADC-78182-60, Sept. 30, 1978.
44. Fortenbaugh, R. L.: "Mathematical Models for the Aircraft Operational Environment of DD-963 Class Ships," Vought Corporation Report No. 2-55800/8R-3500, Sept. 26, 1978.
45. Johnson, W. A.; and Teper, G. L.: "Analysis of Vortex Wake Encounter Upsets," NASA CR-127491, Aug. 1974.
46. Campbell, C. W.; and Sanborne, V. A.: "A Spatial Model of Wind Shear and Turbulence," Journal of Aircraft, Dec. 1985.
47. Zhu, S.; and Etkin, B.: "Model of the Wind Field in a Downburst," Journal of Aircraft, July 1985.
48. "NTSB Assays Iberia Accident at Logan," Aviation Week & Space Technology, April 7, 1975; and "Wind Factor Studies in Iberia Crash," Aviation Week & Space Technology, April 14, 1975.

**QUESTION:** Walter Frost (FWG Associates). In your spectral rolling moment, is there a problem with transferring from coordinate systems? Generally those are developed for?

**ANSWER:** Generally, I think there can be but it's one of these things where at this stage using something is much better than the absence of a model, which is really the case right now.

**FROST:** How do you recommend calculating  $L_w$ .

**HEFFLEY:** That is up to the model user, although the value typically used for low altitude is height above ground.

**COMMITTEE SUMMARY REPORTS**



COMMITTEE: DESIGN

CHAIRMAN: David O'Keefe

MEMBERS: Ben F. Dotson  
Richard Heimbaugh  
John C. Houbolt  
Robert T. Meyer  
Richard N. Moon  
Joe J. Nishikawa  
Elijah Turner

ISSUE:

Two primary issues:

1. How Accurate Gust Measurements or Predictions Do We Need; and What is the Impact on Gust Analysis?
2. How Can Data be Obtained for High Altitudes?

DISCUSSION:

1. First, gusts are statistical in nature and thus it is not possible to define a "worst possible" gust and then design for this gust. Second, criteria and design analysis are intertwined, that is, design levels are based upon the strength of existing satisfactory airplanes. The limit design frequency of exceedance is set such that if loads are determined for existing airplanes in accordance with proposed criteria, these loads will correspond to the limit strength of the airplane. Gust intensity profiles then are essentially backed out of known data in accordance with this criteria.

If accurate "real time" gust measurements were suddenly available, then the entire inter-related criteria/design process would have to be reassessed in accordance with the airplane limit strength loads concept.

The basic question may be: How and what data base can be used to update the information originally used in establishing the design criteria given in FAA-ADS-53?

2. High-altitude clear-air turbulence data are not well established. Vehicle operations in this regime appear likely within the next decade. Trans-atmosphere vehicles (TAV), space re-entry vehicles, high aspect ratio endurance vehicles, and lightweight highly flexible structures are typical candidates.

To obtain such data, extensive use of research aircraft, flight recorders, lidar/radar, in situ, and remote sensing devices may all have to be used.

#### RECOMMENDED ACTION:

On-going research and development funding should be provided to support acquisition of required data and to update existing data bases. Inherent in this recommendation may be the need to reassess the inter-related criterion/design aspects of the gust analysis process. A start would be to complete reduction/evaluation/incorporation of existing measured data for large transports (i.e., Norman Crabill work, B-57B gust gradient data, etc.).

#### RESPONSIBLE AGENCIES:

The driving force for this probably must come from the licensing agencies and user community, basically, FAA, DoD, and NASA. NASA is the logical candidate to coordinate the concerns of all three.

PRIORITY: High

#### ISSUE:

Avoidance and Awareness: How Can Aircraft Crews be Provided with Sufficient Information to Basically Avoid Turbulence or Make Decisions Based on Knowledge of a Potential Adverse Level of Turbulence?

#### DISCUSSION:

Satisfactory structural strength in itself is not sufficient. Aircraft/passenger can still be lost/injured due to upsets and loss of control. Operational rules and restrictions are major factors in reducing encroachment into turbulence. But an additional aid would be reliable avoidance and awareness capabilities.

Avoidance, as used here, implies in-flight detection followed by corrective actions to bypass turbulence. Awareness implies some optional decision-making process based upon assessment of the degree of adversity. Awareness could range from "don't," "go ahead, but it is rough," "no problem, it's mild" signals to true definition of intensity profiles allowing pilot to react (i.e., slow down, speed up, etc.).

Devices, techniques, and procedures with these capabilities appear to be available with a somewhat qualified satisfaction level.

Design processes for current and next-generation aircraft are basically satisfactory (with the exception of highly exotic aircraft). Therefore, for existing fleets and near-term production, avoidance and awareness may be most vital.

#### RECOMMENDED ACTION:

Provide funding to expand research, development, and validation procedures in this area.

RESPONSIBLE AGENCIES: Private industry, NASA, FAA

PRIORITY: High

ISSUE:

What Effect Has Turbulence on Active Controls, Relaxed Stability, and Flight Controls?

DISCUSSION:

The effects of control surfaces employed for purposes of load alleviation or for primary maneuver and control purposes are becoming more prevalent (i.e., L-1011-3ACS, X-29). Historical data bases used in FAR-ASD-53 probably do not reflect such phenomena. Past accounting for systems such as yaw damper has been included by obtaining exceedance curve separately for with and without yaw damping. Results are then combined to reflect rational off/on percentages. The effects of the multi-surface control systems on aircraft response to turbulence penetrations are either unknown or not yet fully determined (i.e., there is some indication that such systems may alleviate gust loading).

RECOMMENDED ACTION:

Provide on-going funding to investigate, measure, and/or provide research activities in this area.

RESPONSIBLE AGENCIES: DoD, NASA

PRIORITY: Low

ISSUE:

What is the Present Status of Turbulence on Criteria, Modeling, Design, and Operation Integration?

DISCUSSION:

The basis for current gust loads criteria, modeling, and basic design analysis procedures should be reviewed. If sufficient evidence is uncovered, consideration should be given to renegotiating criteria, or altering design procedures. Possibility of agency/manufacturer/user agreement on standardization should be considered.

Omission or oversights should be accounted for as part of an overall integrated approach. For example, helicopter criteria is not defined, operational usage considerations are not fully accounted. Basic methodology and approach need to be reviewed and reassessed in light of recent work.

RECOMMENDED ACTION:

A start may be to revisit TARC 78-55 (Transportation Airworthiness Recommendation Committee met in Washington, D.C., May 25, 1978) to reassess its pluses and minuses. Consideration of John Houbolt's approach, as presented at the workshop and included as a paper in the workshop proceedings, should be reviewed. Impact of turbulence prediction techniques and airline meteorology predictions should be included. Evaluate and include as appropriate available recent gust data.

RESPONSIBLE AGENCY: NASA

PRIORITY: Medium

COMMITTEE: OPERATIONS

CHAIRMAN: John J. Pappas

MEMBERS: James C. McLean, Jr.  
W. Dale Meyer  
Douglas J. Miller  
Creighton Pendarvis  
Michael A. Tomlinson  
J. Allen Zak

ISSUE:

Measurement of CAT with Doppler Radar

DISCUSSION:

Atmospheric turbulence is known to be associated with spatial and temporal fluctuations of temperature and velocity. However, there is evidence that turbulence is not the only atmospheric process which can cause these fluctuations. For example, observations suggest these fluctuations may also be caused by non-turbulent internal atmospheric gravity waves. Research is required to develop signal analysis techniques which can distinguish between fluctuations associated with atmospheric turbulence and those associated with non-turbulent atmospheric accelerations.

RECOMMENDED ACTION:

OFCM should be asked to sponsor the subject research. The NEXRAD Special Projects Office should be asked to comment on issue.

RESPONSIBLE AGENCIES: OFCM, FAA, DoD, NOAA

PRIORITY: High

ISSUE:

State of Understanding of Atmospheric Turbulence

DISCUSSION:

An effort should be undertaken to document the state of the science in understanding atmospheric turbulence phenomena, including the frequency of occurrence and duration of significant (greater than "moderate") turbulence events. The effort should also define the current state of the understanding of the spatial and temporal distribution of these turbulence events.

RECOMMENDED ACTION:

OFCM should be asked to sponsor this effort.

RESPONSIBLE AGENCY: OFCM

PRIORITY: High

ISSUE:

Joint Research for Improved Techniques in Turbulence

DISCUSSION:

Areas which deserve increased attention include: Aircraft-mounted turbulence measuring/warning equipment and ground-based equipment; test techniques on operational aircraft; multiple approaches to turbulence avoidance (i.e., passive infrared (IR) sensors, Doppler radar, lidar--high altitude and very high altitude); and finally, better pilot education and awareness of turbulence avoidance techniques.

Concerning on-board turbulence avoidance systems, present systems under development can only look straight ahead. Future systems need to be able to scan in horizontal and vertical mode (to give the pilot knowledge as to whether he/she should climb, descend, or turn in order to avoid or miss the most intense turbulence). Military aviation has a need for better turbulence avoidance in areas such as low-level helicopter operations, wind conditions for airdrops, and large aircraft low-altitude operations.

RECOMMENDED ACTION:

Convince air carriers that on-board turbulence avoidance equipment has a potential for lowering their liability insurance rates, improvement of passenger comfort, as well as reducing structural stresses which will increase the service life of their aircraft.

RESPONSIBLE AGENCIES: NASA, FAA, DoD

PRIORITY: High -- On-Going

ISSUE:

Numerical Models and Space Observational Data for High-Altitude Turbulence for Orbital Insertion and Transatmospheric Vehicle Operations

DISCUSSION:

Data collection efforts and models are just now beginning to focus on this turbulence problem.



RECOMMENDED ACTION:

Support further research, data collection, and model development in high-altitude turbulence characterization.

RESPONSIBLE AGENCIES: NASA, DoD

PRIORITY: Medium

ISSUE:

Realistic Numerical Models to Characterize Turbulence in the Lowest 1000 ft (305 m) of the Atmosphere for Flight Simulator Use

DISCUSSION:

Turbulence in this context includes wind shear produced by downbursts, fronts, sea breezes, and other local scale phenomena.

Observational data bases are not available to represent the low-level wind structure. Doppler radar has difficulty due to ground clutter. Instrumented towers are typically not high enough, not closely spaced, and infrequently capture important events. It is understood that there is a concomitant need for flight simulators capable of fully utilizing detailed three-dimensional inputs to produce realistic instruments and motion responses for aircrew training. Although microbursts are frequently singled out as the only real hazard to aviation, turbulence and wind shear produced from any mechanism can be catastrophic when combined with other problems such as heavy rain or equipment malfunctions in this critical region of flight.

RECOMMENDED ACTION:

Sponsor the continued development of high-resolution models capable of depicting three-dimensional turbulent wind fields.

RESPONSIBLE AGENCIES: FAA, NASA, OFCM

PRIORITY: Very High

ISSUE:

Affordability or Practicality of Present Atmospheric Prediction Models Capable of Resolving the Higher Frequency Turbulence Components for Real-Time Operational Environments

DISCUSSION:

Existing models with fine resolution time and space scales as well as sophisticated treatment of diffusion fluxes, friction, and so forth need large research-oriented computers and long running times to produce prognostic output even for limited areas.

RECOMMENDED ACTION:

Support efforts to scale down models by focusing on pieces of the turbulence problem. For example, a model might be specifically tuned to treat mountain waves, convection, or Kelvin Helmholtz waves.

RESPONSIBLE AGENCIES: OFCM, NASA

PRIORITY: Medium

ISSUE:

Improvements in Turbulence Forecasts Using Existing or Foreseeable Models to Gain Outputs Better Oriented to Provide Turbulence Information

DISCUSSION:

Existing synoptic scale models provide wind, temperature, and moisture fields for spacing larger than most turbulence events. Can they provide valid fields at higher resolutions? Can the existing fields be used to infer higher resolution turbulence values? Can mesoscale models be run using synoptic scale model outputs and/or post-model-run observations to provide mesoscale turbulence information?

RECOMMENDED ACTION:

These questions should be addressed and, if feasible, improved mesoscale information should be developed for operational use.

RESPONSIBLE AGENCIES: NWS, DoD (FNOC, AFGWC)

PRIORITY: Medium -- Medium to Long Range

ISSUE:

Scope and Nature of the Turbulence Problem for Aircraft Operations

#### DISCUSSION:

There is a need for a clear definition of what is the operational objective of understanding turbulence. Questions of cost and cost/benefit must have answers that explain why turbulence is a problem and not just a phenomena.

#### RECOMMENDED ACTION:

Define the turbulence problem for aviation operations.

RESPONSIBLE AGENCIES: FAA, DoD, NTSB

PRIORITY: High -- Short Term

#### ISSUE:

The Meaning of Terminology Used to Describe Turbulence for Researchers, Forecasters, Pilots, and Passengers

#### DISCUSSION:

Turbulence intensity terms and reports are subjective and, to a large extent, aircraft and/or pilot dependent. This means that controllers, flight service specialists, and forecasters must interpret and evaluate reports. Reports which may appear to say the same thing may be interpreted differently by each person receiving them and may have meant something different to each person providing them.

#### RECOMMENDED ACTION:

Turbulence intensity terms and reports should be standardized and "objectivized" or quantified.

RESPONSIBLE AGENCY: OFCM

PRIORITY: High -- Short Term

#### ISSUE:

Current Techniques for Predicting En-Route Turbulence and Terminal Area Wind Variations Including Turbulence and Shear

#### DISCUSSION:

While the operational impacts of turbulence may be significant, particularly for DoD, the number of fatalities associated with en route turbulence is small and the cost of injuries is perceived as relatively small. The forecasts provided by the existing system are perceived as needing improvement but the

point at which the cost/benefit ratio becomes too large is thought to be close. An effort to evaluate the existing prediction techniques would provide an opportunity to re-evaluate the turbulence hazard and determine the current cost/benefit ratio, as well as the state of available observational data. This should include operational evaluations of newer techniques which might otherwise have too small a set of verification data.

On the other hand, the number of low-level turbulence and wind shear fatalities is relatively large as are the attendant liability and legal costs. The nature of the objectives and techniques for forecasting these conditions is fundamentally different from those associated with turbulence in the en route environment. These techniques also need evaluation for appropriateness and effectiveness.

RECOMMENDED ACTION:

The appropriateness and operational effectiveness of existing forecast techniques should be evaluated with the objective of quantifying the hazard's significance and identifying the most effective forecast techniques and any deficiencies in the current data used as a basis for these techniques.

RESPONSIBLE AGENCY: OFCM

PRIORITY: High -- Short Term

ISSUE:

Resolution of the Numerous Turbulence Forecasting Techniques and Rules of Thumb into a Set of Validated, Standard Techniques

DISCUSSION:

There are many subjective and objective turbulence forecasting techniques and rules which are based on data as old as 35 years and as new as GOES moisture channel data. There has been little organized effort to evaluate and validate or discard these rules and techniques. The result is a lack of standardized turbulence forecasts, contradictory forecasts, and an uneven level of forecast quality.

RECOMMENDED ACTION:

The body of turbulence forecast techniques and rules should be reviewed and evaluated. Validated ones should be published and their use encouraged.

RESPONSIBLE AGENCIES: OFCM, NWS, DoD

PRIORITY: High -- Medium Term

COMMITTEE: REMOTE SENSING

CHAIRMAN: Gary P. Ellrod

MEMBERS: Alan Bohne  
Diana Collier  
G. David Emmitt  
Phil Rogers  
James R. Scoggins  
Robert W. Smith  
Laj Utreja

ISSUE:

What is the Status of Remotely Sensing Turbulence from Ground Stations?

DISCUSSION:

Considerable research has been performed in the quantification of turbulence intensity in regions of precipitation. Methods such as the NEXRAD turbulence algorithm may be used with Doppler radars to identify regions of turbulence in the non-hazardous and hazardous ranges with relatively high probability of detection. The clear-air boundary layer (1-3 km) is routinely observed with Doppler radars to ranges of about 60 km. Again, accuracy of turbulence severity estimates, when compared with in situ aircraft measurements, has been shown to be quite high.

Above the boundary layer, UHF radars may detect layers of CAT to heights of 6-10 km and moderate ranges, perhaps 30-40 km. Wind profilers, which will play an adjunct role with radiosondes, will be able to routinely measure winds in the vicinity of the sensor up to the tropopause.

In summary, in precipitation, radars such as those to be incorporated in the NEXRAD system will routinely measure turbulence severity indices up to 130 km. In clear air, measurements are restricted to 30-40 km.

RECOMMENDED ACTION: None

RESPONSIBLE AGENCY:

PRIORITY:

ISSUE:

What Plans are There for Directly Measuring Turbulence Remotely from Space?

DISCUSSION:

A space-based lidar would be a means of direct clear-air turbulence detection. Current sensors are capable of reasonably accurate measurements of winds and

gust velocities, but currently they are technically feasible only for polar and equatorial orbiting satellites. There are plans for putting a lidar profiler on the Space Station or polar platform scheduled to be launched in the 1990's.

RECOMMENDED ACTION:

Continue evaluation and improvement of lidars for eventual use on space platforms.

RESPONSIBLE AGENCY: NASA

PRIORITY: Low

ISSUE:

What is the Status of an On-Board Warning Indicator of Turbulence for Aircraft?

DISCUSSION:

A lead time of 20 to 40 seconds is needed to allow jet aircraft to respond to a warning of impending turbulence in flight. An infrared radiometer now available has a maximum range of 60 km and high accuracy (~94%) for detecting clear-air turbulence. Current lidar instruments have limited range and would not provide sufficient warning.

The addition of a low-cost Doppler radar or direct readout from ground-based Doppler would be desirable for detection of downbursts on approaches to airports.

RECOMMENDED ACTION:

1. Evaluate existing infrared radiometers as to their usefulness in in-flight CAT detection.
2. Determine feasibility of on-board Doppler radar systems.

RESPONSIBLE AGENCY: FAA

PRIORITY: Medium

ISSUE:

How Can Remote Sensing Data Best be Utilized to Improve the Prediction of Turbulence?



### DISCUSSION:

The primary data needed are winds, temperatures, and pressure heights with a higher resolution than that provided by the radiosonde network. Many new sources of remotely sensed data will become routinely available by 1990 (VAS soundings, ASDAR, profilers). Due to the high volume of data, automatic collection and processing will be needed. In order to evaluate improvements in prediction, a high density of verifiable turbulence reports will be needed. Ground-based sensors such as Doppler radar and lidar may contribute in this effort. Even with improvements in the objective forecast of winds, wind shears or turbulence indices, some interpretation and inference will likely be required by meteorologists in the operational environment. Qualitative image features will continue to be useful for short-range turbulence prediction.

### RECOMMENDED ACTION:

1. Determine if the addition of aircraft, VAS, or profiler data will lead to improvement of numerical models.
2. Improve the current system of collecting and disseminating standardized aircraft turbulence reports.
3. Refine techniques for detecting and short-range prediction of turbulence using VAS sounding data and multi-spectral imagery.

RESPONSIBLE AGENCIES: NWS(NMC), FAA, NESDIS(SAL)

PRIORITY: High

### ISSUE:

How Does Turbulence Impact Space Operations?

### DISCUSSION:

Launch pad operations and the launch of a rocket are affected by wind and wind shear. These are normally handled well at the launch site. Any improvement in measuring upper winds and temperatures would benefit this phase.

In the future, satellite recovery vehicles will be required and will probably use the atmosphere between 70 and 120 km to accomplish orbital plane changes. Large amplitude, small-scale fluctuations in density are known to exist, but, at present, we have no real time method to measure in this region.

### RECOMMENDED ACTION:

1. Study existing data from past rocket-grenade experiments to understand the problem.

2. Develop a remote sensor capable of measuring density in the 70 to 120 km region.

RESPONSIBLE AGENCIES: NASA, DoD

PRIORITY: Medium

**COMMITTEE:** SIMULATION

**CHAIRMAN:** Robert L. Ireland

**MEMBERS:** Roland L. Bowles  
Sue-li (Kingsley) Chuang  
Richard E. Dickson  
John Klehr  
Burnell T. McKissick  
Bill Melvin

The primary thrust of our committee discussions centered around the several reasons for simulation and the resultant types of turbulence models needed. We certainly furthered understanding among the participants, but did not reach any earth-shattering conclusions.

First, we recognized and discussed the requirement for fully researched, state-of-the-art, physically complete turbulence models. It was agreed that such simulations must form the groundwork for any follow-on models of simpler nature, but more importantly, they further the understanding of the phenomenon itself.

The first subset of turbulence models may differ little from the first. These models would be applicable to the design, testing, and certification for airframes and systems. In order to assess the impact of turbulence on the structure, and to guarantee that auto flight systems work well, physically representative models of turbulence must be available. The better these models become through research, the more reliable the results. It is "Mom and apple pie," really.

The committee's point of disagreement was reached regarding turbulence simulation for training purposes. While some participants felt strongly that equally complete models were required, others, myself included [Ireland], are quite certain that such simulations for training need only provide approximate instrument and motion responses. As a compromise, we recommended piloted studies.

The committee also surfaced the question of turbulence versus wind shear. The two may be differentiated by scale length (workshop committee meeting notes) or by pilot response required. The boundary conditions are important. Ultimately both disturbances surround a mean; however, wind shear initiates deviations from the mean for periods of time which require pilot response to avoid aircraft upset or ground impact. Once again, the same set of models: research, engineering, and training, is foreseen. The training models may range from the very simple to teach specific pilot techniques, to the complex for demonstration of workload and complications clouding recognition.

ISSUE:

What is a good turbulence model? How is it simulated? Do we need a new standard?

DISCUSSION:

Theoretical model to start Tailor solution to need. For training: If pilot cannot tell the difference, complex model unnecessary. Complex theoretical models necessary for research and testing of auto flight systems.

RECOMMENDED ACTION:

Piloted studies in simulators, compare responses to theoretically accurate models to those with simplified models.

RESPONSIBLE AGENCY: NASA

PRIORITY: High

ISSUE: What is wrong with superimposing linearly?

DISCUSSION:

Have to simulate mechanism that transports energy into the smaller scales. (The real thing is nonlinear.)

RECOMMENDED ACTION:

RESPONSIBLE AGENCY: NASA

PRIORITY: Medium

ISSUE:

Use of turbulence motion simulation: Is it merely an annoyance to the pilot or does it provide a valuable piece of realism?

DISCUSSION:

Melvin: Causes problems for the pilot which are irrelevant to the airplane.

RECOMMENDED ACTION: Piloted study.

RESPONSIBLE AGENCY: NASA

PRIORITY: High

ISSUE: Differentiation of turbulence versus wind shear.

DISCUSSION:

Upset of aircraft? Bowles proposed that wind shear is scale length  $>5b$  or  $>10c$ . Simulate turbulence with zero mean. Depends on effect on vehicle. In general, wind shear may be expected to cause a gross disturbance necessitating corrective action while "turbulence" is of short scale length about a mean--control inputs unnecessary.

RECOMMENDED ACTION:

Need a definition of turbulence versus/or including wind shear. (Is wind shear a subset or a separate entity. Need consensus.)

RESPONSIBLE AGENCY: Can only be addressed by open forum.

PRIORITY: Low

COMMITTEE: MEASURING

CHAIRMAN: Robert A. McClatchey

MEMBERS: Pat Adamson  
L. Jack Ehernberger  
George Gal  
Robert K. Sleeper  
Anthony Smart  
Jim Usry

ISSUE:

Instrumentation Needed for Avoiding Turbulence, Wind Shear, and Microbursts

DISCUSSION:

Development of in situ and remote sensors, e.g., Doppler radar, passive radiometry, lidar, other electro-optical sensors and techniques for using data is required.

RECOMMENDED ACTION:

1. Develop small, lightweight instrumentation instrumentation for measuring turbulence to altitudes of 30 km.
2. Test sensors and techniques on aircraft.

RESPONSIBLE AGENCIES: DoD, NASA, USAF

PRIORITY: High

ISSUE:

Adequacy of High-Altitude Turbulence Understanding

DISCUSSION:

The understanding of turbulence to high altitudes (>30 km), effects of turbulence on the shuttle, and aerospace plane was discussed in detail.

RECOMMENDED ACTION:

Develop measurement techniques for altitudes greater than 30 km.

RESPONSIBLE AGENCIES: DoD, NASA

PRIORITY: High

PRECEDING PAGE BLANK NOT FILMED



ISSUE:

Measurements for Extending the Turbulence Design Data Base

DISCUSSION:

1. Design of expanded aircraft flight envelopes, new control system design evaluation, and laser communications.
2. Operational implications.

RECOMMENDED ACTION:

Develop and implement techniques to update and extend global turbulence data base.

RESPONSIBLE AGENCIES: NASA, SDIO, USAF

PRIORITY: High

ISSUE:

Verification and Standardization of Turbulence Forecasting Techniques

DISCUSSION:

1. PIREPS are "happen-stance."
2. Need comprehensive measures of forecast method skills.

RECOMMENDED ACTION:

1. Gather selective sets of digital flight recorder data.
2. Analyze and establish a national repository of turbulence data.

RESPONSIBLE AGENCIES: NASA, FAA, DoD, NOAA, NTSB

PRIORITY: High

ISSUE:

Process and Use of Currently Available On-Board Sensor Data to Help Pilots Avoid Turbulence and Wind Shear

DISCUSSION:

Information presently on-board may provide a real-time decision aid for avoiding turbulence.

RECOMMENDED ACTION:

Develop algorithms for processing on-board information.

RESPONSIBLE AGENCIES: FAA, DoD, NASA

PRIORITY: High

ISSUE:

Specifications of Operational Requirements for Turbulence and Wind Shear Warning Techniques

DISCUSSION:

The need for quantitative specifications at all altitudes.

RECOMMENDED ACTION:

The operation community needs to document the requirements, i.e., utility or benefit to them vs. warning skill as a function of intensity, lead time, etc.

RESPONSIBLE AGENCIES: USAF, FAA

PRIORITY: High

ISSUE:

Need for In Situ On-Board Profilers to Measure Temperature, Wind, Turbulence, and Composition

DISCUSSION:

The Measuring Committee did not have a scheduled meeting with the Understanding Committee but feels the above issue should receive immediate action.

RECOMMENDED ACTION:

Assemble a comprehensive sensor system to provide cost-effective flight research of fluid dynamic instabilities in the atmosphere.

RESPONSIBLE AGENCIES: NASA, NOAA, DoD, FAA

PRIORITY: High

ISSUE:

Strategic Defense Initiative Office (SDIO) Turbulence Requirements

DISCUSSION:

The SDIO turbulence research and operational requirements are an important subject area but largely omitted at this workshop.

RECOMMENDED ACTION:

Do not drop from subject list, include in a future workshop.

RESPONSIBLE AGENCY: DoD (SDIO)

PRIORITY: High

**COMMITTEE:** MODELING

**CHAIRMAN:** Robert K. Heffley

**MEMBERS:** Stephen D. Burk  
Warren Campbell  
William D. Mark  
C. M. Tchen  
George Trevino  
Morton G. Wurtele

This committee considered a number of modeling-related topics both from a general perspective and with regard to the four interactive group meetings (simulation, design, operations, and remote sensing). The results of our discussions are summarized according to selected issues identified during our individual and interactive group meetings. These results are loosely categorized according to model type or area of interest (i.e., Monte Carlo models, flux models, simulation applications, design applications, operations applications, and remote sensing issues).

The information which is presented is not claimed to be complete nor is it presented in a consistent form. The synopses of issues and discussions were prepared by individual committee members having a close association or strong interest.

One common factor among the various applications and disciplines is that communication between those engaged in model development and those using models is difficult and limited. Perhaps the most effective solution is meetings or workshops such as this. Problems are then quickly detected in articulation of model developers and model users.

A summary of major points is given in Table 1. This is the basis of the oral summary presented on the final day of the workshop.

TABLE 1. Summary of Major Points.

---

1. Monte Carlo Models

- a) The Dryden form of the turbulence spectrum is still most widely used although rational von Karman forms are readily available.
- b) Non-Gaussian turbulence models are available but are in limited use. Factors which call for implementation of these models are correctness, less regularity to pilot with more "surprise," and more faithful compliance with the nonlinear governing equations.
- c) Coherence and cross-correlation models exist but have not been developed to the point where simulation usefulness is recognized.
- d) Non-stationary models can produce "patchiness" as with non-Gaussian.
- e) Future models in progress will have better correlation between turbulence and shear.

TABLE 1. (continued).

---

**2. Models of Turbulence Closure (Flux Models, CFD-Related)**

- a) CFD turbulence models work reasonably well for shear flows but are less effective where there exists buoyancy forces, recirculation zones, rapid accelerations, and large scale turbulence.
- b) Two-equation turbulence models are more general than algebraic models; the higher order models are better than lower order as a general trend.
- c) No clear rational approach to coupling of CFD and Monte Carlo models was indicated but it is attractive to use CFD for mean profiles and Monte Carlo for high frequency.
- d) A group-kinetic approach was presented by C. P. Tchen which transforms the prime equation into a system of macro-equations having the same form as the primitive equations, with added transformation coefficients (eddy viscosity, eddy damping) derived from kinetic theory.

**3. Simulation Applications**

- a) There is a desire for models which are practical and reliable but they should be reasonably correct physically--shear/turbulence interaction is a major area of interest.
- b) Pilot's perception of turbulence features is not well documented but is needed for engineering, modeling, information choices.
- c) A clear consistent handbook or users guide on model implementation is needed.

**4. Design Applications**

- a) There is a need for structural, flight control, flying qualities specification models (specific turbulence ranges of interest span 0.03 to 300 rad/sec).
- b) Despite advanced turbulence models being available, it is difficult to incorporate new models in specs as illustrated in the recent flying qualities (F.Q.) specifications update. That is, even when specifications are updated, it is hard to get new models incorporated (even in background handbook/instruction guidelines which is a highly reasonable document to list new models).
- c) An appropriate rotary wing model is needed. No turbulence model in new F.Q. specifications (MIL-H-8501).
- d) It would be helpful to designers if the characterization of turbulence model is compatible with system response model, especially calculated statistics.

TABLE 1. (concluded).

---

5. Operations Applications

- a) Turbulence prediction models are desired but even if available computation power may be a fundamental limitation--mesoscale models are on threshold of numerical weather prediction (NWP) use.
- b) Improved training simulator "turbulence" models are desired to broaden available simulated conditions, but credibility is essential.
- c) JAWS data are becoming increasingly useful but need to be implemented in training systems. However, it is believed these data do not reflect the most severe conditions.

6. Remote Sensing Issues

- a) There is a clear connection of remote sensing with model development activities.
  - b) There is a need for better understanding of model requirements and sensing capabilities--clear definition of parameters needed.
  - c) There is a data assimilation problem (lots to handle).
  - d) Use of turbulence simulation models as a data source for lidar simulation application is a possibility.
- 

1. Monte Carlo Models

Monte Carlo models, in a variety of forms, are used in flight simulation and aircraft design applications. A key factor setting this class of model apart from the flux models is the relative simplicity and ease of computation of the former.

The main discussion presented is an overview of the status of such models. Special aspects considered are probability density function modeling, anisotropy, and dispersion of passive contaminants. A special issue deserving mention is generation of "simple" functional models based on measured data.

ISSUE:

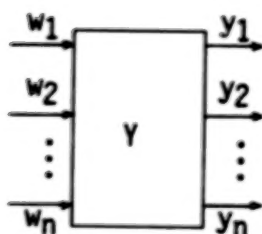
Status of Monte Carlo Models

DISCUSSION:

- 1. Simple Gaussian Models -- The Dryden model (so called because of the form of the spectrum used in the filter) is well known and has a computationally rational form. Some good rational approximations to von Karman spectra are also available (e.g., Campbell or Boeing model forms).



2. Non-Gaussian Models -- Gaussian models can be modulated or acted on by nonlinear filters to generate non-Gaussian models, which are more representative of atmospheric data.
3. Coherence and cross-correlation models -- Several approaches to incorporate coherence or cross-correlations into the models have been developed. Some have been implemented and others proposed. The general problem of this type is as shown in the figure; given a number,  $n$ , of desired outputs with given auto- and cross-correlations, and  $n$  input white noise sources,  $w_i$ , find the set of filters indicated by "Y". "Y" is the unknown set of filters.



Preferably the box should be composed of rational filters for computational efficiency or the simulation community will probably not use these models.

4. Nonstationary models -- Non-stationary models and non-Gaussian models are similar.

#### RECOMMENDED ACTION:

1. Investigate the general Monte Carlo (turbulence) simulation problems described above. Look into coupling Monte Carlo techniques with CFD.
2. Investigate the influence of probability density functions (pdf) on aircraft response. This can be done simply using a Monte Carlo simulation model with different pdf's. Feed the simulated "turbulence" into a fixed-stick aircraft model flying a glide slope and study landing footprints.

RESPONSIBLE AGENCY: NASA

PRIORITY: Medium to High

#### ISSUE:

Modeling Probability Density Function (pdf) of Turbulence,  $p\{u(x)\}$

DISCUSSION:

1. Variation of pdf with position (i.e., How does it vary from one location to another?).
2. Definite non-Gaussian structure of pdf for both  $p\{u(x)\}$  and  $p\{u(x), u(x+r)\}$  (Is it necessary to incorporate the effects of skewness?).

RECOMMENDED ACTION:

1. Data to model these characteristics need to be generated.
2. Pursue self-similar model of the form  $p\{u(x + \Delta x)\} \approx \eta p\{\xi u(x)\}$  where  $\eta$  and  $\xi$  are  $x$ -dependent scale factors.

RESPONSIBLE AGENCIES: NASA, DoD

PRIORITY: Medium

ISSUE:

Anisotropy of Turbulence (What is it and what does it mean?)

DISCUSSION:

1. Anisotropy means that the turbulence intensities (and integral scales) are different from one direction to another.
2. Anisotropy is crucial whenever strong shear is present (particularly boundary-layer turbulence).
3. The time decay of "low" Reynolds number anisotropic turbulence is still an unsolved problem.

RECOMMENDED ACTION:

1. Model (at least crudely) anisotropy in wind shear turbulence.
2. Attempt to formulate a "rule-of-thumb" estimate of decay rate.

RESPONSIBLE AGENCIES: NASA, DoD

PRIORITY: Medium

ISSUE:

Dispersion of Passive Contaminants

#### DISCUSSION:

Both in the earth's planetary boundary layer and in the stratosphere, the Lagrangian problem of passive contaminant dispersion is of great interest. Theoretical models of dispersion have become highly sophisticated, far exceeding the capacity of observational data sets for validation. Model simulations of Eulerian turbulence can, with some additional effort, also simulate dispersion.

#### RECOMMENDED ACTION:

Modelers should be encouraged to treat turbulence and diffusion as two ways of describing the same phenomena.

RESPONSIBLE AGENCIES: NOAA, NASA

PRIORITY: Low to Medium

#### ISSUE:

Generation of "Simple" Functional/Probabilistic Models of Measured Turbulence Time Histories

#### DISCUSSION:

One approach to Monte Carlo model development is to develop the simplest functional/probabilistic models that will represent all obvious features of measured turbulence time histories. For such models to be useful it is necessary to be able to extract model parameters, e.g., standard deviations, integral scales, probability densities, etc. from measured turbulence time histories.

#### RECOMMENDED ACTION:

The underlying philosophy is simplistic and functional depending, of course, on the projected use. This should be stated in applied research efforts and should be considered in approaching any modeling application.

RESPONSIBLE AGENCIES: NASA, DoD

PRIORITY: Medium

## 2. Models of Turbulent Closure (Flux Models)

This class of models can be categorized according to the following:

- a. Truncation models
- b. Constant dissipation models

- c. High-order closure (either by mixing length or normality)
- d. Kinetic methods (either probability or group-kinetic methods)
- e. Numerical simulation models.

A discussion of the status of turbulent closure models is followed by a description of Dr. Tchen's "group-kinetic" modeling, analytical foundation of Monin-Obukhov similarity theory, and turbulence parameterization in operational numerical weather prediction.

#### ISSUE:

Status of Turbulence Closure Models and Coupling of CFD, Engineering Applications, and Monte Carlo Turbulence Simulation

#### DISCUSSION:

Most turbulence closure models work reasonably well for simple shear flows (i.e., jets, wakes, etc.) but for flows with boundary forces, recirculation zones, or rapid accelerations, they do not work as well. In general, the two-equation models have more generality than algebraic models and higher order models are better than lower order models. Recently, a new turbulence model, the multiple scale model developed by C. P. Tchen (NRC fellow at Marshall Space Flight Center), has had great success in predicting complex flows (i.e., with swirl and associated recirculation), which were previously difficult to predict. This four-equation model shows great promise for a wide variety of problems. One area it cannot handle is flows where regions of countergradient diffusion are present.

Generalizations are being added by Tchen to account for countergradient diffusion. The question of coupling CFD analyses with Monte Carlo simulation is relevant for many applications. At the same time, a rational approach is not clear for doing this. One possibility is to use CFD to predict the mean values of the flow. The calculation can be done with a two-equation turbulence model which provides turbulent kinetic energy and length scale. The problem is with the spectrum. Some approach for computing the spectrum function with the CFD model is also required. With this information, Monte Carlo simulation can be performed and added to the mean wind speeds to give the turbulent fluctuations.

Treatment of boundary conditions is an issue of considerable interest. In the CFD community, boundary condition treatment is controversial. Some believe surface treatment with wall functions is completely unacceptable in complex flows. Others believe it is a necessary evil.

#### RECOMMENDED ACTION:

Cross coupling of CFD with Monte Carlo simulation should be investigated. Methods for generating spectra, turbulence intensity length scale, etc. should be evaluated. The sources of any such a technique need to be tested. The best hope for conclusive tests is in a controlled laboratory environment.

Comparisons of calculations and "tuning" of models can proceed from an experimental data base.

RESPONSIBLE AGENCIES: NASA, DoD, NCAR, NOAA

Each agency has its own applications and requires its own models. Generality from one application to the next is not guaranteed.

PRIORITY: High!

ISSUE:

Group-Kinetic Method of Modeling Large-Scale Turbulence

DISCUSSION:

Dr. Tchen described a group-kinetic theory which he is developing. With the group-kinetic method, the system of primitive equations (Navier-Stokes equations) that describe the microdynamic state of turbulence are transformed into the equations of evolution in turbulence that are similar to the primitive equations with added terms containing transport coefficients that represent the statistical effects of small-scale turbulence. The transport coefficients are derived analytically by the group-kinetic method and take the form of an eddy viscosity for small-scale transport or of a damping coefficient for large-scale transport. Thus, the outcome of the group-kinetic theory is to transform the primitive equations into a system in the macro-form without escalating a hierarchy. The method is valid for the determination of mean profiles, the probability functions, and the spectral distributions. A nonlinear dynamical system in the form of a non-homogeneous and nonlinear partial differential equation is transformed into a homogeneous master equation in the  $t, x, v$  space. It is decomposed into three transport equations: the macro-group describes the spectral evolution, the micro-group describes the transport properties, and the sub-group describes the relaxation. The memory loss in the relaxation defines the closure. The kinetic equation is derived.

The transport coefficients (eddy viscosity, damping coefficients) are calculated. The equation of spectral flow is obtained, including all the transport functions, i.e., production, coupling, cascades (direct and inverse) and dissipation. The solutions yield the spectral distributions and the probability function.

The group-kinetic theory derives the spectral laws  $k^{-5/3}$ ,  $k^{-1}$ , gap,  $k^{-3}$  for the spectral density of velocity fluctuations at increasing scales.

By using the Prandtl hypothesis of mixing length, Monin and Obukhov had derived a similarity theory of profiles for mean velocity, temperature, and humidity. The Monin-Obukhov theory cannot determine the universal functions that characterize the neutral, stable, and unstable stratifications. A



group-kinetic method of closure could analytically determine these universal functions.

RECOMMENDED ACTION:

Dr. Tchen should pursue the following issues in his current program:

1. The group-kinetic theory should be extended to include the interactions between turbulence and internal gravity wave, Rossby waves with uniform and differential rotation, geostrophic planetary waves, and other large-scale motions, e.g., vortex motions, in order to investigate the coupling and the reverse cascade.
2. In an atmosphere with rain and snow, the coupling between phases of turbulence should be investigated.
3. The method of lidar sensing should be analytically investigated for multi-phases.

RESPONSIBLE AGENCY: NASA

PRIORITY:

The three topics are listed in the order of their priority.

ISSUE:

Turbulence Parameterization in Operational Numerical Weather Prediction (NWP)

DISCUSSION:

Operational numerical weather prediction models have to cover a sizable region of the atmosphere in order to provide useful meteorological forecasts. This necessitates the use of computational grid volumes which are so large that a considerable portion of the atmospheric turbulence is subgrid and must be parameterized. There is a need to improve these parameterizations.

RECOMMENDED ACTION:

Results from finer resolution models can be used to improve parameterizations in the coarser resolution models. Models should be made more flexible to handle remotely sensed data, such as scatterometer measurements of surface stress over the ocean. New modeling approaches to parameterization should be investigated.

RESPONSIBLE AGENCIES: DoD, NOAA, NASA

PRIORITY: Medium



### 3. Simulation Applications

Simulation is an important use of turbulence models and can span a range of applications. Simulation involves engineering (design and research) and training (airline and military) applications. It was also suggested that there are possibly important non-aviation applications of turbulence simulation, namely, atmospheric circulation (as was suggested by the presentation made by Dr. John Theon of NASA HQ).

#### ISSUE:

Pragmatic Solution of Turbulence Wind Shear Simulation Using a Linear Combination of Random Turbulence and Deterministic Wind Profile

#### DISCUSSION:

This is an approach commonly used in engineering simulation applications. Ease of implementation is a major benefit, but some credibility questions persist (as suggested by the Operations Committee). Also, basic incorrectness of probability distribution (due to linear combination) is another negative argument for this approach.

#### RECOMMENDED ACTION:

Continue to develop physically correct flow models which will provide the potential for better formulation of this modeling technique.

RESPONSIBLE AGENCY: NASA

PRIORITY: High

#### ISSUE:

Pilot Perception of Simulated Turbulence Effects

#### DISCUSSION:

This issue is not well documented but is crucial to making engineering tradeoffs between computational complexity and "realism."

Microscale turbulence is important to effects on instruments even though it is beyond the frequency response of aircraft.

A major limitation in "realism" is outside the turbulence or aircraft models, i.e., limited by visual or motion systems.

While a comprehensive turbulence model is theoretically desirable, more pragmatic approaches must be taken because of economics and of the status of existing models.

Realism, *per se*, may not be as important as identifying critical design conditions.

RECOMMENDED ACTION:

Carry out a systematic investigation and determination of effects which can be perceived by a pilot and their relative level of importance for performance of various flight tasks.

RESPONSIBLE AGENCIES: NASA, DoD

PRIORITY: Medium to High

4. Design Applications

One central concern is the use of turbulence models in conjunction with design standards, specifications, and criteria. These include structures, flying qualities, and flight controls.

ISSUE:

Revision of Military Specification (MIL spec) Models

DISCUSSION:

In spite of recent revisions of specifications (flying qualities military standard, MIL-F-8785C), there are not substantial changes from previous models.

Specification handbooks should contain explicit guidance in how to implement, define the parameters, and use the model.

RECOMMENDED ACTION:

Review current MIL spec models for structural, flying qualities, and flight control applications.

RESPONSIBLE AGENCIES: DoD, NASA

PRIORITY: Medium

ISSUE:

Modeling of Deterministic Features such as Wind Shear and Microbursts

DISCUSSION:

Need meaningful statement of turbulence conditions relative to critical design points.

An initial model has been developed by FWG Associates, Inc.

RECOMMENDED ACTION:

Continue development of understanding and models.

RESPONSIBLE AGENCIES: NASA, FAA

PRIORITY: High

ISSUE:

Needs of Rotary Wing Designers/Users

DISCUSSION:

One area lacking guidance is application of turbulence models in design of rotary wing aircraft. Rotor aerodynamics are important in defining modeling forms and may require time-space dependence.

RECOMMENDED ACTION:

Develop suitable models for rotary wing design and simulation.

RESPONSIBLE AGENCIES: Army, NASA

PRIORITY: High in view of near-term LHX (proposed U.S. Army advanced light scout/attack helicopter family) and J VX (joint services advanced vertical lift aircraft (V-22)) design activities.

5. Operations Applications

Three needs expressed by the Operations Committee were:

1. A better three-dimensional turbulence model for general purpose training simulator use,
2. A better low-level (<500 ft) model for training in terminal area operations (especially regarding wind shear), and

3. An improved model for turbulence forecasting.

ISSUE:

Improved Low-Level Models with Emphasis on Training for Wind Shear

DISCUSSION:

1. Presently, most training likely to be with very limited set of profiles (JFK, MSY, DEN).
2. Pilots learn specific wind shear profiles quickly; therefore, a large variety of cases is needed.
3. Lack of credibility is the reason for not employing direct Monte Carlo modeling.

RECOMMENDED ACTION:

Activities such as those being carried out by NASA LaRC, i.e., viable solution with credibility based on physics and computationally manageable, should be supported.

RESPONSIBLE AGENCIES: NASA, DoD

PRIORITY: High

ISSUE:

Improved Three-Dimensional Turbulence Simulation for Training Simulator

DISCUSSION:

1. Need credible, flexible turbulence model for broad flight envelope application.
2. Objective is training.
3. Need more detailed statement of requirements.
4. Need operational definition for modelers (i.e., what elements of turbulence are observable by pilot and reproducible by simulator).
5. This model would blend into low-level model (or be same).

RECOMMENDED ACTION:

Study the necessity of a three-dimensional model for training application.

RESPONSIBLE AGENCIES: FAA, NASA

PRIORITY: Low

ISSUE:

Turbulence Forecasting: Is Improved Numerical Guidance Available or Possible?

DISCUSSION:

Many high-resolution research models currently in existence hold promise for improved turbulence forecasting. Models which simulate individual thunderstorms, mountain-lee waves, etc. on the mesoscale are currently used primarily in research applications. They show many realistic features of the physical processes involved. With anticipated computing power increases and data assimilation increases associated with advances in satellite and other remote sensing techniques, these models should become true numerical weather prediction models in the next decade.

RECOMMENDED ACTION:

Continue to support development of high-resolution research models.

RESPONSIBLE AGENCIES: NOAA, DoD, NASA

PRIORITY: Medium

**6. Remote Sensing Issues**

Two topics of discussion were explored:

1. Remote sensing requirements for supplying various modeling needs, and
2. How particular models could be used in studying development of remote sensing techniques.

Discussion of the first of these led to the "wind shear" training simulator requirement. This, in turn, led to the solution posed by current use of JAWS data. The second issue centered on the discussion of requirement for models in lidar simulation.

It was again found that clear communication of requirements is needed across disciplines.

ISSUE:

What Modeling Needs are Supported by Remote Sensing Techniques?

DISCUSSION:

1. There is a very broad range of needs spanning "wind shear" to mesoscale.
2. For "wind shear," JAWS data have led to a set of improved models for low-level training simulator applications.
3. Limitations of remote sensing need to be defined and understood by modelers (e.g., resolution of lidar regarding the need to generate simulator wind/turbulence profiles which affects flight path and airspeed).

RECOMMENDED ACTION:

Modelers should establish more direct contact with appropriate individuals in the remote sensing community.

RESPONSIBLE AGENCIES: NOAA, NASA, DoD

PRIORITY: Medium

ISSUE:

What Models/Approaches Might be Available for Lidar Simulation (Connected with Development of Lidar Usage Techniques)?

DISCUSSION:

Use of large eddy simulation models could be used as numerical data source for lidar simulation application.

RECOMMENDED ACTION:

Lidar developers should define needs and present them to the modeling community.

RESPONSIBLE AGENCIES: NOAA, DoD, NASA

PRIORITY: Medium



COMMITTEE: PREDICTING

CHAIRMAN: John L. Keller

MEMBERS: C. L. Chandler  
Dave Forrester  
George Modica  
Charles H. Sprinkle  
Donald Wylie

ISSUE:

Simulation of Turbulence

DISCUSSION:

There were differing opinions as to the importance of simulating CAT. The line-of-flight training (LOFT) approach would seem to require more sophisticated representations of both boundary layer and high-level non-convective turbulence (CAT).

RECOMMENDED ACTION:

The NASA/Ames work using flight recorder data with the equations governing aircraft motion may provide a more realistic representation of individual events. These could be superimposed over the large-scale wind fields associated with CAT outbreaks. It is recommended this work be continued.

RESPONSIBLE AGENCY: NASA

PRIORITY: Very Low

ISSUE:

Need for Ground-Based and Airborne Remote Sensing of Convective and Non-Convective (CAT) Turbulence

DISCUSSION:

Direct sensing of turbulence in the boundary layer seems feasible using ground-based Doppler radar and lidar.

Airborne Doppler lidar data collection efforts for research efforts at the present time. The use of lidar sensors on commercial air carriers at a later time was also discussed.

Use of satellite cloud picture was discussed.

RECOMMENDED ACTION:

Investigate techniques for possible long-term implementation.

RESPONSIBLE AGENCIES: NASA, FAA

PRIORITY: Low

ISSUE:

Operations: Validation and Standardization of CAT Forecasting Techniques/  
Quality of PIREPS

DISCUSSION:

Problems exist for validating both the qualitative techniques currently used by airlines and quantitative numerical techniques under development. Parameterization techniques related to specific turbulence indices could also benefit numerical weather prediction accuracy.

RECOMMENDED ACTION:

1. Use INS-based automatic PIREPS.
2. Evaluate and validate CAT forecast techniques.
3. Standardize forecast techniques (numerical and qualitative).

RESPONSIBLE AGENCIES: NASA, NOAA, DoD

PRIORITY: Medium

ISSUE:

Effects on Aircraft Design

DISCUSSION:

An improvement in turbulence forecasting may lead to an increase in the average life span of the aircraft fleet. Design and forecast validation share a need for the data base.

RECOMMENDED ACTION:

NASA should sponsor a study to determine benefit thresholds of effects on the increased life span of aircraft due to improved clear-air turbulence forecasting methods.

RESPONSIBLE AGENCIES: NASA, FAA

PRIORITY: Medium to High

ISSUE:

Central Automated PIREPS Assimilation Center

DISCUSSION:

There seems to be a unanimous consensus that a need for a reliable turbulence validation data base exists. The development of a quantitative clear-air turbulence (or CAT) index is greatly hindered by the current lack of such information. INS-based automated PIREPS, which are gradually increasing in number, represent a potential resource for providing a quantitative measure of turbulence intensity as well as wind, temperature, and altitude which can be used for improving short-term forecasting at cruising altitude.

RECOMMENDED ACTION:

The Prediction Committee wishes to second the recommendation, which is expected to be made by the FAA's Aviation Weather Task Force, that a centrally located automated PIREPS assimilation center be established within the next several years. This includes the implementation of necessary communications systems and the systematic archiving of these data. The problem of aircraft avoidance of CAT will remain.

RESPONSIBLE AGENCIES: FAA, NOAA, NASA

PRIORITY: Very High

COMMITTEE: UNDERSTANDING

CHAIRMAN: Rodney Wingrove

MEMBERS: Ray Arritt  
Alfred J. Bedard  
Coleman D. Donaldson  
Jean T. Lee  
Peter F. Lester  
James K. Luers  
Ernest W. Millen  
Fred H. Proctor  
J. D. A. Walker

ISSUE:

Produce a Better Definition of Atmospheric Turbulence as It Influences Aircraft

DISCUSSION:

There is a need for a better definition of atmospheric turbulence that includes the broad range of atmospheric phenomena encountered by aircraft. Specialists currently have differing perspectives on the nature and effects of turbulence. The definition should include turbulence in the statistical sense as well as organized instabilities.

RECOMMENDED ACTION:

Encourage representatives from several agencies and sectors of the industry to work to develop and to disseminate a standard that clearly encompasses all aspects of aircraft turbulence.

RESPONSIBLE AGENCIES: Multi-Agency (Research Organizations, NASA, FAA, DoD, etc.)

PRIORITY: Medium

ISSUE:

NEXRAD Application to Turbulence Recognition

DISCUSSION:

Questions were asked as to how well does the measured spectrum width/energy dissipation rate represent (indicate) turbulence in convective situations.

PRECEDING PAGE BLANK NOT FILMED

RECOMMENDED ACTION:

Education and communication of present information are strongly encouraged. Prior to commissioning the NEXRAD radars, users and operators need to be trained as to the interpretation of the data and the limitations brought about by the sampling mode, the mode in which the radar is operated--the algorithm used and the problem area in very weak reflectivity regions.

RESPONSIBLE AGENCIES: NWS, FAA, USAF Air Weather Service

PRIORITY: High

ISSUE:

Evaluation of Wind Profiler and Thermodynamic Profiler Capabilities for Predicting and Monitoring Atmospheric Turbulence

DISCUSSION:

Recent results indicate that thermodynamic profilers can monitor the fluctuations of constant pressure surfaces and provide data on the amplitude and spectral content. Wind profiling radars have also detected short period fluctuations, and the mean wind fields will be valuable for prediction.

RECOMMENDED ACTION:

Document present state of knowledge on the use of profilers for monitoring turbulence aloft. Encourage NOAA to test collocated wind and thermodynamic profilers. Encourage agencies responsible for prediction and warning to consider how higher time resolution data on mean winds aloft could be incorporated into turbulence prediction models.

RESPONSIBLE AGENCY: NOAA

PRIORITY: Medium

ISSUE:

Standardization of Turbulence Reporting Procedures

DISCUSSION:

There is a need for regular, dependable reporting procedures of turbulence for forecast development and verification, for research and for encouraging more reports for operational purposes.

RECOMMENDED ACTION:

Develop a simple, automated, standard, quantitative turbulence reporting procedure for use by all domestic and international flights.

RESPONSIBLE AGENCIES: FAA, Military

PRIORITY: High

ISSUE:

A More Objective and Accessible Way to Measure G-Forces

DISCUSSION:

On many aircraft (commercial and general aviation) quantitative measurements of g-forces are often not available or of poor quality. There exists no method of providing objective pilot reports quantifying the hazard level encountered in real time.

RECOMMENDED ACTION:

Encourage the development of a simple and low-cost "g" meter, permitting easy visual readout (of max g) and reset capability.

RESPONSIBLE AGENCIES: FAA, NASA, Industry

PRIORITY: Low

ISSUE:

Unsteady Flow Structure

DISCUSSION:

There is a need to understand and categorize the different types of unsteady flow structures that occur in the atmosphere and that the aircraft may encounter.

1. Turbulent boundary layers -- Production in the lower portion of turbulent boundary layers is known to take place through abrupt and intermittent eruptions of fluid from the region near the wall (bursts); the burst is then followed by a rapid inrush of fluid toward the wall (the sweep). Similar phenomena undoubtedly occur in the planetary boundary layer; a rough calculation suggests eruptions for a vertical scale of several hundred feet are possible. This may pose a threat to landing aircraft.



2. Three-dimensional vortex motions are common near airports, e.g., (a) trailing aircraft vortices, (b) vortices created near the ground due to downwash, and (c) structured unsteady vortices shed from topographical features.
3. Convected roll cells and waves are also a feature of atmospheric flows. These convected vorticular disturbances (flow structures) will have an affect on aircraft which might be broadly classified as turbulence. However, although they will contain small-scale background turbulence, they are really organized, defined, and unsteady flow structures. As such structures evolve and are convected, updrafts, downdrafts, and sharp shearing regions will occur. All of these effects pose a potential problem for aircraft but on an intermittent or discrete basis. There is a need to understand and categorize such motions, which may be thought of as structured unsteadiness. How do such vortices evolve with time? What types of flow do they induce as they move (particularly near the ground)? Do they generate more vortices near the ground?

RECOMMENDED ACTION:

1. Efforts are needed relative to detailed flow visualization and/or measurements of unsteady phenomena (not the mean quantities--they are not relevant to these kinds of phenomena).
2. Theoretical calculations of the evolution of three-dimensional vortices and their effects on the flow near the ground plane should be accomplished. Interactions with other vortices should also be investigated.
3. Develop an understanding of the most important types of unsteadiness near airports and/or topographical features.

RESPONSIBLE AGENCIES: NSF, NASA, Research

PRIORITY: Medium

ISSUE:

Characterization of Low-Altitude (Terminal) Turbulence

DISCUSSION:

Standardization of data output becomes important for comparison/education of forecasted data from NEXRAD, TDR, LLWSAS facilities.

RECOMMENDED ACTION:

Education; communication among interested technical communities.

RESPONSIBLE AGENCY: NASA, FAA

PRIORITY: Medium

ISSUE:

Turbulence Data Base

DISCUSSION:

There is a need to update and expand the turbulence data base including both old but unused data and new information such as DFDR and Doppler/lidar outputs. These data are needed for an updated physical description of observed turbulence for better understanding, training, and design as aircraft fly higher and composite constructions become common.

RECOMMENDED ACTION:

Inventory current data bases; expand as needed; analyze; and develop a catalog of turbulence describing each type of turbulence, its frequency content (or discrete structure), its altitude range, its pitch size, and its average duration.

RESPONSIBLE AGENCIES: FAA, NASA

PRIORITY: Medium

ISSUE:

Turbulence Knowledge/Understanding "Gap"

DISCUSSION:

Despite the rapid developments in our understanding of turbulence through 1973 and the steady, albeit, slower developments since that time, it appears that there has developed a knowledge gap between the scientist/researcher and the user. This problem has been exacerbated by the growth in our capabilities to detect turbulence and turbulence-related structures via remote sensing devices (sodar, radar, lidar, etc.). The interpretation and use of these data are not immediately obvious to many users including both operational meteorologists and pilots.

RECOMMENDED ACTION:

Develop a systematic program of information/education to include a comprehensive review of the appropriate literature and the preparation of circulars and manuals. In view of the continued impetus towards the establishment of networks of remote sensors in the near future, continued regular updates in this material is encouraged.

RESPONSIBLE AGENCIES: Multi-Agency

PRIORITY: Medium

## CLOSING REMARKS

Walter Frost  
FWG Associates, Inc.  
Tullahoma, Tennessee

I think the workshop was pretty successful relative to our objectives and goals. We had a very good exchange of information. As usual, you don't always achieve exactly what you hoped and there were a few areas where we fell a little short. First of all, not through a fault of ours, at least not because we didn't try, we did miss our presentation on SDI. That was an area in which I believe a number of you were interested. A definition of what may be some of the anticipated problems relative to disturbances and turbulence in the atmosphere was not discussed in too much detail. We'd hoped to do that.

There was also a gap, and some mentioned it toward the end, relative to the fact that we should have had a presentation on the atmospheric boundary layer. There is a lot of work going on in the atmospheric boundary in terms of turbulence modeling that the diffusion people are doing and we intentionally did not invite a large contingency from diffusion modeling because we felt that would be trying to cover too broad an area. But there is a lot of work on turbulence modeling in terms of the effects of buoyancy on turbulence models and the effects of terrain on turbulence models. One of things I'd hoped might come out of the discussion but I didn't see it in any of the presentations is whether we really need to be able to simulate better terrain effects, stability effects, etc. in the atmospheric boundary layer.

There was no real discussion on aircraft wake turbulence, and that is an area that is being researched in the FAA. Unfortunately, the FAA personnel we invited had no travel funds.

I thought the issue of non-stationary turbulence might have been discussed a lot more than it was. That is one place where we are bogging down in turbulence modeling. We have a lot of turbulence models in terms of isotropic and homogeneous turbulence but, how we model non-stationary turbulence, how do you do ensemble averaging, etc. didn't seem to receive much discussion.

One of the things that came out as a recommendation was that we need to define operational requirements. I had hoped that definition would be a result of this workshop. There are no current reports summarizing these requirements. John Houbolt did it in 1972\*, and the recommendation is we need to do it again. A similar recommendation was made relative to design: It was to review criteria modeling and design procedures. The workshop in its final documentation might provide some specific recommendations on areas that we needed further data for design, but basically the recommendation is that there needs to be a specific study.

There was a good point made that we really didn't address the non-rotary wing application problem. That wasn't entirely by design either. We had invited people from the rotary wing community who did not come and a number we

\*Houbolt, John C.: Atmospheric Turbulence. AIAA Journal, vol. 11, no. 4, pp. 421-437, April 1973.

asked turned us down. I think most of the rotary wing people I talked to don't think they have a wind problem. Some how or other we have to get the word out to the rotary wing aircraft community that there are wind problems.

Finally, there could have been a little more discussion on joint and integrated programs. We don't have the money for everybody to go out and study their own thing. We had hoped to generate cooperation between the groups who are measuring statistical turbulence parameters for design working with the group who is doing computational fluid mechanics. There was some discussion of this topic.

In general, I think that the recommendations which came out of this workshop were very good and I believe they gave us guidance. The workshop provided a good opportunity to get together and summarize where we are currently. I hope Hal Murrow felt the same. He was one of the leaders in getting this workshop together. John Houbolt, John Theon, Joe Stickle, and Ed Harrison were also very instrumental in this regard. I hope they are happy with what we achieved. I personally feel we had a very effective workshop.

Harold N. Murrow  
NASA Langley Research Center  
Hampton, Virginia

I don't have much to add. I think Walter Frost summarized it very well. I think we all owe a debt of gratitude to Walter Frost and Dennis Camp for putting together such a group for both the interactive working sessions and the presentations. I thought you might be interested in just where the participants at our workshop came from. I summarized from the attendance list that we had 30 from industry, 10 from universities, 9 from DoD, 5 from NOAA, 17 from NASA, and 3 from other government agencies. As you know, this was an international meeting. We hope that you feel this was as profitable as we think it was.

## ATTENDEES

Pat Adamson  
Adaptive Instruments Corp.  
2450 Central Avenue, Suite H  
Boulder, CO 80301  
303/443-1319

Dr. Ray Arritt  
Dept. of Atmospheric Science  
Colorado State University  
Ft. Collins, CO 80325  
303/491-8293

Dr. Alfred J. Bedard  
Environmental Research Laboratories  
NOAA/WPL  
325 Broadway  
Boulder, CO 80303  
303/497-6508

Dr. Alan Bohne  
Air Force Geophysical Lab/LYR  
Hanscom AFB, MA 01731  
617/377-4406

Dr. Roland L. Bowles  
MS 156A  
NASA Langley Research Center  
Hampton, VA 23665-5225  
804/865-3621

Dr. Stephen D. Burk  
Naval Environmental Protection Research Facility  
US Navy  
Monterey, CA 93943-5106  
408/646-2856

Dennis W. Camp  
FWG Associates, Inc.  
Rt. 2, Box 271A  
Tullahoma, TN 37388  
615/455-1982

Dr. Warren Campbell  
The BDM Corporation  
2227 Drake Avenue  
Huntsville, AL 35805  
205/882-7540



C. L. Chandler  
Operation Center, Dept. 091  
Delta Air Lines  
Hartsfield International Airport  
Atlanta, GA 30320  
404/765-6478

Dr. Sue-11 (Kingsley) Chuang  
SASC Technologies, Inc.  
17 Research Dr.  
Hampton, VA 23666  
804/865-3621

Diana Collier  
Lockheed Calif. Co.  
P.O. Box 551  
Burbank, CA 91520  
818/847-7128

Richard Dickson  
AMSMI/RD-SS-SD  
Army Missile Command  
Redstone Arsenal, AL 35898-5252  
205/876-1951

Coleman DuPont Donaldson  
Aeronautical Research Associates of Princeton  
1800 Old Meadow Rd., #114  
McLean, VA 22102  
703/734-1930

Ben F. Dotson  
MS 3304  
Advance Airplane Branch  
Boeing Military Aircraft Company  
P.O. Box 3707  
Seattle, WA 98124  
206/241-4435

Earl Dunham  
MS 247  
NASA Langley Research Center  
Hampton, VA 23665-5225  
804/865-3274

L. Jack Ehernberger  
MS OFA  
NASA Ames Research Center  
Dryden Flight Research Facility  
P.O. Box 273  
Edwards, CA 93523-5000  
805/258-3699

Gary P. Ellrod  
Satellite Application Lab.  
NOAA NES/DIS  
E/RA21:GE  
Washington, DC 20233  
301/763-8251

G. David Emmitt  
Simpson Weather Associates  
P.O. Drawer 5508  
Charlottesville, VA 22903  
804/979-3571

Bruce D. Fisher  
MS 247  
NASA Langley Research Center  
Hampton, VA 23665-5225  
804/865-3274

Dave Forrester  
Special Investigations Branch  
Meteorological Office  
London Road  
Bracknell, Berkshire  
England  
011-44-0344-420242, x. 2306

Dr. Walter Frost  
FMG Associates, Inc.  
Rt. 2, Box 271A  
Tullahoma, TN 37388  
615/455-1982

George Gal  
Dept. 97-01/Bldg. 201  
Lockheed RDD  
3251 Hanover St.  
Palo Alto, CA 94306-1187  
415/424-2332

William D. Grantham  
MS 489  
NASA Langley Research Center  
Hampton, VA 23665-5225  
804/865-2132

Capt. Edward J. Harrison, Jr.  
Military Asst. for Environmental Sciences  
R&AT/E&LS  
Office of the Under Secretary of Defense  
The Pentagon  
Washington, DC 20301  
202/695-9604

George C. (Cliff) Hay  
ADL-15  
FAA  
800 Independence Ave., SW  
Washington, DC 20591  
202/426-3677

Robert K. Heffley  
Technical Director  
Manudyne Systems, Inc.  
349 First St.  
Los Altos, CA 94022  
415/949-1747

Richard M. Heinbaugh  
McDonnell Douglas Corp.  
Douglas Aircraft Co.  
Dept. C1, E84  
Mail Code 35-05  
3855 Lakewood Blvd.  
Long Beach, CA 90846  
213/593-0563

Dr. John C. Houbolt (Retired NASA Consultant)  
MS 246A  
NASA Langley Research Center  
Hampton, VA 23665-5225  
804/865-2037

Robert L. Ireland  
United Airlines Flight Center  
Stapleton International Airport  
Denver, CO 80207  
303/398-4553

John L. Keller  
Senior Meteorologist  
WSI Corporation  
41 North Road  
Bedford, MA 01730  
617/275-5300

John T. Klehr  
Link Flight Simulation Division  
Singer Co.  
Kirkwood Industrial Park  
Binghamton, NY 13902  
607/772-4695

Dr. V. Klein  
George Washington University  
JIAFS  
Attn: AMB  
MS 489  
NASA Langley Research Center  
Hampton, VA 23665-5225  
804/865-4887

Jean T. Lee (Retired)  
NOAA/NSSL  
1313 Halley Circle  
Norman, OK 73069  
405/321-8011

Peter F. Lester  
Dept. of Meteorology  
San Jose State University  
San Jose, CA 95192  
408/277-2311

James K. Luers  
University of Dayton Research Center  
College Park Drive  
Dayton, OH 45469  
513/229-3921

Dr. William D. Mark  
Bolt, Beranek, and Newman, Inc.  
10 Moulton St.  
Cambridge, MA 02238  
617/497-3527

Dr. Robert A. McClatchey  
Director, Atmospheric Sciences Division  
Air Force Geophysics Lab/LY  
Hanscom AFB, MA 01731  
617/377-2975

Dr. Burnell T. McKissick  
MS 156A  
NASA Langley Research Center  
Hampton, VA 23665-5225

James C. McLean, Jr.  
National Transportation Safety Board  
800 Independence Ave., SW  
Washington, DC 20594  
202/382-6679

William W. Melvin  
ALPA  
1101 West Morton  
Denison, TX 75020  
214/463-1246

Robert T. Meyer  
Stability & Control Group Eng.  
Lockheed Georgia Co.  
86 S. Cobb Dr.  
Marietta, GA 30063  
404/424-2866

Dr. W. Dale Meyer  
HQ Air Weather Services/DNXS  
Scott AFB, IL 62225-5008  
618/256-4781

Ernest W. Millen  
MS 156A  
NASA Langley Research Center  
Hampton, VA 23665-5225  
804/865-3621

Major Douglas Miller  
HQ AFISC/SEFB  
Norton AFB, CA 92409-7001  
714/382-2226

George Modica  
Air Force Geophysics Lab/LYP  
Hanscom AFB, MA 01731-5000  
617/377-2956

Richard N. Moon  
Lockheed California Co.  
Dept. 76-11, Bldg. 63, Plant A1  
P.O. Box 551  
Burbank, CA 91503  
818/847-1732

Harold N. Murrow  
MS 243  
NASA Langley Research Center  
Hampton, VA 23665-5225  
804/865-3451

Jerry R. Newsom  
MS 243  
Head, Aeroservoelasticity Branch, LAD  
NASA Langley Research Center  
Hampton, VA 23665-5225  
804/865-3451

Joe J. Nishikawa  
MS 08-40  
Boeing Commercial Airplane Co.  
P.O. Box 3707  
Seattle, WA 98124  
206/342-4871

David O'Keefe  
Project Loads Dept., Bldg. 63, Plant A-1  
Lockheed-California Co.  
P.O. Box 551  
Burbank, CA 91520  
818/847-3198

John J. Pappas  
Manager Meteorology/Flight Planning  
Western Airlines  
6060 Avion Drive  
Los Angeles, CA 90009  
213/646-9267

Creighton Pendarvis  
Instructor Pilot, Advanced Aeronautics  
SimuFlite Training International  
P.O. Box 611011  
Dallas/Ft. Worth Airport, TX 75261  
214/456-8066/8000 (1-800-527-2463)

Fred H. Proctor  
Meso  
28 Research Drive  
Hampton, VA 23666  
804/865-7800

Phil Rogers  
Lockheed California Company  
P.O. Box 551  
Burbank, CA 91503  
818/847-4550

Dr. James R. Scoggins  
Dept. of Meteorology  
Texas A&M University  
College Station, TX 77843  
409/845-7671



Robert K. Sleeper  
MS 243  
NASA Langley Research Center  
Hampton, VA 23665-5225  
804/865-2273

Anthony Smart  
Spectron Development Labs., Inc.  
3303 Harbor Blvd., G3  
Costa Mesa, CA 92626-1579  
714/549-8477

Robert Smith  
Chief  
Night Vision & EO Labs  
ASL Ft. Belvoir Met Team  
Ft. Belvoir, VA 22060-5677  
703/664-1188

Charles H. Sprinkle  
Chief, Aviation Services Branch (W/OM13)  
NOAA/NWS  
8060 - 13th St.  
Silver Spring, MD 20910  
202/427-7726

Dr. C. M. Tchen, Professor Emeritus  
City College of the City University of New York  
Dept. of Mechanical Engineering  
900 West 190th Street  
New York, NY 10040  
212/781-4111 (Home)

Dr. John S. Theon  
Mail Code EET  
NASA HQ  
600 Independence Ave., SW  
Washington, DC 20546  
202/453-1474

Michael Tomlinson  
National Weather Service  
W/OM13X1  
8060 - 13th St.  
Silver Spring, MD 20910  
301/427-7726

Dr. George Treviño  
Dept. of Mechanical Engineering and Engineering Mechanics  
Michigan Technological University  
Houghton, MI 49931  
906/487-2551

Elijah W. Turner  
Air Force Flight Dynamics Lab  
AFWAL/FIBEB  
Wright-Patterson AFB, OH 45433-6553  
513/255-6434

Jim Usry  
MS 247  
NASA Langley Research Center  
Hampton, VA 23665-5225  
804/865-3274

Dr. Laj Utreja  
The BDM Corporation  
2227 Drake Avenue  
Huntsville, AL 35805  
205/882-4970

Harry A. Verstynen  
Manager, FAA Langley Development  
and Logistics Field Office  
MS 250  
Langley Research Center  
Hampton, VA 23665-5225  
804/865-4595

Dr. J. D. A. Walker  
Packard Lab #19  
Dept. of Mechanical Engineering  
Lehigh University  
Bethlehem, PA 18015  
215/861-3789

Rodney Wingrove  
MS 210-9  
NASA Ames Research Center  
Moffett Field, CA 94035  
415/694-5429

Dr. Morton G. Wurtele  
Professor, Dept. of Atmospheric Sciences  
UCLA  
Los Angeles, CA 90024  
213/825-1751

Dr. Donald Wylie  
Space Science & Engineering Center  
University of Wisconsin  
1225 West Dayton St.  
Madison, WI 53706  
608/263-7458

Dr. E. Carson Yates, Jr.  
MS 243  
NASA Langley Research Center, LAD  
Hampton, VA 23665-5225  
804/865-3451

Dr. J. Allen Zak  
SASC Technologies, Inc.  
17 Research Drive  
Hampton, VA 23666  
804/865-0214

## Standard Bibliographic Page

1. Report No. NASA CP-2468	2. Government Accession No.	3. Recipient's Catalog No.	
4. Title and Subtitle Atmospheric Turbulence Relative to Aviation, Missile, and Space Programs		5. Report Date April 1987	
		6. Performing Organization Code 505-63-21-05	
7. Author(s) Dennis W. Camp and Walter Frost, Editors		8. Performing Organization Report No. L-16296	
		10. Work Unit No.	
9. Performing Organization Name and Address NASA Langley Research Center Hampton, Virginia 23665-5225		11. Contract or Grant No.	
		13. Type of Report and Period Covered Conference Publication	
12. Sponsoring Agency Name and Address National Aeronautics and Space Administration Washington, DC 20546-0001 and U.S. Department of Defense, Washington, DC 20301		14. Sponsoring Agency Code	
15. Supplementary Notes  Dennis W. Camp and Walter Frost: FWG Associates, Inc., Tullahoma, Tennessee.			
16. Abstract  This report is a compilation of proceedings of a workshop conducted at the NASA Langley Research Center April 2-4, 1986. The purpose of the workshop was to bring together representatives of various disciplines of aviation, missile, and space programs involved in predicting, measuring, modeling, and understanding processes of atmospheric turbulence, and to assess the status of knowledge and define work needed to satisfy stated requirements. The contents include 14 invited papers that were presented at plenary sessions and summary reports from 8 committees that were formed from all attendees and which met interactively with other committees.			
17. Key Words (Suggested by Author(s)) Atmospheric turbulence Aerospace environment Gusts Aerospace meteorology Air transportation and safety		18. Distribution Statement  Unclassified-Unlimited  Subject Categories 03, 05, 47	
19. Security Classif.(of this report) Unclassified	20. Security Classif.(of this page) Unclassified	21. No. of Pages 265	22. Price A12

**END  
DATE  
FILMED**

JUL 27 1987

NASA Conference Publication 2469

# Double Layers in Astrophysics

(NASA-CP-2469) DOUBLE LAYERS IN  
ASTROPHYSICS (NASA) 321 p Avail: NTIS HC  
A14/HF AC1 CSCL 03B

N87-23313  
--THRU--  
N87-23335  
Unclas  
H1/88 0072144

*Proceedings of a workshop held at  
George C. Marshall Space Flight Center  
Huntsville, Alabama  
March 17-19, 1986*

**NASA**



NASA Conference Publication 2469

# Double Layers in Astrophysics

*Edited by*  
Alton C. Williams and Tauna W. Moorehead  
*NASA George C. Marshall Space Flight Center*  
*Marshall Space Flight Center, Alabama*

Proceedings of a workshop sponsored by  
the National Aeronautics and Space Administration,  
Washington, D.C., and the Universities Space Research  
Association, Washington, D.C., and held at  
George C. Marshall Space Flight Center  
Huntsville, Alabama  
March 17-19, 1986

**NASA**

National Aeronautics  
and Space Administration

Scientific and Technical  
Information Branch

1987

## PREFACE

An international symposium with the theme "Double Layers in Astrophysics" was held at Marshall Space Flight Center in March 1986. The symposium was sponsored by NASA and the Universities Space Research Association (USRA). Participants from six countries came together for 3 days to discuss their latest research efforts in the experimental, theoretical, and astrophysical application aspects of double layers.

This was the third such symposium. The other two were held at Riso National Laboratory in Roskilde, Denmark, and at the University of Innsbruck in Innsbruck, Austria, in 1982 and 1984, respectively. Whereas, the first two symposia concentrated on laboratory and numerical simulation studies of double layers, this symposium placed emphasis on astrophysical application of double layers.

Most of the applications involved the magnetosphere-ionosphere plasma environment of the Earth because of its accessibility to direct observatories. However, other astrophysical applications were discussed. These included the heliospheric circuit, double radio sources, the solar prominence circuit, magnetic substorms, x-ray and gamma ray bursts, cosmic ray acceleration, x-ray pulsars, and the critical velocity phenomenon.

It is widely felt by the participants that much more work in double layer research needs to be done, especially in the theoretical aspect. A particular area of concern are the effects of physical boundaries and boundary conditions on the formation and nature of double layers.

A recommendation was made by the participants to adopt a standard symbol for the double layer when shown in an electric circuit. This is discussed in more detail in the Recommendations Section of this report.

### ORGANIZING COMMITTEE

H. Alfvén  
L. Lyons  
T. Moore  
M. Weisskopf  
A. Williams

PRECEDING PAGE BLANK NOT FILMED

## TABLE OF CONTENTS

	Page
AGENDA .....	vii
ATTENDEES .....	ix
KEYNOTE ADDRESS (H. Alfvén) .....	1
I. DOUBLE LAYERS IN THE LABORATORY	
Formation Mechanisms of Laboratory Double Layers (Chung Chan).....	35
Some Dynamical Properties of Very Strong Double Layers in a Triple Plasma Device (T. Carpenter and S. Torvén) .....	55
Pumping Potential Wells (N. Hershkowitz, C. Forest, E. Y. Wang, and T. Intrator) .....	73
A Laboratory Investigation of Potential Double Layers (Philip Leung).....	89
Experimental Observation of Ion-Acoustic Double Layers in Laboratory Plasma (Y. C. Saxena) .....	105
II. THEORY AND SIMULATION OF DOUBLE LAYERS	
A New Hydrodynamic Analysis of Double Layers (Heinrich Hora).....	109
Ion Phase-Space Vortices and Their Relation to Small Amplitude Double Layers (Hans L. Pécseli) .....	139
Effect of Double Layers on Magnetosphere-Ionosphere Coupling (Robert L. Lysak and Mary K. Hudson) .....	147
Current Driven Weak Double Layers (Gérard Chanteur) .....	167
Electric Fields and Double Layers in Plasmas (Nagendra Singh, H. Thiemann, and R. W. Schunk) .....	183
Electron Acceleration in Stochastic Double Layers (William Lotko) .....	209
Anomalous Transport in Discrete Arcs and Simulation of Double Layers in a Model Auroral Circuit (Robert A. Smith) .....	211
Weak Double Layers in the Auroral Ionosphere (M. K. Hudson, T. L. Crystal, W. Lotko, and C. Barnes) .....	225
Particle Simulation of Auroral Double Layers (Bruce L. Smith and Hideo Okuda) .....	247

### III. SPACE APPLICATIONS

Conditions for Double Layers in the Earth's Magnetosphere and Perhaps in Other Astrophysical Objects (L. R. Lyons).....	265
Some Aspects of Double Layer Formation in a Plasma Constrained by a Magnetic Mirror (W. Lennartsson).....	275
Electric Potential Distributions at the Interface Between Plasmasheet Clouds (D. S. Evans, M. Roth, and J. Lemaire) .....	287
Double Layers Above the Aurora (M. Temerin and F. S. Mozer) .....	295
Beamed Emission from Gamma-Ray Burst Sources (R. Epstein) .....	305
Double Layers and Plasma-Wave Resistivity in Extragalactic Jets: Cavity Formation and Radio-Wave Emission (Joseph E. Borovsky) .....	307
Accretion onto Neutron Stars with the Presence of a Double Layer (A. C. Williams, M. C. Weisskopf, R. F. Elsner, W. Darbro, and P. G. Sutherland) .....	317
The Formation of a Double Layer Leading to the Critical Velocity Phenomenon (A. C. Williams).....	319
RECOMMENDATIONS .....	327

## AGENDA

Monday, March 17

Chairman, A. Williams

W. Lucas	Welcome from MSFC
A. Dessler	Welcome from Space Science Laboratory
H. Alfvén	Keynote Address
	Summary of the Two Previous Symposia
J. Borovsky	Theory
N. Hershkowitz	Laboratory
T. Moore	Space Observations

Chairman, K. Wright

H. Hora	A New Hydrodynamic Analysis of Double Layers
C. Chan	Formation Mechanisms of Laboratory Double Layers
T. Carpenter	Double Layers in a Triple Plasma Device
N. Hershkowitz	Pumping Potential Wells
P. Leung	Formation of Potential Double Layers
Y. C. Saxena	Ion-Acoustic Double Layers in Laboratory Plasma

Tuesday, March 18

Chairman, T. Moore

H. L. Pécseli	Phase Space Structures in Turbulent Plasmas
R. L. Lysak	Double Layers in Magnetosphere-Ionosphere Coupling
G. Chanteur	Nonlinear Ion Hole Instability and Weak Double Layers

Chairman, J. H. Waite

N. Singh	Double Layer Formation and Dynamics
W. Lotko	Electron Acceleration in Stochastic Double Layers
R. A. Smith	Double Layers in a Model Auroral Circuit
M. K. Hudson	Weak Double Layers in the Ionospheric Plasma
B. L. Smith	Particle Simulation of Auroral Double Layers

Wednesday, March 19

Chairman, J. Horwitz

L. R. Lyons	Why Double Layers in the Earth's Auroral Regions?
W. Lennartsson	Double Layers in a Magnetic Mirror Constrained Plasma
D. S. Evans	Electric Potential Between Plasmasheet Clouds
M. Temerin	Double Layers Above the Aurora

Chairman, R. Bussard

R. Epstein	Beamed Emission from Gamma Ray Burst Sources
J. E. Borovsky	Double Layers and Extragalactic Jets
A. Williams	X-Ray Pulsars and the Critical Velocity Phenomenon
H. Alfvén	Concluding Remarks



## ATTENDEES

Hannes Alfvén  
Royal Institute of Technology  
10044 Stockholm, Sweden

Joseph Borovsky  
Mail Stop D438  
Los Alamos National Lab.  
Los Alamos, NM 87545

Roger W. Bussard  
Space Science Lab./ES65  
NASA Marshall Space Flight Center, AL 35812

Tom Carpenter  
University of Iowa  
Iowa City, Iowa 52242

Gérard Chanteur  
CNET/CRPE  
38-40 rue du General Leclerc  
92131 Issy-les-Moulineaux, France

Chung Chan  
ECE Dept.  
Northeastern University  
Boston, MA 02115

Richard H. Comfort  
Physics Dept.  
The University of Alabama in Huntsville  
Huntsville, AL 35899

Wesley Darbro  
Space Science Lab./ES65  
NASA Marshall Space Flight Center, AL 35812

William Dent  
Space Science Lab./ES65  
NASA Marshall Space Flight Center, AL 35812

James H. Derrickson  
Space Science Lab./ES62  
NASA Marshall Space Flight Center, AL 35812

A. J. Dessler  
Space Science Lab./ES01  
NASA Marshall Space Flight Center, AL 35812

R. F. Elsner  
Space Science Lab./ES65  
NASA Marshall Space Flight Center, AL 35812

Richard Epstein  
Los Alamos National Lab.  
Mail Stop D436  
Los Alamos, NM 87545

David Evans  
SEL/NOAA  
325 Broadway  
Boulder, CO 80303

Carl-Gunne Fälthammar  
Dept. of Plasma Physics  
Royal Institute of Tech.  
10044 Stockholm, Sweden

Gerald J. Fishman  
Space Science Lab./ES62  
NASA Marshall Space Flight Center, AL 35812

Heinrich Hora  
553A Van Allen Hall  
Iowa City, IO 52242

Noah Hershkowitz  
Dept. of Nucl. Eng.  
Univ. Wisconsin-Madison  
1500 Johnson Dr.  
Madison, WI 53706

James L. Horwitz  
Dept. of Physics  
The University of Alabama in Huntsville  
Huntsville, AL 35899

Mary K. Hudson  
Physics & Astron. Dept.  
Dartmouth College  
Hanover, NH 03755

Craig Kletzing  
CASS C-011  
UCSD  
La Jolla, CA 92093

Walter Lennartsson  
Lockheed Palo Alto Res. Lab.  
D/91-20, B/255  
3251 Hanover St.  
Palo Alto, CA 94304

Philip Leung  
MS144-218  
Jet Propulsion Lab.  
Pasadena, CA 91109

William Lotko  
Thayer School of Engineering  
Dartmouth College  
Hanover, NH 03755

Larry Lyons  
Space Sciences Lab. M2-260  
The Aerospace Corp.  
P.O. Box 92957  
Los Angeles, CA 90009

Robert L. Lysak  
School of Physics & Astronomy  
University of Minnesota  
Minneapolis, MN 55455

Shigeki Miyaji  
Space Science Lab./ES65  
NASA Marshall Space Flight Center, AL 35812

Thomas E. Moore  
Space Science Lab./ES53  
NASA Marshall Space Flight Center, AL 35812

Hans L. Pécseli  
Riso National Lab.  
Physics Dept.  
P.O. Box 49  
DK-4000 Roskilde, Denmark

David L. Reasner  
Space Science Lab./ES53  
NASA Marshall Space Flight Center, AL 35812

Y. C. Saxena  
Physical Res. Lab.  
Navrangpura  
Ahmedabad 380009  
India

N. Singh  
CASS, UMC 3400  
Utah State University  
Logan, UT 84322

L. L. Smalley  
Space Science Lab./ES65  
NASA Marshall Space Flight Center, AL 35812

Bruce L. Smith  
Princeton Plasma Physics Laboratory  
Princeton, NJ 08544

Robert A. Smith  
SAIC, Div. 157  
1710 Goodridge Dr.  
McLean, VA 22102

Nobie H. Stone  
Space Science Lab./ES53  
NASA Marshall Space Flight Center, AL 35812

E. A. Tandberg-Hanssen  
Space Science Lab./ES01  
NASA Marshall Space Flight Center, AL 35812

Michael A. Temerin  
Space Sci. Lab.  
Univ. of Calif.  
Berkeley, CA 94720

Roy R. Torbert  
D4A-R1  
The University of Alabama in Huntsville  
Huntsville, AL 35899

M. C. Weisskopf  
Space Science Lab./ES65  
NASA Marshall Space Flight Center, AL 35812

A. C. Williams  
Space Science Lab./ES65  
NASA Marshall Space Flight Center, AL 35812

K. H. Wright, Jr.  
Dept. of Physics  
The University of Alabama in Huntsville  
Huntsville, AL 35899

## KEYNOTE ADDRESS

H. Alfvén

Department of Plasma Physics, Royal Institute of Technology  
Stockholm, Sweden

and

Department of Electrical Engineering and Computer Sciences  
University of California, San Diego, California

### ABSTRACT

As the rate of energy release in a double layer with voltage  $\Delta V$  is  $P = I\Delta V$ , a double layer must be treated as part of a circuit which delivers the current  $I$ .

As neither double layer nor circuit can be derived from magnetofluid models of a plasma, such models are useless for treating energy transfer by means of double layers. They must be replaced by particle models (Lyons and Williams, 1985) and circuit theory (Alfvén, in Chapter III of *Cosmic Plasma*, 1981, hereafter referred to as CP).

A simple circuit (Fig. 1) is suggested which is applied to the energizing of auroral particles, to solar flares, and to intergalactic double radio sources. Application to the heliographic current system leads to the prediction of two double layers on the Sun's axis which may give radiations detectable from Earth.

Double layers in space should be classified as a new type of celestial object (one example is the double radio sources). It is tentatively suggested that x-ray and gamma ray bursts may be due to exploding double layers (although annihilation is an alternative energy source).

M. Azar has studied how a number of the most used textbooks in astrophysics treat important concepts like double layers, critical velocity, pinch effects and circuits. He has found that students using these textbooks remain essentially ignorant of even the existence of these, in spite of the fact that some of them have been well known for half a century [e.g., double layers (Langmuir, 1929) and pinch effect (Bennett, 1934)]. The conclusion is that astrophysics is too important to be left in the hands of the astrophysicists. The billion-dollar telescope data must be treated by scientists who are familiar with laboratory and magnetospheric physics and circuit theory, and of course with modern plasma theory. At least by volume the universe consists of more than 99 percent of plasma, and electromagnetic forces are  $10^{39}$  times stronger than gravitation.

### I. GENERAL PROPERTIES OF DOUBLE LAYERS

#### A. Double Layers as a Surface Phenomenon in Plasmas

Since the time of Langmuir, we know that a double layer is a plasma formation by which a plasma — in the physical meaning of this word — protects itself from the environment. It is analogous to a cell wall by which a plasma — in the biological meaning of this word — protects itself from the environment.

If an electric discharge is produced between a cathode and an anode (Fig. 2) there is a double layer, called a cathode sheath, produced near the cathode that accelerates electrons which carry a current through the plasma. A positive space charge separates the cathode sheath from the plasma. Similarly, a double layer is set up near the anode, protecting the plasma from this electrode. Again, a space charge constitutes the border between the double layer and the plasma. All these double layers carry electric currents.

The lateral limitation of the plasma is also produced by double layers which reduces and slows down the escape of the rapid electrons and accelerates the positive ions outwards so that an ambipolar diffusion is established (no net currents). If the plasma is enclosed in a vessel, its walls get a negative charge and a positive space charge is set up which, again, is the border between the double layer and the plasma. If the discharge constricts itself, the walls can be taken away (without removing the space charge they carry). In these double layers the net electric current is zero.

If the cathode itself emits electrons; e.g., if it is a thermionic or photoelectric emitter, the sign of the cathode fall may be reversed, so that the double layer is limited by a negative space charge which acts as a "virtual cathode." The anode fall may also be reversed.

The lateral double layers may also change sign. This occurs in a dusty plasma if the dust is negatively charged (e.g., by absorbing most of the electrons). In this case we have a "reversed plasma" in which the ions form the lighter component. A magnetized plasma in which the Larmor radius of the ions is smaller than that of the electrons may also be a reversed plasma.

If a plasma is inhomogeneous so that the chemical composition, density, and/or electron temperature differs in different parts of the plasma, the plasma may set up double layers which split the plasma into two or more regions, each of which become more homogeneous. For example, a Birkeland current flowing between the ionosphere and the magnetosphere may produce one or more double layers in this way when they flow through regions with different densities.

There are innumerable variations and complications of the simple case we have discussed, in the same way as biological cell walls show innumerable variations. If we try to increase the current by increasing the applied voltage, the plasma may produce a double layer (see Fig. 2) which takes up part of the voltage so that the plasma current density does not exceed a certain value. Hence, the plasma divides itself into two cells, analogous to what a biological cell does when it gets a large energy input.

The voltage difference  $\Delta V$  over a double layer is usually of the order 5 to 10 times the equivalent of the temperature energy  $kT_e/e$ . However, if there are two independent plasmas produced by different sources, the double layer which is set up at the border between them may be 100 or 1000  $kT_e/e$  or even larger (see Torvén and Andersson, 1979).

## B. Noise in Double Layers

There is one property of a double layer which often is neglected: a double layer very often (perhaps always) produces noise. By this we mean irregular rapid variations within a broad band of frequencies. Lindberg (1982) studied the noise in a stationary fluctuating double layer and demonstrated what a profound influence it has. It broadens the energy spectrum of the electrons and the plasma expands perpendicular to the magnetic field. The electrons in the beam which is produced in the double layer are scattered much more by the noise than by collisions. (Some people claim that noise is essential for the formation and sustenance of a double layer. This is actually a "chicken-egg" problem.)

An analogy to this is that the "critical velocity" phenomenon also seems to be associated with noise. Noise production is often associated with strong currents through plasmas.

The noise is such an important property of plasmas that theories which do not take it into consideration run some risk of being irrelevant. It is difficult to include noise in numerical simulations of double layers, which means

that we should also regard the simulations with some scepticism. It is claimed that supercomputers are powerful enough to treat a noisy plasma. With so many prominent theoreticians present, I believe that the noise problem will be clarified.

### C. Theoretical and Experimental Approaches

Since thermonuclear research started with Zeta, Tokamaks, Stellarators (not to forget the Perhapsotron!), plasma theories have absorbed a large part of the energies of the best physicists of our time. The progress that has been achieved is much less than was originally expected. The reason may be that from the point of view of the traditional theoretical physicist, a plasma looks immensely complicated. We may express this by saying that when, by an immense number of vectors and tensors and integral equations, theoreticians have prescribed what a plasma must do, the plasma — like a naughty child — refuses to obey. The reason is either that the plasma is so silly that it does not understand the sophisticated mathematics, or it is that the plasma is so clever that it finds other ways of behaving, ways which the theoreticians were not clever enough to anticipate. Perhaps the noise generation is one of the nasty tricks the plasma uses in its IQ competition with the theoretical physicists. I am confident that the prominent theoreticians and the plasma will be reconciled before the end of this meeting.

One way out of this difficulty is to ask the plasma itself to integrate the equations; in other words, to make plasma experiments. Confining ourselves to cosmic plasmas, presently there are two different ways of doing this.

1. By performing scale model experiments in the laboratory. This requires a sophisticated technique, which in part we can borrow from the thermonuclear plasma physicists. It also requires methods to "translate" laboratory results to cosmic situations (see CP, 1.2; Alfvén, 1986). Great progress has been made in this respect, but much remains to be done.

2. By using space as a laboratory and performing the experiments in space. This is a fascinating new technology which is most promising, but somewhat more expensive. We shall shortly discuss the laboratory experiments in later sections. There are a number of good surveys on the program of this meeting.

### D. Field and Particle Aspects of Plasmas

Space measurements of magnetic fields are relatively easy; whereas, direct measurements of electric currents are very difficult and in many cases impossible. (Roy Torbert is now developing a technique which makes direct measurements of space current: possible.) Hence, it is natural to present the results of space exploration (from spacecrafts and from astrophysical observations) with pictures of the magnetic field configuration. Furthermore, in magnetohydrodynamic theories, it is convenient to eliminate the current ( $i$  = current density) by curl  $B$ . This method is acceptable in the treatment of a number of phenomena (see Fig. 3).

However, there are also a number of phenomena which cannot be treated in this way, but which require an approach in which the electric current is taken account of explicitly. The translation between the magnetic field description and the electric current description is made with the help of Maxwell's first equation

$$\nabla \times B = \mu_0 \left( i + \frac{\partial D}{\partial t} \right)$$



in which the displacement current can usually be neglected. (However, it is sometimes convenient to account for the kinetic energy of a magnetized plasma by introducing the permittivity  $\epsilon = \epsilon_0[1 + (c/V_{MH})^2]$ , where  $c$  and  $V_{MH}$  are the velocities of light and of hydromagnetic waves (Alfvén, 1950, 3.4.4). If this formalism is used, the displacement current is often large.)

Phenomena which cannot be understood without explicitly accounting for the current are:

1. Formation of double layers.
2. Energy transfer from one region to another.
3. The occurrence of explosive events such as solar flares, magnetic substorms, possibly also "internal ionization" phenomena in comets (Wurm et al., 1963; Mendis, 1978), and stellar flares.
4. Double layer violation of the Ferraro corotation. Establishing "partial corotation" is essential for the understanding of some features of the solar system.
5. Formation of filaments in the solar atmosphere, in the ionosphere of Venus, and in the tails of comets and in interstellar nebulae.
6. Formation of current sheets which may give space a "cellular structure."

Exploration of those plasma properties which can be described by the magnetic field concept has in general been successful. However, this is not the case for those phenomena which cannot be understood by this approach.

## E. Recent Advances

There is a rapidly growing literature concerning double layers and their importance for different cosmic situations. Of special interest is the work of Knorr and Goertz (1974), Block (1978), and Sato and Okuda (1980, 1981). A balanced review of these achievements is given by Smith (1983). Further, to judge from the abstracts of this present symposium, we can look forward to important new results.

As indicated by the title of the present lecture, I will concentrate my attention on the astrophysical applications of double layer theory. The development of the theory of double layers, including numerical simulation, is covered by a number of other papers.

## II. LABORATORY EXPERIMENTS

### A. Electrical Discharges in Gases

Toward the end of the nineteenth century electric discharges in gases began to attract increased interest. They were studied in Germany and in England; and, as there were few international conferences, the Germans and the English made the same discoveries independently. Later, a strong group in Russia was also active. The best survey of the early development is Engel-Steenbeck, *Theorie der Gasentladungen*; see also Cobine (1958). Some modern textbooks are those by Loeb (1961), Papoular (1963), and Cherrington (1974).



## **B. Birkeland**

At the turn of the century geophysicists began to be interested in electrical discharges, because it seemed possible that the aurora was an electrical discharge. Anyone who is familiar with electrical discharges in the laboratory and observes a really beautiful aurora cannot avoid noting the similarity between the multi-colored flickering light in the sky and in the laboratory. Birkeland was the most prominent pioneer. He made his famous terrella experiment in order to investigate this possibility (Birkeland, 1908). Based on his experiments and on extensive observations of aurora in the auroral region, he proposed a current system which is basically the same as is generally accepted today. However, the theory of electric discharges was still in a very primitive state, and the importance of double layers was not obvious.

When Sydney Chapman began his investigations on magnetic storms and aurora one or two decades later, he proposed a current system [the Chapman and Vestine system (Chapman and Vestine, 1938)] which was located entirely in the ionosphere. His most important argument against Birkeland's current system was that above the atmosphere there was a vacuum, and hence there could be no electrons or ions which could carry any currents. [The relation between Chapman and Birkeland is analyzed by Dessler (1983)].

## **C. Langmuir and Plasma**

The interest in double layers made a great leap forward when Langmuir began his investigations. He introduced the term "plasma" in his paper "Oscillation in Ionized Gases" (Langmuir and Tonks, 1929a; see also Langmuir and Tonks, 1929b). Curiously enough, he does not give any motivation for choosing this word, which was probably borrowed from medical terminology. He just states: "We shall use the name 'plasma' to describe this region containing balanced charges of ions and electrons." His biographers do not give any explanation either. Langmuir also made the first detailed analyses of double layers (Langmuir, 1929).

Irving Langmuir was probably the most fascinating man of the plasma pioneers. As his biographers describe him, he was far from being a narrow-minded specialist. His curiosity was all-embracing, his enthusiasm indiscriminate. He liked whatever he looked upon, and he looked everywhere. He was not far from the ideal which Roederer, in a recent paper (1985), contrasts with the insulated specialists that dominate science today (see Section VIII).

Langmuir once wrote, "Perhaps my most deeply rooted hobby is to understand the mechanism of simple and familiar phenomena..." and the phenomena might be anything from molecules to mountains. One of his friends said, "Langmuir is a regular thinking machine: put in facts and you get out a theory." And the facts his always active brain combined were anything from electrical discharges and plasmas to biological and geophysical phenomena. Science as fun was one of his cardinal tenets.

From this one gets the impression that he was very superficial. This is not correct. He got a Nobel prize in chemistry because he was recognized as the father of surface chemistry. He knew enough of biology to borrow the term plasma from this science, and the mechanism of double layers from surface chemistry. Langmuir's probes were of decisive value for the early exploration of plasmas and double layers, and they are still valuable tools.

All magnetospheric physicists must regret that as far as is known, he probably never saw a full-scale auroral display. Schenectady, where he spent most of his life, is rather far from the auroral zone, and he seems never to have traveled to the auroral zone. If he had, his passion for combining phenomena in different fields might very well have made him realize that the beautiful flickering multi-colored phenomenon in the sky was basically the same as the beautiful flickering multi-colored phenomenon he had observed so many times in his discharge tubes. At a time

when Birkeland was dead he might have saved magnetospheric physics from half a century when it was a credo that the road to magnetic storms and aurorae should go through a jungle of misleading mathematical formulae where trees and trees prevented you from seeing the woods — but you can never reconstruct history.

In 1950 I published a monograph, *Cosmical Electrodynamics* (Alfvén, 1950), in which Chapter III deals with electrical discharges in gases. Essential parts of this is devoted to plasma physics; I mention Langmuir only in passing because a quarter of a century after his breakthrough the results were considered as "classical": all experimental physicists were familiar with his works on plasmas, double layers, probes, etc. However, many theoreticians were not; they had no knowledge of Langmuir's work. They do not mention the word "plasma" and had no idea that experiments in close contact with theory had shown that plasmas were drastically different from their "ionized gases." I tried to draw the attention to this by pointing out: "What is urgently needed is not a refined mathematical treatment (referring to Chapman-Cowling) but a rough analysis of the basic phenomena" (referring to the general knowledge of plasmas).

Today, 60 years after Langmuir, most astrophysicists still have no knowledge of his work. The velocity of the spread of relevant knowledge to astrophysics seems to be much below the velocity of light (compare Section VIII).

#### **D. The Energy Situation in Sweden and Exploding Double Layers**

In Sweden the waterpower is located in the north, and the industry in the south. The transfer of power between these regions over a distance of about 1000 km was first done with a.c. When it was realized that d.c. transmission would be cheaper, mercury rectifiers were developed. It turned out that such a system normally worked well, but it happened now and then that the rectifiers produced enormous over-voltages so that fat electrical sparks filled the rectifying station and did considerable harm. In order to get rid of this, a collaboration started between the rectifier constructors and some plasma physicists at the Royal Institute of Technology in Stockholm.

An arc rectifier must have a very low pressure of mercury vapor in order to stand the high back voltages during half of the a.c. cycle. On the other hand, it must be able to carry large currents during the other half-cycle. It turned out that these two requirements were conflicting, because at a very low pressure the plasma could not carry enough current. If the current density is too high, an exploding double layer may be formed. This means that in the plasma a region of high vacuum is produced: the plasma refuses to carry any current at all. At the sudden interruption of the 1000 km inductance produces enormous over-voltages, which may be destructive.

In order to clarify this phenomenon, a series of laboratory experiments were made, in close contact with theoretical work on the same phenomenon. Nicolai Herlofson was the leader of this activity.

At low current densities, a drift motion  $v_d \ll v_T$  is superimposed on the thermal velocity  $v_T$  of the electrons in the plasma. If the current density increases so that  $v_d > v_T$  the motion becomes more similar to a beam, and an instability sets in which is related to the two-beam instability. This produces a double layer which may be relatively stable (although it often is noisy and may move along the tube.) If the voltage over the tube is increased in order to increase the current, the higher voltage is taken up by the double layer and the current is not increased. However, under certain conditions the double layer may explode.

A simple mechanism of explosion is the following. The double layer can be considered as a double diode, limited by a slab of plasma on the cathode side and another slab on the anode side. Electrons starting from the cathode get accelerated in the diode and impinge upon the anode slab with a considerable momentum which they transfer to the plasma. Similarly, accelerated ions transfer momentum to the cathode slab. The result is that the anode and cathode plasma columns are pushed away from each other. When the distance between the electrodes in the diodes becomes larger the drop in voltage increases. This run-away phenomenon leads to an explosion.

Today the mercury arc rectifiers are long since replaced by semiconductors, but our work with them led to an interesting spin-off in cosmic physics. We had since long been interested in solar physics and had interpreted solar prominences as caused by pinching electric currents. With this as background, Jacobsen and Carlqvist (1964) suggested that the violent explosions called solar flares were produced by the same basic mechanism as made the mercury arc rectifiers explode. It drew attention to the fact that every inductive circuit carrying a current is intrinsically explosive.

Further consequences were:

1. The obvious connection between laboratory and space plasma led to a long series of plasma experiments planned to clarify cosmic phenomena.
2. It inspired Carlqvist (1969; 1982a,b,c) to work out a detailed theory of solar flares, and later to develop a theory of relativistic DL's.
3. It inspired Boström (1974) to develop a theory of magnetic substorms which, in important respects, is similar to Akasofu's theory (Akasofu, 1977).

In general, the connection between a technical difficulty and an astrophysical phenomenon led to what Roederer (1985) calls an "interdisciplinaryfication," which turned out to be very fruitful.

### **E. Extrapolation to Relativistic Double Layers**

In most of the DL's in the magnetospheres and those studied so far in the laboratory, the electrons and ions have such low energies that relativistic effects are usually not very important. However, in solar flares, DL's with voltages of  $10^9$  V or even more may occur, and in galactic phenomena we may have voltages which are several orders of magnitude larger.

Carlqvist (1969, 1982a,c) finds that in a relativistic double layer the distribution of charges  $Zn_+(x)$  and  $n_-(x)$  can be divided into three regions: two density spikes near the electrodes and one intermediate region with almost constant charge density. The particles are mainly accelerated in the spikes; whereas, they move with almost constant velocity in the intermediate region. Examples are given of possible galactic DL voltage differences of  $10^{12}$  V. This means that by a straightforward extrapolation of what we know from our cosmic neighborhood, we can derive acceleration mechanisms which brings us up in the energy region of cosmic radiation.

### III. DOUBLE LAYERS AND FROZEN-IN MAGNETIC FIELD LINES

#### A. Frozen-In Field Lines — A Pseudo-Pedagogical Concept

In *Cosmical Electrodynamics*, I tried to give a survey of a field in which I had been active for about two decades. In one of the chapters, I treated magnetohydrodynamic waves. I pointed out that in an infinitely conductive magnetized fluid the magnetic field lines could be considered as "frozen" into the medium — under certain conditions — and this concept made it possible to treat the waves as oscillations of the frozen-in medium.

The "frozen-in" picture of magnetic field lines differs from Maxwell's views. He defined a magnetic field line as a line which everywhere is parallel to the magnetic field. If the current system which produced the field changes, the magnetic field changes and field lines can merge or reconnect. However, if the current system is constant the magnetic field is also constant. To speak of magnetic field lines moving perpendicular to the field makes no sense. They are not material.

In a detailed analysis of the motion of magnetic lines of force, Newcomb (1958) has demonstrated that "it is permissible to ascribe a velocity  $\vec{v}$  to the line of force if and only if  $\nabla \times (\vec{E} \times \vec{v} \times \vec{H})$  vanishes identically."

I thought that the frozen-in concept was very good from a pedagogical point of view, and indeed it became very popular. In reality, however, it was not a good pedagogical concept but a dangerous "pseudo-pedagogical concept." By pseudo-pedagogical I mean a concept which makes you believe that you understand a phenomenon whereas in reality you have drastically misunderstood it.

I never totally believed in it myself. This is evident from the chapter on "Magnetic Storms and Aurora" in the same monograph. I followed the Birkeland-Störmer general approach; but, in order to make that applicable to the motion of low-energy particles in what is now called the magnetosphere, it was necessary to introduce an approximate treatment (the "guiding-center" method) of the motion of charged particles. (As I have pointed out in *CP*, III.1, I still believe that this is a very good method for obtaining an approximate survey of many situations and that it is a pity that it is not more generally used.) The conductivity of a plasma in the magnetosphere was not relevant.

Some years later criticism by Cowling made me realize that there was a serious difficulty here. According to Spitzer's formula for conductivity, the conductivity in the magnetosphere was very high. Hence the frozen-in concept should be applicable and the magnetic field lines connecting the auroral zone with the equatorial zone should be frozen-in. At that time (~1950) we already knew enough to understand that a frozen-in treatment of the magnetosphere was absurd, but I did not understand why the frozen-in concept was not applicable. It gave me a headache for some years.

In 1963 Carl-Gunne Fälthammar and I published the second edition of *Cosmical Electrodynamics* (Alfvén and Fälthammar, 1963). He gave a much higher standard to the book and new results were introduced. One of them was that a non-isotropic plasma in a magnetic mirror field could produce a parallel electric field  $E_{\parallel}$ . We analyzed the consequences of this in some detail and demonstrated with a number of examples that in the presence of an  $E_{\parallel}$ , the frozen-in model broke down. On page 191 we wrote:

"In low density plasmas the concept of frozen-in lines of force is questionable. The concept of frozen-in lines of force may be useful in solar physics where we have to do with high- and medium-density plasma, but may be grossly misleading if applied to the magnetosphere of the earth. To plasma in interstellar space it should be applied with some care."



## B. Magnetic Merging — A Pseudo-Science

Since then I have stressed in a large number of papers the danger of using the frozen-in concept. For example, in a paper "Electric Current Structure of the Magnetosphere" (Alfvén, 1975), I made a table showing the difference between the real plasma and "a fictitious medium" called "the pseudo-plasma," the latter having frozen-in magnetic field lines moving with the plasma. The most important criticism of the "merging" mechanism of energy transfer is due to Heikkilä (1973) who with increasing strength has demonstrated that it is wrong. In spite of all this, we have witnessed at the same time an enormously voluminous formalism building up based on this obviously erroneous concept. Indeed, we have been burdened with a gigantic pseudo-science which penetrates large parts of cosmic plasma physics. The monograph *CP* treats the field-line reconnection (merging) concept in I.3, II.3, and II.5. We may conclude that anyone who uses the merging concepts states by implication that no double layers exist.

A new epoch in magnetospheric physics was inaugurated by L. Lyons and D. Williams' monograph (1985). They treat magnetospheric phenomena systematically by the particle approach and demonstrate that the fluid dynamic approach gives erroneous results. The error of the latter approach is of a basic character. Of course there can be no magnetic merging energy transfer.

I was naive enough to believe that such a pseudo-science would die by itself in the scientific community, and I concentrated my work on more pleasant problems. To my great surprise the opposite has occurred; the "merging" pseudo-science seems to be increasingly powerful. Magnetospheric physics and solar wind physics today are no doubt in a chaotic state, and a major reason for this is that some of the published papers are science and part pseudo-science, perhaps even with a majority for the latter group.

In those parts of solar physics which do not deal with the interior of the Sun and the dense photospheric region (fields where the frozen-in concept may be valid), the state is even worse. It is difficult to find theoretical papers on the low density regions which are correct. The present state of plasma astrophysics seems to be almost completely isolated from the new concepts of plasma which the in situ measurements on space plasma have made necessary (see Section VIII).

I sincerely hope that the increased interest in the study of double layers — which is fatal to this pseudo-science — will change the situation. Whenever we find a double layer (or any other  $E_{\parallel} \neq 0$ ) we hammer a nail into the coffin of the "merging" pseudo-science.

## IV. DOUBLE LAYER AS A MECHANISM FOR ENERGY RELEASE

### A. Double Layer as a Circuit Element

It is a truism to state that a DL which releases a power  $P = I\Delta V$  is part of a circuit in which a current  $I$  flows. We shall investigate the properties of such a circuit by starting with a conventional simple circuit and step by step adopt it to cosmical conditions.

Figure 1 depicts a simple circuit which, besides the double layer DL, contains an inductance in which is stored an energy ("circuit energy").

$$W_L = \frac{1}{2} LI^2 = \frac{1}{2\mu_0} \int B_I^2 d\tau \quad (1)$$

where  $B_I$  is the magnetic field produced by the current  $I$  and  $d\tau$  is a volume element.

If a magnetized plasma (field  $B_0$ ) moves with velocity  $\vec{v}$  in relation to the circuit it produces an emf

$$V = \int \vec{v} \times \vec{B}_0 \cdot d\vec{s} \quad (2)$$

where  $d\vec{s}$  is a line element in the direction of  $\vec{I}$ .

If  $V > 0$  we have a generator transferring plasma energy  $I\Delta V$  into the circuit; if  $V < 0$  we have a motor transferring circuit energy into kinetic energy of the plasma. In Figure 1 we have introduced a symbol  $\oplus$  with the arrow parallel to  $I$  to represent a generator and a similar  $\ominus$ , but with the arrow antiparallel to  $I$ , to represent a motor. Finally, the circuit may contain a resistance  $R$  which dissipates energy  $I^2 R$  into heat, etc.

An electrotechnical circuit like Figure 1 consists essentially of metal wires. Is it realistic to use this for cosmic plasma problems? Apparently not. There are no metal wires in space. Further, if we want to use the circuit in connection with a cosmic problem, most or all the circuit elements are distributed over cosmic distances. There have been many detailed studies made concerning the relations between kinetic energy of a plasma and currents which give a deeper understanding of these processes than our circuit approach.

However, our purpose is not to study the detailed problems but to get a general survey of energy transports in cosmical physics. Is the circuit approach useful as a first approximation to such problems? Maybe.

A map of a city is useful in spite of the fact that it does not describe all the houses, or rather because it does not attempt to do so. For calculating the motion of charged particles the guiding center method is often preferable to the Störmer method even if it does not give the exact position of a particle at a certain moment, or rather because it does not.

In space, charged particles move more easily parallel to  $B$  than perpendicular, and parallel currents are often pinched to filaments. A wire is not too bad an approximation to a pinched filament. Moreover, the generators-motors as well as the double layer are often confined to relatively small volume. Hence, with all these reservations in mind we are going to apply the simple circuit of Figure 1 to a number of cosmical problems in Section VI.

However, the circuit representation could — and must — be developed in many respects. For example when a current flows in large regions, the simple inductance  $L$  should be replaced by a transmission line (see Fig. 4).

We should also observe that a theory of certain phenomena need not necessarily be expressed in the traditional language of different equations, etc. It could also be expressed as an equivalent circuit. The pioneer in the field is Boström who summarized his theory of magnetic substorms in the circuit shown in Figure 11. If this method is developed, it is quite possible that it will be recognized as the best way to represent energy transfer in cosmic plasmas.

## B. Properties of the Circuit

Every circuit which contains an inductance  $L$  is intrinsically explosive (cf. Section II.D). The inductive energy  $W_L = 1/2 L I_0^2$  can be tapped at any point of the circuit. If we try to interrupt the current  $I_0$ , the inductance tends to supply its energy to the point of interruption where the power  $P = I\Delta V$  is delivered ( $\Delta V$  = voltage over the point of interruption and  $I$  the current at this point). This means that most of the circuit energy may be released in a double layer, and if large, cause an explosion of the DL. (If the inductance is distributed over a considerable region, there are transient phenomena during which  $I$  is not necessarily the same over the whole circuit.)



In electro-technical literature in general, the resistors and inductances in the circuit may often be non-linear and sometimes distributed over larger volumes. Similarly, the DL symbol may mean one double layer but also a multiple DL. We should also allow this circuit element to represent other types of  $E_{\parallel}$ ; for example, mirror-produced fields. Hasagawa and Uberoi (1982) have shown that under certain conditions a hydromagnetic wave produces a magnetic field-aligned electric field, which also should be included as DL. This means that DL stands for any electric field parallel to the magnetic field.

### C. Local Versus Global Plasma Theories

Consider a long, homogeneously magnetized uniform plasma. It is confined laterally by tube walls or by a magnetic field. It carries no longitudinal current. Information/energy is transmitted in a time  $T$  from one end to the other by sound waves or diffusion. Phenomena with a time constant  $\ll T$  can be treated by local theories (because one end does not know what happens in the other). The Chapman-Cowling (1970) theory may be valid. However, if a longitudinal current  $I$  flows through the plasma and returns through an outer wire (or circuit), the situation is different. Except for rapid transients the current must be the same in the whole tube and in the wire. If the current is modulated in one end, this information is rapidly transferred to the other end and to the wire. The current may produce double layers which accelerate electrons (and ions) to kV, MV, GV, etc. It may pinch the plasma, producing filaments. These effects also produce coupling between the two ends of the plasma column and reduce the coupling to its local environment.

Electrons accelerated in a DL in the plasma column may travel very rapidly from one end of the plasma column to the other.

Hence, if there is a current through a plasma, we must use global theories, taking account of all the regions through which the current through the plasma column flows. Local theories are not valid (except in special cases).

The theoretical treatment of a current-carrying plasma must start with locating the whole region in which the current flows. It is convenient to draw the circuit and determine the resistances, the inductances, the generators, and DL's. These elements are usually distributed and non-linear, and the circuit theory may be rather complicated.

The return current need not flow through a wire. It could very well flow through another plasma column. An example of this is the auroral current system. As pointed out in Section VI.A the energy is transferred from the cloud C to DL not by high energy particles nor by waves (and of course, not by magnetic reconnection!). It is a property of the circuit. A global theory is necessary which takes account not only of the plasma cloud in the equatorial but also of the ionosphere and double layers which may be found in the lower magnetosphere. Another still more striking example is given in Section VI.C.

## V. TRANSFER OF KNOWLEDGE BETWEEN DIFFERENT PLASMA REGIONS

In CP it is pointed out that the basic properties of a plasma are likely to be the same in different regions of cosmic plasmas. This is represented by Figure 5, called the Cosmic Triple Jump.

The linear dimensions of plasma vary by  $10^{27}$  in three jumps of  $10^9$ : from the laboratory plasmas  $\sim 0.1$  m, to magnetospheric plasmas  $\sim 10^8$  m, to interstellar plasmas  $\sim 10^{17}$  m, up to the Hubble distance  $\sim 10^{26}$ . Including laser fusion experiments, brings us up to  $10^{27}$  orders of magnitude. New results in laboratory plasma physics and in situ

measurements by spacecraft in the magnetospheres (including the heliosphere) make sophisticated plasma diagnosis possible out to the reach of spacecraft ( $\sim 10^{13}$  m). Plasmas at larger distances should to a large extent be investigated by extrapolation. This is possible because of our increased knowledge of how to translate results from one region to another.

The figure shows us an example of how cosmogony (formation of the solar system) can be studied by extrapolation from magnetospheric and laboratory results, supplemented by our knowledge about interstellar clouds. When better instruments for observing the plasma universe in x rays and gamma rays are developed, we may get more information from these than from visual observations.

Figure 6 contains essentially the same information as Figure 5. It demonstrates that plasma research has been based on highly idealized models, which did not give an acceptable model of the observed plasma. The necessary "paradigm transition" leads to theories based on experiments and observations. It started in the laboratory about 20 years ago. In situ measurements in the magnetospheres caused a similar paradigm transition there. This can be depicted as a "knowledge expansion," which so far has stopped at the reach of spacecraft. The results of laboratory and magnetospheric research should be extrapolated further out. When this knowledge is combined with direct observations of interstellar and intergalactic plasma phenomena, we can predict that a new era in astrophysics is beginning, largely based on the plasma Universe model.

## VI. EXAMPLES OF COSMIC DOUBLE LAYERS

In order to demonstrate the usefulness of the equivalent circuit methods, we shall apply it here to a variety of different cosmical problems.

### A. Auroral Circuit

The auroral circuit is by far the best known. It is derived from a large number of measurements in the magnetosphere and in the ionosphere which were pioneered by the Applied Physics Laboratory at Johns Hopkins.

Zmuda and Armstrong (1974) observed that the average magnetic field in the magnetosphere had superimposed on it transverse fields which they interpreted as due to hydromagnetic waves. Inspired by discussions with Fälthammer, Dessler suggested that the transverse field components instead indicated electric currents essentially parallel to the magnetic field lines (Cummings and Dessler, 1967).

This means that it was Dessler who discovered the electric currents which Birkeland had predicted. Dessler called them "Birkeland currents," a term which is now generally accepted and sometimes generalized to mean all currents parallel to the magnetic fields. I think that it is such a great achievement by Dessler to have interpreted the magnetospheric data in what we now know is the correct way that the currents should be called Birkeland-Dessler currents.

In the auroral current system the central body (Earth and ionosphere) maintains a dipole field (Fig. 7).  $B_1$  and  $B_2$  are magnetic field lines from the body. C is a plasma cloud near the equatorial plane moving in the sunward direction (out of the figure) producing an electromotive force

$$V = \int_{C_1}^{C_2} (\vec{v} \times \vec{B}) \cdot d\vec{s}$$

which gives rise to a current in the circuit  $C_1, a_1, a_2, C_2$  and  $C_1$ . The circuit may contain a double layer DL with the voltage  $\Delta V$ , in which the current releases energy at the rate  $P = I\Delta V$  which essentially is used for accelerating auroral electrons. The energy is transferred from C to DL not by high energy particles or waves (and, of course, not by magnetic merging or field reconnection). It is a property of the electric circuit (and can also be described by the Poynting vector, see Fig. 7).

## B. Heliospheric Current

In a way which is described in CP, II.4.2, we go from the auroral circuit to the heliospheric circuit (Fig. 8).

The Sun acts as a unipolar inductor (A) producing a current which during odd solar cycles goes outward along the axes ( $B_2$ ) in both directions and inward in the equatorial plane  $B_1$ . The current closes at large distances ( $B_3$ ), but we do not know where. The equatorial current layer is often very inhomogeneous. Further, it moves up and down like the skirt of a ballerina. In even solar cycles the direction of the current is reversed.

By analogy with the magnetospheric circuit we may expect the heliospheric circuit to have double layers. They should be located at the axis of symmetry, but only in those solar cycles when the axial current is directed away from the Sun.

No one has yet tried to predict how far from the Sun they should be located. They should produce high energy electrons directed toward the Sun, and synchrotron radiation from these should make them observable as radio sources. Further, they should produce noise. They may be observable from the ground, but so far no one has cared to look for such objects.

## C. Double Radio Sources

If in the heliospheric circuit we replace the rotating magnetized Sun by a galaxy, which is also magnetized and rotating, we should expect a similar current system, but magnified by about 9 orders of magnitude (Fig. 9, CP, II.4). This seems to be a very large extrapolation, but in fact a number of successful extrapolations from the laboratory to the magnetosphere are by almost the same ratio. (Of course all theories of plasma phenomena in regions which cannot be investigated by in situ measurements are by definition speculative!)

The emf is given by equation (2), taken from the galactic center out to a distance where the current leaves the galaxy, which may be the outer edge. Inside the galaxy the current may flow in the plane of symmetry similar to the current sheet in the equatorial plane of the Sun, but whether the intragalactic picture is correct or not is not really important to our discussion here. The emf which derives from the galactic rotation is applied to two circuits in parallel, one to the "north" and one to the "south" (see Fig. 9). As galaxies in general are highly north-south symmetric, it is reasonable that the two circuits are similar. Hence, we expect a high degree of symmetry in the current system (at least under idealized conditions).

In the magnetosphere, the current flowing out from the ionosphere produces double layers (or magnetic mirror induced fields) at some distance from the Earth. Because of the similarity of the plasma configuration, we may expect double layers at the axis of a galaxy and a large release of energy in them. It has been suggested that the occurrence of such double layers is the basic phenomenon producing the double radio sources.

In the galactic circuit, the emf is produced by the rotating magnetized galaxy acting as a homopolar inductor, which implies that the energy is drained from the galactic rotation, but from the interstellar medium, not from the stars. By the same mechanisms as in the auroral circuit, it is transferred first into circuit energy and then to the

double layers where the power  $P = I\Delta V$  is released. In a single DL or a series of DL's on each side of the galaxy, an acceleration of charged particles takes place. From the magnetosphere, we know that layers are produced when the current flows outward. (Whether double layers can be formed when the current flows inward is still an open question.) If the same is true in the galactic case, there is a flow of thermal electrons to the layer from the outside and when passing a series of double layers, the electrons are accelerated to very high energies. Hence, a beam of very high energy electrons is emitted from the double layer along the axis toward the central galaxy. This process is the same as the one which produces auroral electrons, only scaled up enormously both in size and energy. In analogy with the current in the magnetotail, the current in the equatorial plane of a galaxy may also produce double layers, which may be associated with large releases of energy.

Figure 9 shows a radio astronomy picture of a double radio source. It is essential in our model that the emf of the galaxy has such a direction that the axial currents flow outward. The DL's they produce should be located at the outer edges of the strong radio source. When electrons conducting the currents outside the double layer reach the double layer, they are accelerated to very high energies. Similarly, ions reaching the double layer on their outward motion from the central galaxy will be accelerated outward when passing the double layers. The strong axial current produces a magnetic field, which pinches the plasma, confining it to a cylinder close to the axis.

Although the electrons are primarily accelerated in the direction of the magnetic field, they will be scattered by magnetic inhomogeneities and spiral in such a way that they emit synchrotron radiation. The accelerated electrons will be more like an extremely hot gas than a beam. With increasing distance from the double layer the electrons will spread and their energy, and hence their synchrotron emission, will decrease. This is in agreement with observations. It is possible that some of them will reach the central galaxy and produce radio emission there. It is also possible that the observed radio emission from the central galaxy is due to some other effect produced by the current (there are several mechanisms possible). Such phenomena in the central galaxy will not be discussed here.

The ions passing the double layer in the outward direction will be accelerated to the same energy as the electrons. Because of their larger rest mass, they will not emit much synchrotron radiation, but there are a number of other mechanisms by which they may produce the observed radio emission from the regions farther away from the central galaxy.

It should be stressed again that, just as in the magnetosphere and in the laboratory, the energy released in the double layer derives from circuit energy and is transferred to it by electric currents which essentially consist of relatively low-energy particles. There is no need for a beam of high energy particles to be shot out from the central galaxy (or plasmons). On the contrary, the central galaxy may be bombarded by high energy electrons which have obtained their energy from the double layer.

A quantitative analysis of the double radio galaxies is given in *CP*. It is possible that some modifications are needed.

#### **D. Solar Prominence Circuit. Solar Flares**

The circuit consists of a magnetic flux tube above the photosphere and part of photosphere (see Fig. 10). The generator is in the photosphere and is due to a whirl motion in sunspot magnetic field.

Generator output increases circuit energy which can be dissipated in two different ways: (1) When current density surpasses critical value, an exploding DL is produced in which most of the circuit energy is released. This causes a solar flare. Hénoux (1985) has recently given an interesting study of solar flares and concludes that a current disruption by DL's is an appealing explanation of solar flares. (2) Under certain circumstances the electromagnetic pressure of the current loop may produce a motor which gives rise to a rising prominence (Alfvén and Carlqvist, 1967; Carlqvist, 1982b).



### **E. Magnetic Substorms**

According to Boström (1974) and Akasofu (1977), an explosion of the transverse current in the magnetotail gives an attractive mechanism for the production of magnetic substorms (see Fig. 11). Boström has shown that an equivalent magnetic substorm circuit is a way of presenting the substorm model. The onset of a substorm is due to the formation of a double layer, which interrupts the cross-tail current so that it is redirected to the ionosphere.

### **F. Currents and Double Layers in Interstellar Space**

As it is relatively easy to measure magnetic fields, it is natural that the first description of the electromagnetic state of interstellar and intergalactic space is based on a magnetic field description. However, as no one claims — at least not explicitly — that the magnetic fields are curl-free, we must have a network of currents. As investigations of DL's (and quite a few other phenomena) require explicit pictures of electric currents, it is essential to apply these pictures.

Filamentary structures were quite generally observed long ago, and may be observed everywhere where sufficient accurate observations can be made. There are a number of processes by which they are generated. For example, the heliospheric current system must close at large distances (cf. Fig. 8), and it is possible — perhaps likely — that this is done by a network of filamentary currents. Many such filaments may produce DL's, and some of these may explode.

### **G. Double Layers as a New Class of Celestial Objects**

The general structure and evolution of such a network of currents, including their production of DL's, has not yet been investigated. It is possible that under certain circumstances the final destiny of a set of currents is DL's, perhaps exploding DL's. DL's may be considered as a new class of celestial objects. We have already given an example of this in the interpretation of double radio sources as DL's.

### **H. X-Ray and Gamma Ray Bursts**

When a number of explosions are observed, such as gamma ray and x-ray bursts, one may try to explain them as exploding DL's. However, another possible source of energy is annihilation (CP, VI.3). There is also a possibility that they may be due to double layers in a baryon symmetric universe.

### **I. Double Layers as a Source of Cosmic Radiation**

As pointed out in Section II.E, relativistic DL's in interstellar space may accelerate ions up to cosmic ray energies (see Carlqvist, 1969; 1982a,c).

## VII. DOUBLE LAYERS IN TEXTBOOKS

As has been pointed out many times (see e.g., *CP I*; Alfvén, 1982) in situ measurements in the magnetospheres and progress in laboratory plasma physics have caused a "paradigm transition" which means that a number of old concepts have to be abandoned and a number of new phenomena must be taken into account. Michel Azar has gone through some of the most generally used textbooks in astrophysics and listed in which of these the new concepts have been presented to the student in astrophysics. The results are shown in Table 1. The table gives the surprising and depressing result that the students in astrophysics still are kept ignorant of what has happened in plasma physics.

Double layers were analyzed in detail by Langmuir (1929). The development described in Section III.A demonstrated that there must be "double layers" in a generalized sense (= magnetic field-aligned electric field) so the first decisive evidence for their existence in the magnetosphere dates from 1962. The real discovery of double layers in the magnetosphere is due to Gurnett (1972), but still there are only 2 out of 17 textbooks which even mention that anything like that could exist.

The critical velocity was postulated in 1942 in order to explain the band structure of the solar system. In a series of experiments especially designed to clarify this and other cosmic plasma phenomena, the critical velocity phenomenon was confirmed in the laboratory by Fahleson (1961), by Angerth et al. (1962), by Eninger (1965), and by Danielsson (1973).

The use of "equivalent circuits" is discussed in Alfvén and Fälthammar (1963) and further in a number of papers. Boström (1974) has given the most interesting account of their use. Still, Akasofu is the only one in the list who has understood the value of this in cosmic physics.

That parallel currents attract each other was known already at the times of Ampere. It is easy to understand that in a plasma, currents should have a tendency to collect to filaments. In 1934, it was explicitly stated by Bennett that this should lead to the formation of a pinch. The problem which led him to the discovery was that the magnetic storm producing medium (solar wind with present terminology) was not flowing out uniformly from the Sun. Hence, it was a problem in cosmic physics which led to the introduction of the pinch effect.

Today everybody who works in fusion research is familiar with pinches. Indeed, several big multimillion dollar thermonuclear projects are based on pinches. Pinches in cosmical physics are discussed in detail in Alfvén and Fälthammar (1963) and further in a large number of papers; see *CP*, II.4. However, to most astrophysicists it is an unknown phenomenon. Indeed, important fields of research, e.g., the treatment of the state in interstellar regions, including the formation of stars, are still based on a neglect of Bennett's discovery more than half a century ago. As shown in the table, present-day students in astrophysics hear nothing about it. A recent survey article in *Science* described some "mysterious" threads which were claimed to be different from anything earlier discovered (Waldrop, 1985). Published photographs indicated that these phenomena are likely to be common filamentary structures; indeed, they have been well known since 1934.

In conclusion, it seems that astrophysics is too important to be left in the hands of theoretical astrophysicists who have gotten their education from the listed textbooks. The multibillion dollar space data from astronomical telescopes should be treated by scientists who are familiar with laboratory and magnetospheric physics, circuit theory, and, of course, modern plasma physics. More than 99 percent of the Universe consists of plasma, and the ratio between electromagnetic and gravitational forces is  $10^{39}$ .



## VIII. ROEDERER'S INTERDISCIPLINARIFICATION

### A. The Roederer Syndrome

In his article "Tearing Down Disciplinary Barriers," Juan G. Roederer (1985) points out the conflict between the demand for "increased specialization on one hand and the pursuit of an increasingly interdisciplinary approach on the other."

This is important. Indeed, in the present state of science specialization is favored to such an extent that science is split up into a number of increasingly small specialties. We lack the global view. This is evident from the preceding section.

We should remember that there once was a discipline which was called "Natural Philosophy" ("reine Naturwissenschaft"). Unfortunately this discipline seems not to exist today. It has been renamed "science," but science of today is in danger of losing much of the Natural Philosophy aspect.

Roederer further discusses the psychological and structural causes for the loss of the global view, and points out that one syndrome of cause is the "territorial dominance, greed, and fear of the unknown." Scientists tend to "resist interdisciplinary inquiries into their own territory... In many instances, such parochialism is founded on the fear that intrusion from other disciplines would compete unfairly for limited financial resources and thus diminish their own opportunities for research."

### B. Microscale Example

All this agrees with my own experience. When running a lab I found that one of my most important activities was to go from room to room and discuss in depth the problems which a certain scientist or a group of scientists was trying to understand. It often happened that one group reported that in their field they had a special problem which they could not possibly understand. I told them that if they cared to open the door to the next room — it was not locked! — just this special problem had been solved half a year ago, and if they injected the solution into their own field, this would take a great leap forward. Often they were not at all happy for this suggestion, probably because of the syndrome which Roederer has discussed, but when faced with "tearing down the disciplinary barriers" within the laboratory they realized how important such action is for progress (cf. Section II.D). This may be considered a mild case of the Roederer syndrome.

Such an example from the microscale structure of science supports Roederer's general views, but examples from the macroscale structure are much more important. Large parts of this lecture have been a series of examples of the malady which Roederer describes.

The lack of contact between Birkeland's and Langmuir's experimental-theoretical approach on the one hand and the Chapman-Cowling mathematical-theoretical approach on the other had delayed progress in cosmic plasma physics by perhaps half a century. The many new concepts which came with the space age begin to be understood by magnetospheric physicists but have not yet reached the textbooks in astrophysics, a delay of one or two decades, often more as seen in the preceding section. Very few if any deny that (at least by volume) more than 99 percent of the Universe consists of plasma but students in astrophysics are kept ignorant even of the existence of important plasma phenomena like those listed in Table 1.

Dr. Roederer's prescription for curing this serious disease is "tearing down disciplinary barriers," indeed "interdisciplinarification" of science. This seems to be wise. However, we must suspect that to many astrophysicists this is bitter medicine. Can we find ways to sweeten it?

## REFERENCES

- Akasofu, S.-I., *Physics of Magnetospheric Substorms*, D. Reidel Publ. Co., Dordrecht, Holland, 1977.
- Alfvén, H., *Cosmical Electrodynamics*, Oxford University Press, London, 1950.
- Alfvén, H., in *Physics of the Hot Plasma in the Magnetosphere*, edited by B. Hultqvist and L. Stenflo, Plenum Press, New York, p. 1, 1975.
- Alfvén, H., *Cosmic Plasma*, D. Reidel Publ. Co., Dordrecht, Holland, 1981.
- Alfvén, H., *Physica Scripta*, T2, 10 (1982).
- Alfvén, H., Plasma Universe, preprint, 1986.
- Alfvén, H., and P. Carlqvist, *Solar Phys.*, 1, 220 (1967).
- Alfvén, H., and C.-G. Fälthammar, *Cosmical Electrodynamics*, Second Edition, Oxford University Press, London, 1963.
- Angerth, B., L. Block, U. V. Fahleson, and K. Soop, *Nucl. Fusion Suppl.*, 3, 9 (1962).
- Bennett, W. H., *Phys. Rev.*, 45, 840 (1934).
- Birkeland, K., in *The Norwegian Aurora Polaris Expedition, 1902-1903*, Vol. 1, Section 1, H. Aschehoug and Co., Christiania, p. 1, 1908.
- Block, L. P., *Astrophys. Space Sci.*, 55, 59 (1978).
- Boström, R., in *Magnetospheric Physics*, edited by B. M. McCormac, D. Reidel Publ. Co., Dordrecht, Holland, p. 45, 1974.
- Carlqvist, P., *Solar Phys.*, 7, 377 (1969).
- Carlqvist, P., in *Symposium on Plasma Double Layers*, edited by P. Michelsen and J. Juul Rasmussen, June 16-18, 1982, Riso National Laboratory, Roskilde, p. 71, 1982a.
- Carlqvist, P., in *Symposium on Plasma Double Layers*, edited by P. Michelsen and J. Juul Rasmussen, June 16-18, 1982, Riso National Laboratory, Roskilde, p. 255, 1982b.
- Carlqvist, P., *Astrophys. Space Sci.*, 87, 21 (1982c).
- Chapman, S., and T. G. Cowling, *The Mathematical Theory of Nonuniform Gases*, Cambridge University Press, London, 1970.
- Chapman, S., and F. H. Vestine, *Terr. Mag.*, 43, 351 (1938).
- Cherrington, B. E., *Gaseous Electronics and Gas Lasers*, Pergamon Press, Oxford, 1974.
- Cobine, J. D., *Gaseous Conductors*, Dover Publications, Inc., New York, 1958.
- Cummings, V. D., and A. J. Dessler, *J. Geophys. Res.*, 72, 1007 (1967).
- Danielsson, L., *Astrophys. Space Sci.*, 24, 459 (1973).
- Dessler, A. J., in *Magnetospheric Currents*, edited by T. A. Potemra (Proceedings of the Chapman Conference on Magnetospheric Currents, Tides Inn, Irvington, Virginia, April 5-8, 1983), p. 22, 1983.
- Eninger, J., *Proc. 7th Int. Conf. Phenom. Ionized Gases*, 1, p. 520, 1965.
- Fahleson, U. V., *Phys. Fluids*, 4, 123 (1961).
- Gurnett, D. A., in *Critical Problems of Magnetospheric Physics*, edited by E. R. Dyer, p. 123 (Proceedings of Joint COSPAR, EAGA, URSI Symposium, Madrid, May 1972), UCSTP, Washington, D.C., 1972.
- Hargrave, P. J., and N. Ryle, *Roy. Astron. Soc. Mon. Not.*, 166, 305 (1974).
- Hasegawa, A., and C. Uberoi, *The Alfvén Wave*, Chapter V, p. 18, Technical Information Center, U.S. Department of Energy, U.S. Printing Office, Washington, D.C., 1982.
- Heikkilä, W. J., *Astrophys. Space Sci.*, 23, 261 (1973).
- Hénoux, J. C., *Dynamo Theories of Solar Flares*, SMA Workshop on Solar Flares, Irkutsk, June 1985.
- Jacobsen, C., and P. Carlqvist, *Icarus*, 3, 270 (1964).
- Knorr, G., and C. K. Goertz, *Astrophys. Space Sci.*, 31, 209 (1974).
- Langmuir, I., *Phys. Rev.*, 33, 954 (1929).
- Langmuir, I., and L. Tonks, *Phys. Rev.*, 33, 195 (1929a).
- Langmuir, I., and L. Tonks, *Phys. Rev.*, 34, 876 (1929b).
- Lindberg, L., in *Symposium on Plasma Double Layers*, edited by P. Michelsen and J. Juul Rasmussen, p. 164, June 16-18, 1982, Riso National Laboratory, Roskilde, 1982.

- Loeb, L., *Basic Processes of Gaseous Electronics*, Cambridge University Press, London, 1961.
- Lyons, L., and D. Williams, *Quantitative Aspects of Magnetospheric Physics*, D. Reidel Publ. Co., Dordrecht, Holland, 1985.
- Mendis, A., *Moon and Planets*, 18, 361 (1978).
- Newcomb, W. A., *Annals of Physics*, 3, 347 (1958).
- Papoular, R., *Electrical Phenomena in Gases*, American Elsevier Publ. Co., New York, 1963.
- Roederer, J. G., *EOS*, 66, 681 (1985).
- Sato, T., and H. Okuda, *Phys. Rev. Lett.*, 44, 740 (1980).
- Sato, T., and H. Okuda, *J. Geophys. Res.*, 86, 3357 (1981).
- Smith, R. A., in *Proc. 107th International Astronomical Union Symposium*, edited by M. R. Kundu and G. Holman, p. 113, College Park, Maryland, 1983.
- Torvén, S., and S. Andersson, *J. Phys. D. Appl. Phys.*, 12, 717 (1979).
- Waldrop, M. M., *Science*, 230, 652 (1985).
- Wurm, in *The Moon Meteorites and Comets*, edited by B. M. Middehurst and G. P. Kuiper, p. 573, University of Chicago Press, Chicago, 1963.
- Zmuda, A. J., and J. C. Armstrong, *J. Geophys. Res.*, 74, 4611 (1974).

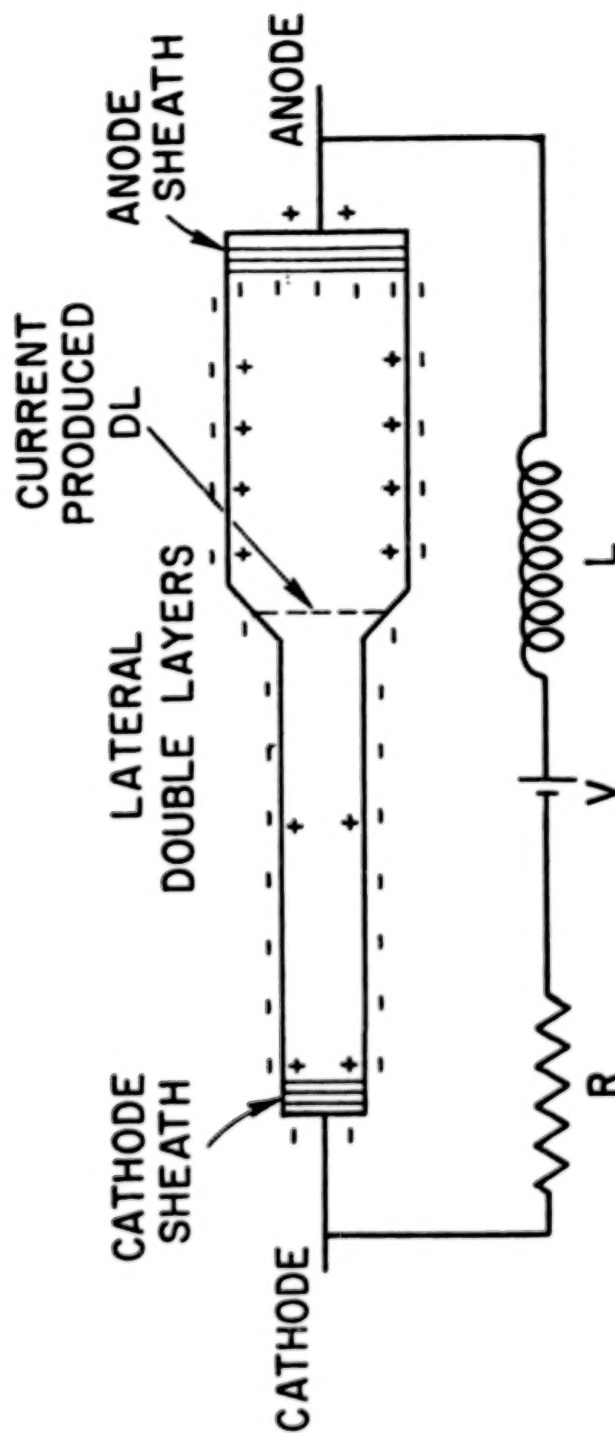


Figure 1. Example of a simple electric circuit where the double layer symbol suggested by Carlqvist (1982c) is used. The double layer is connected in series with a voltage source  $V$ , an inductance  $L$ , and a resistance  $R$ . A current  $I$  flows in the circuit. The usual symbol for an emf (which is derived from a galvanic element) is replaced by the suggested symbol for a "generator." The arrow points in the direction of the current  $I$ . The same symbol with the arrow antiparallel to  $I$  represents a "motor" in which circuit energy is used to accelerate the plasma.

## DUALISM IS COSMIC PLASMA PHYSICS

### TRANSLATION FORMULA

$$\nabla \times B = \mu_0 i$$

#### MAGNETIC FIELD DESCRIPTION

MAGNETIC FIELDS ARE:  
MEASURED RATHER EASILY  
BASIC FOR PLASMA ANISOTROPY  
INCLUDING HIGH ENERGY PARTICLE MOTION  
GIVES A GOOD DESCRIPTION OF SOME  
WAVES IN PLASMAS

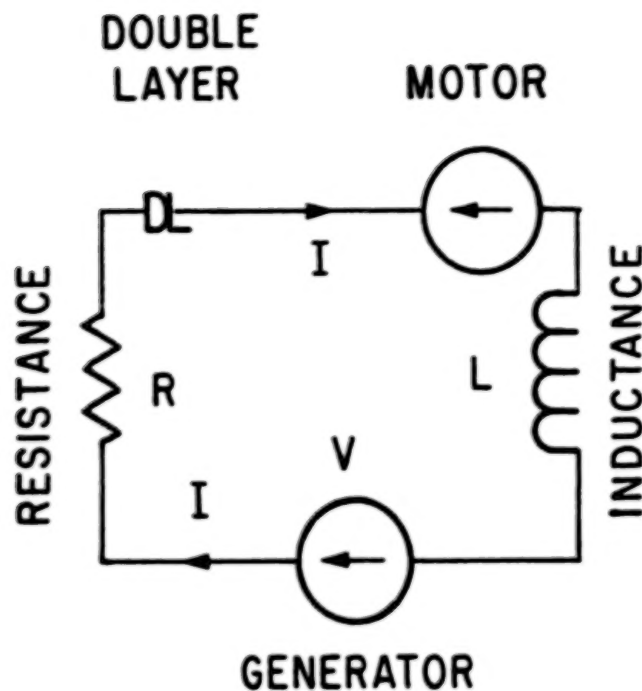
#### ELECTRIC CURRENT DESCRIPTION

ELECTRIC CURRENTS ARE:  
DIFFICULT TO MEASURE DIRECTLY BUT  
ESSENTIAL FOR UNDERSTANDING:  
DOUBLE LAYERS  
TRANSFER OF ENERGY FROM ONE REGION  
TO ANOTHER  
CURRENT SHEET DISCONTINUITIES  
CELLULAR STRUCTURE OF SPACE  
MAGNETIC SUBSTOMS, SOLAR FLARES

THE PLASMA DUALISM IS SOMEWHAT ANALOGOUS TO THE GENERAL PARTICLE-FIELD DUALISM IN PHYSICS.  
THE CURRENT DESCRIPTION REQUIRES A NEW FORMALISM WITH DOUBLE LAYER AND ELECTRIC CIRCUITS  
AS IMPORTANT INGREDIENTS.

Figure 2. Plasma produced by an electric discharge. In case the plasma is inhomogeneous, either because its cross section varies or its chemical composition or its density varies, one or more double layers may be produced between the electrodes (cf. Lindberg, 1982).

# SIMPLE CIRCUIT



CIRCUIT ENERGY  $W_C = 1/2 L I^2$

GENERATOR VOLTAGE  $V_G = \int_{\text{GEN}} \vec{v} \times \vec{B} \cdot d\vec{s}$

MOTOR VOLTAGE  $V_M = \int_{\text{MOT}} \vec{v} \times \vec{B} \cdot d\vec{s}$

GENERATOR POWER  $P_G = I V_G$

MOTOR POWER  $P_M = I V_M$

DOUBLE LAYER VOLTAGE  $\Delta V$

POWER DELIVERED TO PARTICLES BY DL  $P_0 = I \Delta V$

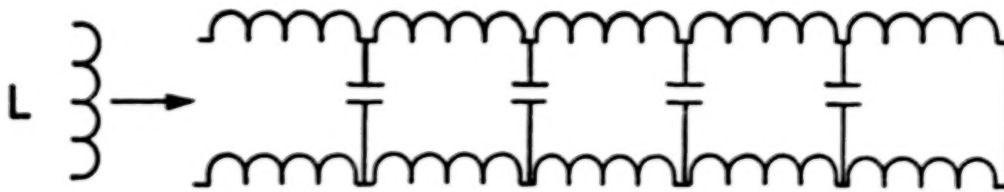
ENERGY LOSSES IN RESISTANCES ETC.  $P_R = 1/2 R I^2$

Figure 3. Dualism in plasma physics (cf. CP, I.3).



## OTHER SYMBOLS

IF INDUCTANCE IS DISTRIBUTED  $L$  SHOULD BE REPLACED BY TRANSMISSION LINE.



MAGNETIZED CELESTIAL  
BODY ACTING AS  
HOMOPOLAR INDUCTOR

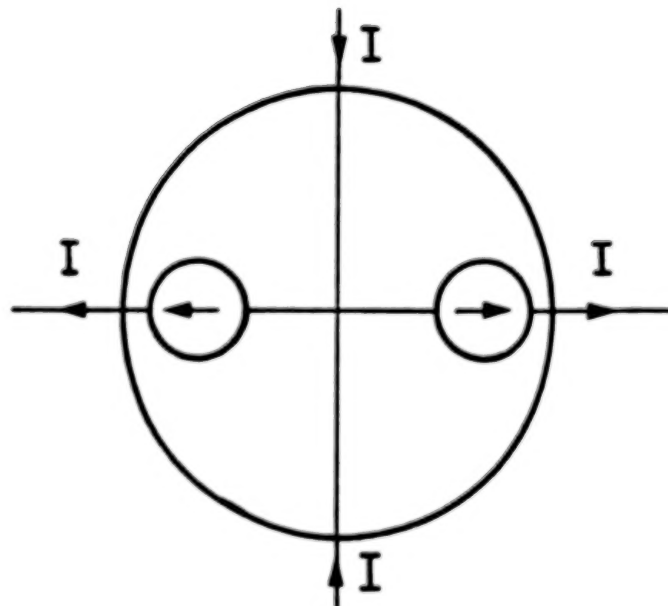
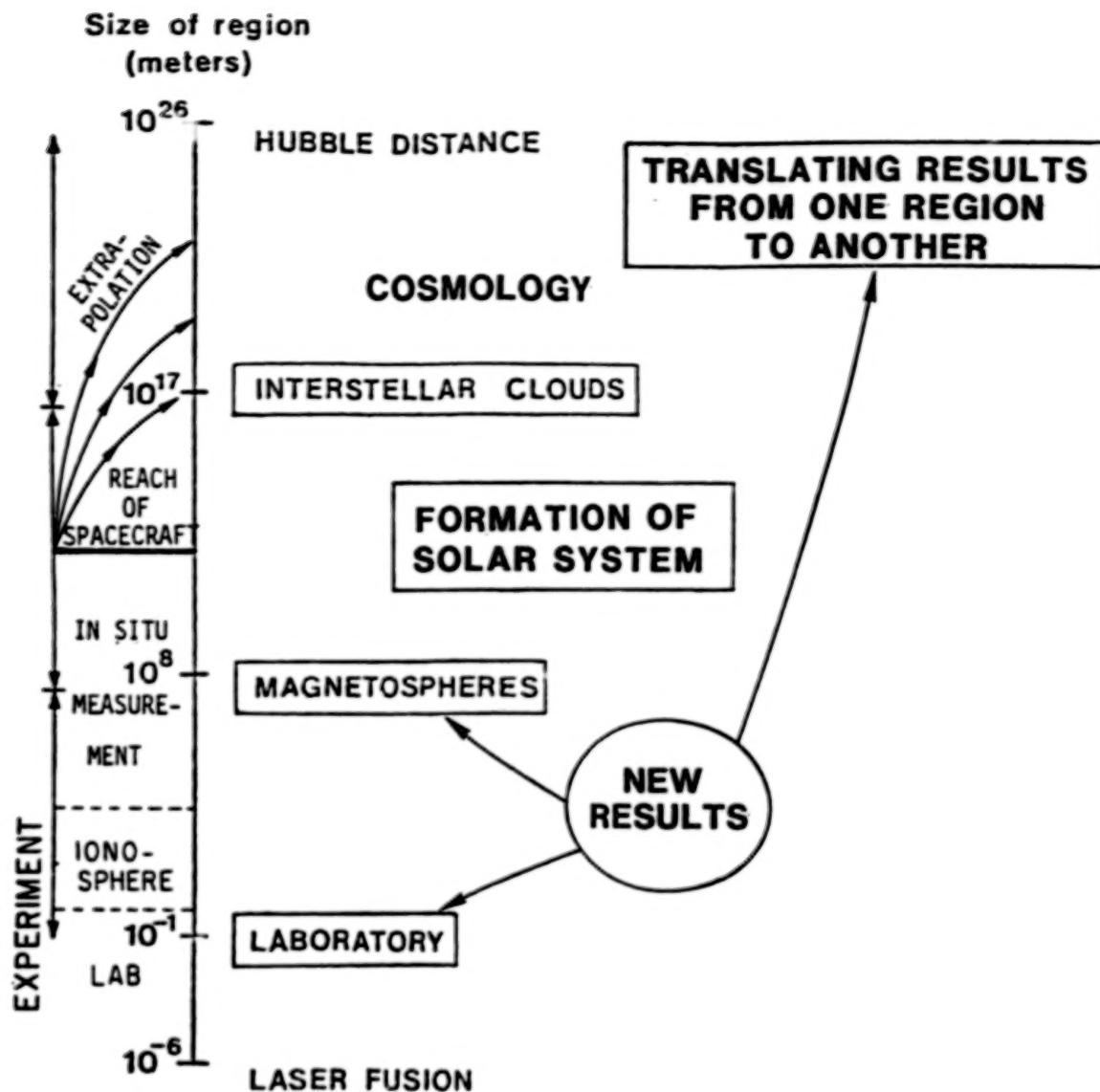


Figure 4. (Upper) In certain cases, e.g., if the circuit has large dimensions, the simple inductance  $L$  should be replaced by a transmission line. (Lower) A rotating magnetized celestial body often acts as a homopolar inductor.

# PLASMA UNIVERSE



**CONSEQUENCE FOR THEORY:**  
**PARADIGM TRANSITION**  
**IS TAKING PLACE IN MAGNETOSPHERE**  
**WILL TAKE PLACE IN ASTROPHYSICS INCL.**  
**COSMOGONY**  
**COSMOLOGY**

Figure 5. Cosmic triple jump.

# PLASMA UNIVERSE

Logarithmic Scale (linear in Lab)

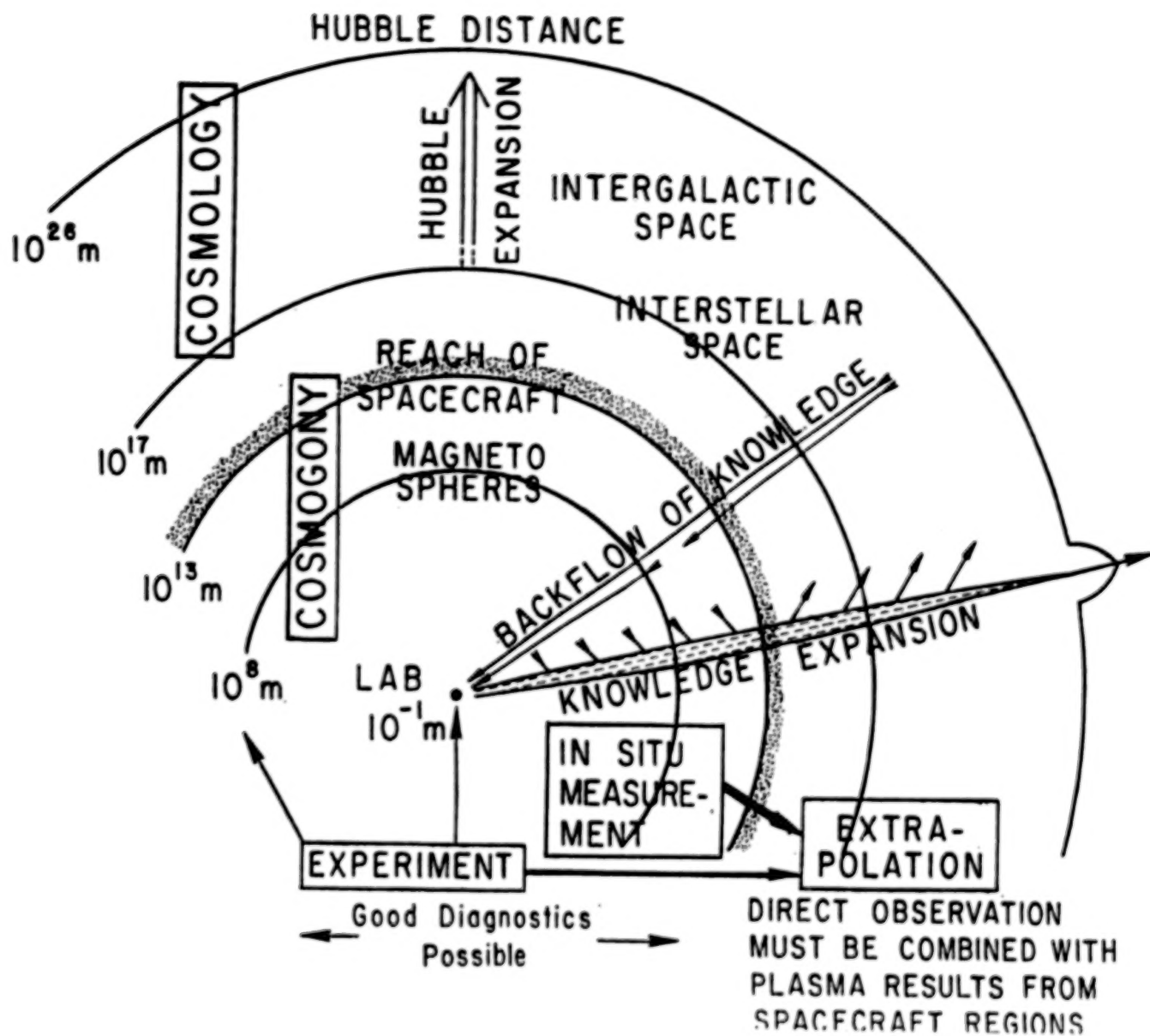


Figure 6. The plasma Universe and knowledge expansion.

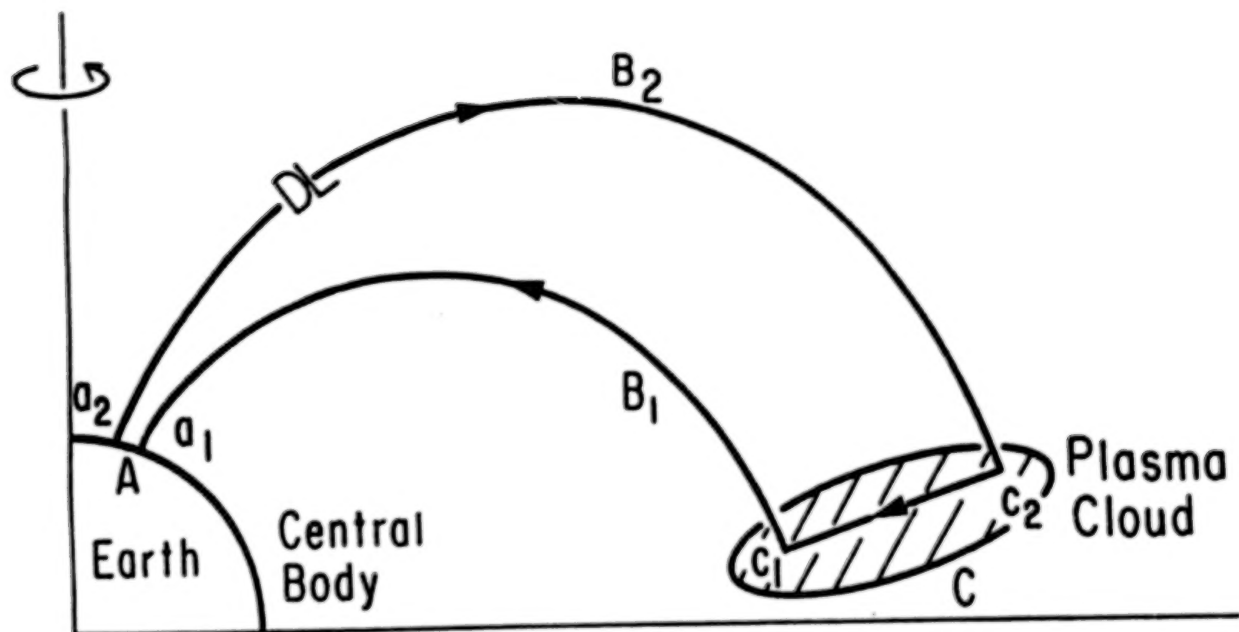


Figure 7. Auroral circuit (seen from the Sun) (cf. CP, Figure II:17).

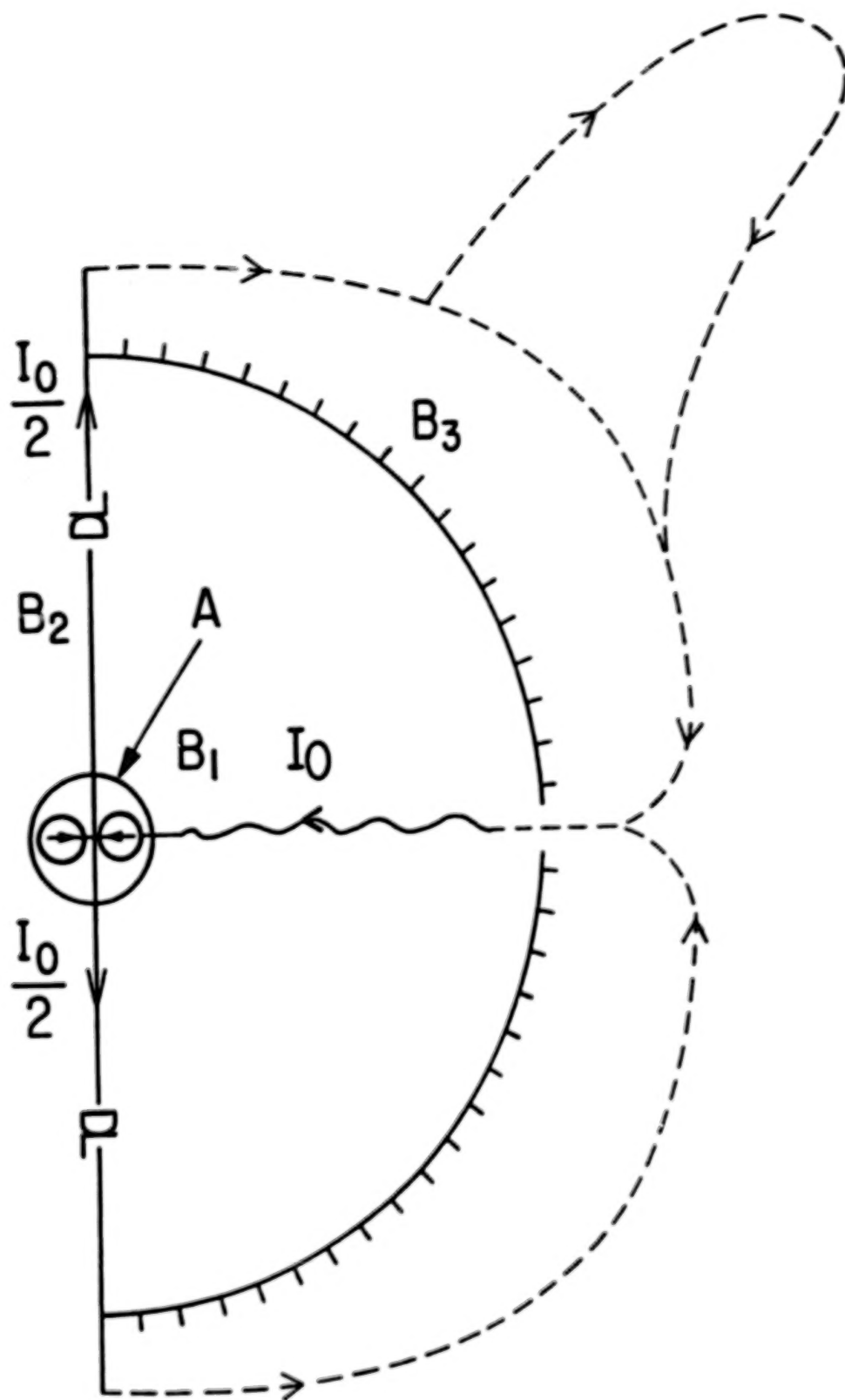


Figure 8. Heliospheric circuit. The Sun acts as a unipolar inductor (A) producing a current which goes outward along both the axes ( $B_2$ ) and inward in the equatorial plane  $C_1$  and along the magnetic field lines  $B_1$ . The current must close at large distances ( $B_3$ ), either as a homogeneous current layer, or — more likely — as a pinched current. Analogous to the auroral circuit, there may be double layers which should be located symmetrically at the Sun's axes. Such double layers have not yet been discovered.

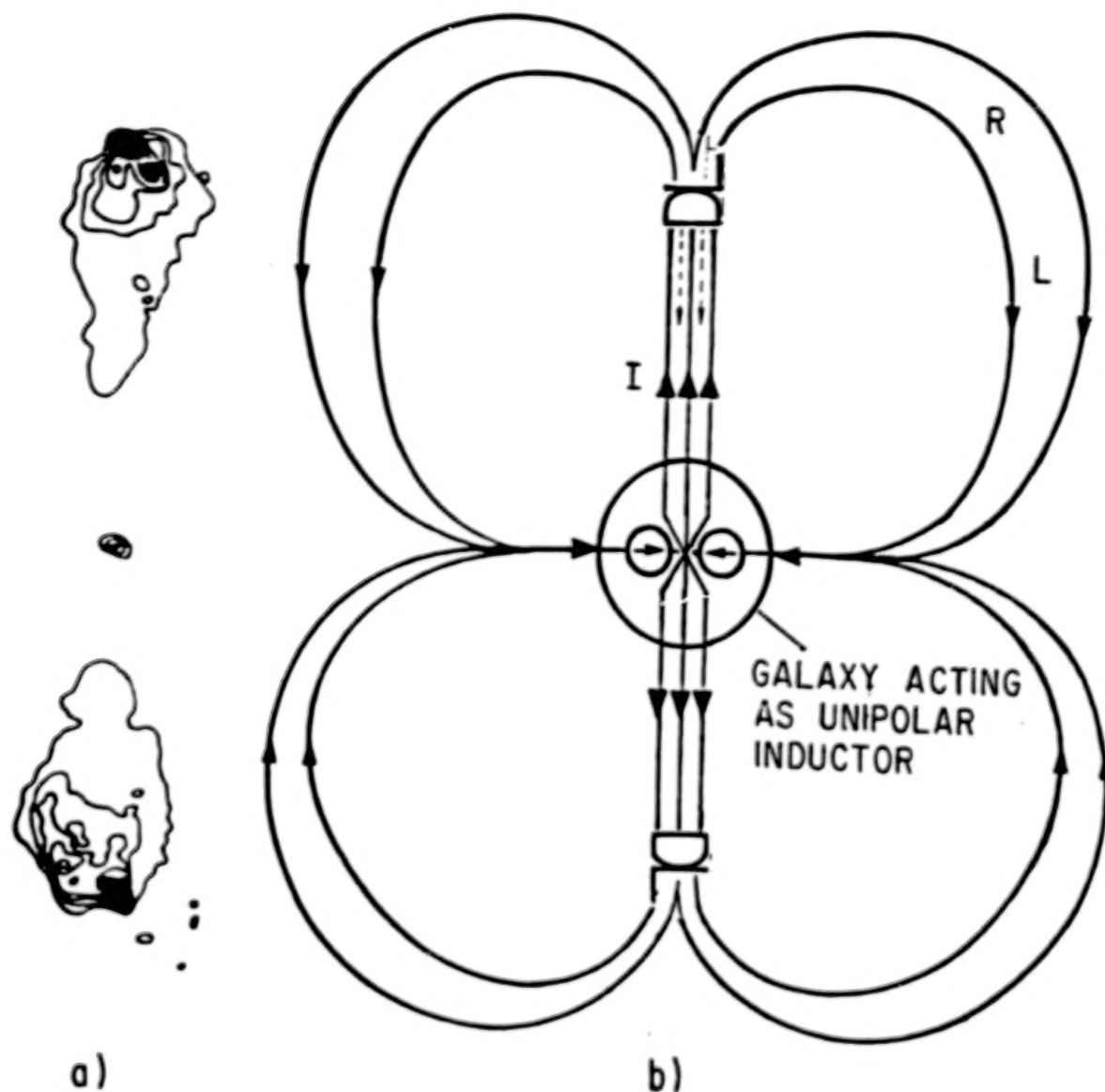


Figure 9. Galactic Circuit. (a) Observed radio emission of Cygnus A (by Hargrave and Ryle, 1974) is attributed to synchrotron emission by electrons accelerated in the double layer. (b) The heliospheric circuit is scaled up by a factor  $10^9$  and the Sun replaced by a galaxy located almost exactly between the radio sources (cf. CP, III.4.4).



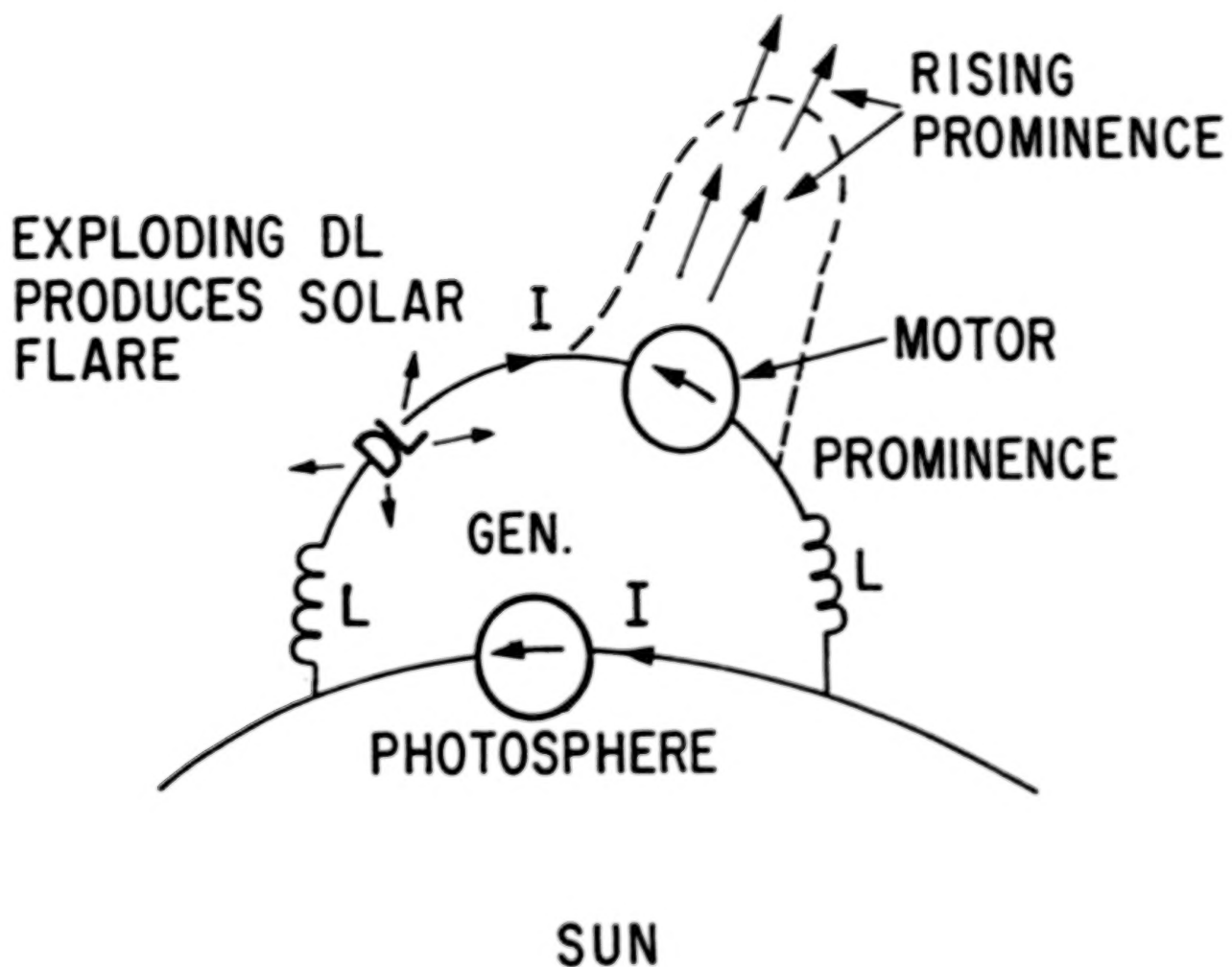


Figure 10. Prominence-solar flare circuit. Whirling motions in the photosphere act as a generator, feeding energy into the circuit (which is similar to Figure 1). The circuit energy can be released either as a solar flare produced by an exploding double layer and/or as a kinetic energy in a rising prominence.

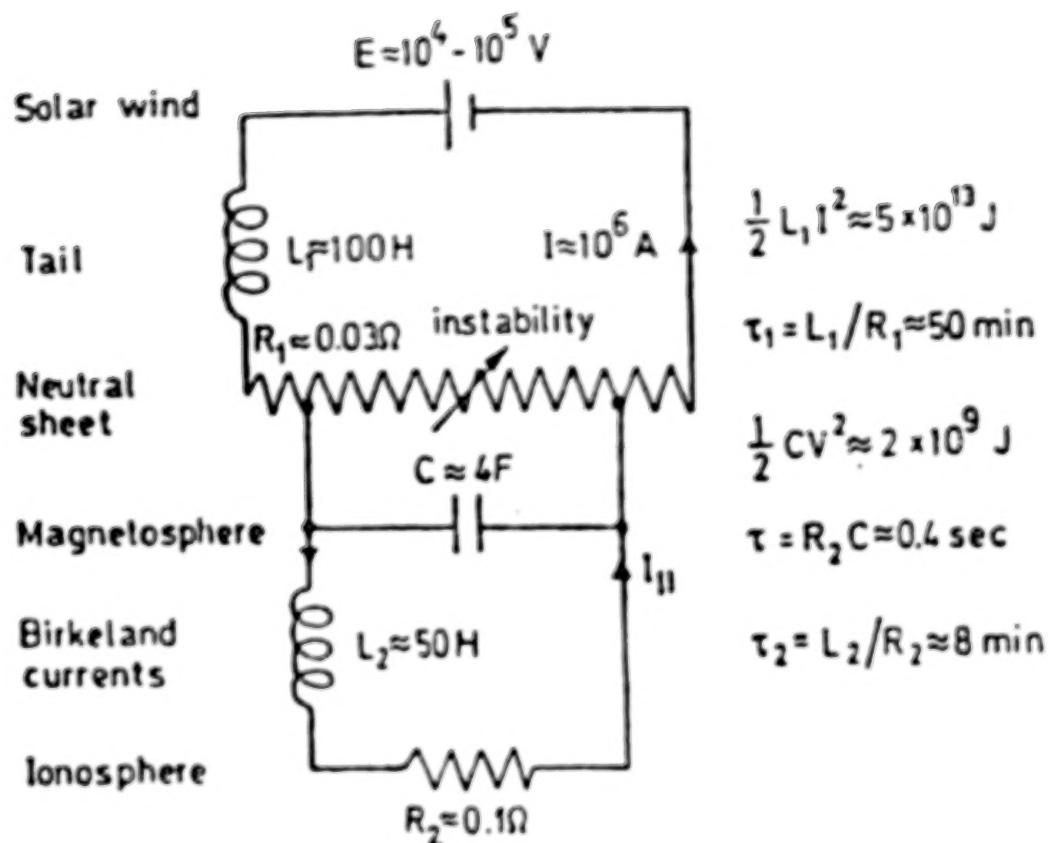


Figure 11. Boström (1974) has given a summary of his theory of magnetic substorms in the form of a circuit. Solar wind energy produces a cross-tail current in the neutral sheet. The arrow indicates that this current can give rise to a very large voltage. (In our terminology, it should be replaced by the DL symbol.) This causes the circuit energy to be discharged over the ionosphere, where it is observed as a magnetic substorm. At substorm onset, the resistance of the neutral sheet increases because a DL is produced and the tail current is redirected to the ionosphere.

TABLE 1. CURRENT TEXTBOOKS DEALING WITH DOUBLE LAYERS  
AND RELATED PHENOMENA\*

	Double Layers	Critical Velocity	Pinch Effect	Circuits
<i>Astrophysical Concepts</i> M. Harwit, 1973 (New York: John Wiley & Sons)				
<i>Theoretical Astrophysics</i> Ambartsumian, 1958 (New York: Pergamon Press)				
<i>Astrophysics: The Atmospheres of the Sun and Stars</i> L. H. Aller, 1963 (New York: The Ronald Press)				
<i>Plasma Astrophysics</i> Kaplan and Tsyrovich, 1973 (New York: Pergamon Press)				
<i>Astrophysics and Space Science</i> A. J. McMahon, 1964 (Englewood Cliffs, NJ: Prentice-Hall)				
<i>Plasma Astrophysics, Vol. 2</i> D. B. Melrose, 1980 (New York: Gordon and Breach, Science Publ.)	X			
<i>Astrophysics and Stellar Astronomy</i> T. L. Swihart, 1968 (New York: John Wiley & Sons)				
<i>General Astrophysics with Elements of Geophysics</i> J. S. Stodolkiewicz, 1973 (New York: Amer. Elsevier Publ.)				
<i>Astrophysics</i> W. K. Rose, 1973 (New York: Holt, Rinehart & Winston, Inc.)				
<i>Cosmic Electrodynamics</i> J. H. Piddington, 1964 (New York: John Wiley & Sons)				
<i>Astrophysics I and II</i> Bowers and Deeming, 1984 (Boston: Jones and Bartlett Publ.)				
<i>Solar Flare Magnetohydrodynamics</i> E. R. Priest, 1982 (Dordrecht, Holland: D. Reidel Publ. Co.)				
<i>Physics of the Solar Corona</i> L. S. Shklovskii, 1965 (New York: Pergamon Press)				
<i>Solar Terrestrial Physics</i> S. I. Akasofu and S. Chapman, 1972 (London: Oxford University Press)	X			X
<i>Introduction to Space Science</i> Haymes, 1971 (New York: John Wiley & Sons)				
<i>Introduction to the Physics of Space</i> Rossi and Albert, 1970 (New York: McGraw-Hill Book Co.)				
<i>Physics of Magnetospheric Substorms</i> S. I. Akasofu, 1977 (Dordrecht, Holland: D. Reidel Publ. Co.)	X			X

\* X means that the field of research is at least mentioned. Blank squares mean that the student is kept ignorant of the fact that such a field exists.

## **I. DOUBLE LAYERS IN THE LABORATORY**

**PRECEDING PAGE BLANK NOT FILMED**

N87

23314

UNCLAS

## FORMATION MECHANISMS OF LABORATORY DOUBLE LAYERS

Chung Chan  
 Center for Electromagnetics Research  
 and  
 Department of Electrical and Computer Engineering  
 Northeastern University  
 Boston, Massachusetts 02115, U.S.A.

## ABSTRACT

The evolution processes of double layers have been studied in a series of laboratory experiments. It was found that the existence of virtual cathode-type potential wells at the electron injection boundary was the dominant triggering mechanism. The rapid growth of the potential well led to collisionless ion trapping and the establishment of the necessary trapped ion population. For double layers with small potential drops, collisionless ion trapping actually induced ion-ion streaming instabilities and the formation of ion phase-space vortices. In this regime, the system often exhibited relaxation-type oscillations which corresponded to the disruption and the recovery of the double layers.

## I. INTRODUCTION

Much of our recent understanding of double layers has come from laboratory experiments and numerical simulations which had rather limited system dimensions. The system boundaries are often in close proximity with the double layer electric field, thus affecting almost all aspects of double layer physics. The situation is obviously different in space plasmas where boundaries are not well defined and often far away from the regions of possible double layer formation. In order to extrapolate the results from laboratory and computer experiments to the space context, it is important to understand the role of the system boundaries on the formation of double layers.

Most double layers experiments (Quon and Wong, 1976; Leung et al., 1980; Singh and Schunk, 1983; Iizuka et al., 1979; Saeki, et al., 1980) have utilized the injection of a drifting electron species to trigger the formation process. It was found that a necessary condition for double layer formation is that the electron drift velocity  $v_d$  exceed the thermal velocity  $v_{te}$  of the ambient electrons. This condition results in the belief that the Buneman instability with an instability threshold of  $v_d \geq v_{te}$  was the triggering mechanism for double layers. However, double layers with potential drops  $\Phi > T_e/e$ , the electron temperature divided by the electron charge, have been observed (Hollenstein et al., 1980) experimentally with  $v_d$  as small as  $0.2 v_{te}$ . Ion-acoustic turbulence instead of the Buneman instability was expected to be the triggering mechanism for double layer formation in that experiment.

Numerical simulation (Sato and Okuda, 1980) of double layers with  $v_d \leq v_{te}$  have found different results. No double layers with  $\Phi > T_e/e$  were found. Rather, a new class of double layers with non-monotonic potential profiles and  $\Phi \leq T_e/e$  was found. These double layers were always preceded by negative potential pulses and associated with current-driven, ion-acoustic turbulence. As such, these double layers have been identified as "ion acoustic" in order to distinguish them from the conventional double layers. Since an electron drift velocity of  $v_d > v_{te}$  may not exist in space (e.g., the auroral plasma), the ion-acoustic double layers have also become a subject of considerable interest.

In this talk, we will discuss previous (Hershkowitz et al., 1981) as well as new experimental results in order to identify the formation mechanism of double layers in our triple plasma device. We begin with the roles of the



boundaries on the steady state characteristics of double layers. It is shown that the drifting electrons provide the initial space charge for double layer formation, while the trapped ions determine the evolution process and the shape of the potential profile. It is also shown that the growth of virtual cathode-type potential wells at the electron injection boundary is the triggering mechanism for double layers. Collisionless ion trapping by the potential well is found to be the main process for the establishment of the necessary trapped ion population.

Furthermore, double layers with  $\phi \leq T_e/e$  are shown to be unstable to the evolution of ion phase-space vortices from ion-ion streaming instabilities. In this regime, the double layer potential profile has a strong resemblance to ion-acoustic double layers. This result may represent an alternative explanation of the small electric field signatures observed in the auroral plasma.

## II. STEADY STATE EXPERIMENT

It is useful to first describe the operational characteristics of the triple plasma device in order to get some insights into the sources of particles that support the double layer. The triple plasma device consists of two source plasmas bounding a target plasma. Each source is separated from the target chamber by two grids. Plasma potential in each chamber is determined by the bias voltages of the grid and the internal anode. The source plasmas are created by filament discharge in argon gas (operating pressure  $P_0 \leq 1 \times 10^{-4}$  Torr) with density  $n_s = 10^9 \rightarrow 10^{10} \text{ cm}^{-3}$  and  $T_e \approx 2 \text{ eV}$ . The ionizing electrons are trapped by surface multidipole magnetic fields in the region closed to the filaments so that they cannot reach the target chamber and produce plasma there directly. We have also confined our study on double layers with  $\phi \leq 10 \text{ V}$ . These procedures ensure that ionization effects are minimized in our double layer experiment. A schematic of the triple plasma device is shown in Figure 1.

Stable double layers with  $\phi \leq 5 T_e/e$  can routinely be achieved using the boundary conditions shown in Figure 2. We chose to investigate these smaller double layers in order to limit the accelerated electron beam energy to below the ionization potential of argon. From the boundary conditions shown in Figure 2, we expect ions to only come from the high potential source. These ions are usually pre-accelerated into the target chamber by the potential difference between the high potential source plasma and the target plasma. These ions are further accelerated by the double layer into the low potential side. These beam ions either exit the target chamber at the left boundary or they charge exchange with neutrals and form cold ions ( $T_i \sim 0.3 \text{ eV}$ ). The cold ions, once formed, are confined electrostatically by the potentials of grids B and C. Although the charge exchange reaction rate is relatively low at our operating neutral pressure, the cold ion density accumulates to a significant fraction of the beam ion density due to their long confinement times.

Electrons which enter the target chamber from the high potential source are those in the tail of the Maxwellian source distribution function. These electrons have almost no drift energy, thus becoming the thermal electron species in the target plasma. This contrasts with the situation at the low potential end. There the tail of the source distribution function, which is energetic enough to get over the barrier provided by grid A, is accelerated into the target plasma. This results in an electron drift with the drift energy determined by the potential difference between grid A and the target plasma.

The boundary conditions in this experiment are believed to play the following roles:

1. The high potential side boundary ensures that the ions will enter the target chamber with a flow velocity  $u_0 > C_s$ . This situation is quite similar to that of a sheath at a plasma boundary. Downward curvature of the plasma potential requires an ion drift velocity  $u_0 > C_s$ . Since the high potential side electrons can be treated as approximately isothermal, the "Bohm sheath criteria" applies in this case for the double layer as well.

2. Grid B acts as a potential barrier for the low potential source ions as well as for the charge exchange cold ions which formed between the double layer and grid B. Since the height of the potential barrier of grid B is roughly 20 times the ion temperature ( $T_i \approx 0.3$  eV), no low potential source ions are expected to enter the target chamber. On the other hand, the high potential source ions are at a much higher energy than grid B and can exit through grid B into the low potential source. As such the only source of thermal ions in the target plasma appears to be that of the charge exchange ions.

3. The low potential side boundary allows only electrons to drift in from the left. Such excess electron space charge may be neutralized only by the ion beam and the charge exchange ions.

4. There is no externally applied electric field across the target plasma since grids B and C are at roughly the same potential. The formation of double layers is a result of the particle flow rather than that of an external electric field.

Using the experimental boundary conditions and the particle distributions at the sources, it is possible to determine the potential profile across the target chamber by solving the Vlasov-Poisson equations. The details of such calculations have been described in an earlier paper (Hershkowitz et al., 1981) and will not be repeated here. Rather we will point out some results which are relevant to our present discussion. A typical solution of the target plasma potential profile and the boundary conditions employed is shown in Figure 3. The model has grid potentials similar to those shown in Figure 2. The double layer is formed in the region  $x_L \leq x \leq x_R$  where  $\phi(x_L) = 0$  and  $\phi(x_R) = \phi_D$ . Using the dimensionless variable  $\psi = e\phi/T_e$ , the density of the free ions  $n_{if}$  and trapped electrons  $n_{et}$  entering from the high potential source are, respectively:

$$n_{if}(\psi) = \frac{N}{2} e^{(T_e/T_i)(\psi_2 - \psi)} \operatorname{erfc} \sqrt{\frac{T_e}{T_i}} (\psi_2 - \psi) \quad (1)$$

and

$$n_{et}(\psi) = N e^{(\psi - \psi_2)} (1 - \operatorname{erfc} \sqrt{\psi - \psi_A}) \quad (2)$$

The density of the free electrons entering from the low potential source is:

$$n_{ef}(\psi) = \frac{N}{2} e^{\psi - \psi_1} \operatorname{erfc} \sqrt{\psi - \psi_A} \quad (3)$$

where  $\psi_1$ ,  $\psi_2$  and  $\psi_A$  are, respectively, the low potential source, high potential source, and grid A potentials normalized to the electron temperature. Both source particles are assumed to be Maxwellian distributed with equal density  $N$ .

The density of the charge exchange ions cannot be calculated from the boundary conditions, thus it can be treated as a variable or:

$$n_{it}(\psi) = \beta n_e(0) e^{-(T_e/T_i)\psi} \quad (4)$$

and

$$\beta = 1 - \frac{n_{if}(0)}{n_e(0)} \quad (5)$$

$\beta$  is a parameter which depends on the density ratio of the trapped ions to the beam ions and  $n_e(0)$  is the total electron density at  $\psi = 0$ .

We show the dependence of the double layer on the trapped ion density with  $\beta$  varying from 0 to 0.35 in Figure 4. As the trapped ion density increases, the double layer becomes more detached from the low potential side boundary. Since  $\beta = 0.35$  corresponds closely to the potential profile in the experiment, it is possible that a significant amount of charge exchange ions are trapped by the double layer at the low potential side; i.e.,  $\beta = 0.35$  corresponds to a trapped ion/beam ion density ratio of 54 percent. The trapped ions neutralize the excess negative space charge created by the drifting electrons, thus maintaining a uniform plasma potential at the low potential region of the double layer.

The contributions of the various particle species on the double layer space charge are shown clearly in Figures 5a and 5b where the charge density profile and particle density profiles are plotted versus axial distance. As discussed earlier, the ion beam provides the positive charge density for the downward curvature of the double layer at the high potential side, while the drifting electrons supply the negative charge density for the upward curvature of the double layer at the low potential side.

### III. THE FORMATION MECHANISM

In order to understand the triggering mechanism for the double layers in our experiment, we examine the temporal evolution of the target plasma potential profile with  $v_D \leq v_{te}$  and  $v_D > v_{te}$ . An extra grid is installed at the low potential side to facilitate the pulsing of the drifting electrons. The boundary conditions for this experiment are shown in Figure 6. A steady state target plasma with  $n_e \cong 10^7 \text{ cm}^{-3}$  is extracted from the high side source, and the target plasma potential is quite uniform axially with  $\phi_T = 4 \text{ V}$ . Low side source electrons and ions are normally excluded from the target plasma by the potential barriers of grid B (biased at -30 V) and grid C (biased at +12 V), respectively.

At time  $t = 0$ , grid B is switched to the ground potential and the low side source electrons are accelerated into the target plasma by the potential difference between  $\phi_T$  and ground, i.e.,

$$v_D \cong \sqrt{\frac{e\phi_T}{T_e}} v_{te} \quad (6)$$

When the un-neutralized electron stream enters the target plasma, the entire target potential decreases rapidly from 4 to 3 V in 10  $\mu$ s which results in  $v_D = 1.2 v_{te}$ . The temporal evolution of the target plasma potential profiles, as obtained with an emissive probe using Boxcar interferometer averaging technique, is shown in Figure 7. A potential well begins to form near the electron injection boundary at  $t = 50 \mu$ s. The potential well grows deeper and widens into a double layer at  $t > 400 \mu$ s. The amplitude of the double layer is  $\phi = 1.1 T_e/e$  and appears to be quite stable. This result can be interpreted as follows.

Electron injection from the low side source creates excess space charge at the injection boundary, and a virtual cathode-type potential well is formed to limit the injected current. The growth of the potential well is accompanied by ion trapping in the potential well. As the density of the trapped ions increases, the double layer becomes detached from the electron injection boundary, in agreement with our earlier result on the effects of trapped ions (see Figure 3). Notice the double layer formation time of  $T_{DL} \leq 400 \mu$ s is considerably shorter than the charge exchange time of  $T_{ex} \cong 1$  ms in this experiment. At such, the trapped ion population cannot come entirely from the charge exchange ions which fall into the potential well. A more possible source is the neighborhood ions which fall into the well during its growing phase. These ions will actually get accelerated down the potential well with energies depending on their locations in the potential well.

We further decrease the drift velocity of the injected electrons by decreasing the target plasma potential to  $\phi_T \cong 3$  V. When the un-neutralized electron stream enters the target plasma,  $\phi_T$  decreases from 3 to 1.5 V in 10  $\mu$ s. As shown in Figure 8, a potential well is once again formed near the electron injection boundary at  $t = 50 \mu$ s when  $v_D \cong 0.7 v_{te}$ . At  $t > 75 \mu$ s, a small double layer with  $\phi \cong 0.5 T_e/e$  has formed. However, in contrast with the earlier experiment, the double layer decays into an ion hole-like potential well. Note the similarity between the potential profile at  $t = 150 \mu$ s and an ion-acoustic double layer.

The time history of the plasma potential ( $\phi_L$ ) at an axial distance of  $x = 10$  cm, the electron current flow across the target chamber from the low potential source ( $I_{eH}$ ), and the ion saturation current ( $I_{iL}$ ) at  $x = 15$  cm are shown in Figure 9 in order to illustrate the double layer formation processes. At  $t > 50 \mu$ s,  $\phi_L = 1$  V, and  $v_D \cong 0.7 v_{te}$ , the growth of the potential well corresponds to the abrupt decrease of  $\phi_L$ . On the other hand,  $I_{eH}$  continues to increase due to the injected electron current until  $\phi_L$  becomes negative where  $I_{eH}$  begins to decrease rapidly. As  $\phi_L$  reaches a minimum at -1.0 V,  $I_{eH}$  returns almost to the level at  $t < 0$ .  $\phi_L$  subsequently becomes slightly more positive, and an intense low frequency noise appears in  $I_{iL}$  which corresponds to the evolution of the ion hole-like pulse.

A similar evolution process is observed when we increase  $v_D$  just slightly. As shown in Figure 10, the double layer breaks into one or more ion hole-like pulses. The long time history of this experiment is shown in Figure 11. The ion saturation current exhibits relaxation-type oscillations in time with a period roughly characterized by the transit time of the ion hole-like pulses across the target plasma. The relaxation oscillation corresponds to the evolution of the double layer from virtual cathode potential well and the subsequent decay into ion hole-like pulses. When the pulses reach the high side boundary (e.g., the ion-hole velocity is the order of the ion thermal velocity), the process repeats itself.



The breaking of the double layer into the ion hole-like pulses can be understood as follows. The magnitude of the virtual cathode potential well  $\phi_w$  is formed to limit the injected current. Since the potential well must become a potential barrier to the injected electrons in order to limit the current,  $\phi_w \cong (v_D/v_{te})^2 T_e/e$ . The potential drop of the double layer  $\phi \cong \phi_w$ ; also, we have  $\phi = (v_D/v_{te})^2 T_e/e$ .

As shown in Figure 9c, the injected current  $I_{ch}$  and  $v_D$  are reduced to very small values as a result of the formation of the double layer. We believe the growth of the potential well and the double layer formation also triggered bursts of counterstreaming ions which are accelerated down each side of the potential well with an average velocity:

$$v_b < \sqrt{\frac{2e\phi}{T_e}} C_s \quad (7)$$

This results in a counterstreaming or "tuning fork" ion phase space configuration at the double layer front. As reported in many numerical and experimental studies (Pécseili and Trulsen, 1984; Chan et al., 1984) of ion-acoustic shocks and ion holes, the ion-ion two-stream region becomes unstable when  $v_b \leq C_s$  and evolves into one or more ion phase-space vortices.

As we have observed double layer formation with  $v_D \leq v_{te}$ , it is doubtful that the Buneman instability plays any roles in triggering the formation of double layers in these experiments. When  $v_D < v_{te}$ , no steady double layer exists as a result of the ion two-stream instability and the evolution of ion phase-space vortices.

#### IV. DISCUSSION

We have reviewed results from a series of laboratory experiments concerning the formation of double layers in a triple plasma device. In steady state, the double layer electric field is sustained by the negative space charge of the drifting electrons and the positive space charge of the ion beam. The low potential boundary condition permits the injection of an un-neutralized electron species which space charge is crucial for the initiation of the virtual cathode potential well. The ion reflecting grid (grid B in Fig. 2) plays two roles; first, to prevent the low potential source ions from entering the double layer and second, to confine the charge exchange cold ions in the low potential side of the double layer. The charge exchange (trapped) ions are needed to neutralize part of the drifting electrons, thus allowing the double layer to move away from the low potential boundary.

The formation phase of the double layers is associated with the growth of virtual cathode-type potential wells at the electron injection boundary. The formation of the virtual cathode potential well is a result of the lack of neutralizing ions at the electron injection boundary. As long as the injected electron density is sufficiently high, the potential well will form independent of  $v_D$  and it need not be associated with instabilities. We have clearly shown the formation of double layers with  $v_D < v_{te}$  which is below the threshold of the Buneman instability.

The movement of the double layer electric field away from the electron injection boundary is probably caused by the accumulation of the trapped ion density at the low potential side of the double layer as demonstrated by Figure 3. Since the double layer formation time is much shorter than the charge exchange time, the source of trapped ions is more likely coming from ions in the neighborhood of the potential well during the growth of the well. As such, these ions are accelerated down the potential well with a maximum velocity of:

$$v_b \leq \sqrt{\frac{2 e \phi_w}{T_e}} C_s \quad (8)$$

When the magnitude of the potential well  $\phi_w < T_e/e$ , the ions become two stream unstable because  $v_b < C_s$ . As such, the double layer decays into ion phase space vortices with potential structures that resemble ion acoustic double layers. This situation is similar to the auroral plasma condition where small electric signatures (Temerin et al., 1982) are often observed along with counterstreaming ions.

For the case of  $v_D > v_{te}$ , the depth of the potential well  $\phi_w > T_e/e$  and results in a stable double layer formation. For the stable double layers, the charge exchange ions will be the main fueling source for the trapped ion population in steady state. In that case, the main loss mechanism for the trapped ions is radial diffusion to the side walls.

*Acknowledgments.* The authors wish to thank N. Hershkowitz, G. Payne, H. Pécseli, J. Juul Rasmussen, H. Schamel, M. Silevitch, and S. Torvén for valuable discussions. This work was supported in part by NSF grant 83-14488.

## REFERENCES

- Chan, C., M. H. Cho, N. Hershkowitz, and T. Intrator, *Phys. Rev. Lett.*, **52**, 1782 (1984).  
Hershkowitz, N., G. Payne, and C. Chan, *Plasma Phys.* **23**, 910 (1981).  
Hollenstein, Ch., M. Guyot, and E. S. Weibel, *Phys. Rev. Lett.*, **45**, 2110 (1980).  
Iizuka, S., K. Saeki, N. Sato, and Y. Hatta, *Phys. Rev. Lett.*, **43**, 1404 (1979).  
Leung, P., A. Y. Wong, and B. H. Quon, *Phys. Fluids*, **23**, 992 (1980).  
Pécseli, H. L., and J. Trulsen, *Phys. Rev. Lett.*, **48**, 1355 (1982).  
Pécseli, H. L., R. J. Armstrong, and J. Trulsen, *Phys. Rev. Lett.*, **81A**, 386 (1980).  
Quon, B. H., and A. Y. Wong, *Phys. Rev. Lett.*, **37**, 1393 (1976).  
Saeki, K., S. Iizuka, and N. Sato, *Phys. Rev. Lett.*, **45**, 1853 (1980).  
Sato, T., and H. Okuda, *Phys. Rev. Lett.*, **44**, 740 (1980).  
Singh, N., and R. W. Schunk, *Phys. Fluids*, **26**, 2781 (1983).  
Temerin, M., K. Cerny, W. Lotko, and F. S. Mozer, *Phys. Rev. Lett.*, **48**, 1175 (1982).



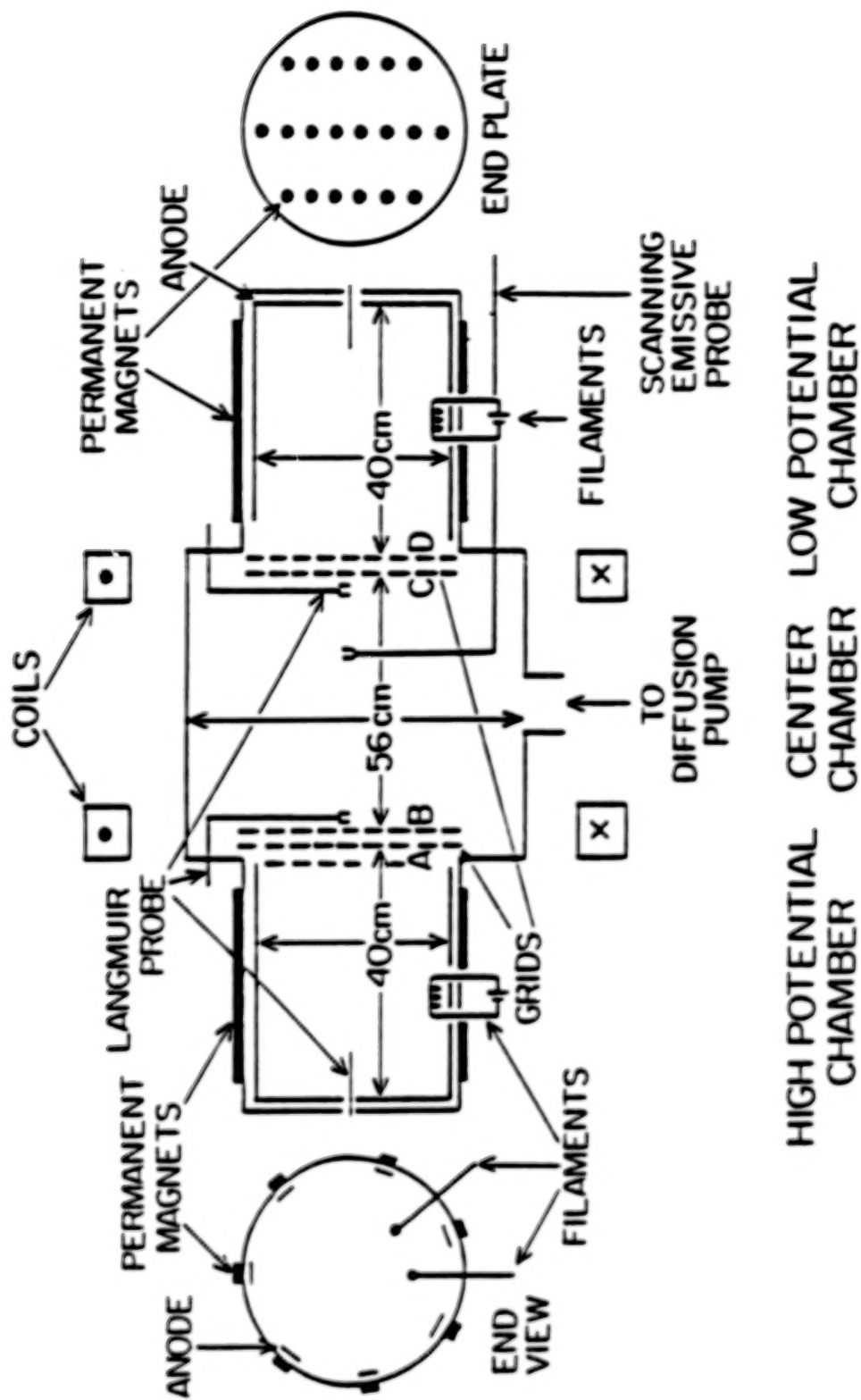


Figure 1. A schematic of the triple plasma device.

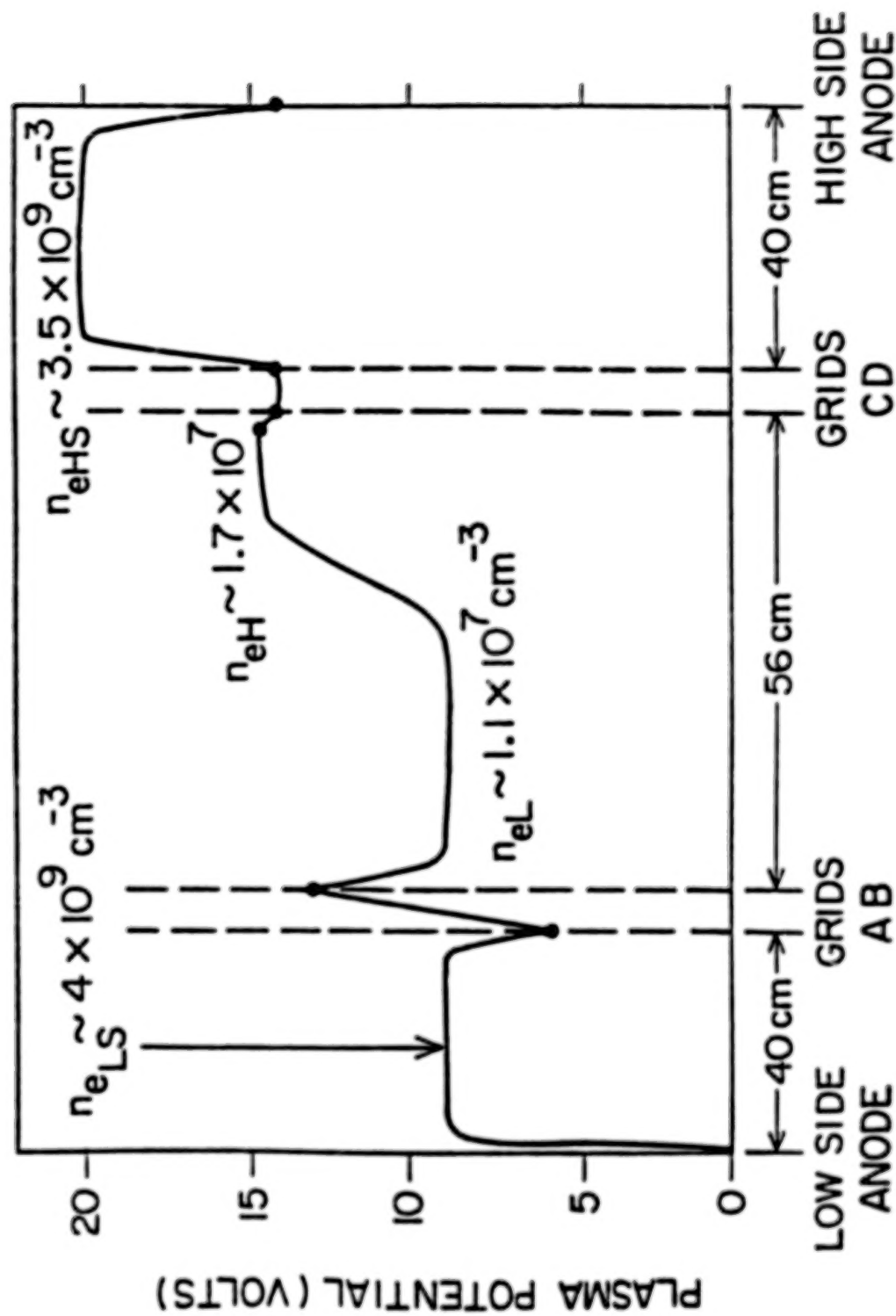


Figure 2. Axial potential profile of the laboratory double layer including the boundary condition.

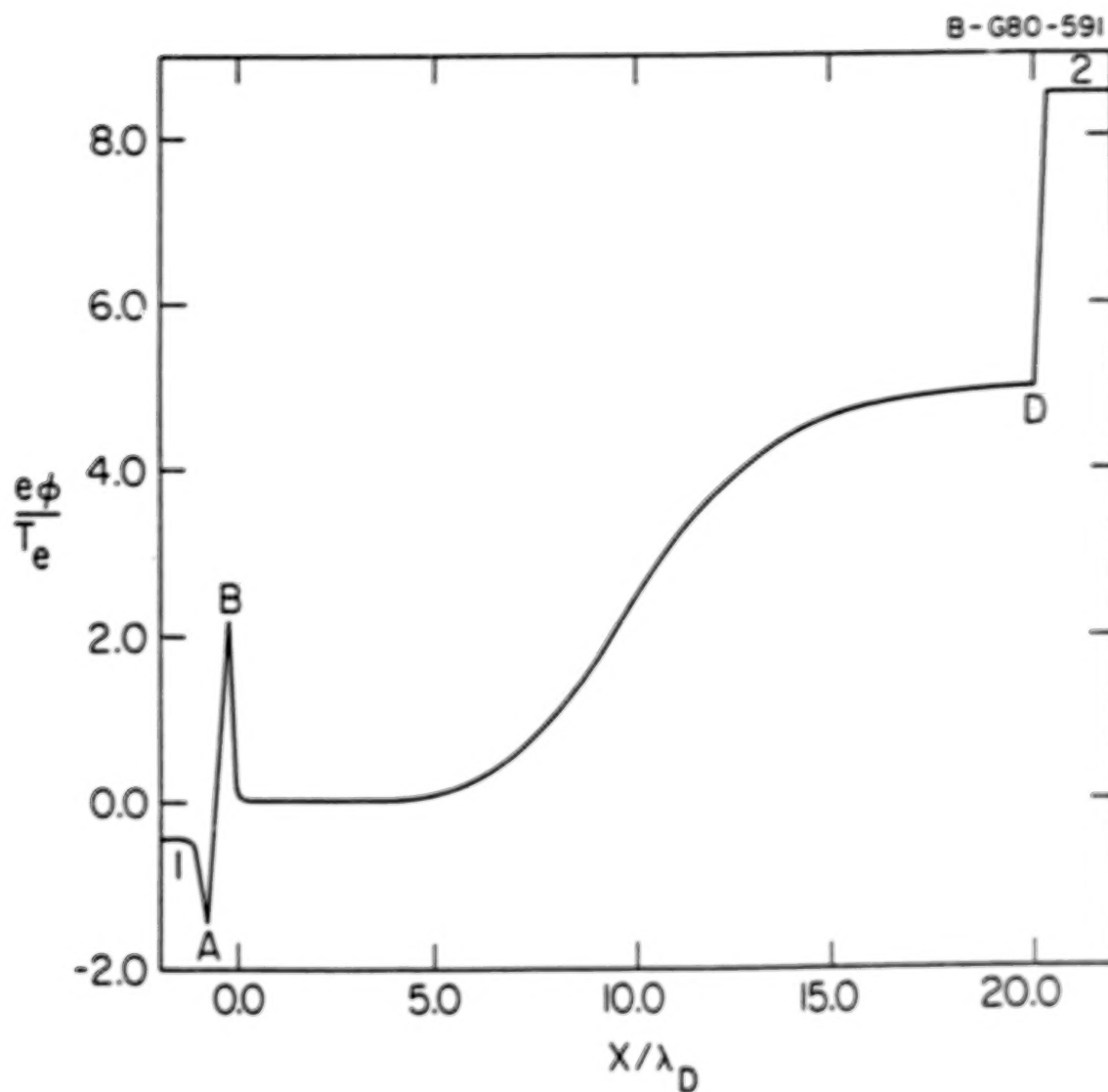


Figure 3. A solution of Poisson's equation  $d^2\psi/dx^2 = n_{ei}(\psi) + n_{et}(\psi) - n_{it}(\psi) - n_{ti}(\psi)$  where  $\psi = e\phi/T_e$ ;  $x = x/\lambda_D$ ;  $n_{it}$ ,  $n_{et}$ ,  $n_{ei}$ , and  $n_{ti}$  are given by equations (1) through (4), respectively.

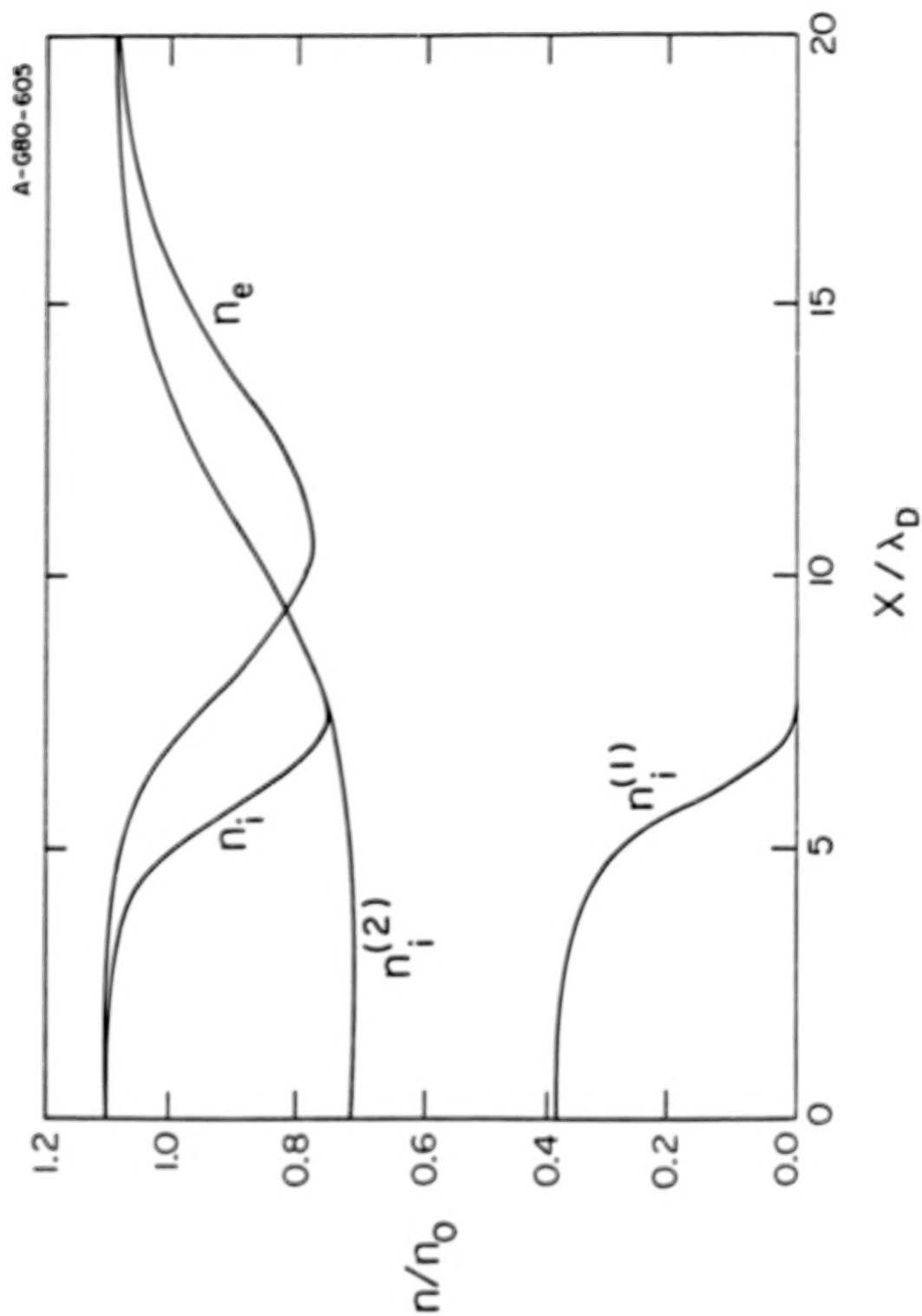


Figure 4a. The total ion and electron density profiles for the model double layer.

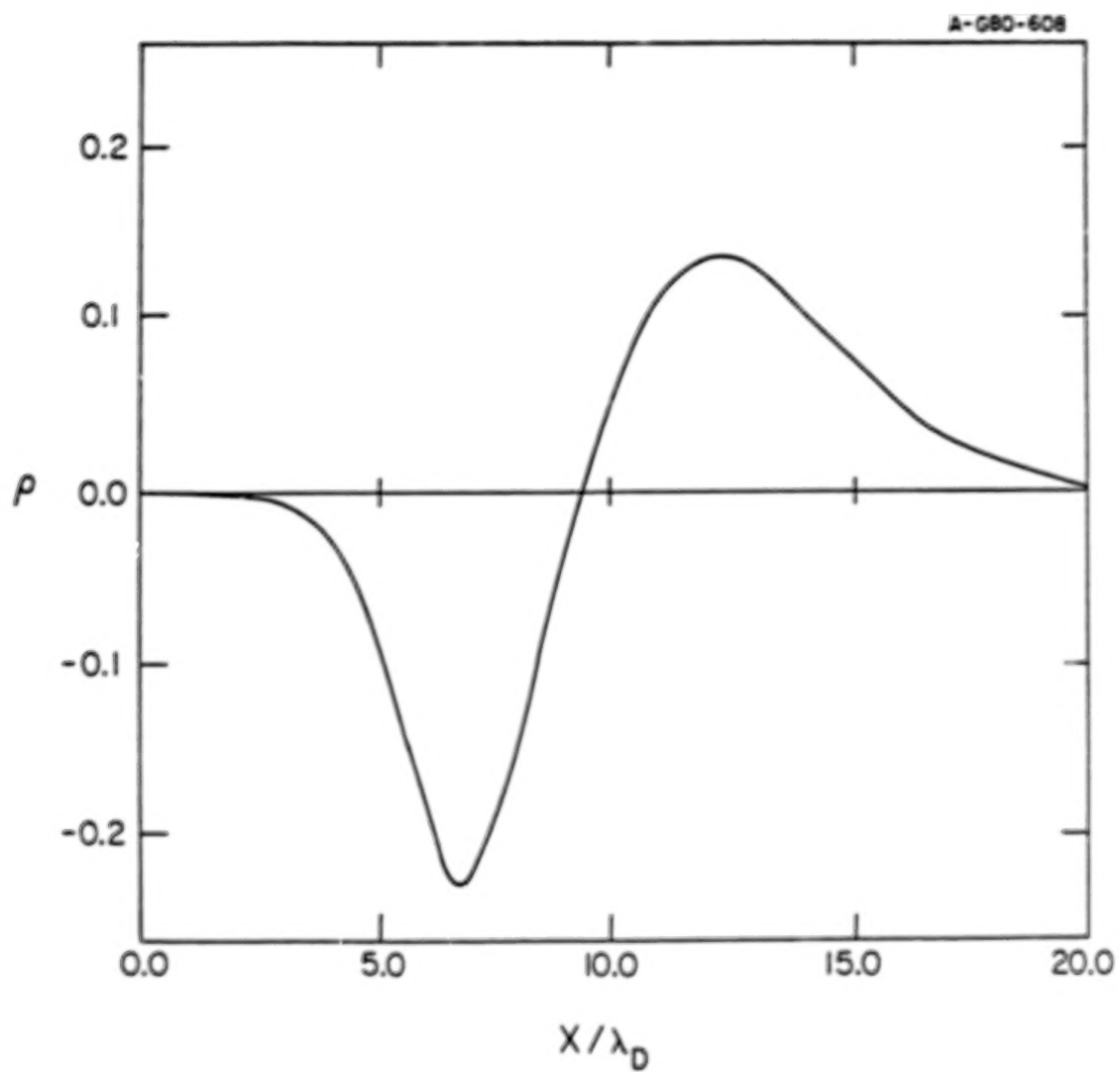


Figure 4b. Total charge density profile for the model double layer.

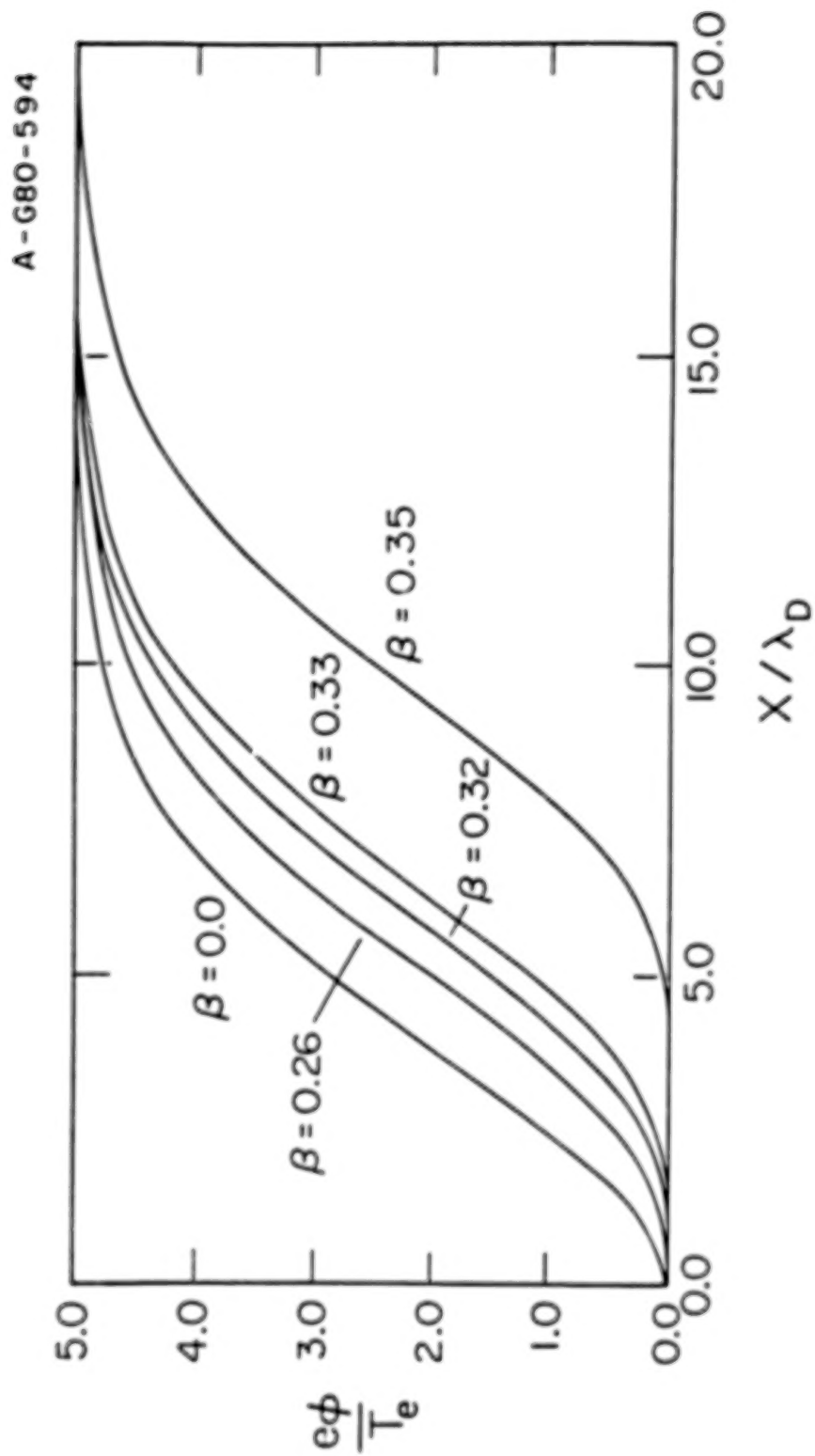


Figure 5. Illustration of the dependence of double layer position on the density of trapped ions. The curve labeled  $\beta = 0.0$  has no trapped ions.



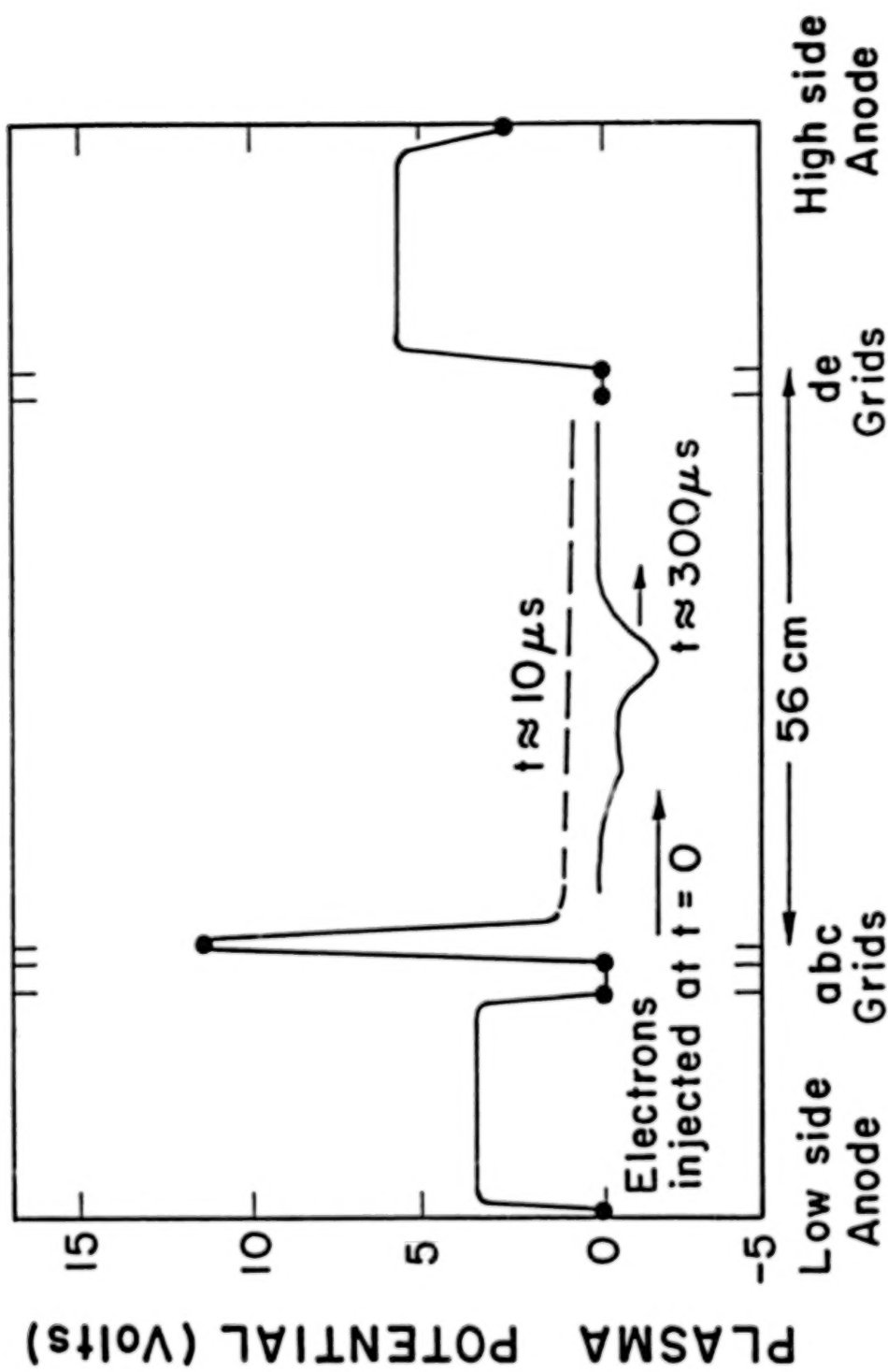


Figure 6. Axial potential profile along the axis of the device. Grid B was switched from -30 V to ground at  $t = 0$ .

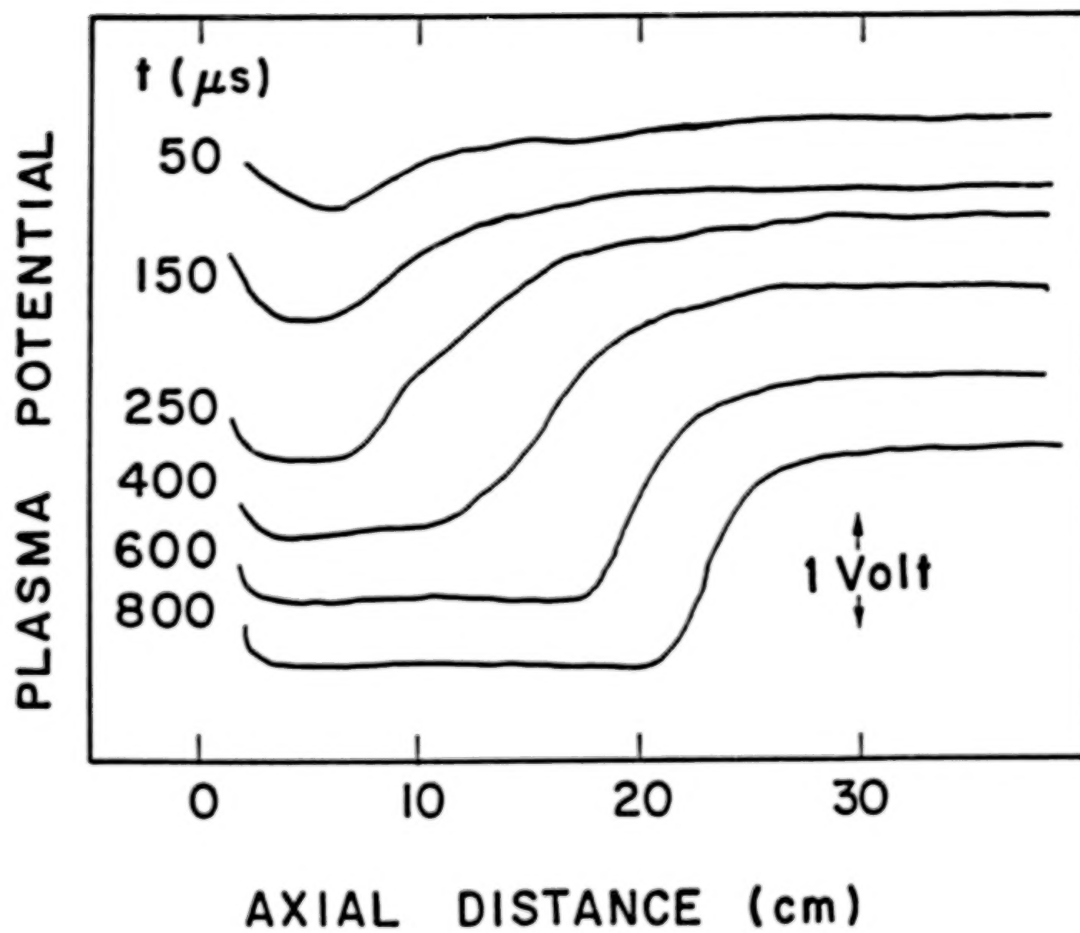


Figure 7. Temporal evolution of the target plasma potential profile when  $v_D > v_{te}$ . Each profile is displaced for clarity.

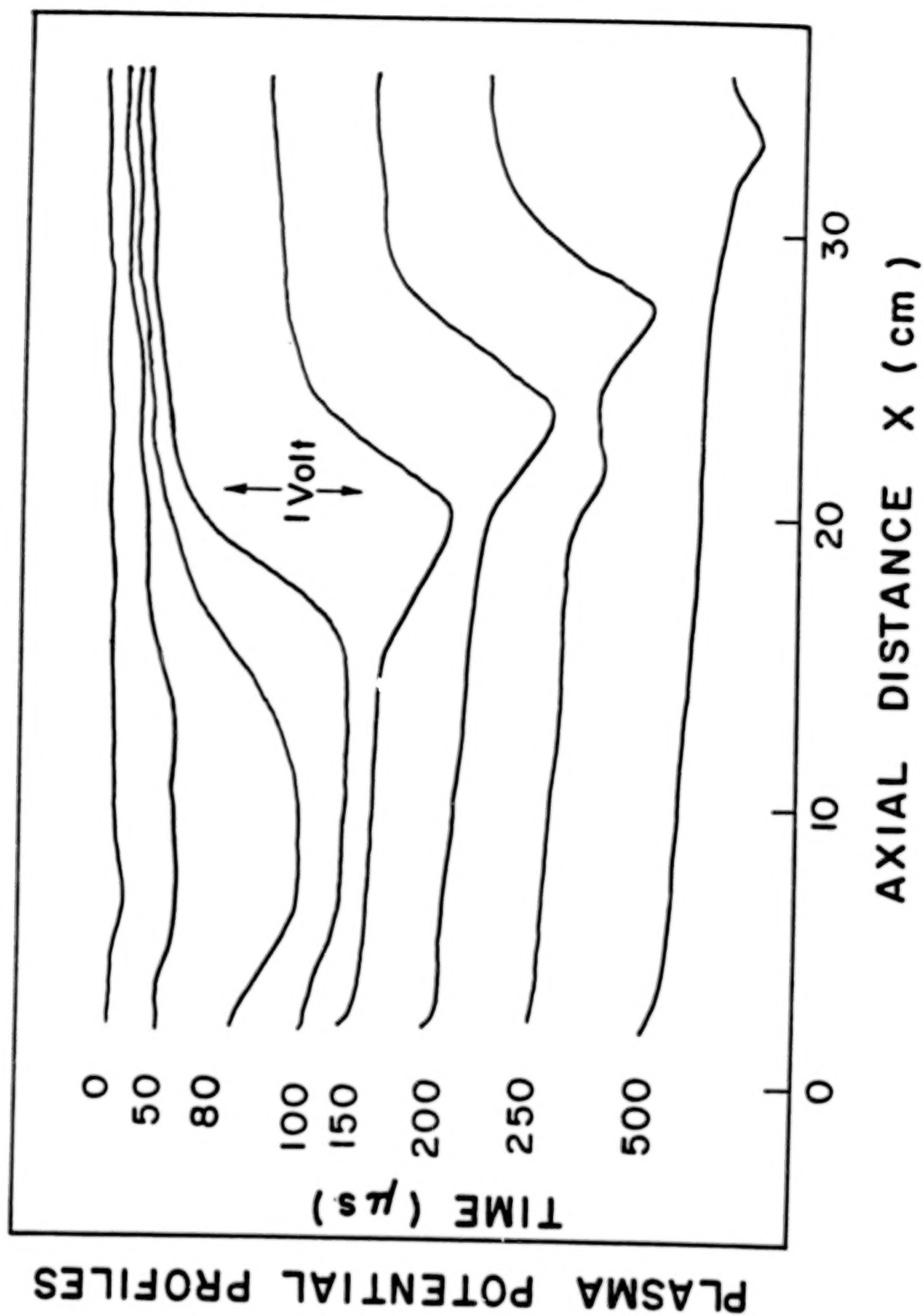


Figure 8. Temporal evolution of the target plasma potential profile when  $v_D > v_{te}$ .

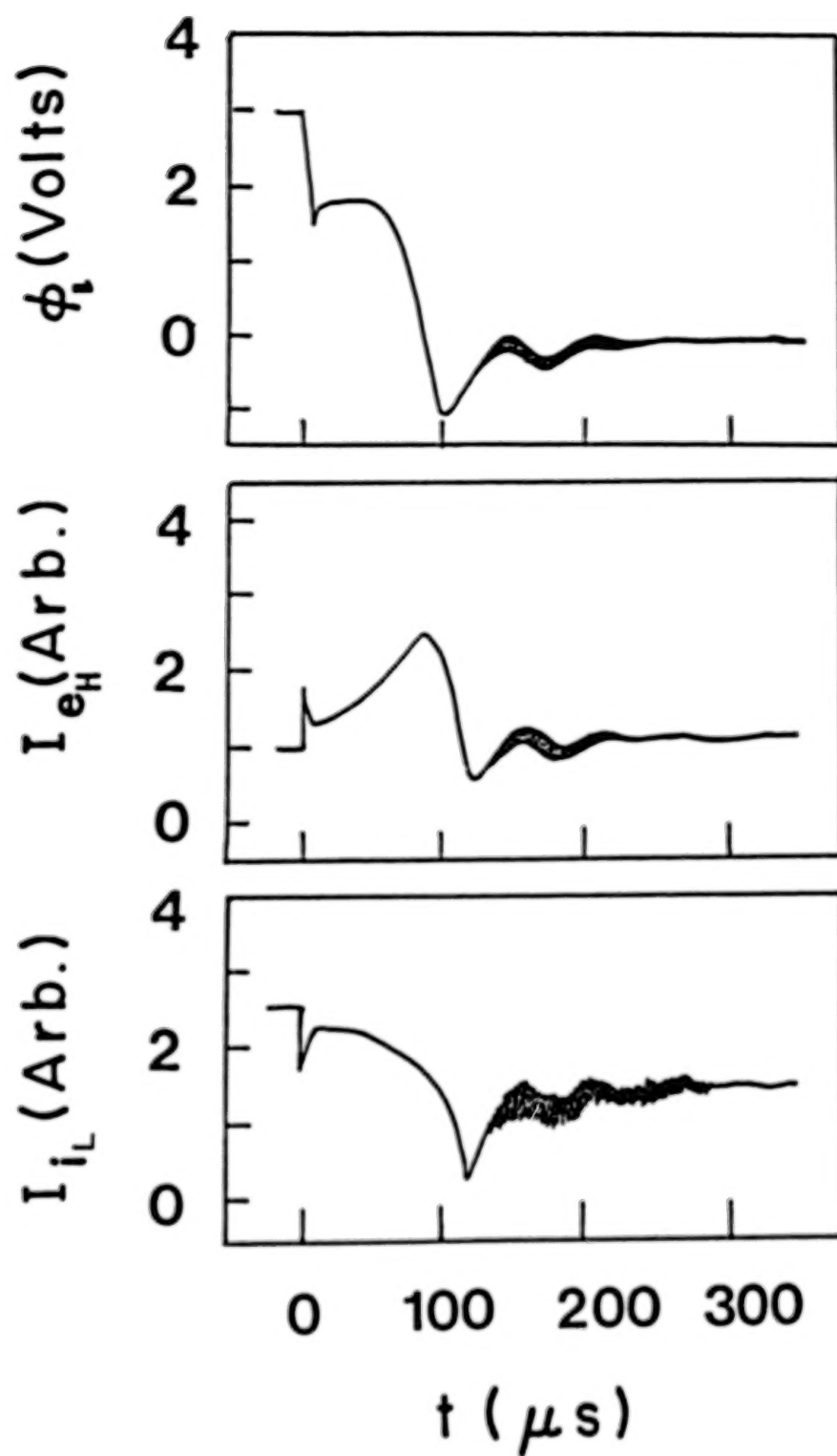


Figure 9. Time history of (a) the target plasma potential ( $\phi_t$ ) as measured by an emissive probe at 10 cm away from grid C; (b) the electron current ( $I_{eH}$ ) collected by a single-sided Langmuir probe facing the low potential source; and (c) the ion saturation current ( $I_{iL}$ ) collected by a wire probe at 15 cm away from grid C.

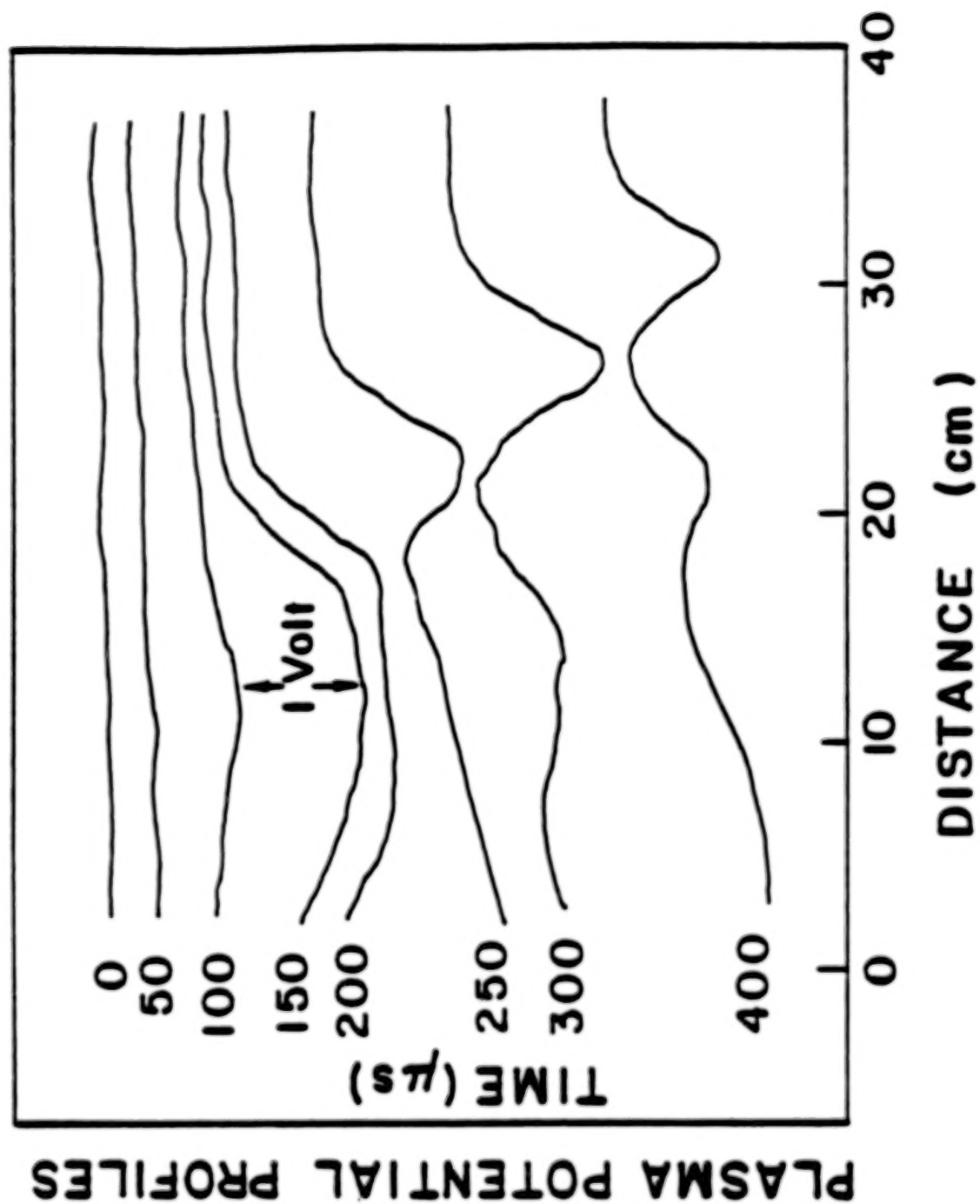


Figure 10. Temporal evolution of the target plasma potential with  $v_D < v_{te}$  and the double layer decays into more than one ion hole-like pulses.

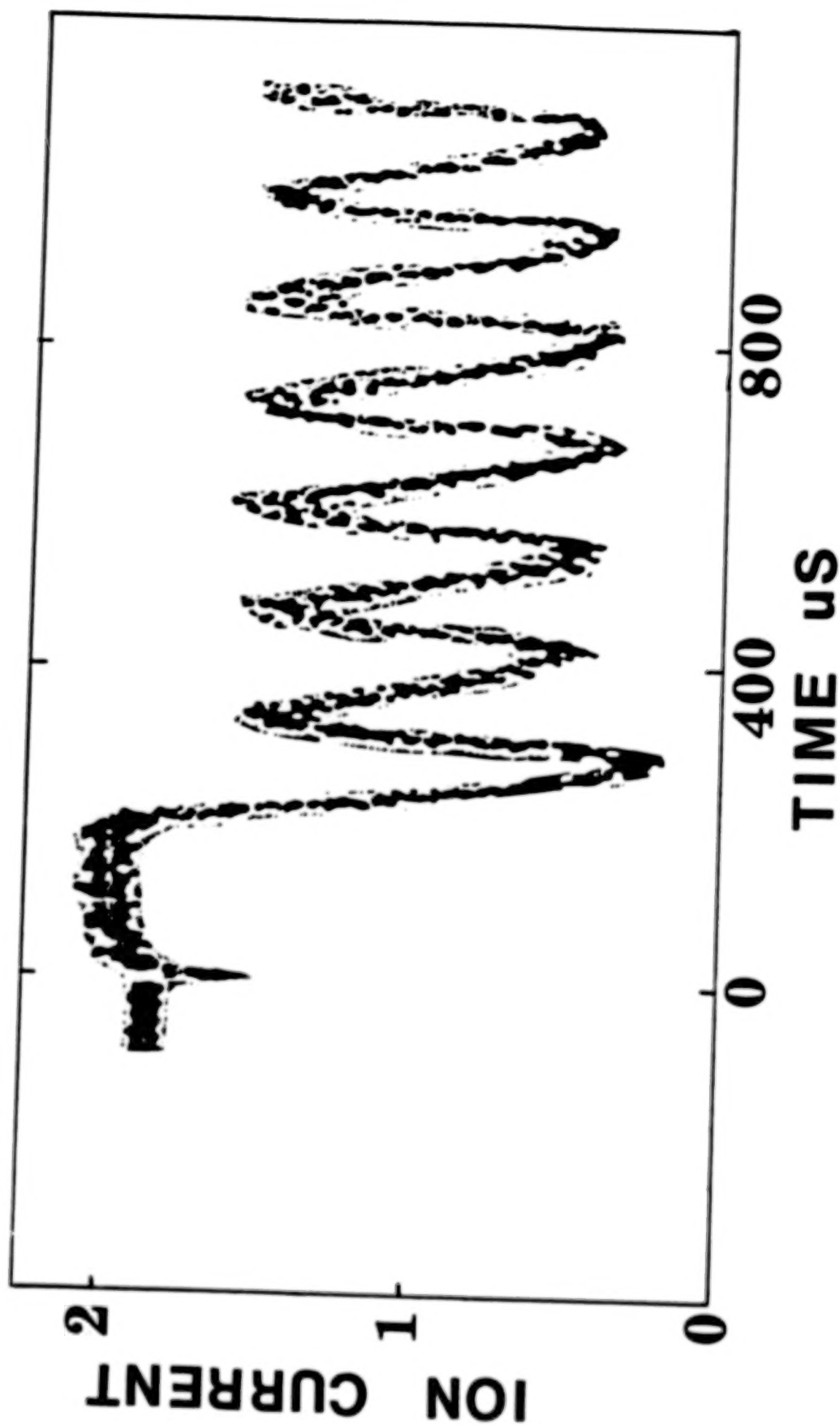


Figure 11. Long time history of the ion saturation current when the system exhibits relaxation oscillation.



N87

23315

UNCLAS

# SOME DYNAMICAL PROPERTIES OF VERY STRONG DOUBLE LAYERS IN A TRIPLE PLASMA DEVICE

T. Carpenter  
Department of Physics  
University of Iowa  
Iowa City, Iowa 52242, U.S.A.

N87-23315

and

S. Torvén  
Department of Plasma Physics, Royal Inst. of Technology, Stockholm, Sweden

## I. INTRODUCTION

Since double layers observed in space and in simulations are rarely if ever static, considerable attention has been given to studies of motions of double layers in the laboratory. Extensive reviews have recently been published of the dynamical properties of very strong double layers ( $eV/kT_e \sim 1000$ ) in a Q machine (Sato et al., 1983; Iizuka et al., 1983) and strong double layers ( $eV/kT_e \sim 10$ ) in a triple plasma device (Hershkowitz, 1985). In both cases the double layers were essentially planar. We report here on some of the dynamical properties of very strong double layers ( $eV/kT_e \sim 200$ ) seen in a differentially pumped triple plasma device (Torvén, 1982). These double layers are V-shaped. In particular, we discuss the following findings: (1) Disruptions in the double layer potential and in the plasma current occur when an inductance is placed in series with the bias supply between the sources in the external circuit. These disruptions, which can be highly periodic, are the result of a negative resistance region that occurs in the I-V characteristic of the device. This negative resistance is due to a potential minimum which occurs in the low potential region of the double layer, and this minimum can be explained as the self-consistent potential required to maintain charge neutrality in this region. (2) When reactances in the circuit are minimized, the double layer exhibits a jitter motion in position approximately equal to the double layer thickness. The speed of the motion is approximately constant and is on the order of 2 times the ion-sound speed. The shape of the double layer does not change significantly during this motion. (3) When the bias between the sources is rapidly turned on, the initial phase in the double layer formation is the occurrence of a constant electric field (uniform slope of the potential) for the first few microseconds. The potential then steepens in the region where the double layer will eventually be formed and flattens in regions above and below this. The double layer is completely formed after about 100 microseconds and then engages in the jitter motion discussed above.

In the following we discuss first the apparatus used in all of the work and then consider each of the three phenomena mentioned above. In the first case it is believed that the phenomenon is rather completely understood and the situation is discussed at some length. The same cannot be said for the last two cases and limited discussion is included. However, these two phenomena have characteristics which differ qualitatively from what is seen in Q machines and these differences are identified.

## II. EXPERIMENTAL DETAILS

The experiment was performed in a triple plasma device (Torvén, 1982) consisting of a central chamber with coaxial plasma sources located on either side as shown in Figure 1. Plasma was produced in the sources by discharges in argon between heated tungsten filaments and the source chamber walls. The electrodes B1 and B2 can also be used as anodes; but, for the present investigation, they were left floating. They, therefore, acquired potentials approximately equal to the respective filament potentials. The sources were independent in the sense that

discharge voltages and currents and gas flow rates could be varied independently in either source with unmeasurably small effects on the plasma parameters in the other source. The potential between the anodes of the two sources was determined by  $U_0$ , which was also taken as the difference in the plasma potentials in the sources. This assumption was tested several times during the course of the experiments using collecting probes in the sources to measure the potentials there and was found to be satisfied within the accuracy with which the potentials could be determined from the probe characteristics, or about  $\pm 0.5$  volt, over a variation of  $U_0$  by more than 200 volts. Plasma diffused into the central chamber from the sources through apertures A1 and A2 in the end plates of the central chamber. These apertures determined the diameter of the plasma column (3.0 cm) which was radially confined by a homogeneous magnetic field of up to 20 mT. Because of the small diameter of the apertures compared to the diffusion pump (25 cm), it was possible to maintain sufficient pressure in the sources for their proper operation (10 to 100 mPa) while restricting the pressure in the central chamber to about 1 mPa, thereby minimizing the importance of ionizing processes in the chamber. It is this property that allows the production of very strong double layers (potential drops up to 3 kV) in this device (Torvén, 1982).

Electric potentials were measured with electron emitting probes which could be moved both radially and axially with electric motors. For low frequency measurements (from d.c. up to about 10 kHz), the probes were operated essentially at their floating potential, which was measured using 100 mohm frequency-compensated voltage dividers. For a.c. signals which are not too large (cf. Torvén et al., 1985), the frequency response of the probe is determined by the product of the dynamic resistance of the plasma near the floating potential and the distributed capacitance of the probe and its heating circuit. This capacitance (about 100 pf) is dominated by the capacitance to ground of the feed wires to the movable probe inside the vacuum chamber. The dynamic resistance of the plasma, defined as the reciprocal of the slope of the probe characteristic, depends on the plasma density and the probe wire temperature. For the present experiment it was on the order of 10 kohm.

### III. DISRUPTIONS WITH AN INDUCTIVE EXTERNAL CIRCUIT

When an inductor of sufficient size is placed in series with the bias source  $U_0$ , it is observed that periodic disruptions of the plasma current and of the double layer potential occur. These disruptions have been previously reported in detail (Torvén et al., 1985) and we review here only those aspects pertinent to the present work.

Figure 2 shows an example of the disruptions when the inductance was 0.1 Hy. The top oscilloscope trace shows that the potential measured on the positive source varied from zero to 400 volts. For these runs  $U_0$  was 100 volts so there was a 300-volt inductive overvoltage. This overvoltage was given exactly by  $L di/dt$ , where  $i$  is the current flowing through the inductor. This current is shown by the bottom trace in Figure 2. The other traces are of potentials measured by probes at fixed positions in the plasma and show that the potential drop does occur over a limited spatial region, that is, in a double layer.

The disruptions are thus seen to be completely explained in terms of variations in the plasma current. The plasma current, in turn, is controlled by the potential structure between the two sources. Figure 3 shows the potential measured in the low potential region for various times during the disruption cycle. There is clearly qualitative agreement between the minimum value of the potential, which should be the only feature of the potential structure that influences the plasma current, and the plasma current. To test the quantitative sufficiency of this mechanism, a series of experiments were performed with the inductance removed and with  $U_0$  varied slowly over the voltage range of interest. Preliminary reports of these results have appeared (Carpenter and Torvén, 1984; Carpenter et al., 1984), and a detailed account will appear (Carpenter and Torvén, 1986), but we will review the pertinent results here.

To obtain I-V characteristics of the device, the potential  $U_0$  between the sources was slowly varied, either by hand or by using a function generator to control the power supply with voltage-control programming, and the resulting plasma current measured using precision 1 ohm shunts. The data were taken using a calibrated X-Y plotter, or a calibrated two-parameter transient digitizer. The emitting probes were used to measure both axial and radial potential profiles for different values of  $U_0$ . An example of the axial potential structure observed between the sources is shown in Figure 4. For these data  $U_0$  was 150 volts. A minimum in the potential is clearly seen at about 15 cm from the left aperture. That the minimum is in fact quite well defined is seen more clearly with the expanded scale. The magnitude of the minimum potential,  $V_m$ , was determined for values of  $U_0$  between zero and 200 volts. For details of how this was accomplished see Carpenter and Torvén (1986). An example of such a measurement is shown in the lower half of Figure 5. The corresponding I-V characteristic is shown as the solid curve in the upper half of this figure.

The purpose of these measurements, as mentioned above, was to test whether or not the variations in  $V_m$  could quantitatively explain the variations in the plasma current. For purposes of this discussion, consider only the case where the right source is biased positive with respect to the left source. Plasma from both sources diffuses into the central chamber. Since a potential minimum exists between the sources, the ion flow will not be affected, but the electron current between the sources will be reduced because of reflection of electrons from both sources by an amount that depends only on the differences between the minimum potential  $V_m$  and the plasma potentials in the sources. These potential differences can be obtained from the data, and the I-V characteristics can accordingly be calculated if the electron distribution functions are known.

Assume that the plasmas in the sources are Maxwellian with temperatures  $T_p$  and  $T_n$  and densities  $n_p$  and  $n_n$ , where the subscripts p and n refer to the positive and negative sources, respectively. These symbols refer to the electrons only. (Ion currents can be easily included, but they contribute much less than 1 percent of the total current and so are ignored in order to simplify the notation.) Then the distribution function at a point where the potential is  $V(x)$  is generally given by

$$f(x,v) = n_0 \left( \frac{2m}{\pi kT} \right)^{1/2} \exp \left[ -\frac{mv^2}{2kT} - \frac{e(V_0 - V(x))}{kT} \right] \quad \text{for} \quad a < v < \infty \quad (1)$$

$= 0$  for velocities outside this range

Here  $n_0$  is the plasma density at a point where the potential is  $V_0$ ,  $e$  is the magnitude of the electronic charge,  $m$  is the electron mass, and  $k$  is the Boltzman constant. The lower velocity limit  $a$  is negative for points between the source and the minimum, since reflected electrons exist in this region, and positive for points beyond the minimum. It is exactly zero at the minimum, so the lower limit is the velocity such that the energy, which is constant, is just equal to  $V_m$ . Thus,

$$a = \pm \left\{ \left( \frac{2e}{m_e} \right) [V(x) - V_m] \right\}^{1/2} \quad (2)$$

The current is of course independent of the point  $x$  where it is evaluated. However, it is convenient to evaluate the contributions to the total current from each source at the position of the potential minimum, since at this point the distribution functions take on their simplest forms. The result is

$$I = Ae \left\{ \left( \frac{2k}{\pi m_e} \right)^{1/2} \left[ n_n T_{en}^{1/2} \exp \left( -\frac{V_n - V_m}{kT_{en}} \right) - n_p T_{ep}^{1/2} \exp \left( -\frac{V_p - V_m}{kT_{ep}} \right) \right] \right. \\ \left. + \left( \frac{2k}{\pi m_i} \right)^{1/2} \left[ n_p T_{ip}^{1/2} \exp \left( -\frac{V_p - V_n}{kT_{in}} \right) \right] \right\} \quad (3)$$



Here  $V_p$  and  $V_n$  are the plasma potentials in the sources and the other quantities have been defined previously. As the applied voltage  $U_0$  is increased, the current increases at first because of the decrease in the magnitude of the second term. That is,  $V_p$  approximately follows  $U_0$  and  $V_n$  stays approximately at ground. After  $U_0$  increases to several times  $kT_p$ , the second term will become negligible, and further changes in  $I$  can only occur if  $V_m$  changes relative to  $V_n$ .

In order to test the sufficiency of this picture, we have used the measured variation of  $V_m$  with  $U_0$  and determined the values of the temperatures and densities that best fit the data with equation (3). That is, the value of  $V_m$  observed at  $U_0 = V_p - V_n$  is used in equation (3) to calculate  $I_{fit}$  and the results compared with the corresponding observed currents  $I_{exp}$ . The parameters in equation (3) are varied in order to minimize the sum

$$\psi = \sum (I_{exp} - I_{fit})^2 \quad (4)$$

The result of a typical fit is shown by the dashed line in the upper part of Figure 5. The main features of the data are certainly rather well explained. However, the temperatures that give acceptable fits are larger than those observed with probes in the sources. For example, the temperatures that give the fit shown in Figure 5 are 12.3 eV for the left source and 21.5 eV for the right source. Measured values for the temperatures were about 8 eV in both sources. However, the probe characteristics showed high energy tails of the type usually seen in discharge sources corresponding to a significant population of ionizing electrons. If distributions corresponding to such electrons were included in the model, the best-fit temperatures of the Maxwellian populations would certainly be reduced. However, the number of parameters to be fit would be doubled, thereby reducing the significance of the small improvement in the fit that might be expected. It is felt that the appropriateness of the model has been adequately demonstrated without this refinement. Data were taken and fits performed in the manner described for 12 different combinations of source parameters, such that the plasma density in both sources varied by an order of magnitude. No unusual characteristics were observed and the fits obtained were in all cases comparable to that described above.

The model can also be used to provide some insight into the role of the potential minimum and its behavior. The basic feature of the region of space below the double layer is its charge neutrality. That is, even though there are variations in the potential here, they occur over many hundreds, even thousands, of Debye lengths, so the departure of the ratio of electron-to-ion densities from unity is expected to be vanishingly small. Therefore, since the electron and ion charge densities depend in different ways on the voltage applied between the sources, some self-adjusting potential is needed between the sources in order to keep the region quasineutral. Mathematically, the requirement that the net charge density at the minimum be zero will insure quasineutrality over a broad region near this point. The electron densities were obtained by integrating the distribution functions given in equation (1) over the appropriate velocity intervals. The ion densities were obtained in a similar way. The form of the distribution functions was the same, but the velocity intervals were different since the ions were accelerated from the sources. The equation giving zero net charge at the minimum is

$$\begin{aligned} n_{ep} \exp\left(-\frac{V_p - V_m}{T_{ep}}\right) + n_{en} \exp\left(-\frac{V_n - V_m}{T_{en}}\right) &= n_{if} \exp\left(\frac{V_p - V_m}{T_{ip}}\right) \\ &\times \left[1 - \operatorname{erf}\left(\sqrt{\frac{V_p - V_m}{T_{ip}}}\right)\right] + n_{in} \exp\left(\frac{V_n - V_m}{T_{in}}\right) \\ &\times \left[1 + \operatorname{erf}\left(\sqrt{\frac{V_p - V_m}{T_{in}}}\right) - 2 \operatorname{erf}\left(\sqrt{\frac{V_n - V_m}{T_{in}}}\right)\right] \end{aligned} \quad (5)$$

where the new subscripts  $i$  and  $e$  refer to the ions and electrons. This equation was solved by simply stepping  $V_m$  in successively smaller steps each time zero was crossed, until the step size was smaller than the accuracy desired. The results are sensitive to the ion temperatures, about which we have little experimental information. Examples showing how  $V_m$  varies as  $U_0 = V_p - V_n$  is changed are shown in Figure 6 for three different sets of ion temperatures. The plasma parameters used were typical of those observed experimentally in the two sources. It seems clear that a rather good fit to the experimental curve of  $V_m$  versus  $U_0$  could be obtained by adjusting the ion parameters, with possibly some small adjustment of the electron parameters, but in view of the number of parameters involved and the fact that the charge exchange ions have been neglected, such an effort hardly appears justified. However, the agreement with the data of the trends shown in Figure 6 provides some confidence in the following explanation: As  $U_0$  is first increased, the biggest change is the reduction in the number of electrons reaching the minimum region from the positive source. To compensate, the minimum becomes less negative so more electrons from the negative source are admitted. This continues until all electrons from the positive source are reflected. Competing with this effect is the reduction of ion density from the positive source due to increasing ion velocity as  $U_0$  increases and when the electrons are eliminated, this effect becomes dominant. Thus, the minimum increases in depth to reduce the flow of electrons from the negative source. It is exactly this last process that gives rise to the negative resistance region according to this model.

The main features of the variation of  $V_m$  with  $U_0$  are obviously rather well explained by these considerations, at least for cases where  $U_0$  varies slowly with time. Thus, the negative-resistance region in the I-V characteristic is explained, and it can be said that the low frequency disruptions are understood. It should be emphasized that in order to observe disruptions of low enough frequency that this explanation applies without modification, additional lumped capacitance must be added in parallel with the distributed capacitance between the sources (Carpenter et al., 1984). At higher frequencies ion-transit times become significant and there is some delay in the charge neutrality condition that can be expected to affect  $V_m$ . Although these effects have not been included, it seems clear that careful consideration of the potential structure in the low potential region must be included in any complete theory of double layers.

#### IV. JITTER MOTION

When the potential indicated by the emissive probe is monitored by a device capable of following high frequency variations, such as an oscilloscope, it is observed that the signal fluctuates wildly when the probe is in the vicinity of the double layer. Observations as the probe moves through the double layer lead quickly to the conclusion that the fluctuations are due to the random motion of the entire potential structure around its equilibrium position. The effect is shown in Figure 7. These data were recorded by plotting single sweeps obtained with a transient digitizer on the same graph. Also shown is an overlay of the double layer obtained with an X-Y plotter during this run. The sweeps were obtained with the probe fixed at the three positions marked A, B, and C on the double layer. For all three sets of sweeps, horizontal lines are shown that correspond to the variation in potential which results when the double layer makes an excursion with a total extent of 1.2 cm centered at each of the three points. Clearly the various amplitudes of the fluctuations which are observed as the probe moves through the double layer are all explained by movements of the structure by a constant amount. Also evident in these data are regions where the potential changes with a constant slope for several microseconds. The velocity of the structure is apparently constant during these times. Since the double layer provides a convenient conversion factor — distance required for a given potential change — the velocity of the motion can be determined if we can determine the change in shape of the double layer (the calibration constant) as it undergoes its random motion.

The X-Y plotter provides a potential profile which is time-averaged over the rapid jitter motion. To obtain instantaneous profiles, a second stationary probe was mounted in the double layer slightly off-axis. The signal from



this probe provided a trigger which gated the output of the moving probe used to map the potential structure. The varying signal from the trigger probe corresponded to varying positions of the structure. Thus, different double layer positions could be selected by choosing different trigger levels. Data obtained with three different levels are shown in Figure 8. If any of the curves is displaced horizontally, it is seen to closely overlap the other two curves. We conclude that the double layer moves with little, if any, change in shape. Another interesting implication of this result should be mentioned. The fact that double layer shapes that have been previously reported are time averages has been invoked by some authors to explain the apparent broadness of laboratory double layers. However, the widths of the instantaneous profiles reported here, defined for example as the distance required for a change from 10 percent to 90 percent of the full height, are not significantly different from those obtained with an X-Y plotter. This is the expected result if the structure between the 10 percent and 90 percent points was a straight line, the velocity was constant, and the maximum excursion was equal to the double layer width, which seems to be approximately the case.

The data in Figure 7 indicate that motion toward the negative source, corresponding to an increasing potential, occurs with a higher velocity than motion toward the positive source. However, this apparent difference is entirely due to experimental effects associated with the distributed capacitance of the emissive probe to ground. This was first suspected when it was noticed that the apparent difference was reduced when the emissive probe was shunted with an external resistor. The distributed capacitance can easily be charged more positively by simply emitting electrons. However, to become more negative it must collect electrons and it has insufficient area to do this rapidly enough. Put another way, the time response of the probe is determined by its RC time constant, where C is the distributed capacitance and R is the dynamic resistance of the plasma, defined as the reciprocal of the slope of the probe's I-V characteristic. The distributed capacitance is on the order of 100 pF and the dynamic resistance of the probe normally is on the order of 10 kohms. Thus, RC is on the order of 1 microsecond and the probe can respond to changes on the order of 1 MHz. However, when the probe is collecting electron saturation current, which would happen if the plasma potential suddenly dropped, the dynamic resistance is on the order of a few megohms, giving RC on the order of a tenth of a millisecond.

In order to overcome this effect, a special emissive probe was constructed in which the heating circuit, which contributed almost all of the distributed capacitance, was mechanically disconnected from the potential measuring circuit during the measurement time. The distributed capacitance during the measuring time was reduced to 10 pF which gives an RC value of 10 microseconds even in the worse case. Some traces of the fluctuating potential taken with this probe are shown in Figure 9. There is still a slight difference between the maximum rates of increase and decrease, but it is small enough that it can be explained as a residual effect of the distributed capacitance of the probe. The details of this probe and a further discussion of the effect of distributed capacitance on probe measurements will appear elsewhere (Torvén, private communication, 1986).

The maximum rates of increase and decrease shown by overdrawn lines in Figure 8 are 36 and 24 volts per microsecond, respectively. The central portion of the double layer observed for this case had a slope of 50 volts per centimeter. Thus, the indicated velocities are  $7.2$  and  $4.8 \times 10^5$  cm/s. As a comparison, the electron temperature observed for this run was 7 eV so the ion-acoustic speed was  $4.1 \times 10^5$  cm/s.

Fluctuations are observed also in double layers formed in Q machines (Iizuka et al., 1983; Sato et al., 1981). In the case of double-ended operation, the mode most comparable to the triple plasma machine, nearly stationary double layers are observed. The fluctuation consists of a more or less periodic variation of the slope of the double layer with the knee at the high potential side remaining approximately fixed. Thus, the knee at the low potential side shows a sort of roughly periodic motion which has been termed a "foot-point oscillation."

## V. INITIAL FORMATION

In order to study the initial formation of the double layer,  $U_0$  was replaced by a transistor-switched power source capable of supplying 100 volts with a rise time on the order of 1 microsecond. Standard boxcar sampling techniques were then used to measure the potential structure at various times after the bias voltage was switched on. Typical results are shown in Figure 10. There is a small structure near the low potential source that seems to propagate toward the high potential source, but the striking feature of the potential structure is that at early times the slope is essentially a constant. As time progresses the slope steepens in the vicinity of the place where the double layer will eventually form while it flattens in regions above and below this. The structure is nearly formed after 50 microseconds and completely formed after 100 microseconds. If one wants to think of the low potential foot-point as propagating toward the high potential source, then its velocity of propagation is about 50 cm in say 100 microseconds or  $5 \times 10^5$  cm/s, a speed which is somewhat supersonic and which seems to be typical of the propagation velocity of the double layers in this device.

The initial formation of double layers has also been studied in a double-ended Q machine (Iizuka et al., 1983). In this work it was observed that immediately following the application of the bias voltage the potential rose to the positive source potential over nearly all of the column, forming an ion-rich sheath near the cathode. This condition persisted for about 100 microseconds, after which the double layer detached itself from the cathode and propagated, as a completely formed structure, toward its final position. The velocity of propagation was approximately 3 times the ion-sound speed.

It has been suggested that the motion of laboratory double layers represents a sort of "hunting" for that position where the Langmuir criterion (the square of the electron-to-ion current ratio equals the ion-to-electron mass ratio) is satisfied (Iizuka et al., 1983; Torvén, 1982). The basis for this explanation is that the ion flux at the double layer should decrease as the length of the high potential region increases because of radial losses of ions along the part of the column at high potential. It should be expected, then, that the larger these losses are, the smaller should be the excursions from the equilibrium position. This may explain why the double layers seen with relatively weak magnetic fields are more stable than those seen in the Q machines. It may also explain the lack of stability of double layers seen in simulations where the use of periodic boundary conditions at the sides is equivalent to the total removal of radial ion losses. In order to investigate this question, a systematic investigation should be made of the motion of double layers as a function of the strength of the magnetic field and the planarity of the plasma column.

*Acknowledgments.* This work was performed at the Royal Institute of Technology in Stockholm. One of us (RTC) would like to thank Carl-Gunne Fälthammer for the stimulating working conditions that were provided and also the Swedish Natural Science Research Council and the Swedish Institute for support during the stay in Sweden.

## REFERENCES

- Carpenter, R. T., and S. Torvén, *Proc. Int. Conf. on Plas. Phys.*, Lausanne, P14-3, 1984.
- Carpenter, R. T., S. Torvén and L. Lindberg, in *Second Symposium on Double Layers and Related Topics*, edited by R. Schrittwieser and G. Eder, p. 159, University of Innsbruck, 1984.
- Carpenter, R. T., and S. Torvén, to be published, 1986.
- Hershkowitz, N., *Space Sci. Rev.*, **41**, 351, (1985).
- Izuka, S., P. Michelsen, J. Juul Rasmussen, R. Schrittwieser, R. Hatakeyama, K. Saeki, and N. Sato, Riso National Laboratory Report RISO-M-2414, 1983.
- Sato, N., R. Hatakeyama, S. Iizuka, T. Mieno, K. Saeki, J. Juul Rasmussen, and P. Michelsen, *Phys. Rev. Lett.*, **46**, 1330 (1981).
- Sato, N., R. Hatakeyama, S. Iizuka, T. Mieno, K. Saeki, J. Juul Rasmussen, P. Michelsen, and R. Schrittwieser, *J. Phys. Soc. Jpn.*, **52**, 875 (1983).
- Torvén, S., *J. Phys. D., Appl. Phys.*, **15**, 1943 (1982).
- Torvén, S., L. Lindberg, and R. T. Carpenter, *Plasma Phys.*, **27**, 143 (1985).

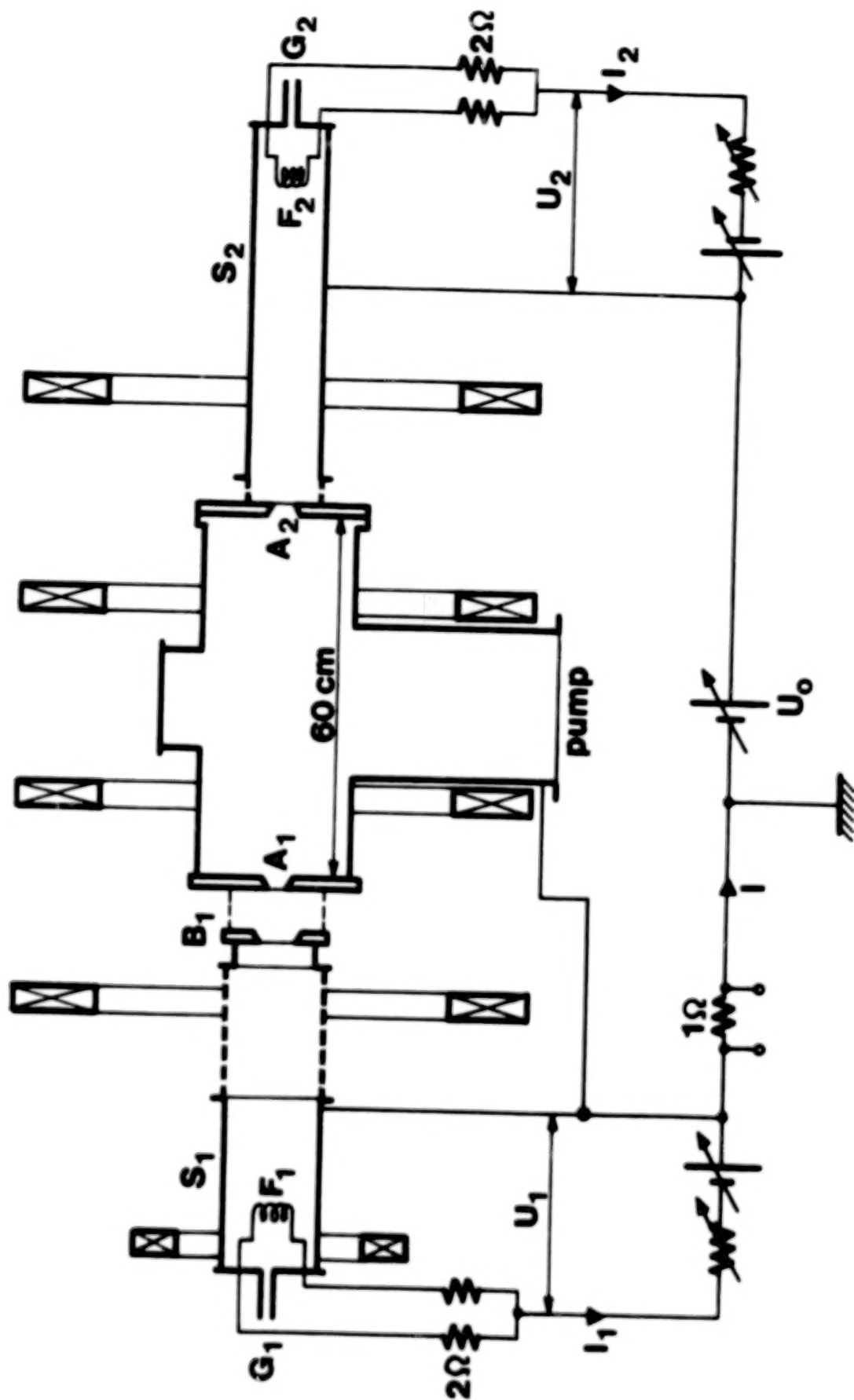


Figure 1. Schematic of the triple plasma machine.

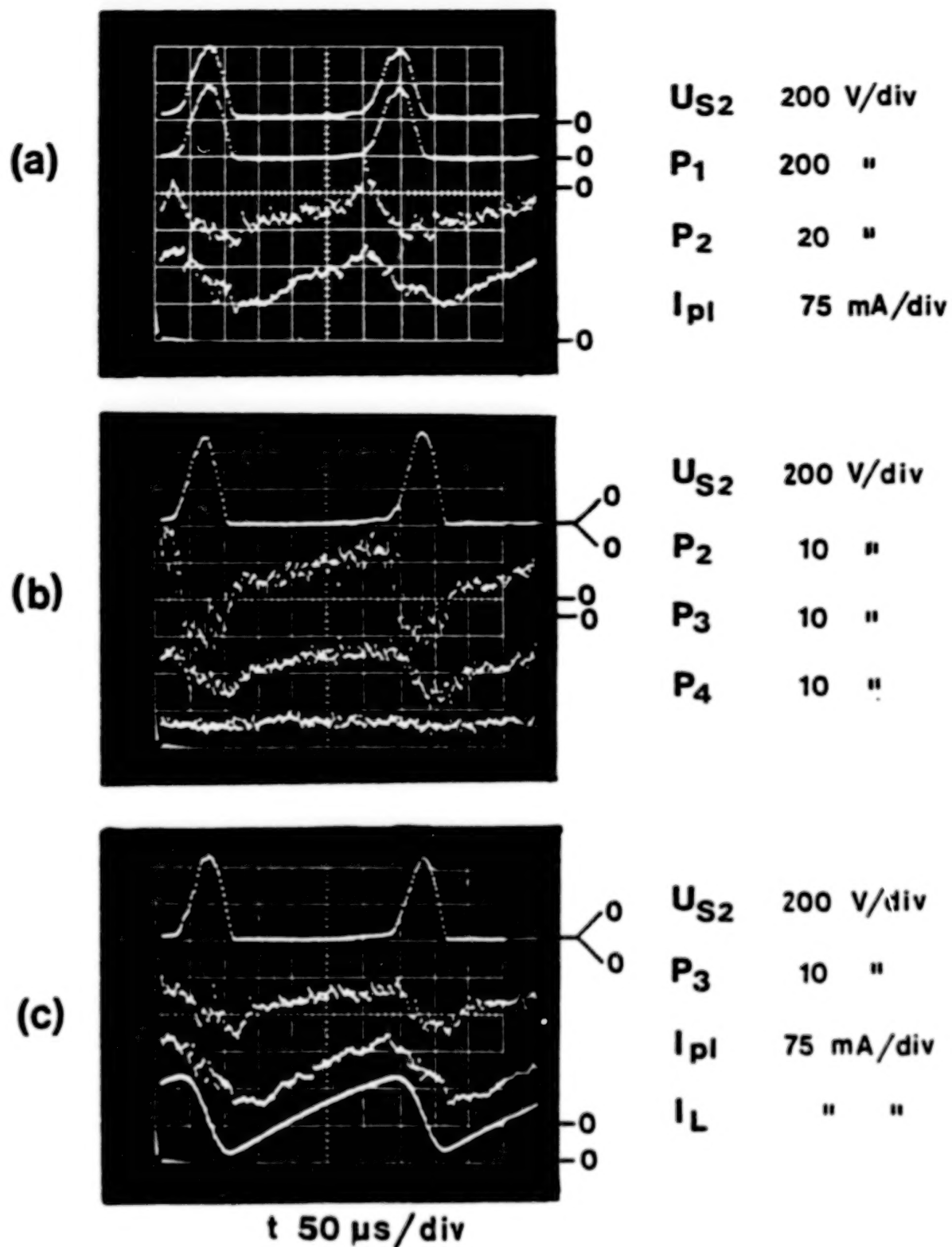


Figure 2. Oscilloscope traces during the disruptions. Probes P1, P2, P3, and P4 were located at 55, 45, 20 and 6 cm from aperture A1. The gain settings and zero levels are different for the various sweeps and are indicated to the right of each trace.

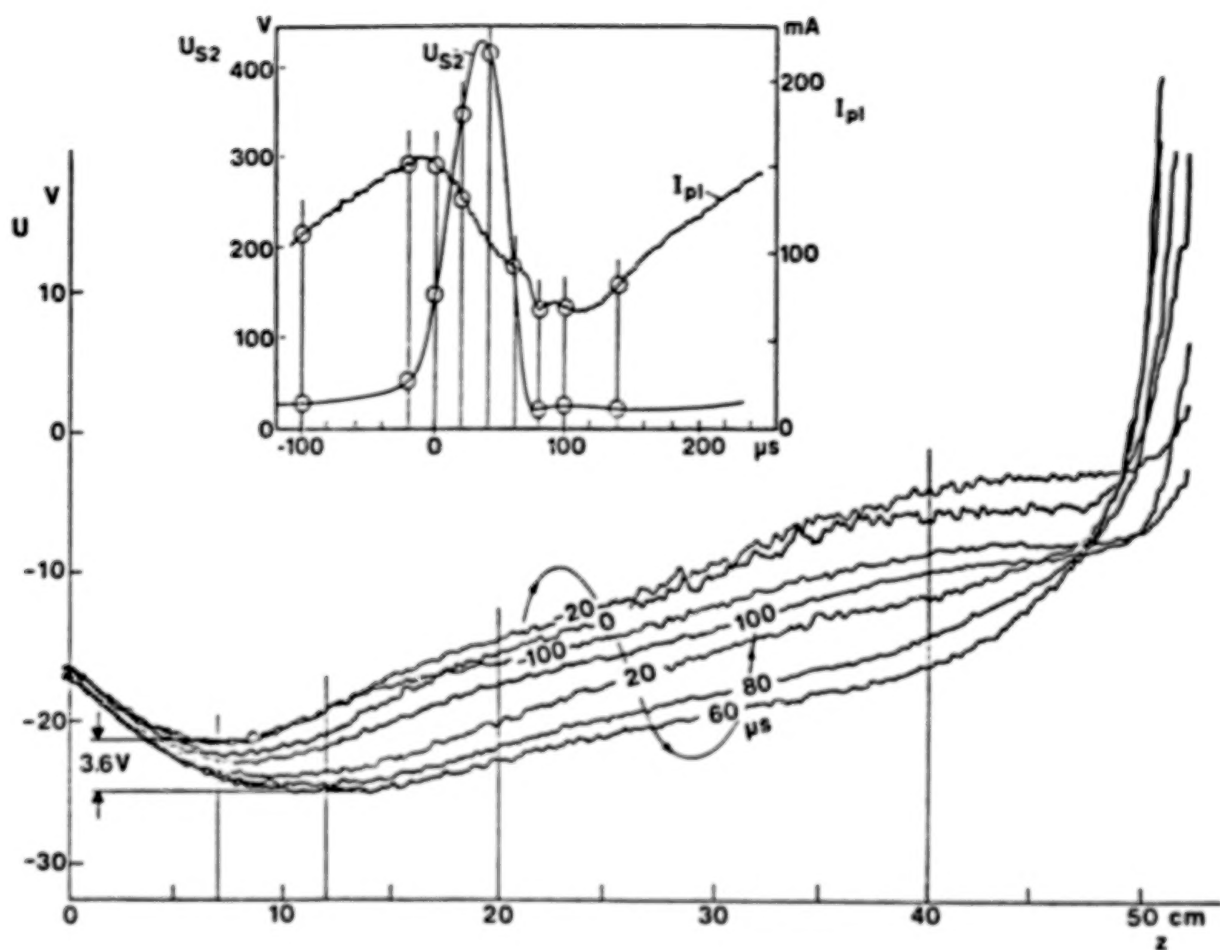


Figure 3. Potential structure in the low potential region sampled at various times, indicated by circles in the inset, during the disruption cycle. The serpentine line shows the timing sequence and the inset shows the time variation of the plasma current and the positive source potential.



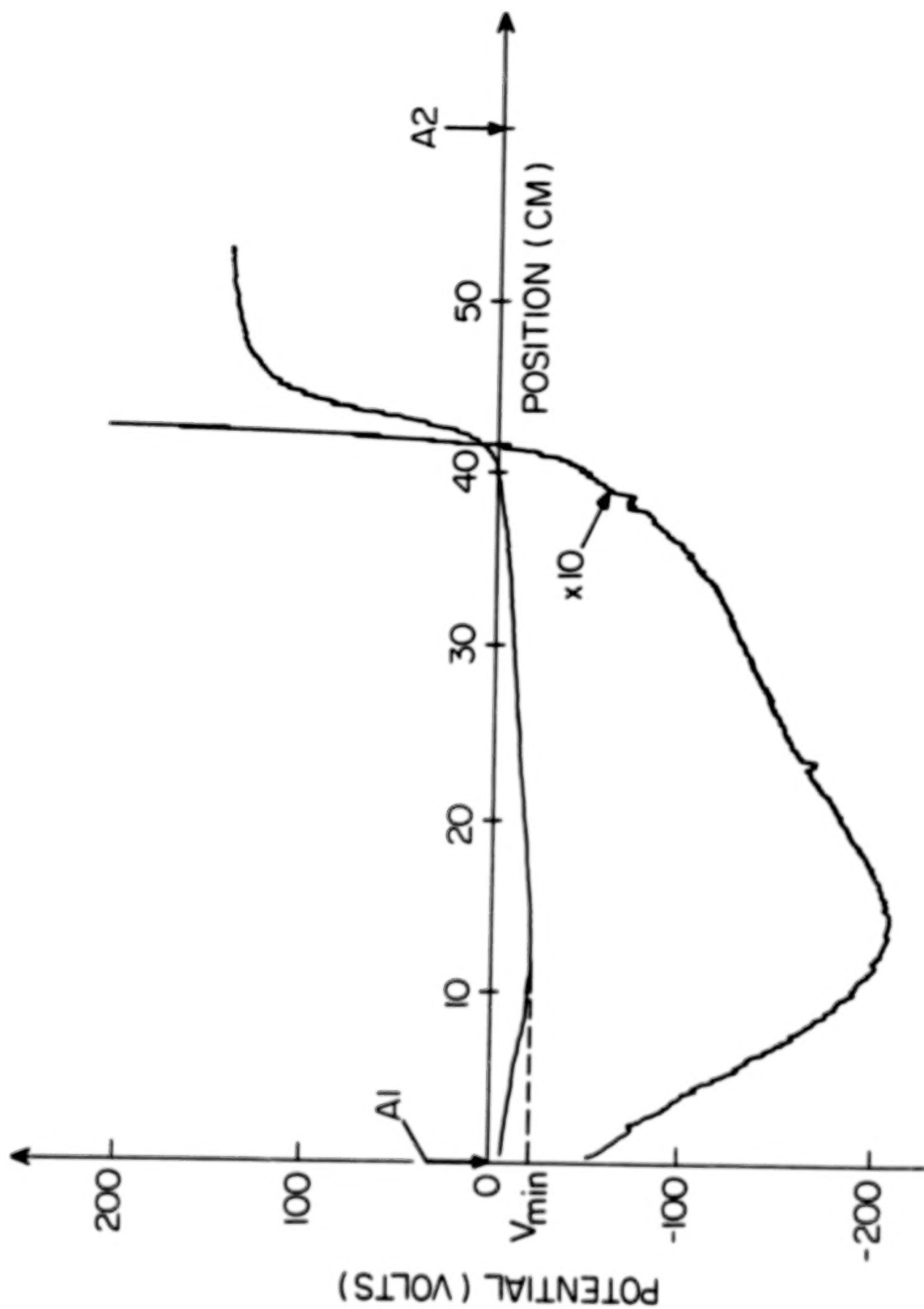


Figure 4. Steady state double layer showing the potential minimum in the low potential region.

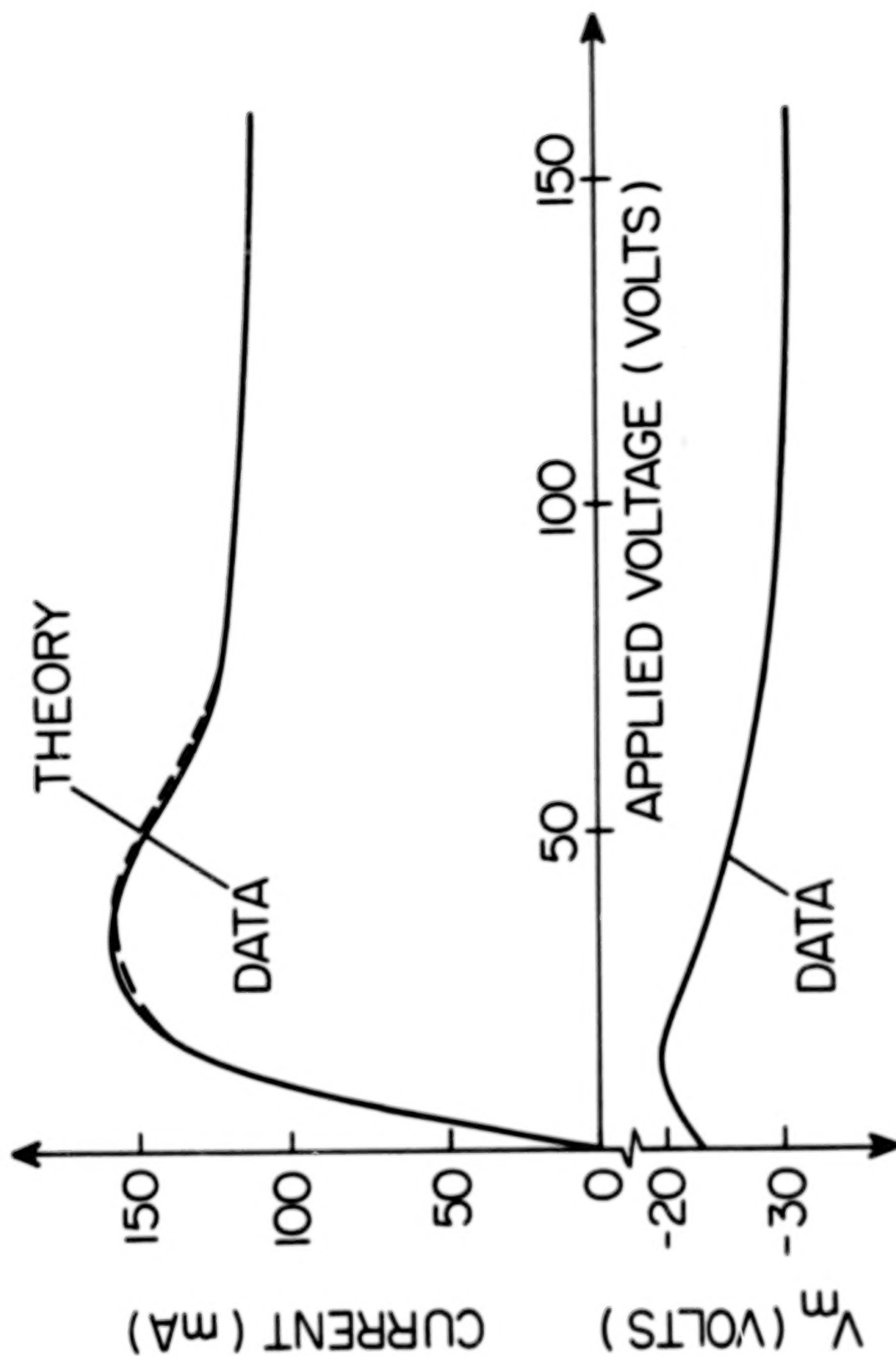


Figure 5. I-V characteristic for the double layer (upper curve) and the variation of the current-limiting minimum (lower curve). A fit to the I-V characteristic, using the data in the lower curve and assuming Maxwellian distributions in the sources, is shown by the dashed curve.

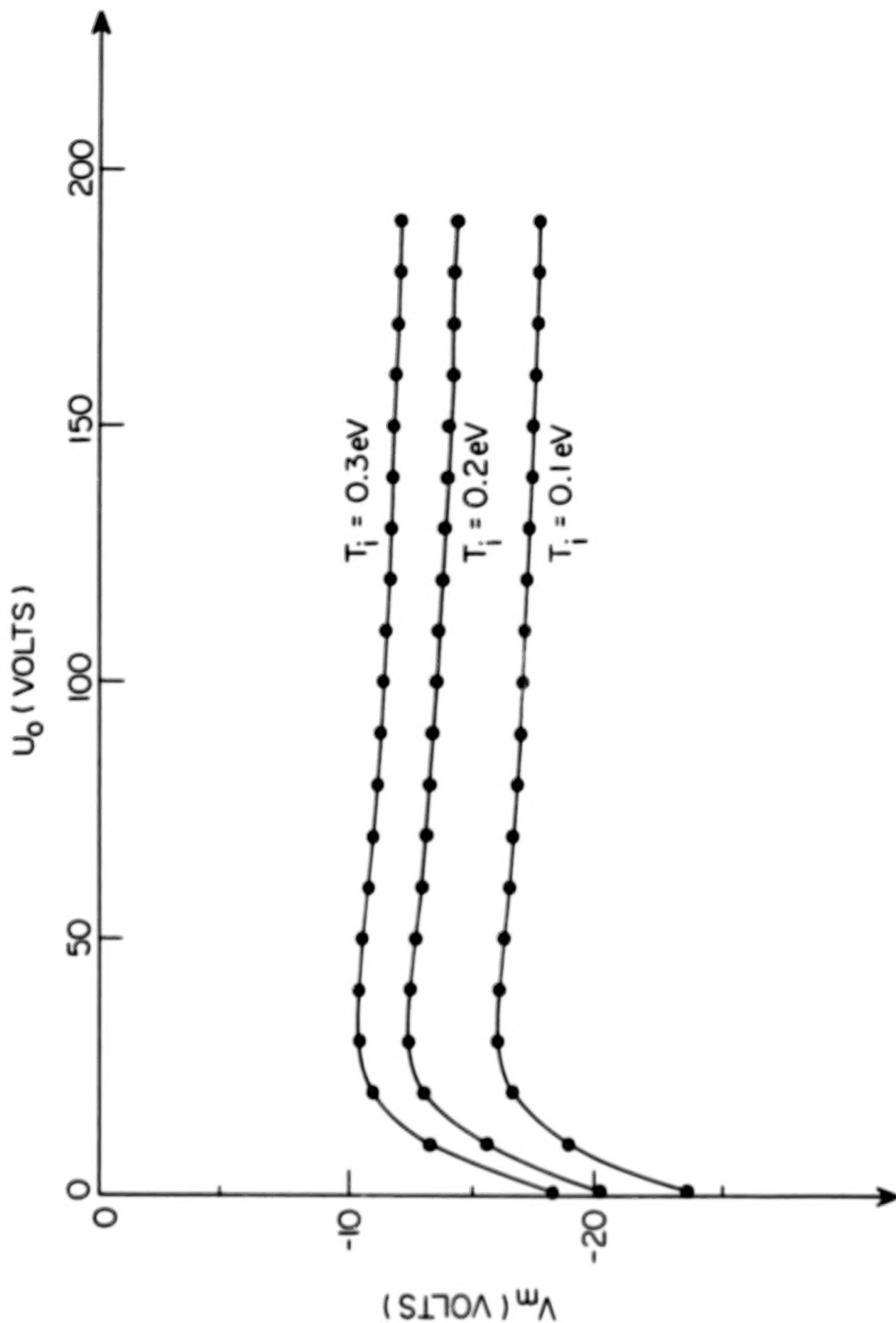


Figure 6. Examples of the calculated variation of the potential minimum  $V_m$  required to produce charge neutrality at the minimum. The ion temperatures were assumed to be the same in both sources.

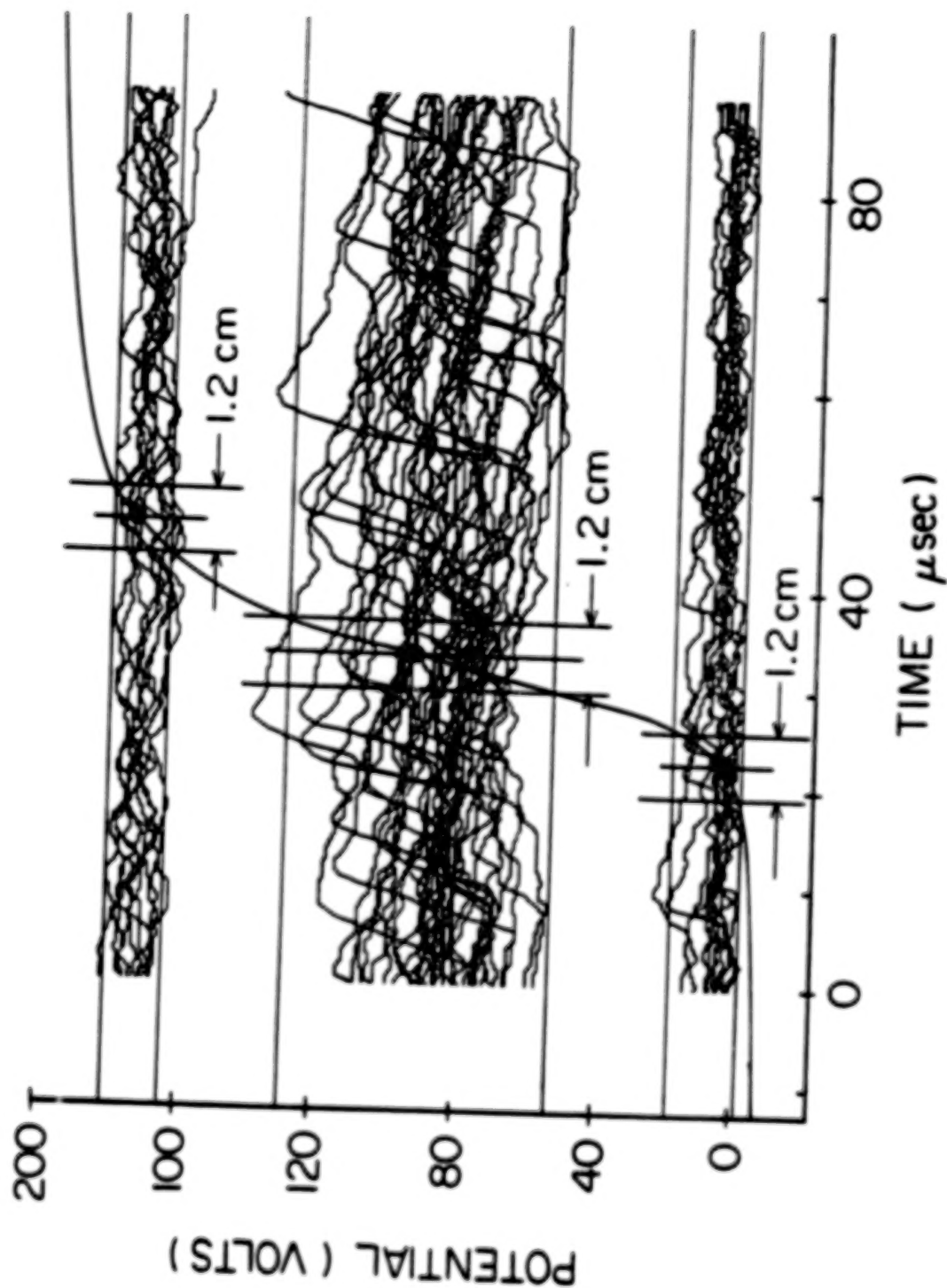


Figure 7. Oscilloscope traces, obtained with a digital transient recorder, of the potential indicated by an emissive probe when the probe was located at three different positions in the double layer. The positions chosen are shown on the overdrawn double layer which also shows potential variations corresponding to excursions in the double layer position by a total of 1.2 cm, centered at the indicated points.

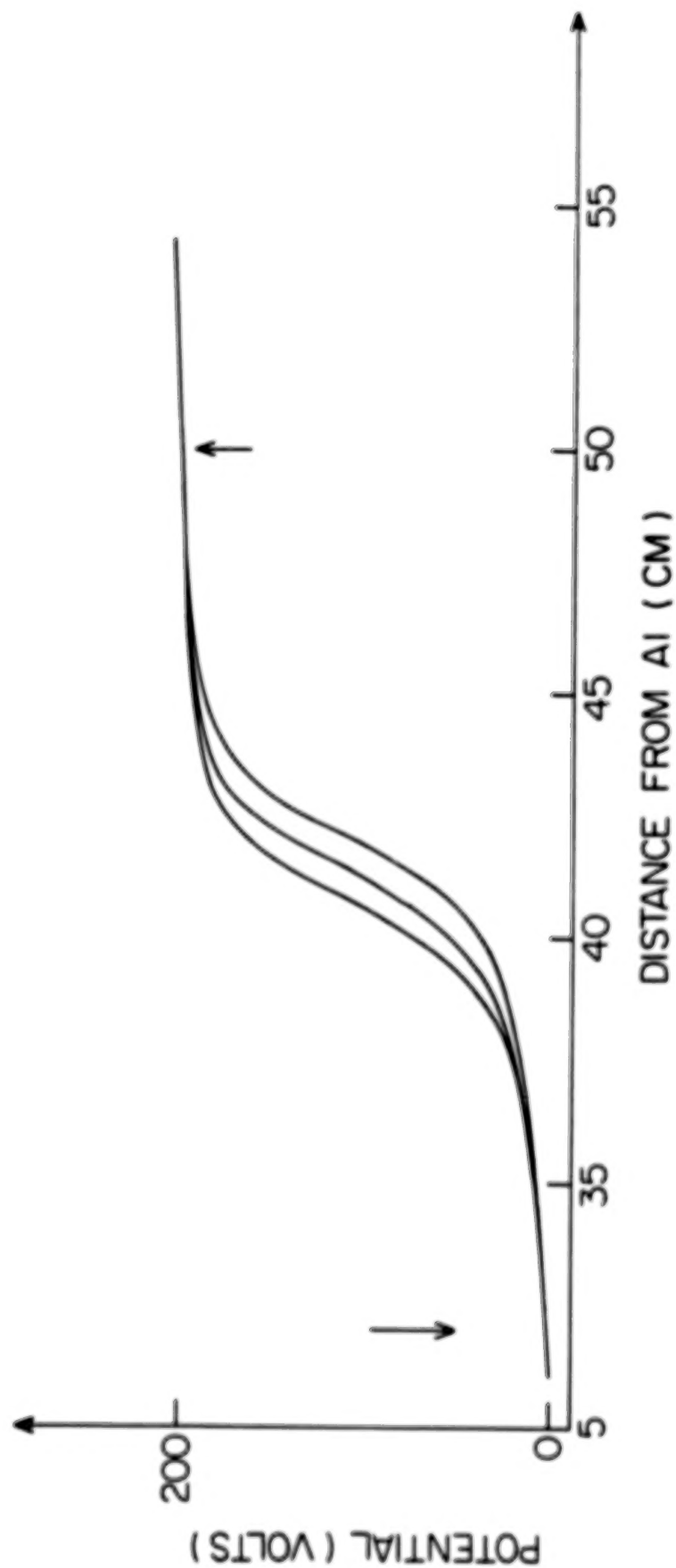


Figure 8. Potential structures obtained using a fixed probe to provide a gate, when the potential reached certain preset values, for the signal from the moving probe. Results for three different trigger levels are shown.

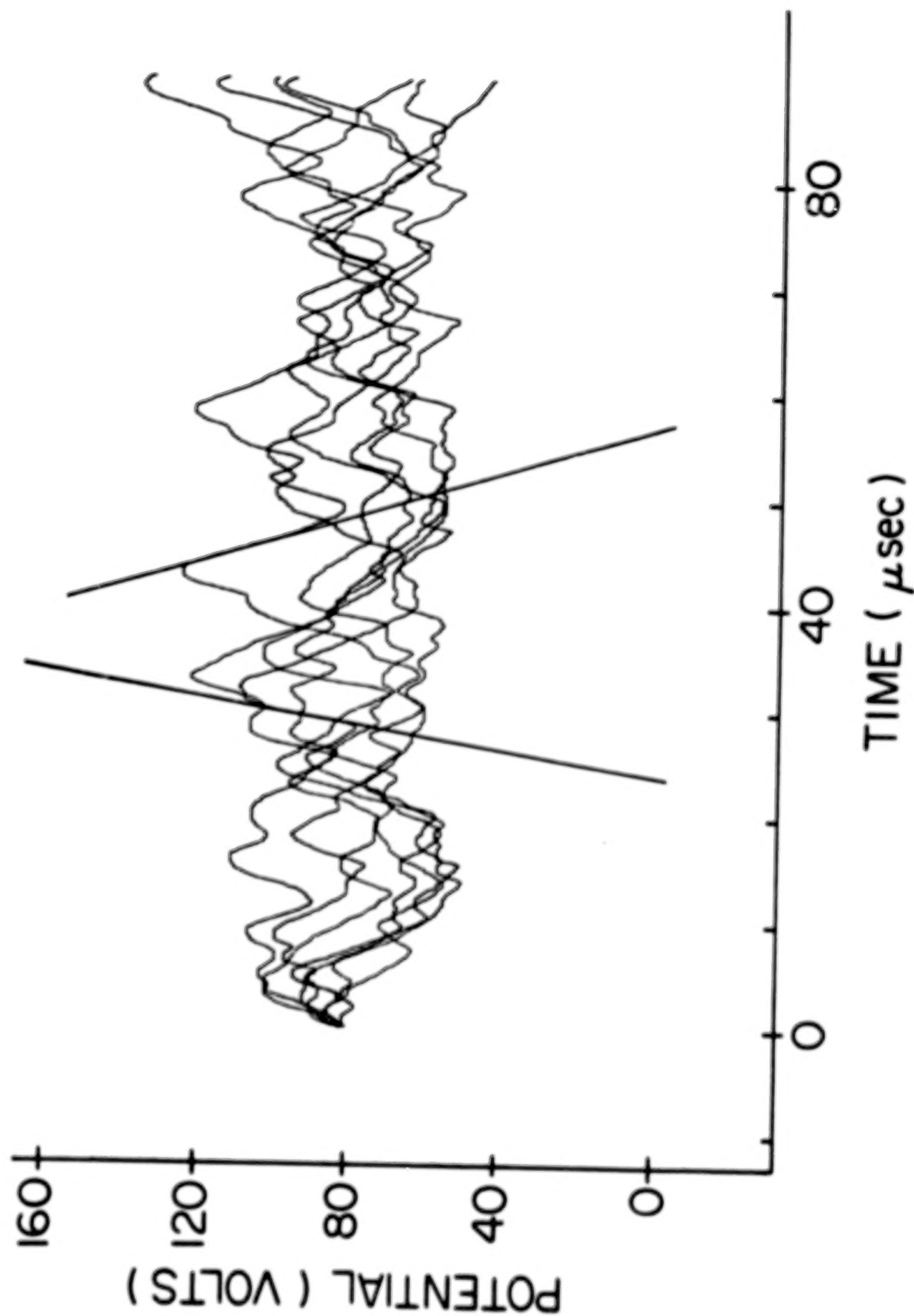


Figure 9. Oscilloscope traces similar to those shown in Figure 8 but taken with a probe with greatly reduced distributed capacitance.



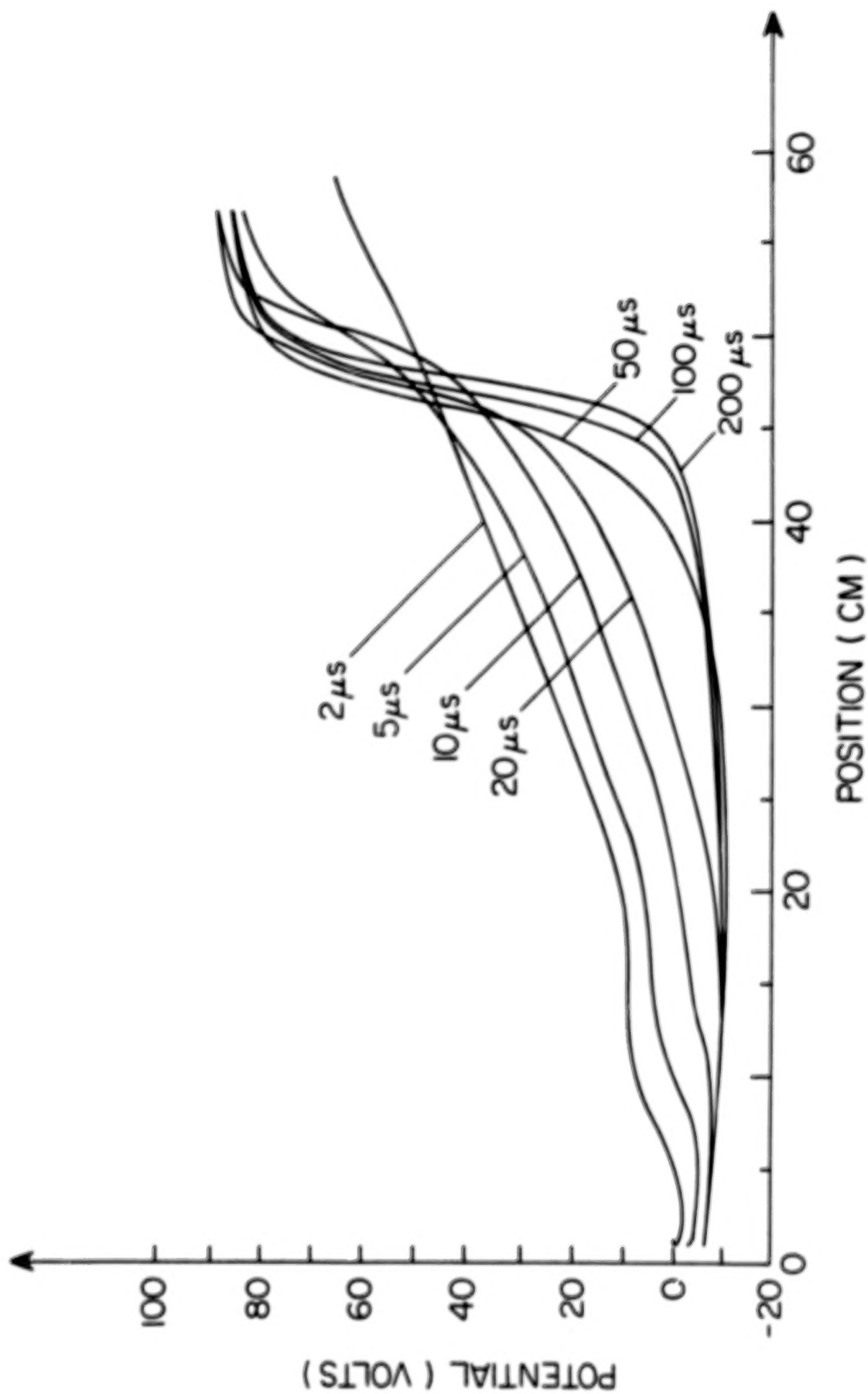


Figure 10. Measured potential structure at various times after the high voltage was switched on. The double layer forms quickly from an initial state where the structure is nearly that of a vacuum capacitor.

N87

23316

UNCLAS

## PUMPING POTENTIAL WELLS

N. Hershkowitz, C. Forest, E. Y. Wang,\* and T. Intrator

Department of Nuclear Engineering

University of Wisconsin-Madison

Madison, Wisconsin 53706, U.S.A.

## ABSTRACT

Nonmonotonic plasma potential structures are a common feature of many double layers and sheaths. Steady state plasma potential wells separating regions having different plasma potentials are often found in laboratory experiments. In order to exist, all such structures must find a solution to a common problem. Ions created by charge exchange or ionization in the region of the potential well are electrostatically confined and tend to accumulate and fill up the potential well. The increase in positive charge should eliminate the well. Nevertheless, steady state structures are found in which the wells do not fill up. This means that it is important to take into account processes which "pump" ions from the well. As examples of ion pumping of plasma wells, we consider potential dips in front of a positively biased electron collecting anode in a relatively cold, low density, multidipole plasma. Pumping is provided by ion leaks from the edges of the potential dip or by oscillating the applied potential. In the former case the two-dimensional character of the problem is shown to be important.

## 1. INTRODUCTION

A variety of experimental measurements of double layer and double layer related phenomena have demonstrated the presence of steady state plasma potential dips, at least in one dimension. Experiments range from glow discharge plasmas (Biboroch et al., 1984), to unmagnetized collisionless laboratory plasmas (Leung et al., 1980), to Q machine experiments (Sato et al., 1981), to fusion experiments (Hershkowitz, 1984). The general problem with all such structures is the question — what prevents the dip from filling up with ions either by charge exchange or by some kind of scattering? This problem has been identified as a key issue in maintaining "thermal barriers" in tandem mirrors (Baldwin and Logan, 1979) for which several techniques have been proposed for "pumping" out trapped ions. The only technique so far tested has been "neutral beam pumping" (Inutake et al., 1985; Grubb et al., 1984) — they use charge exchange of trapped ions on energetic neutral beams injected into the thermal barriers.

Although a dip may be present in one-dimensional data, it is not immediately apparent that ions are electrostatically confined in the dip in the perpendicular dimensions. Many structures have been found to have only minima in the potential in one dimension, while, in the other dimension the potential might be a relative maximum. In this case ions are not confined, pumping is not an issue, and potential variations in the perpendicular dimension can dominate the self-consistent solution to the problem. It is clear that the double layer is the wrong structure upon which to concentrate. This paper considers the problem of pumping steady state and slowly time varying potential dips in a multidipole laboratory plasma.

Representative double layers with dip structures that have been previously reported are shown in Figures 1 through 4. The data in Figure 1 (Coakley et al., 1978) were obtained in a triple plasma device for which  $T_e = 0.2$  eV. The various steady state structures were obtained by varying the bias on a boundary grid on the low potential

\*On leave from Southwestern Institute of Physics, Leshan, Sichuan, China.

side. Note that potential dips as deep as 5 V, equal to  $25 T/e$ , were achieved. For these data the pumping mechanism was later identified to be ion leaks in the perpendicular dimension. Another example is a discharge tube double layer shown in Figure 2 (Maciel and Allen, 1984). Examination of the associated radial potential profile also showed that the potential minimum was a relative maximum in the perpendicular dimension and that ions could again leak out.

While the first two examples are ones for which the ions can easily leak out, the data shown in Figure 3 (Suzuki et al., 1984) give a different situation. In that case a double layer was found at a B field minimum in a magnetized plasma. Ions trapped in the dip had to cross the magnetic field. In addition it was also found that the dip was an absolute minimum in potential in the radial direction. As the neutral pressure was increased to  $7 \times 10^{-6}$  from  $10^{-7}$  Torr, the dip was substantially reduced and eventually disappeared (as seen in Figure 4) (Suzuki et al., 1984). The pumping mechanism of this dip is not yet understood, but it is possible that instabilities provided wave energy which energized the trapped ions or that trapped ions were lost to the diagnostic used to determine the dip's presence.

## II. EXPERIMENTAL RESULTS

Consider the potential near a positively biased plate (Forest and Hershkowitz, 1986). A copper plate, radius = 3 cm, coated with a ceramic insulator on the back side and support, was introduced into an argon plasma with plasma density  $n = 10^8 \text{ cm}^{-3}$  and electron temperature  $T_e = 3.5 \text{ eV}$ . The plate was biased to +20 V and the chamber walls were grounded. The plasma was produced in a conventional multidipole device (Leung et al., 1975).

The plasma potential measured with an emissive probe along the axis of the plate is given in Figure 5. Note that a potential dip equal to  $\Delta\phi \approx 1.7 \text{ V}$  is found a distance  $d_{\text{MIN}}$  from the plate and that the potential far from the plate is only 3 V compared to the plate bias potential of 20 V.

We have also achieved a similar result (Wang et al., 1986) by looking at the potential on the axis of a set of parallel plates mounted in the same device. One was grounded and one biased to an oscillating potential at 100 kHz whose amplitude was approximately 12 V. The resulting plasma potential profiles at the maximum and minimum part of the cycle are shown in Figure 6. Note that once again a potential dip is also apparent in front of the positively biased electrode. In this case the backs of the plates were not insulated. The data shown in Figure 6 were taken using a new technique based on differentiated time-averaged emissive probe I-V characteristics which has been described elsewhere (Wang et al., 1986).

We can separate the interpretation of the results shown in Figures 5 and 6 into two issues. The first is the dip characteristics and the second is the question of why the dip does not fill in. Figure 7a shows that the size of the potential dip in Figure 5 scales linearly with electron temperature and is approximately equal to  $T_e/2$ . In Figure 7b it is also shown that the dip separation  $d_{\text{MIN}}$  from the plate decreases as the plasma density is increased. In Figure 8 we compare the dip separation to the predictions of the Child-Langmuir law and show that there is good agreement. This indicates that the self-consistent potential is established to make the electron loss from the plasma consistent with space charge limited emission as only electrons from the plasma are present near the front of the plate.

The question of why the dip does not fill in requires a look at the two-dimensional equipotential contours for a somewhat different case (shown in Figure 9) which also exhibits a dip (labeled 16). For that particular case, contours are apparent (indicated by +4 to +14) which are negative with respect to the potential dip. These were identified as being associated with a fingerprint on the plate. These suggest that the presence of an insulator on the surface could provide the necessary ion leaks. A careful examination of the contours near a cleaned plate is given in Figure 10. The potential dip is still present. Note that the dip contours terminate on the edges of the plate at the insulator which coats the back of the plate. The pumping is clearly provided by these leaks. Note also that the contours are quite one-dimensional near the center of the plate and that the radius of the plate is equal to approximately 30 Debye lengths.

We investigated the spatial profile near the plate as a function of neutral pressure and found that the dip is reduced as the neutral pressure increased (as shown in Figure 11). This can be understood as the leaks out of the end of the dips not being able to keep up with the charge exchange filling of the dip.

We believe that ion pumping is a necessary condition for the presence of the dip. We can test this conjecture by removing the pumping from the system. For the static case, we removed the source of the pumping, i.e., the insulator from the back of the plate. This resulted in a very different plasma potential axial profile shown in Figure 12. These data correspond to the same conditions as those shown in Figure 5. The only difference is that the insulator on the back of the plates was not present for the data in Figure 12 but was present for the data in Figure 5. It is apparent that when pumping is not present, the plasma potential is everywhere more positive than the plate. This means that the self-consistent solution that the plasma finds is determined by the coating on the back of the plate, 30 Debye lengths from the center of the plate. This result strongly suggests that double layer potential profiles may be determined by the presence of, for example, an insulating boundary on the edge of the device. We demonstrated that the insulator must be in a location where it can pump the dip by removing the insulator from the plate while still locating it within the plasma volume. In this case the plasma potential also remained more positive than the plate.

The data shown in Figure 7 indicate that a similar potential dip can also occur in front of a capacitor plate during the part of the cycle that it is biased positively. However, in that case there is no problem with trapped ions because such ions empty out during the part of each cycle when the plate is negatively biased.

### III. SUMMARY

We have shown that a plasma potential dip can exist in front of positively biased plates because of "ion pumping" of trapped ions from the dip. The dips were located in front of a steady state positively biased plate and also when the maximum positive bias was applied during an oscillating potential. Pumping was achieved by providing ion leaks, i.e., decreasing potential contours leading far from the structure that is usually measured, and indicates that boundary conditions far from the axes of experimental devices may play key roles in determining measured structures. A similar plasma potential structure was found when an oscillating potential was applied to a plate and no insulator was present. In that case ions were emptied from the dip by the time varying potential.

*Acknowledgment.* This work was supported by NASA grant NAGW-275.

## REFERENCES

- Baldwin, D. E., and B. G. Logan, *Phys. Rev. Lett.*, **43**, 1318 (1979).
- Biborosch, L., G. Popa, and M. Sanduloviciu, in *Second Symposium on Double Layers and Related Topics*, edited by R. Schrittwieser and G. Eder, p. 154, University of Innsbruck, 1984.
- Coakley, P., N. Hershkowitz, R. Hubbard, and G. Joyce, *Phys. Rev. Lett.*, **40**, 230 (1978).
- Forest, C., and N. Hershkowitz, *Journal of Applied Physics*, in press, (1986).
- Grubb, D. P. S. et al., *Phys. Rev. Lett.*, **53**, 783 (1984).
- Hershkowitz, N., in *Second Symposium on Double Layers and Related Topics*, edited by R. Schrittwieser and G. Eder, p. 55, University of Innsbruck, 1984.
- Inutake, M. et al., *Phys. Rev. Lett.*, **55**, 939 (1985).
- Leung, K. N., T. K. Samec, and A. Lamm, *Phys. Lett.*, **A51**, 490 (1975).
- Leung, P., A. Y. Wong, and B. H. Quon, *Phys. Fluids*, **23**, 992 (1980).
- Maciel, H. S., and J. E. Allen, in *Second Symposium on Double Layers and Related Topics*, edited by R. Schrittwieser and G. Eder, p. 218, University of Innsbruck, 1984.
- Sato, N., R. Hatakeyama, S. Iizuka, T. Mieno, K. Saeki, J. Juul Rasmussen, and P. Michelsen, *Phys. Rev. Lett.*, **45**, 1330 (1981).
- Suzuki, Y., R. Hatakeyama, and N. Sato, in *Second Symposium on Double Layers and Related Topics*, edited by R. Schrittwieser and G. Eder, p. 243, University of Innsbruck, 1984.
- Wang, E. Y., N. Hershkowitz, T. Intrator, and C. Forest, *Rev. of Sci. Instrum.*, submitted, 1986.



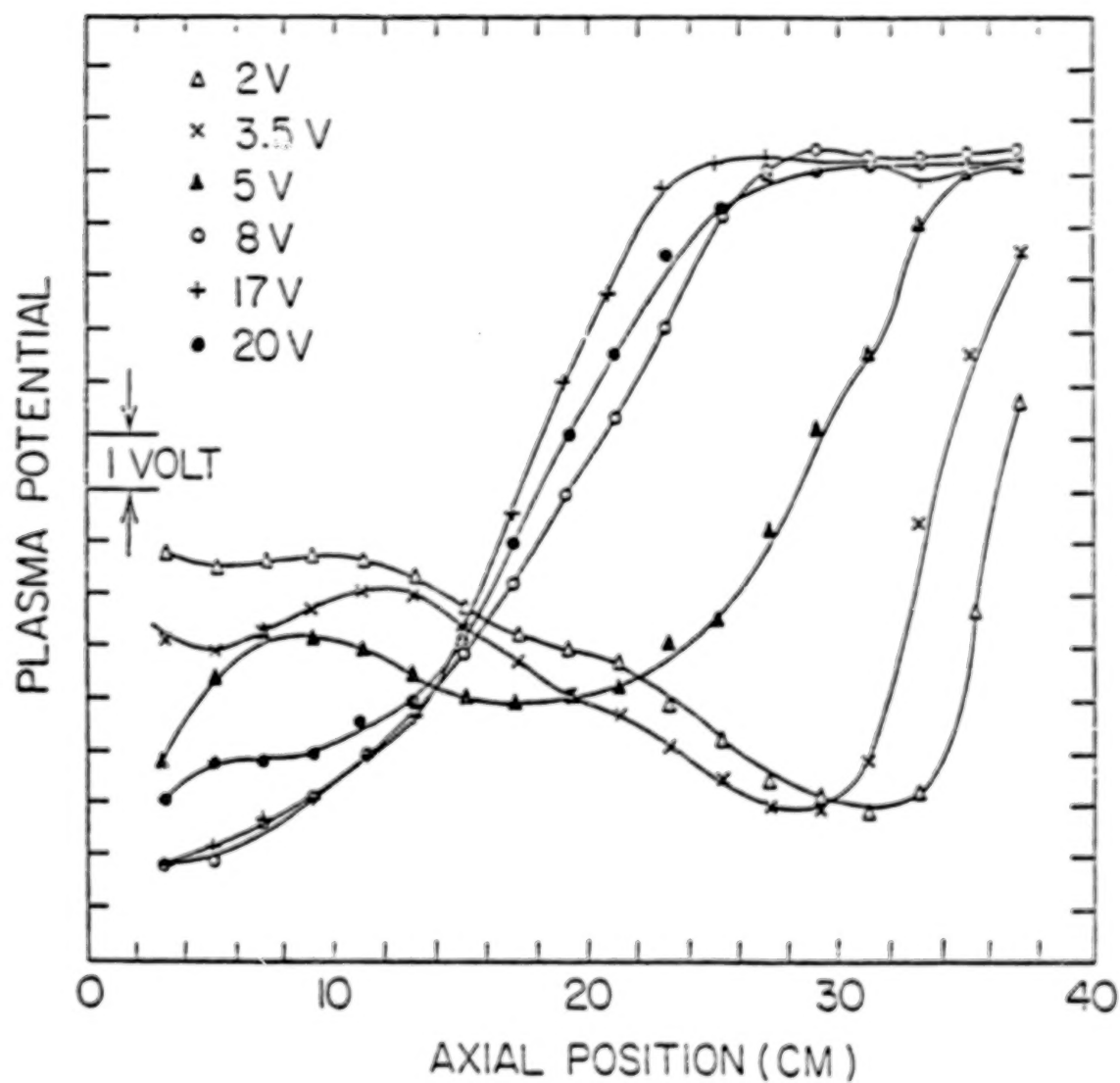


Figure 1. Stationary double layers showing potential dips on the low potential side. Axial potential profiles are given as a function of the bias of a grid on the low potential boundary. Multidipole double layers are apparent for bias voltages of 2-5 V. A bias voltage of 18 V was applied across the two source chambers.

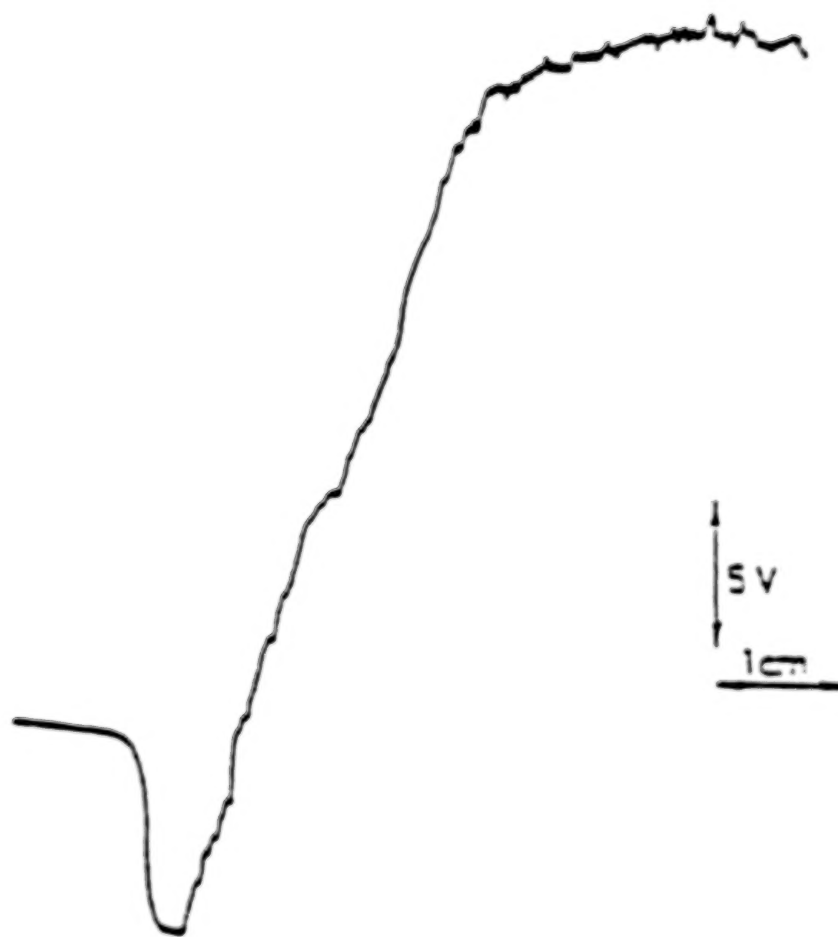


Figure 2. Triple layer axial potential profile obtained in a low pressure Hg arc discharge. This solution was identified to depend only on the boundary conditions; i.e., it was found to be a BGK solution.

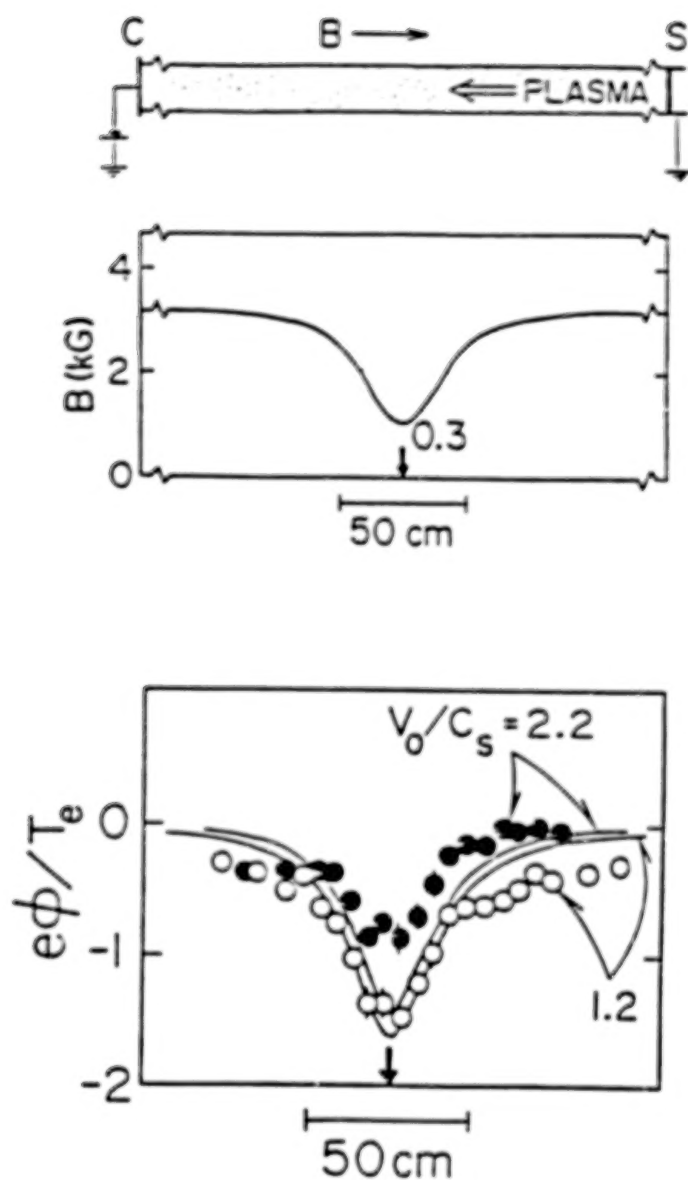


Figure 3. Schematic of the Q machine setup used by Suzuki et al. (1984) and the corresponding axial magnetic field profile. The axial potential profiles corresponding to two ion flow speeds are also shown.

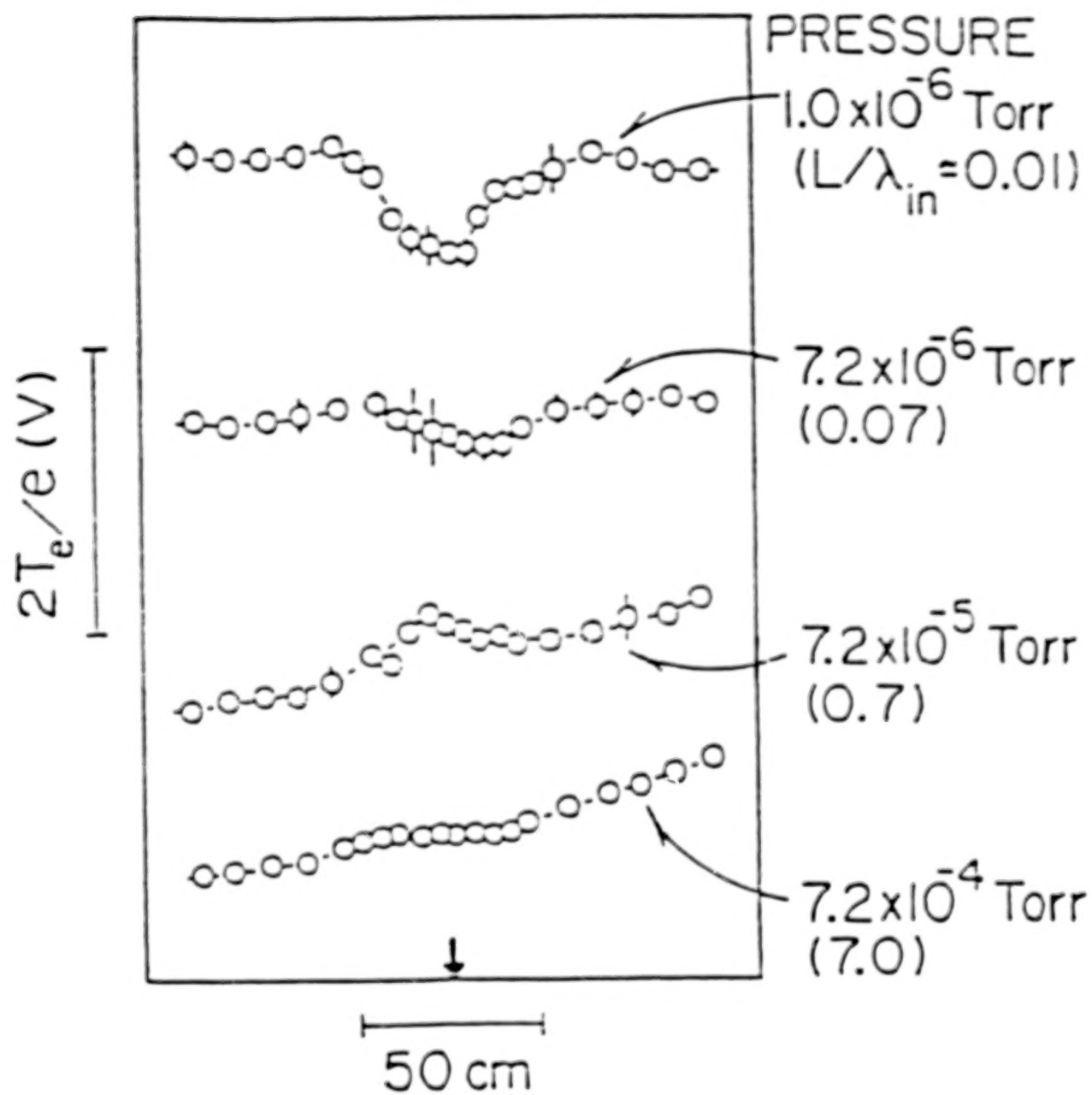


Figure 4. Axial potential profiles as a function of neutral gas pressure in the magnetic well ( $R_m = 0.3$ ).

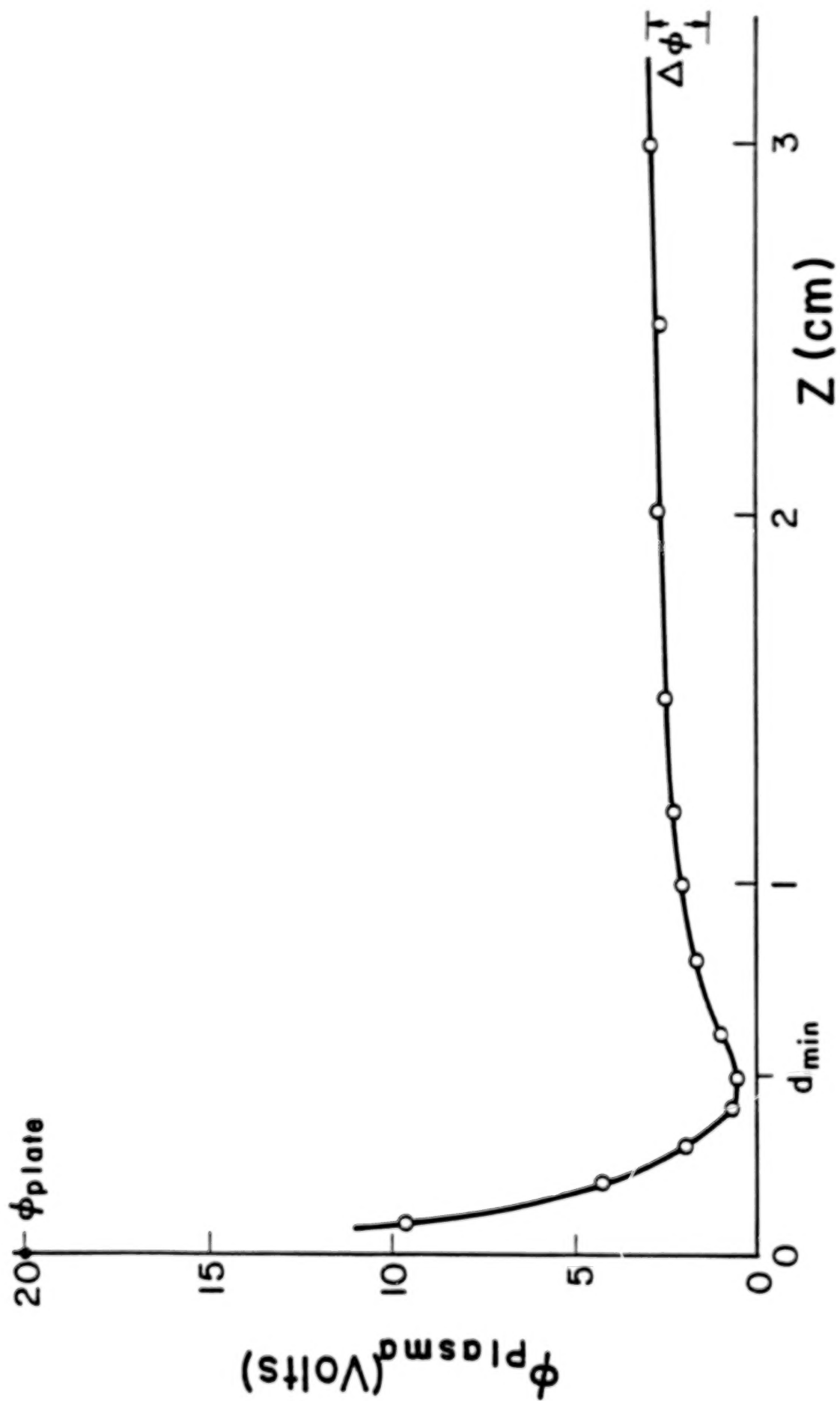


Figure 5. The plasma potential, measured with an emissive probe on-axis of a circular plate biased at +20 V. The electron temperature was measured to be  $T_e = 3.5$  eV.

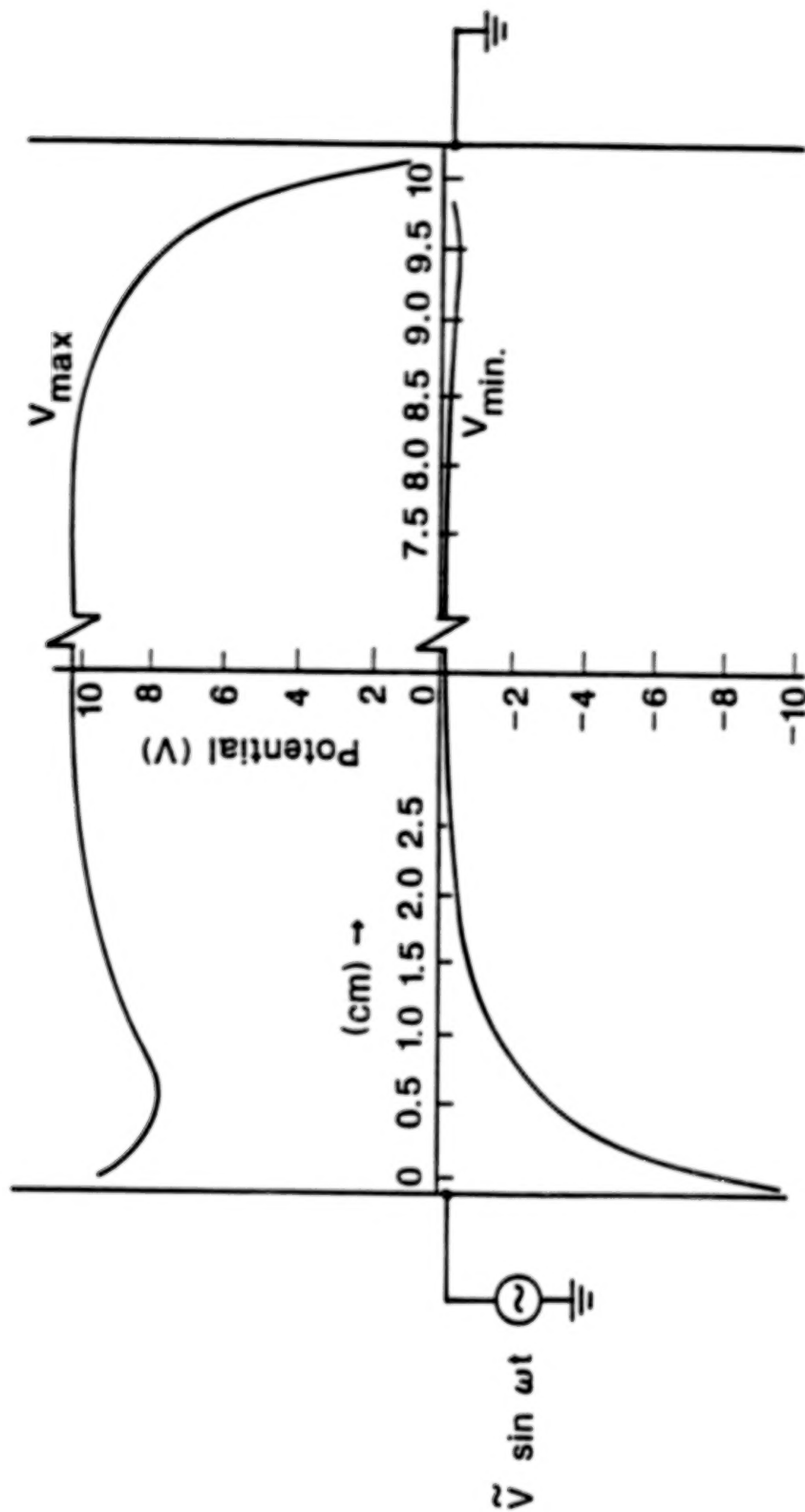


Figure 6. The maximum and minimum potential profiles between two parallel plates; a 100 kHz potential was applied between the plates. Data were obtained using emissive probes and a time-averaging method.



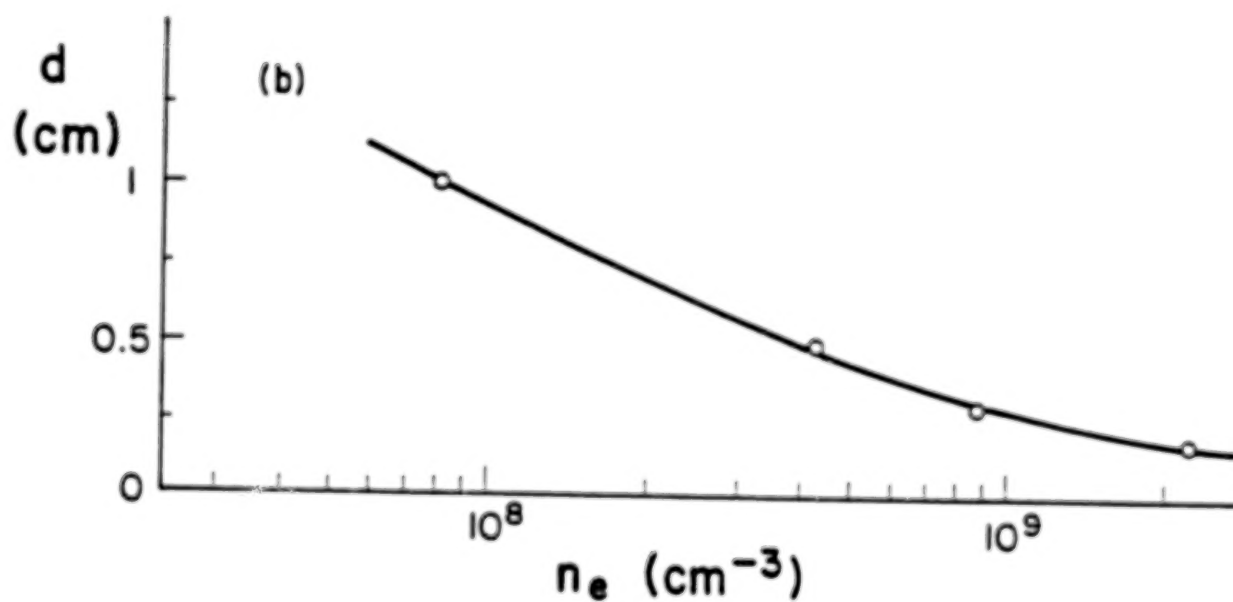
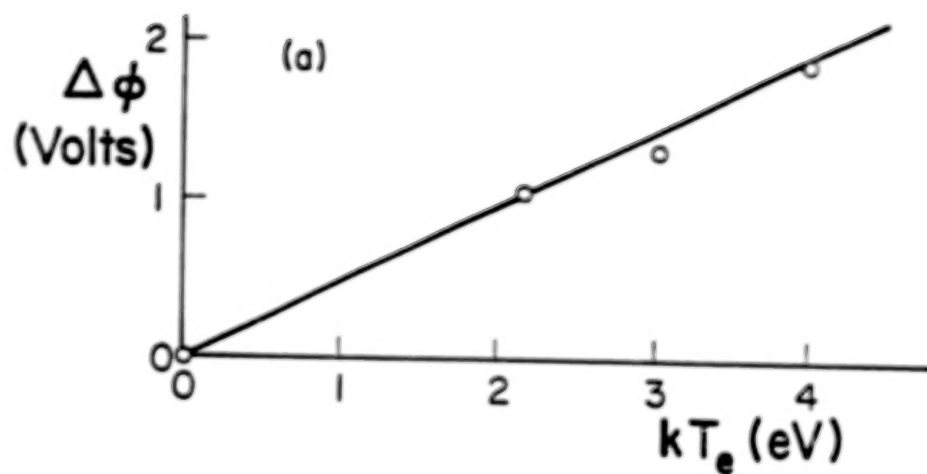


Figure 7. (a) The potential difference  $\Delta\phi$  between the plasma and the inflection point of the dip, as a function of electron temperature. A straight line is drawn through the data. (b) The penetration of the dip ( $d$ ) as a function of plasma density. A smooth curve is drawn through the data.

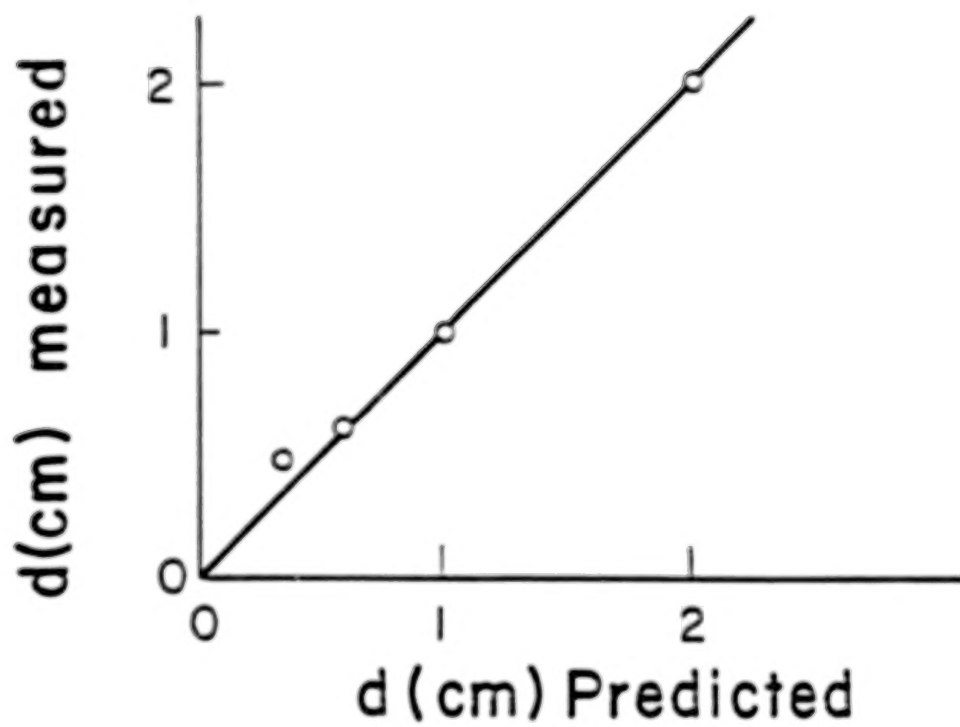


Figure 8. A comparison between measured values of  $d_{\min}$  and values predicted by using space charge limited electron flow to the plate.

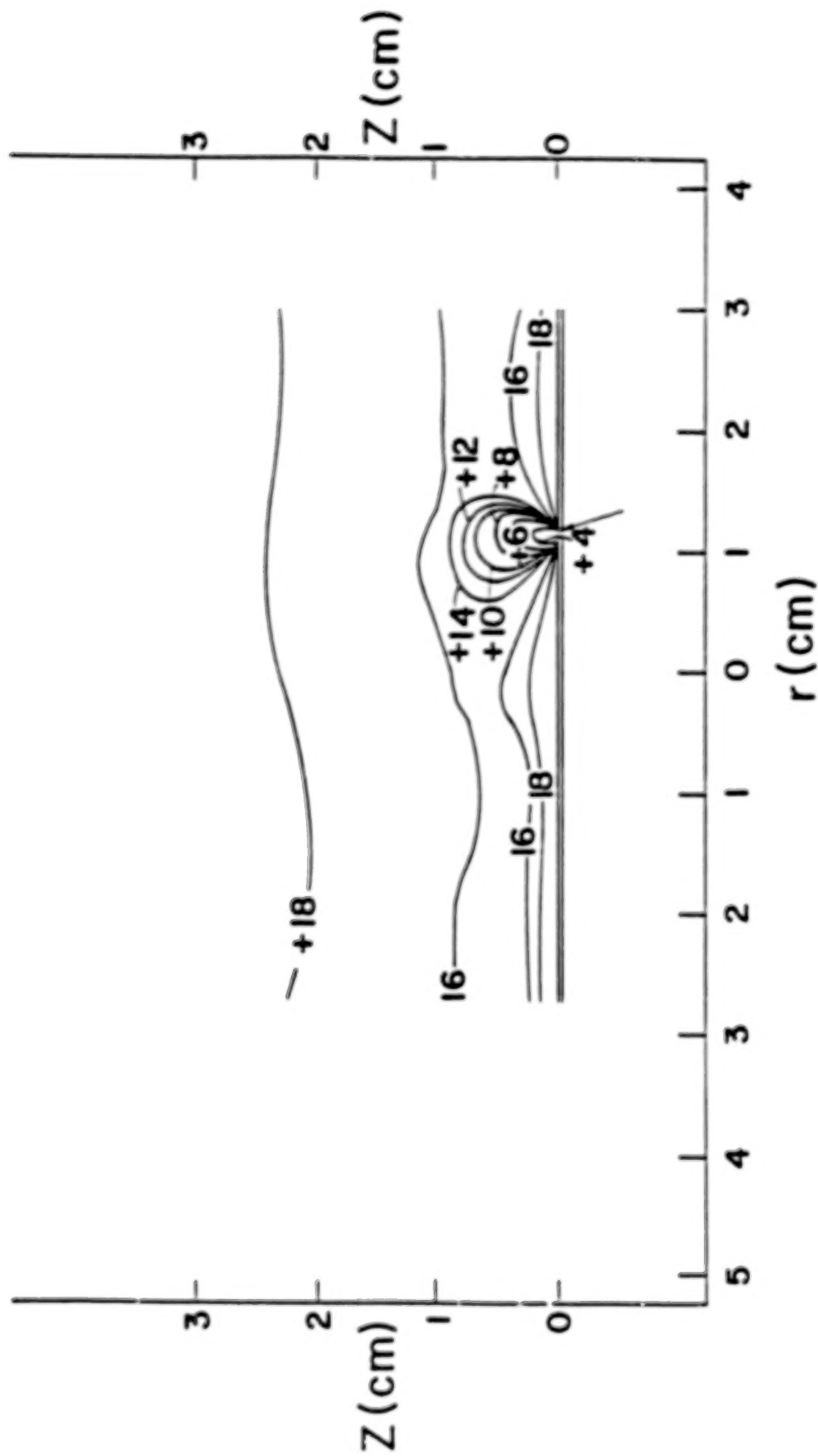


Figure 9. The equipotential contours near a circular brass plate ( $r = 3.5$  cm, 2 mm thick). Note the contours near a grease fingerprint (labeled by the arrow). The plate is in the center of the multidipole soup pot device, 10 cm from one end.

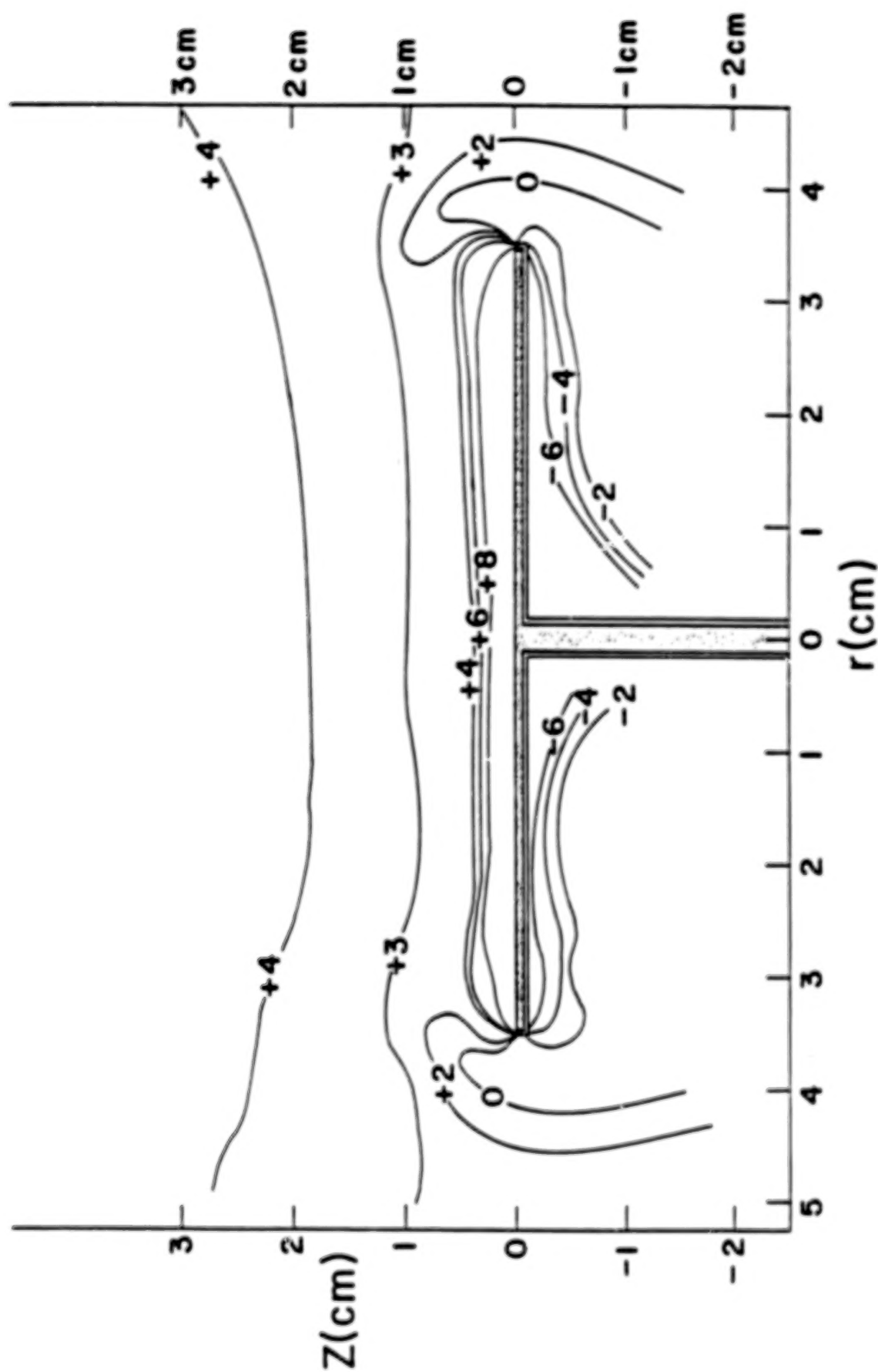


Figure 10. The equipotential contours near a clean plate. The back of the plate, the edges of the plate, and the support are covered with ceramic.

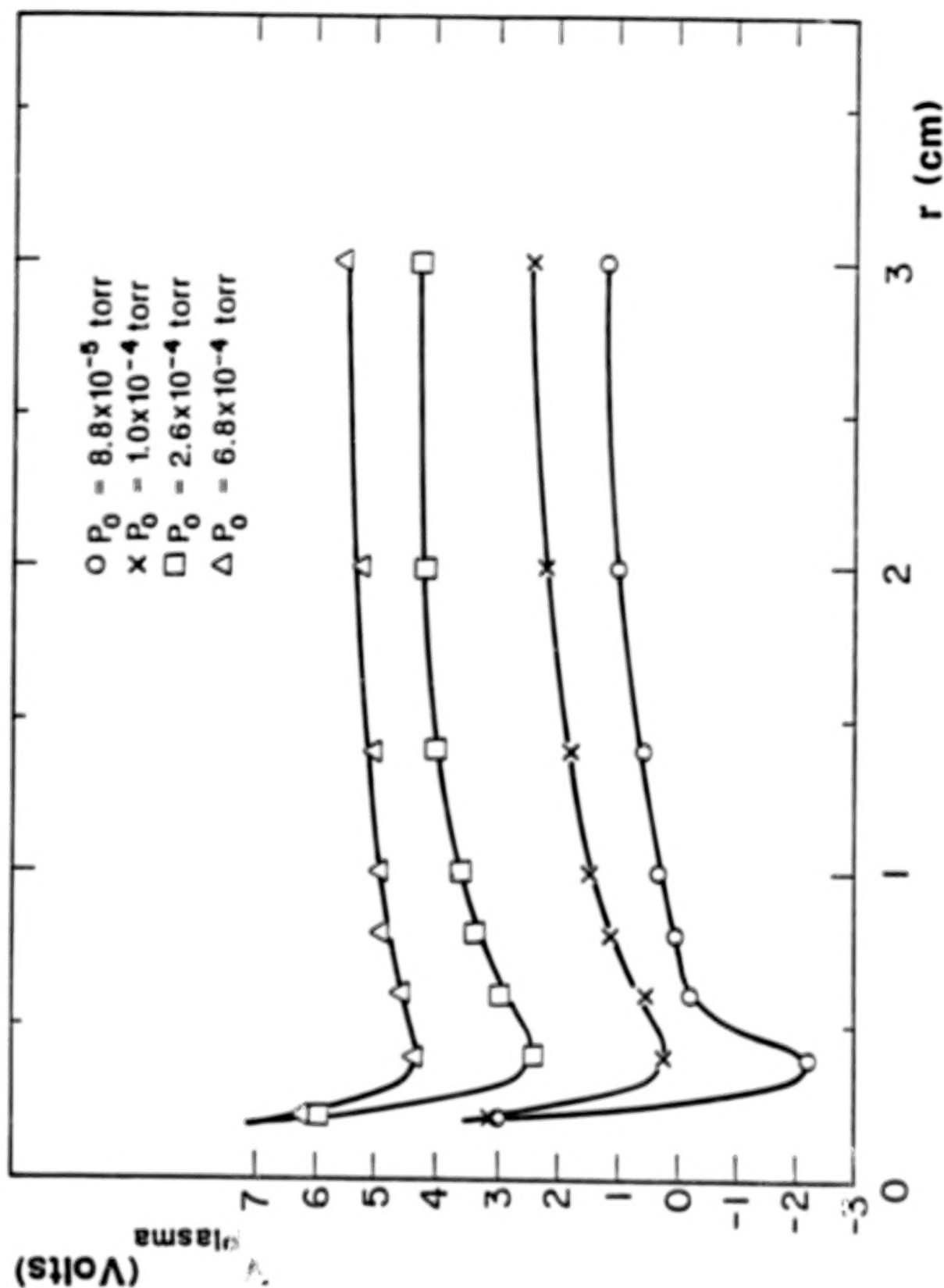


Figure 11. Axial potential profiles, near the positively biased disc, at several neutral pressures. As the neutral pressure is increased, the size of the dip  $\Delta\phi$  is seen to be reduced.

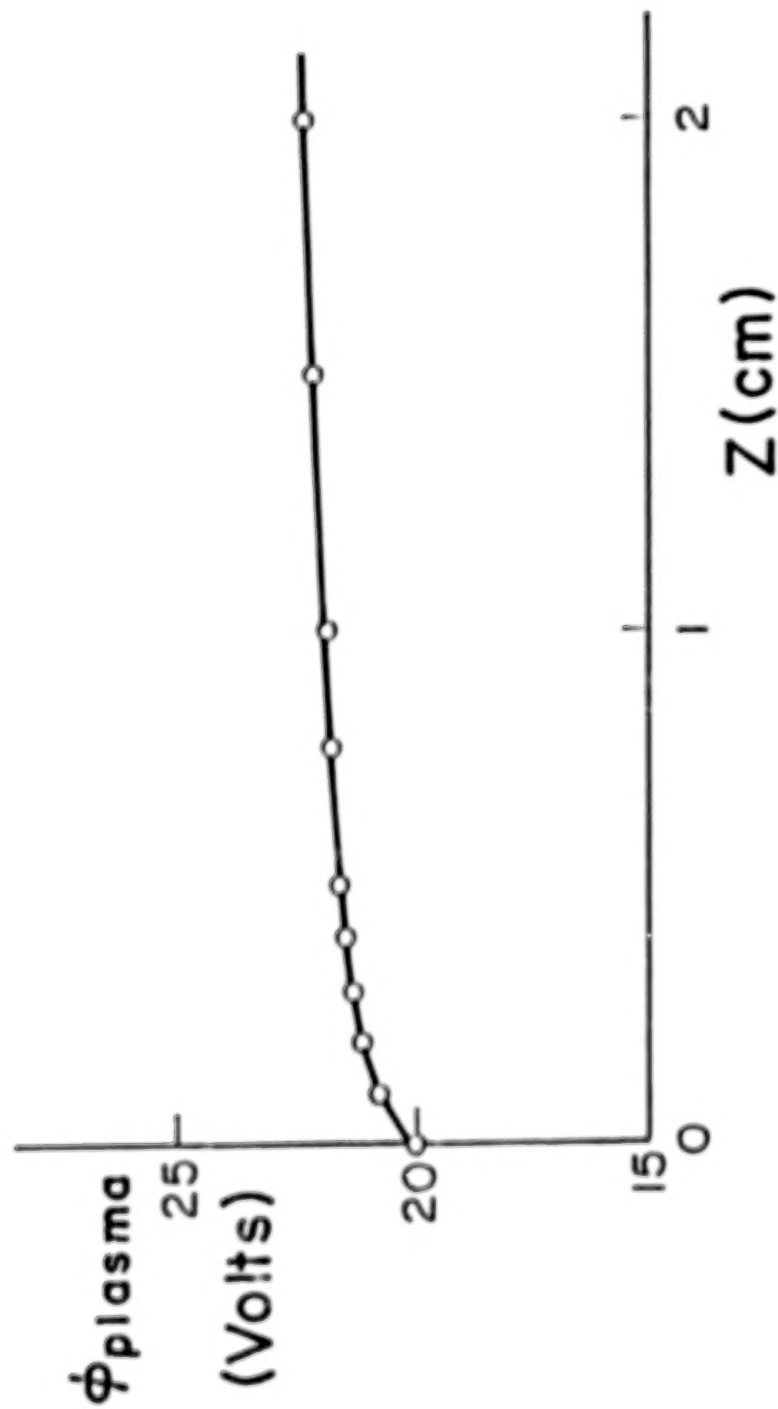


Figure 12. The plasma potential measured on the axis of the plate with ceramic removed from the back.



N87

23317

UNCLAS

**A LABORATORY INVESTIGATION OF POTENTIAL DOUBLE LAYERS**

Philip Leung  
Jet Propulsion Laboratory  
California Institute of Technology  
Pasadena, California 91109, U.S.A.

**ABSTRACT**

In a triple plasma device, the injection of electron current from the source chamber to the target chamber causes the formation of a potential double layer. At a low current density, the space charge of the injected current produces a virtual cathode-type potential double layer. This double layer is stable, and various wave instabilities are observed to associate with this double layer. As the current density is increased, the double layer becomes unstable, and a moving double layer results. As the current density is increased further, the enhanced ionization causes the neutralization of the space charge of the electron beam, and the "beam plasma discharge" is ignited.

**I. INTRODUCTION**

The importance of potential double layers in astrophysical phenomena is well known (Alfvén, 1958). Theoretical work on potential double layers has indicated that wave instabilities may be responsible for the formation of potential double layers. However, different theoretical models have predicted different instabilities in order for a double layer to form. These instabilities include ion-acoustic (Sato and Okuda, 1980), ion hole (Schamel and Bujarbarua, 1983), Langmuir turbulence (Levine and Crawford, 1978), and Buneman (Iuzuka et al., 1979) instabilities. This paper presents experimental measurements of the characteristics of instabilities associated with a potential double layer. The double layers were produced in a conventional triple plasma device by the injection of an electron current from the source chamber to the target chamber. Different types of wave turbulences were observed to be associated with a stable double layer. Despite the presence of these wave instabilities, the virtual cathode-type mechanism (Leung et al., 1980) associated with the space charge of the injection electron current was found to be the single most important mechanism responsible for the double layer formation. Experimental data on the transition of the double layer phenomenon into the beam plasma discharge phenomenon (Bernstein et al., 1978) will also be discussed. This transition was due to the transition from space charge-limited electron current flow to source temperature-limited electron current flow. This transition further illustrates the importance of space charge effects in the stability and formation of potential double layers.

Part II of this paper describes the experimental setup, part III presents the measurements of wave instabilities associated with a stable double layer, part IV discusses the transition of a stable double layer into the beam plasma discharge phenomenon, and part V is the conclusion.

**II. EXPERIMENTAL SETUP**

The experiments were performed in a modified triple plasma device. The details of this setup have been described elsewhere (Leung et al., 1980). In most of the experiments, the system was operated as a double plasma device. The diagnostics consist of a two-sided Langmuir probe and an emissive probe, both mounted on the same

\*

C-2

probe shaft. This permits measurements of plasma potential and plasma electron distribution function simultaneously. An electron gun (5-9 keV, 100 nA) is available for electric field measurements. This gun provides a non-perturbative diagnostic to verify the existence of a double layer. The ion dynamics are measured by an electrostatic energy analyzer.

A shielded RF probe is used to measure the unstable wave spectrum. Wavelength measurements are made by two probe correlational methods. In this series of experiments, the frequency of unstable waves ranges from 50 kHz to 100 MHz.

### III. RESULTS

A steady state double layer is produced by operating the system in a double plasma device configuration. The potential profile and the grid biases are shown in Figure 1. The plasma parameters associated with this double layer are shown in Figure 2. In the high potential side, the electron distribution function is in the form of a bump-on-tail distribution. In the low potential region, the electron distribution function is a modified drifting Maxwellian. In the low potential region, counterstreaming ion beams are present; whereas, in the high potential region, only thermal ions are present. These particle distributions are very important for the understanding of a potential double layer since they are responsible for both the self-consistent potential profile and the wave instabilities.

The typical frequency spectrum associated with a stable double layer is shown in Figure 3. The frequency spectrum can be divided into two regions: (1) the high frequency spectrum around the electron plasma frequency and (2) the low frequency spectrum in the vicinity of the ion plasma frequency. The unstable waves at  $\omega_{pe}$  only have significant amplitude at the high potential side. This is because the bump-on-tail electron distribution on the high potential side excites beam plasma instabilities. The cross-spectral intensity obtained by a two-probe correlation method is shown in Figure 4a. The value of the wavelength derived from this interferometer trace indicates that the waves propagate at approximately the same velocity as the electron beam that is present in the high potential region. Consequently, the waves are excited by the beam-plasma (Schmidt, 1979) instabilities.

The waves around the ion plasma frequency range from  $0.1 \omega_{pi}$  to  $3 \omega_{pi}$ , where  $\omega_{pi}$  is the ion plasma frequency. The amplitudes of these waves are significant only in the low potential region. Figure 4b shows a typical cross-spectral density function obtained by the two-probe correlation measurement technique. The dispersion relationship of these low frequency waves is shown in Figure 5. The data displayed in Figure 5 show that the phase velocity of most waves is faster than  $V_b$ , where  $V_b$  is the ion beam velocity associated with the stable double layer. Due to their fast phase velocity and the fact that the unstable waves are present above the ion plasma frequency, the waves cannot be excited by the ion-beam plasma instabilities.

A theoretical model was developed to interpret the dispersion relationship shown in Figure 5. The details of this model are discussed in a previous publication (Leung, 1980). The model indicates that the waves around the ion plasma frequency are excited by a modified Buneman-type (Buneman, 1959) instability. The main interaction mechanism is operating between the drifting electrons and the ion beam that is propagating at the same velocity as the electron drift. In the stationary frame of the ion beam, the excited waves have Buneman-type properties. The observed dispersion relationship is just the Buneman dispersion relationship after a transformation from the stationary frame of the ion beam to the stationary frame of the laboratory. The drifting electrons should also interact with the ion beam that propagates in the opposite direction; however, the resulting unstable waves will be subjected to strong Landau damping. This is because the phase velocity of this unstable wave in the laboratory frame will be very close to the velocity of the preceding (rightward in Figure 2) ion beam. Consequently, this mode was not observed in the measurements. The theoretical model discussed in Leung (1980) predicts a very high growth rate. In our measurements, the growth of the Buneman-type waves was not observed. This could be due to the fact that the high growth rate caused the waves to saturate near the grid.

#### IV. TRANSITION OF A STABLE DOUBLE LAYER INTO THE BEAM PLASMA DISCHARGE

The current that flows from the source to the target region can be increased by increasing the grid bias. As the grid bias is increased, the potential drop across the double layer also increases. This trend continues until the potential drop reaches 14 V, which is approximately the first ionization potential of argon. Beyond this point, a sudden increase in the grid bias causes an abrupt increase in the current; and, at the same time, the double layer potential profile collapses (Fig. 6). The plasma density in the target chamber increases by more than an order of magnitude and the "beam plasma discharge" (Bernstein et al., 1978) is excited. The ignition of the beam plasma discharge (BPD) phenomenon is characterized by abrupt increases in the following plasma parameters: (1) optical emission, (2) plasma density, (3) plasma current (Fig. 7), and (4) wave turbulence (Fig. 8).

It should be noted that before the ignition of BPD, the double layer becomes unstable, and large amplitude potential fluctuations are observed. Figure 9a shows the fluctuations in the local electric field as measured by the diagnostic electron beam. The electric field fluctuates at a frequency of approximately 1 kHz. Figure 9b shows the signal detected by the Langmuir probe. The fluctuation in the probe current was due to the change in local plasma potential induced by the moving double layer. The temporal change in potential profile was obtained by performing a time sampling of the emissive probe trace. Figure 10 shows the time development of the potential profile. In this figure,  $t = 0$  is chosen arbitrarily. The data show that the double layer is no longer stable but is moving toward the end of the chamber, i.e., away from the source. The velocity of propagation varies, but under most conditions it is faster than the ion-acoustic speed. The data presented in Figure 10 indicate the significance of the space charge of the electron current in double layer formation. At  $t = 150 \mu\text{s}$ , the normalized potential of the low potential region has a value of 2, and the amount of electron current that can flow from source chamber to target chamber is very large (Figs. 11a,b). At  $t = 200 \mu\text{s}$ , the normalized potential has a value of 6, the flow of current from source to target is severely limited, and the potential double layer is not well defined. The cycle for the formation and disappearance of a potential double layer repeats itself. This is responsible for the observed fluctuation in the potential profile. A detailed model (Leung et al., 1980) on double layer formation has been discussed elsewhere and will not be discussed in this article.

Referring again to Figure 10, at  $t = 150 \mu\text{s}$ , the current limitation by the space charge effect is at its minimum. If the absolute potential of the low potential region is further reduced, the current flow is significantly increased (Figs. 11a,b). This increase in current increases the rate of ionization in the high potential region. The increase in the ion fluxes further reduces the space charge in the low potential region, and eventually the space charge limitation of the electron current flow is eliminated. The uninhibited flow of current leads to the ignition of the beam plasma discharge.

It should be noted that the transition from double layer (DL) to BPD is not a reversible process. By lowering the bias, the BPD will not transform back to a DL immediately. A DL is formed only when the bias voltage is lowered to a value such that the ionization cross-section is substantially reduced.

The injection of electron current from the source to the target chamber is very similar to the injection of an electron beam from a rocket to the ionosphere. BPD has been observed in several rocket experiments (Hallinan et al., 1978). In some of the beam injection experiments, large amplitude fluctuations (Winckler, 1980) in the electron return current and in the optical emission were also observed. This type of fluctuation could be due to the excitation of moving double layer-type potential structures in the ionosphere. The space shuttle and the future Space Station, with its diverse sophisticated diagnostic instruments, should be able to provide a test bed for beam-excited double layer structures in the ionosphere.

## V. CONCLUSIONS

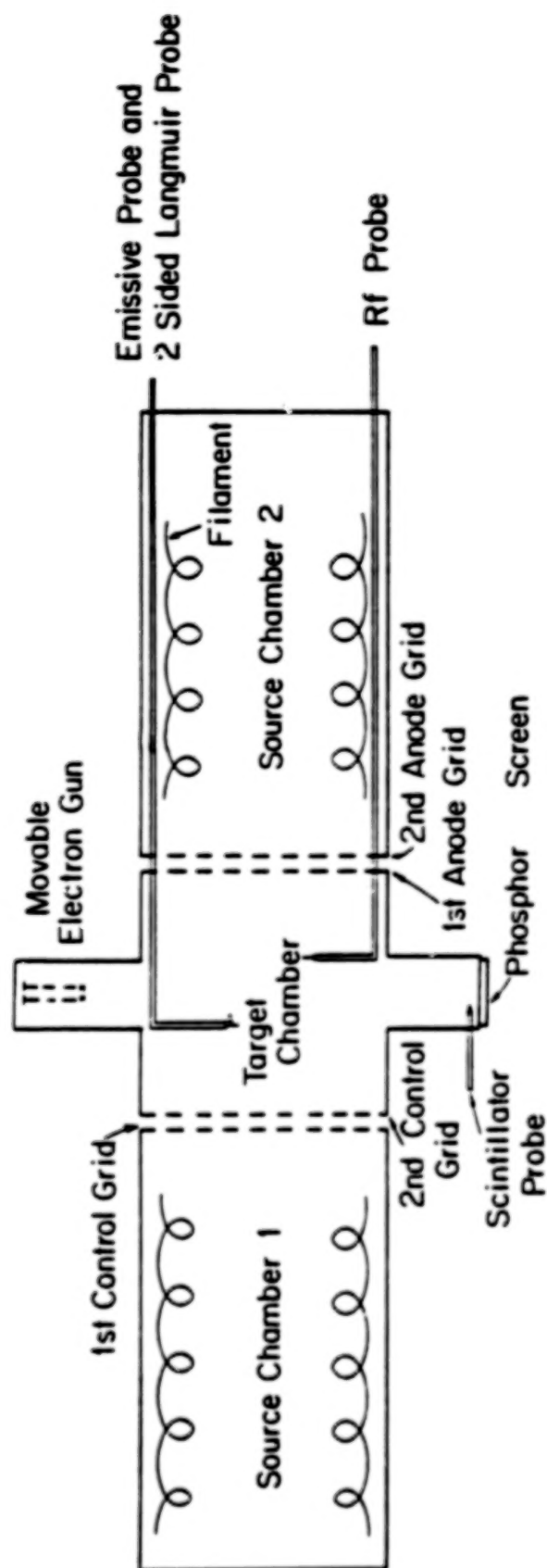
This paper has discussed the instabilities associated with a stable double layer. The unstable wave spectrum around the electron plasma frequency is due to the excitation of the beam plasma instabilities by the electron beam that is present in the high potential region. The unstable waves around the ion plasma frequency are due to the excitation of the Buneman-type waves by the electron current.

The data in our experiments show that as the grid bias is increased, there is a transition from a stable double layer to a moving double layer, followed by the ignition of beam plasma discharge. This transition shows that the space charge of the injected electron current plays a very important role in double layer formation. The role of instabilities is not evident in our experimental measurements. Since wave instabilities are always associated with double layers, their role in modifying the characteristics of DLs is undeniable and should be further investigated.

## REFERENCES

- Alfvén, H., *Tellus*, 10, 104 (1958).  
Bernstein, W., et al., *Geophys. Res. Lett.*, 5, 127 (1978).  
Buneman, O., *Phys. Rev.*, 115, 503 (1959).  
Hallinan, T., H. C. Stenbaek-Nielsen, and J. R. Winckler, *J. Geophys. Res.*, 83, 3263 (1978).  
Iizuka, S., K. Saeki, N. Sato, and Y. Hatta, *Phys. Rev. Lett.*, 43, 1404 (1979).  
Levine, J., and F. Crawford, SU-IPR Report 78-7, Stanford University, CA, 1978.  
Leung, P., "Interaction Between Particle Beams and Nonlinear States," Ph.D. Thesis, University of California, Los Angeles, 1980.  
Leung, P., A. Wong, and B. Quon, *Phys. Fluids*, 23, 992 (1980).  
Sato, T., and H. Okuda, *Phys. Rev. Lett.*, 44, 740 (1980).  
Schamel, H., and S. Bujarbarua, *Phys. Fluids*, 26, 190 (1983).  
Schmidt, G., *Physics of High Temperature Plasmas*, Academic Press, 1979.  
Winckler, J. R., *Rev. Geophys. Space Phys.*, 18, 659 (1980).





# POTENTIAL PROFILE

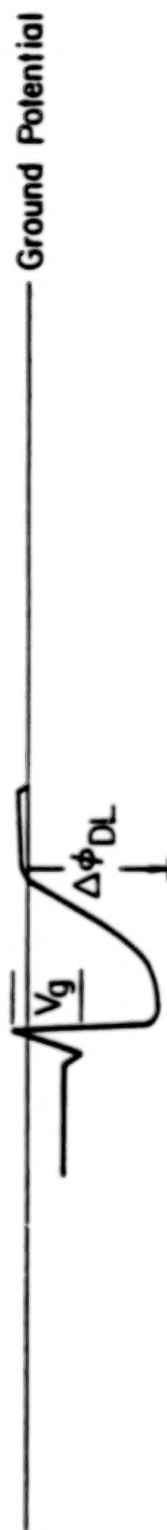


Figure 1. Schematics of the triple plasma device.



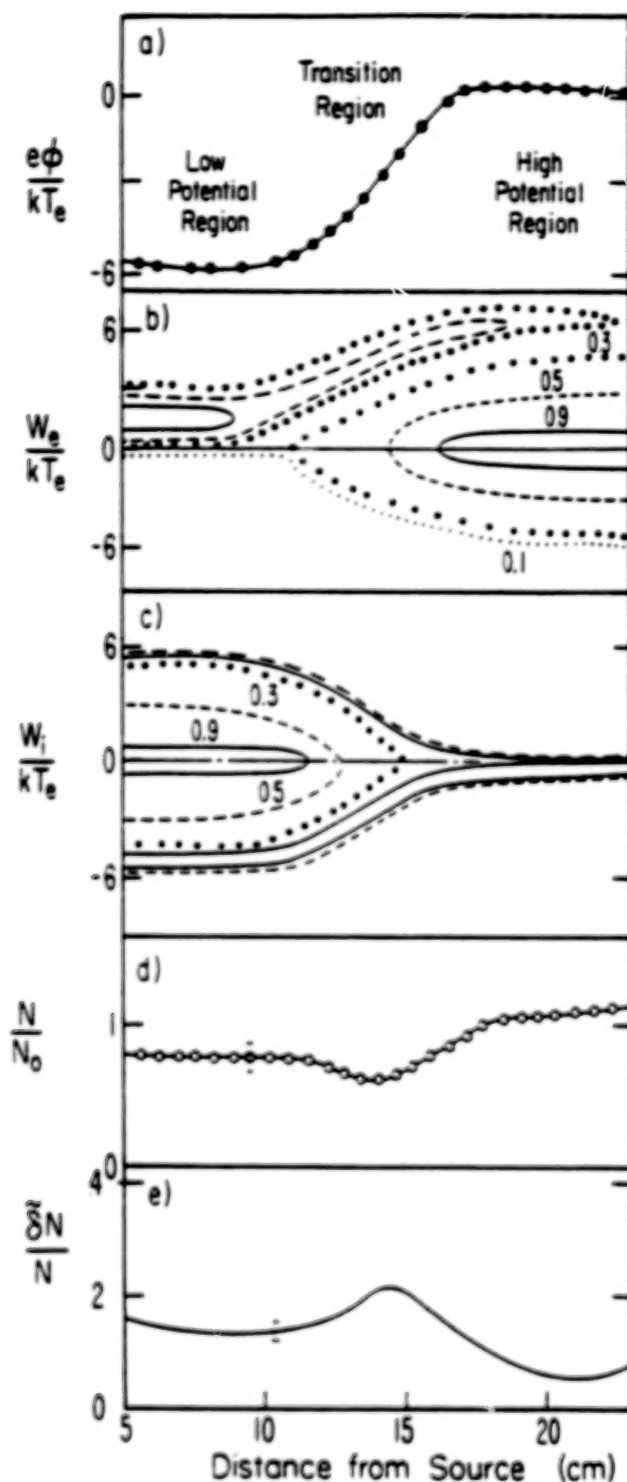


Figure 2. The plasma parameters associated with a potential stable double layer. The plasma parameters are normalized with respect to electron temperature  $T_e$  and the electron density at the high potential side. (a) Plasma potential profile. (b) One-dimensional phase-space representation of electron distribution,  $W_e = 1/2 m_e v^2$ , where  $W_e$  is the normalized electron energy. The numbers on the curves indicate the normalized height of the distribution function. The negative values of  $W_e/kT_e$  represent velocity in the opposite direction, (c) Phase representation of the ion distribution function,  $W_i = 1/2 M_i v^2$ . (d) Relative electron density.  $N$  is the spatial density in the target region. (e) Relative peak-to-peak density fluctuation.

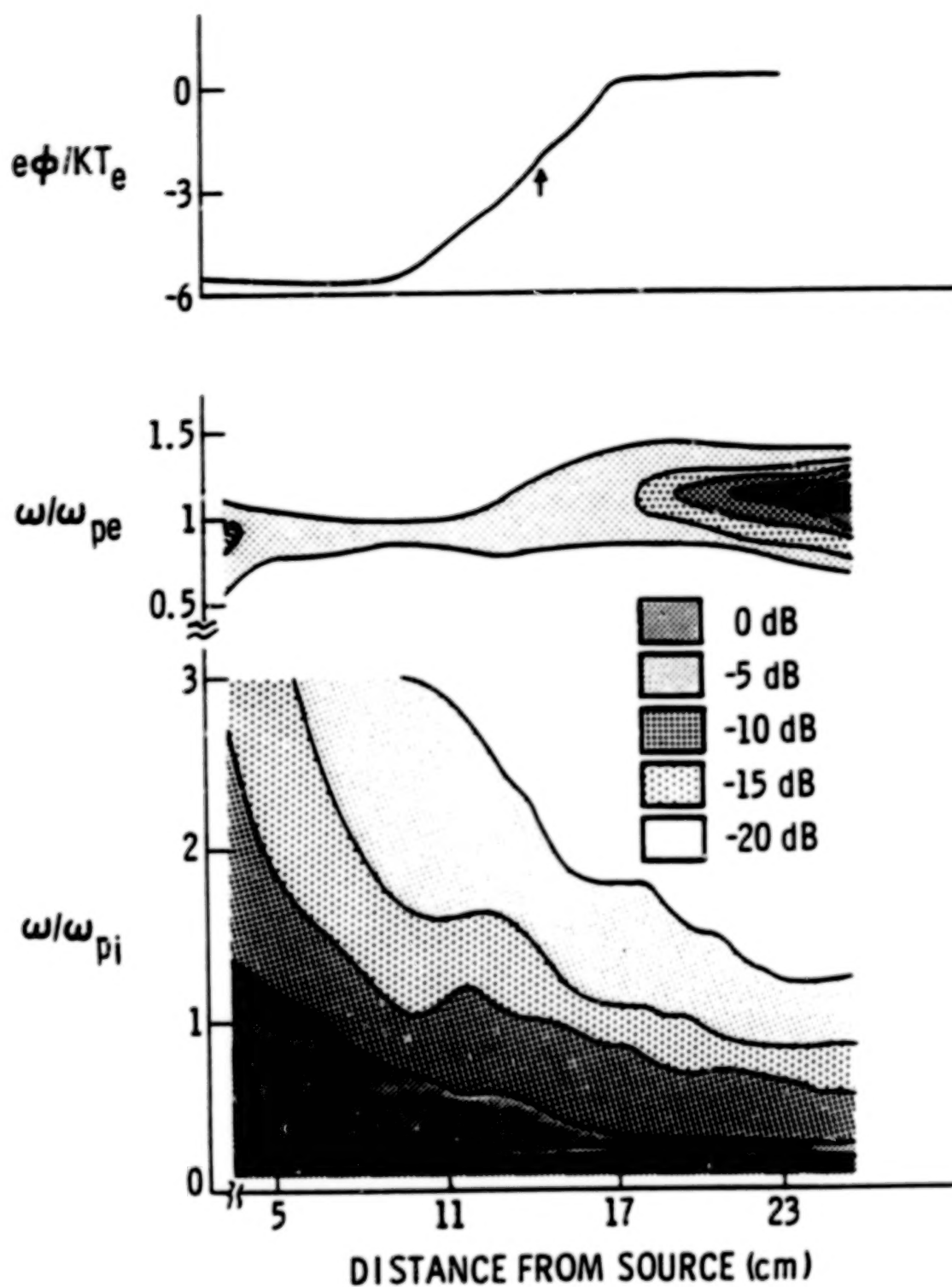


Figure 3. The power spectrum of unstable waves associated with a stable double layer, showing the power level of different frequencies present at different points along the potential profile (top). The power levels are divided into five arbitrary levels. The frequencies of unstable waves are normalized to electron plasma frequency ( $\omega_{pe}$ ) and ion plasma frequency ( $\omega_{pi}$ ).

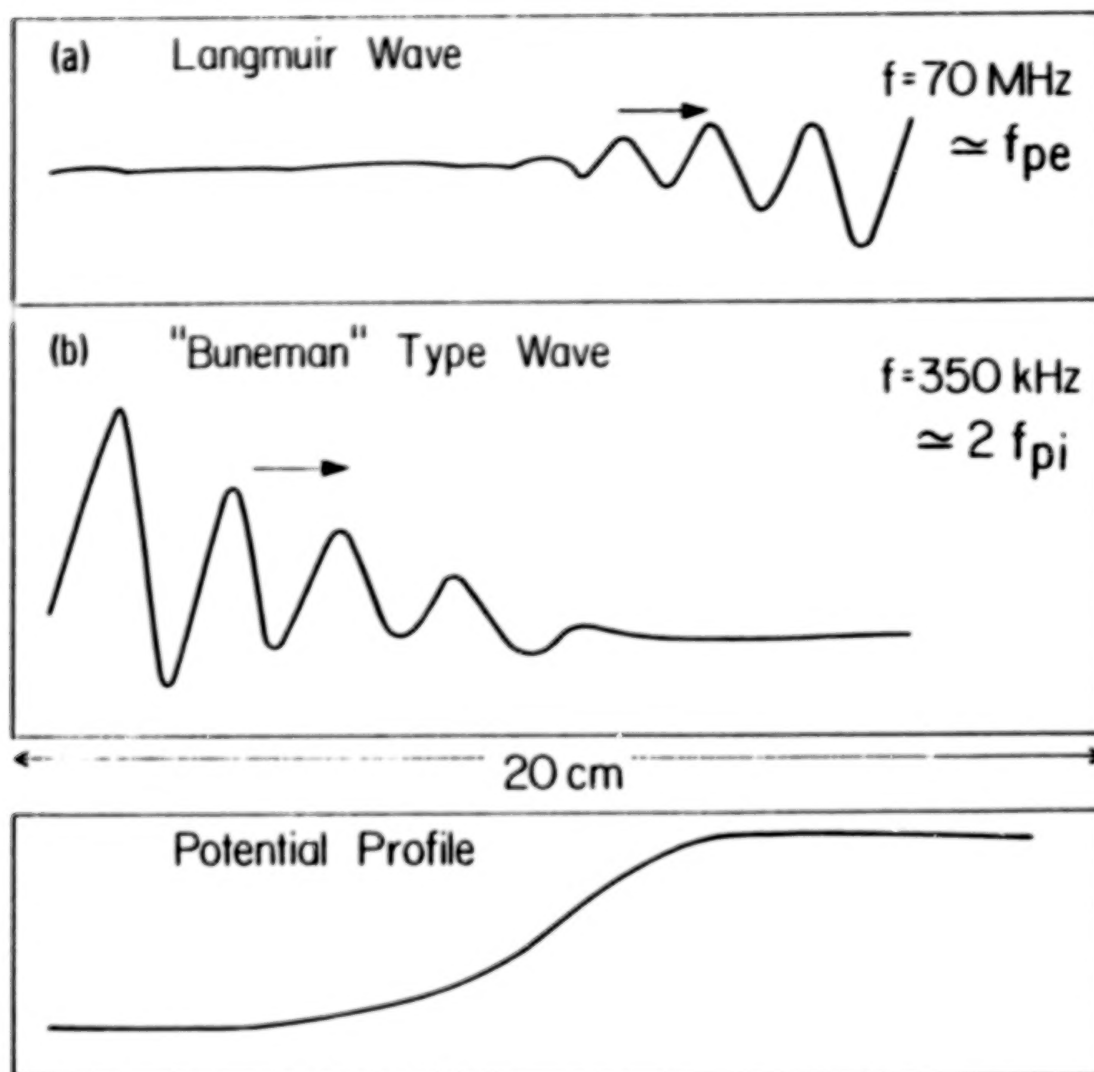


Figure 4. The cross power spectral density of the Langmuir wave and Buneman-type waves. The potential profile is also shown here for reference.

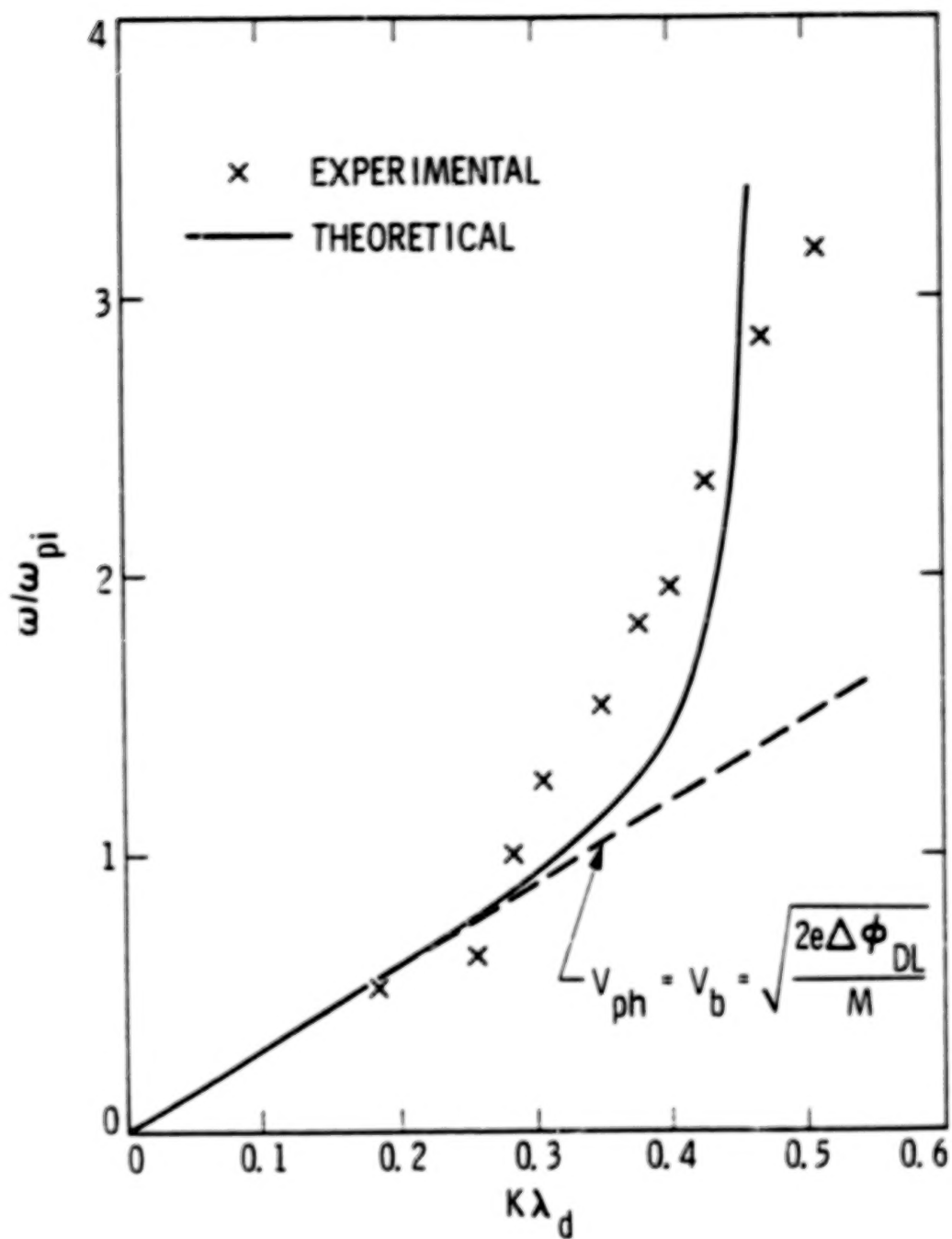


Figure 5. The dispersion relationship of the Buneman-type wave: x represents the experimental data, and the solid line is the theoretical dispersion relationship.

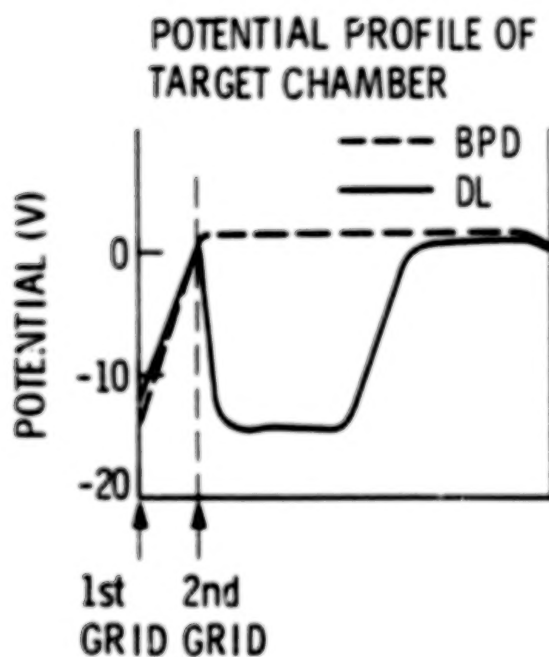
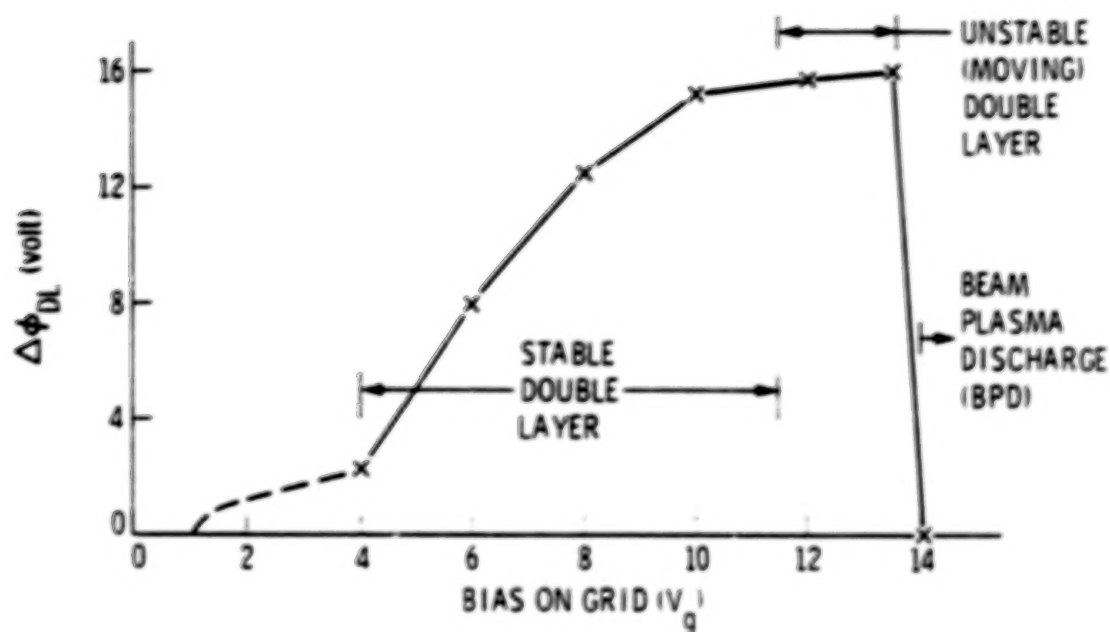


Figure 6. The change in potential drop of the double layer as the grid bias is increased. The beam plasma discharge is ignited when the grid bias exceeds 13 V. The potential profile of the target chamber before and after the ignition of the BPD is shown in the lower diagram.

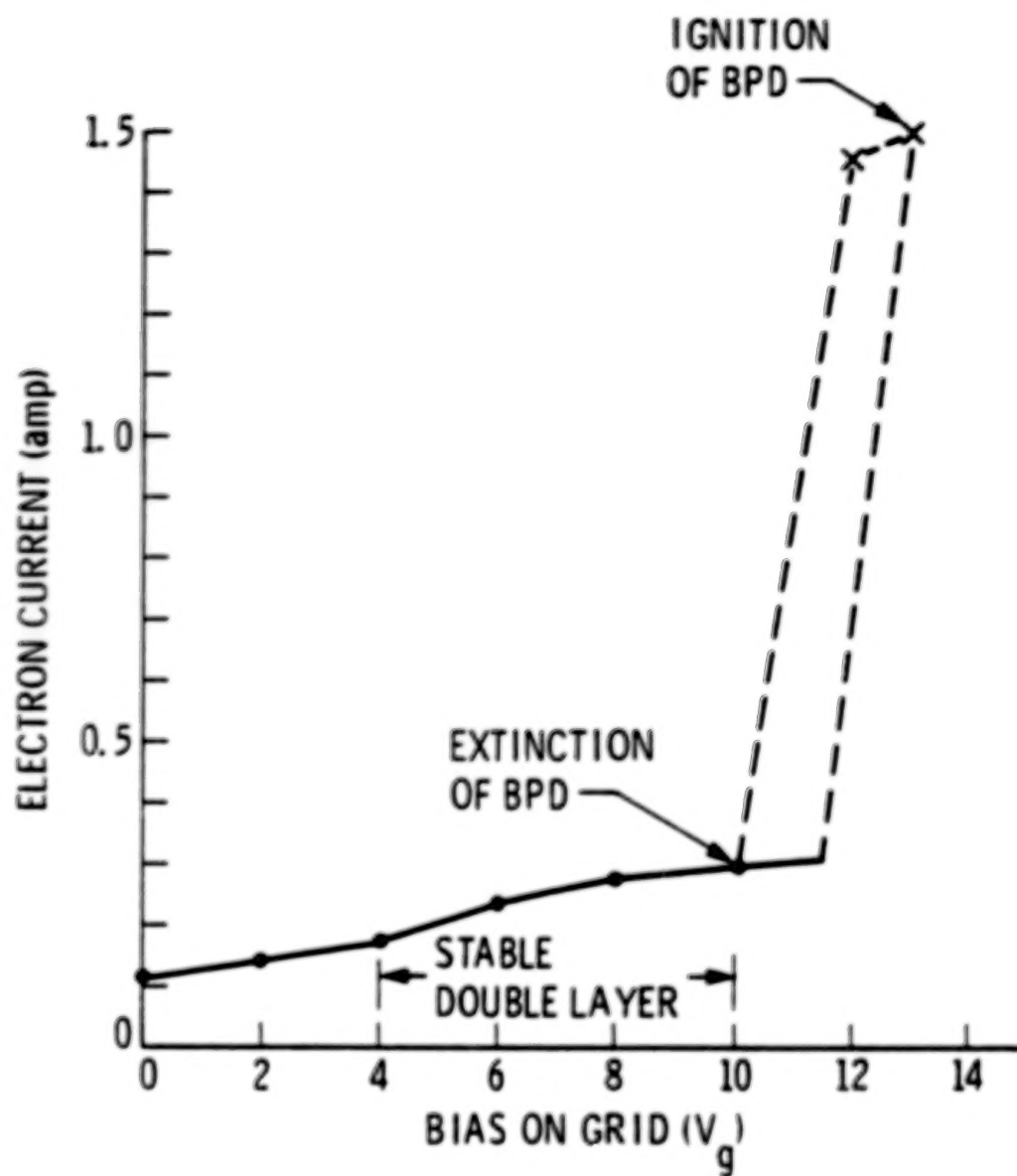


Figure 7. The injected electron current as a function of the grid bias showing the ignition of the BPD.



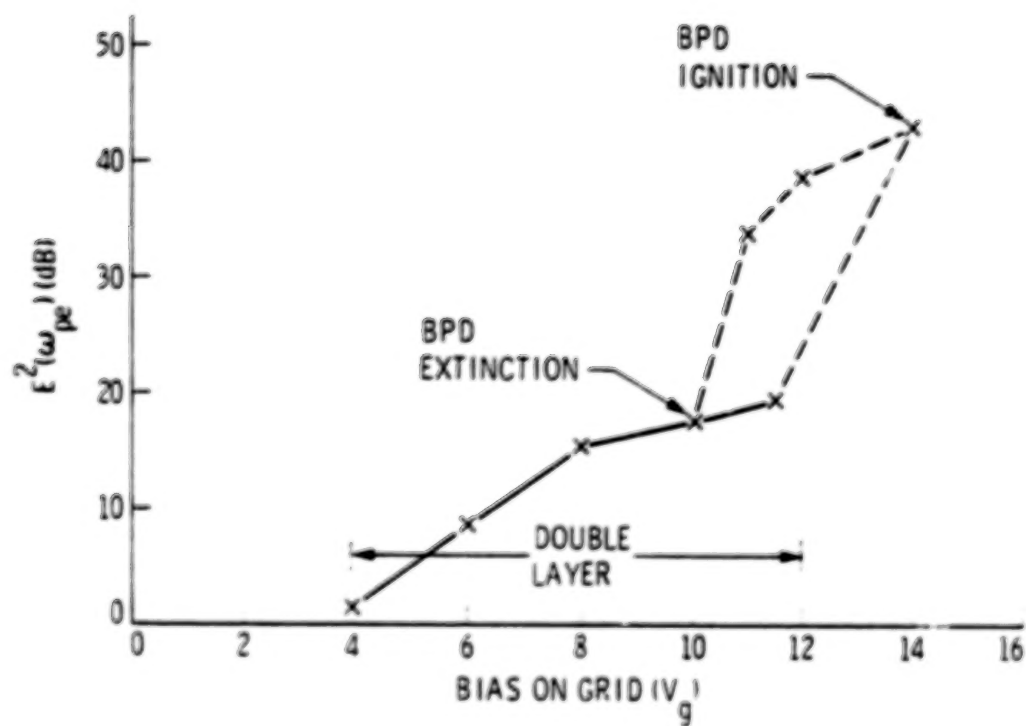


Figure 8. The wave turbulence level as a function of grid bias showing the ignition of BPD. When the BPD is ignited, the electron distribution function is a bump-on-tail distribution.

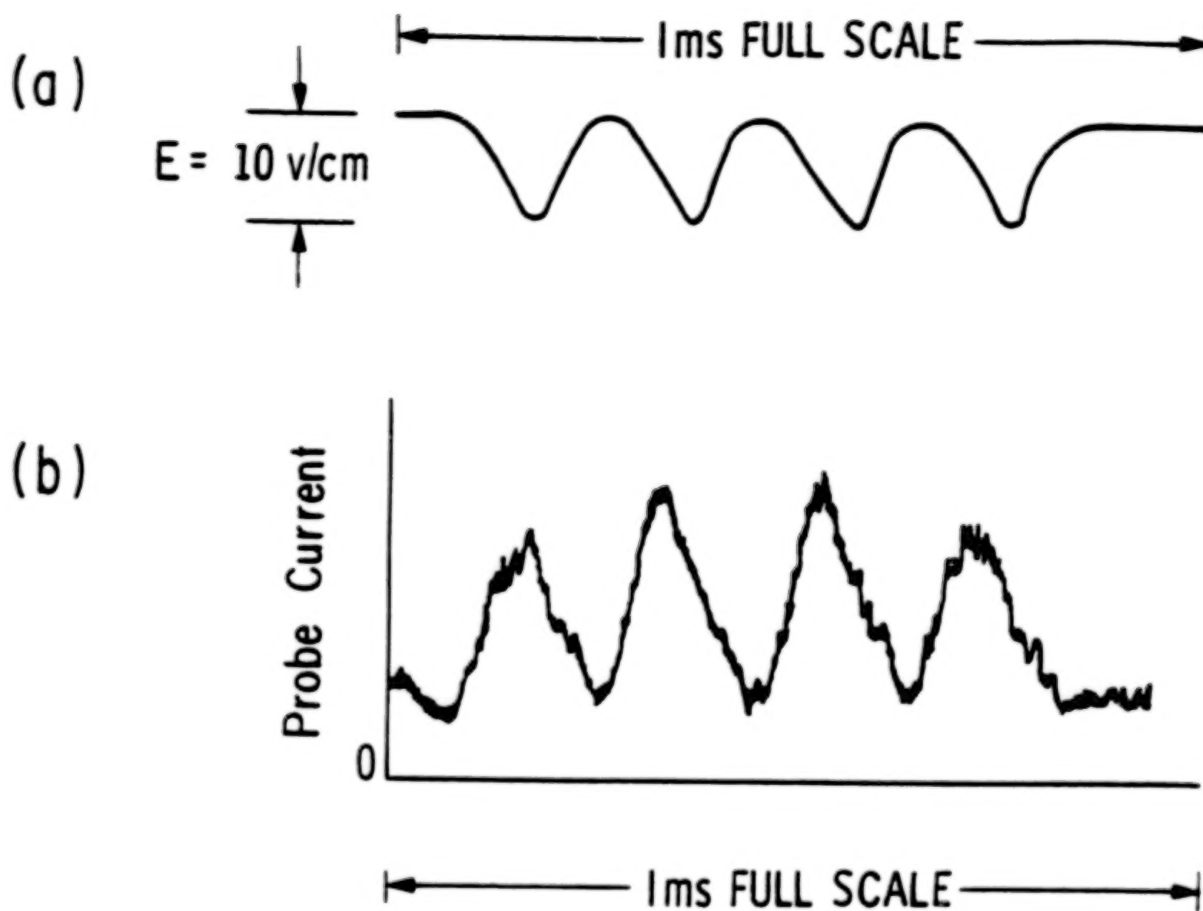


Figure 9. The top trace (a) shows the fluctuation in the local electric field as measured by the diagnostic electron beam. The fluctuation is due to the motion of the double layer. The corresponding fluctuation in the Langmuir probe current is shown in the bottom trace (b).

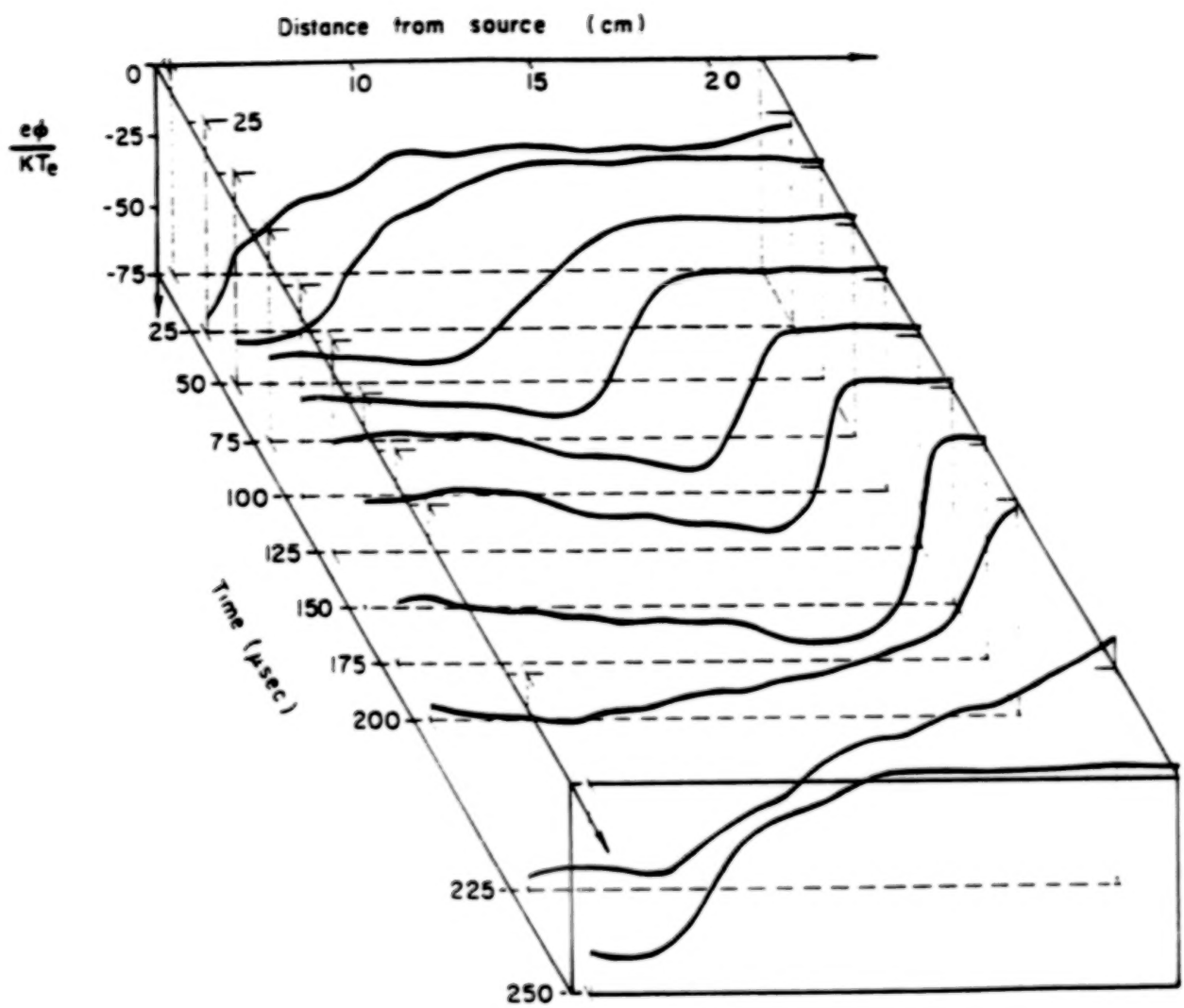


Figure 10. Time development of moving double layers.

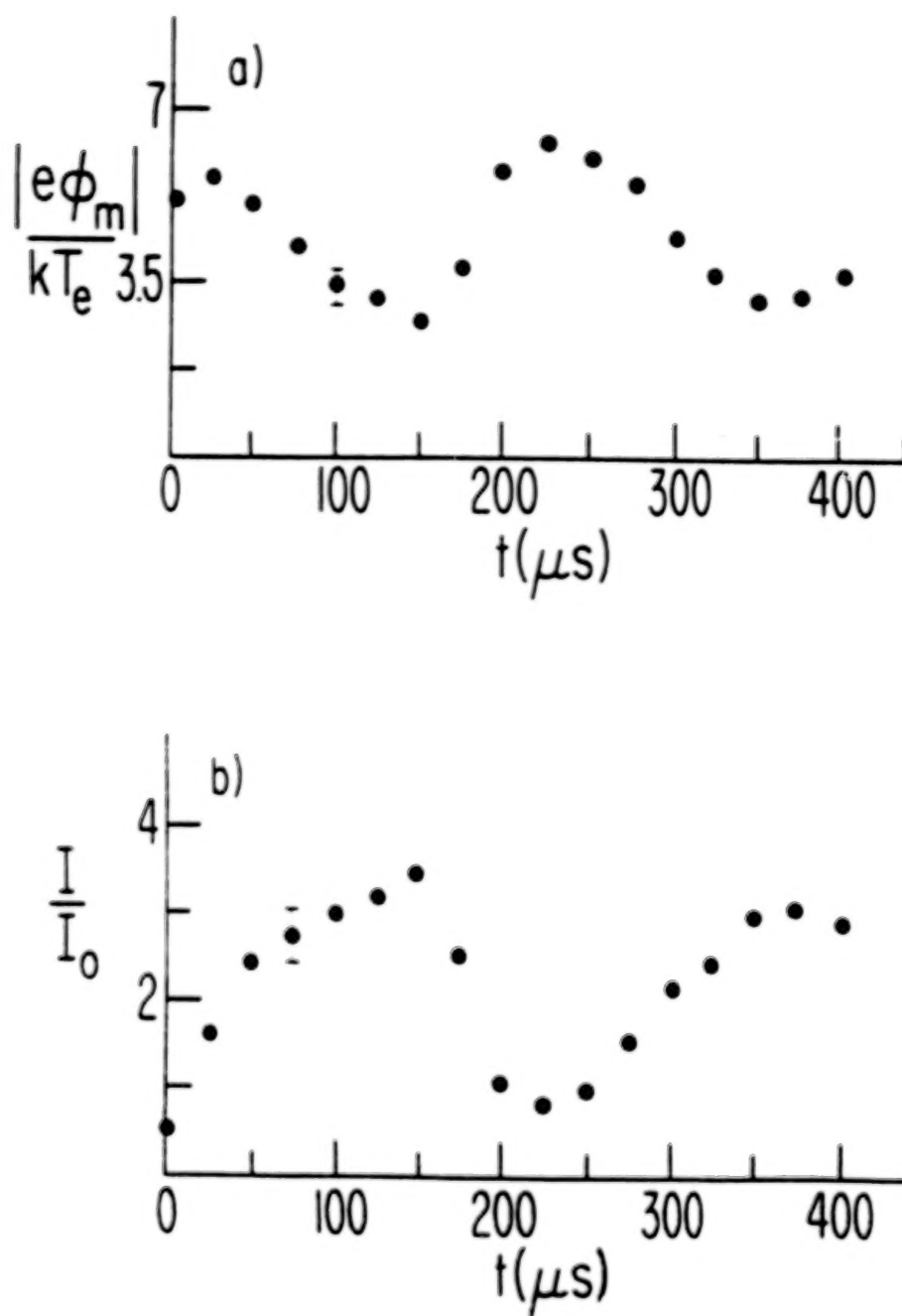


Figure 11. The two important parameters that control the moving double layers: (a) the potential of the low potential region and (b) the injection current as a function of time.

N87

23318

UNCLAS

**EXPERIMENTAL OBSERVATION OF ION-ACOUSTIC DOUBLE LAYERS  
IN LABORATORY PLASMA**

Y. C. Saxena  
Plasma Physics Programme  
Physical Research Laboratory  
Ahmedabad 380009, India

**ABSTRACT**

Computer simulations indicate existence of weak, electrostatic potential structure with  $e\Delta\phi/kT_e \lesssim 1$ , having a negative potential dip on low potential side in a current carrying plasma (DeGroot et al., 1977; Sato and Okuda, 1980). These types of structures, known as ion-acoustic double layers, have been analytically correlated with the ion-holes which are known to be nonlinear extensions of normally damped slow ion-acoustic modes (Schamel, 1979; Hasegawa and Sato, 1982). Ion-acoustic double layers have also been evoked for explaining recent satellite observations (Hudson et al., 1983).

In this paper we present experimental results on the observation of ion-acoustic double layers in laboratory plasma. In a double-plasma device, modified suitably to inject electron beam into the target plasma, modulation of the beam through a step potential leads to excitation of ion-acoustic fluctuations. The fluctuations, growing away from the separating grids, develop into weak asymmetric ion-acoustic double layers. The observations are compared with the scenario emerging out of the computer simulations and analytical results on ion-acoustic double layers.

**REFERENCES**

- DeGroot, J. S., C. Barnes, A. E. Walstead, and O. Buneman, *Phys. Rev. Lett.*, **38**, 1283 (1977).  
Hasegawa, A., and T. Sato, *Phys. Fluids*, **25**, 632 (1982).  
Hudson, M. K., W. Lotko, I. Roth, and E. Witt, *J. Geophys. Res.*, **88**, 916 (1983).  
Sato, T., and H. Okuda, *Phys. Rev. Lett.*, **44**, 740 (1980).  
Schamel, H., *Physica Scripta*, **20**, 336 (1979).

PRECEDING PAGE BLANK NOT FILMED



## **II. THEORY AND SIMULATION OF DOUBLE LAYERS**

**PRECEDING PAGE BLANK NOT FILMED**

N87

23319

UNCLAS

## A NEW HYDRODYNAMIC ANALYSIS OF DOUBLE LAYERS

Heinrich Hora  
Department of Physics and Astronomy  
and  
Iowa Laser Facility  
The University of Iowa  
Iowa City, Iowa 52242, U.S.A.

## ABSTRACT

A genuine two-fluid model of plasmas with collisions permits the calculation of dynamic (not necessarily static) electric fields and double layers inside of plasmas including oscillations and damping. For the first time a macroscopic model for coupling of electromagnetic and Langmuir waves was achieved with realistic damping. Starting points were laser-produced plasmas showing very high dynamic electric fields in nonlinear force-produced cavitous and inverted double layers in agreement with experiments. Applications for any inhomogeneous plasma as in laboratory or in astrophysical plasmas can then be followed up by a transparent hydrodynamic description. Results are the rotation of plasmas in magnetic fields and a new second harmonics resonance, explanation of the measured inverted double layers, explanation of the observed density-independent, second harmonics emission from laser-produced plasmas, and a laser acceleration scheme by the very high fields of the double layers.

## 1. INTRODUCTION

There is a close similarity between the double layers in the surface of laser-produced plasmas and a wide class of astrophysical plasmas (Hora, 1975). In both cases a high temperature plasma is produced which expands into vacuum or into gases of much less density. During this dynamic process, a separation of space charges will happen at the plasma surfaces when the equithermal electrons with their much higher velocity than that of the ions will expand much faster generating first a negatively charged cloud followed by a positively charged cloud of the ions. Then the more or less homogeneous and space charge quasi-neutral plasma follows. The separation of the electrons and ions with a net neutral charge is a double layer (DL) in which electric fields persist within these plasma areas (Fig. 1). These fields were suggested for explaining phenomena in extraterrestrial plasmas by Alfvén (1958) not without hefty opposition of other plasma theoreticians. Even the more advanced presentation (Alfvén, 1981) was commented by Kulsrud (1983) as "Alfvén's electric fields whose origin is intuitively not clear." These fields and double layers were also suggested to be involved with the solar atmosphere (Alfvén and Carlqvist, 1967; Carlqvist, 1979, 1982; Torvén et al., 1985), in the ionosphere and magnetosphere of the Earth and the magnetosphere of Jupiter (Shawhan, 1976), and with the striated structure of the barium clouds when expanding in the ionosphere (Haerendel et al., 1976).

In laser-produced plasmas, these double layers in the surface of the expanding plasma were thought to be involved with the measured speeding up of the ions to multi-kiloelectronvolt energies as measured by Linor (1963) while the particle temperatures were 100 eV or less. However, the analysis of the double layer (Hora et al., 1967) with a derivation of its thickness being of a Debye length (Hora, 1975) arrived at a number of accelerated ions which was  $10^5$  times less than measured. A completely different acceleration mechanism had to be derived by nonlinear forces (as a generalization of the ponderomotive forces) of nonthermal electrodynamic interaction of the laser radiation with the plasma (Hora, 1969).

The direct experimental proof of the double layer and high electric fields in laser-produced plasmas was given by Mendel and Olson (1975) where the bending of an ion beam passing the double layer led to the measurement of electric fields of 10 kV/cm. The generation of electrostatic potentials was measured by Pearlman and Dahlbacka (1977), and a more detailed study using Rogowski coils (Eliezer and Ludmirsky, 1983), Figure 2, with a high temporal resolution to 50 psec or less (Ludmirsky et al., 1985; Eliezer et al., 1986) arrived at the discovery of the inverted double layers and spatially oscillating behavior of the double layers (Hora et al., 1984).

The first measurement of the double layers in space plasmas was not before 1977 (Mozer et al., 1977; Temerin et al., 1982; Temerin and Mozer, 1984) using S3-3 satellite data. These results, together with the laboratory experiments on double layers as reviewed by Hershkovitz (1985), emerged from the initial theory on plasma double layers by Langmuir (1929), Bohm (1949), Bernstein et al. (1957), and Knorr and Goertz (1974), and from computer simulations by DeGroot et al. (1977) and Sato and Okuda (1980). Turbulence theory by Yabe et al. (1981) arrived at electric fields inside of these turbulence areas and may be interpreted as some sort of a double layer behavior. The laboratory experiments showed double layers in mercury discharges (Torvén, 1981; Stangeby and Allen, 1973), Q machines (Sato et al., 1976), and triple devices where two plasmas at different electric potential are connected through grids by a plasma which has then a double layer according to the difference of the voltages plus the difference of the temperatures between the two outer plasmas (Coakley and Hershkovitz, 1981; Quon and Wong, 1976; Leung et al., 1980). The geometry can be one-dimensional (Hershkovitz et al., 1981), two-dimensional (Baker et al., 1981), or three-dimensional (Merlino et al., 1984).

A special motivation for studying the double layer in laser-produced plasma was given from the theory of the nonlinear force (Hora, 1969, 1974, 1981; Lindl and Kaw, 1971; Peratt and Watterson, 1977; Peratt, 1979). The electrodynamic, dielectrically caused acceleration of plasma by laser radiation is based on the force acting on the high density electron gas in the plasma being pushed or pulled and the ion gas has to follow then by the electric fields generated between the two fluids. When the essential properties of the nonlinear force were derived from the space charge quasi-neutral plasma model (Hora, 1969), the mentioned fields were disguised by the presumptions of the model. However, the existence of the fields of the description of the single electron motion (Hora, 1971) was evident, and a search was overdue since the beginning of the work on the nonlinear force in 1965.

While the treatment of the double layers and the high electric fields is essentially no problem on the basis of the kinetic theory with the Vlasov equation (Knorr and Goertz, 1974), the inclusion of collisions for the conditions of the high density laser-produced plasmas would have been necessary for which the complications of the collision processes for the kinetic theory would be a problem. How important the collision processes are in laser-produced plasma can be seen from several examples. Simply, the classical optical constants (Hora, 1981) can be evaluated only by carefully watching the numerical problems close to a pole of the related functions where the change of the real part or the imaginary part of the optical constant can be by a factor  $10^3$  or much more for a change of the plasma temperature or the plasma density by less than 1 percent. Another drastic example is the theory of Denisov's resonance absorption (to distinguish from a new resonance found by Hora and Ghatak, 1985) where the derivation based on the electric field by White and Chen (1974) arrived at a negative infinite pole of the function for the effective dielectric function of the plasma was collisionless. Introducing a tiny little bit of absorption (collisions), however, caused a swap of the pole from minus infinity to nearly plus infinity (Hora, 1979). Collisions are therefore essential in laser-produced plasmas.

The use of N-particle simulation of the plasma (with  $N = 10^6$ ) by computers could again not be used as the physics of the collisions could be covered yet only in a limited way and only first attempts have been done to correctly treat Coulomb collisions now in a simplified way by using supercomputers (Yabe, 1985). The difficulties in this macroscopic theory, however, are in the presumptions of space charge quasi-neutrality that could not at all be used to treat the electric fields or double layers in plasmas. It even could not describe the coupling of the longitudinal ("electrostatic") Langmuir waves with transversal electromagnetic waves in plasma (Schamel, 1979).

## II. THE GENUINE TWO-FLUID MODEL

The macroscopic hydrodynamic theory for the consequent description of the double layers and the generated electric fields required the use of the complete two fluids for electrons and ions including collisions, viscosity, equipartition of temperatures between ions and electrons, optical constants with the correct nonlinear dependence on the laser intensity (about an incorrect formula, see e.g., Duderstadt and Moses, 1983), and including the general expression of the nonlinear force apart from the thermokinetic force given by the gas dynamic pressure (Hora, 1969, 1981, 1985a). In one spatial dimension, the problem was then to solve the following seven quantities depending on the spatial coordinate  $x$  and the time  $t$  for given initial and boundary values: the density, temperature and velocity (in the  $x$ -direction) for electrons, the same for ions ( $n_e$ ,  $T_e$ ,  $v_e$ ,  $n_i$ ,  $T_i$ ,  $v_i$ ) and the electric field  $E$  (in the  $x$ -direction) differing from the external electric and magnetic fields  $E_L$  and  $H_L$  of the incident laser radiation. For the seven functions, seven differential equations are available: the equations of continuity for electrons and ions, the equations of motions for electrons and ions, the equations of energy conservation for electrons and ions, and the Poisson (or better Gaussian) equation (Lalousis and Hora, 1983). For the whole three-dimensional description there have to be added the two variables for the other components of the electron velocity and the same for the ion velocities for which the four further velocity components of the equation of motion are accounted. Instead of the longitudinal electric field component  $E$  of the one-dimensional case, all three components of  $E$  and that of the magnetic field  $H$  generated in the plasma during the complex dynamics have to be included for which instead of the Gaussian law in one dimension, the six components of the Maxwellian equations have to be used. All together, there are 16 equations for the 16 quantities to be determined in space and time, automatically also reproducing the complete development of the so-called spontaneous magnetic fields in the laser-produced plasmas.

The solution of the one-dimensional problem allowed for numerics is very complicated in this general property of the plasma because the time steps have to be very much shorter than the shortest plasma oscillation time. For the plasmas at irradiation with neodymium glass laser radiation, the time steps have then to be shorter than 0.1 fs. In order to arrive at physically detectable results in the picosecond scale, long computer runs have to go on, where for each time step the Maxwellian equations also have to be solved for the incident laser radiation with the correct conditions for the reflected wave. For the treatment of the reflection field, a very quick computation by a matrix procedure was invented (Lalousis, 1983). The whole computation had to be using a very unusual Eulerian code instead of the usual Lagrangian codes because of the appropriate inclusion of the description of the electric fields produced inside the plasma. The basic problem of the boundary conditions in this case ran into instabilities, and a special new method for a stable solution had to be discovered as derived by numerical experiments (Lalousis, 1983; Lalousis and Hora, 1984).

The results described in the following were attained by using a CD 7600 computer and a Cray 1. The stability of the computation and the correctness of the output was confirmed after the runs up to the picosecond range by checks of the conservation of energy. Also the fact that the gain or loss of energy of relativistic electrons, fired through the then not longer static and conservative electric fields with potentials, but having the dynamic electric fields  $E$  where

$$\oint E \cdot dx \neq 0 \quad (1)$$

resulted in reasonable numbers of the gain or loss of electron energies (Green et al., 1986), was a proof of the correct computations.



### III. ELECTRIC FIELDS, DL'S, AND OSCILLATIONS IN PLASMA WITHOUT LASER INTERACTION

When using the genuine two-fluid code, the appearance of strong electric oscillations was marked. For a plasma without laser irradiation, the following initial condition was chosen; a fully ionized hydrogen plasma slab of  $10 \mu\text{m}$  thickness with a linear increase of the electron density from  $5 \times 10^{20} \text{ cm}^{-3}$  at  $x = 0$  to  $10^{21} \text{ cm}^{-3}$  at  $x = 10 \mu\text{m}$  was taken at time  $t = 0$  with same ion density and an electron and ion temperature  $T_e = T_i = 10^3 \text{ eV}$  at  $t = 0$ . The initial velocities were  $v_e = v_i = 0$  everywhere at  $t = 0$  and, consequently, the electric field  $E = 0$  at  $t = 0$ . Working with time steps of  $1.5 \times 10^{-16} \text{ s}$  (1/30 of the shortest plasma period of  $5 \times 10^{-15} \text{ s}$ ) at  $x = 10 \mu\text{m}$ , expanding plasma showed a very strong oscillation of the electric field displayed by electrons moving down the ramp and being returned. The field was always negative, never positive, because the electron cloud went back to the initial position within the ions or less. At later times an "ambipolar" oscillation field was noted (Figs. 3 to 5) which decayed faster when the initial plasma temperature was lower (higher collision frequency). The oscillations were damped out and a bent profile of the electric field resulted, nearly unchanged along the whole expanding plasma profile. The field had the highest negative values at  $x = 0$  of  $2.6 \times 10^6 \text{ V/cm}$ . This value was interpreted for a temperature of  $10^3 \text{ eV}$  and a length of  $10^{-3} \text{ cm}$ , reaching a value of  $3 \times 10^6 \text{ V/cm}$ , of a "potential" of  $10^3 \text{ kT}$  was assumed. As we have a time-dependent evaluation of the field  $E$  due to the plasma dynamics, we have no longer a conservative field and therefore no potential. These fields are then, strictly speaking, no longer electrostatic fields, and the generated double layer is, strictly speaking, not an electrostatic double layer, though the result is close to the picture of one.

An analytical description of the numerically very general result is possible with some approximations: The Poisson equation, which was formulated for a potential as an inhomogeneous differential equation to the homogeneous Laplace differential equation, is then only an approximation as the fields are, strictly speaking, no longer conservative. The following Gauss law was used where  $n_e$  and  $n_i$  have to be considered as time-dependent. The non-conservative character of these fields, equation (1), can be used to produce an acceleration or a stopping of charged particles by manipulating the time dependence of  $n_e$  and  $n_i$ . From the time-dependent electric field, we get the Gauss law by time differentiation, substitution of the equations of continuity, and integration over the spatial coordinate (without discussing the integration constant),

$$\frac{\partial}{\partial t} E = 4\pi e(n_e v_e - Z v_i n_i) \quad (2)$$

Further time differentiation, substitution by the equations of motion and re-arrangement of the terms with the collision frequency  $\nu$  results in

$$\frac{\partial^2 E}{\partial t^2} + \nu \frac{\partial E}{\partial t} + \omega_{po}^2 E = E_0 \omega_{po}^2 + \frac{4\pi e}{m_e} \frac{\partial}{\partial x} (E_L^2 + H_L^2)/8\pi + 4\pi e \nu (n_e v_i - Z n_i v_e) \quad (3)$$

where

$$E_0 = \frac{4\pi e}{\omega_{po}^2} \left[ \frac{\partial}{\partial x} \left( \frac{3n_i k T_i}{m_i} + 2n_i v_i^2 \right) - \frac{\partial}{\partial x} \right] \frac{3n_e k T_e}{m_e} + n_e v_e^2 \quad (4)$$



and

$$\omega_{po}^2 = 4\pi e^2 \frac{n_e}{m_e} + \frac{Z^2 n_i}{m_i} \quad (5)$$

The driving laser field  $E_L$  and  $H_L$  were used for the following section. Neglecting (3) for  $\nu \ll \omega_p$  and assuming a vanishing laser field ( $E_L = H_L = 0$ ), the local solution of (3) results in an electric field,

$$E = E_0 \left\{ 1 - \exp\left(-\frac{\nu}{2}t\right) \left[ \cos\left(\sqrt{\omega_{po}^2 - \nu^2}t\right) + \frac{\nu}{2\sqrt{\omega_{po}^2 - \nu^2}} \sin\left(\sqrt{\omega_{po}^2 - \nu^2}t\right) \right] \right\} \quad (6)$$

which oscillates with a frequency close to the plasma frequency. These oscillations, however, are damped (exponentially decaying) by the collision frequency such that after a time  $t \gg 2/\nu$  a nearly constant electric field  $E$  remains, as seen numerically (Fig. 5). This field  $E$  is determined by the spatial gradients of the enthalpy of the ions and electrons given in the brackets within the square bracket of equation (4) divided by the particle masses.

The (nearly static) electric field has an understandable order of magnitude at least for the early time of the damping processes of an initially stationary inhomogeneous plasma where any electron and ion velocity is small and from the big ratio of the ion to the electron mass. It follows,

$$E \approx \frac{4\pi e}{\omega_{po}^2 m_e} \frac{\partial}{\partial x} 3n_e kT_e \quad (7)$$

or

$$eE \approx \frac{1}{n_e} \frac{d}{dx} 3n_e kT_e \quad (8)$$

We see that the electric field  $E$  is simply caused by the gradients of the electron density and/or the temperature temporally changing. Therefore the expression "inhomogeneity field" or "dynamic electric field" has been used. In the stationary approximation (8) the inhomogeneity field corresponds to the (thermionic) work function for the electrons that moved from the plasma interior to the vacuum (or an electrode) outside corresponding to the spread Debye sheath (Hara, 1983).

This result of a quasi-potential value  $eE_0 \lambda = eV_e = 3kT_e$  corresponds to the measured 600 volts in a tokamak of a maximum temperature of 200 eV where the missing factor 3 was mentioned as an unexplained result (Razumova, 1983). If there are experimental conditions where, instead of a factor 3, a factor 10 (Eliezer and Ludmirsky, 1983) has been measured from the electric fields in laser-produced plasmas with (spread) Debye lengths over 10 to 100 times of its usual value, this may be explained for the more general conditions of the time developing enthalpy in (4) which was simplified in (8). Higher values than a factor 3 were also measured in cases of double layer experiments.

#### IV. ELECTRIC FIELDS AND DL'S WITH LASER INTERACTIONS

For the case of incident laser radiation, the computer output of the following cases will be discussed (Hora et al., 1984). A 25  $\mu\text{m}$  thick plasma slab of initial  $10^3$  eV temperature and zero velocity with an ion and electron density of symmetric parabolic shape very close to the value in Figure 6 for  $t = 0.5$  ps is given. No laser interaction occurs during the first 0.5 ps such that the minor thermal expansion does not change much of the initial density profiles while this time is long enough to damp down the fast electric oscillations. At  $t = 0.5$  ps, a neodymium glass laser field incident from the left-hand side is switched on with a vacuum amplitude of  $10^{16}$  W/cm<sup>2</sup>. The resulting electric field density  $\bar{E}_L^2/8\pi$  averaged over a laser period is given in Figure 7 showing an exponential decay for  $x > 8$   $\mu\text{m}$  because of superdense plasma there. At several time steps up to 1.5 ps, the resulting densities (Fig. 6) and ion velocity (Fig. 8) are given. The density (Fig. 6) shows a strong minimum (caviton) at  $x = 5$   $\mu\text{m}$  indicating the predominance of the nonlinear force-driven ponderomotion. Plasma blocks with ion velocities up to  $10^7$  cm/s are created in agreement with simplified estimates of the strong acceleration densities.

The resulting differences of the ion and electron densities are given in Figure 9. They cause fast changing electric fields  $E$  given in Figure 10 reaching values beyond  $10^8$  V/cm. This value corresponds to the expected numbers: the dielectrically swollen laser field  $E_L$  in the plasma can be up to  $10^{11}$  V/cm decaying to zero within  $10^{-3}$  cm.

Using similar simplifying approximations as in equation (6), including the oscillating laser field, the longitudinal (dynamic electric) field  $E$  from (3) is given by

$$E = 4\pi e \left[ \frac{\partial}{\partial x} \left( \frac{3n_i k T_i}{m_i} + Z n_i v_i^2 \right) - \frac{\partial}{\partial x} \left( \frac{3n_e k T_e}{m_e} + n_e v_e^2 \right) + \frac{1}{m_e} \frac{\partial}{\partial x} (E_L^2 + H_L^2) \right] \left[ 1 - \exp \left( -\frac{\nu}{2} t \right) \cos \omega_p t \right] + \frac{\omega_p^2 - 4\omega^2}{(\omega_p^2 - 4\omega^2)^2 + \nu^2 \omega^2} \times \frac{4\pi e}{m_e} \frac{\partial}{\partial x} (E_L^2 + H_L^2) \cos 2\omega t + \frac{2\nu\omega}{(\omega_p^2 - 4\omega^2)^2 + \nu^2 \omega^2} \frac{4\pi e}{m_e} \frac{\partial}{\partial x} (E_L^2 + H_L^2) \sin 2\omega t, \quad (9)$$

where the first term represents the former quasi-static field  $E$ , (4) with its damped-fast oscillations but modified by the amplitude of the fast time-averaged laser field density  $E_L^2 + H_L^2$  which is dominant before the gas dynamic pressure  $n_e k T_e$  acts. As  $E_L^2 + H_L^2$  changes fast (still very slow compared to the laser oscillation time), a quite complicated result for  $E$  can be seen in Figure 12, in which the exact result is given without the simplification of equation (9). Considering the complicated time dependence of  $n_i$ ,  $n_e$ ,  $T_i$ ,  $T_e$ ,  $E_L$  and  $H_L$ , the term "potential" is no longer applicable and  $E$  is a dynamic electric field following equation (1). Only at stationary conditions, the pressure may be a potential or one may consider a ponderomotive potential.

The second and last terms in equation (9) oscillate quickly with twice the laser frequency. As  $E_x$  is directed to the  $x$ -direction, i.e., perpendicular to the  $E_L$  of the laser field, we have — obviously for the very first time — the coupling of the transverse electromagnetic wave with the longitudinal plasma waves which is made possibly only by overcoming the restriction of the quasi-neutrality of the earlier two-fluid theory, and without the artificial inclusions of microscopic model assumptions. The last term in equation (9) has a resonance denominator, causing a very steep increase of the oscillation amplitude at  $2\omega = \omega_p$ . As we consider a case of purely perpendicular incidence without

any surface rippling and no self-focusing, we have here a new type of resonance mechanism acting in the evanescent part of the wave in a depth of 4 times the critical density, if there is still sufficient laser intensity. This resonance is basically different from Denisov's resonance absorption which works at oblique incidence for p-polarization only (Denisov, 1957). The new type of perpendicular incidence resonance can be significant (Hora and Ghatak, 1985) as will be discussed in Section V with other phenomena.

The numerical result of Figure 9 can explain the inverted double layers in laser-produced plasmas if cavitons are produced by the nonlinear forces. The existence of the electric fields in plasma surfaces had been shown directly by electron beam probes and from electrostatic acceleration of a small number of the nonlinear force-accelerated ions. A more systematic experiment was done by Eliezer and Ludmirsky (1983), Ludmirsky et al. (1985), and Eliezer et al. (1986) where the temporal dependence of charge of the expanding plasma and the temporal change of the target potential were measured. A very unexpected observation was that the plasma leaving the target was first positively charged and then negatively charged. This was in contrast to the general expectation that an electron cloud should first leave the plasma. The picture changes, however, if we look at all fields at the surface and in the interior of the plasma in the genuine two-fluid model if a nonlinear force-driven caviton is generated. Figure 9 shows, near  $x = 25 \mu\text{m}$ , where no laser light acts, that a negatively charged plasma expands before the positively charged plasma follows. Near  $x = 0$ , one sees that first a strong positively charged plasma is emitted and then a negatively charged plasma before a nearly neutral plasma follows. This is the result of the caviton generation. Though the experiment (Eliezer and Ludmirsky, 1983) was on the nanosecond time scale, the comparison with the picosecond processes should be justified not only by the correct polarity of the plasma charges but also from other experiments that showed the picosecond buildup of the cavitons (Briand et al., 1985). The experiment of Eliezer and Ludmirsky (1983) is an indirect proof that they had also generated cavitons.

A further experiment which can be explained is the energy upshift of alpha particles from laser fusion pellets. It was observed (Gazit et al., 1979) that the DT-alpha particles from laser fusion pellets had not the expected maximum energy of 3.56 MeV but showed an upshift by  $\Delta\epsilon$  of up to 0.5 MeV. The exact description of the interaction of the alphas with the spatially and temporally varying electric field  $E(x,t)$  in the (one-dimensional) plasma corona is very complicated as the field is non-conservative. The velocity of the alpha particle,  $v$ , with an initial velocity,  $v_0$  and mass,  $m_\alpha$  is given by the complex integral equation,

$$v(x) = v_0 + \frac{2e}{m_\alpha} \int_{t_1}^{t_2} E[x(t), t] dt \quad ; \quad x = v(t)dx \quad (10)$$

For a very simplified estimate we use,

$$d\left(\frac{m_\alpha}{2} v^2\right) = 2eE[x, t(x)] dx \quad , \quad (11)$$

with an average value  $\bar{E}$  of  $E$  to give the increase of the alpha energy,

$$\Delta\epsilon = 2e\bar{E} \Delta x \quad , \quad (12)$$

after acceleration along a length  $\Delta x$  of the plasma corona. In order to reach  $\Delta\epsilon = 0.5 \text{ MeV}$  for  $\Delta x = 10 \mu\text{m}$ , we find  $\bar{E} = 2.7 \times 10^3 \text{ V/cm}$ . Such fields for Nd glass laser pulses of  $10^{16} \text{ W/cm}^2$  are possible only if the nonlinear force-produced cavitons (Fig. 10) are present, since lengths very much larger than  $10 \mu\text{m}$  are not realistic. Thermally produced fields of up to  $10^6 \text{ V/cm}$  could not produce the measured upshifts of 0.5 MeV. Our results, therefore, are

not only a rough explanation of the alpha upshift by the large electric fields in the cavitons but are also a clear indication that no thermal electric field can cause the measured upshifts.

We have preliminary results on the exact numerical solution of equation (10) from E-values derived from laser plasma dynamics (Green et al., 1985). It was discovered that broad E-maxima move within 0.3 to 0.9 of the speed of light (Fig. 10). The correct phasing of the charged particles in the field does lead to an acceleration by multiples of the estimate of equation (12). It can be shown how today available CO<sub>2</sub> lasers (Antares) with 80 TW short laser pulses and a sequence of several pulses can shift electron clouds of GeV energy to TeV electron energy. The caviton (nonlinear force) fields of the type in Figure 12 of 10<sup>11</sup> V/cm act like the (non-conservative) pump fields in the microwave cavities of an accelerator. The phasing of the nonlinear force field electron acceleration is an extension of the concept based on many years of work on the nonlinear force and the then recent results on high electric fields in plasmas (Clark et al., 1985).

## V. DISCUSSION AND FURTHER RESULTS

Against all prior assumptions of space charge quasi-neutrality of plasmas, our analysis of genuine two-fluid hydrodynamics has shown very high electric fields inside of plasmas. These are simply given by gradients of density and/or temperature (inhomogeneity fields) modified by plasma oscillations due to changes in mechanical motion for free expansion or due to the nonlinear force-produced block motion or cavitons. A consequence for laser fusion of the resonance at perpendicular incidence may be significant, but it is only one of numerous anomalous and nonlinear phenomena known. A more important consequence, however, is the fact that the electric fields in the double layers change the thermal conductivity drastically. In order to fit experiments with too low temperatures of the interior of the plasma-irradiated pellet and the low fusion neutron emission with the computations, fitting factors *f* for reduction of the thermal conduction were used since 1979 (Ding et al., 1983; Richardson et al., 1986) which were around 1/100. The results of the double layers offer a quantitative theory for this reduction. This and further consequences of the reviewed results will be discussed in this section (Hora, 1985b).

### A. Double Layers and Reduction of Thermal Conduction

The generation of electric fields and double layers inside of plasmas at gradients of density and/or temperature can cause the inhibition (reduction) of thermal conductivity below the Spitzer-value for the plasma electrons. This inhibition was detected indirectly from laser fusion experiments when the interior of the compressed pellet did not reach the temperatures expected from electronic thermal conduction (Cicchitelli et al., 1984), expressed by a reduction factor *f*. This can be understood simply from Figure 11 where a double layer is produced between a hot laser-irradiated corona and the cold pellet interior.

The energetic electrons have left the positive area (causing a mostly negligible preheat), and the following electrons are returned by the positive charges. If a total disconnection of the electron transport through the double layer is considered because of the return current of the electrons, only the ions can transport the heat. The thermal conductivity  $\kappa$  is then that of the ions,  $\kappa_i$  given by that of the electrons  $\kappa_e$ ,

$$\kappa = \kappa_i = \kappa_e (m/m_i)^{1/2}, \quad (13)$$

where *m* is the electron mass and *m<sub>i</sub>* is the ion mass. This gives the factor  $\kappa/\kappa_e = 1/70$  for the ion mass of deuterium and tritium used in the experiments where a computation fit with a factor 1/100 was shown (Ding et al., 1983; Richardson et al., 1986).



This explanation of the reduced thermal conduction by the double layer does not take into account that the electrons in the hot plasma may have a Maxwellian equilibrium distribution of their energy with a small number of very fast electrons penetrating the double layer. The factor  $f$  of the thermal conduction by the fast electrons through the double layer is given by the ratio of the energy flux density of the electrons (of temperature  $T$ ) in the  $x$ -direction  $E_{out}$  at  $x = x_2$  in Figure 11 over the energy flux density  $E_{in}$  of the electrons incident from the left-hand side at  $x = x_1$ ,

$$f = E_{out}/E_{in} \quad (14)$$

Based on an equilibrium distribution  $n$  of the electrons with the velocity  $\mathbf{v} = (v_x; v_y; v_z)$

$$n(v_x, v_y, v_z) = \left(\frac{m}{2\pi kT}\right)^{3/2} n_0 \exp\left(-\frac{mv^2}{2kT}\right), \quad (15)$$

where  $n_0$  is the (spatial) electron density, we find,

$$E_{in} = \int_{-\infty}^{+\infty} v_x \frac{m}{2} v^2 n dv_x dv_y dv_z = 4\pi n_0 m (kT/2\pi m)^{3/2}. \quad (16)$$

The flux density  $E_{out}$  must take into account the fact that the energy of the electrons beyond the double layer is reduced by the electric potential  $eV_0$  of the layer and only electrons with a velocity component in the  $x$ -direction  $v_x > v_{x0} = (2eV_0/m)^{1/2}$  will be transmitted. This results in,

$$E_{out} = \int_{+\infty}^{+\infty} \int_{+\infty}^{+\infty} dv_y dv_z \int_{v_{x0}}^{\infty} v_x (mv^2/2 - eV_0) n dv_x \quad (17)$$

$$= 4\pi n_0 m (kT/2\pi m)^{3/2} \exp(-\alpha), \quad (18)$$

where

$$\alpha = eV_0/(kT). \quad (19)$$

The final result

$$f = \exp(-eV_0/kT) \quad (20)$$

is then a simple Boltzmann factor.

From the experiments (Eliezer et al., 1985) there may be good reasons that  $eV_0$  is more than 5 kT up to at least 10 kT. In this case  $f$  is less than 1/70 given from the thermal ion conduction for D-T plasma. If we, however, work with the simple (one-dimensional) adiabatic relation  $eV_0 = 3kT$ , the factor  $f$  is 1/20, showing a well reduced but electronically dominated thermal conduction.

We conclude that the reduction of the thermal conductivity by the electrostatic double layer between hot and cold plasma does not necessarily drop down to the low value of the ion conductivity, and a reduced electronic thermal conduction by the energetic tail of the electron energy distribution may remain. For the analysis of future experiments, these variables of thermal conductivity factors have to be taken into account if no further competitive mechanisms (e.g., turbulence, classical thermal conductivity in inhomogeneous media) are taken into account. With respect to the energetic (so-called "hot") electrons in laser-produced plasmas, it has been found that there does not exist a fast Maxwellian tail of the energy distribution (McCall, 1983) proving that these energies are due to nonthermal quiver motion. These electrons would not be able to contribute to the thermal conduction mechanism discussed here. Another indication that these energetic electrons are not of a thermal nature (very probably representing the coherent quiver motion) is the very anisotropic "butterfly" directivity of the x-ray emission.

The reduced thermal conductivity in the double layers at steep thermal or density gradients, as given by the dynamic electric field strength  $E$  (inhomogeneity field), equation (9), is an important consideration in pellet ablation-compression computations whether the driving is by particle beams or by lasers. As long as no nonlinear forces, nonlinear optical response (absorption), and parametric effects are involved, there is a lot of similarity to the laser driving where the computer evaluation of the hydrodynamics automatically results in a compression of the plasma below the driver heated ablating corona. As a sufficient temperature is needed for the compressed plasma in the pellet core, the heat transport between corona and core is essential. If the classical electronic conductivity is used (without change by the inhomogeneity fields or the space charges of the double layers), it is no surprise that the laser ablation resulted in high core densities well after the mechanical recoil, but the temperatures were too low (Yaakobi et al., 1984) and the neutron gains from fusion were  $10^4$  times less than expected at this ablation mode (Hora, 1981).

It should be noted that the inhibition of electron transport by the double layer (Fig. 11) is valid also for the energetic (erroneously called "hot") electrons. Even if their energy is some 100 keV as in  $\text{CO}_2$  laser-irradiated fusion pellets, the number of electrons to produce a Debye layer only can move to the pellet interior to preheat the plasma. The following electrons, especially if they have no fast Maxwellian tail of a distribution, cannot pass the 100 keV DL. The usual electron preheat in pellets is then only a few mJ at some 100 J absorption of laser radiation.

## **B. New Resonance at Perpendicular Incidence**

The only resonance phenomenon (to be distinguished from parametric instabilities) at laser-plasma interaction is Denisov's (1957) resonance absorption which only may work at oblique incidence of laser radiation for p-polarization. White and Chen (1974) published the first derivation with the electric field description for a collisionless plasma, showing a resonance maximum of the electric field component of the laser field in the direction perpendicular to the surface at the critical density for laser light which is obliquely incident and p-polarized. The resonance in this case is in the evanescent field region below the reflection point of the propagating radiation. When generalizing this derivation (Hora, 1979) to the case with collisions, the pole of the effective dielectric constant suddenly changes from minus infinity to a high positive value and the width of Denisov's resonance maximum can be directly calculated in a transparent way (Hora, 1981).

In difference to this, a resonance was found (Hora and Ghatak, 1985) at perpendicular incidence of the (laser driven) longitudinal dynamic plasma field  $E$  (not the laser field) of such magnitudes that some phenomena at perpendicular incidence may be explained now where Denisov resonance was mentioned hoping that density ripple provides the necessary oblique incidence. This was questionable with respect to the low angle of incidence.

While the results on the numerical theory of the genuine two-fluid model were most general, the simplified analytical evaluation of the equations was possible by neglecting terms because of the electrons to ion mass ratios,



dropping discussions of integration constants and reducing to local differentiations and by coupling with Maxwell's equations. In a laser-irradiated plasma for perpendicular incidence, an inhomogeneous oscillation equation is then derived (with driving terms) for the (longitudinally oscillating dynamic) electric field  $E$  which is perpendicular to the driving laser field  $E_L$  (and  $H_L$ ). The solution of the differential equation resulted in equation (9).

The last term in equation (9) significantly indicated a resonance of  $\omega_p = 2\omega$  (4 times the critical density). This was noted approximatively before and evaluated roughly numerically (Hora et al., 1984; Hora and Ghatak, 1985). The more precise evaluation was performed by Goldsworthy et al. (1986). It is stressed again that in evaluating the last term in equation (9) before time averaging, the whole nonlinear force needs to be strong enough such that the term proportional to  $\sin(2\omega t)$  resonantly dominates. The coefficient of this term is

$$E_R = \frac{2\nu\omega}{(\omega_p^2 - 4\omega^2)^2 + 16\nu^2\omega^2} \frac{e}{2m} \frac{\partial}{\partial x} (E_L^2 + H_L^2) \quad (21)$$

In order to get the solutions  $E_L$  and  $H_L$  from the inhomogeneous plasma we especially select the condition that the electron density is increasing linearly in the region of the evanescent field. In this case, the wave equation can be solved by Airy functions (Lindl and Kaw, 1971; Goldsworthy et al., 1986). The full resonance amplitude given in equation (21) can now be evaluated numerically for any slope of the linear density profile and a constant temperature (collision frequency) by numerically solving  $E_L$ , deriving  $H_L$  from Maxwell's equations and calculation  $\tilde{n}$ , and using these values to compute the resonance amplitude  $E_R$ .

Numerical evaluation of the resonance phenomenon described in the previous sections was carried out for a plasma irradiated by neodymium glass laser light.

In Figure 12 the value of  $E_R$  of the resonant field amplitude is plotted as a function of depth  $x$  where the zero of the depth axis represents the critical layer. Noting that the resonant field depends linearly on the incident laser intensity, only the results of the realistic case, an initial intensity of  $10^{16} \text{ W/cm}^2$ , are discussed.

The electron collision frequency  $\nu$  is density dependent and is given by

$$\nu = 2.72 \times 10^{-5} \frac{n_e}{T_e^{3/2}} \ln \Lambda \quad (22)$$

where  $n_e$  is the electron density per cubic centimeter,  $T_e$  is the electron temperature in electron volts (eV), and  $\ln \Lambda$  is the Coulomb logarithm.

Results have been obtained for several different plasma temperatures, of which the case for 1 keV is given in Figure 12. The gradient of the density profile was varied as a parameter of the curves. The gradient is determined by  $\alpha$ ,

$$\alpha^2 = (\partial n_e / \partial x)^{-1} \omega / c \quad (23)$$

where the maximum of each curve is at such depth  $x$  where the density has reached 4 times the critical density. Figure 12 shows the results for the conditions  $T_e = 1 \text{ keV}$  for different depths of the maxima. The density gradients  $\alpha^2$  range from 140 to 240.  $T_e$  is the effective temperature (chaotic plus coherent motion of the electrons) which can well have the values of  $10^4 \text{ eV}$  at high laser intensities. Figure 13 evaluates the maximum field  $E_{\text{max}}$  of  $E_R$  as  $E_{\text{max}}/E_L$  related to the amplitude of the laser field in vacuum for various plasma temperatures.

Figure 13 shows that any strong resonance effect can be expected only when the profile has a very high steepening such that 4 times the density is reached at one wavelength or less below the critical density. This high steepening, however, is not unusual in cases where the nonlinear force is dominating the plasma dynamics (Ahlstrom, 1982; and Montes and Willi, 1982).

For laser-plasma interaction at perpendicular incidence a resonance is analyzed which produces high electric fields oscillating with the second harmonic perpendicular to the plasma surface (longitudinal oscillations). These fields are found in the application of a new genuine two-fluid hydrodynamic theory which is not restricted by space charge quasi-neutrality. For linear density profiles beyond the critical density, the resonance maxima are evaluated on the basis of the Airy functions and reach considerably high values for such profiles which can be generated by nonlinear force driving of the laser-plasma dynamics. Even the necessary high temperatures (appearing then as quiver energy as in the theory of the optical constants) seem to be reasonable. This perpendicular resonance mechanism may possibly be distinguished from the ordinary nonlinear force acceleration by the appearance of electron bursts.

### C. Density Independent Second Harmonics Emission

A rather surprising phenomenon was reported by Mayer et al. (1982). Irradiating a plane target in vacuum by a neodymium glass laser, a side-on time-integrated picture in the second harmonic frequency showed the large plasma plume in nearly constant  $2\omega$  intensity though the plasma density has been lower by orders of magnitudes in the outermost parts of the plasma than in the focus. A similar observation was detected more precisely (Aleksandrova et al., 1985) from a 400  $\mu\text{m}$  diameter pellet irradiated by a 2 ns rectangular neodymium glass laser pulse (Delfin), where a nearly constant  $2\omega$  radiation from a sphere of 2 mm diameter (to which the pellet corona had expanded during the laser irradiation) was detected. The fact that the very low peripheric plasma density emits the same  $2\omega$  radiation as the inner part of the cut-off density can be explained by the middle term of equation (9). The factor is nearly density-independent at low  $\omega_p$  ( $\omega_p \ll \omega$ ), and the standing wave pattern may result in a constant nonlinear force factor; therefore, this term of equation (9) should produce a spatially constant term of the dynamic electric field  $E_d$  as long as the laser is shining.

While this gives a qualitative explanation of the observation, a quantitative evaluation of the transfer of the dipole oscillation of  $E$  into emission of electromagnetic radiation results in an emission power of about  $10^6$  watts (Goldsworthy et al., 1986). The experimental evaluation of the calibration of the experimental results in a  $2\omega$ -power of about  $10^5$  watts (Fedotov et al., 1985).

### D. $E \times B$ Rotation of Plasmas

Since the dynamic electric fields, e.g., (9), in plasmas are (apart from the oscillations, damping, and transient effects of internal and/or external plasma dynamics) in a simplified way due to gradients of electron density and/or temperature, their  $E \times B$  interaction with external magnetic fields  $B$  may cause drift motion or rotation of plasmas. We shall first discuss this as examples with plasmas without laser irradiation, e.g., with tokamaks and stellarators, and then consider the extremely high  $E$ -fields by the nonlinear forces in laser-produced plasmas that describe fast block acceleration of plasma. There is a similarity to the simple ambipolar field effects.

The consequences for dynamic inhomogeneity electric fields in tokamaks are not only the modification of the thermal conduction but also the resulting basic change in the dynamics. The radial decay of density and temperature in any plasma column produces an inhomogeneity field in the radial direction which under stationary conditions is given by equation (9)

$$E_s = \frac{3}{en_e} \frac{d}{dx} n_e k T_e \quad (24)$$

This field combines with the toroidal magnetic field  $B$  and causes a drift with the velocity of the poloidal plasma rotation in meters/second (Fig. 14)

$$v_{\text{rot}} = 3T/rB \quad (25)$$

where the electron temperature is in electronvolts, the radius  $r$  of the plasma column is in meters, and  $B$  is in Tesla.

Measurements from tokamaks fully agree with the result of equation (25). Bell (1979) measured rotation velocity  $v = 2 \times 10^3$  m/s for  $r = 2 \times 10^{-2}$  m,  $B = 0.5$  T,  $T_e = 50$  eV for which case equation (25) results in  $v = 2.4 \times 10^3$  m/s. These plasma rotations were detected from the Doppler shift of  $H\alpha$ -lines, with similar agreement with equation (25), by Sigmar et al. (1974) who did not interpret them as plasma rotation, but as an anomaly of hot protons in the banana and plateau regimes. The agreement with equation (25), however, favors an interpretation of a simple rotation.

The same is with the experiment at the stellarator W7, where the result of 1980 agrees with a rotation according to equation (25). As this experiment was with tangential neutral beam injection, one would have had to exclude the rotation of these neutrals, which is difficult. Recent measurements at W7 without neutral beam injection but with plasma production by intensive microwave irradiation and heating (Thumm, 1985) result in exactly the same rotation given by equation (25).

## REFERENCES

- Ahlstrom, H. G., *Physics of Laser Fusion*, National Technical Service, Springfield, Virginia, 1982.
- Aleksandrova, I. V., W. Brunner, S. I. Fedotov, R. Guthrie, M. P. Kalashnikov, G. Korn, A. M. Maksimchuk, Y. A. Mikhailov, S. Ploze, R. Rieker, and G. V. Shlizkov, *Laser and Particle Beams*, 3, 197 (1985).
- Alfvén, H., *Tellus*, 10, 104 (1958).
- Alfvén, H., *Cosmic Plasmas*, Reidel Publ. Co., Dordrecht, Holland, 1981.
- Alfvén, H., and P. Carlqvist, *Solar Phys.*, 1, 220 (1967).
- Baker, K. D., N. Singh, L. P. Block, R. Kist, W. Kampa, and H. Thiemann, *J. Plasma Phys.*, 26, 1 (1981).
- Bell, M., *Nucl. Fusion*, 13, 33 (1979).
- Bernstein, I. B., J. M. Green, and M. D. Kruskal, *Phys. Rev.*, 108, 546 (1957).
- Bohm, D., *Characteristics of Electric Discharges in Magnetic Fields*, edited by A. Guthrie and R. K. Wakerling, McGraw Hill, New York, 1949.
- Briand, J., V. Adrian, M. El Tamer, A. Gomes, Y. Quemener, J. P. Dinguiraud, and J. C. Kieffer, *Phys. Rev. Lett.*, 54, 38 (1985).
- Carlqvist, P., *Solar Phys.*, 63, 353 (1979).
- Carlqvist, P., *Astrophys. Space Sci.*, 87, 21 (1982).
- Cicchitelli, L., S. Eliezer, J. S. Elijah, A. K. Ghatak, M. P. Godsworthy, H. Hora, and P. Lalouis, *Laser and Particle Beams*, 2, 467 (1984).
- Clark, P. J., S. Eliezer, F. J. M. Farley, M. P. Godsworthy, F. Green, H. Hora, J. C. Kelly, P. Lalouis, B. Luther-Davies, R. J. Stening, and J. C. Wang, *Laser Acceleration of Particles*, AIP Conf. Proc. 130, edited by C. Joslin et al., p. 380, AIP, New York, 1985.

- Coakley, P. G., and N. Hershkowitz, *Phys. Lett.* 83A, 131 (1981).
- DeGroot, J. S., C. Barnes, A. E. Walstead, and O. Buneman, *Phys. Rev. Lett.*, 38, 1283 (1977).
- Denisov, N. G., *Sov. Phys. JETP*, 4, 544 (1957).
- Ding, L. M., T. W. Hai, and W. R. Wen, *Plasma and Nuclear Fusion in China*, 1, 187 (1983).
- Duderstadt, J. J., and G. A. Moses, *Laser and Particle Beams*, 1, 216 (1983).
- Eliezer, S., and A. Ludmirsky, *Laser and Particle Beams*, 1, 251 (1983).
- Eliezer, S., A. D. Krumbein, H. Szichman, and H. Hora, *Laser and Particle Beams*, 3, 207 (1985).
- Eliezer, S. et al., *Laser Interaction and Related Plasma Phenomena*, edited by H. Hora and G. H. Miley, Vol. 7, p. 345, Plenum, New York, 1986.
- Fedotov, S. J., Y. A. Mikhailov, and G. V. Sklizkov, Private Communication, 1985.
- Gazit, Y., J. Delettretz, T. C. Bristow, A. Entenberg, and J. Soures, *Phys. Rev. Lett.*, 43, 1943 (1979).
- Goldsworthy, M. P., H. Hora, and R. J. Stening, *Phys. Fluids*, to be published, 1986.
- Green, F., G. W. Kentwell, H. Hora, and S. Tapalaga, *International Conference on Laser Sciences*, AIP Conf. Proc. 146, edited by W. C. Stwalley, p. 386, AIP, New York, 1985.
- Haerendel, G., E. Rieger, A. Valenzuela, H. Föppl, H. Stenback-Nielsen, and E. M. Wescott, *European Space Programmes on Sounding-Rocket and Balloon Research in the Auroral Zone*, Report ESA SP-115, European Space Agency, Neuilly, France, 1976.
- Hershkowitz, N., *Space Sci. Rev.*, 41, 351 (1985).
- Hershkowitz, N., G. L. Payne, C. Khan, and J. K. Dekock, *Plasma Phys.*, 23, 903 (1981).
- Hora, H., *Phys. Fluids*, 12, 182 (1969).
- Hora, H., *Laser Interaction and Related Plasma Phenomena*, edited by H. Schwarz and H. Hora, Vol. 1, p. 383, Plenum, New York, 1971.
- Hora, H., *Phys. Fluids*, 17, 939 (1974).
- Hora, H., *Laser Plasmas and Nuclear Energy*, Plenum, New York, 1975.
- Hora, H., *Nonlinear Plasma Dynamics*, Springer, Heidelberg, 1979.
- Hora, H., *Physics of Laser Driven Plasmas*, Wiley, New York, 1981.
- Hora, H., *Laser and Particle Beams*, 1, 151 (1983).
- Hora, H., *Phys. Fluids*, 28, 3705 (1985a).
- Hora, H., *Laser and Particle Beams*, 3, 87 (1985b).
- Hora, H., and A. K. Ghatak, *Phys. Rev.*, 31A, 3473 (1985).
- Hora, H., D. Pfirsch, and A. Schlüter, *Z. Naturforsch.*, 22A, 278 (1967).
- Hora, H., P. Lalouis, and S. Eliezer, *Phys. Rev. Lett.*, 53, 1650 (1984).
- Knorr, G., and C. Goertz, *Astrophys. Space Sci.*, 31, 309 (1974).
- Kulsrud, A., *Phys. Today*, 36(4), 54 (1983).
- Lalouis, P., Ph.D. Thesis, Univ. New South Wales, 1983.
- Lalouis, P., and H. Hora, *Computational Techniques and Application*, CTAC-83, edited by J. Noye and C. Fletcher, p. 699, Elsevier, North-Holland, 1984.
- Langmuir, I., *Phys. Rev.*, 33, 954 (1929).
- Leung, P., A. Y. Wong, and B. H. Quon, *Phys. Fluids*, 23, 992 (1980).
- Lindl, J., and P. Kaw, *Phys. Fluids*, 14, 371 (1971).
- Linlor, W. I., *Appl. Phys. Lett.*, 3, 210 (1963).
- Ludmirsky, A., S. Eliezer, B. Arad, A. Borowitz, Y. Gazit, S. Jackel, A. D. Krumbein, D. Salzmann, and H. Szichman, *IEEE Trans. Plasma Sci.*, 13, 132 (1985).
- Mayer, F. J. et al., *Abstracts, European Conference on Laser Interaction with Matter*, Schliersee, Germany, 1982.
- McCall, G., *Phys. Fluids*, 26, 1943 (1983).
- Mendel, C. W., and J. N. Olson, *Phys. Rev. Lett.*, 34, 859 (1975).
- Merlino, R., S. Cartier, M. Alport, and G. Knorr, *Second Symposium on Double Layers and Related Topics*, edited by R. Schrittwieser and G. Eder, p. 224, University of Innsbruck, 1984.
- Montes, A., and O. Willi, *Plasma Phys.*, 24, 671 (1982).
- Mozier, F. S., C. W. Carlson, M. K. Hudson, R. B. Torbert, B. Parady, and J. Yatteau, *Phys. Rev. Lett.*, 38, 292 (1977).



- Pearlman, J. S., and G. H. Dahlbacka, *Appl. Phys. Lett.*, **31**, 414 (1977).
- Peratt, A. L., *Phys. Rev. A*, **A20**, 2555 (1979).
- Peratt, A. L., and R. L. Watterson, *Phys. Fluids*, **20**, 1911 (1977).
- Quon, B. H., and A. Y. Wong, *Phys. Rev. Lett.*, **37**, 1393 (1976).
- Razumova, K. A., *Plasma Phys.*, **26**, 37 (1983).
- Richardson, M. C. et al., *Laser Interaction and Related Plasma Phenomena*, edited by H. Hora and G. H. Miley, Vol. 7, p. 624, Plenum, New York, 1986.
- Sato, T., and H. Okuka, *Phys. Rev. Lett.*, **44**, 740 (1980).
- Sato, N., G. Popa, E. Märk, E. Mravlag, R. Schrittwieser, *Phys. Fluids*, **19**, 70 (1976).
- Schamel, H., *Physica Scripta*, **20**, 336 (1979).
- Shawhan, S. D., *J. Geophys. Res.*, **81**, 3373 (1976).
- Sigmar, D. J., J. F. Clarke, R. V. Neidigh, and K. L. Vander-Sluis, *Phys. Rev. Lett.*, **33**, 1376 (1974).
- Stangeby, P. C., and J. E. Allen, *J. Phys.*, **D6**, 224 (1973).
- Temerin, M., K. Cerny, W. Lotko, and F. S. Mozer, *Phys. Rev. Lett.*, **48**, 1175 (1982).
- Temerin, M., and F. S. Mozer, *Second Symposium on Double Layers and Related Topics*, edited by R. Schrittwieser and G. Eder, p. 119, University of Innsbruck, 1984.
- Thumm, M., Private Communication, 1985.
- Torvén, S., *Phys. Rev. Lett.*, **47**, 1053 (1981).
- Torvén, S., L. Lindberg, and R. T. Carpenter, *Plasma Phys.*, **27**, 143 (1985).
- White, R. B., and F. F. Chen, *Plasma Phys.*, **16**, 565 (1974).
- Yaakobi, B., J. Delettrez, R. F. McCrory, R. Marjoribanks, M. C. Richardson, D. Shvarts, J. M. Soures, C. Verdon, D. M. Villeneuve, T. Boehly, R. Hutchinson, and S. Letzring, *Laser Interaction and Related Plasma Phenomena*, edited by H. Hora and G. H. Miley, Eds., Vol. 6, p. 731, Plenum, New York, 1984.
- Yabe, T., K. Mima, K. Yoshikawa, H. Takabe, and M. Hamano, *Nucl. Fusion*, **21**, 803 (1981).
- Yabe, T., Private Communication, 1985.

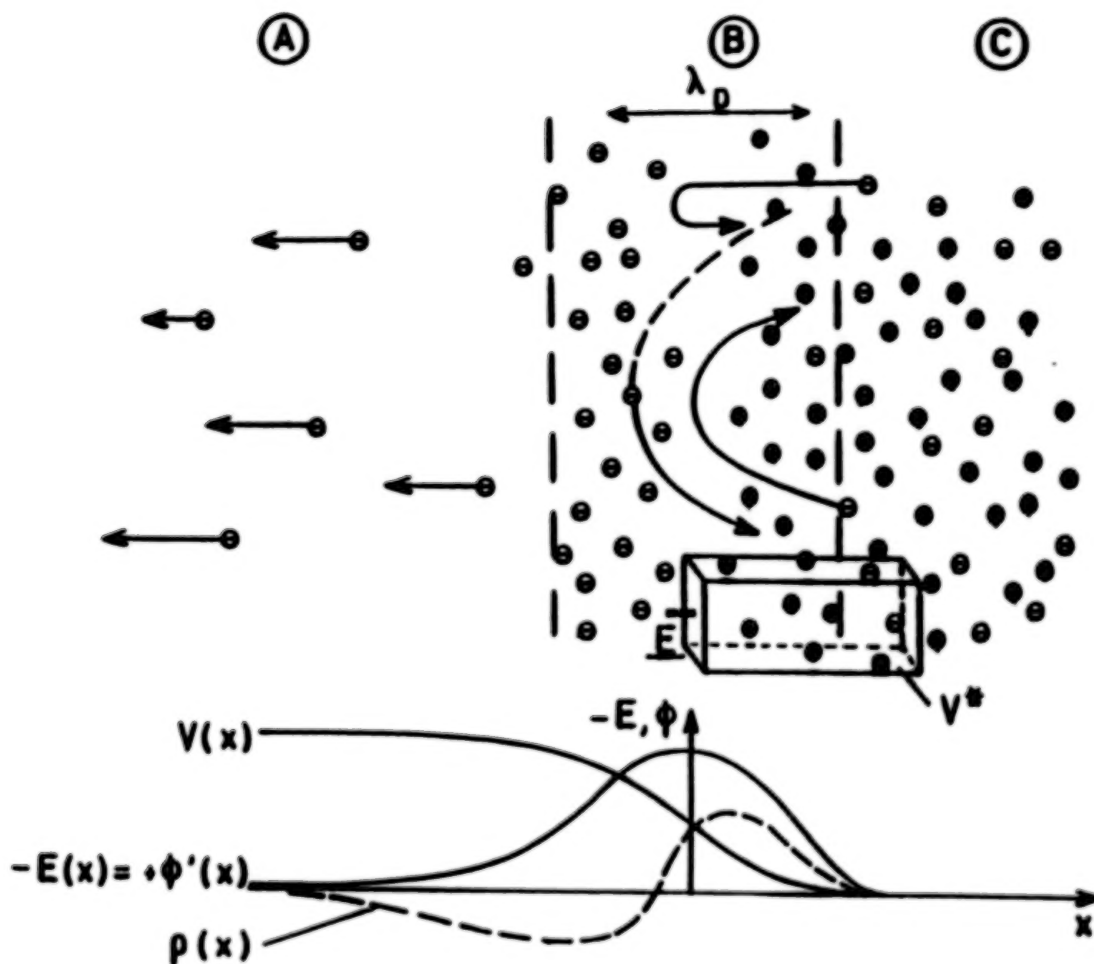


Figure 1. Between the vacuum range A and the space charge neutral interior of homogeneous plasma C, the plasma surface sheath is depleted by the escape of fast electrons until such a strong space charge is built up that the following fast electrons from the plasma C are electrostatically returned into C. The electric field  $E(x)$ , due to the space charge density  $\rho(x)$ , and the resulting potential  $V$  are given schematically (Hora, 1975).



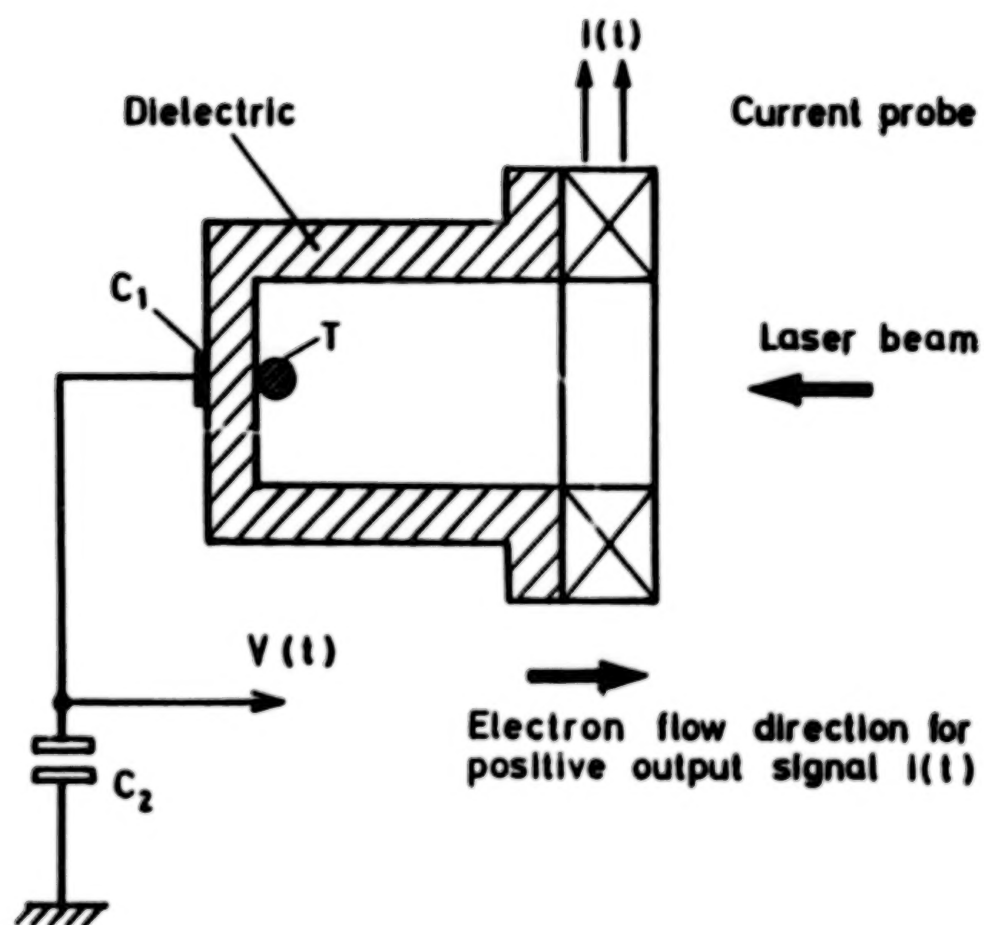


Figure 2. Experiment for a laser-irradiated pellet whose potential and the field [by the Rogowski coil  $I(t)$ ] are measured.

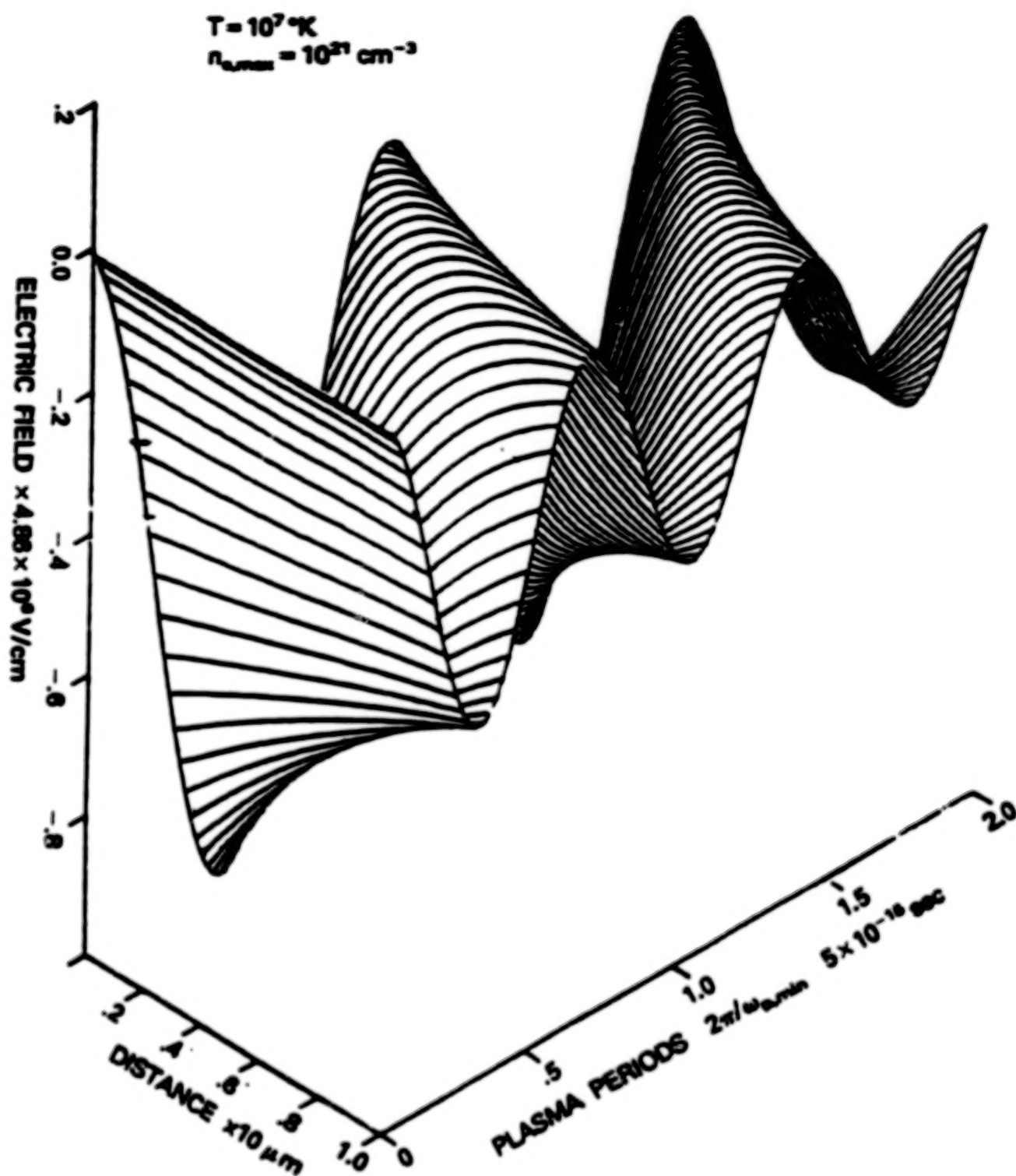


Figure 3. Time-dependent development of the longitudinal dynamic electric field  $E_z$  along the density with an initial ramp of linear plasma of initial temperature  $10^7 \text{ K}$  of  $5 \times 10^{20} \text{ cm}^{-3}$  at  $x = 0$  and  $10^{21} \text{ cm}^{-3}$  at  $x = 10 \text{ } \mu\text{m}$  (Lalousis and Hora, 1983).

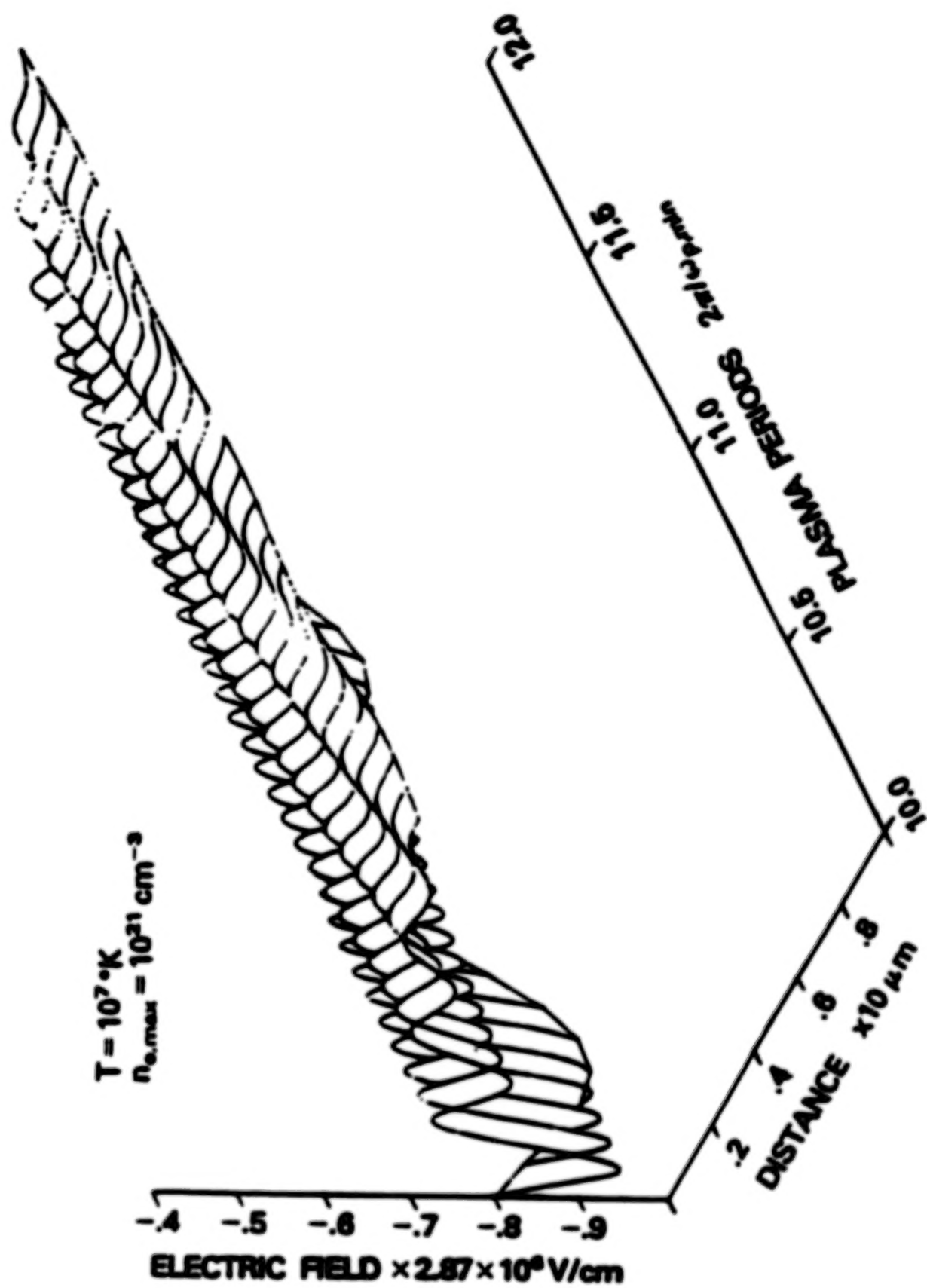


Figure 4. Same as Figure 3 for times of 10 and 12 plasma oscillation period (Lalousis nad Hora, 1983).

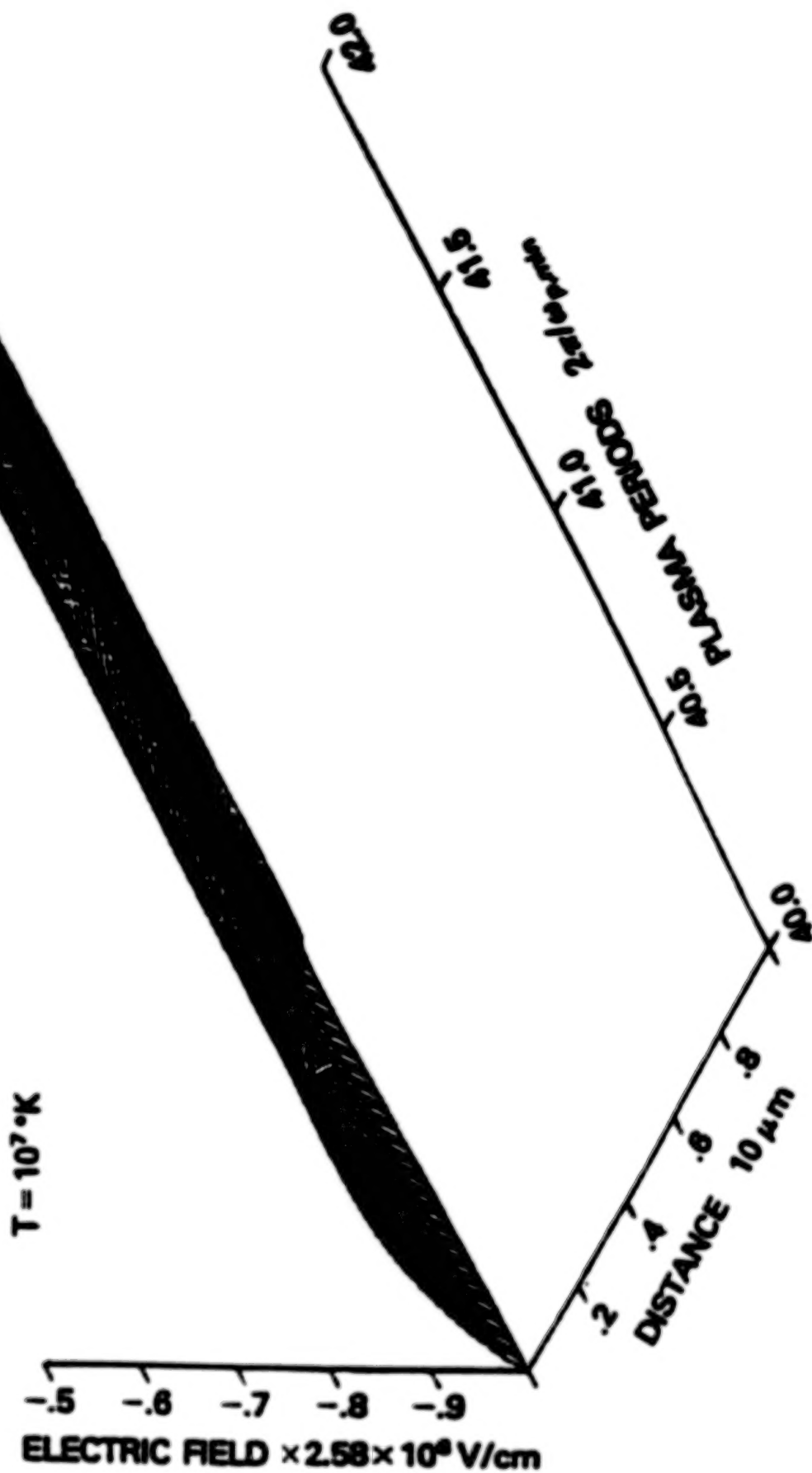


Figure 5. Same as Figure 3 for times of 40 to 42 periods (Lalouis and Hora, 1983).

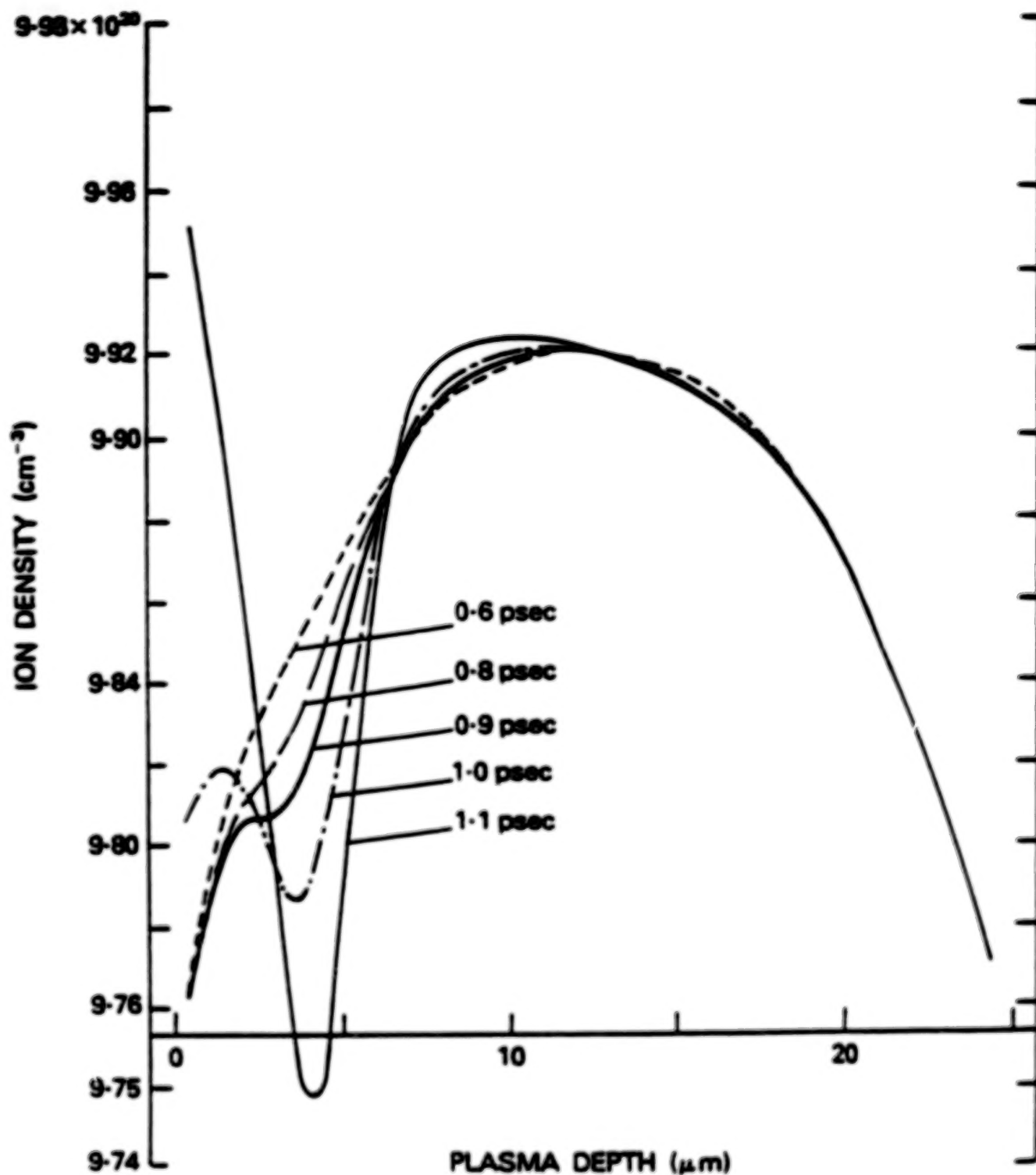


Figure 6. Ion density of a  $25 \mu\text{m}$  thick hydrogen plasma slab initially at rest and 1 keV temperature irradiated from the left-hand side by a  $10^{16} \text{ W/cm}^2$  Nd glass laser. At  $t = 0.6 \text{ ps}$  the density is very similar to its initial value. The energy maximum near  $x = 4 \mu\text{m}$  produces a caviton by nonlinear forces.

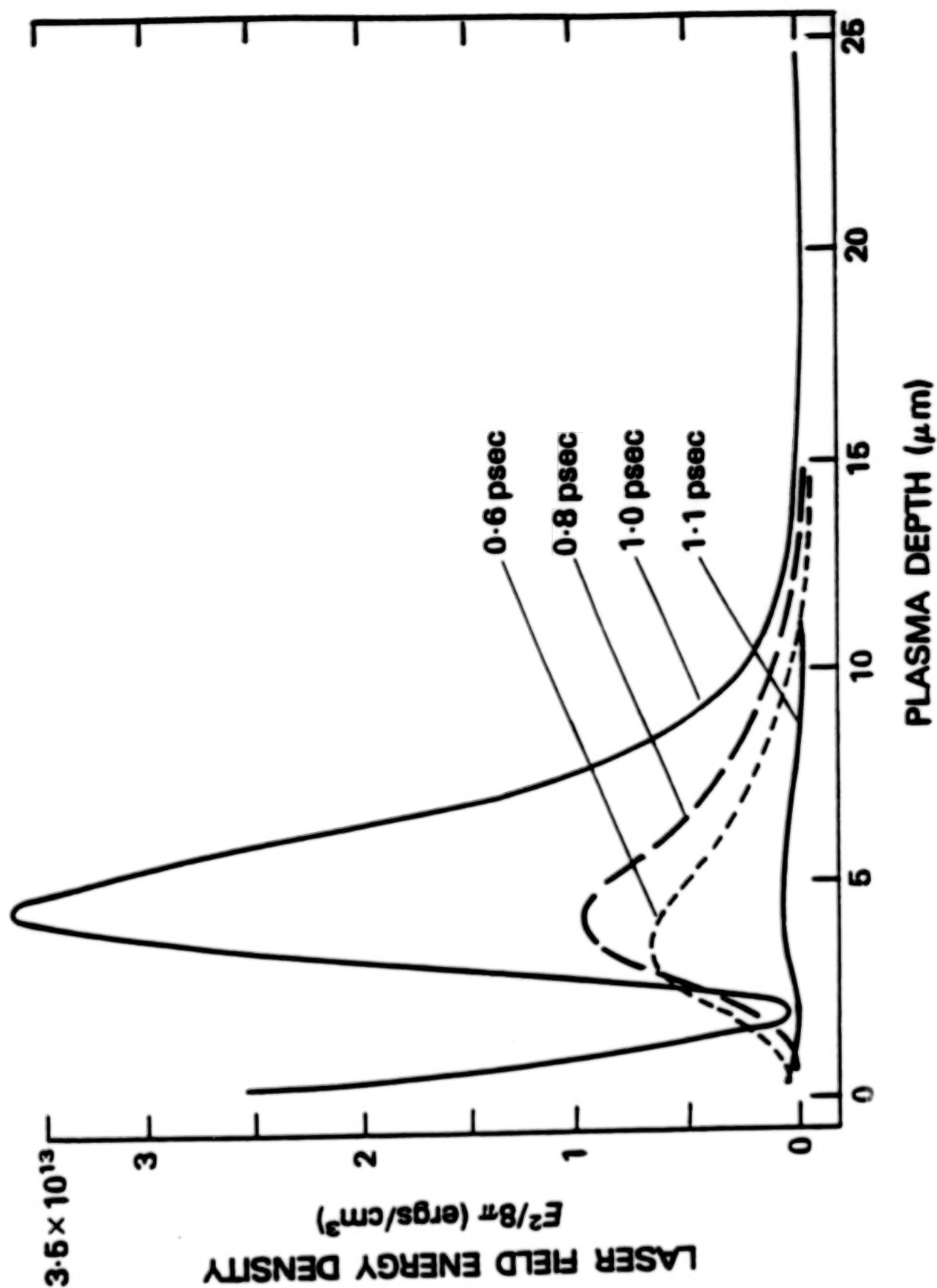


Figure 7. Density of the electric field energy of the laser (without the electrostatic fields generated within the plasma).



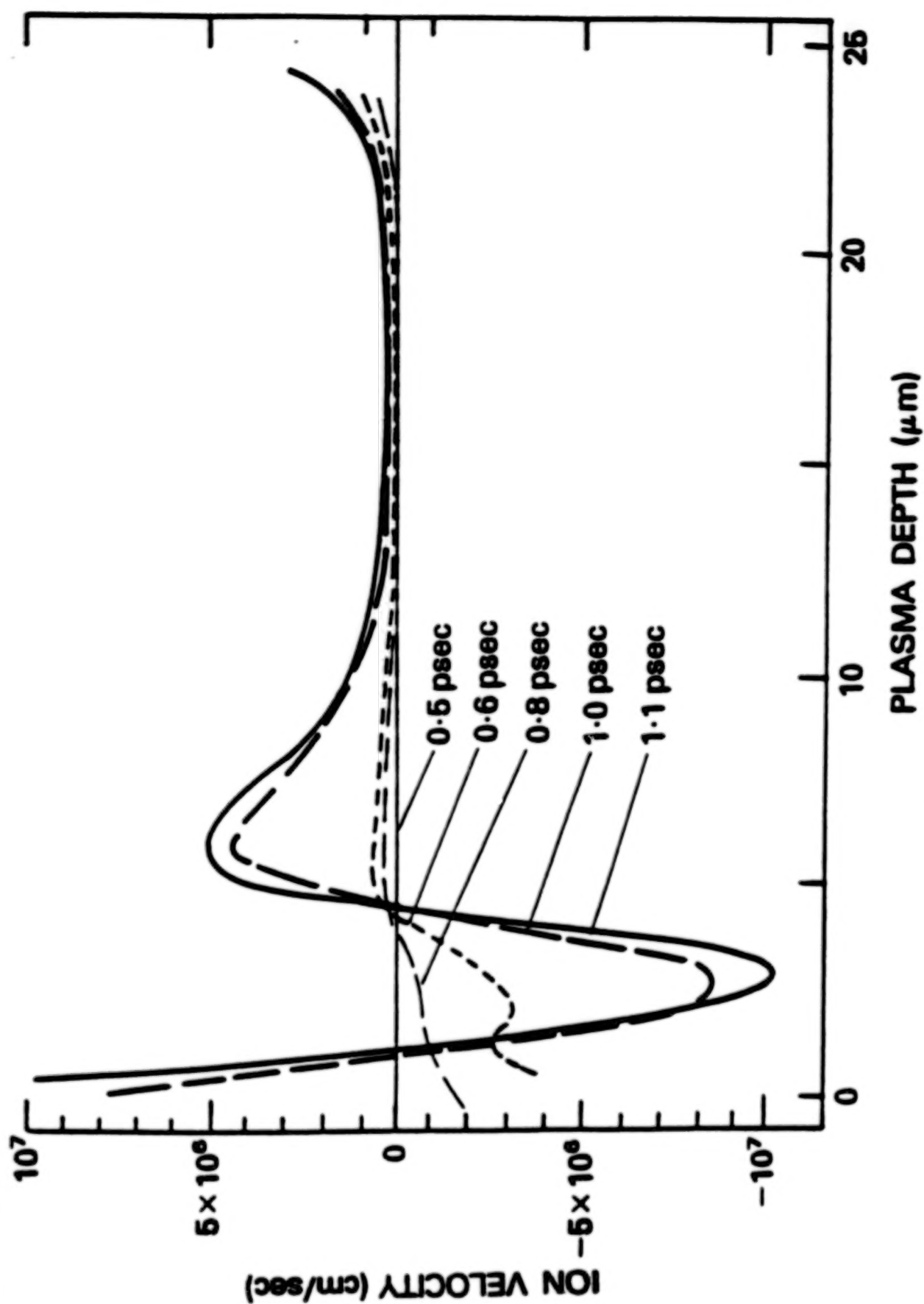


Figure 8. Ion velocity  $v_o$  at several time steps for a plasma, as in Figure 3. A block of plasma is generated with a velocity up to  $10^7 \text{ cm/s}$ .

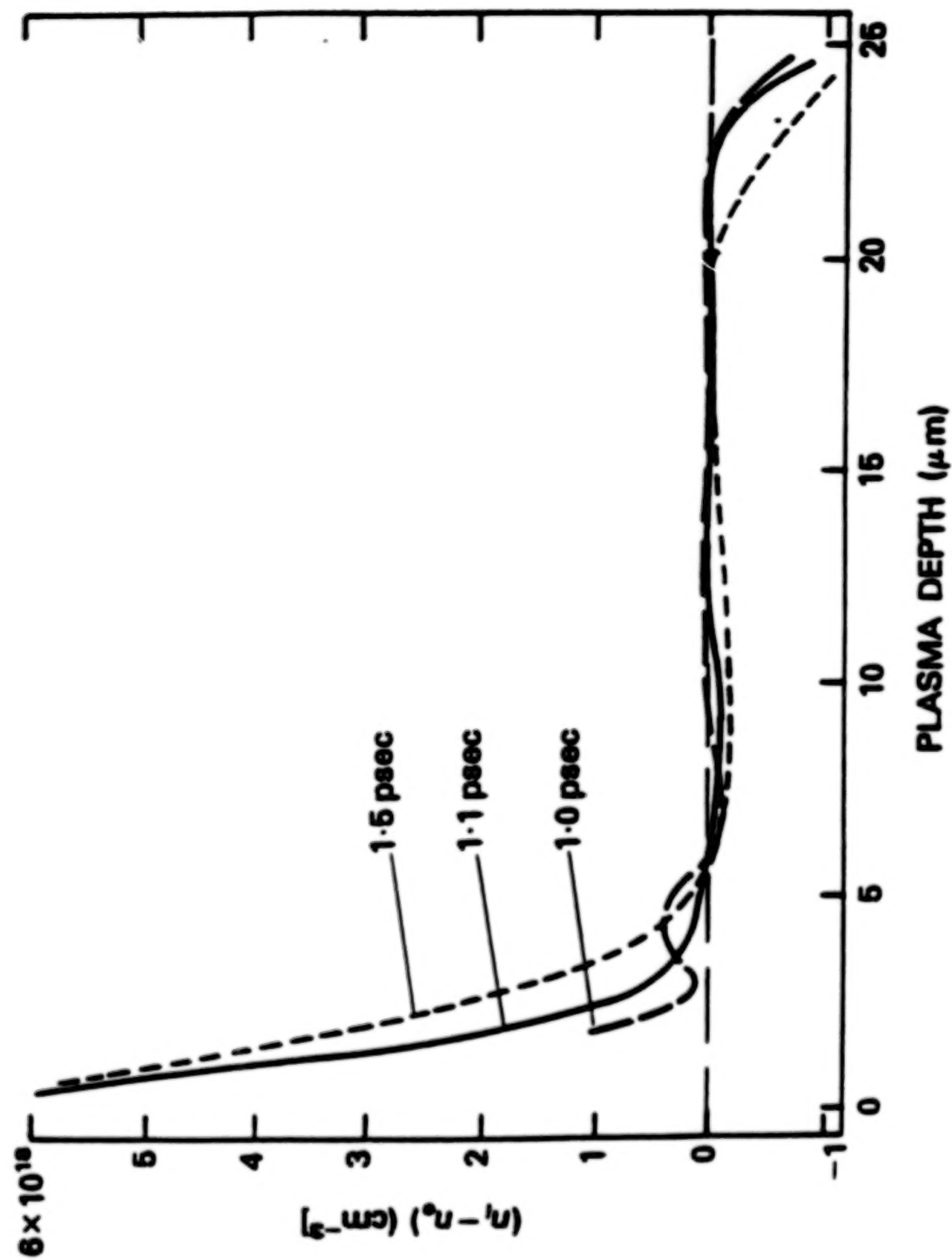


Figure 9. The genuine two-fluid model shows the difference between ion density  $n_i$  and electron density  $n_e$  with the surprising result of a positive difference (space charge) before the caviton and a negative region behind the caviton (inverted double layer as observed by Eliezer and Ludmirsky, 1983). Near  $x = 25 \mu\text{m}$  the laserless plasma expands normally with a negative periphery.

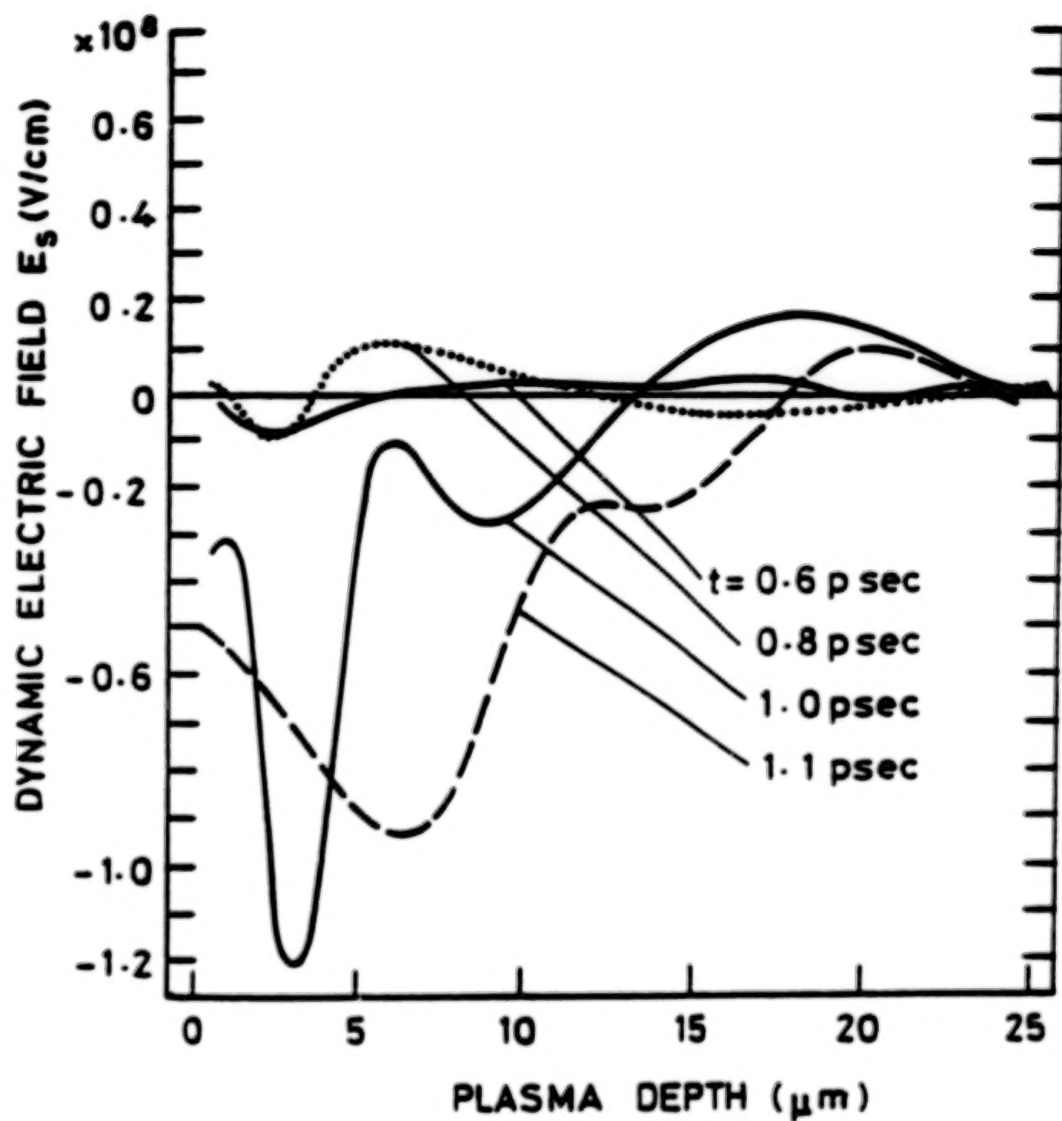


Figure 10. Electric field  $E = E_s$  inside the plasma of Figure 3 dynamically evolving with absolute values beyond  $10^8$  V/cm near the caviton produced by the nonlinear laser forces at times (in picoseconds) 0.6-; 0.8...; 1.0-; 1.1... .

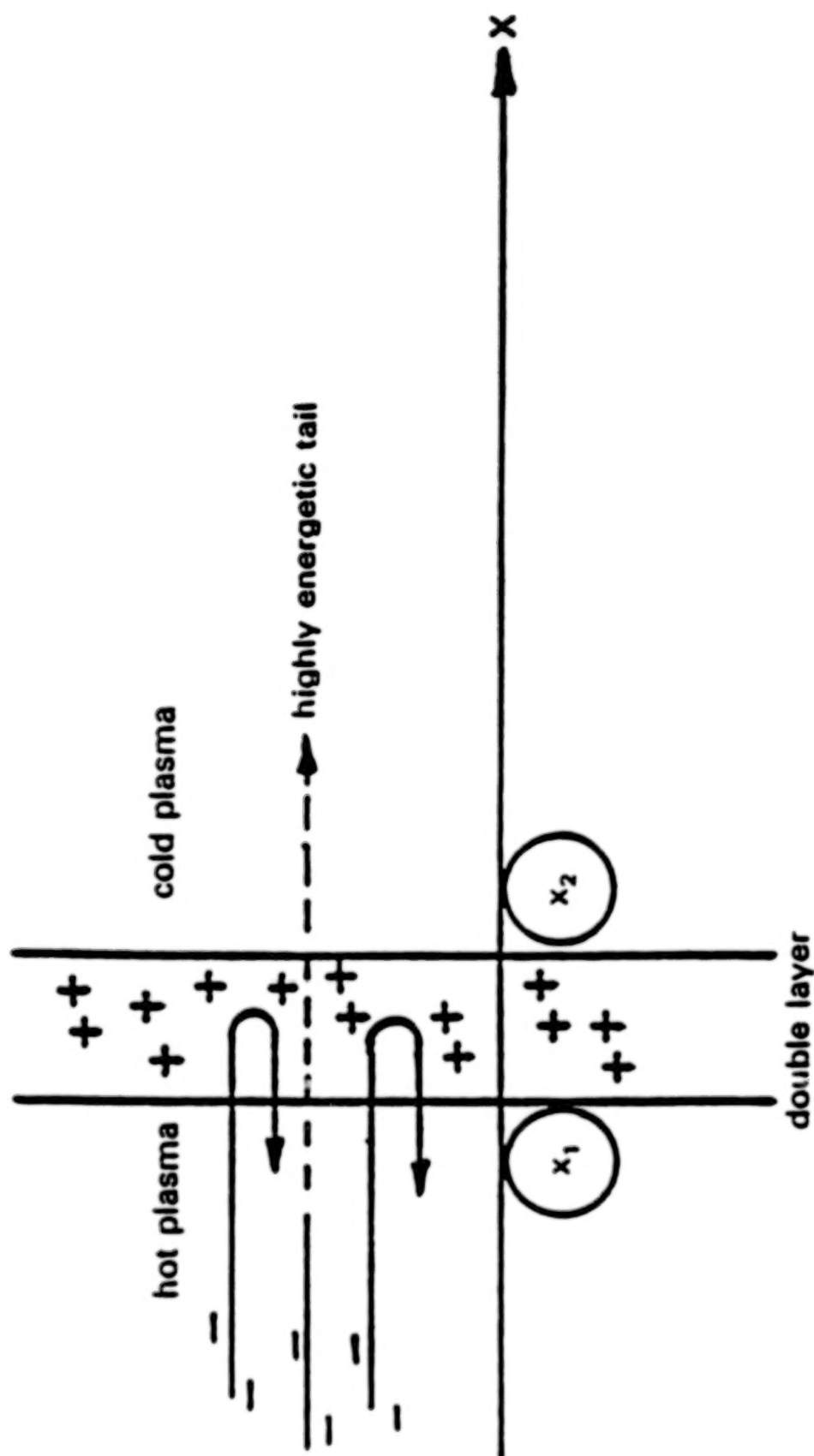


Figure 11. The positive charge of the double layer between the hot and the cold plasma causes a return of the electrons to the hot plasma with the exception of the electrons from the energetic tail of the energy distribution (Cicchitelli et al., 1984).

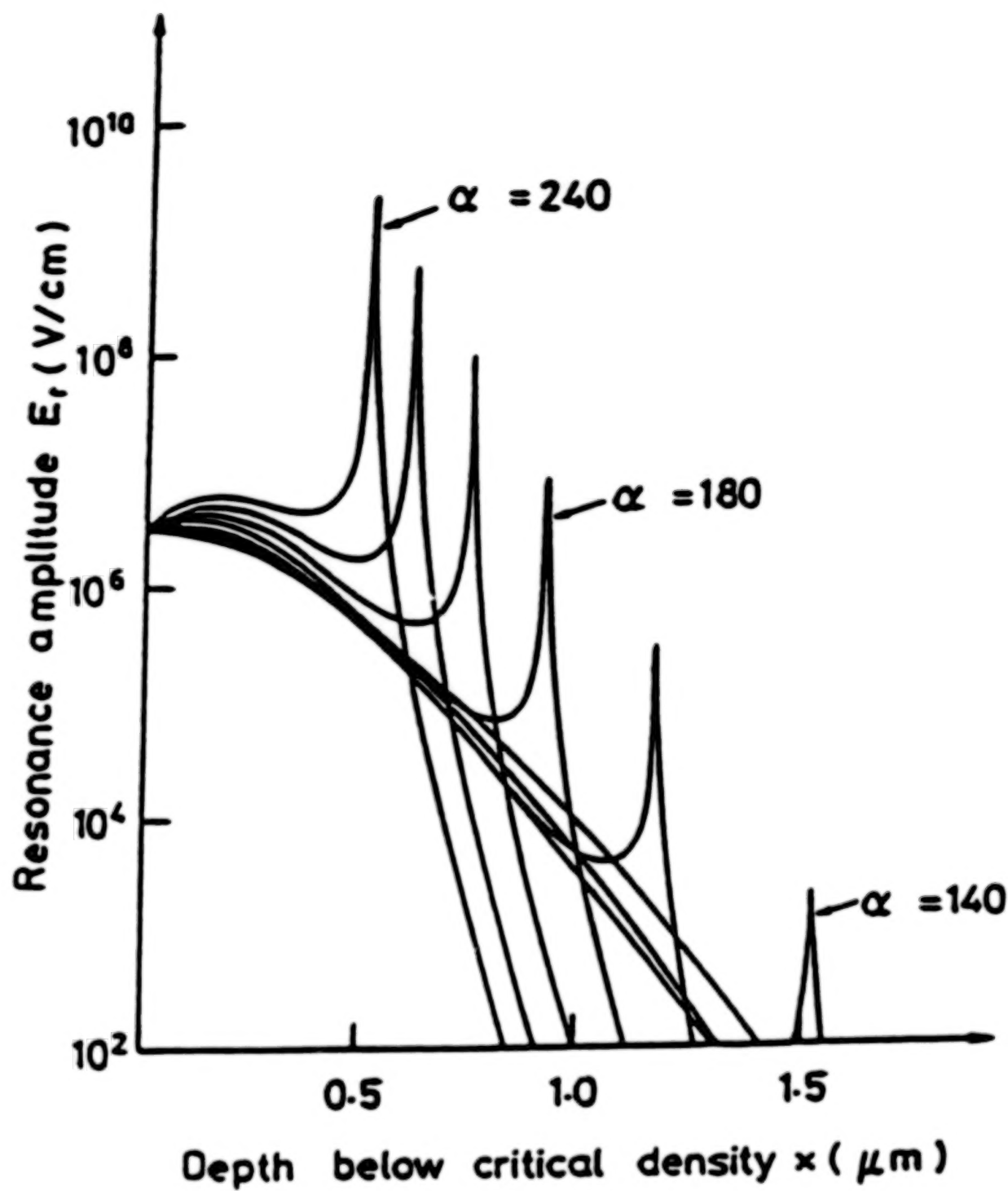


Figure 12. Resonance amplitude  $E_R$  of the longitudinal electric field, as a function of the depth  $x$  below the critical density, for neodymium glass laser irradiation of  $10^{16}$  W/cm<sup>2</sup> into plasma with a temperature of 1 keV. The parameter for profile steepening  $\alpha^2$  ranges from 100 to 240. The critical density  $n_c$  corresponds to the axis  $x = 0$ .

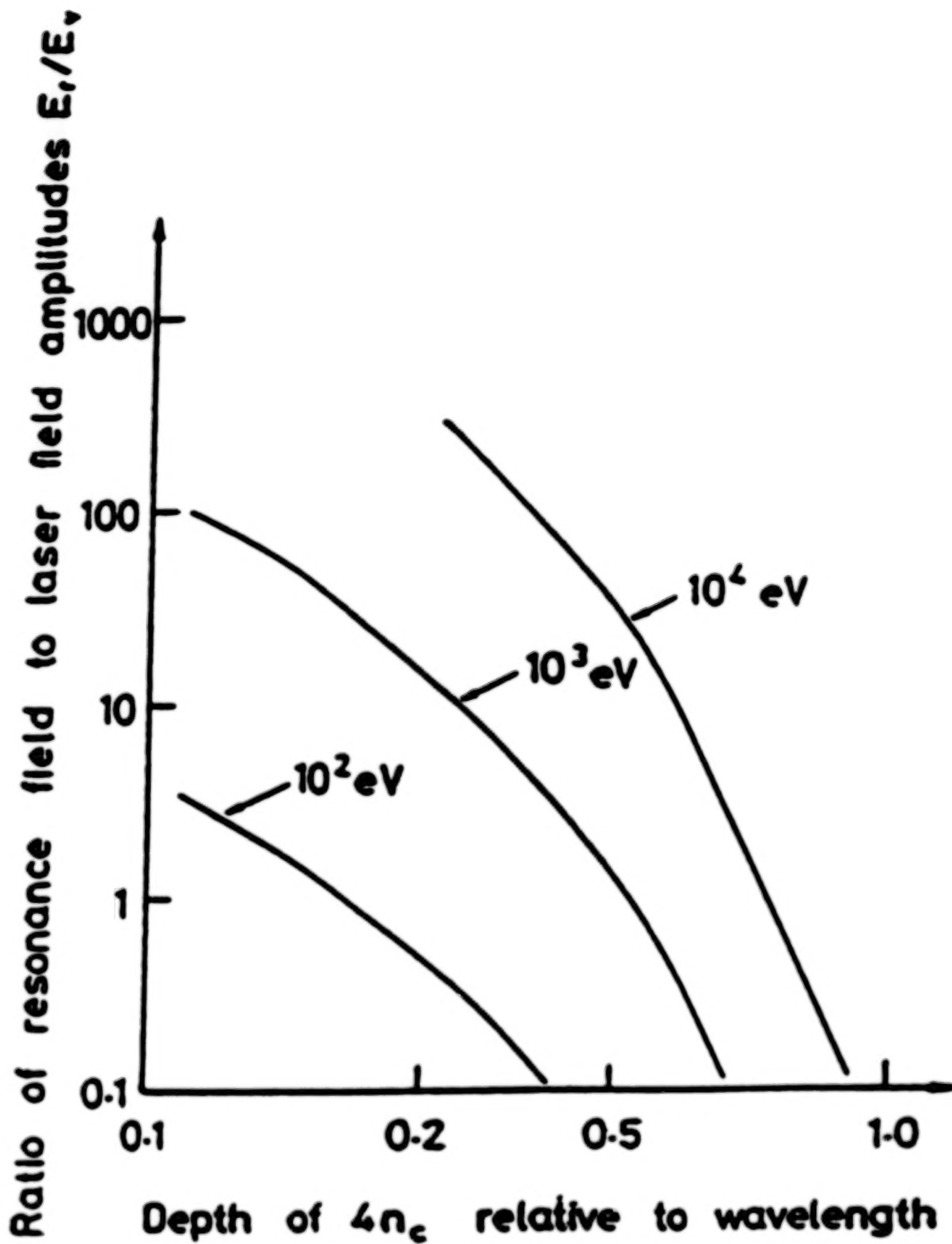


Figure 13. Combining the resonance maxima of Figure 12 and for other temperatures given as ratio to the incident laser amplitude for various plasma temperatures in electron volts depending on the depth  $x$  below the critical density for neodymium glass laser radiation.



# TOKAMAK PLASMA

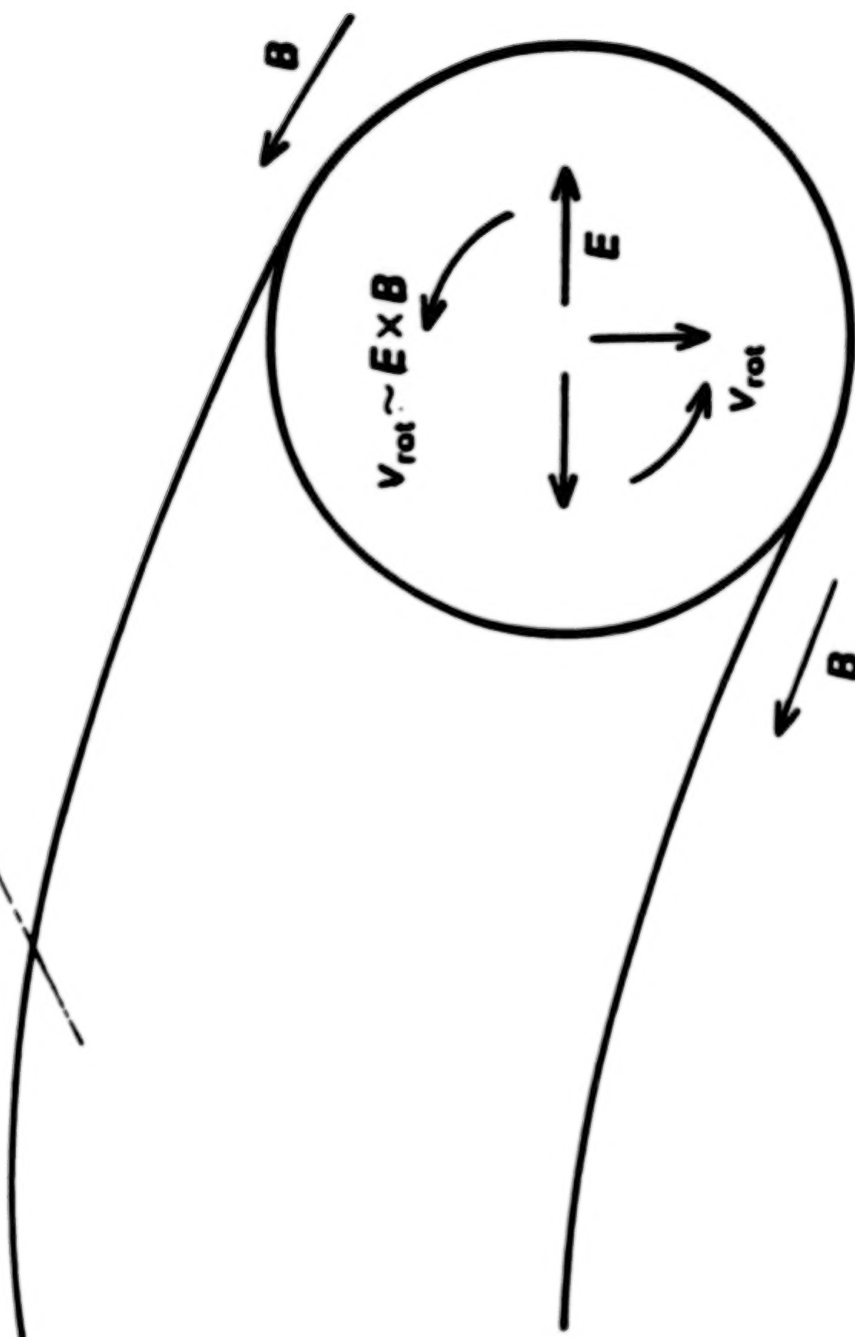


Figure 14. Poloidal rotation of tokamak plasma by  $E \times B$  forces where the electric field  $E$  is the inhomogeneity field.

N87

23320

UNCLAS

# ION PHASE-SPACE VORTICES AND THEIR RELATION TO SMALL AMPLITUDE DOUBLE LAYERS

Hans L. Pécseli

Association EURATOM-Riso National Laboratory  
Physics Department, Riso National Laboratory  
P.O. Box 49, DK-4000 Roskilde, Denmark

## ABSTRACT

The properties of ion phase-space vortices are reviewed with particular attention to their role in the formation of small amplitude double layers in current-carrying plasmas. In a one-dimensional analysis, many such double layers simply add up to produce a large voltage drop. A laboratory experiment is carried out in order to investigate the properties of ion phase-space vortices in three dimensions. Their lifetime is significantly reduced as compared with similar results from one-dimensional numerical simulations of the problem.

## I. INTRODUCTION

A plasma can support a large variety of stationary (or quasi-stationary) double-layer-like structures. The proceedings (Michelsen and Rasmussen, 1982; Schrittwieser and Eder, 1984) of the first two double layer symposia at Riso and in Innsbruck contain an extensive summary of theoretical, numerical, and experimental investigations. A number of these investigations, however, refer to conditions with very carefully chosen initial or boundary conditions imposed on the plasma. These conditions may often be highly idealized, or even unrealistic representations of those met in, for example, ionospheric conditions. However, not all examples have this shortcoming. One of these seems to be small amplitude double layers occurring in current-carrying plasmas. One possible mechanism for their generation is reflection of electrons by a negative potential dip associated with an ion plasma-space vortex, which consequently acts as a "seed" for the double layer (Sato and Okuda, 1980; Hasegawa and Sato, 1982; Nishihara et al., 1982; Berman et al., 1985; Pécseli, 1984). This is a spatially localized process and thus independent of any boundary conditions. The potential drop associated with one such double layer will be rather small. If, however, the system is large and the ion phase-space vortices sufficiently frequently occur, many of these small double layers may be generated and will eventually add up to a significant potential drop. With this scenario in mind, we found it worthwhile to investigate the properties of the ion phase-space vortices in detail. These properties will be summarized in the following paragraphs.

## II. ION PHASE-SPACE VORTICES IN ONE-DIMENSIONAL SYSTEMS

The properties of ion phase-space vortices are discussed in some detail in Berman et al., 1985; Pécseli, 1984; Burjarbarua and Schamel, 1981; Pécseli et al., 1984, 1984, and Trulsen, 1980. They represent one particular type of Bernstein-Green-Kruskal (BGK) equilibria (Bernstein et al., 1957) which appear to be very stable. An ion phase-space vortex thus represents a careful balance between trapped and untrapped particles maintaining a local potential dip, resulting in a corresponding plasma density depletion. It was demonstrated (Bujarbarua and Schamel, 1981) that a simple analytical model, characterized by only three parameters, can be constructed for the ion velocity distribution function. The electrons were assumed to be Boltzmann-distributed. In spite of its simplicity, this model accounts very well for the properties of ion vortices. The analysis is formally very similar to that of electron holes

(Bujarbarua and Schamel, 1981; Lynov et al., 1979, 1985) especially if electron modes in a strongly magnetized plasma waveguide are considered (Pécseili, 1984). A particularly important result of the analysis (Bujarbarua and Schamel, 1981) predicts that ion vortices cease to exist (i.e., their amplitude goes to zero) as the electron-to-ion temperature ratio  $T_e/T_i$  becomes smaller than  $\sim 3.5$ . This result was confirmed in a numerical particle simulation (Pécseili et al., 1981, 1984; Trulsen, 1980).

The dynamic properties of ion phase-space vortices can be most conveniently accounted for by considering them as quasi-particles. A simplified analysis demonstrates that an ion vortex can be assigned a negative charge and a negative mass (Pécseili, 1984; Dupree, 1983). Numerical simulations (Pécseili, 1984; Bujarbarua and Schamel, 1981; Pécseili et al., 1981, 1984; Trulsen, 1980) demonstrated that two ion vortices may coalesce into one when they are sufficiently close in phase space, very much like electron vortices (Lynov et al., 1979, 1980). A detailed parameter study of this process remains to be carried out. Isolated ion holes, on the other hand, appeared to be very stable (Pécseili et al., 1981, 1984; Trulsen, 1980) in a description where the electron component is assumed to be in Boltzmann equilibrium at all times. This simplification becomes inappropriate in current-carrying plasmas, where the interaction between ion vortices and individual electrons becomes important. In this case, the reflected electrons give up a net momentum to the ion vortex, which consequently decelerates, since its effective mass is negative. However, as its velocity is decreased, it can move into regions of increasing ion phase-space density. The result is a slow increase in amplitude of the phase-space vortex, which consequently becomes more efficient in reflecting electrons. The process is thus accelerated. The charge distribution of the reflected electrons gives rise to localized double-layer-like structures. Eventually, the phase-space vortex is destroyed. The very simplified physical picture outlined here is elaborated in more detail by Berman et al. (1985) and Dupree (1983) and also by Nishihara et al., (1982) and Pécseili (1984). In particular, Berman et al. (1985) describe very spectacular one-dimensional numerical particle simulations, showing the slow time evolution of ion phase-space vortices under conditions like those discussed here. It is important to emphasize that the unstable growth of the ion vortices is due to a slowly growing nonlinear instability, which can be excited for bulk electron flow velocities well below those giving the linear two-stream instability. The only criterion for the nonlinear instability seems to be that long-lived ion vortices are formed. In the simulations reported in Berman et al. (1985), this formation occurred for a rather wide class of initial phase-space distributions of simulation particles. The formation of large ion vortices was investigated by Pécseili et al. (1981, 1984) and Trulsen (1980). It could be analytically demonstrated that such vortices are formed in the saturated stage of the one-dimensional ion-ion, two-stream instability of Pécseili and Trulsen (1982). Alternatively, the formation could be due to ion bursts (which after all can be considered as a segment of an ion beam).

### III. ION PHASE-SPACE VORTICES IN THREE DIMENSIONS

The properties of ion phase-space vortices described in the previous section referred mainly to one-dimensional investigations. The experimental investigation reported in Pécseili et al. (1981, 1984) and Trulsen (1980) is of course three-dimensional, but it refers to very carefully chosen initial and boundary conditions. Numerical investigations (Morse and Nielson, 1969) of electron phase-space vortices demonstrated that an ensemble of these was very stable in one dimension, while the phase-space structures were very rapidly eroded in two or, in particular, three spatial dimensions. In order to investigate the properties of ion vortices in three dimensions, we performed a laboratory experiment where the vortices were generated by the ion-ion beam instability, which gives linear instability for wave directions in a cone around the beam velocity.

Our investigations were carried out in the double-plasma device at the University of Tromsø (Johnsen, 1986; Johnsen et al., 1985). The vacuum vessel has an inner diameter of 60 cm and is divided into source and target parts (length 40 cm and 80 cm, respectively) by a fine meshed grid. The device was operated at a typical neutral argon pressure of  $1.5 \times 10^{-4}$  Torr, with plasma densities in the range 2 to  $10 \times 10^8$  cm<sup>-3</sup>. The electron temperature was  $T_e \approx 2.5$  eV, while  $T_i \approx 0.15$  eV in the absence of a beam. By adjusting the bias of the source, an ion beam was injected into the target plasma. Typical beam energies were 4-8 eV. The density ratio between beam and background ions is

adjustable in the setup and was chosen to be around one. The fluctuation level increases along the direction of beam propagation ( $Z$  axis in the following, with  $Z = 0$  corresponding to the position of the separating grid) and saturates roughly at a distance of  $Z = 9$  cm, with a density fluctuation level of  $\bar{n}/n_0 \sim 1$ -5 percent. The increase in noise level is accompanied by a significant scattering of the incoming ion beam, as observed by using both conventional three-grid and the novel directional electrostatic energy analyzers. It is not experimentally possible to obtain information about spontaneously generated individual ion vortices. Instead, we performed a statistical analysis of the experimental data. The turbulent plasma fluctuations in the frequency range 10 kHz to 1 MHz were investigated by the fluctuations in electron saturation current to two movable Langmuir probes with an exposed spherical tip of 1 mm in diameter. Realtime signal sequences of 800  $\mu$ s duration were recorded with a sample rate of 2.5 MHz. At each combination of probe positions, five such sequences formed the basis of a statistical analysis. With the realtime signals available, we thus performed a statistical analysis on a conditional basis. The signal  $n_A$  from the fixed probe (A) at position  $\vec{r}$  was chosen as a reference. Choosing a certain value of the density perturbation, say  $n_1$ , the corresponding time records are subsequently searched for times  $t'$ , where the signal takes a value within the narrow interval  $(n_1, n_1 + \Delta)$ , where  $\Delta$  is taken as the minimum amplitude resolution of the record. Each time this condition on signal A is satisfied, the signal from the movable probe B is recorded in a certain prescribed time interval  $(t' - \tau, t' + \tau)$ . These conditionally chosen time series are then considered as independent realizations for the ensuing statistical analysis. The analysis is repeated for varying positions  $\vec{r}$  of probe B. The result is most conveniently expressed in terms of the electrostatic potential by the relation  $\bar{n}/n_0 \sim e\bar{\phi}/T_e$ , which is adequate for the relatively low fluctuation level in the experiment. A record of 800  $\mu$ s duration is sufficiently long to give an adequate representation of many realizations in the ensemble. By the procedure outlined above, we thus obtained the conditional ensemble average, where  $t'$  is just a dummy variable for time stationary turbulence

$$\bar{\phi} = \langle \phi(\vec{r}, t + t') | \phi(\vec{r}, t') = \phi_1 \rangle. \quad (1)$$

This quantity has the following rather self-evident physical interpretation: given that a particle is located in a potential  $\phi_1$  at a position  $\vec{r}$  at time  $t'$ , then  $\bar{\phi} = \bar{\phi}(\vec{r}, t + t')$  is the average potential variation it will experience in the vicinity of  $\vec{r}$  at the same or at different times.

One important question to be discussed in the following is the lifetime  $\tau_L$  of a conditional structure (or eddy for simplicity) described by equation (1), compared to the average bounce time  $\tau_B$  of a charged particle derived from  $\bar{\phi}$ . Thus, if  $\tau_B \leq \tau_L$ , a small cloud of test particles released at  $(\vec{r}, t')$  will be likely to stay together with the trajectories being correlated for a substantial time. Ions with velocities close to that of the eddy will, if  $\phi_1 < 0$ , be trapped, on average, by the (average) potential, thus exhibiting the features of three-dimensional ion phase-space vortices. On the other hand, if  $\tau_L$  is very short, the particles will disperse rapidly with a large probability, and vortex or "clump-like" features will be immaterial for the description of the turbulent fluctuations in question. In our case, we find  $\tau_L \approx \tau_B$ . In Figures 1a,b we show equipotential contours for  $\phi$  in a rectangular cross-section of the plasma for two different values of the reference potential  $\phi_1$ . The position of the reference probe is indicated by  $\bullet$ . The full spatial variation is obtained by rotating the figure around the  $Z$  axis. This symmetry was explicitly verified in the experiment. For the region of measurements, we may consider the turbulence to be homogeneous and isotropic in the plane perpendicular to the axis of the device. In particular we note that since full time records are available, it is perfectly feasible to let  $t$  be negative, i.e., to consider the formation of the conditional eddy. Evidently the eddy rapidly assumes a roughly spherical shape and propagates in the direction of the ion beam. A lifetime of 60  $\mu$ s for the eddy is estimated for the present plasma conditions. By fitting a parabola to the local minimum of the conditional spatial potential profile, we obtain an inverse angular ion bounce frequency  $\omega_B^{-1} \approx 8 \mu$ s for the largest eddy, indicating that the trapping of ions is a significant dynamic process. The observed structures corresponding to large negative values of  $\phi_1$  can thus be considered as evidence for quasi-static three-dimensional ion holes. Using the electrostatic energy analyzer, we verified (Johnsen et al., 1985) that there was indeed a significant number of ions in the velocity range where they can be trapped by the conditional eddy. From measurements such as those summarized in Figure 1, it is easy to deduce the eddy velocity.



An eddy described by equation (1) and shown in Figure 1 is an average quantity. In each individual realization we may find eddies which may deviate significantly from the average. However, we expect these to have little statistical weight. This statement can be given support by a theoretical analysis.

Being particularly interested in ion-hole formation, we concentrated on negative values for  $\phi_1$  in the present summary of our results. Of course, positive values of  $\phi_1$  can be chosen as well, where now the electrons can be trapped. We found that the evolution of conditional structures corresponding to  $\phi_1 > 0$  was somewhat similar to the overall features given in Figure 1, with some deviations in the actual shapes and velocities. A more general account of these results is in preparation.

#### IV. CONCLUSIONS

In this work we discussed experimental observations of conditional structures in ion beam driven turbulence, presenting the actual variation of the average potential deduced from a conditional analysis of measured fluctuations. Given the propagation velocity and lifetime of these structures, we obtained evidence for the formation of quasi-stationary, ion phase-space vortices. We find it worthwhile to emphasize that the conditionally averaged potential need not coincide with the most probably conditional potential variation. An analysis of this problem requires investigations of the conditional amplitude probability distribution of potential in each spatial point as a function of time. This (rather lengthy) investigation was also carried out. However, the differences between the resulting spatial potential variations and those shown in Figure 1 were not sufficiently pronounced to necessitate a separate figure here. Although we have obtained evidence for the formation of three-dimensional ion phase-space vortices, it seems conclusive that their lifetime is much shorter than for those found in one-dimensional numerical simulations (Pécseľi et al., 1981, 1984; Trulsen, 1980; Pécseľi et al., 1982). In particular, we find that the vortex lifetime is too short to manifest coalescence of two vortices, which is a relatively slow process in units of bounce time. Several reasons for this difference between one and higher dimensions can be found. First of all, a stability analysis (Schamel, 1982) has demonstrated that one isolated vortex is unstable with respect to transverse perturbations in three dimensions, although the growth rate of this instability is rather small for realistic conditions. Probably more important, however, is the possibility of two or many such vortices colliding at an angle in three dimensions, thus destroying the simple trapped particle orbits. Finally, the interaction between ions and potential structures is rather different in one and in higher spatial dimensions, as illustrated in Figure 2. Thus, in one dimension (Fig. 2a), an ion coming in from infinity may give up momentum to an isolated positive quasi-stationary potential structure (top trace) while it only gives a transient perturbation to a negative potential variation (lower trace). In two or three dimensions, an ion may give up momentum to both polarities of a potential variation as indicated in Figure 2b. We see no obvious method to discriminate between these effects in our experiment. Numerical simulations such as those reported in, for example, DeGroot et al. (1977) and Barnes et al. (1985) may provide some insight into these features. It is rather evident that the experimental conditions discussed here do not exactly match those met in current-carrying plasmas. It seems fair, however, to assume that the properties of ion phase-space vortices are, at least in a first approximation, independent of a small electron drift. The conclusion based on the results summarized here will consequently be that the lifetime of ion vortices in three-dimensional unmagnetized systems is not sufficiently long to allow an analysis in terms of quasi-particles interacting with individual electrons, in contrast to the one-dimensional investigations discussed in Berman et al. (1985) and Dupree (1983). The growth of very small vortices, or holes, from an initial low-level noise is thus improbable for a small electron drift. If, however, the electron drift exceeds the threshold for the linear current-driven instability, a rapid growth of negative potential spikes may occur (Barnes et al., 1985) which subsequently form ion vortices by particle trapping (Nishihara et al., 1982). The instability may then evolve nonlinearly as described in Section II. Although the ion vortices have a relatively short lifetime, they have in this case a large amplitude and are thus effective local barriers for the slow electrons. One might expect that these conclusions should be modified for magnetized plasmas with electron drifts



along B-field lines. However, the two-dimensional numerical simulations in Barnes et al. (1985) do not reveal any particular variations of the results with the intensity of an externally applied magnetic field. Unfortunately, practical limitations imply that most numerical simulations are restricted to at most two spatial dimensions.

Although ion phase-space vortices were discussed here with reference to one particular plasma phenomenon, it may be worth mentioning that they present a nonlinear plasma mode which may be interesting also in a different context [see, for instance, the discussion by Hershkovitz (1984)].

*Acknowledgments.* The authors thank R. J. Armstrong, H. Johnsen, J. P. Lynov, P. Michelsen, J. J. Rasmussen, K. Saeki, J. Trulsen, and V. A. Turikov for their collaboration in this work and for many illuminating discussions on the subject of this summary. The expert technical assistance of T. Brundtland in connection with the experiment discussed in Section III is gratefully acknowledged.

## REFERENCES

- Barnes, C., M. K. Hudson, and W. Lotko, *Phys. Fluids*, **28**, 1055 (1985).  
Berman, R. H., D. J. Tetrauli, and T. H. Dupree, *Phys. Fluids*, **28**, 155 (1985).  
Bernstein, I. B., J. M. Green, and M. D. Kruskal, *Phys. Rev.*, **108**, 546 (1957).  
Bujarbarua, S., and H. Schamel, *J. Plasma Phys.*, **25**, 515 (1981).  
DeGroot, J. S., C. Barnes, A. E. Walstead, and O. Buneman, *Phys. Rev. Lett.*, **38**, 1283 (1977).  
Dupree, T. H., *Phys. Fluids*, **26**, 2460 (1983).  
Hasegawa, A., and T. Sato, *Phys. Fluids*, **25**, 632 (1982).  
Hershkovitz, N., in *Second Symposium on Double Layers and Related Topics*, edited by R. Schrittwieser and G. Eder, p. 55, University of Innsbruck, 1984.  
Johnsen, H., *Physica Scripta*, **33**, 84 (1986).  
Johnsen, H., H. L. Pécseli, and J. Trulsen, *Phys. Rev. Lett.*, **55**, 2297 (1985).  
Lynov, J. P., P. Michelsen, H. L. Pécseli, J. J. Rasmussen, K. Saeki, and V. A. Turikov, *Physica Scripta*, **20**, 328 (1979).  
Lynov, J. P., P. Michelsen, H. L. Pécseli, and J. J. Rasmussen, *Phys. Lett.*, **80A**, 23 (1980).  
Lynov, J. P., P. Michelsen, H. L. Pécseli, J. J. Rasmussen, and S. H. Sorensen, *Physica Scripta*, **31**, 596 (1985).  
Michelsen, P., and J. J. Rasmussen (editors), *Symposium on Plasma Double Layers*, Riso National Laboratory, Roskilde, Denmark, 1982.  
Morse, R. L., and C. W. Nielson, *Phys. Rev. Lett.*, **23**, 1087 (1969).  
Nishihara, K., H. Sakagami, T. Taniuti, and A. Hasegawa, in *Symposium on Plasma Double Layers*, edited by P. Michelsen and J. J. Rasmussen, p. 41, Riso National Laboratory, Roskilde, Denmark, 1982.  
Pécseli, H. L., in *Second Symposium on Double Layers and Related Topics*, edited by R. Schrittwieser and G. Eder, p. 81, University of Innsbruck, 1984.  
Pécseli, H. L., and J. Trulsen, *Phys. Rev. Lett.*, **48**, 1355 (1982).  
Pécseli, H. L., R. J. Armstrong, and J. Trulsen, *Phys. Lett.*, **81A**, 386 (1981).  
Pécseli, H. L., J. Trulsen, and R. J. Armstrong, *Physica Scripta*, **29**, 241 (1984).  
Sato, T., and H. Okuda, *Phys. Rev. Lett.*, **44**, 740 (1980).  
Schamel, H., *Phys. Lett.*, **89A**, 280 (1982).  
Schrittwieser, R., and G. Eder (Editors), *Second Symposium on Double Layers and Related Topics*, University of Innsbruck, 1984.  
Trulsen, J., University of Tromsø Report, 1980.

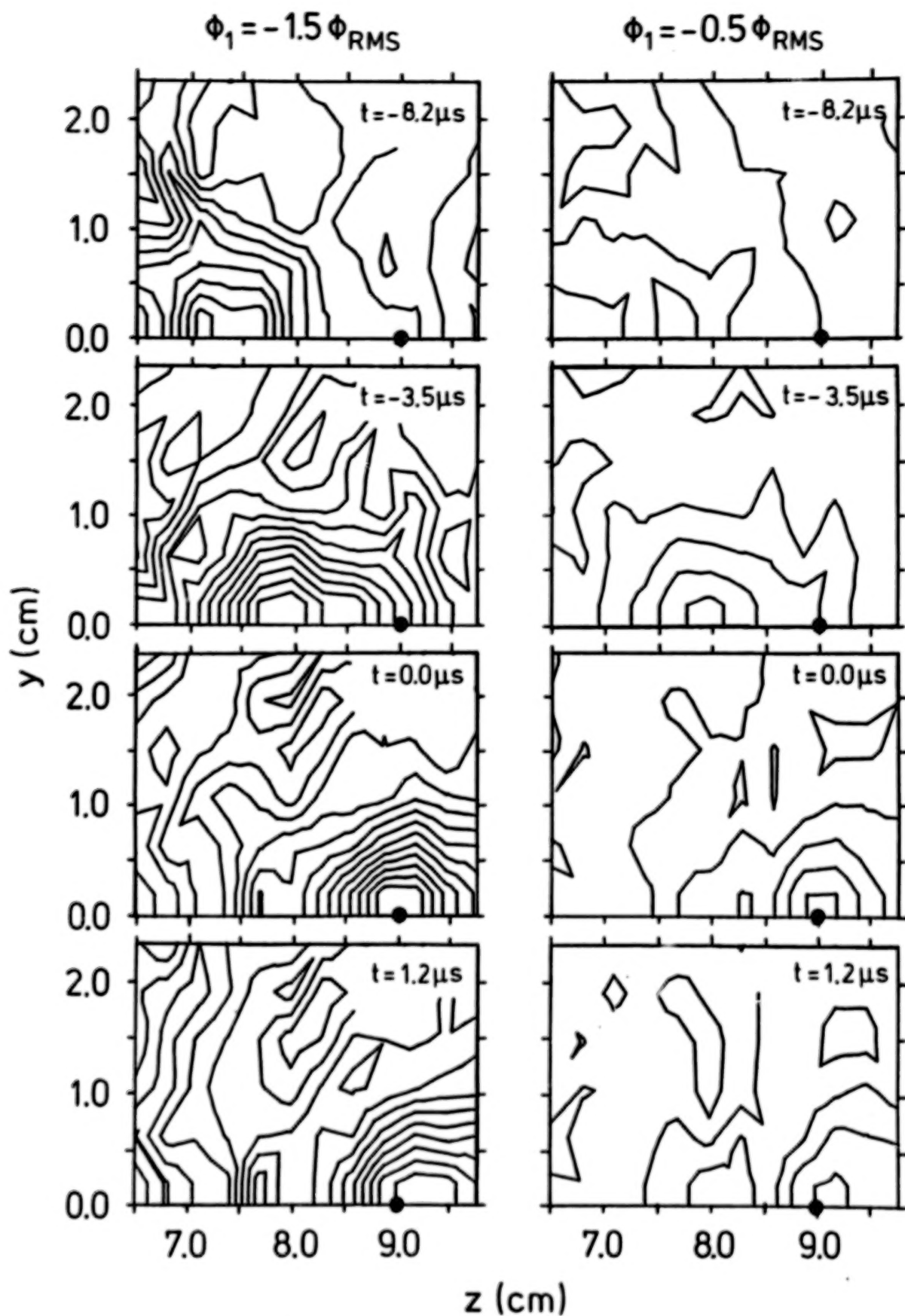


Figure 1. Contour plots of conditional eddies for two different reference values  $\phi_1$  in equation (1) measured in units of the rms value of the potential fluctuations  $\phi_{rms}$ . The position of the reference probe is  $Z = 9$  cm measured from the separating grid of the double-plasma device. The spacing between contours is  $0.1 \phi_{rms}$ .

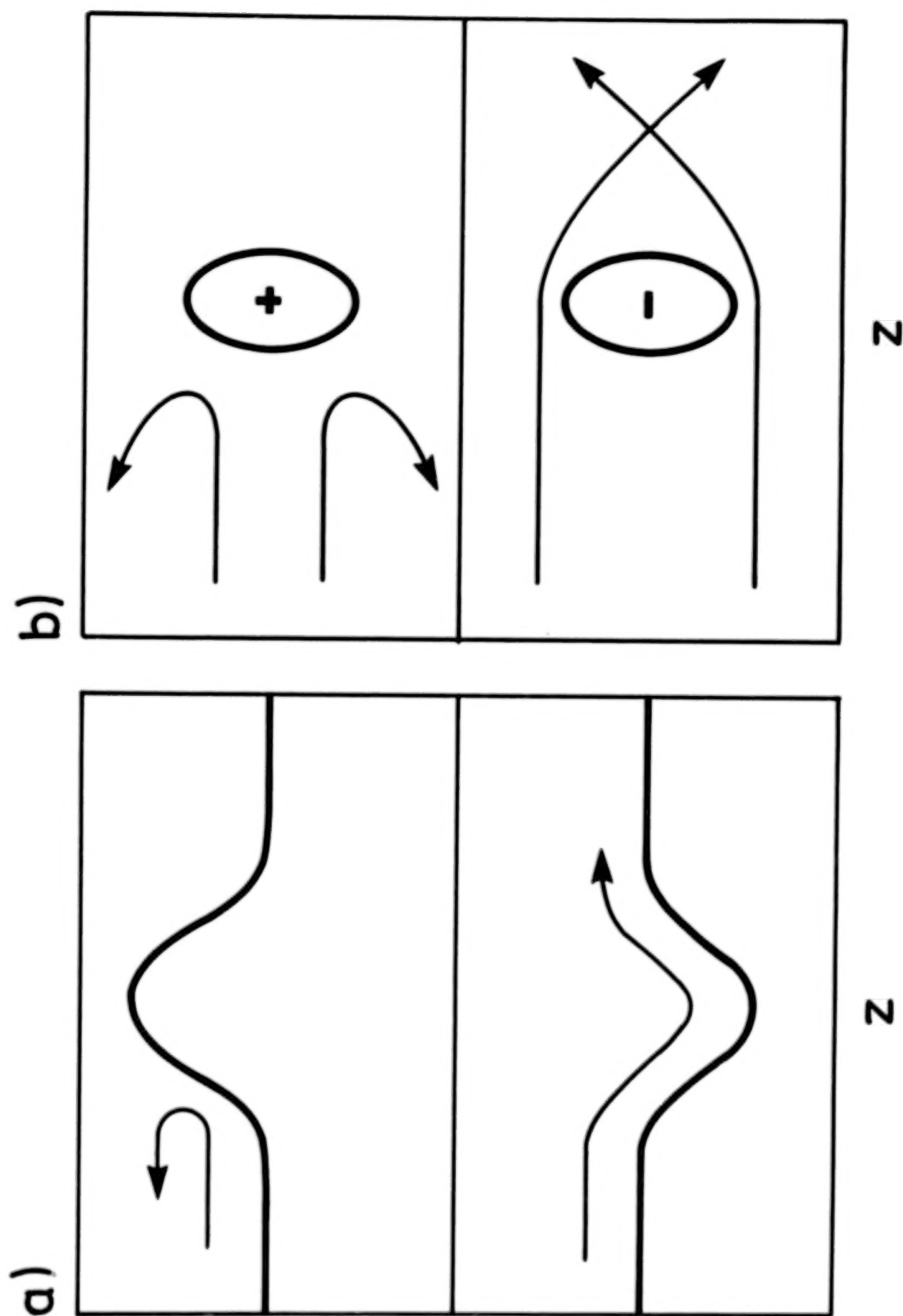


Figure 2. Schematic diagram for discussing the difference between particles interacting with localized potential variations in one and in higher dimensions.

N87

23321

UNCLAS

# EFFECT OF DOUBLE LAYERS ON MAGNETOSPHERE-IONOSPHERE COUPLING

Robert L. Lysak

School of Physics and Astronomy, University of Minnesota  
Minneapolis, MN 55455, U.S.A.

N87-23321

Mary K. Hudson

Department of Physics and Astronomy, Dartmouth College  
Hanover, NH 03755, U.S.A.

## ABSTRACT

The Earth's auroral zone contains dynamic processes occurring on scales from the length of an auroral zone field line (about  $10 R_E$ ) which characterizes Alfvén wave propagation to the scale of microscopic processes which occur over a few Debye lengths (less than 1 km). These processes interact in a time-dependent fashion since the current carried by the Alfvén waves can excite microscopic turbulence which can in turn provide dissipation of the Alfvén wave energy. This review will first describe the dynamic aspects of auroral current structures with emphasis on consequences for models of microscopic turbulence. In the second part of the paper a number of models of microscopic turbulence will be introduced into a large-scale model of Alfvén wave propagation to determine the effect of various models on the overall structure of auroral currents. In particular, we will compare the effect of a double layer electric field which scales with the plasma temperature and Debye length with the effect of anomalous resistivity due to electrostatic ion cyclotron turbulence in which the electric field scales with the magnetic field strength. It is found that the double layer model is less diffusive than in the resistive model leading to the possibility of narrow, intense current structures.

## 1. INTRODUCTION

Auroral arcs and the auroral current structures which produce them occur in a variety of scale sizes and time scales. While electrostatic models of auroral electrodynamics (Lyons et al., 1979; Fridman and Lemaire, 1980; Chiu and Cornwall, 1980) have had success at describing the overall current-voltage relationship of the auroral zone and in defining the scale size of the inverted-V precipitation signature, they are not well suited to describing the dynamics of small-scale auroral arcs, multiple auroral arcs, and time-dependent auroral structures. In this realm a fluid picture of auroral electrodynamics has advantages and can describe a number of auroral processes (Sato, 1978; Goertz and Boswell, 1979; Miura and Sato, 1980; Lysak and Dum, 1983; Lysak, 1985, 1986). The difficulty with the fluid models is that the kinetic processes which play an important part in defining the auroral potential drop must be described by means of assumed transport coefficients which should be determined by a consideration of the microscopic plasma processes.

The formation of parallel potential drops in laboratory and computer simulated plasmas has been covered in many of the reviews in this workshop. The problem with applying most of these results to the auroral zone is the high sensitivity of the results to the initial and boundary conditions which are imposed. In the auroral plasma, there are no grids to be set to a certain voltage and, perhaps more fundamentally, the scale of the system is vastly larger than the sizes of a thousand Debye lengths or so which are typical in laboratory and computer studies. Therefore a description of the auroral potential drop should consider the large-scale dynamics of the auroral zone as well as the microscopic processes which can directly produce parallel electric fields.

The remainder of this review will consist of two major sections. In the first, we will consider some of the time-dependent aspects of auroral current structures and the implications these structures have for models of microscopic plasma turbulence. In particular, we will argue that auroral currents are closely associated with Alfvén wave



signatures that tend to define the current which flows along auroral field lines and that include a transient parallel electric field which can set up the particle distributions necessary to support double layer structures. In the second part of the review, we will discuss some numerical experiments in which the form of the parallel electric field is changed. We will consider two extreme cases. In the first, we assume a double layer model in which a potential drop that scales with the electron temperature is distributed over distances which scale with the Debye length when the current exceeds a threshold. We will compare this model with a model of nonlinear resistivity due to electrostatic ion cyclotron turbulence in which the effective resistivity increases with the current over a threshold. These models produce rather different overall current structures, since in the resistive model the current diffuses across the magnetic field producing broader structures, while in the double layer model narrow current structures can persist.

## II. A BRIEF REVIEW OF AURORAL ELECTRODYNAMICS

The Earth's auroral zone is a region in which the ionosphere and the outer magnetosphere are coupled by means of magnetic field-aligned currents which flow between the two regions. These currents must close across field lines in the ionosphere and also somewhere in the outer magnetosphere. Ionospheric current closure is described by the current continuity equation, which is generally integrated along the field line over the thin layer (about 50 km) in which the ionospheric currents flow. To simplify the description, we will consider a two-dimensional geometry in which variations in longitude are ignored. This assumption is well justified on the dawn and dusk flanks of the magnetosphere, although it should be modified to take into account the more complicated current structures at noon and midnight. With these approximations ionospheric current continuity can be expressed as follows:

$$j_z = \frac{\partial I_x}{\partial x} = \frac{\partial}{\partial x} [\Sigma_p E_x] \quad (1)$$

where  $\Sigma_p$  is the height integrated Pedersen conductivity and the geometry is defined in Figure 1. Note that here a positive current is parallel to the magnetic field line, i.e., downward in the northern hemisphere.

In the steady state and in the absence of parallel electric fields, the north-south electric field  $E_x$  simply maps along the field line, which, in the dipolar coordinates of Figure 1, means that it stays constant. (More details on the dipolar coordinate system can be found in Lysak, 1985.) However, if we assume that a linear relationship exists between the parallel current and the parallel potential drop:

$$j_z = -K(\Phi_i - \Phi_e) \quad (2)$$

where  $\Phi_i$  and  $\Phi_e$  represent the potential in the ionosphere and in the equatorial plane, respectively, the perpendicular field must change along the field line so that the curl of the total electric field vanishes. In this case, we can combine equations (1) and (2) to relate the potential in the ionosphere to the equatorial potential:

$$\left[ 1 - \frac{\Sigma_p}{K} \frac{\partial^2}{\partial x^2} \right] \Phi_i = \Phi_e \quad (3)$$

This relationship indicates that large-scale potential structures in the equatorial plane, with sizes large compared to  $L = \sqrt{\Sigma_p/K}$ , will pass unattenuated to the ionosphere with no potential drop along the field line. On the other hand, equatorial structures with sizes less than  $L$  will not be mapped to the ionosphere, and the resulting difference will



appear as a parallel potential drop. For auroral zone parameters, this scale length  $L$  is about 100 km. This scale size is appropriate for the largest scale auroral structures, but is large compared to the sizes of individual auroral arcs which have a scale of about 1 km.

Consequences of this type of model in the steady state have been considered by Lyons et al. (1979), Chiu and Cornwall (1980), and others. Two critical assumptions are made in these models. First, it is assumed that a linear current-voltage relationship as in equation (2) is present. These authors associate such a relationship with plasma sheet particle motion in the dipolar magnetic field, as was shown by Fridman and Lemaire (1980). As we shall see below, such an approximate linear relationship is not restricted to these adiabatic models. A second assumption is that the driving force in the outer magnetosphere is characterized by a fixed potential as a function of position represented by the right-hand side of equation (3). Such a potential could be related to the  $E \times B$  motion of the equatorial plasma, in which case treating it as constant implies that the equatorial convection is not affected by conditions on the field line which connects it to the ionosphere.

On the other hand, it has been known for some time that the ionosphere exerts a frictional influence on magnetospheric convection due to the dissipation caused by the finite Pedersen conductivity (e.g., Vasyliunas, 1970; Sonnerup, 1980). Information on ionospheric conditions is transmitted to the equatorial region by means of shear mode Alfvén waves which can propagate along the field line between the two regions, which have a travel time from the ionosphere to the equator of about 30 s in the auroral zone, as is evidenced by the existence of Pi2 pulsations with periods of about 2 min (Southwood and Hughes, 1983), which would correspond to the travel time from one ionosphere to the conjugate ionosphere and back.

The presence of Alfvén waves on auroral field lines should cause one to rethink the steady state model presented above. For one thing, the steady state model assumes that currents perpendicular to the magnetic field only exist at the ionosphere and in the equatorial plane, while Alfvén waves carry with them a polarization current which depends on the rate of change of the perpendicular electric field. In a static structure, these currents will vanish, but the possibility exists that a standing wave structure could be set up in which the polarization currents could persist. Such a situation is shown in Figure 2, which shows results from a time-dependent, two-dimensional MHD model of auroral currents (Lysak and Dum, 1983; Lysak, 1985). The contours in this figure represent flow lines of the current for a case in which a potential structure is propagated across the field line. Alternatively, this figure could be viewed as the current pattern produced by a potential structure in the presence of a north-south component of plasma convection in the auroral zone. As can be seen, the multiple reflections of the Alfvén wave pulses give rise to wave structure in which interference occurs between up- and downgoing waves. This wave interference decouples the field-aligned currents which connect to the ionosphere from those which flow up to the equatorial plane. In a structure such as this, which may be typical of multiple auroral arc structures, the steady state model is clearly inappropriate.

This structure can be described by a generalization of the model given above by replacing the assumption that a fixed equatorial potential structure is present by a more general assumption that a relation exists between the electric field and the perpendicular currents. For the case of polarization currents, this relation involves the so-called Alfvén conductance (Mallinckrodt and Carlson, 1978),  $\Sigma_A = c^2/4\pi V_A$ , where  $V_A$  is the Alfvén speed. If it is assumed that the ionospheric currents close via these polarization currents, a relation with the form of equation (3) results but with the scale length becoming:

$$L = \left[ \frac{\Sigma_p \Sigma_A}{K (\Sigma_p + \Sigma_A)} \right]^{1/2} \quad (4)$$

The Alfvén conductance  $\Sigma_A$  is plotted along an auroral field line in Figure 3, where it can be seen that its value over the field line is generally less than the Pedersen conductivity, which is typically over 1 mho. For the Case  $\Sigma_A \ll \Sigma_P$ , equation (4) shows that the scale length depends on the Alfvén conductance rather than the Pedersen conductivity, leading to smaller scales than those predicted by equation (2). Thus, the 1-km scale size of discrete auroral arcs may in fact be a result of current patterns such as those shown in Figure 2.

Another process which violates the steady state assumption is the enhancement of the ionospheric conductivity due to the enhanced energetic electron precipitation produced by the parallel electric field. This can give rise to a feedback instability (Sato, 1978; Rothwell et al., 1984; Lysak, 1986) in which traveling enhancements of the conductivity and the field-aligned current occur (Fig. 4). Numerical modeling of this instability (Lysak, 1986) shows periods of about 1 s which appear to be due to Alfvén wave reflections at altitudes of  $2 R_E$  or less, so these currents also close well before they reach the equatorial region. The structures shown in Figure 4 have scale sizes of about 10 km, approaching the size of the discrete aurora.

The discussion above indicates that while the steady state model can describe the large-scale properties of the aurora, time-dependent effects may be important at creating short-scale current structures on auroral field lines. Parallel electric fields thus form in a current environment which can fluctuate on time scales as quickly as 1 s. On these time scales, Alfvén waves carry changes in the field-aligned currents. Parallel electric fields form as a result (Goertz and Boswell, 1979) of the current required to flow because of the magnetic perturbation associated with the Alfvén wave. Plasma turbulence will form when the current exceeds the threshold for instabilities. The effect of this turbulence will be examined in the following section.

### III. MACROSCOPIC EFFECTS OF PLASMA TURBULENCE

If plasma turbulence does develop, it can affect the development of the current structure which produced it. Lysak and Carlson (1981) showed that the introduction of parallel resistivity modified the Alfvén wave dispersion relation, producing a reflection and dissipation of the wave which reduces the current. From the point of view of the MHD equations, this is the result of the well-known magnetic diffusion equation in the presence of resistivity. Plasma turbulence in a strong magnetic field will most likely give rise to a non-isotropic conductivity. In the case of double layer formation of electrostatic ion cyclotron turbulence, the dominant effect is that of parallel resistivity (Lysak and Dum, 1983). It can be shown that this term gives rise to diffusion across the magnetic field:

$$\frac{\partial B_y}{\partial x} = \frac{\partial}{\partial x} \left[ \eta_{\parallel} \frac{\partial B_y}{\partial x} \right] \quad (5)$$

in the geometry of Figure 1 with gradients in  $y$  ignored. Thus, the presence of plasma turbulence will in general lead to a broadening of current structures and the reduction in the current strength.

In this section, we will compare three models of parallel electric fields caused by current-driven turbulence. In order to incorporate these effects into a MHD model, a simple relationship between the fluid properties of the plasma, such as density, drift velocity and temperature, and the parallel electric field, must be introduced. Clearly, a satisfactory model of this type has not yet been found and, indeed, it is likely that the complexities of plasma turbulence cannot be so easily parameterized. Nevertheless, some simple models of this type can be considered and will serve to indicate some of the relevant effects.

The first model we will consider will be based on simulations of current driven double layers (e.g., Sato and Okuda, 1981; Kindel et al., 1981; Barnes et al., 1985). When the drift velocity in these models is about half the electron thermal speed, double layers with amplitude  $e\Phi/T_e \approx 1$  are produced and, in long enough systems, will recur at intervals of the order of 1000 Debye lengths, where a Debye length is the order of a few meters in the auroral plasma. Since the MHD model has a grid size along the magnetic field of about 500 km, it is appropriate to consider the average electric field, which for the above numbers leads to:

$$E_z = 0.001 [4\pi n T_e]^{1/2} \quad (6)$$

Although the drifts in excess of the threshold cause these double layers to grow and decay more quickly (Barnes et al., 1985), the average electric field over the time step of the MHD model (about 0.01 s) may remain roughly constant. To avoid a discontinuity in the electric field, the parallel field is increased linearly [using the linear resistivity given by equation (9) below] until the double layer electric field given above is reached. It should be noted that double layer electric fields are not present when the plasma frequency exceeds the electron cyclotron frequency (Barnes et al., 1985). This effect has not been explicitly included in the model; however, in the region in which the critical current is the lowest, the plasma frequency remains below the cyclotron frequency.

As an alternate to the double layer model, we consider a model for electrostatic ion cyclotron (EIC) turbulence due to resonance broadening (Dum and Dupree, 1970; Lysak and Dum, 1983). In this model, a resistive potential drop is introduced whenever the current exceeds the threshold for the EIC instability, i.e., about 0.3 of the electron thermal speed for  $T_e = T_i$ . The amplitude of the fluctuating electric field, and thus the effective resistivity, increases quadratically as the current increases. Thus, the electric field becomes:

$$E_z = \frac{mv^*}{ne^2} (j_z - j_{crit}) \quad (7)$$

where the effective collision frequency is:

$$\nu^* = 0.4 \Omega_i \left[ 1 + 0.1 \left( \frac{j_z - j_{crit}}{j_{crit}} \right)^2 \right] \quad (8)$$

Note that in this case the parallel electric field will scale with the strength of the background magnetic field through the ion gyrofrequency  $\Omega_i = eB/m_i c$ , in contrast to the double layer model described by equation (6).

These two models have very differing behavior in that the double layer model is electric field-saturated in the sense that once the critical current is reached, the parallel electric field does not increase further. The nonlinear resistive model described by equations (7) and (8) is in a sense current-saturated since the electric field rises very rapidly after the critical current is reached. This enhances the diffusion of the current and reduces it to a lower level. The third model that will be considered will be one in which an effective collision frequency is assumed as in equation (7) but the collision frequency is independent of the current once the threshold is reached. Thus, equation (8) is replaced by:

$$\nu^* = 0.4 \Omega_i \quad (9)$$



when the drift velocity exceeds 0.3 of the electron thermal speed. This model will be referred to as the linear resistivity model.

In order to assess the macroscopic consequences of these models, a series of runs were done with the MHD model described earlier. In these runs, a current loop of a fixed magnitude and width is introduced on the field line, propagates toward the ionosphere, and enters a region of parallel electric field described by one of the three models. The ionospheric conductivity is taken to be fixed at 1 mho, and the density profile is of the form:

$$n(r) = 10^5 e^{-(r-r_0)/h} + 5 (r - 1)^{-1.5} \quad (10)$$

where  $n$  is measured in  $\text{cm}^{-3}$ ,  $r$  is in  $R_E$ , the base altitude for the ionosphere is  $r_0 = 1.05 R_E$ , and the scale height  $h = 0.1 R_E$ . The electron temperature is 1 eV and the upper boundary condition is taken to absorb Alfvén waves which are incident upon it after being reflected from lower altitudes (Lysak, 1985). As the runs proceed, the maximum potential drop and the field-aligned current at the ionosphere are monitored, as the system approaches a steady state. Since the ionosphere is a very good conductor, the current of a reflected Alfvén wave is in the same direction as that of the incident wave (Mallinckrodt and Carlsson, 1978); thus, the final value of the current will be twice the injected current in the limit of infinite ionospheric conductivity ( $\Sigma_p \gg \Sigma_A$ ) and no parallel electric field. Such a case is shown in Figure 5 in which the injected current was  $20 \mu\text{A}/\text{m}^2$  and the final current of  $36 \mu\text{A}/\text{m}^2$  is nearly double this value. Because of the diffusion associated with the parallel electric field, the current reaching the ionosphere is reduced when a parallel electric field is present. This effect is shown for the double layer model and the nonlinear resistivity model in Figures 6 and 7, respectively. In these figures the injected current was  $20 \mu\text{A}/\text{m}^2$ . It can be seen that the double layer model is much less diffusive than the resistive model, with the final currents being  $30 \mu\text{A}/\text{m}^2$  and  $6 \mu\text{A}/\text{m}^2$  for the two runs.

The final current-voltage characteristics for a series of runs are shown in Figure 8. First of all, note that each of the models produces potentials in the kilovolt range for currents of a few microamps per square meter. This is significant since the parameters of the parallel electric field model were determined purely from the local properties of the auroral plasma without any requirement that the global current-voltage relation come out right. Therefore, none of the models can be ruled out on this basis.

Turning to differences in the models, we see that the double layer model exhibits the voltage-saturation effect referred to earlier. As the current increases, more of the field line can support the formation of double layers, leading to an increased total potential drop. Since it is assumed that the parallel electric field does not increase further as the current increases, the addition of more current does not further increase the total potential drop.

The linear resistivity model produces a linear current-voltage characteristic. At first glance this may appear obvious, but actually the situation is complicated by the scaling of the fields and currents along the field line. It was shown by Lysak and Dum (1983), however, that these factors cancel when the resistivity scales with the magnetic field strength, preserving the linear relationship between the total potential and the field-aligned current at the ionosphere. The approximate linear relationship has been invoked by Lyons (1980) to support the nonlocal current-voltage relationship based on adiabatic particle motions (e.g., Fridman and Lemaire, 1980). However, the present argument shows that this interpretation is not unique.

The current limiting effect of the nonlinear resistivity model is apparent from Figure 8. Here an attempt to increase the current simply causes an enhancement in the diffusion, leading to large potentials and a broader current structure as is seen in Figures 9 and 10, which compare the field and current profiles for the double layer and non-linear resistivity models. Here the enhanced diffusion due to the nonlinear resistivity is evident.

Figure 11 shows the effective diffusion in the entire set of runs by plotting the ratio between final and input currents against the input current. As discussed above, the maximum value of this ratio is 2 for the case of infinite Pedersen conductivity. The open squares represent runs with no parallel electric field and a Pedersen conductivity of 1 mho. The small reduction from 2 in these cases represents the effect of ionospheric dissipation. Note that the linear and nonlinear resistive models have comparable diffusion for small currents where the nonlinear part of the resistivity is not important; but, at larger currents, the nonlinear model is more diffusive. The double layer model is comparable to the other models at low currents, but an increase in the current decreases the effective diffusion since the potential drop does not increase for increasing current.

In summary, the three models for a local current voltage relation produce results consistent with the observed global relationship. Thus, this type of model cannot be distinguished from the kinetic models of parallel potential drop on this basis. The double layer model allows for very strong currents to flow in a narrow channel since the potential drop and thus the effective diffusion do not increase much as the current increases. The nonlinear resistive model has the opposite effect in that the strong increase in the potential drop for an increase in the current causes an enhanced diffusion which broadens the current channel, in effect causing the current to flow around the region of parallel electric field.

#### IV. SUMMARY AND CONCLUSIONS

The simplified models of parallel electric fields presented here have provided some insight into the development of the auroral potential drop, but are clearly limited in their applicability to the auroral plasma. Auroral conditions can be quite varied, and the presence of turbulence along the field line can result in the heating of the plasma as well as a decrease in the plasma density as transversely heated ions are expelled from the acceleration region. Therefore, there is more to auroral dynamics than can be found in the simple cold plasma model used here.

Density decreases in the auroral zone serve to decrease the critical current necessary for the generation of microscopic turbulence, and therefore will increase the total potential drop for a given level of current. Numerical results indicate that this result is more important in the double layer model because of the "switch-on" nature of the double layer electric field. Since the double layer electric field scales with the plasma pressure, the potential drop is localized at the lowest altitudes at which the critical current is exceeded. This is in contrast with the resistive electric field which depends on the excess current over the critical current, and thus maximizes at the point where the critical current is lowest. A set of runs in which a current of  $10 \mu\text{A}/\text{m}^2$  is injected showed that the potential drop increased by 25 percent in the double layer model when the ionospheric scale height [see equation (10)] is reduced to  $0.05 R_E$  from the value of  $0.1 R_E$  used in the other runs, while in the nonlinear resistivity model the increase was only 18 percent. Thus, the effect of a density cavity would be to produce an increase in the potential drop, especially in the double layer model.

The temperature of the topside ionosphere can also vary under auroral conditions, and may be expected to increase as the result of microscopic turbulence. Increases in the temperature will tend to decrease the extent of the turbulent region since the critical current scales as the electron thermal speed. Thus, potential drops due to nonlinear resistivity would be expected to decrease. A similar result is true in the double layer model; however, this effect is counteracted by the increase of the average electric field due to double layers since this field scales with the square root of the temperature. Runs at  $10 \mu\text{A}/\text{m}^2$  indicate that the potential drop in the nonlinear resistivity model decreased by 35 percent when the temperature was raised by a factor of 10, while in the double layer model the potential increased by 12 percent. Thus, the increase of temperature favors the double layer model, at least until the point at which the current becomes sub-critical.

In the actual auroral zone, these two effects will be necessarily connected. The transverse heating of ions observed in the auroral zone can create density cavities since the heated ions are subject to the magnetic mirror force that expels them from the low-altitude auroral zone. One can imagine a scenario in which the increase of the current magnitude excites turbulence, leading to the heating of ions and the creation of the density cavity. This hot, low density plasma would lead to conditions under which the formation of double layers could further accelerate electrons into the atmosphere and ions out of the atmosphere. This would result in the density cavity progressively extending to lower and lower altitudes, with a corresponding increase in the total potential drop along the field line. While the existing numerical model is too crude to account for all these effects, this scenario seems plausible based on the results above. A more complete model including the effects of the thermal evolution of the plasma will be the subject of future work.

In conclusion, this work has shown first of all that models of the auroral potential drop based on microscopic turbulence, whether due to double layers or a nonlinear resistivity, can account for the correct magnitude of the auroral potential drop for typical auroral currents. The two models differ in that the nonlinear resistivity model limits the current density by spreading the current over a broader area. In contrast, the double layer model proposed above has a limit to its total potential drop and can sustain currents with a high density. At such high current densities, however, this model will most likely be too simplified, since plasma heating and the formation of a density cavity, effects not included in the cold plasma model presented here, will likely change the nature of the current-voltage relation.

The oversimplified models presented here represent an attempt to incorporate kinetic effects of the plasma into a fluid model. In order to model the global structure of the auroral zone, some such approximation must be made since particle-in-cell or Vlasov models of any large volume of the auroral zone are technically not feasible with present or anticipated computer resources. The question of a satisfactory parameterization of the kinetic effects for use in a fluid model remains an open question, which can only be answered by a combination of fluid modeling and kinetic modeling, as well as analytic theory of the auroral current region.

*Acknowledgments.* The authors would like to thank W. Lotko and D. S. Evans for useful discussions on this work. This work was supported in part by NSF grants ATM-8451168 and ATM-8508949 and NASA grant NAGW-809. Computing costs were supported by the University of Minnesota Supercomputer Institute.



## REFERENCES

- Barnes, C., M. K. Hudson, and W. Lotko, *Phys. Fluids*, 28, 1055 (1985).
- Chiu, Y. T., and J. M. Cornwall, *J. Geophys. Res.*, 85, 543 (1980).
- Dum, C. T., and T. H. Dupree, *Phys. Fluids*, 13, 2064 (1970).
- Fridman, M., and J. Lemaire, *J. Geophys. Res.*, 85, 664 (1980).
- Goertz, C. K., and R. W. Boswell, *J. Geophys. Res.*, 84, 7239 (1979).
- Kindel, J. M., C. Barnes, and D. W. Forslund, in *Physics of Auroral Arc Formation*, American Geophysical Union Geophysical Monograph 25, edited by S.-I. Akasofu and J. R. Kan, p. 296, 1981.
- Lyons, L. R., *J. Geophys. Res.*, 85, 17 (1980).
- Lyons, L. R., D. S. Evans, and R. Lundin, *J. Geophys. Res.*, 84, 457 (1979).
- Lysak, R. L., and C. W. Carlson, *Geophys. Res. Lett.*, 8, 269 (1981).
- Lysak, R. L., and C. T. Dum, *J. Geophys. Res.*, 88, 365 (1983).
- Lysak, R. L., *J. Geophys. Res.*, 90, 4178 (1985).
- Lysak, R. L., *J. Geophys. Res.*, accepted for publication, 1986.
- Mallinckrodt, A. J., and C. W. Carlson, *J. Geophys. Res.*, 83, 1426 (1978).
- Miura, A., and T. Sato, *J. Geophys. Res.*, 85, 73 (1980).
- Rothwell, P. L., M. B. Silevitch, and L. P. Block, *J. Geophys. Res.*, 89, 8941 (1984).
- Sato, T., *J. Geophys. Res.*, 83, 1042 (1978).
- Sato, T., and H. Okuda, *J. Geophys. Res.*, 86, 3357 (1981).
- Sonnerup, B.U.O., *J. Geophys. Res.*, 85, 2017 (1980).
- Southwood, D. J., and W. J. Hughes, *Space Sci. Rev.*, 35, 301 (1983).
- Vasyliunas, V. M. in *Particles and Fields in the Magnetosphere*, edited by B. McCormac, p. 29, D. Reidel, Hingham, Massachusetts, 1970.

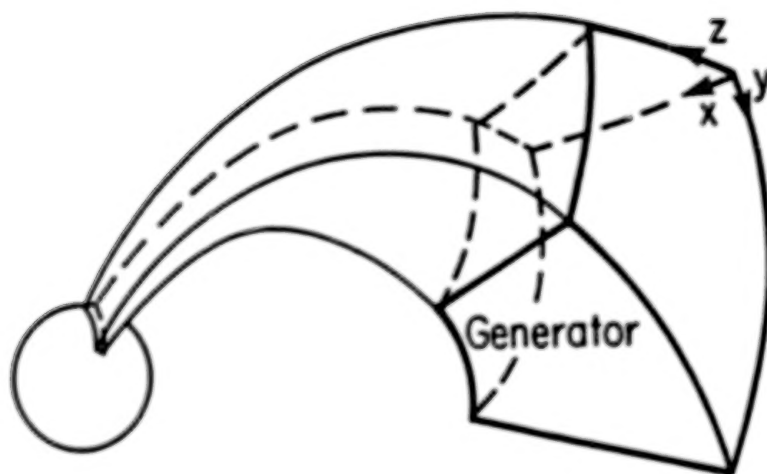


Figure 1. A sketch of the dipolar coordinate system used in this paper. Here  $z$  is the coordinate along the geomagnetic field,  $y$  is the longitude, and  $x$  is a coordinate proportional to the inverse of the  $L$  value of the field line.

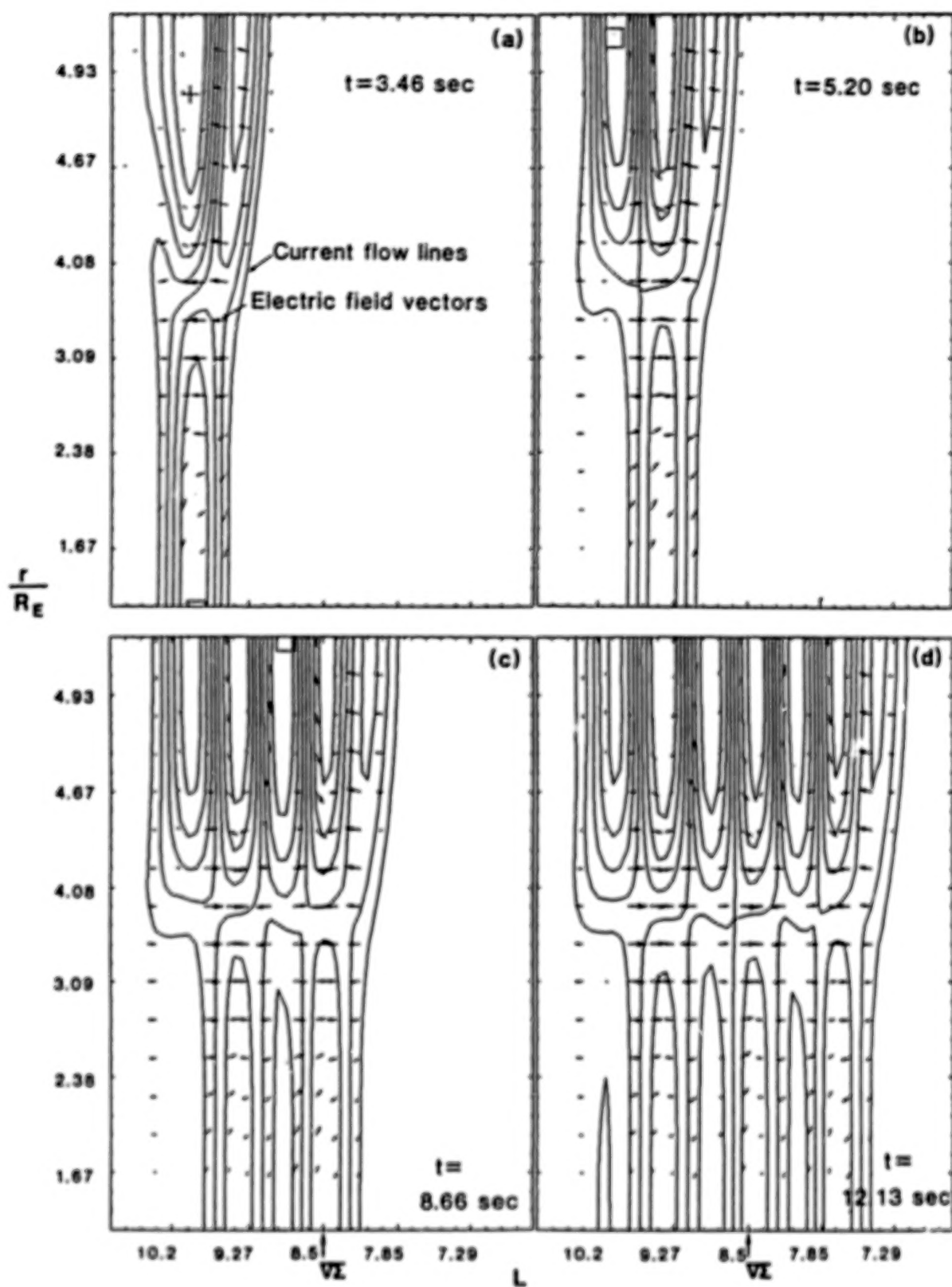


Figure 2. A set of snapshots showing the evolution of a run in which a moving voltage pulse travels across field lines (Lysak, 1985). The contour lines represent current flow lines in the  $xz$  plane of Figure 1. Note that the currents which reach the ionosphere close in the region between  $3$  and  $4 R_E$  where up- and downgoing waves interfere.

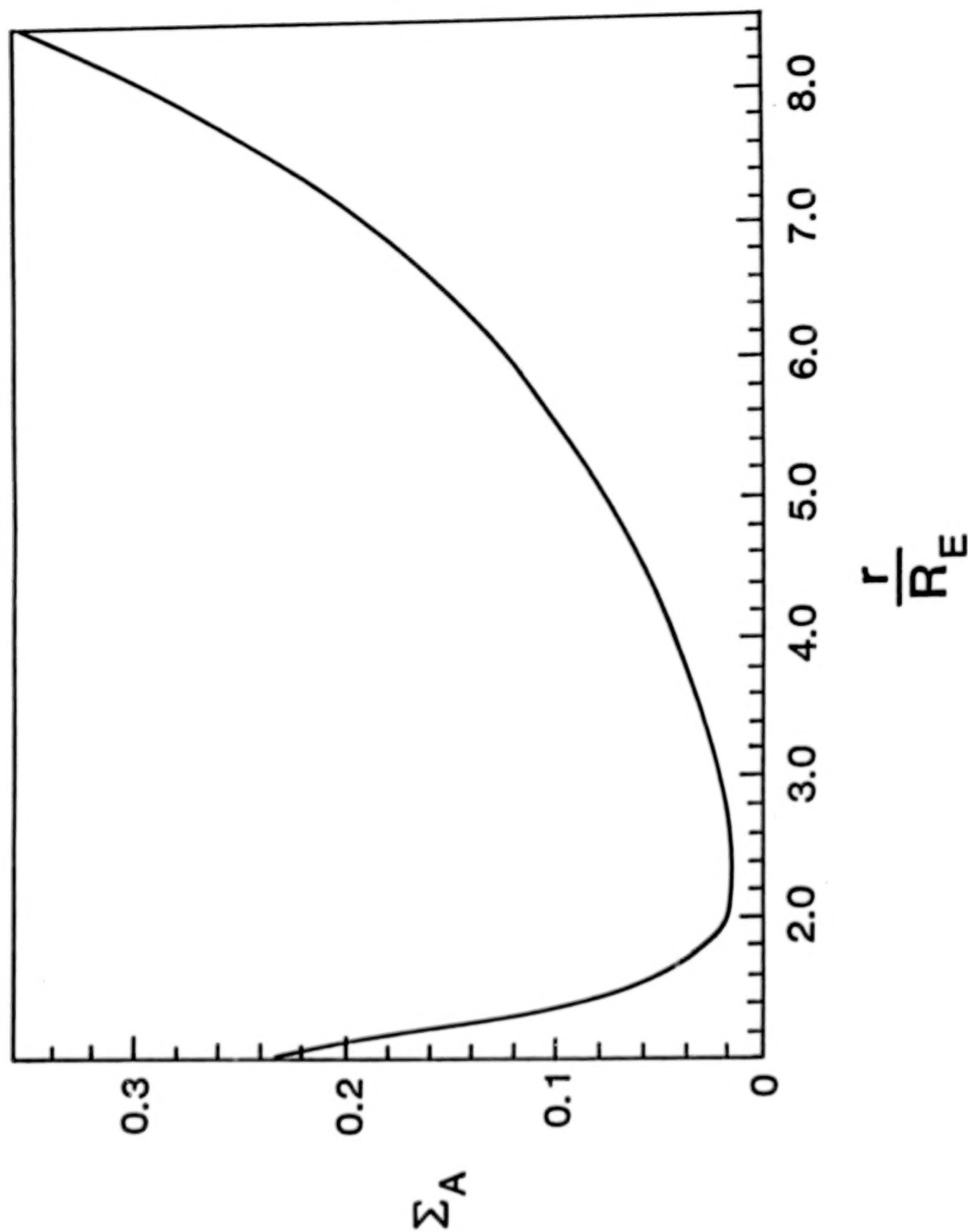


Figure 3. A sketch of the Alfvén wave admittance  $\Sigma_A$  (in mho) as a function of radial distance for the density profile given by equation (10).

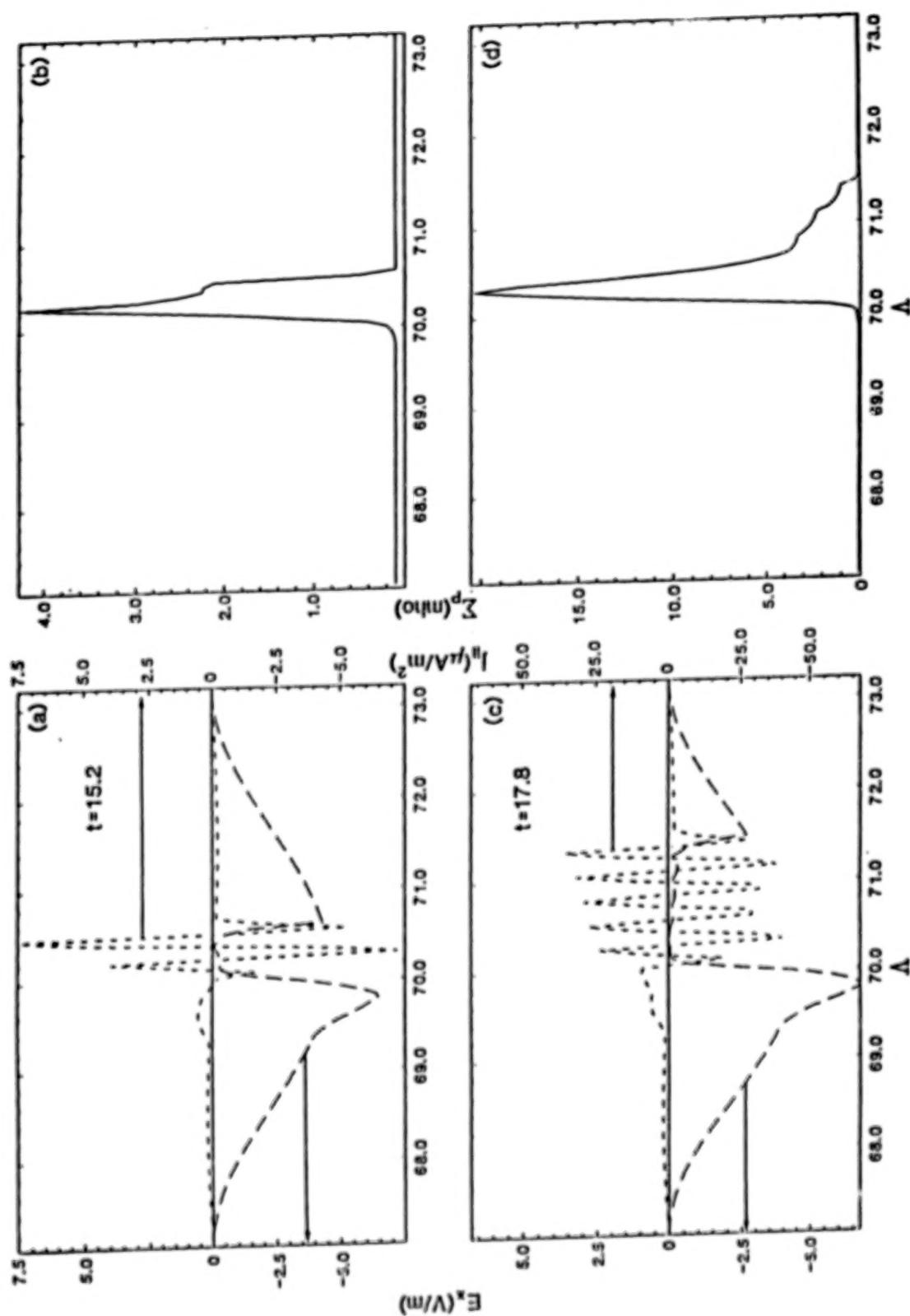


Figure 4. Ionospheric electric field, field-aligned currents, and Pedersen conductivity for a run in which the conductivity increases due to electron precipitation and a feedback instability results (Lysak, 1986). The oscillations in the current have a wavelength of about 20 km and a frequency of near 1 Hz, indicative of wave reflection from the region of minimum wave admittance.

## Run number 258, Ionospheric current history

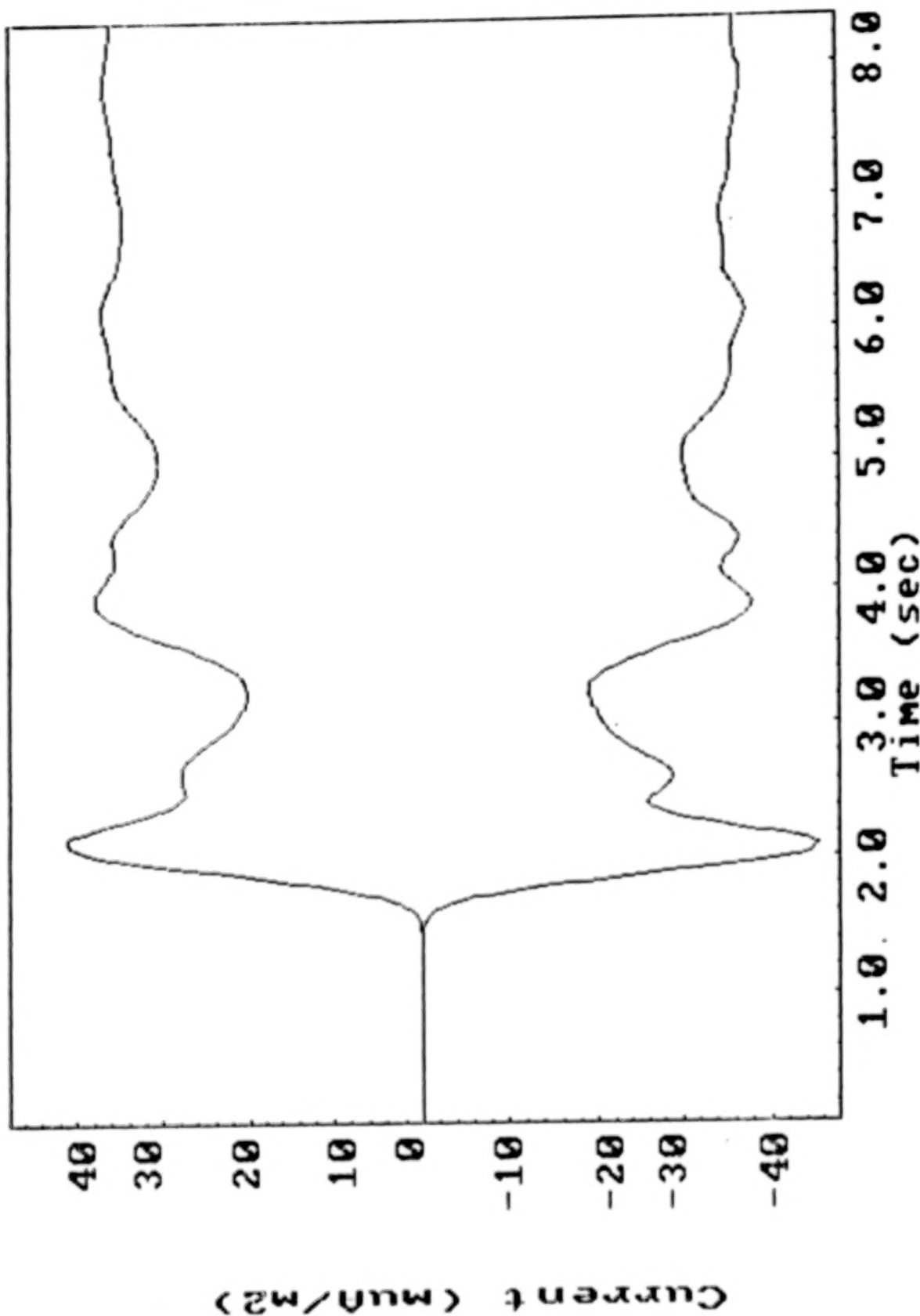


Figure 5. Maximum and minimum field-aligned currents at the ionosphere for a run with a Pedersen conductivity of 1 mho, an injected current of  $20 \mu\text{A}/\text{m}^2$ , and no parallel electric field. The maximum current attainable in this system is  $40 \mu\text{A}/\text{m}^2$ , and the final value of  $36 \mu\text{A}/\text{m}^2$  is due to losses in the ionosphere.



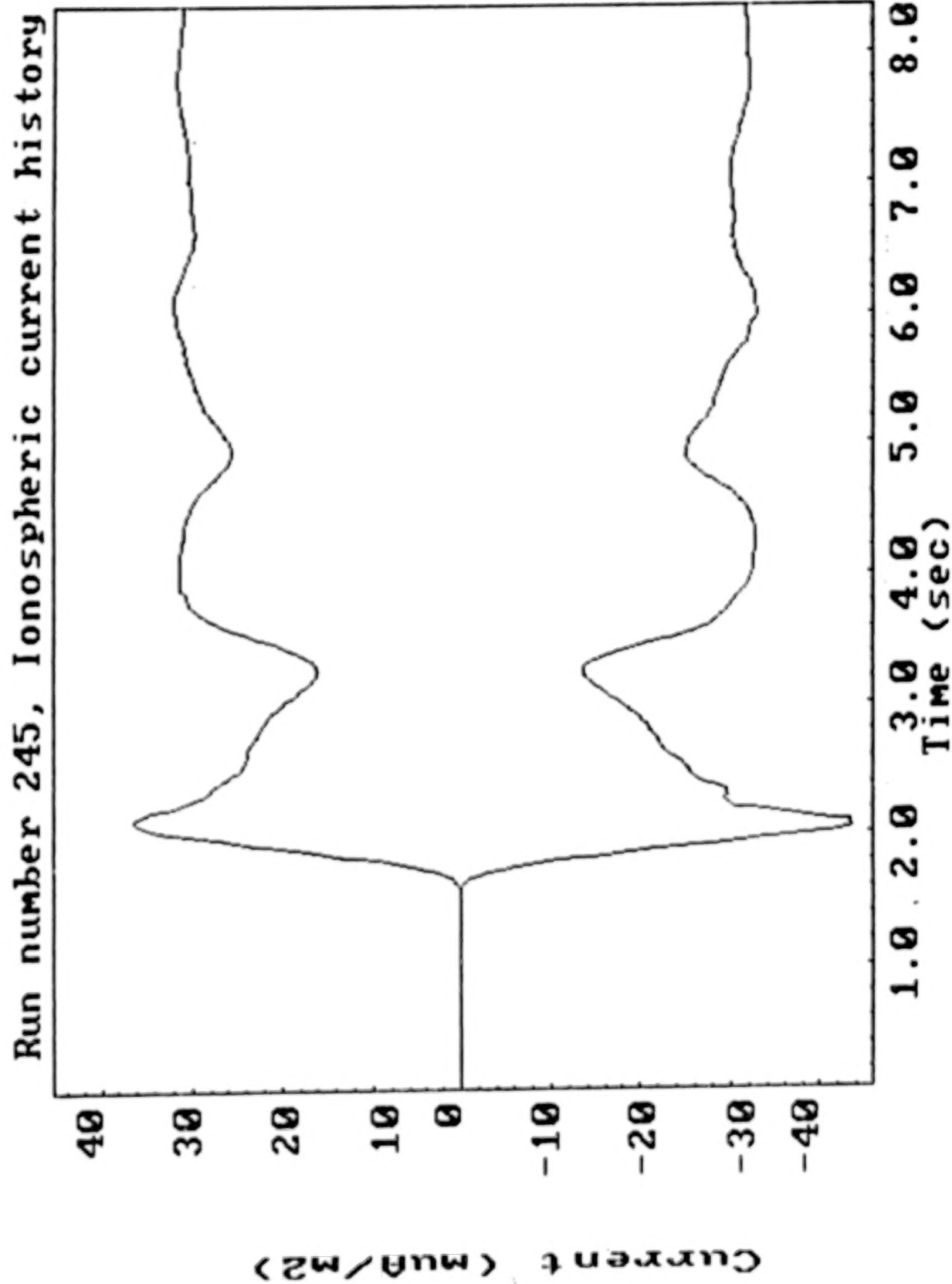


Figure 6. Similar to Figure 5 except that a double layer electric field has been included. The maximum current is reduced to  $30 \mu\text{A}/\text{m}^2$  in this case.

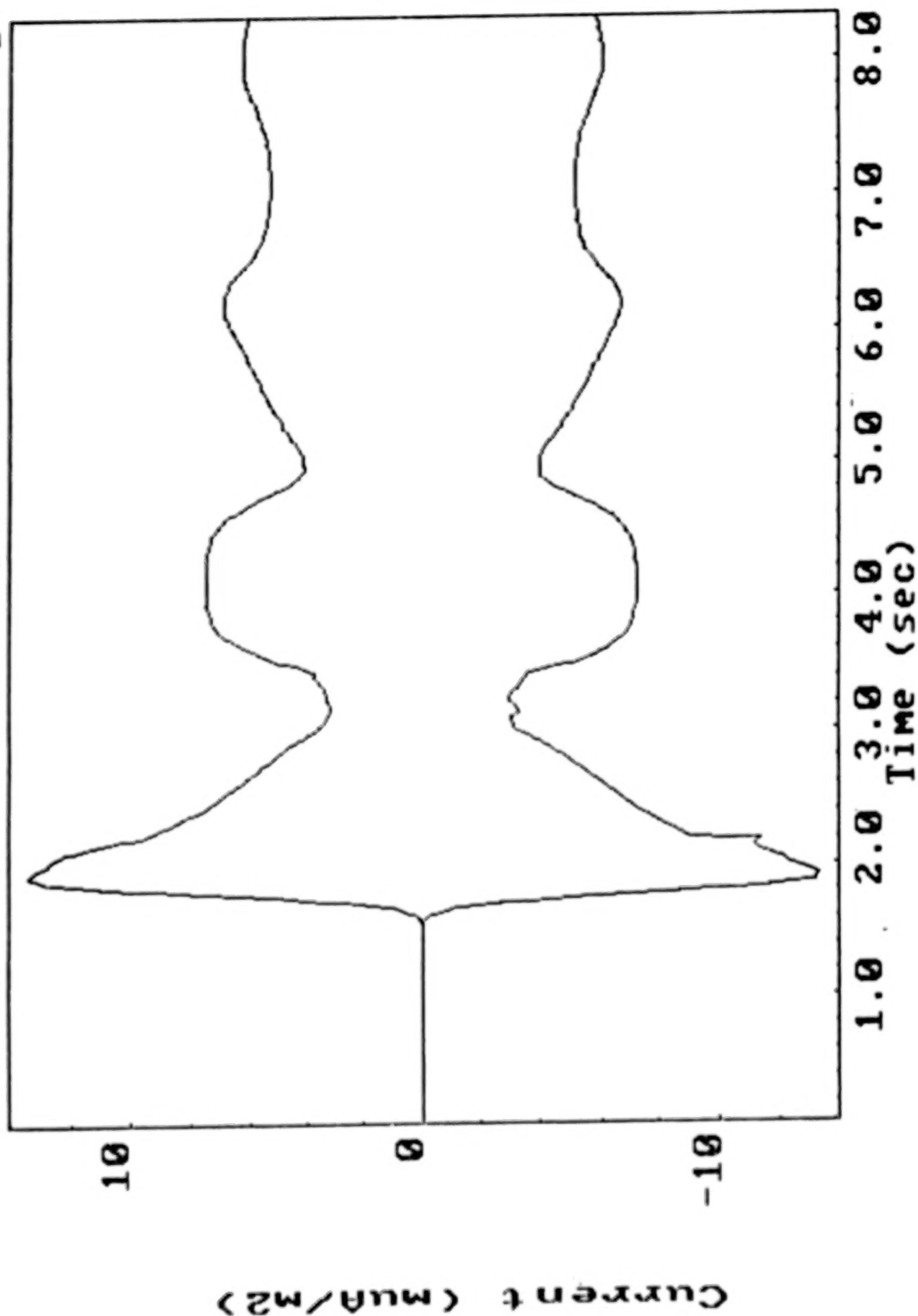


Figure 7. Similar to Figures 5 and 6 but including a nonlinear resistivity. The maximum current is drastically reduced due to the diffusion of the current structure to  $6 \mu\text{A/m}^2$ .

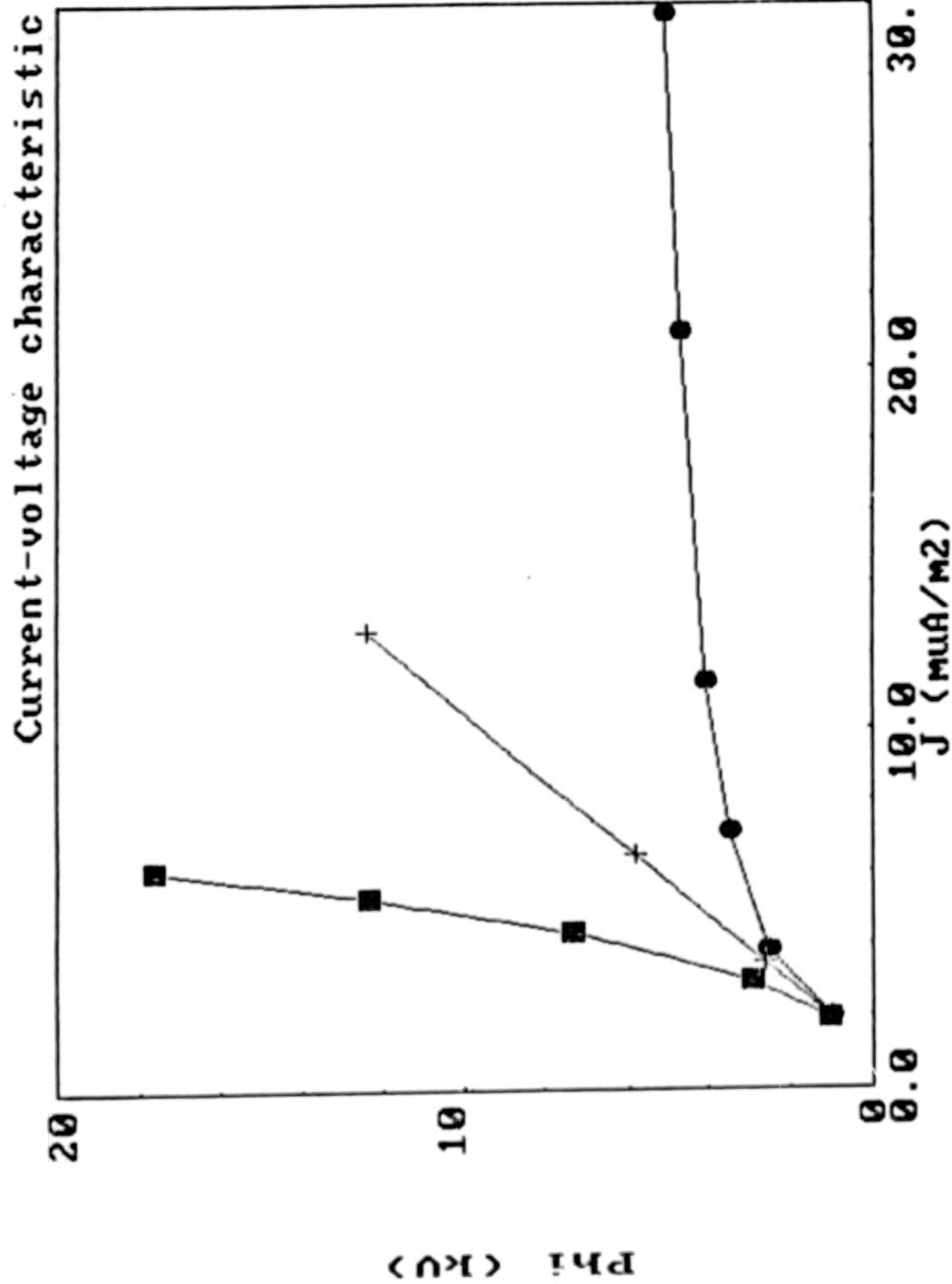


Figure 8. Current-voltage characteristics for a set of runs comparing the double layer model (dots), linear resistivity model (crosses), and the nonlinear resistivity model (squares).

Run 245, Fields, t=8.35, r=1.99

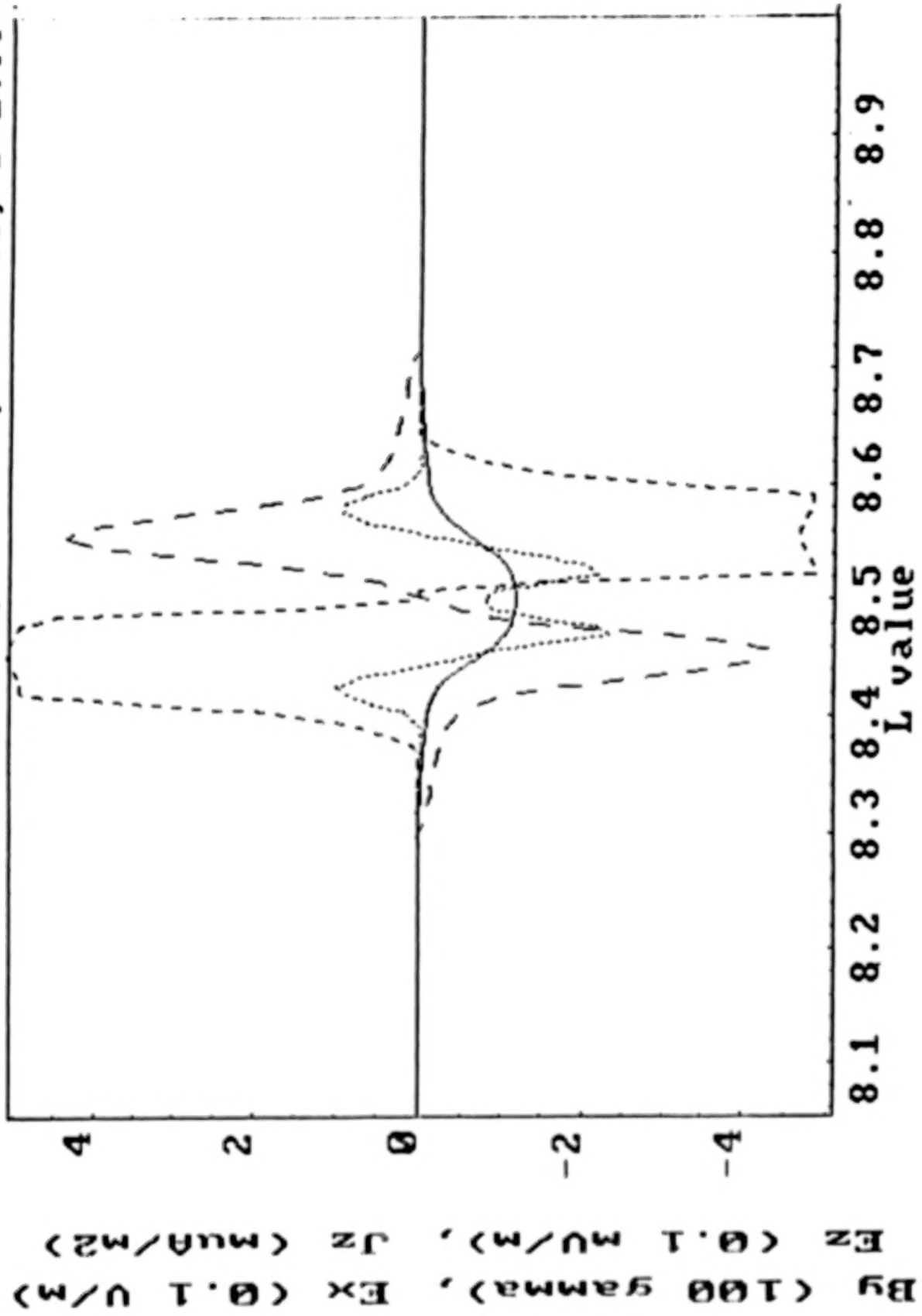


Figure 9. Field profiles at  $2 R_E$  for the double layer run of Figure 6. The solid line gives the magnetic perturbation, the dotted line the perpendicular electric field, the short dashed line the parallel electric field, and the long dashed line the field-aligned current. These fields are in units of 100  $\gamma$ , 0.1 V/m, 0.1 mV/m, and  $\mu A/m^2$ , respectively.

Run 246, Fields,  $t=8.35$ ,  $r=1.99$

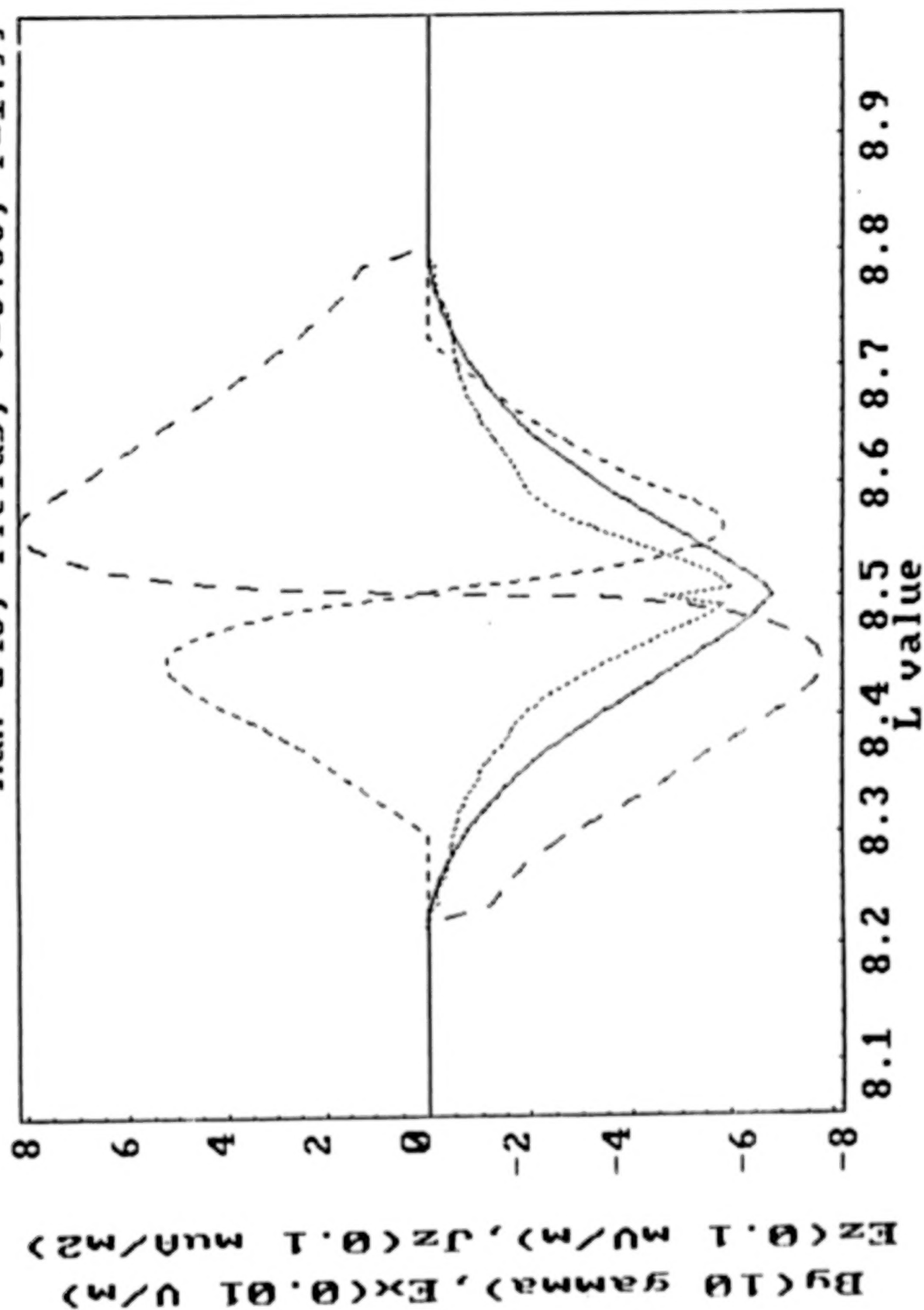


Figure 10. Same as Figure 9 but for the nonlinear resistivity run of Figure 7. The units in this case are  $10 \gamma$ ,  $0.01$  V/m,  $0.1$  mV/m, and  $0.1 \mu\text{A}/\text{m}^2$  for  $B_y$ ,  $E_x$ ,  $E_z$ , and  $J_z$ , respectively.

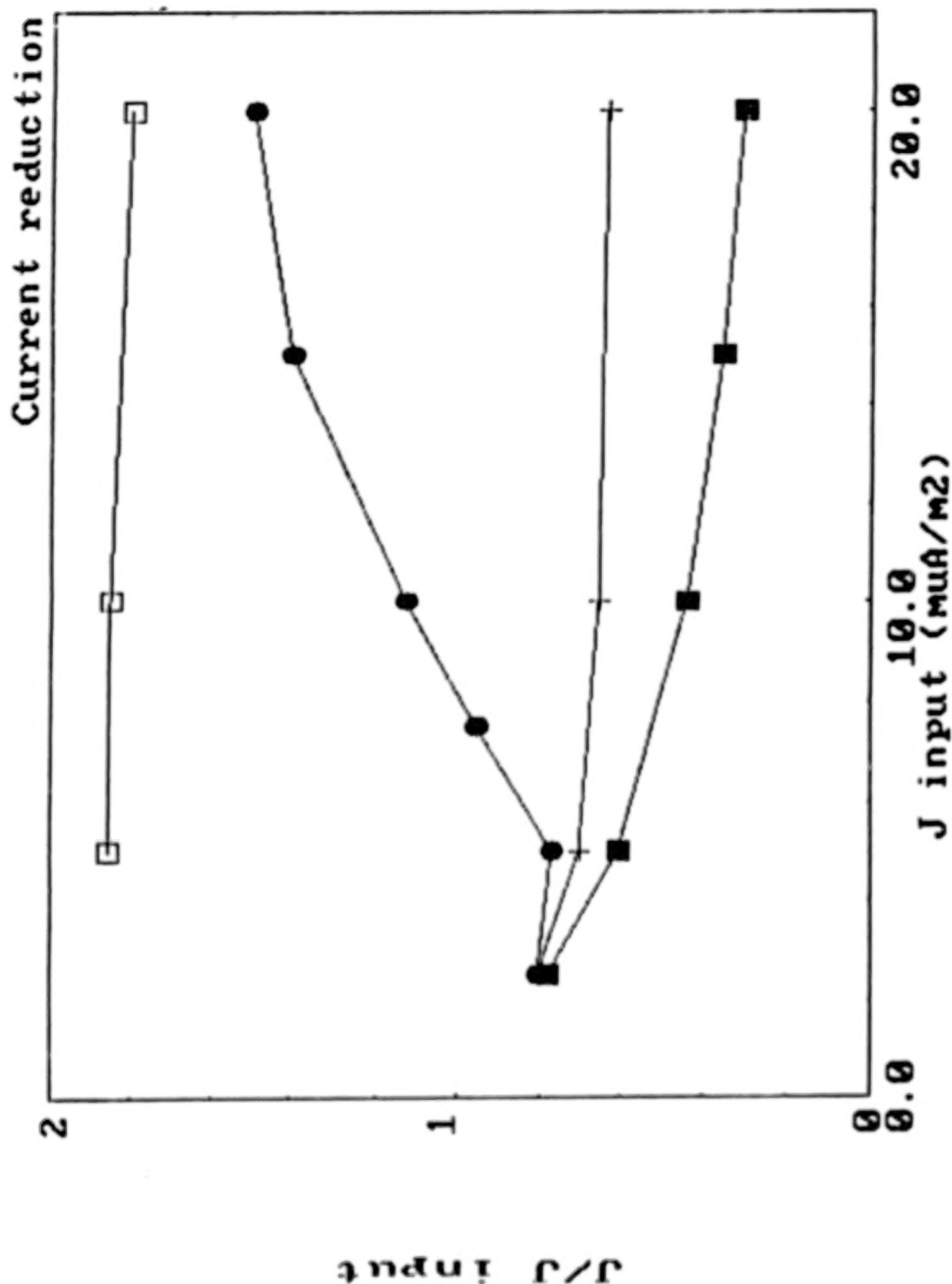


Figure 11. A comparison of the final currents to the injected currents for the runs of Figure 8, using the same symbols. In addition, runs in which no parallel electric fields were included are indicated by open squares.



N87

23322

UNCLAS

## CURRENT DRIVEN WEAK DOUBLE LAYERS

Gérard Chanteur

CRPE/CNET, 92131 Issy-les-Moulineaux, France

## ABSTRACT

Double layers in plasmas can be created by different means. For example, a potential difference forms between two plasmas with different temperatures (Hultqvist, 1971; Ishiguro et al., 1985), in a plasma jet flowing along a converging magnetic field (Serizawa and Sato, 1984), in a quiescent plasma submitted to an external difference of potential, or in a turbulent plasma carrying an electric current. The first three cases can be current-free, but not necessarily, although the numerical simulations have been made under such conditions for the first two points (Ishiguro et al., 1985; Serizawa and Sato, 1984). Apart from the third case, which is mainly of interest for laboratory experiments, these double layers are good candidates for accelerating the auroral electrons to the few kiloelectron volts observed.

## I. INTRODUCTION

This paper is devoted to the fourth case, i.e., to weak double layers driven by an electric current. Two papers have triggered the studies in this field: DeGroot et al. (1977) showed the formation of localized potential jumps in an homogeneous plasma with a suprathermal electron drift; later, Sato and Okuda (1980) gave evidence for the formation of small double layers under ion-acoustic instability conditions, i.e., a large electron-to-ion temperature ratio and a subthermal electron drift. Our present understanding of weak double layers built by electric currents has mainly grown from the analysis of numerical simulations with either superthermal (DeGroot et al., 1977; Singh et al., 1985; Singh and Schunk, 1984) or subthermal (Sato and Okuda, 1980, 1981; Kindel et al., 1981; Hudson and Potter, 1981; Okuda and Ashour-Abdalla, 1982; Hasegawa and Sato, 1982; Nishihara et al., 1982; Chanteur et al., 1983; Chanteur, 1984, 1986; Barnes et al., 1985) electron drifts, but always in linearly unstable conditions. The formation mechanism seems to be different in these two cases; furthermore, it is likely to be sensitive to the boundary conditions in the superthermal case. The basic mechanism which produces weak ion-acoustic double layers is a current interruption caused by a negative potential spike. This fact was primarily recognized in one-dimensional periodic simulations (Sato and Okuda, 1981; Kindel et al., 1981; Hasegawa and Sato, 1982; Nishihara et al., 1982; Chanteur et al., 1983) and has been recently confirmed in the two-dimensional case with a strong magnetic field and under various boundary conditions (Barnes et al., 1985). The theoretical explanation given to the appearance and the growth of a double layer (Hasegawa and Sato, 1982; Nishihara et al., 1982; Chanteur et al., 1983; Chanteur, 1984) turns out to be more or less independent of the linear instability. The goal of this paper is to specify this point, and it will be shown that small and localized differences of potential can be built by a partial current interruption under linearly stable conditions. It has been demonstrated (Dupree, 1983; Berman et al., 1985; Pécseli, 1984) that phase space holes can be unstable for electron drifts less than the critical value which destabilizes the ion-acoustic modes. Although different from our work in many respects, it invokes the same physical basis, i.e., the reflection of the current carrying electrons by coherent structures. Section II gives an account of the formation of weak ion-acoustic double layers under linearly unstable conditions. Section III is a first presentation of recent simulations demonstrating that small double layers can be produced by a localized current interruption in a marginally stable plasma. A more thorough presentation of these numerical experiments is in preparation (Verga et al., 1986).

## II. UNSTABLE CASE

Most of the numerical studies concerning ion-acoustic double layers have been made with electrostatic particle codes that allow for the existence of thermal fluctuations. Indeed, the relatively small number of particles per Debye length (usually a few  $10^1$  or  $10^2$ ) gives rise to an artificially high level of thermal fluctuations. Besides, the probability of "big" fluctuations of the electric potential increases with the length of the system and should not be dismissed. Since ion-acoustic waves are weakly dispersive, we can argue that a big and negative potential spike present in the "initial" condition has a coherence time long enough to interact resonantly with the electrons. The word "initial" deserves a short explanation: a particle run is usually started with particles regularly distributed in space and attributing each particle a velocity given by a random number generator. The electric field usually taken equal to zero everywhere at  $t = 0$  is built self-consistently by the thermal motion of the particles in a few tens of time steps. It appears that the "initial" condition on the field is determined by the microscopic details of the loading of the particles. The longer the system, the greater the probability to find a negative potential spike sufficiently above the thermal level to produce a persistent interruption of the current by reflecting the electrons. In a short and periodic system without any externally applied electric field, this current interruption goes on for the transit time of the electron flow through the system and a stable BGK state results with a large fraction of trapped electrons. If the system is long enough for the establishment of this BGK state to be delayed and if the negative spike is not too close downstream of another big spike, the evolution will be qualitatively different, giving rise to a weak and transient double layer, as will be seen below. Increasing the length of the system, we increase the probability of the large fluctuations and delay the appearance of the BGK state; the combination of these two facts is likely to explain both the reason why double layers have never been observed in short periodic systems and the reason for the mean distance between double layers in very long systems. Instead, open boundary conditions not only provide a continuous input of energy into the system but new potential fluctuations are usually created near the input boundary (i.e., where the incoming flux of electrons is greater) and propagate through the system, giving rise to the observed temporal recurrence of double layers even in short open systems (Barnes et al., 1985). Consequently, the spatial and temporal recurrences of double layers in open systems are mainly governed by the chosen injection process of the particles at the boundaries. On the other hand, it has been shown (Barnes et al., 1985) that the formation mechanism of a weak double layer reported in detail in Nishihara et al. (1982), Chanteur et al. (1983), Chanteur (1984, 1986), and Barnes et al. (1985) is independent of the boundary conditions. Let us now recall the main features of this process.

In a system driven unstable by an electric current, the perturbations propagating against the electron flow are strongly damped, and the perturbations close to the most unstable wave number are rapidly selected among the other ones. On the basis of the linear instability theory for an homogeneous plasma, we expect the turbulence to develop homogeneously. Instead, it is observed that the evolution of long systems is dominated by one or few coherent structures, as was shown initially by Sato and Okuda (1980). For example, Figure 1 shows a negative potential spike (the figure in fact represents the potential energy of an electron), with  $e\phi/T_e \sim 1$  which has emerged from the thermal noise in a one-dimensional electrostatic and periodic particle simulation with the following parameters: length  $L = 512 \lambda_D$ , ion-to-electron mass ratio  $m_i/m_e = 100$ , electron-to-ion temperature ratio  $T_e/T_i = 20$ , and electron drift to thermal speed ratio  $V_d/V_{th} = 0.8$ . As previously discussed, this pulse originates in a thermal fluctuation present in the "initial" condition. This negative spike of potential is initially amplified by the linear instability taken over by the nonlinear instability discussed in Nishihara et al. (1982) and Chanteur (1983). The electrons having a kinetic energy less than the height of the potential barrier are reflected on both sides of the pulse; yet, due to the current, more electrons impinge on the left side of the barrier than on the right side and, consequently, more electrons are reflected upstream of the barrier than downstream. This simple fact has important implications. First, the resulting charge separation in the vicinity of the barrier develops a difference of potential between the two sides of the pulse, as can be seen around  $x = 120 \lambda_D$  in Figure 1, the low electric potential being on the upstream side of the barrier (upstream with respect to the electron drift). Second, quasi-neutrality of the plasma being preserved outside of the pulse, the electron density in excess on the upstream side is compensated for by an increased ion

density. Thus, the deep density trough associated with the potential pulse separates the upstream region of inflated plasma density from the depleted downstream region. Third, taking into account the velocity of the barrier, the mechanism of the instability can be easily understood. Let  $\vec{V}_0$  be the velocity of the barrier and  $\vec{V}$  the velocity of an incoming electron in the frame of reference moving with the barrier; assuming that the potential does not change during the interaction with this electron (a reasonable assumption considering the time scales in the numerical experiments), the collision is elastic and the particle leaves with a velocity  $-\vec{V}$ . The kinetic energy of the particle in the laboratory frame has changed from  $1/2 m_e (\vec{V}_0 + \vec{V})^2$  to  $1/2 m_e (\vec{V}_0 - \vec{V})^2$ ; i.e., an energy  $2m_e \vec{V}_0 \cdot \vec{V}$  has been transferred to the barrier. The potential barrier moving primarily in the direction of the electron flow receives more energy from the electrons impinging on the upstream side than it gives the downstream side, and the field energy locally grows! Detailed energy and momentum balances have been made theoretically (Nishihara et al., 1982; Chanteur et al., 1983; Pecseli, 1984) and checked in the simulations (Chanteur et al., 1983).

Due to the relatively small number of particles per Debye length, local diagnostics in phase space (for example the distribution function of electrons at a given location) are poorly done in particle simulations. Instead, Vlasov simulations are free of this limitation, but in return suffer, at least for this study, from the absence of thermal noise. Starting with an initial condition strictly independent of  $x$ , a good Vlasov code can be run a long time before truncation and round-off errors seed a potential instability. An initial perturbation has to be put, whether random or not, in the system; an account of weak double layer formation under such circumstances has been given in Chanteur (1984). For the present discussion, we just recall the simulation presented in Chanteur et al. (1983). This Vlasov run was initialized with the same physical parameters as the aforementioned particle run, the initial perturbation being a localized 10 percent density depression on both species. Although qualified "perhaps unphysical" in Borovsky (1984), this initial condition reproduces what is built from the exaggerated thermal noise present in particle simulations. In fact, the potential energy of an electron shown versus  $x$  and  $t$  in Figure 2 is strikingly similar to the result of the particle simulation (see Fig. 1). This temporal evolution of the system is not an artifact of the periodic boundary conditions; doubling the length of the system while keeping the same physical parameters does not change anything. On the other hand, this behavior is also observed in bounded systems and for different physical parameters (Barnes et al., 1985). Thus, it is not due either to some numerical coincidence for a magic set of parameters; in turn, the boomerange motion of the localized wave seems to be an artifact of one-dimensionality (Barnes et al., 1985). Figure 3 displays the electron phase space in the vicinity of the double layer at three different times during its propagation in the direction of the electron flow. The reflections of the electrons are clearly visible on both sides of the structure, and the electron holes are seen to be formed in the depleted downstream region [see also Chanteur (1984) and Barnes et al. (1985)].

The slowing down and the late evolution of the weak double layer cannot be understood without taking into account the ion dynamics (Chanteur et al., 1983; Chanteur, 1984). Figures 4a and b are local representations of the ion phase space just around the double layer for the above-mentioned particle and Vlasov simulations, respectively. It again emphasizes the similarity of the two runs. In the beginning, the negative pulse of potential is moving subsonically ( $\sim 0.8 c_s$ ) toward the right in Figures 1 and 2, consistently with the negative velocity perturbation seen at times 320 and 340 in Figures 4a and b. The pulse first undergoes a very faint slowing down (Chanteur et al., 1983) of purely hydrodynamic origin because of the extremely small number of resonant ions. It has been emphasized in Chanteur (1986) that resonant ions are by no means responsible for this slowing down and the point can be stated in the following way. Weakly nonlinear ion-acoustic waves in a stable plasma with a large electron-to-ion temperature ratio are well accounted for by assuming a cold fluid behavior of the ions and a Boltzmannian distribution of the electrons in the electrostatic potential. The evolution of the potential is then determined by a Korteweg-de Vries (KdV) equation, and the numerical integration of this evolution equation shows that a localized and rarefactive ion-acoustic wave is very slightly slowed down, and simultaneously weakly damped by the radiation of a dispersive tail on its trailing edge (Nishihara et al., 1982; Fornberg and Whitham, 1978; Okutsu and Nakamura, 1979). In the unstable case presently under investigation, the alteration of the pulse by the reflection of the electrons has been incorporated in a dissipative KdV equation (Nishihara et al., 1982; Chanteur et al., 1983). The resulting amplification strengthens the deceleration of the pulse caused by the quadratic nonlinearity  $\phi (\partial \phi / \partial x)$  of the evolution equation (Nishihara et al., 1982). Of course, the validity of this dissipative KdV equation relying on a fluid description of the ions progressively breaks down with the onset of the ion trapping. The growth of the potential



pulse occurs on a time scale comparable to the transit time of the ion through the pulse; thus, the closer to resonance the ions, the greater the non-adiabatic effect they suffer (which eventually traps them inside the pulse). The onset of the trapping is visible in Figures 4a and b at times 448 and 512, respectively. The transfer of momentum to these ions enhances the slowing down of the pulse, which in turn makes the trapping more efficient as the pulse velocity moves toward the central part of the ion distribution, as shown in Figures 4a and b where the pulse velocity is indicated at each time by a heavy horizontal line. The trapping is completed when the pulse velocity comes to zero, at times around 600 in both simulations; yet, the trapped ions are not phase-mixed inside the pulse, and the highly asymmetric trapped population is responsible for the backward acceleration of the pulse with the subsequent detrapping of the ions. The burst of ions accelerated up to  $C_s$  is formed during this process (Fig. 4b) in the downstream region. Such bursts up to  $2 C_s$  are commonly observed in Vlasov simulations started with random initial conditions (Chanteur, 1986). In a two-dimensional system, the trapping acts differently since the ions can enter sideways the potential well, which leads to a trapped population much more symmetric than in one dimension. Barnes et al. (1985) actually observed in two-dimensional simulations that the pulse does not move backward after it has stopped. We can thus conclude that the observed boomerang motion of the structure is an artifact of one-dimensionality.

Except for this rather secondary point, one- and two-dimensional simulations agree on the basic process responsible for the formation of weak double layers driven by the ion-acoustic instability. This process recently received an experimental confirmation in the laboratory experiment done by Sekar and Saxena (1985).

### III. AROUND THE MARGINAL STABILITY

It has been suggested in Chanteur (1986) and Pecseli (1984) that the formation mechanism discussed at length in Section II can work with electron drift velocities unable to destabilize the ion-acoustic mode. A series of Vlasov simulations have been done to check that point. More generally, we have studied both subthermal and superthermal drift cases, but always near or below the marginal stability of the plasma. The marginal stability condition referred to is the classical one computed for an infinitesimal harmonic perturbation of the plasma and thus, strictly speaking, is not of concern for the initial condition used to start the simulations. Nevertheless, it indicates that the thermal noise, absent in the Vlasov simulation, would be marginally stable. We chose the same initial condition previously used in Chanteur et al. (1983) and Chanteur (1984) and reported to in the preceding section, i.e., a 10 percent density dip on both species. The drift motion of the electrons relative to the ions rapidly creates a potential trough, the depth of which strongly depends on the drift velocity  $V_d$  and on the initial amplitude of the density dip. It is worth noticing that the weak double layers triggered by initial density dips almost vanish when the initial amplitude of these dips is reduced to 1 percent. Thus, under marginally stable conditions, the formation mechanism of weak double layers needs a rather strong initial depression of the plasma density to be effective. In this respect, the linear instability helps a lot in the unstable case. In the present case, the initial density dip has to be produced by other means. The length of the system has been chosen equal to  $1024 \lambda_D$  and  $2048 \lambda_D$  in some cases to prevent an early influence of the periodic boundary conditions in the circulating electrons. As said in the introduction, we only present a small sample of our simulation results. A full account of these results will be given in the paper by Verga et al. (1986), presently under preparation. The physical parameters of the five selected runs are listed in Table 1. Figures 5 to 8 illustrate runs 1 to 4, respectively, each figure being composed of an upper panel for the electric potential (averaged over two plasma periods) in unit  $T_e/e$ , and of a lower panel for the electron phase space. The results are conveniently organized with respect to the ion-to-electron temperature ratio.

TABLE 1. PHYSICAL PARAMETERS OF THE SELECTED RUNS

Run Number	$T_i/T_e$	$V_c/V_{th}$	$V_d/V_{th}$	Linearly Stable?	System Length ( $\lambda_D$ )
1	0.30	0.55	0.50	yes	1024
2	0.30	0.55	0.60	no	1024
3	0.50	0.88	0.85	yes	1024
4	1.00	1.44	1.25	yes	1024
5	1.00	1.44	1.50	no	2048

Note: The mass ratio is  $m_i/m_{e_c} = 100$  for the five runs, and  $V_c$  is the critical electron drift which destabilizes the plasma.

The case of relatively cold ions ( $T_i/T_e = 0.30$ ) is illustrated by runs 1 and 2, which are linearly stable and unstable, respectively, but both marginally, as appears from Table 1. The two upper panels in Figures 5 and 6 show that the electric potential in the vicinity of the moving density depression has the same spatial variation as the one discussed in Section II for strongly unstable cases. Only quantitative differences occur; the amplitude of the negative pulse and the difference of potential between the downstream (on the right of the figures) and upstream sides which were of the order of one in the Section II cases are now reduced to 0.05 for run 1 and 0.10 for run 2. It is worth noticing that the linear instability, although weak, helps building a difference of potential which is twice the one of the stable case. The electron phase spaces drawn with the same contour levels (lower panels in Figs. 5 and 6) show the same enhancement of the structure; moreover, tiny electron holes are formed downstream of the double layer in run 2. These electron holes can be associated one to one with the small positive pulses seen on the high potential side (Fig. 6, upper part). Run 3 for  $T_i/T_e = 0.50$  differs from run 1 by the formation of electron holes, which are even deeper than in run 2, as shown by the phase space (Fig. 7, lower part) and the associated pulses of potential, also more pronounced than in case 2. The potential trough and jump have values twice those of the corresponding values in run 1. Going on to higher ion temperature with  $T_i/T_e = 1$ , a superthermal drift velocity is now required to get the marginal stability of the plasma, and differences with the colder ion cases can be seen both on the potential and in the electron phase space. First, the potential trough is not as sharp as in the previous cases. Second, the difference of potential, although greater than previously, is much less steep, apart from the large pulses associated with very deep electron holes. Correspondingly, the acceleration region of the electrons in the vicinity of the potential well (see Fig. 8, lower part) is not as well defined as in the cold ion case. To briefly summarize the observations, we can say that, except for very weak drift velocities, electron holes moving at velocities close to  $0.5 V_{th}$  are recurrently formed in the density depression which moves subsonically. The region of high potential extends between the density depression and the leading electron hole.

Run 5 differs from run 4 by the initial condition, which is now made of two identical density depressions separated by  $512 \lambda_D$ . Snapshots of the averaged potential presented in Figure 9 show that the two structures evolve independently, as long as they are disconnected, yet a blowup of the potential occurs when the two depleted regions join together. This behavior has not yet been investigated in detail and needs to be confirmed for other sets of parameters.



#### IV. CONCLUSION

The physics of the formation of weak double layers by current interruption seems now to be satisfactorily understood after a few years of both theoretical and numerical work. We have presented the first evidence of weak double layer formation in stable conditions: they share conditions, except for those associated to the ion dynamics. Their weakness explains why they have almost no effect in the ion phase space. An interesting point associated with these structures is the recurrent formation of electron holes; we believe that it deserves further work, as well as the blowup of the field observed during the coalescence of two depleted regions.

*Acknowledgments.* The author greatly acknowledges the organizing committee of the Workshop on Double Layers in Astrophysics for financial support. The scientific collaboration of R. Pellat and A. Verga has been greatly appreciated. The author is also grateful to N. Dupin for her careful reading and efficient typing of the manuscript.

#### REFERENCES

- Barnes, C., M. K. Hudson, and W. Lotko, *Phys. Fluids*, 28, 1055 (1985).  
Berman, R. H., D. J. Tretault, and T. H. Dupree, *Phys. Fluids*, 28, 155 (1985).  
Borovsky, J. E., in *Second Symposium on Plasma Double Layers*, edited by R. Schrittwieser and G. Eder, University of Innsbruck, p. 33, 1984.  
Chanteur, G., in *Computer Simulation of Space Plasmas*, edited by H. Matsumoto and T. Sato, Terra Scientific Publ Co., p. 279, 1984.  
Chanteur, G., in *Proceedings of the International Conference on Comparative Study of Magnetospheric Systems*, Cepedues Editions, Toulouse, to appear, 1986.  
Chanteur, G., J. C. Adam, R. Pellat, and A. S. Volokhitin, *Phys. Fluids*, 26, 1584 (1983).  
DeGroot, J. S., C. Barnes, A. E. Walstead, and O. Buneman, *Phys. Rev. Lett.*, 38, 1283 (1977).  
Dupree, T. H., *Phys. Fluids*, 26, 2460 (1983).  
Fornberg, B., and G. B. Whitham, *Phil Trans. Roy Soc. London, A*, 289, 373 (1978).  
Hasegawa, A., and T. Sato, *Phys. Fluids*, 25, 632 (1982).  
Hudson, M. K., and D. Potter, in *Physics of Auroral Arc Formation*, Geophys. Monogr. Series #25 (American Geophysical Union: Washington, D.C.), p. 260 (1981).  
Hultqvist, B., *Planet. Space Sci.*, 19, 749 (1971).  
Ishiguro, S., T. Kamimura, and T. Sato, *Phys. Fluids*, 28, 2100 (1985).  
Kindel, J. M., C. Barnes, and D. W. Forslund, in *Physics of Auroral Arc Formation*, Geophys. Monogr. Series #25 (American Geophysical Union: Washington, D.C.), p. 296, 1981.  
Nishihara, K., H. Sakagami, T. Taniuti, and A. Hasegawa, in *First Symposium on Plasma Double Layers*, edited by P. Michelsen and J. J. Rastrassen, p. 41, Risoe National Laboratory, Denmark, 1982.  
Okuda, H., and M. Ashour-Abdalla, *Phys. Fluids*, 25, 1564 (1982).  
Okutsu, E., and Y. Nakamura, *Plasma Physics*, 21, 1053 (1979).  
Pécseli, H., in *Second Symposium on Plasma Double Layers*, edited by R. Schrittwieser and G. Eder, University of Innsbruck, p. 81, 1984.  
Sato, T., and H. Okuda, *Phys. Rev. Lett.*, 44, 740 (1980).  
Sato, T., and H. Okuda, *J. Geophys. Res.*, 86, 3357 (1981).  
Sekar, A. N., and Y. C. Saxena, *Plasma Physics and Controlled Fusion*, 27, 181 (1985).  
Serizawa Y., and T. Sato, *Geophys. Res. Lett.*, 11, 595 (1984).  
Singh, N., and R. W. Schunk, in *Second Symposium on Plasma Double Layers*, edited by R. Schrittwieser and G. Eder, University of Innsbruck, p. 364, 1984.  
Singh, N., H. Thiemann, and R. W. Schunk, *J. Geophys. Res.*, 90, 5173 (1985).  
Verga, A., G. Chanteur, and R. Pellat, in preparation (1986).

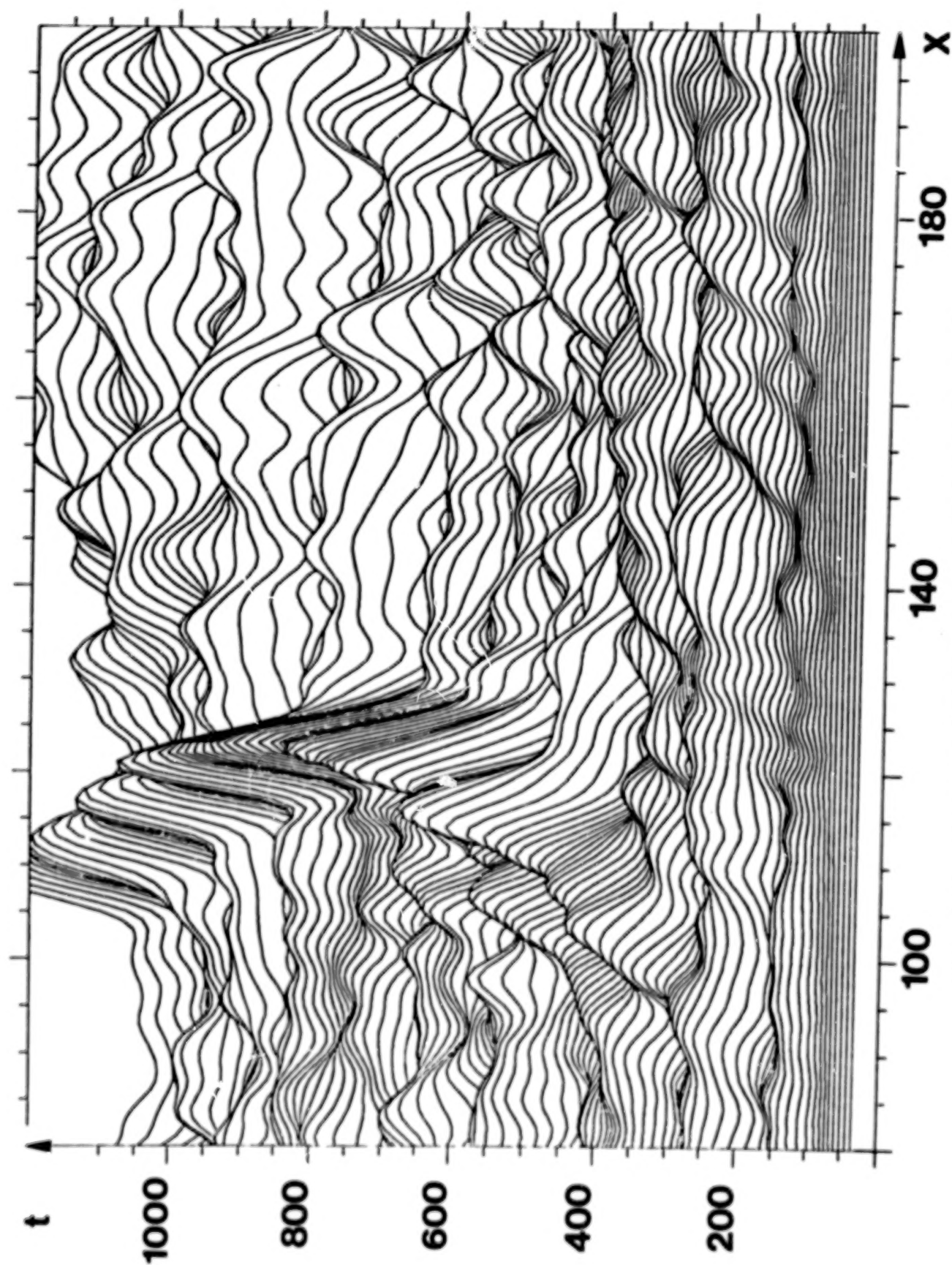


Figure 1. Potential energy of an electron versus  $x$  and  $t$  in the vicinity of the moving density dip (particle simulation).

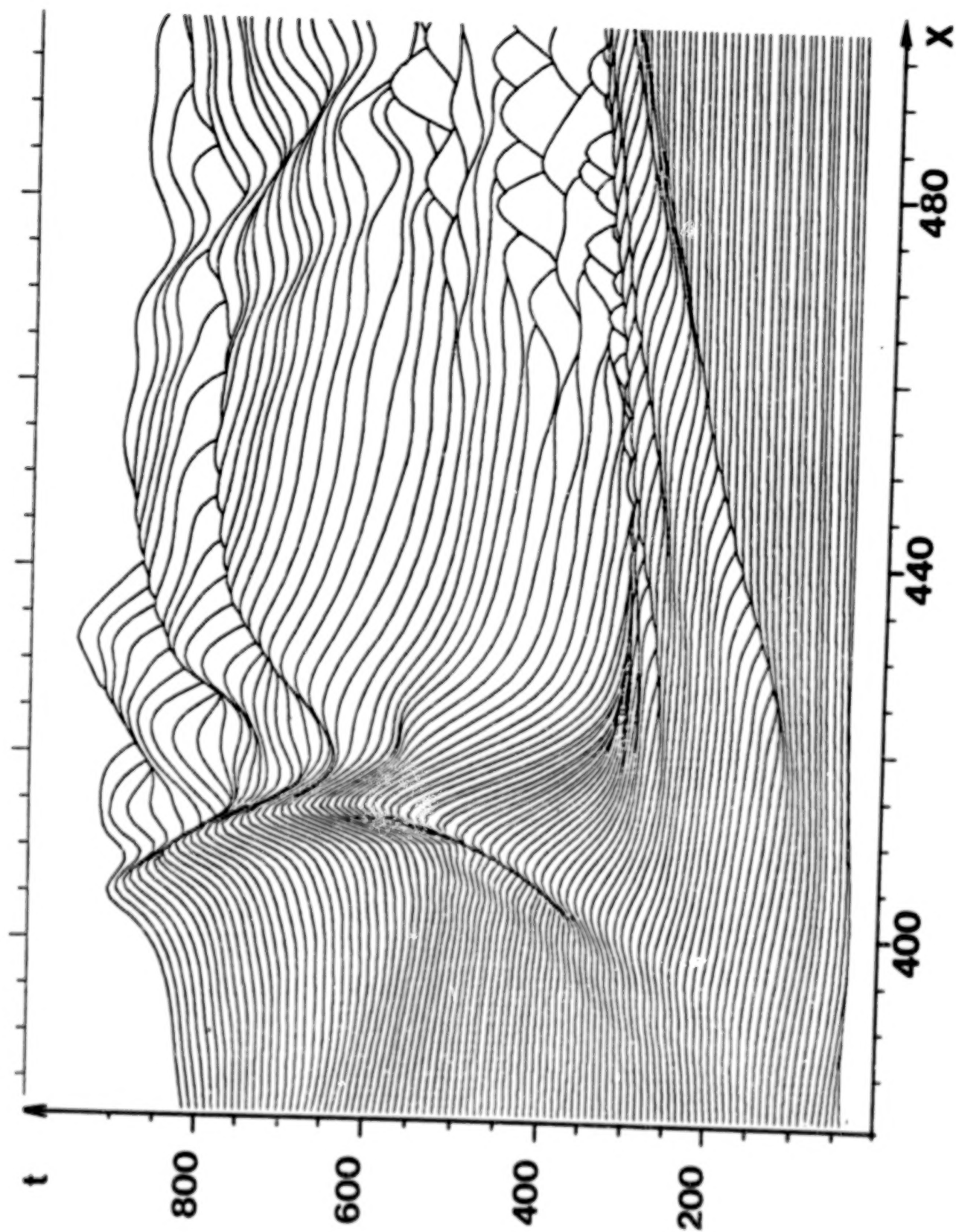


Figure 2. Same as Figure 1 but for the Vlasov simulation.

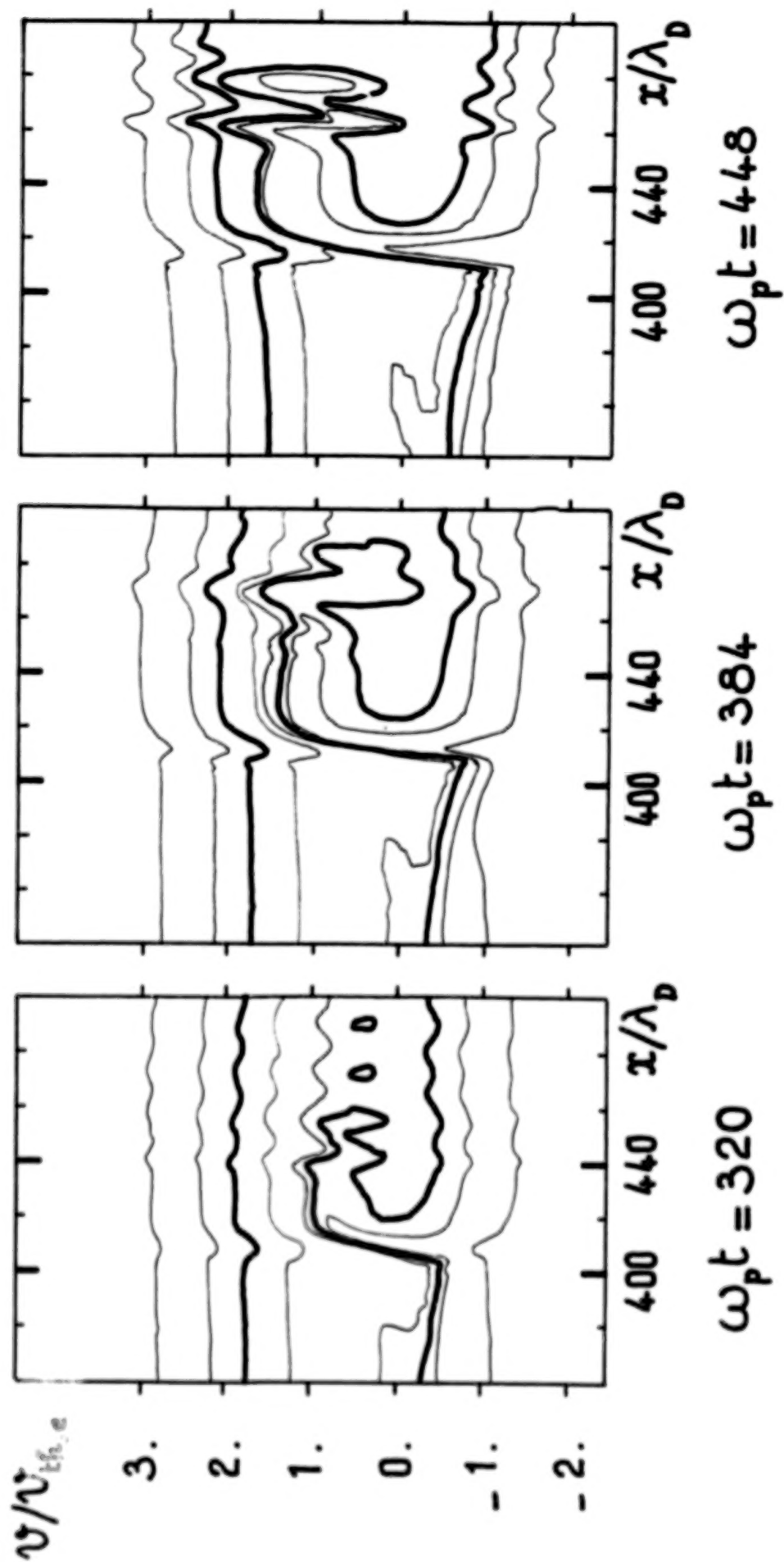


Figure 3. Electron phase space at three different times in the vicinity of the double layer at three different times (Vlasovs simulation).



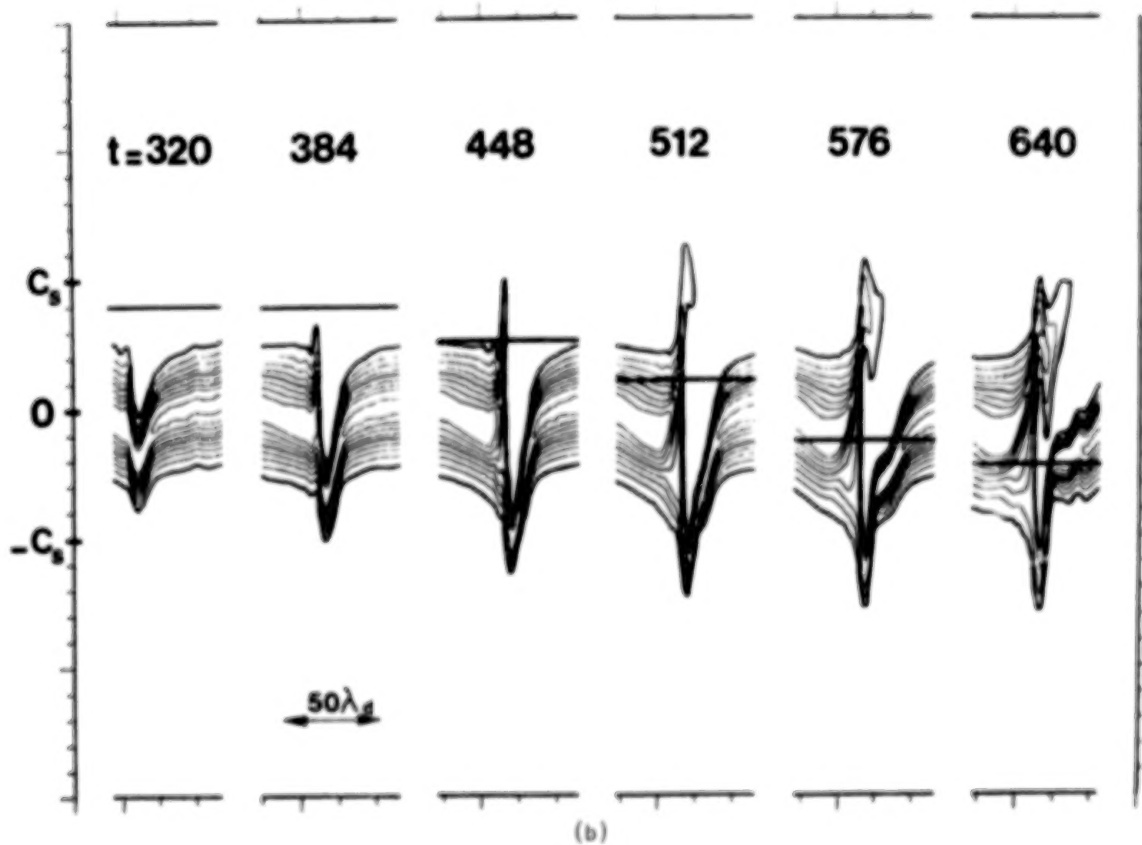
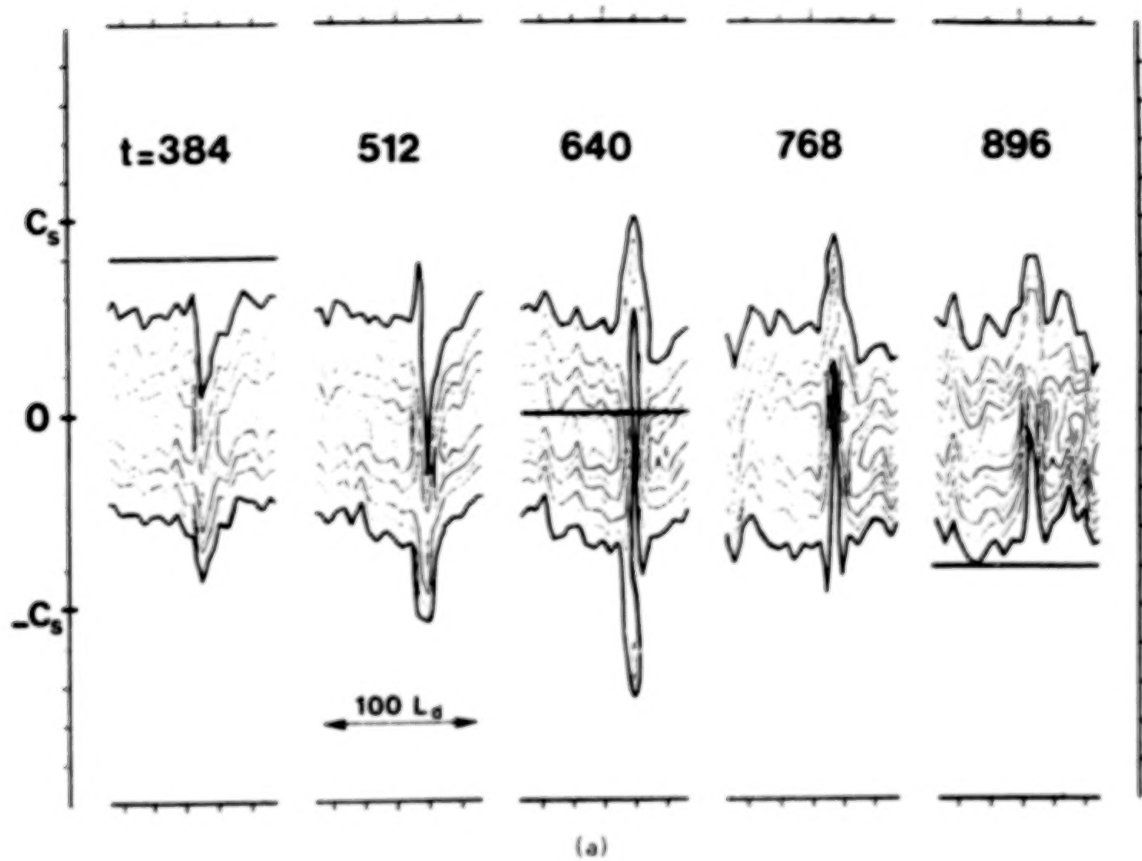
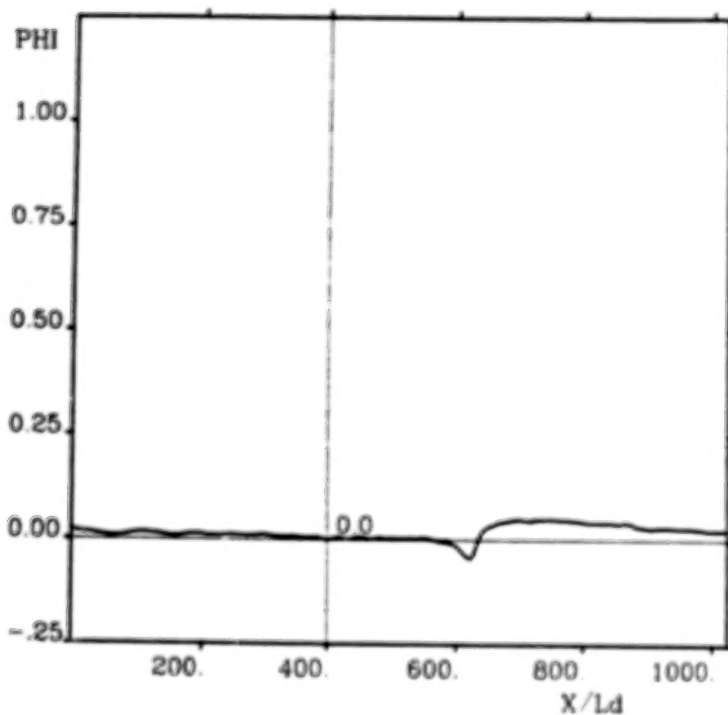


Figure 4. Ion phase spaces around the double layer at different times. (a) Particle simulation; (b) Vlasov simulation. The heavy horizontal line indicates the velocity of the localized wave.

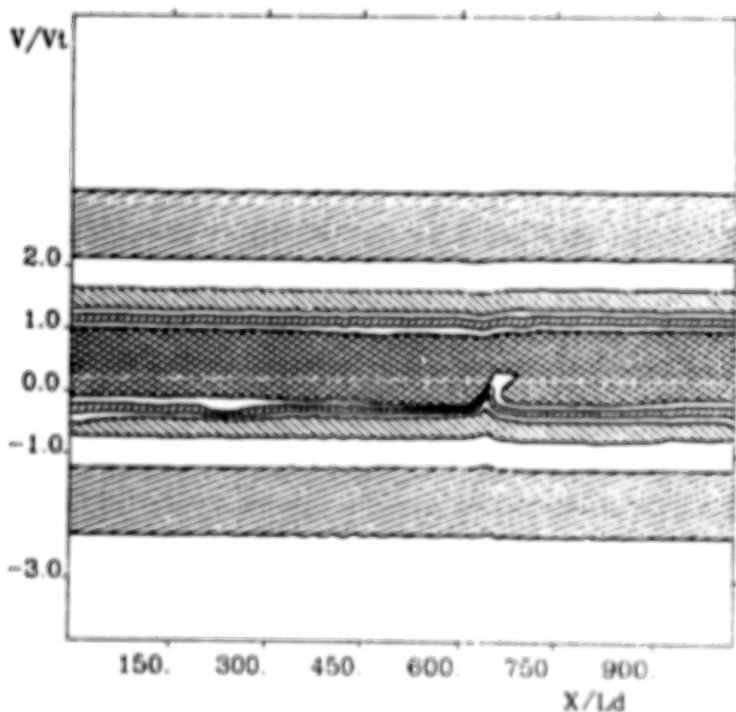
# OF POOR QUALITY

AVERAGED POTENTIAL (over  $4\pi/\omega_p$ )  
 $v_d/v_t=0.50$   $t_i/t_e=0.30$   $m_i/m_e=100$ .



DRHO	=	-0.10
NX	=	1024
DX	=	1.00
NT	=	2048
DT	=	0.50

ELECTRON PHASE SPACE vlasov code  
 $v_d/v_t=0.50$   $t_i/t_e=0.30$   $m_i/m_e=100$ .



TIME 1024

DRHO	=	-0.10
NX	=	1024
DX	=	1.00
VMIN	=	-4.00
VMAX	=	+6.00

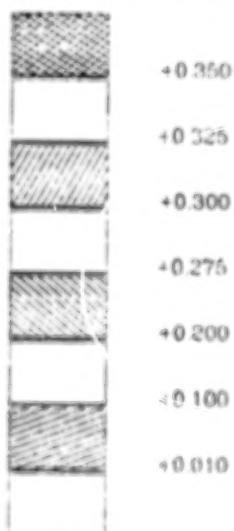
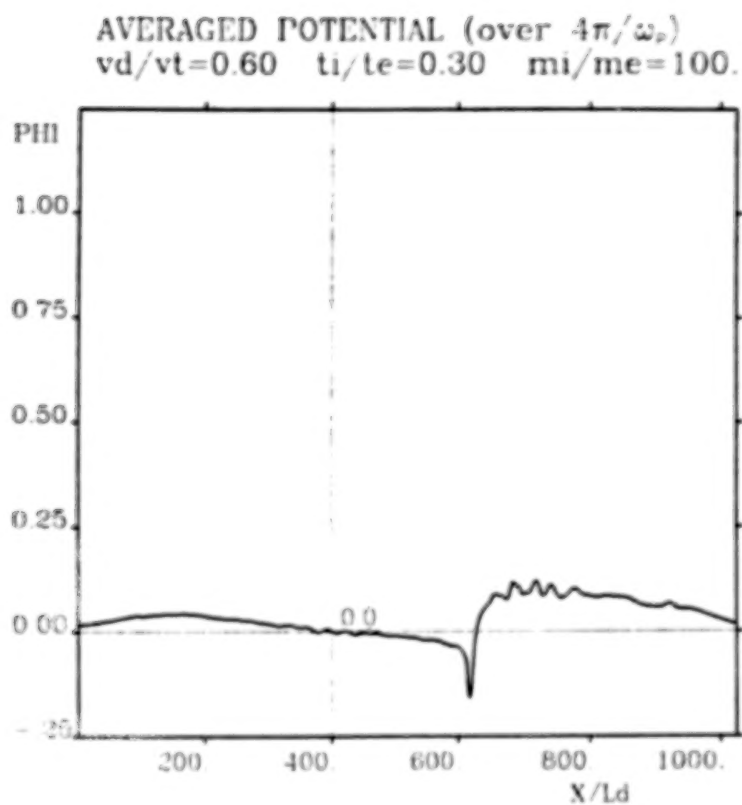
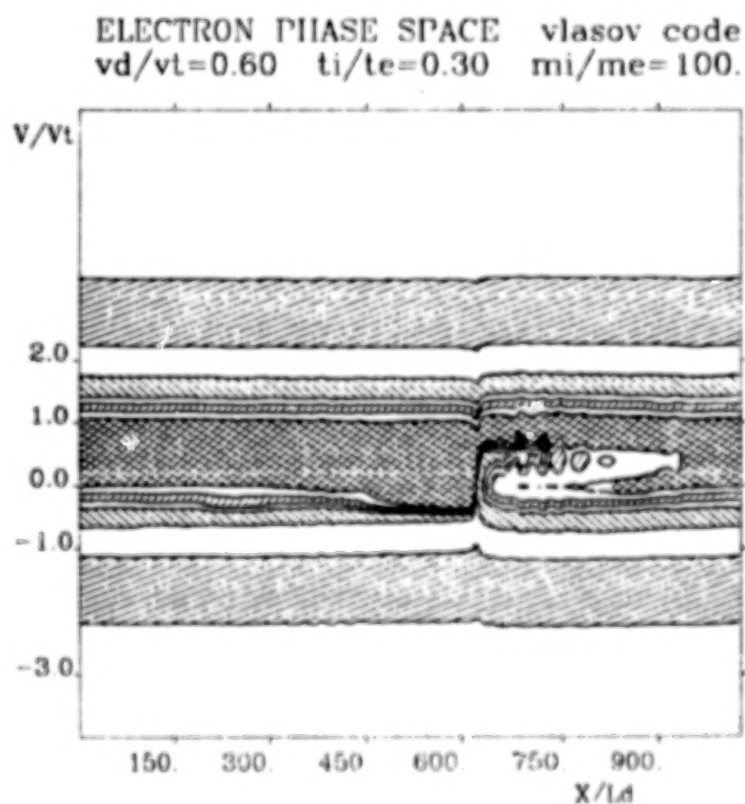


Figure 5. Upper: averaged electrostatic potential around  $t = 1024$  for run 1 of Table 1.  
 Lower: corresponding electron phase space.





DRHO	=	-0.10
NX	=	1024
DX	=	1.00
NT	=	2048
DT	=	0.50



TIME 1024.

DRHO	=	-0.10
NX	=	1024
DX	=	1.00
VMIN	=	-4.00
VMAX	=	+6.00

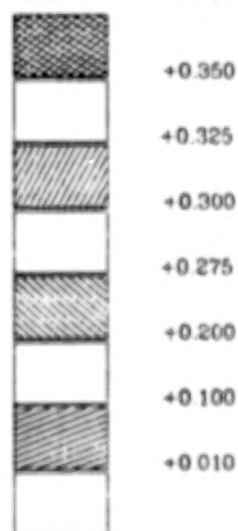
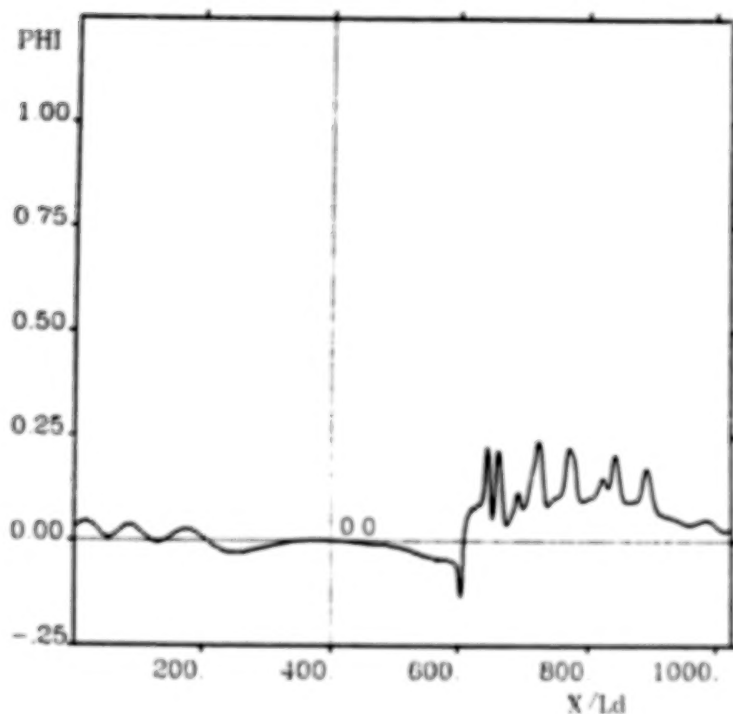


Figure 6. Same as Figure 5 for run 2.

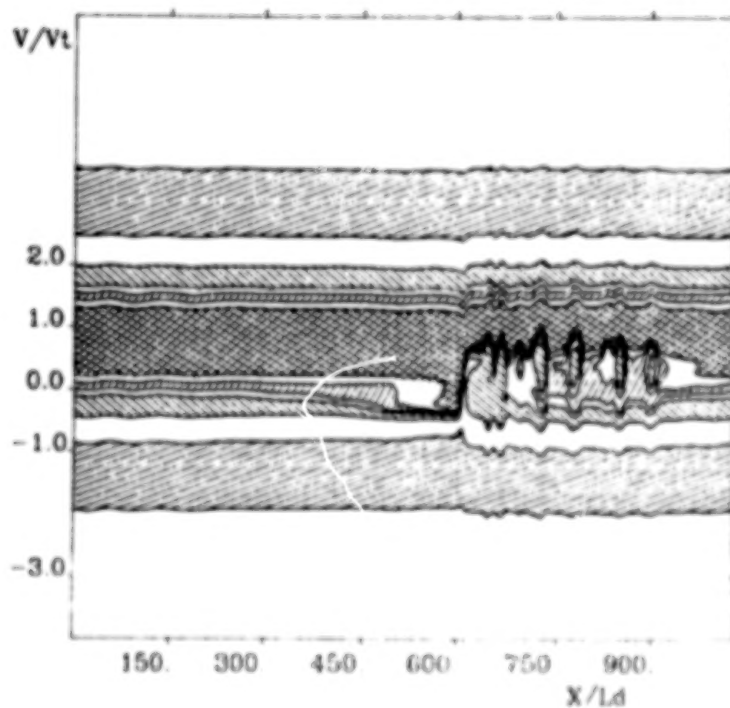
ORIGINAL PAGE IS  
OF POOR QUALITY

AVERAGED POTENTIAL (over  $4\pi/\omega_p$ )  
 $v_d/v_t=0.85$   $t_i/t_e=0.50$   $m_i/m_e=100$ .



DRHO	=	-0.10
NX	=	1024
DX	=	1.00
NT	=	2048
DT	=	0.50

ELECTRON PHASE SPACE vlasov code  
 $v_d/v_t=0.85$   $t_i/t_e=0.50$   $m_i/m_e=100$ .



TIME 1024.

DRHO	=	-0.10
NX	=	1024
DX	=	1.00
VMIN	=	-4.00
VMAX	=	+6.00

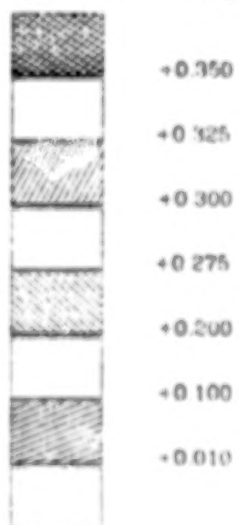
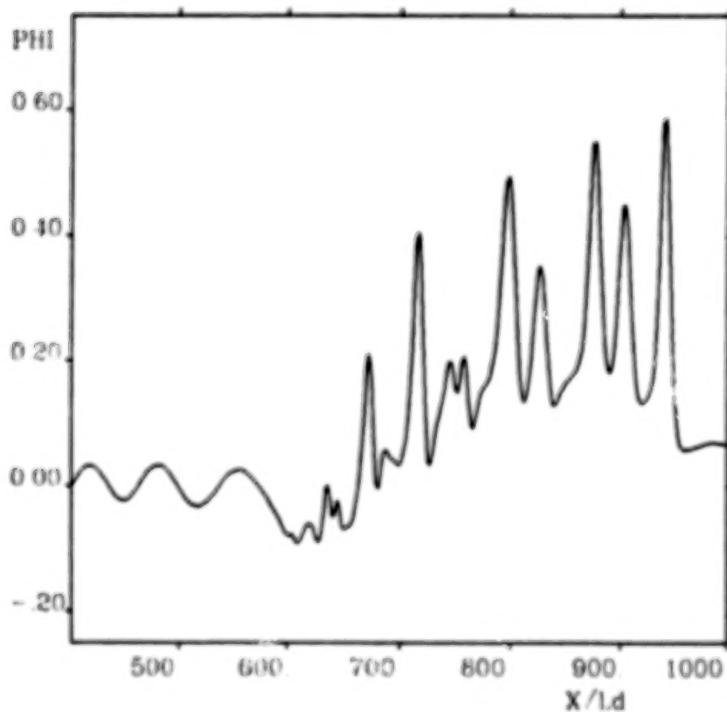


Figure 7. Same as Figure 5 for run 3.

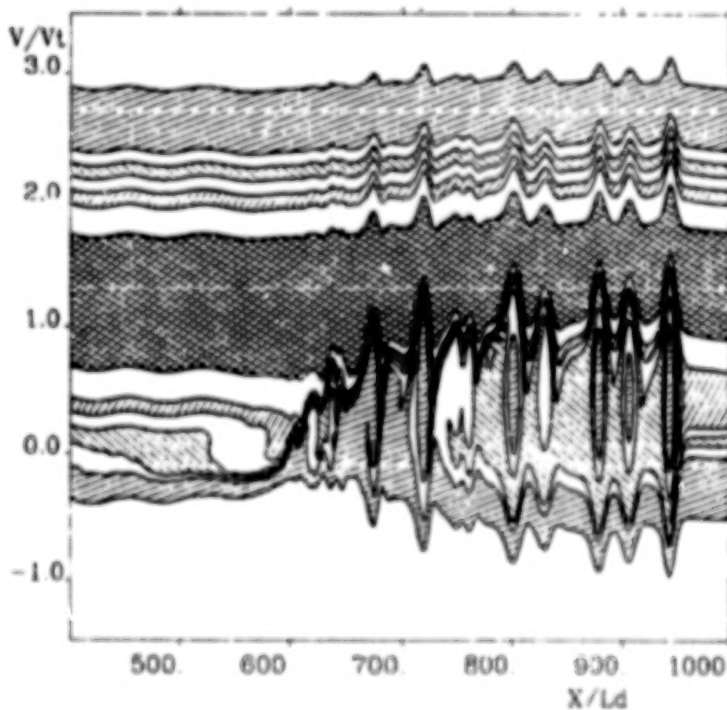
ORIGINAL PAGE IS  
OF POOR QUALITY

AVERAGED POTENTIAL (over  $4\pi/\omega_p$ )  
 $v_d/v_t = 1.25$   $t_i/t_e = 1.00$   $m_i/m_e = 100$ .



DRHO	=	-0.10
NX	=	1024
DX	=	1.00
NT	=	2048
DT	=	0.50

ELECTRON PHASE SPACE vlasov code  
 $v_d/v_t = 1.25$   $t_i/t_e = 1.00$   $m_i/m_e = 100$ .



TIME 1024

DRHO	=	-0.10
NX	=	1024
DX	=	1.00
VMIN	=	-1.00
VMAX	=	+6.00

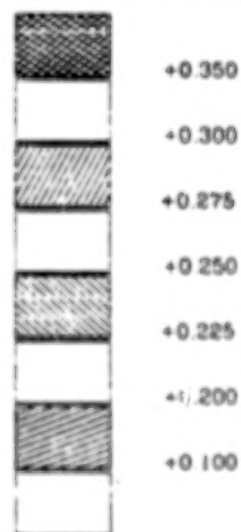


Figure 8. Same as Figure 5 for run 4.

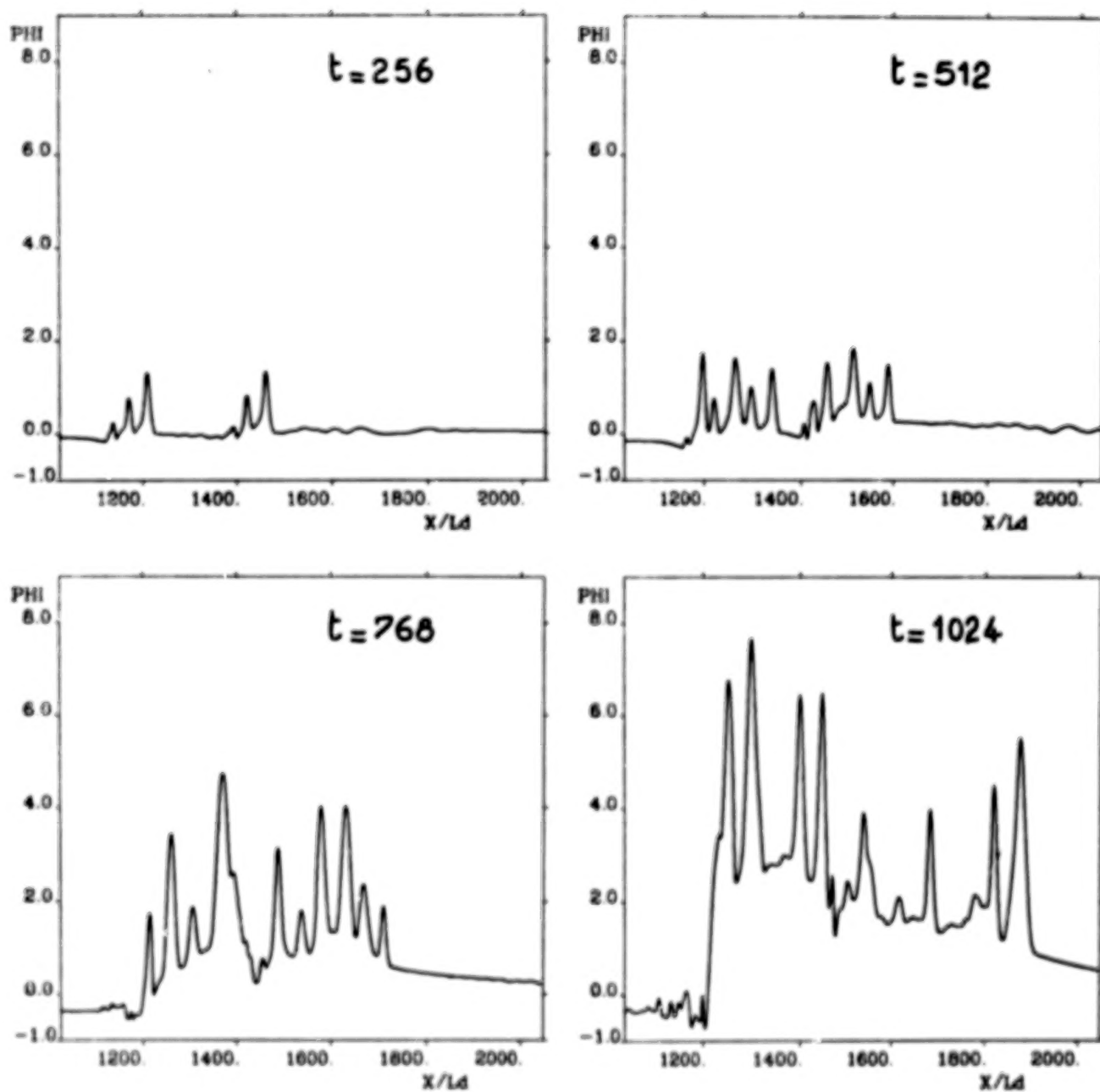


Figure 9. Averaged electric potential at times 256, 512, 768, and 1024  $\omega_{pe}^{-1}$  for run 5.  
Notice the blowup of the potential after time 768.

N87

23323

UNCLAS

## ELECTRIC FIELDS AND DOUBLE LAYERS IN PLASMAS

Nagendra Singh, H. Thiemann, and R. W. Schunk  
Center for Atmospheric and Space Sciences  
Utah State University  
Logan, Utah 84322-3400, U.S.A.

## ABSTRACT

Various mechanisms for driving double layers in plasmas are briefly described, including applied potential drops, currents, contact potentials, and plasma expansions. Some dynamical features of the double layers are discussed. These features, as seen in simulations, laboratory experiments, and theory, indicate that double layers and the currents through them undergo slow oscillations which are determined by the ion transit time across an effective length of the system in which the double layers form. It is shown that a localized potential dip forms at the low potential end of a double layer, which interrupts the electron current through it according to the Langmuir criterion, whenever the ion flux into the double is disrupted. The generation of electric fields perpendicular to the ambient magnetic field by contact potentials is also discussed. Two different situations have been considered; in one, a low-density hot plasma is sandwiched between high-density cold plasmas, while in the other a high-density current sheet permeates a low-density background plasma. Perpendicular electric fields develop near the contact surfaces. In the case of the current sheet, the creation of parallel electric fields and the formation of double layers are also discussed when the current sheet thickness is varied. Finally, the generation of electric fields (parallel to an ambient magnetic field) and double layers in an expanding plasmas is discussed.

## I. INTRODUCTION

Since the early days of double layer (DL) research (e.g., Block, 1972), considerable progress has been made in the understanding of the formation of DL's and their dynamical features. The purpose of this summary is to highlight some of the major findings on the generation of electric fields in collisionless plasmas and on the formation, dynamics, and structure of double layers. We define double layers as electrostatic potential structures that can support localized electric fields in collisionless plasmas. The nomenclature "double layer" is derived from the fact that the electric field is primarily supported by two layers of charges (positive and negative). Such potential structures can form in current carrying plasmas as well as in the absence of a current.

Figure 1 shows a summary of the various mechanisms that can create double layers in a plasma. Broadly speaking, the mechanisms can be categorized as follows:

1. Applied potential drop across a plasma
2. Current through a plasma
3. Contact potentials
4. Plasma expansion.



These mechanisms are not as distinct from each other as it may appear. For example, when a potential drop is applied across a plasma, a current develops (Singh, 1980, 1982; Singh and Schunk, 1982a), or when a current is drawn through a plasma, a potential drop develops (Singh and Schunk, 1982b, 1984a). The characteristics of double layers driven by an applied potential drop and by a current through the plasma have been compared, and they have been shown to be very similar (Singh and Schunk, 1983a).

Contact potentials develop when plasmas with different properties come into contact. The difference in the ion and electron gyroradii plays an important role in creating perpendicular electric fields when the contact surfaces are parallel to the ambient magnetic field. Typically, the scale length of such electric fields is of the order of the ion Larmor radius. The potential structures associated with such electric fields appear as perpendicular or oblique double layers. When the perpendicular electric fields are shorted out at some location away from the source region, it is possible to generate two-dimensional potential structures with electric fields parallel to the ambient magnetic field. Such two-dimensional potential structures are known to play an important role in auroral electrodynamics. It is worth mentioning that the generation of a parallel potential drop by shorting out the perpendicular electric fields away from their source region is, in a sense, equivalent to applying a potential drop. Here, the perpendicular potential drop becomes a parallel potential drop due to the conducting boundary condition.

Current sheets or filaments of a finite thickness in plasmas are examples where the plasma processes driven by both the contact potential and the current take place. Multi-dimensional double layers form in such cases (Singh et al., 1983, 1984, 1985, 1986).

When a high-density plasma expands along an ambient magnetic field into a low-density plasma or into a vacuum, electric fields are set up. Near the expansion front, a double-layer type-charge separation occurs. Thus, currentless double layers form in expanding plasmas (Singh and Schunk, 1984b).

The purpose of this paper is to present a summary of our studies on the above mechanisms for generating electric fields and double layers. These studies have been performed either with a one-dimensional Vlasov-Poisson solver (Singh, 1980) or with a two-dimensional particle-in-cell (PIC) code (Singh et al., 1983, 1985).

## II. APPLIED POTENTIAL DROP

Basically, the process of DL formation is creating a potential drop. Thus, the application of a potential drop across a collisionless plasma may drive a double layer along with a host of other plasma processes (Singh and Schunk, 1982a). There are several laboratory experiments (Coakley and Hershkowitz, 1979; Iizuka et al., 1983, 1985) and numerical simulations (Joyce and Hubbard, 1978; Singh, 1980, 1982; Singh and Thiemann, 1980a,b; Singh and Schunk, 1982a,c, 1983a; Johnson, 1980) in which DL's have been driven by applied potential drops. Some of these experiments and simulations (Singh, 1982; Singh and Schunk, 1982a, 1983a) show remarkable similarities in both the processes leading to the formation of a DL and its dynamics. It is found that these processes are cyclic; the DL formation leads to current interruption, as the DL moves the currents recuperate, leading to the reformation of a new DL. In connection with several space and cosmic plasma phenomena, Alfvén (1982) has invoked the role of exploding double layers, which are cyclic. Thus, it is relevant here to discuss the cyclic behavior of double layers as seen in laboratory experiments and simulations.

Here we illustrate some important plasma processes taking place during recurring DL formation by presenting results from one-dimensional Vlasov simulations (Singh, 1982; Singh and Schunk, 1982a,c, 1983a) in which the dynamics of the plasma of length  $0 \leq x \leq d$  is followed by solving the Vlasov and Poisson equations after a potential drop  $\Delta\phi_0$  is applied across the plasma. In Figure 2 we present a summary of a simulation in which  $d = 100 \lambda_D$  and  $\Delta\phi_0 = 30 k_B T_e / e$ , where  $\lambda_D$  is the plasma Debye length with  $T_e$  as the electron and ion temperature.

Applying a potential drop across a quasi-neutral plasma is equivalent to applying a uniform electric field  $E_0$  (see the potential profile at  $t = 0$  in Figure 2a), whose strength depends on the applied drop  $\Delta\phi_0$  and the length of the system;  $E_0 \approx \Delta\phi_0/d$  (Fig. 2a). This field accelerates electrons and ions in opposite directions. However, during very early time ion acceleration is not important, but the electrons are accelerated to the extent that a current is set up in the plasma which may exceed the current at the cathode boundary,  $x = 0$  (Fig. 2b). When this happens a positive space charge appears near the cathode ( $x = 0$ , in Fig. 2) modifying greatly the initial linear potential profile (Fig. 2a). This potential perturbation evolves into an electron hole in the form of a positive potential pulse which propagates in the direction of the initial electric field (Fig. 2a) and it is destroyed when it reaches the anode end. During the phase of the electron hole propagation, counterstreaming electron beams form (Singh, 1982). After this phase the plasma is subject to a strong high frequency turbulence, which modifies the plasma greatly. One important modification is the expulsion of the plasma and creation of plasma cavity. In simulations with very short lengths (Singh, 1980) ( $L < 100 \lambda_{de}$ ), the formation of an extended cavity is not seen. However, as the system length increases, the extended cavity becomes an important feature of the plasma (Singh, 1982; Singh and Schunk, 1982a). Also, the ion flux into the plasma from the anode boundary is totally disrupted; as a matter of fact, an outflux of ions occurs.

The potential step near the cathode evolves into a double layer (Figs. 2a, c, and d) self-consistently modifying the electron and ion velocity distribution functions. Soon after its formation, the DL develops a potential dip (potential profiles marked with "A" in Fig. 2e) at its low potential end which interrupts the electron current (bottom panel in Fig. 2e) and it moves toward the anode (compare potential profiles "A" and "B" in Fig. 2e). The moving double layer sits on an expanding plasma density front moving approximately at the ion-acoustic speed (Singh and Schunk, 1982b). The expanding plasma and the ion acceleration by the double layer produce counterstreaming ion beams near the low potential end of the DL (Singh and Schunk, 1982a). In the frame of reference of the moving double layer, the electron and ion current continuity conditions are maintained (Singh and Schunk, 1982a).

As the double layer moves, the ion flux (current) at the anode reverses from outflux to influx (Fig. 2e). As the ion current through the DL recuperates, so does the electron current approximately satisfying the Langmuir condition (Singh and Schunk, 1982c). In the presence of the ion beam and the electron current on the low potential side, any positive potential perturbation near the cathode triggers the reformation of the double layer and the above plasma processes repeat in a cyclic fashion (Fig. 2e). The time constant of this cyclic process is the ion transit time ( $\tau_i$ ) across the system or equivalently the transit time of the double layer across the system. The above cyclic phenomenon of DL formation is summarized in Figure 3. The cyclic reformation of double layers has been seen in simulations with applied potential drops reported by other authors (Joyce and Hubbard, 1978; Borovsky and Joyce, 1983).

Some of the cyclic processes seen in the simulations have also been seen in laboratory experiments (Iizuka et al., 1983, 1985). These experiments were carried out in a Q machine with both single- and double-ended operations. In the single-ended operation only the cathode plasma source was operative. On the other hand, in the double-ended operation both the cathode and anode plasma sources were operative. Iizuka et al. (1983) clearly show that in both types of operations, cyclic behaviors were seen, but there were some differences between them as discussed below. With the single-ended operation, the double layer formed near the cathode and subsequently moved toward the anode and disappeared there, and with the applied potential drop persisting, a new double layer formed near the cathode and moved away from it. Thus, the double layer appears to show a forward (toward anode) and backward motion. However, the backward motion (toward cathode) was found to be so fast that the details of the plasma processes during this phase could not be resolved in the experiments. From our simulations we find that the time scale of the rise in the potential at the low potential end of the double layer, which eventually leads to the formation of a new double layer (Fig. 2f), is roughly  $\tau_r < 100 \omega_{pe}^{-1}$ . For the plasma densities ( $\sim 10^8 \text{ cm}^{-3}$ ) in the experiment,  $\tau_r \approx 0.1 \mu\text{s}$  which is much smaller than the temporal resolution of about  $1 \mu\text{s}$  in the experiments.

C - 3

In double-ended operations, Iizuka et al. did not see the motion of the whole double layer; instead, a back and forth motion of the low potential end of the double layer was seen. In agreement with the single-ended operation, the backward motion was found to be so fast that it could not be resolved in the experiment while the forward motion was slow. These motions were correlated with the oscillation in the current at a frequency determined by the transit time of the low potential end during its forward motion. Such features of double layers seen in the Q machine with the double-ended operations are common in simulations with very short system lengths (Singh, 1980; Singh and Thiemann, 1980a).

The cyclic behavior seen in the simulations and laboratory experiments driven by applied potential drops has also been seen in simulations (Singh and Schunk, 1982b, 1983a, 1984a) and experiments (Leung et al., 1980) in which double layers were driven by current injections.

It is important to assert here that the cyclic behavior seen in the simulations and experiments do not appear to be an artifact of the boundary conditions. The primary cause of the cyclic behavior appears to be the fundamentally different time scales associated with the electron and ion dynamics. The plasma processes which lead to the double layer formation interrupt the ion flux into the double layer. Due to the lack of the ion flux, the double layer moves and also the current through it disrupts according to the Langmuir condition (Singh and Schunk, 1982c). When the ion flux recuperates slowly, so does the electron current. Some plasma fluctuations on the low potential side, after the current recovery, start the process of double layer reformation. In the simulations, the fluctuations are found to be growing electron holes, which appear to be caused by the rarefaction instability (Carlqvist, 1972; Block, 1972; Singh, 1982).

The cyclic oscillations discussed above appear to be in accord with the theoretical work of Silevitch (1981), who showed that in an unbounded plasma, strong double layers have a negative dynamic resistance. Thus, only when the system (circuit), of which the double layer is a part, is sufficiently "lossy," it is possible to create a steady double layer. Otherwise, the double layer oscillates with a frequency determined by an effective ion transit time (Silevitch, 1981).

It is worthwhile to mention that Smith (this proceedings) draws quite different conclusions from those drawn here regarding the cyclic behavior of double layers as seen in simulations and experiments. His discussion on the experimental results with the double-ended operation of the Q machine and the comparison of the results from experiments (Iizuka et al., 1983) with those from simulations (Singh and Schunk, 1982a,c) are misleading.

The cyclic behaviors of the double layer and the current through it, as discussed here, may be relevant to some space and cosmic plasma phenomena such as magnetic storms, solar flashes, and solar flares, which are found to be repetitive (Alfvén, 1982). It has been suggested that these phenomena may be caused by exploding double layers (Alfvén, 1982) which are caused by the inductive effects in the current systems in the plasma. When the double layer forms, the current interrupts. The decreasing current may induce large voltages which add to the double layers. The repetitive feature appears because of the subsequent current recovery. The time scale ( $\tau_c$ ) of such recovery may be determined by the circuit properties. If  $\tau_c \ll \tau_i$ , the current recovery through a DL is dictated by the time scale of the ion transit time. Otherwise ( $\tau_c \gg \tau_i$ ), the repetition time is determined by  $\tau_c$ . For a given space or cosmic situation it is possible to make rough estimates of  $\tau_i$  (Singh and Schunk, 1982c), but it is difficult to estimate  $\tau_c$  because of the distributed nature of the circuit properties associated with the currents.

As an illustrative example, let us consider the auroral circuit. If we assume that circuit length parallel to the geomagnetic field is  $\ell_{\parallel} \approx R_e$ , the Earth radius, the transit time of an ionospheric hydrogen ion with thermal energy  $\sim 1$  eV is  $\tau_i \approx 500$  s. For an auroral circuit, Alfvén (1982) estimated the inductance  $L \approx 30$  H. Assuming the resistance in the circuit to be  $R \approx 0.1$  ohm,  $\tau_c = 300$  s. However, we note that these numbers are highly tentative. It is not even certain that for the auroral double layer, which exists in extended auroral cavity, the transit times across or along the field lines are relevant (Singh and Schunk, 1982c).



### III. CURRENT INJECTION

The above cyclic process leading to double layer reformation has been seen in laboratory experiments (Leung et al., 1980) and simulations (Singh and Schunk, 1982b, 1984a) when electron current is injected into the plasma. However, there are some important differences in the formation processes of the double layers driven by current injection or applied potential drop. In the former case when the electron drift velocity is sufficiently large the Buneman instability leads to the double layer formation. In the early stage of the Buneman mode relatively small scale waves grow (see early time ( $\bar{t} < 1920$ ) plots Fig. 4a). During the nonlinear stage of the instability the small scale oscillations transform into long wavelength ones ( $1920 < \bar{t} < 2000$ ; Fig. 4a). Further evolution of the waves leads to formation of solitary pulses ( $\bar{t} \geq 2000$ ; Fig. 4a). The double layers evolve from these pulses by self-consistent modification of the electron and ion distributions.

### IV. DOUBLE LAYER STRUCTURE

During their temporal evolution, double layers undergo considerable modification in their potential distribution which critically depends on the current through the double layers. In this section we illustrate this through an example in which the plasma was driven by a current as discussed in Section III. However, it is important to note that the features discussed here are quite general. Figure 4b shows the temporal evolution of the double layer potential profile after the initial evolution shown in Figure 4a. The corresponding temporal evolutions of the average electron drift ( $\bar{V}_{de}$ ), electron thermal velocity ( $\bar{V}_{te}$ ), electron current ( $\bar{J}_e$ ), and electron temperature ( $\bar{T}_e$ ), all quantities being on the low potential side ( $\bar{x} = 50$ ), are given in Figure 4c. At early time ( $\bar{t} < 2340$ ), when the current density is large ( $|\bar{J}_e| > 1.5$ ), multiple double layer formations with typical double layer dimension  $\ell_{DL} \approx 20 \lambda_{de}$  are seen. On the other hand, when the current interrupts suddenly at  $\bar{t} = 2345$ , the double layer develops a localized potential dip at its low potential side. At such times  $\bar{V}_{de} < \bar{V}_{te}$ . The sudden electron current interruption is seen to be accompanied by a disruption in the ion influx caused by the strong solitary pulse at  $\bar{t} = 2345$ . Figure 4d shows the structure of the double layers with a dip by plotting the electron and ion density profiles along with the potential profile. Considering the charge separation (Fig. 4d) we note that the potential distribution is a triple layer. However, its predominant nature, as determined by the large electric field, is still of double layer type. The dip plays the role of a current interruptor to adjust the electron current in accordance with the ion influx so that the Langmuir condition is met.

The formation of a dip at the low potential end of a weak ion-acoustic (IA) double layer has been known since its first observation in numerical simulations (Sato and Okuda, 1981). The interesting fact to note is that the formation of an IA double layer itself depends on such dips (Hasegawa and Sato, 1982). On the other hand, we have shown here that in the case of an already existing double, whether weak or strong (Singh et al., 1985), the current interruptions lead to the formation of such dips.

### V. DOUBLE LAYER SCALE LENGTHS

Several simulations and laboratory experiments have indicated that for strong double layers the scale length  $L$  is given by (Joyce and Hubbard, 1978, Singh, 1980),

$$L \approx 6 (e\Delta\phi_{DL}/k_B T_e)^{1/2} \quad (1)$$

This scaling has been empirically derived from simulations based on applied potential drops. We find that when double layers evolve from waves or wavelets, such as the electron holes (Fig. 4b), the double layer scale length is typically of the order of the scale length of the perturbations from which the DL evolves.

## VI. CONTACT BETWEEN DIFFERENT PLASMAS

The existence of contact potentials (electric fields) near the contact surface between two materials having different electrical properties is a well-known phenomenon. In plasmas, the existence of such potentials has been investigated in connection with plasma confinement (e.g., see Sestero, 1964). In space plasmas, the studies related to the structure of the magnetopause indicate that this is a region where contact potentials can develop (e.g., see Whipple et al., 1984 and references therein). Several years ago, Hultqvist (1971) suggested that the contact between the hot plasma in the plasma sheet and the cold ionospheric plasma may create magnetic field-aligned (parallel) electric fields which could account for the observed precipitating energetic ions along the auroral field lines. More recently, Barakat and Schunk (1984) suggested that the contact between the cold polar wind electrons and the hot polar rain electrons may create parallel electric fields.

It is now clear that electric fields perpendicular to the geomagnetic field are an important feature of the auroral plasma. However, the mechanisms for creating such fields have not been well established. It is possible that they are supported by discontinuities in the plasma properties (such as particle temperatures and densities) across magnetic field lines. Such discontinuities, in which the normals to the plane of the discontinuities are perpendicular to the magnetic field lines, are known as tangential discontinuities.

Even though the existence of perpendicular electric fields in the auroral plasma is well established, the nature of the plasma discontinuities (associated with the fields), if they exist, remains virtually unexplored. Recently, however, Evans et al. (1986) have presented observational evidence that tangential discontinuities do occur in association with discrete auroral arcs. They also conducted one-dimensional steady-state calculations on the generation of perpendicular electric fields through the contact of a high-density hot plasma with a low-density relatively cold plasma. They obtained electric fields having scale lengths of both the electron and ion Larmor radii. This is expected because in their model the electrons were not highly magnetized; they used  $\Omega_e/\omega_{pe} < 1/3$ , where  $\Omega_e$  and  $\omega_{pe}$  are the electron-cyclotron and electron-plasma frequencies, respectively. However, in the auroral plasma, where the large perpendicular electric fields have been observed, typically  $\Omega_e \gg \omega_{pe}$ , implying highly magnetized electrons.

Motivated by the observations of large perpendicular electric fields in the auroral plasma, we have pursued two different approaches for creating perpendicular fields by contact potentials as follows:

1. When a low-density containing sufficiently hot ions is sandwiched by high-density cold plasmas, it is possible to generate electric fields having strengths comparable to those observed in the auroral plasma. In such a situation the electric fields occur near the edges of a cavity in the plasma density as it is sometimes the case in the auroral plasma (Mozer and Temerin, 1983).
2. Upward field-aligned currents are a well-known phenomenon in the auroral plasma. These currents can occur in the form of thin sheets or filaments. We study such a situation by driving currents through a background plasma. The currents flow in sheets of finite thicknesses. The contact between the plasmas inside and outside the sheet produces perpendicular electric fields.

By means of numerical simulations, we have studied the above mechanisms for the generation of perpendicular electric fields. We briefly summarize our studies in the following two subsections.

## A. Perpendicular Electric Fields Near the Contact Surface Between Hot and Cold Plasmas

Figure 5 shows the geometrical scheme of our simulations. Using a standard particle-in-cell code (Morse, 1970), we simulate a two-dimensional plasma of size  $L_x \times L_y$ . The magnetic field  $\mathbf{B}$  is along the  $y$ -axis. It is assumed that all field quantities and plasma properties are invariant along the  $z$ -axis. In order to study the generation of the perpendicular electric fields, the plasma is stratified along the  $x$ -axis. The simulation plasma is divided into regions I, II, and III, which are initially (time  $t = 0$ ) filled with plasmas with different properties. For this study, the plasmas are as follows. In region I,  $n_{i1} = n_{e1} = n_0$ , where  $n$  denotes density and subscripts  $e$ ,  $i$ , and  $l$  refer to electrons, ions, and region I, respectively; the electron temperature  $T_{e1} = T_0$  and the ion temperature  $T_{i1}$  is varied in the different simulations. In regions II and III, the plasma properties are the same:  $n_{i2} = n_{e2} = n_{i3} = n_{e3}$  and  $T_{i2} = T_{e2} = T_{i3} = T_{e3} = T_c$ . The temporal evolution of the plasmas for  $t > 0$  is followed by calculating the particle dynamics with the self-consistent electric fields.

In our simulations we use the electrostatic approximation. Thus, the electric fields are calculated by solving the Poisson equation with the following boundary conditions:  $\phi(x = -L_x/2, y) = \phi(x = L_x/2, y) = 0$ . Note that these are the Dirichlet conditions on the electric potential  $\phi$ . Along  $y$  we use a periodic boundary condition, implying  $\phi(x, y = 0) = \phi(x, y = L_y)$ . The electric field  $\mathbf{E}$  is obtained from  $\mathbf{E} = -\nabla\phi$ .

In the simulations described here, we ignore the magnetic fields generated by the plasma currents, which flow near the plasma interfaces. Thus, the ambient magnetic field remains unperturbed. Such an assumption appears justified at altitudes up to a few Earth radii, where the geomagnetic field is strong and the particle pressures are much smaller than the magnetic pressure.

We use the following definitions and normalizations: density  $\tilde{n} = n/n_0$ ; temperature  $\tilde{T} = T/T_0$ , where  $n_0$  and  $T_0$  are the initial (time  $t = 0$ ) density and electron temperature in region I; distance  $\tilde{x} = x/\lambda_{d0}$ ; velocity  $\tilde{V} = V/V_{to}$ ; time  $\tilde{t} = t\omega_{p0}$ ; electric potential  $\tilde{\phi} = e\phi/k_B T_0$ ; electric field  $\tilde{E} = E/E_0$ ; current  $\tilde{J} = J/(n_0 e V_{to})$ , where  $V_{to} = (k_B T_0/m_e)^{1/2}$ ,  $\omega_{p0} = n_0 e^2/m_e \epsilon_0$ ,  $\lambda_{d0} = V_{to}/\omega_{p0}$ ,  $E_0 = k_B T_0/e\lambda_{d0}$ ,  $k_B$  is Boltzmann's constant, and  $m_e$  is the electron mass. In the simulations we use an artificial ion mass,  $m_i = 64m_e$ .

The results described in the following sections are taken from simulations in which  $L_x \times L_y = 64 \times 64 \lambda_{d0}^2$ ,  $d = 32 \lambda_{d0}$ ,  $\Omega_e/\omega_{p0} = 4$ , where  $\Omega_e$  is the electron cyclotron frequency, and where the number of electrons and ions per cell of dimension  $\lambda_{d0}^2$  was 4 in region I and 16 in regions II and III.

When the plasma properties change along a direction perpendicular to the magnetic field, as in Figure 5, the ions play a crucial role in creating the contact potential near the interfaces between the different plasmas. As long as the ion temperature  $T_i > (m_e/m_i)^{1/2} T_e$ , where  $T_e$  is the electron temperature, the ion Larmor radius  $\rho_i > \rho_e$ , the electron Larmor radius. Thus, ions from the neighboring plasmas penetrate the interface more effectively than do the electrons. Thus, depending on the relative densities and the ion temperatures in the neighboring plasmas, a contact potential may develop.

There are numerous possibilities for choosing the relative densities and temperatures in region I to III of Figure 5. In this study, we were primarily motivated by the observations of perpendicular electric fields near the edges of density cavities (Mozer and Temerin, 1983). Thus, we chose  $\tilde{n}_2 = \tilde{n}_3 = 4$  and  $\tilde{n}_1 = 1$ . We assumed that the dense plasmas in regions II and III were cold and that they had the same temperature  $T_c < T_0$ . On the other hand, the electrons and ions in region I were assumed to be warmer than those in the other two regions. We present results on the effect of the variation of the warm ion temperature on the perpendicular electric fields that developed near the contact surfaces.



Figure 6 shows the distributions of the electric potential, the perpendicular electric field, and the plasma density as functions of  $\bar{x}$  at  $\bar{t} = 100$  for  $T_c = 0.2 T_o$ , and  $T_{i1} = 20 T_o$ . Recall that  $T_{e1} = T_o$ . Thus, in the low-density plasma of region I, the ions are hotter than the cold ions in regions II and III by a factor of 100. We note that the average Larmor radius of the hot ions  $\rho_H \approx 9 \lambda_{do}$ . The quantities shown in Figure 2 are time-averaged over a time interval of  $\Delta \bar{t} = 50$  centered at  $\bar{t} = 100$ .

Figure 6a shows that a negative potential valley develops in region I ( $|\bar{x}| < 16$ ). The large perpendicular electric fields develop near the contact surfaces, where sharp gradients occur in the density (Fig. 6b). The maximum magnitude of the electric fields is approximately  $\bar{E}_\perp \approx 0.6$  and the scale length of the electric field near each interface is about  $\rho_H \approx 9 \lambda_{do}$ .

We find that such large electric fields develop only when the ions in region I are sufficiently warm. In order to show this we carried out simulations by varying the hot ion temperature  $T_{i1}$ . For  $T_{i1} = T_o$ , we did not find any enhancement in  $E_\perp$  near the interfaces. As the ion temperature  $T_{i1}$  was increased, bipolar electric fields developed near the interfaces; for  $T_{i1}/T_o = 5$ ,  $E_{\perp \max} \sim 0.2$ . It was found that for  $T_{i1}/T_o > 10$ ,  $E_{\perp \max}$  does not increase indefinitely, but for the parameters used in the simulation it is limited to about  $\bar{E}_{\perp \max} \lesssim 0.6$ .

A noteworthy feature was found that is that the electric fields maximize just inside the low-density plasma and not at the interface (Fig. 6). This happens because the gyrating cold ions in the high-density plasmas of regions II and III partially neutralize the space charges created by the hot gyrating ions near the interfaces. In Figure 6 the magnitude of the hot ion Larmor radius  $\rho_H$  is indicated. The electric fields at the interfaces have scale lengths of the order of the Larmor radius.

The temporal evolution of the potential drop  $\Delta\phi = \phi(x=0)$  in the simulations show that at early times ( $\bar{t} < 20$ ) the potential drop grows and afterward undergoes a slow oscillation, with time-averaged values depending on the hot ion temperature  $T_{i1}$ . It is worth mentioning that the time constant ( $\tau_{\text{cont}}$ ) for the development of the contact potential ( $\Delta\phi$ ) is approximately given by

$$\tau_{\text{cont}} \sim 20 \omega_{po}^{-1} \sim \Omega_i^{-1}, \quad (2)$$

where  $\Omega_i$  is the ion-cyclotron frequency ( $\Omega_i \approx eB/m_i$ ). By varying  $\Omega_e/\omega_{po}$ , we found that the above scaling of  $\tau_{\text{cont}}$  with  $\Omega_i$  is generally valid. Thus, the contact potential sets up with a time constant that is associated with the ion cyclotron motion.

The slow oscillations occur at the ion-plasma frequencies of the plasmas in regions I and II. Comparing the relative amplitudes of  $E_\perp$  and  $E_\parallel$  associated with the oscillations, we find that  $E_\perp \gg E_\parallel$ . Thus, these oscillations are not of the ion-acoustic type, but are associated with the lower hybrid frequencies in regions I to II.

It is important to note that the geometry of our simulations does not allow the excitation of drift modes propagating in the direction of the diamagnetic currents near the interfaces at  $x = \pm d/2$ . These currents flow along the  $z$ -axis. We have assumed in our simulations that all physical quantities are invariant with respect to  $z$ . Thus, no wave modes are allowed to propagate in this direction.

The contact potential develops because the hot ions in region I, while gyrating, penetrate into the neighboring plasmas of regions II and III. In order to show this, the ion velocity distribution function ( $F$ ) is plotted in Figure 7 as a function of the  $x$ -component of the ion energy,  $W_x = 1/2 m_i V_x^2 = 32 \hat{V}_x^2 k_B T_o$ , at several locations for the simulation with  $T_{i1}/T_o = 15$ . The distribution at  $x = 0$  (center of region I) clearly matches the initial Maxwellian distribution with a temperature  $\bar{T}_{i1} = 15$ , as shown by the asymptote marked with this temperature. On the other

hand, at  $\bar{x} = 32$  (near the end of region III) the ion population is cold. At  $\bar{x} = 24$ , we see that the hot and cold ions have mixed together. The average ion Larmor radius for the hot ions in region I for  $T_{i1} = 15$  is  $\bar{\rho}_{H1} \approx 8$ . Thus, we expect the penetration of a large number of hot ions from region I ( $|\bar{x}| < 16$ ) into region III up to a distance of about  $\bar{x} \approx 24$ . This is verified by the distribution function at  $\bar{x} = 24$ . The distribution at  $\bar{x} = 16$  is near the initial interface, where we see that compared to the numbers of ions in the cold and hot populations at  $\bar{x} = 24$ , the number of ions in the cold population has decreased, while that in the hot population has increased.

We summarize this section by noting that when a low-density plasma containing hot ions comes into contact with a high-density cold plasma with the contact surface being parallel to the magnetic field, it is possible to create perpendicular electric fields. The time constant for creating such fields is roughly  $\Omega_i^{-1}$  and the scale length is approximately  $\rho_{H1}$ , the Larmor radius of the hot ions.

The above results indicate that when the hot ion temperature  $T_{i1} > 10 T_o$ , a rough estimate of the strength of the perpendicular electric field is

$$E_{\perp} \sim 0.5 E_o \quad (3)$$

where the normalizing electric field  $E_o$  critically depends on  $n_o$  and  $T_o$ . When  $n_o$  varies from 1 to  $10 \text{ cm}^{-3}$  and  $T_o$  varies from 1 to 100 eV, the strength of  $E_{\perp}$  ranges from several tens to several hundreds of mV/m. Satellite observations indicate that the electric fields associated with electrostatic shocks (Mozar et al., 1980) have a similar strength. For example, if we assume that the hot plasma in region I is of plasma sheet origin and the electron temperature  $T_o = 100 \text{ eV}$ , then it is possible to create perpendicular electric fields of several hundreds of mV/m if the hot ion temperature  $T_{i1} > 1 \text{ keV}$ , which is common in the plasma sheet. For  $T_o = 100 \text{ eV}$ , the cold plasma temperature assumed in our simulations is  $T_c = 20 \text{ eV}$ . We find that when  $T_c$  is reduced below  $0.2 T_o$ , as assumed here, this does not significantly affect the electric fields. Thus, the cold plasma may originate in the ionosphere.

However, the question of how the stratification of the plasma assumed in our simulations (Fig. 5) is created in space plasmas still needs to be answered. It now appears that plasma blobs and clouds are created in the magnetotail region. When these blobs of plasma move closer to the Earth where a colder plasma exists, the stratification of the plasma assumed in our simulations may be created.

In this section we were mainly concerned with the generation of perpendicular electric fields. In the near future we will study the creation of parallel electric fields, the formation of double layers, the parallel acceleration of electrons and ions, and the generation of parallel currents that occurs when the perpendicular electric fields generated by contact potentials are shorted out by a conducting boundary. Such studies will complement our previous studies on current sheets as summarized in the next section.

## B. Double Layer Structures Associated with Current Filaments or Sheets

There are evidences that the current systems in space and cosmic plasmas are filamented (e.g., see Alfvén, 1982 and references therein). Thus, there is a need to study double layer structure in filamentary currents. The available temporal and spatial resolutions for the plasma measurements in the auroral region indicate that the field-aligned currents are highly structured in the form of current sheets with north-south thicknesses of a few kilometers (Dubinin et al., 1985). Probably even thinner sheets exist but they have not been resolved.

Here we briefly summarize our recent efforts on simulations of double layers driven by current sheets (Singh et al., 1983, 1984, 1985; Thiemann et al., 1984). Figure 8 shows our simulation scheme. A two-dimensional

plasma of size  $L_x \times L_y$  is driven by a magnetic field-aligned current sheet having a current density  $J_0$ . Initially the simulation region is filled with a plasma of density  $n_0$  and temperature  $T_0$ . At later times, particles are injected both at the top and lower boundaries. Electrons and ions injected at the top boundaries have temperature  $T_{e0}$  and  $T_{i0}$  ( $T_{i0}$ ) while those at the lower boundary  $T_{e\ell}$  and  $T_{i\ell}$ . Various simulations were performed by varying these temperatures using a standard particle-in-cell (PIC) code. The electron current is set up in the sheet by injecting electrons at the top of the current sheet at rates to produce desired current (flux) densities. These electrons were also given a downward drift  $V_{de}$ . Overall, charge neutrality of the simulation plasma was maintained by counting the number of electrons and ions and injecting an appropriate number of the deficient particles at the lower boundary. The electrostatic boundary conditions are as follows; the plane  $y = 0$  is assumed to be conducting,  $\phi(x, y = 0) = 0$ ; at the top boundary we set  $E_y(x, y = L_y) = 0$  and a periodic boundary condition was used in  $x$ .

We use the following definitions:  $\lambda_{d0}$  is the Debye length based on the temperature  $T_0$  and on the initial density of  $n_0 = 4$  particles per cell,  $\Omega_e$  is the electron-cyclotron frequency and  $\omega_{pe}^2 = n_0 e^2 / m \epsilon_0$ , where  $\epsilon_0$  is the permittivity of free space and  $m$  is the electron mass. The ion-electron mass ratio was chosen to be  $M/m = 64$ . In the analysis that follows, we use the following normalizations: distance  $\tilde{y} = y/\lambda_{d0}$ , time  $\tilde{t} = t\omega_{pe}$ , velocity  $\tilde{V} = V/V_{te}$ , potential  $\tilde{\phi} = e\phi/k_B T_0$ , electric field  $\tilde{E} = E/E_0$ ,  $E_0 = (k_B T_0 / e \lambda_{d0})$ , and current density  $\tilde{J} = J / (en_0 V_{te})$ , where  $V_{te} = (k_B T_0 / m_e)^{1/2}$ . The numerical technique used here has been previously described in much greater detail by Singh et al. (1985).

Figure 9 shows an example of the potential structure as seen in a simulation in which  $\ell = 12 \lambda_{d0}$ ,  $\rho_{i0} = 9 \lambda_{d0}$ ,  $\rho_{i\ell} = 4 \lambda_{d0}$ ,  $\Omega_e/\omega_{pe} = 2$ ,  $\tilde{J}_0 = 1.25$ ,  $T_{i0}/T_0 = 5$ ,  $T_{e\ell} = T_{i\ell} = T_0$ , and  $L_x \times L_y = 64 \times 128 \lambda_{d0}^2$ , where  $\rho_{i0}$  and  $\rho_{i\ell}$  are the Larmor radii of the ions injected at the top and bottom of the simulation plasma, respectively. The potential structure is illustrated by plotting (a) equipotential surfaces, (b) contours of constant  $E_\perp$ , the component of the electric field perpendicular to the magnetic field, and (c) contours of constant  $E_\parallel$  in  $x - y$  plane. The current sheet edges are indicated by the arrows at the bottom of each panel. The solid and broken line contours show positive and negative values of the quantities. A V-shaped potential structure is evident from panel (a); a negative potential valley develops in the upper portion of the current sheet. Panel (b) shows the occurrence of a large bipolar perpendicular electric field near the edges of the current sheet at the top of the simulation plasma. The perpendicular electric fields develop due to the contact between the high-density plasma inside the sheet with a low-density plasma around it (Kan and Akasofu, 1979; Wagner et al., 1980; Singh et al., 1983). The hot ion Larmor radius determines the perpendicular scale length of the electric fields. The V-shaped potential structure develops when the perpendicular electric fields originating near the top of the simulation plasma are shorted out by the conducting surface at  $y = 0$ , thus, creating a parallel potential drop.

Panel (c) of Figure 10 shows the localized parallel upward electric fields as indicated by the "H" inside the current sheet. These parallel fields are of double layer type. There are three double layers stacked on top of each other inside the current sheet. The existence of these double layers can also be inferred from the equipotential surfaces in Figure 9a. Typically the maximum electric field strength in the double layers is about  $\tilde{E} = 0.25$ . The scale length of the double layers along the magnetic field is found to be about  $10 \lambda_{d0}$ , while they fill the entire width of the current sheet.

The double layers shown here are not dc, but they undergo considerable temporal variations at time scales ranging from electron to ion-plasma periods. Figure 10a shows the temporal variation in the double layer potential profile after averaging out the fast electron oscillations. Note the considerable changes in the potential profile and as well as in the magnitude of the net potential drop across the double layer. The temporal variations in  $E_\parallel$  and  $E_\perp$  at the point (0, 100) in the region of double layer formation, are shown in Figure 10b. Even at the times when  $E_\parallel$  has a dc component, there are considerable fluctuations in both  $E_\parallel$  and  $E_\perp$ . These fluctuations appear to have frequencies ranging from below the ion-cyclotron frequency to above the lower hybrid frequency. In addition,  $E_\parallel$  is found to have high frequency oscillations up to electron-plasma frequency and its harmonic which are averaged out in Figure 10b. The high frequency oscillations are not seen in  $E_\perp$ .

In a narrow current sheet, as discussed above in context of Figures 9 and 10, it is difficult to distinguish clearly between the double layers inside the current sheet and the large perpendicular electric fields occurring near the edges of the sheet. On the other hand, in wide sheets ( $\ell \gg \rho_H$ ), the double layers inside the current sheets are well separated from the large  $E_\perp$  occurring near the edges. Figure 11 shows an example of a potential structure associated with a current sheet of thickness  $\ell = 32 \lambda_{de}$ , and  $\ell/\rho_H \approx 10$ . Panel (a) shows the equipotential surfaces in the  $x-y$  plane, panel (b) shows the perpendicular distributions of  $E_\perp(x)$  and  $\phi(x)$  at  $y = 120 \lambda_{de}$ , and panel (c) shows the perpendicular distribution of  $J_\parallel(x)$  at  $y = 120 \lambda_{de}$ . In this simulation maximum possible value of the upward current in the sheet is  $J_0 \approx 0.6 n_0 e V_{te}$ . Note that only weak potentials ( $\sim k_B T_e/e$ ) develop inside the sheet, and the regions exterior to the sheet near the top (panel a) are highly positive. The perpendicular potential profile in the sheet is quite flat (panel b). Thus,  $E_\perp$  is mostly confined near the edges. In the region of large  $E_\perp$  near the edges we find that  $E_\perp \gg E_0$ , which is an important feature of the electrostatic shocks observed in the auroral plasma (Mozer et al., 1980). On the other hand, inside a wide sheet where double layers from  $E_\perp \sim E_0$  and both  $E_\perp$  and  $E_\parallel$  are considerably smaller than the perpendicular electric field near the edges. It is found that near the edges

$$E_\perp \sim E_{\perp m} \sim E_0 \quad (4)$$

We note that  $E_0$  depends on  $n_0$  and  $T_e$ ; when  $n_0$  varies from 1 to  $10 \text{ cm}^{-3}$  and  $T_e$  from 1 to 100 eV,  $E_0$  ranges from about 100 to 1300 mV/m. Thus, the large perpendicular electric fields occurring near the edges of the current sheets resemble the phenomenon of electrostatic shocks observed in the auroral plasma Mozer et al. (1980).

Whether or not the double layers are well separated from the large  $E_\perp$  near the current sheet edges, it is found that

$$E_{\text{DL}} \ll E_0 \quad (5)$$

Depending on  $n_0$  and  $T_e$ ,  $E_{\text{DL}}$  may range from a few mV/m to several tens of mV/m. So far only weak double layers ( $E_\parallel < 15 \text{ mV/m}$ ) have been observed in space plasmas (Temerin et al., 1982).

We find that in the case of wide sheets it is possible to develop relatively large downward parallel electric fields outside the current sheets (panel a, Fig. 11). These fields drive downward return currents (panel c).

In these simulations we have seen both parallel and perpendicular accelerations of ions (Singh et al., 1986). Most energetic ions are seen to be at pitch angles near  $90^\circ$ . Ion beams are seen only in narrow sheets with thicknesses  $\ell \lesssim \rho_H$ .

It is found that the double layers play a key role in electron acceleration, even though, all the features of the accelerated electrons cannot be explained by a simple picture of electron acceleration by dc double layers. The double layers act as a trigger mechanism for a host of plasma processes, which determines the velocity distribution function of the accelerated electrons.



## VII. PLASMA EXPANSION

Plasma expansions have been studied since the pioneering work of Gurevich et al. (1966), who studied the expansion of a plasma into a vacuum using the quasi-neutrality approximation. In this case the plasma equations allow self-similar solutions. However, this approximation breaks down in the low-density region where the local plasma Debye length becomes comparable to the scale length in the density gradient. Thus, a positive-negative charge separation occurs like in a double layer (Singh and Schunk, 1984b). However, it is worth noting that there is no current through such a double layer. The charge separation is supported by a relative smooth variation in the electron density while the ion density has a sharp density jump creating an ion density front. The plasma expansion is preceded by such a density front, behind which the self-similar solutions are found to be valid.

When a high-density ( $n_I$ ) plasma expands into a plasma of low density ( $n_{II}$ ), the expansion properties critically depend on the density ratio  $R = n_I/n_{II}$  (Mason, 1971). An example of such a dependence is shown in Figure 12, in which we have compared the potential profiles associated with expanding plasmas as the ratio  $R$  is varied from  $R = 0.001$  to  $0.2$ . The potential profiles shown in this figure are obtained as follows. We consider that initially (time  $t = 0$ ) the high- and low-density plasmas occupy the regions I ( $x \leq 300 \lambda_{di}$ ) and II, respectively. At times  $t > 0$ , the expansion is studied solving Vlasov equations for the ions in a self-consistent electric field obtained by solving the Poisson equation. The electrons are assumed to obey the Boltzmann law. In the calculations presented here we assume that the electron temperature  $T_e = 10 T_i$ , where  $T_i$  is the initial ion temperature in regions I and II. The potential profiles shown in Figure 12 are at  $t = 60 \omega_{pi}^{-1}$ , where  $\omega_{pi}$  is the ion-plasma frequency in region I and  $\lambda_{di} = V_{ti}/\omega_{pi}$  with  $V_{ti}$  being the ion thermal velocity. The different curves shown in Figure 12 are for different values of  $R$  as marked.

The noteworthy feature of the potential profile shown in Figure 12 is that as the density in region II is increased, the potential profiles steepen over a localized region in the expansion zone. When  $R$  is increased from  $0.001$  to  $0.01$ , we note the formation of a "knee" in the potential profile near  $x \sim 625 \lambda_{di}$ . When  $R$  is increased further this "knee" steepens and for  $R = 0.1$  and  $0.2$  we note the presence of two sharp transitions in the potential profiles; one occurs in region I in which the rarefaction wave propagates in the backward direction, and the other occurs in the expansion region II. Near the transitions localized electric fields, like that in a double layer, occur. It is important to note that the sharp transitions in the potential profiles (double layers) occurring in regions I and II move in opposite directions. With increasing time the potential profile in region I becomes less and less steep while that near the sharp transition in region II maintains its profile giving a localized electric field nearly constant with time. The features associated with occurrence of localized electric fields also occur when a multi-ion plasma expands into a vacuum (Singh and Schunk, 1983b).

## VIII. CONCLUSION

We have presented a brief summary of our studies related to the generation of electric fields in plasmas. Some of the mechanisms we discussed are as follows. When a potential drop is applied across a plasma, localized electric fields in the form of double layers occur. Double layers also form when a current is drawn through a plasma. The dynamical feature of such a double layer shows a cyclic behavior with a frequency determined by the transit time of the ions across an effective length of the system, in which the double layer forms. The formation of a potential dip at the low potential end of a DL and the current interruption are intimately related phenomena.

We have also discussed the generation of electric fields perpendicular to the ambient magnetic field in a plasma. Such fields can be generated by contact potentials near discontinuities in plasma properties. It was found that ion gyration plays an important role in generating the fields. The cases presented indicate that the scale length of the perpendicular electric field is of the order of the ion Larmor radius. Two complementary situations, in which perpendicular electric fields can be generated, were discussed. In one situation, we considered a low-density hot plasma sandwiched between high-density cold plasmas. It was shown that even if the hot ion density is low these ions are effective in creating electric fields of the magnitude observed in the auroral plasma. In the other situation, we considered a current sheet in a plasma. The density gradient across the sheet created the perpendicular electric fields. The formation of double layers in the sheet were studied.

The generation of electric fields in expanding plasmas was briefly discussed. It was shown that when a high-density plasma expands into a low-density plasma, the nature of the spatial distribution of the electric field critically depends on the density ratio of the two plasmas. A currentless double layer forms near the expanding plasma front.

*Acknowledgment.* This research was supported by NASA grant NAGW-77 and NSF grant ATM-8417880 to Utah State University.

## REFERENCES

- Alfvén, H., *Cosmic Plasma*, Reidel, Dordrecht, 1982.
- Barakat, A. R., and R. W. Schunk, *J. Geophys. Res.*, **89**, 9771 (1984).
- Block, L. P., *Cosmic Electrodyn.*, **3**, 349 (1972).
- Borovsky, J. E., and G. Joyce, *J. Geophys. Res.*, **88**, 3116 (1983).
- Carlqvist, P., *Cosmic Electrodyn.*, **3**, 377 (1972).
- Coakley, P., and N. Hershkowitz, *Phys. Fluids*, **22**, 1171 (1979).
- Dubinin, E. M., et al., *Kosm. Issled.*, **23**, 466 (1985).
- Evans, D. S., M. Roth, and S. Lemaire, "Electrical potential distribution at the inference between plasma sheet clouds," Presented at the Workshop on Double Layers in Astrophysics, Marshall Space Flight Center, Huntsville, Alabama, March 17-19, 1986.
- Gurevich, A. V., L.-V. Pariiskaya, and L. P. Pitaevskii, *Sov. Phys. JETP, Eng. Transl.*, **22**, 449 (1966).
- Hasegawa, A., and T. Sato, *Phys. Fluids*, **25**, 632 (1982).
- Hultqvist, B., *Planet. Space. Sci.*, **19**, 749 (1971).
- Iizuka, S., P. Michelsen, J. J. Rasmussen, R. Schrittwieser, R. Hatakeyama, K. Saeki, and N. Sato, *Riso Report-M-2414*, Riso National Laboratory, Denmark, 1983.
- Iizuka, S., P. Michelsen, J. J. Rasmussen, R. Schrittwieser, R. Hatakeyama, K. Saeki, and N. Sato, *J. Phys. Soc. (Japan)*, **54**, 2516 (1985).
- Johnson, L. E., *J. Plasma Phys.*, **23**, 433 (1980).
- Joyce, G., and R. F. Hubbard, *J. Plasma Phys.*, **20**, 391 (1978).
- Kan, J. R., and S.-I. Akasofu, *J. Geophys. Res.*, **84**, 507 (1979).
- Leung, P., A. Y. Wang, and B. H. Quon, *Phys. Fluids*, **23**, 952 (1980).
- Mason, R. J., *Phys. Fluids*, **14**, 1943 (1971).
- Morse, R. L., in *Computational Physics*, edited by Alder, Fernbach, and Rotinberg, Vol. 9, p. 213, Academic Press, New York, 1970.
- Mozer, F. S., C. D. Cattell, M. K. Hudson, R. L. Lysak, M. Temerin, and R. B. Torbert, *Space Sci. Rev.*, **27**, 155 (1980).
- Mozer, F. S., and M. Temerin, in *High-Latitude Space Plasma Physics*, edited by B. Hultqvist and T. Hagfors, p. 43, Plenum, New York, 1983.



- Sato, T., and H. Okuda, *J. Geophys. Res.*, **86**, 3357 (1981).
- Sestero, A., *Phys. Fluids*, **7**, 44 (1964).
- Silevitch, M. B., *J. Geophys. Res.*, **86**, 3573 (1981).
- Singh, N., *Plasma Phys.*, **22**, 1 (1980).
- Singh, N., *Plasma Phys.*, **24**, 639 (1982).
- Singh, N., and R. W. Schunk, *J. Geophys. Res.*, **87**, 3561 (1982a).
- Singh, N., and R. W. Schenk, *Geophys. Res. Lett.*, **9**, 1345 (1982b).
- Singh, N., and R. W. Schunk, *Geophys. Res. Lett.*, **9**, 446 (1982c).
- Singh, N., and R. W. Schunk, *J. Geophys. Res.*, **88**, 10081 (1983a).
- Singh, N., and R. W. Schunk, *Phys. Fluids*, **26**, 1123 (1983b).
- Singh, N., and R. W. Schunk, *Plasma Phys. Controlled Fus.*, **26**, 859 (1984a).
- Singh, N., and R. W. Schunk, in *Second Symposium on Plasma Double Layers and Related Topics*, edited by R. Schrittwieser and G. Eder, p. 272, University of Innsbruck, 1984b.
- Singh, N., and H. Thiemann, *Geophys. Res. Lett.*, **8**, 737 (1980a).
- Singh, N., and H. Thiemann, *Phys. Rev. Lett.*, **76A**, 383 (1980b).
- Singh, N., H. Thiemann, and R. W. Schunk, *Geophys. Res. Lett.*, **10**, 745 (1983).
- Singh, N., R. W. Schunk, and H. Thiemann, *Adv. Space Res.*, **4**, 481-490 (1984).
- Singh, N., H. Thiemann, and R. W. Schunk, *J. Geophys. Res.*, **90**, 5173 (1985).
- Singh, N., H. Thiemann, and R. W. Schunk, in *Ion Acceleration in the Magnetosphere and Ionosphere*, *Geophysical Monograph*, **38**, edited by Tom Chang, pp. 343-347, AGU, Washington, D.C., 1986.
- Temerin, M., K. Cerny, W. Lotko, and F. S. Mozer, *Phys. Rev. Lett.*, **48**, 1175 (1982).
- Thiemann, H., N. Singh, and R. W. Schunk, *Adv. Space Res.*, **4**, 511 (1984).
- Wagner, J. S., T. Tajima, J. R. Kan, J. N. Leboeuf, and J. M. Dawson, *Phys. Rev. Lett.*, **45**, 803 (1980).
- Whipple, E. C., J. R. Hill, and J. D. Nichols, *J. Geophys. Res.*, **89**, 1508 (1984).

## DOUBLE LAYER FORMATION

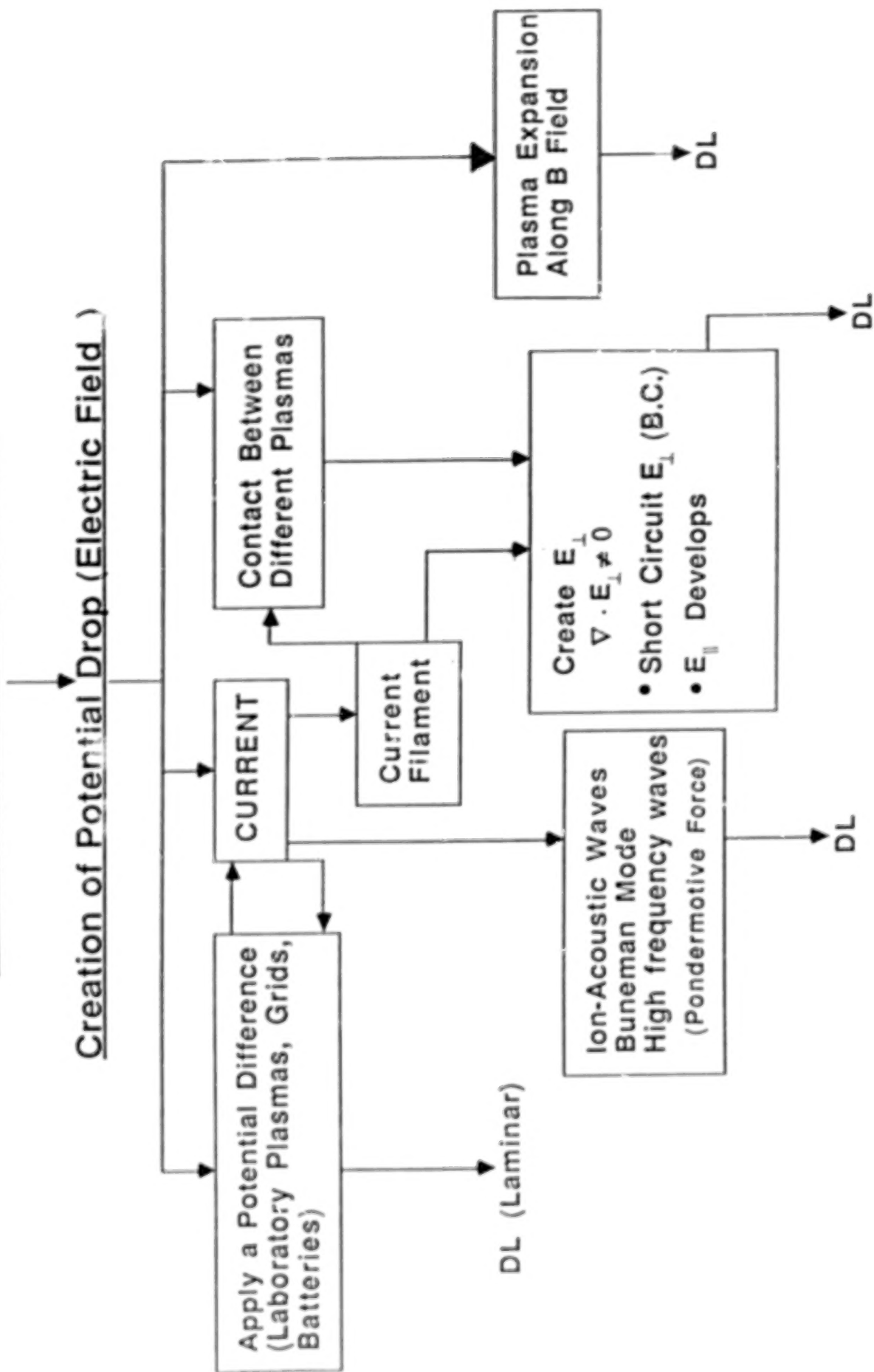


Figure 1. Summary of mechanisms for driving double layers.

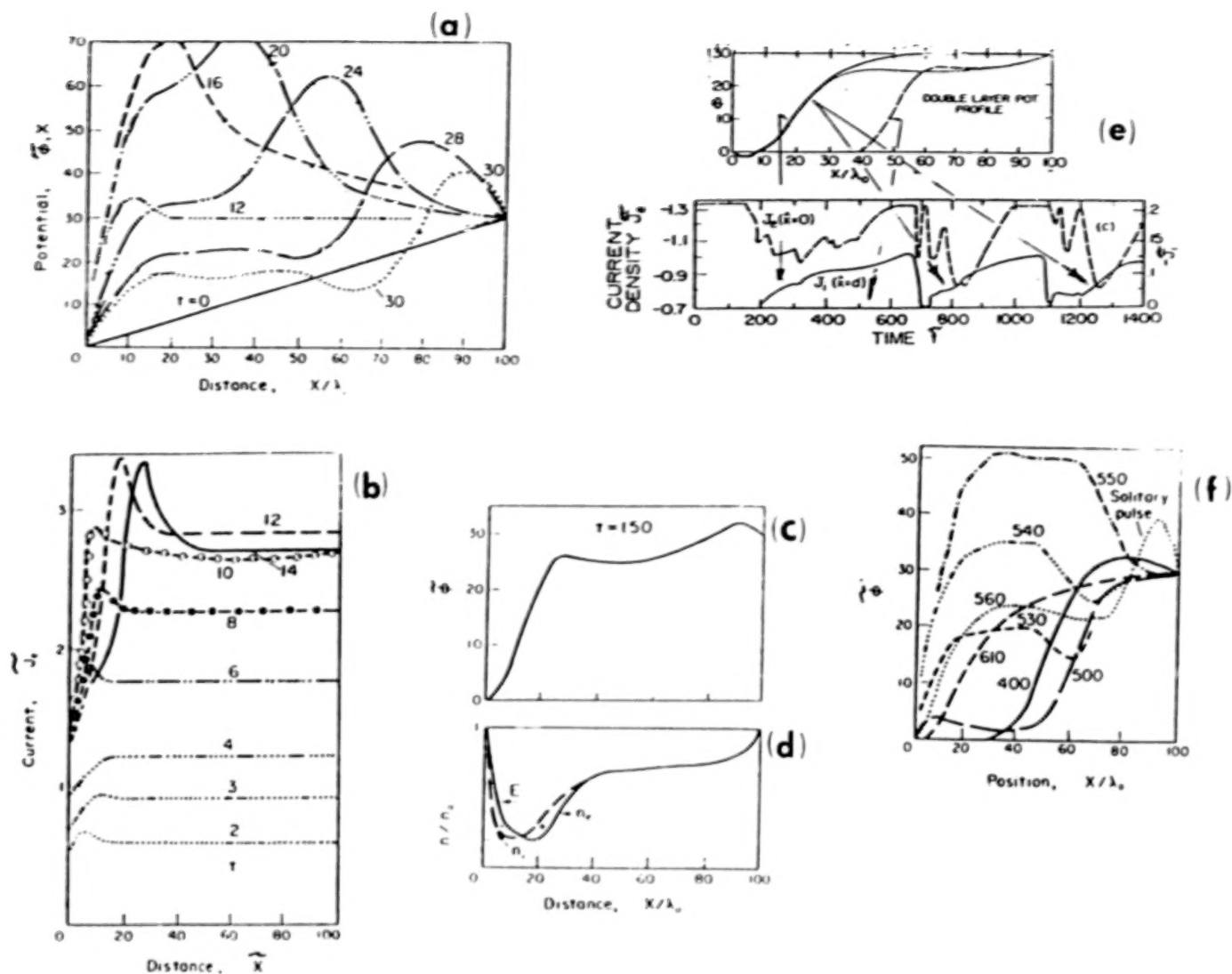


Figure 2. Double layer formation and dynamics as seen in one-dimensional Vlasov simulations. In the simulation, the plasma occupied the region  $0 \leq x \leq 100 \lambda_D$ , where  $\lambda_D$  is the Debye length in the initial plasma ( $t = 0$ ) across which a potential drop of  $\Delta\phi_0 = 30(k_B T_0/e)$  was applied, where  $T_0$  is the initial plasma temperature. We used the following normalizations:  $\tilde{x} = x/\lambda_D$ , velocity  $\tilde{V} = V/V_{t0}$ , time  $\tilde{t} = t\omega_{p0}$ , temperature  $\tilde{T} = T/T_0$ , potential  $\tilde{\phi} = e\phi/k_B T_0$ , current  $\tilde{J} = J/n_0 e V_{t0}$ , where  $V_{t0} = (k_B T_0/m_e)^{1/2}$ ,  $\omega_{p0}$  is the electron plasma frequency with the initial density  $n_0$ ,  $k_B$  is the Boltzmann constant,  $m_e$  is the electron mass, and  $m_i/m_e = 64$ , with  $m_i$  the ion mass; (a) temporal evolution of the potential profile, (b) temporal evolution of the current density profile,  $\tilde{J}_c(\tilde{x})$ , (c) double layer potential profile at  $\tilde{t} = 150$ , (d) density profiles and space charges supporting the DL in (c), and (e) recurring DL formation (top) and electron and ion current interruptions and recovery (bottom). The arrows indicate the times of the potential profiles; the arrows originating from the potential profiles marked with "A" indicate that these profiles correspond to the early stages of the electron current interruptions and to the beginning of the ion influx into the double layer during the three cycles of the double layer formation. Note the dip at the low potential end. The potential profile marked with "B" corresponds to the current recovery stage during the first cycle. (f) Potential profiles during a reformation of the DL; at  $\tilde{t} = 400$  there is a DL, a positive potential perturbation near  $x = 0$  is seen at  $\tilde{t} = 500$ ; at later times this perturbation grows and eventually a new DL forms at  $\tilde{t} \sim 610$ .

## CYCLIC NATURE OF DOUBLE LAYERS

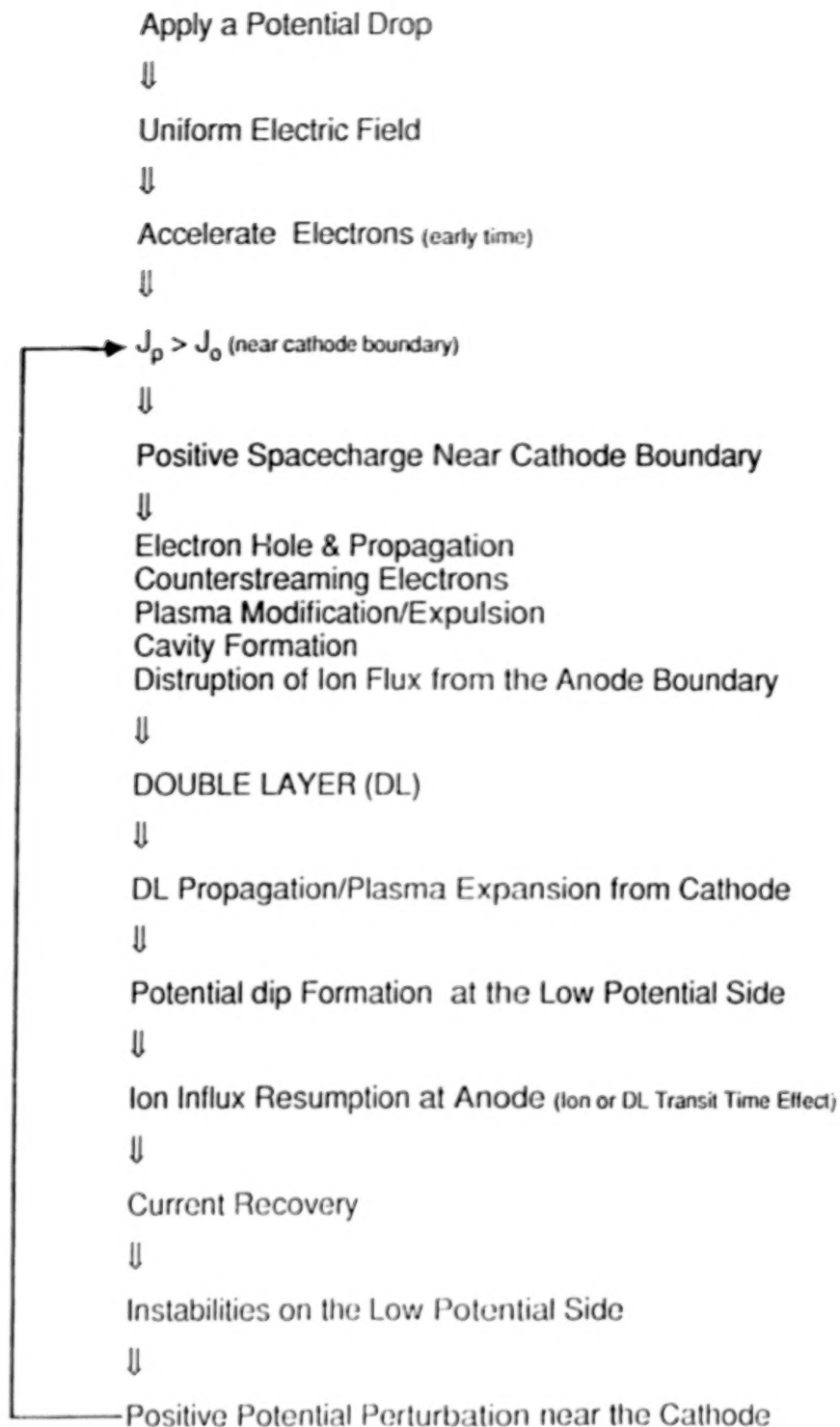


Figure 3. Summary of the various plasma processes occurring during the formation and reformation of a DL when a potential drop is applied across a plasma.

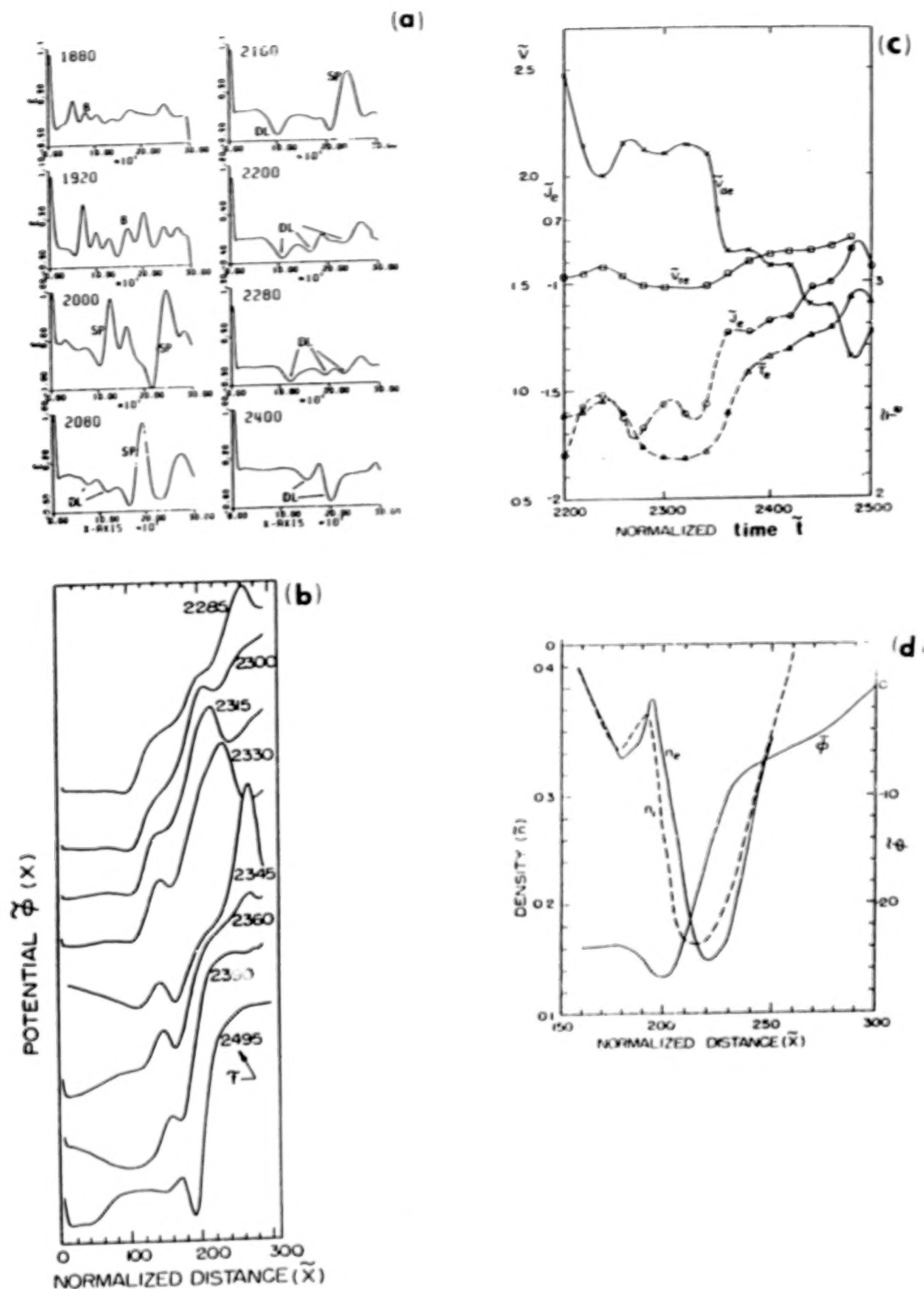


Figure 4. (a) Double layer evolution from the Buneman instability. Spatial profiles of the electric field  $E$  are shown at different times. At early times,  $1880 < \tilde{t} < 2000$ , small wavelength waves grow. At later times, in the nonlinear regime, these waves coalesce into long wavelength oscillations, which evolve into solitary pulses and double layers. (b) Temporal evolution of the double layer potential profile, (c) the corresponding temporal evolutions of the electron current  $J_e$ , electron drift velocity  $V_{de}$ , thermal velocity  $V_{te}$ , and temperature  $T_e$  at  $\tilde{x} = 50$ , and (d) spatial profiles of the electron and ion densities and the potential profile for a DL with a dip at its low potential end. The charge separation indicates the presence of a triple charge layer.

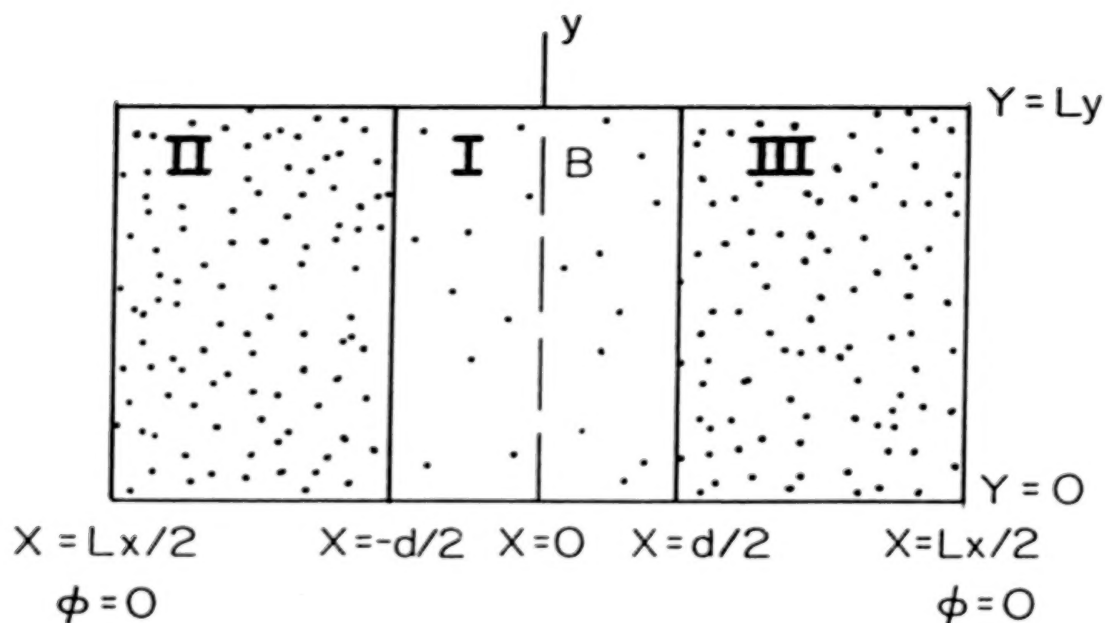


Figure 5. Geometry of the simulation scheme. A two-dimensional plasma of size  $L_x \times L_y$  is simulated. Initially ( $t = 0$ ), regions I to III are filled with plasmas. In the simulations described in this paper, the plasma in region I ( $-d/2 < x < d/2$ ) is assumed to be hot, while the plasmas in regions II and III ( $|x| > d/2$ ) are assumed to be cold and have similar properties. The  $B$  field is along the  $y$ -axis. The particles leaving the simulation plasmas at  $y = 0$  and  $L_y$  are recirculated according to a periodic boundary condition, while those leaving at  $x = \pm L_x/2$  are replaced from plasma reservoirs at the boundaries.



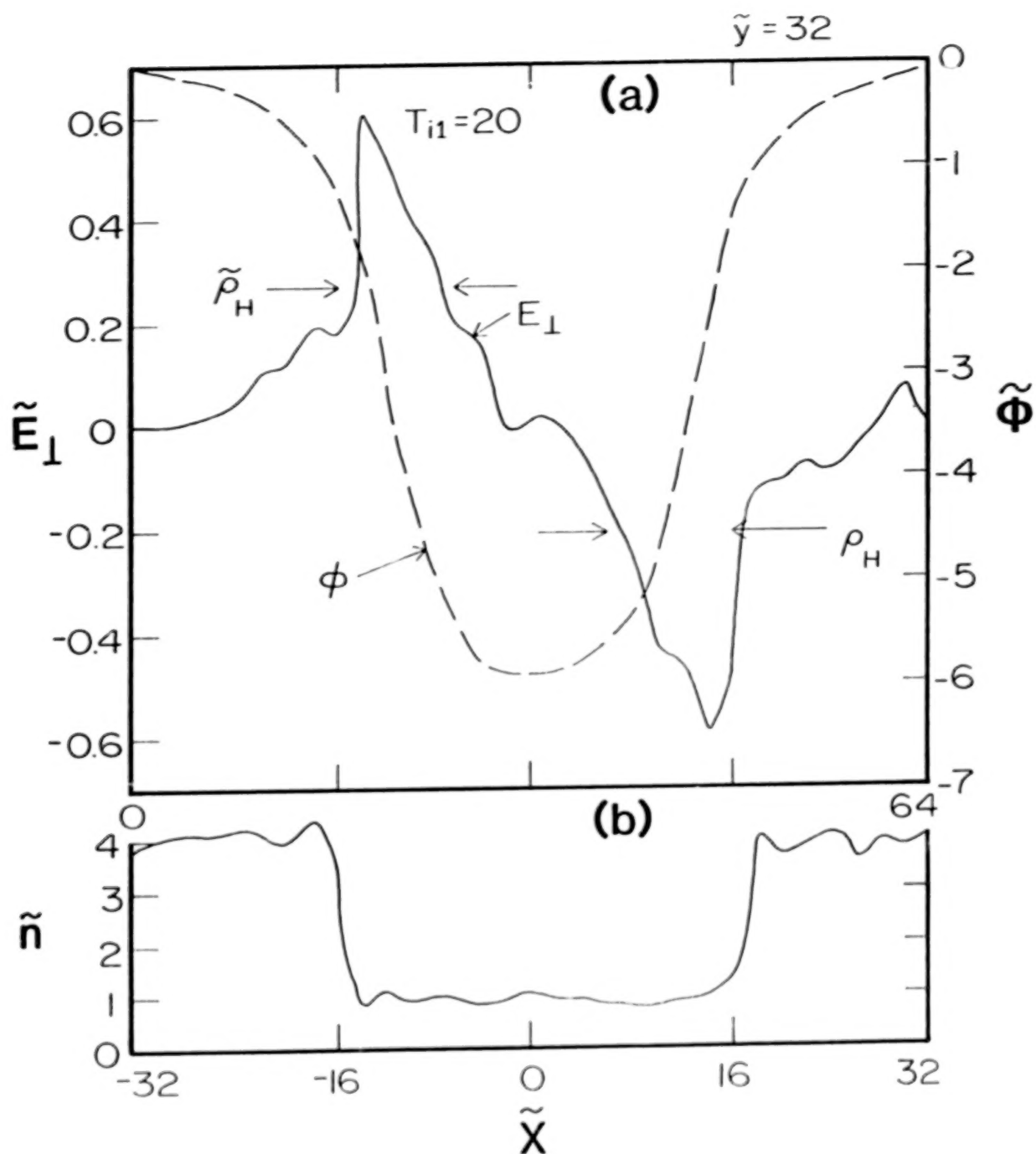


Figure 6. Variations of (a) electric potential and perpendicular electric field, and (b) plasma density as a function of  $x$  from a simulation with  $T_{i1} = 20$ . The average value of the hot in Larmor radius  $\rho_H$  is indicated in (a).

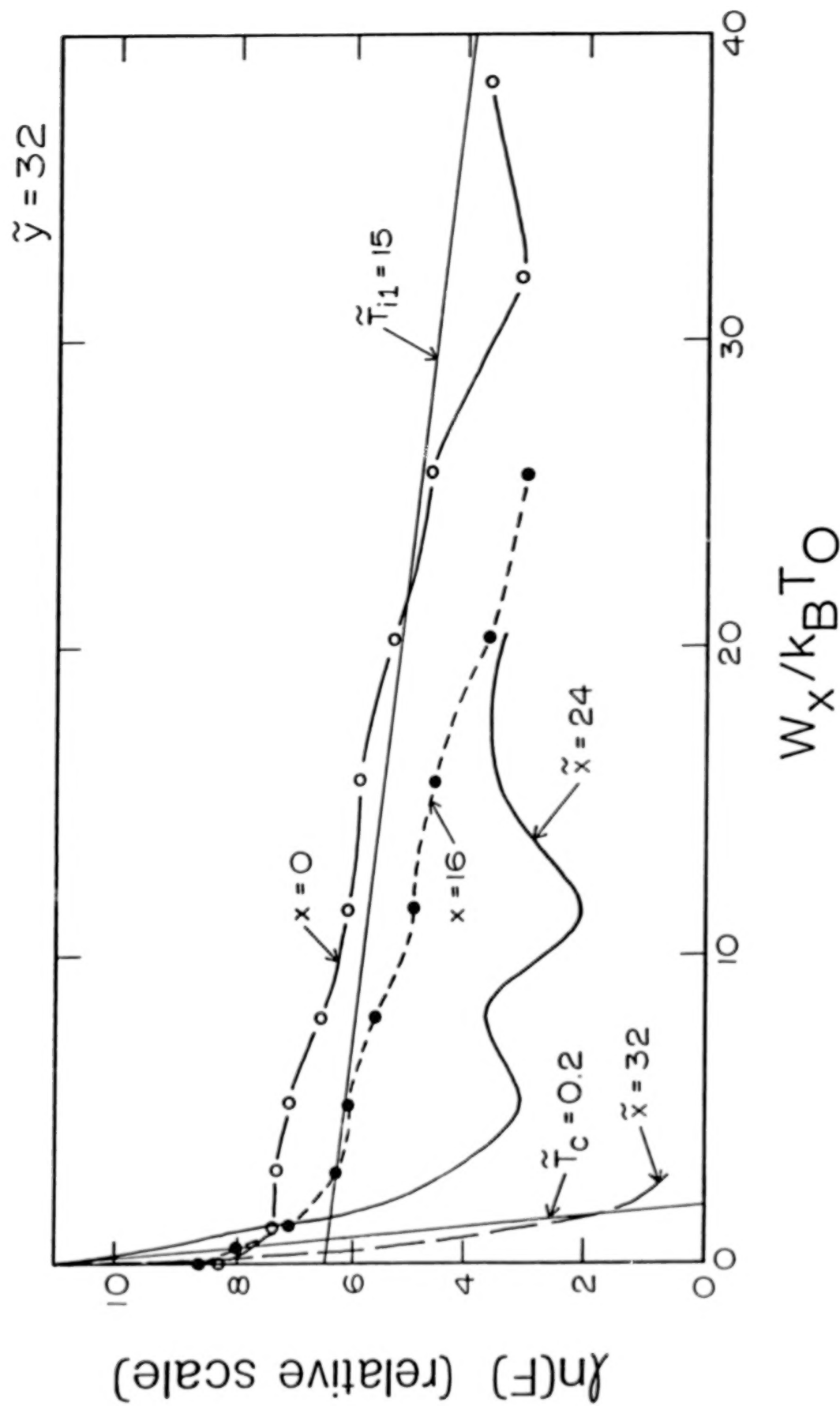


Figure 7. Ion energy distribution function  $F(W_x = 1/2 m_i V_x^2)$  at several locations for  $x \approx 0$ . The distribution functions for  $x < 0$  are nearly the same. Note that the two asymptotes marked with  $\tilde{T}_{i1} = 15$  and  $\tilde{T}_c \approx 0.2$  show the initial Maxwellian distributions.

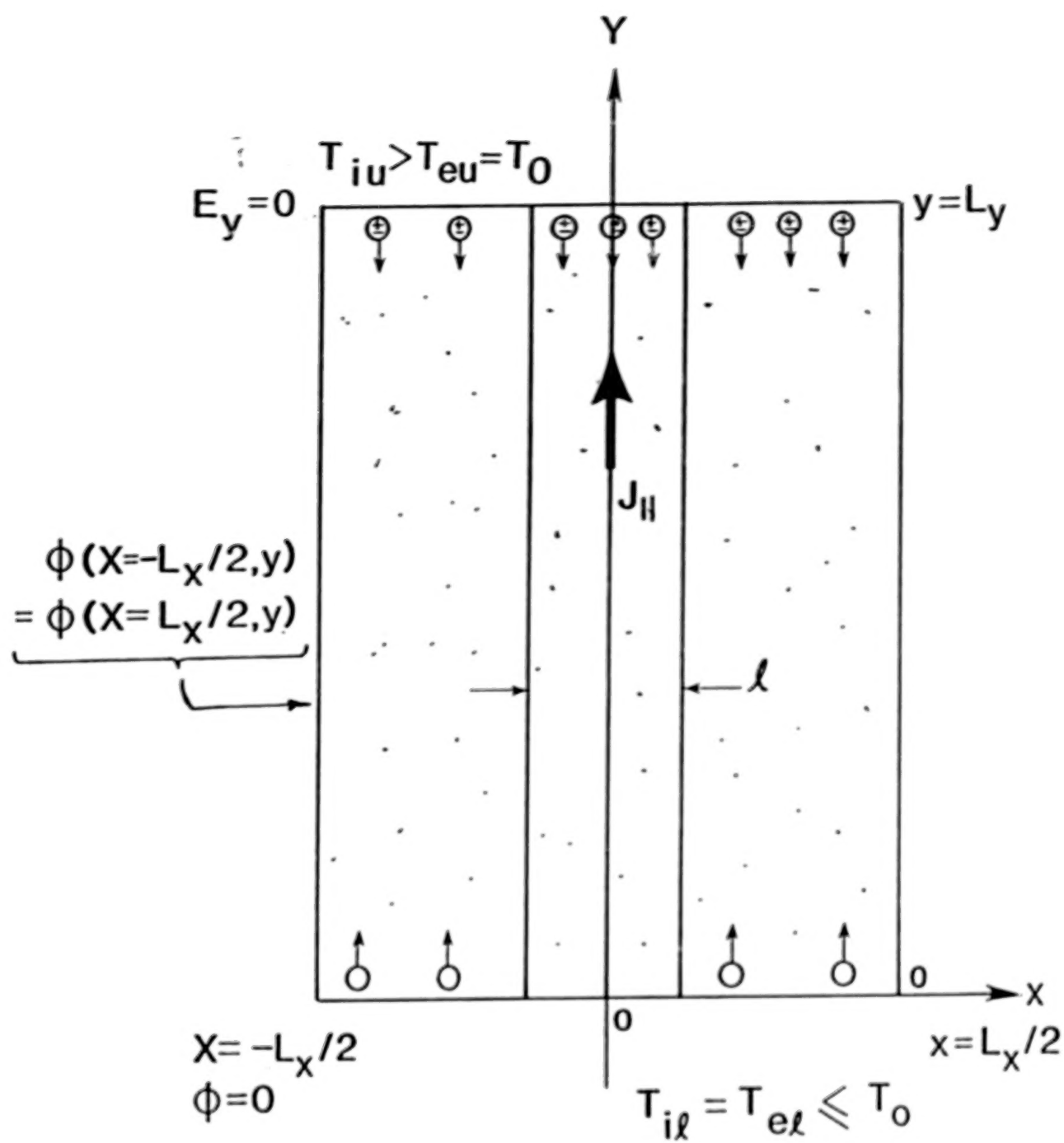
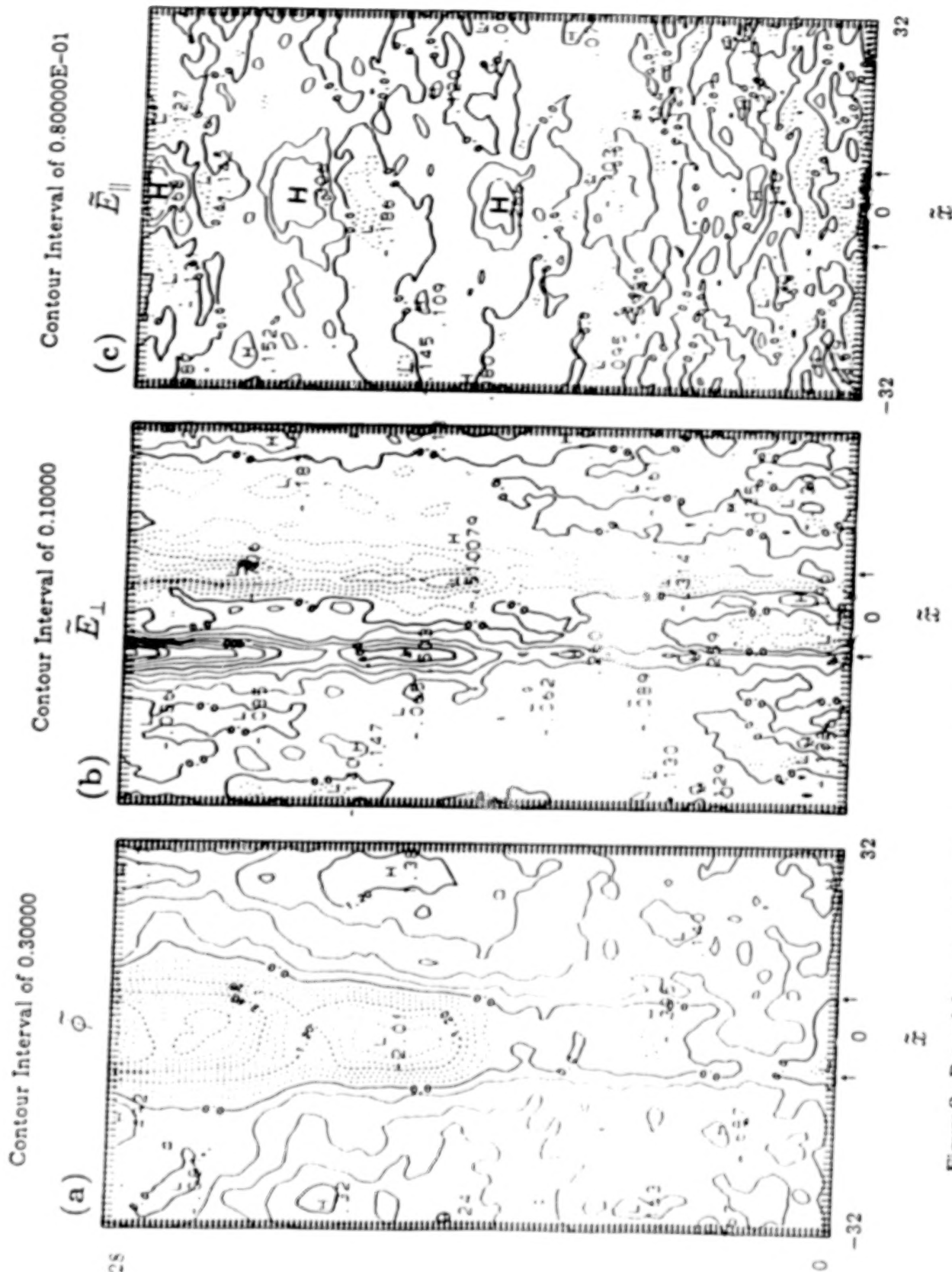


Figure 8. Scheme for simulating double layers driven by a current sheet.

ORIGINAL PAGE  
OF POOR QUALITY



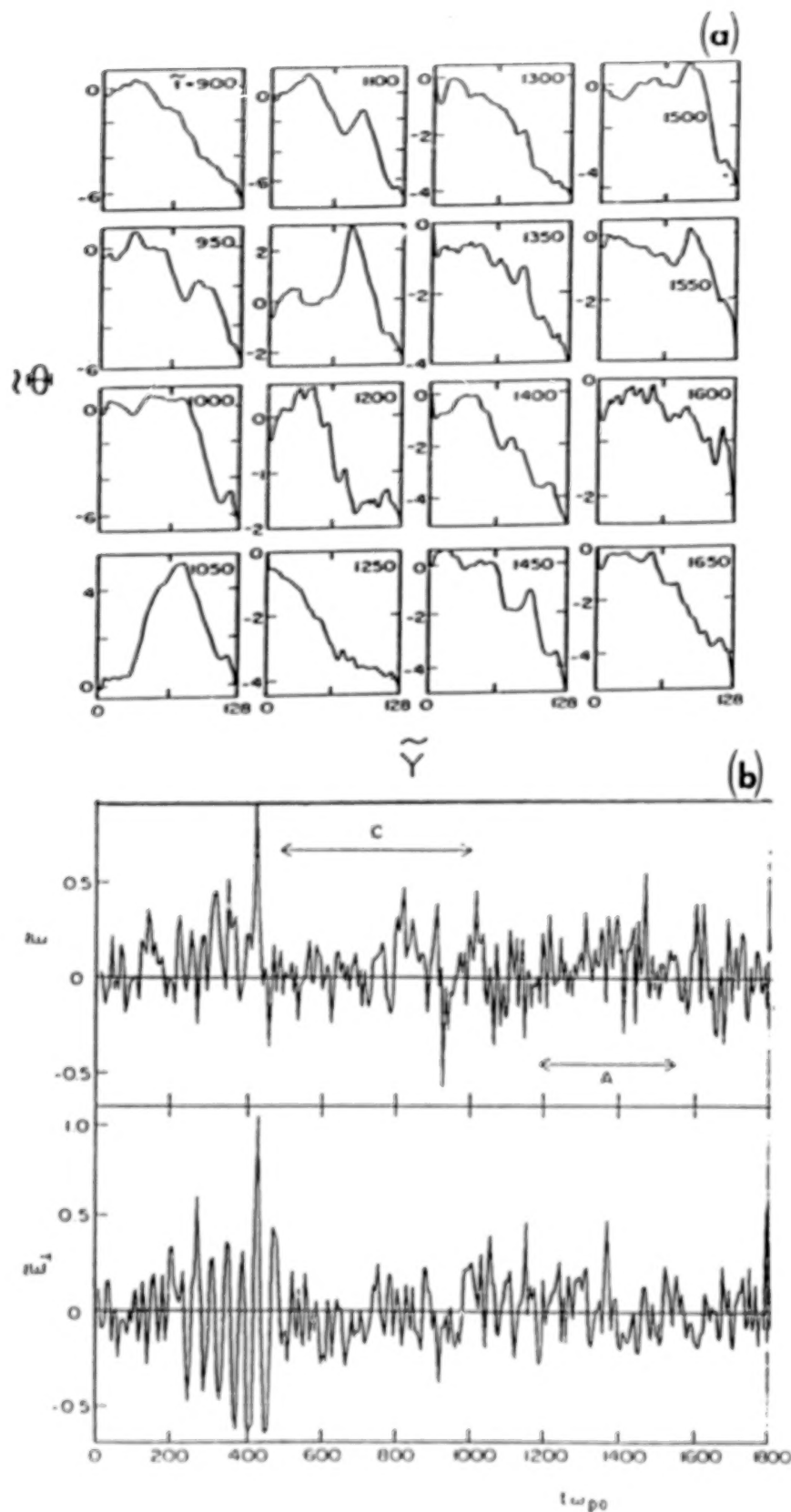


Figure 10. (a) Temporal evolution of the double layer potential profile along the axis of the current shown in Figure 8 and (b) fluctuations in  $E_{\parallel}$  and  $E_{\perp}$  in the region of the DL formation.

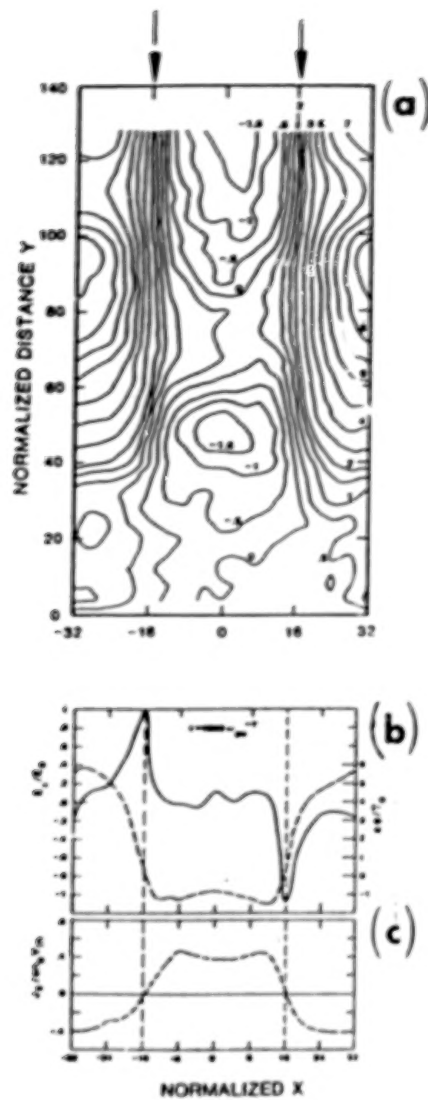


Figure 11. (a) Potential structure associated with a wide current sheet, with  $\ell = 32 \lambda_{de}$ ,  $\rho_H = 3 \lambda_{de}$ , and  $J_0 = 0.6 n_0 e V_{te}$ . The current sheet edges are indicated by the arrows at the top of the panel. Equipotential surfaces are shown. (b) Perpendicular distribution of  $E_{\perp}$  and  $\phi$  near the top ( $\tilde{y} = 1120$ ) of the potential structure in (a). Note that  $E_{\perp}$  is primarily confined near the edges of the current sheet. (c) Perpendicular distribution of the parallel current density  $J_{\parallel}$ ; note the positive (upward) current inside the sheet, while outside the sheet the current is negative (downward). The downward current is caused by the upward acceleration of the electrons by the downward (parallel) electric field (see the potential distribution outside the sheet in (a)).



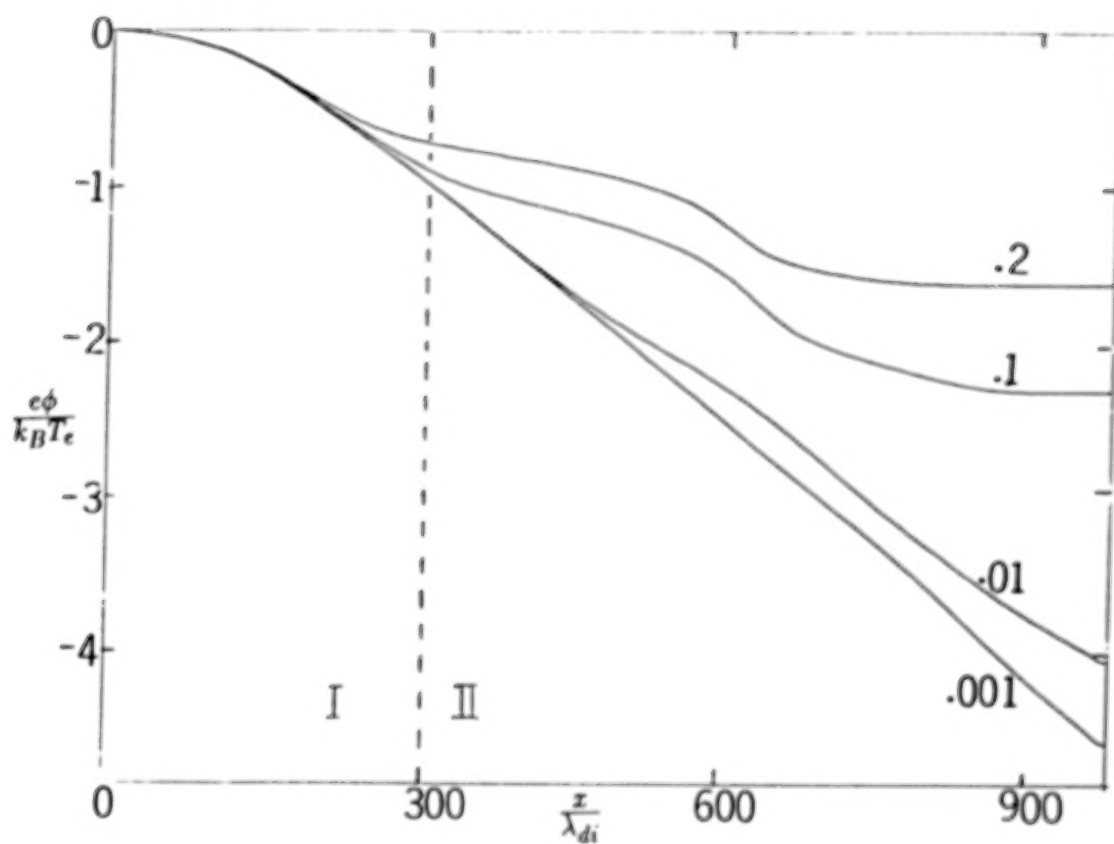


Figure 12. Snapshot ( $t = 60 \omega_{pe}^{-1}$ ) of the potential profile associated with the expansion of a high-density plasma into region II. The different profiles are for different values of the density ratio  $n_i/n_H$ , as indicated.

N87

23324

UNCLAS

## ELECTRON ACCELERATION IN STOCHASTIC DOUBLE LAYERS

William Lotko

Dartmouth College, Hanover, New Hampshire 03755, U.S.A.

## ABSTRACT

Transversely localized double layers evolve randomly in turbulent regions of strongly magnetized plasma carrying current along the magnetic field. Results from numerical simulations and spacecraft observations in the auroral plasma indicate that the parallel electric field in such regions is microscopically intermittent or stochastic. The implications of stochastic double layer fields on electron acceleration will be discussed here in terms of a statistical process involving ensemble averages over test particle motion. A Fokker-Planck equation can be derived for the electron phase space density, which depends on the mean and rms amplitudes of the double layers, the mean double layer density, and the initial electron velocity distribution. It is shown that the resulting electron acceleration is very sensitive to the ratio of the initial electron energy to the rms double layer amplitude. When this ratio is large, the acceleration process differs little from that expected in a dc electric field. When it is small, stochastic "heating" competes with directed acceleration. Evidence for both cases can be found in the auroral ionosphere in association with so-called inverted-V precipitation and collimated edge precipitation.

N87  
23325  
UNCLAS

**ANOMALOUS TRANSPORT IN DISCRETE ARCS AND SIMULATION OF  
DOUBLE LAYERS IN A MODEL AURORAL CIRCUIT**

Robert A. Smith  
Plasma Physics Division  
Science Applications International Corporation  
McLean, Virginia 22102, U.S.A.

**ABSTRACT**

The evolution and long-time stability of a double layer (DL) in a discrete auroral arc requires that the parallel current in the arc, which may be considered uniform at the source, be diverted within the arc to charge the flanks of the U-shaped double layer potential structure. A simple model is presented in which this current redistribution is effected by anomalous transport based on electrostatic lower hybrid waves driven by the flank structure itself. This process provides the limiting constraint on the double layer potential. The flank charging may be represented as that of a nonlinear transmission line. A simplified model circuit, in which the transmission line is represented by a nonlinear impedance in parallel with a variable resistor, is incorporated in a one-dimensional simulation model to give the current density at the DL boundaries. Results are presented for the scaling of the DL potential as a function of the width of the arc and the saturation efficiency of the lower hybrid instability mechanism.

**I. INTRODUCTION**

A vast body of ground-based, rocket, and satellite observations reveals that auroral-zone acceleration processes occur in a hierarchy of latitudinal scale widths. On the scale of the inverted-V region ( $\Delta\lambda > 1^\circ$ ) parallel electric fields are observed in narrow, soliton-like structures interpreted as weak or ion-acoustic double layers (DL's) (Temerin et al., 1982). Assuming statistical homogeneity of the distribution of these weak DL's over an altitude range comparable to  $1 R_e$ , one infers a total potential drop of up to a few kV, typical of the inverted-V region. On smaller spatial scales ( $\Delta\lambda < 0.1^\circ$ ) more energetic precipitation is observed in discrete arcs, which have projected widths  $\sim 1$  km in the ionosphere. Discrete arcs (DA's) are associated with electrostatic shocks (Torbert and Mozer, 1978; Kletzing et al., 1983). We adopt the hypothesis that electrostatic shocks constitute the nearly field-aligned "flanks" of the paradigmatic U-shaped potential structure of a strong double layer. Although this hypothesis seems plausible, many questions exist concerning the conditions under which DL's may exist in space, their dynamics, and their structure. These questions are vital for understanding the complex observational morphology of fields and particles in the auroral zone. At present, investigations of such questions must to a large extent be motivated by and proceed from consideration of the fast-growing literature on experiments and simulations, although usually the applicability of these situations to DL's in space is indirect (Smith, 1985, 1986a).

In this paper, we first discuss theoretically the question of what limits the potential of DL's in auroral arcs, and report results of recent simulations of DL's in a model circuit. Somewhat more detailed expositions are given by Smith (1986b, c).

PRECEDING PAGE BLANK NOT FILMED

## II. THEORY

Experiments and simulations (Goertz and Joyce, 1975; Coakley and Hershkowitz, 1979) reveal a scaling law for the DL potential in terms of its length  $\ell_{DL}$  and the electron density  $n_{eK}$  on the low potential (cathode:K) side; we write this law as

$$\phi_{DL}(\text{kV}) \approx 300 \left( \frac{n_{eK}}{10^2 \text{ cm}^{-3}} \right) \left( \frac{\ell_{DL}}{1 \text{ km}} \right)^2 \quad (1)$$

where  $\ell_{DL} \equiv \phi_{DL}/\max|E_{\parallel}|$ . In space,  $\ell_{DL}$  is not limited a priori and, absent other constraints, equation (1) implies that the potential may grow to much larger values than the observed limit on the auroral precipitation energy, which is a few tens of keV.

This dilemma is resolved by considering how the field-aligned flanks of the arc become charged during the evolution of the DL's. We adopt as a starting point the basic idea of the recent MHD models discussed by Haerendel (1983) and Goertz (1985, 1986) in which the DL evolves in the parallel current sheet of a kinetic Alfvén wave. This scenario limits the thickness of the sheet a priori to a few times the ion gyroradius at an energy representative of the distant plasma population in the generator region. Taking this energy to be  $\sim 1$  keV, we may estimate  $j_{\parallel}$  by

$$j_{\parallel} = neU_{ei} \sim \frac{c}{4\pi} \frac{\delta B_{\perp}}{R_i}$$

Using  $n \sim 10^2 \text{ cm}^{-3}$ ,  $B_0 \sim 0.05 \text{ G}$ ,  $\delta B_{\perp} \sim 10^{-3} \text{ G}$ , and assuming a current sheet of a few kilometers thick, this equation gives a relative drift velocity  $U_{ei}$  greater than the electron thermal velocity  $V_e$ . At such a relative drift velocity, the current sheet is unstable to a variety of instabilities, including the ion cyclotron and Buneman instabilities. We expect the instability to be triggered at some altitude  $z_*$  where the density and magnetic field profiles first combine such that  $U_{ei}$  exceeds the threshold drift. In addition, experiments reveal that the U-shaped structure, with the field-aligned flanks curved toward the low potential side as is required for Earthward-directed Poynting flux (Smith, 1986a), requires  $\omega_e < \Omega_e$ , where  $\omega_e$  and  $\Omega_e$  are the electron plasma frequency and gyrofrequency, respectively. This is just the condition for strong magnetization ( $\omega_e/\Omega_e = R_e/\lambda_e$ ), and is fulfilled in a limited altitude range along the auroral field lines (Gurnett, 1974).

Simulations show that DL's evolve from current-driven instabilities when the current is interrupted by trapping (Smith, 1982a, b). Trapping creates local regions of macroscopic non-neutrality; in the finite-thickness current sheet, the plasma tends to expel charge in the transverse direction in an attempt to neutralize the local electric field (Fig. 1). Electrons are tightly magnetized and cannot be expelled very far, but the ion motion is essentially ballistic (the evolution time scale is  $< \Omega_i^{-1}$ ), and ions are accelerated in the transverse direction out to some distance greater than their gyroradius. Owing to mirror forces, the expelled charge spreads upward, providing the initial charging of the flanks.

The charging mechanism described above operates in the transient phase. The characteristic time scale of the evolution is  $\tau_{DL} \sim \ell_{DL}/U_{iA}$ , where  $U_{iA} > C_s$  the ion inflow velocity in the frame of the DL. The charge spreads along the flank at velocity  $c/\sqrt{\epsilon_{\perp}}$ , where  $\epsilon_{\perp}$  is the dielectric constant. In the MHD limit,  $\epsilon_{\perp} \approx c^2/V_A^2$ , but we shall see later that  $\epsilon_{\perp} < c^2/V_A^2$  in the DL flank. In any case, however, we find that the time  $\tau_{ind} = \int ds c/\sqrt{\epsilon_{\perp}}^{1/2}/c$  for the charge to spread along the field lines back to the generator region (Fig. 2) is long compared to  $\tau_{DL} < t < \tau_{ind}$ , the spreading



charge would thin out along **B** and the flank would not sustain the DL potential; then the DL would discharge. This would occur in a time short compared with the typical lifetime of discrete arcs. Therefore, asymptotic stability of the DA requires a transport mechanism producing a cross-field current density  $J_x(\phi)$ , which persists as  $\partial\phi_{DL}/\partial t \rightarrow 0$ .

If such a mechanism exists, then in the time-asymptotic regime, the density  $n_{eK}$  in equation (1) is determined by current continuity and is of the form

$$n_{eK}(z_*) = n_{e\infty} - g \int_{z_*}^{\infty} dz J_x(\phi, z) \quad , \quad (2)$$

where  $g$  is a constant. Substituted in equation (1), equation (2) provides the physical constraint on the DL potential, which is transparently self-stabilizing for  $J_x$ , a monotonically increasing function of  $\phi$ .

A mechanism to maintain a distributed  $J_x$  in the time-asymptotic regime is discussed by Smith (1986b). The mechanism is based on anomalous transport due to lower hybrid waves which are driven by the inhomogeneous structure of the flank itself. The discussion above implies that the initial scale length  $\ell_f$  of the perpendicular electric field  $E_x$  in the flank is  $\ell_f > R_i$ . As this field is established along **B**, the electrons acquire the local polarization drift velocity  $cE_x/B_0$ . The ions, however, encounter an inhomogeneous electric field over the scale of their gyroradius, and so their drift orbit is modified by finite-Larmor-radius (FLR) effects. For  $\ell_f > R_i$ , the ion drift speed is approximately given by the first non-vanishing order of the phase-averaged FLR correction:

$$V_{Di} \approx \left(1 + \frac{1}{4} R_i^2 \nabla^2\right) \frac{cE_x}{B_0} \approx \left(1 - \frac{R_i^2}{4\ell_f^2}\right) \frac{c\phi}{B_0\ell_f} \quad (3)$$

Then there is a relative drift

$$U_{ei} = V_{De} - V_{Di} \approx \frac{R_i^2}{4\ell_f^2} \left( \frac{c\phi}{B_0\ell_f} \right) \quad ;$$

if  $U_{ei} > V_i$ , this relative drift drives the electrostatic modified two-stream instability (MTSI) studied by McBride et al. (1972). (Other instabilities are also possible, of course, but for simplicity we consider only the MTSI.) The most unstable mode has frequency  $\omega \sim \omega_{LH} = \omega_i/(1 + \omega_e^2/\Omega_e^2)^{1/2}$ , with growth rate  $\gamma \sim \omega_{LH}$ , and parallel wave number  $k_{\parallel} \sim (m/M)^{1/2} k_{\perp}$ .

The salient property of the MTSI for our purposes is that it saturates by trapping ions in the perpendicular drift direction and electrons in the parallel direction; in the saturation process, the ions and electrons are heated to a fraction  $\alpha^2$  of the relative drift energy:

$$T_{\perp i} \approx T_{\parallel e} \approx \alpha^2 M U_{ei}^2 / 2 \quad .$$

From simulations, McBride et al. (1972) find  $\alpha \approx 0.5$ , with a wave energy density  $W$  at saturation of  $W/nMU_{ei}^2 \sim$  a few percent.

Motivated by these results, Smith (1986b) postulates a self-scaling model in which the flank is assumed to be always at saturation (marginal instability) with respect to an instability such as the MTSL. The model characterizes the instability by two parameters  $\alpha, \beta$ , defined by

$$V_{\perp i} = \alpha (cE_x/B_0) ; \quad U_{ei} = \beta (cE_x/B_0) , \quad (4)$$

where  $U_{ei}$  is now the threshold drift speed and  $E_x \sim \phi/\ell_f$ . Using equations (3) and (4), we find the self-similar scalings

$$R_i^2/\ell_f^2 = \alpha\beta ; \quad T_{\perp i}/T_{eo} = (\alpha^3\beta)^{1/2} (e\phi_{DL}/T_{eo}) ;$$

$$V_{De} \equiv \frac{cE_x}{B_0} = \left(\frac{\beta}{\alpha}\right)^{1/4} \left(\frac{m}{M}\right)^{1/2} \left(\frac{e\phi_{DL}}{T_{eo}}\right)^{1/2} ; \quad \left(\frac{\alpha}{\beta}\right)^{1/4} \left(\frac{M}{m}\right)^{1/2} \left(\frac{\omega_{eo}}{\Omega_{eo}}\right) \left(\frac{e\phi_{DL}}{T_{eo}}\right)^{1/2} ; \quad (5)$$

where  $\lambda_{eo}$ ,  $T_{eo}$ , and  $\omega_{eo}$  are reference values of the electron Debye length, temperature, and plasma frequency.

Owing to momentum conservation, there is a wave-modulated friction between the electrons and ions, which may be described by an anomalous collision frequency (Davidson and Krall, 1977)  $\nu_* \approx \epsilon \omega_{LH}$ , where  $\epsilon \equiv W/nMU_{ei}^2$ . Thus, the electron and ion fluids are acted on by volume forces  $F_{yi} = -F_{ye}$ , leading to an  $\mathbf{F} \times \mathbf{B}$  drift velocity in the  $x$ -direction, i.e., opposite to  $E_x$  (the coordinate system is defined by Fig. 3). This drift velocity is given by  $V_{xe} = V_{xi} \equiv V_x(n_e, \phi_{DL})$ , where

$$V_x = \epsilon (\alpha^3\beta^5)^{1/4} \left(\frac{m}{M}\right)^{1/2} \frac{\omega_{LH}}{\Omega_i} \left(\frac{e\phi_{DL}}{T_{eo}}\right)^{1/2} V_{eo} , \quad (6)$$

and  $V_{eo} = (T_{eo}/m)^{1/2}$ . Thus, above the DL, plasma is transported from the center of the arc to the flanks, concentrating the parallel current there (Fig. 3). Although  $V_{xe} = V_{xi}$ , there is a net current  $J_x$  because above the region of strong  $E_{\parallel}$  in the DL, we expect an extended region of small charge density  $\rho$  which sustains a weak parallel density field  $E_{\parallel}$  driven by beam-plasma instabilities. Then the continuity equation is

$$\partial J_z / \partial z \approx - \partial J_x / \partial x \approx - \partial(\rho V_x) / \partial x ,$$

Upon solving and integrating along the field line, we obtain (Smith, 1986b)

$$J_x(\infty) - J_x(0) \approx C(\alpha, \beta) (\phi_{DL}/\ell_a^2)^{5/8} \quad (7)$$

where  $C(\alpha, \beta)$  is a constant and  $\ell_a$  is the perpendicular scale length of the arc (Fig. 3). The RHS of equation (7) is just the term  $\int J_x dz$  in equation (2). Assuming  $J_x(0) \ll J_x(\infty)$ , equation (7) gives a scaling law

$$\phi_{DL} \lesssim (J_z(\infty)/c)^{8/5} \ell_a^2 \quad (8)$$

For typical auroral-zone parameters equation (8) yields  $\phi_{DL} \sim 10$  kV for  $\ell_a \sim 1$  km, in general accord with observations.

### III. SIMULATION

In the context of the above discussion, the flank may be modeled as a transmission line with local potential  $\phi = E_x \ell_f$ , where  $\ell_f \sim \phi^{1/2}$ . Once the DL potential has reached a threshold value  $\phi_*$  required to drive the MTSI, the transmission line is charged by the distributed (in  $z$ ) perpendicular current  $J_x = \rho V_x$  of equation (7). We shall report elsewhere on simulations in which the transmission-line equations (Smith, 1986c) are solved simultaneously with a one-dimensional simulation of the DL evolution; this procedure provides the necessary self-consistent boundary condition on the current density  $J_{DL}(t)$  at the simulation boundaries. In this paper, we replace the transmission line with a simple model circuit.

If the flank were uniform between the DL ( $z = z_* \equiv 0$ ) and the generator, the transmission line would appear to the DL as a pure impedance over the evolution time of the DL, with value  $Z_T = (L_T/C_T)^{1/2}$ , where  $L_T = \ell_f/4\pi c^2$ ,  $C_T = 4\pi\epsilon_1/\ell_f$ . We model the impedance by the same form, with variable  $\ell_f(\phi)$ . We thus adopt the model circuit shown in Figure 4 where the diode symbol represents the DL and the variable resistor  $R(\phi)$  represents leakage current in the flank; this term is modeled by using the same form for  $J_x$  as derived above, but over the perpendicular scale length  $\ell_f$  instead of  $\ell_a$ , by integrating  $J_x \sim n^{1/2}(z)$  over the length  $z_K(t) = ct/\sqrt{\epsilon_1}$ . The dielectric constant is defined by

$$\epsilon_1 = 1 + (\omega_{e0}^2/\Omega_e^2) + (\omega_{i0}^2/\Omega_i^2) [(1-\alpha\beta)^2 + \alpha^2(1+\gamma_e)] \quad (9)$$

where  $\gamma_e \equiv T_{he}/T_{li}$ .

The heuristic definition [equation (9)] is such that the total energy stored in the dielectric is  $\epsilon_1 E_x^2/8\pi$ : the first term in [] represents the reduced ion drift speed, while the second term accounts for ion and electron heating by saturation of the self-scaled modified two-stream instability.

For the purpose of testing the scaling of  $\phi_{DL}$  with  $\ell_a$  and  $\alpha$ , we adopt the philosophy that owing to the separation between the perpendicular scale lengths  $\ell_a$  and  $\ell_f$ , the flank may be represented by these circuit elements while the DL will evolve in an essentially one-dimensional fashion in the central region of the arc. The DL evolution is simulated with the one-dimensional Vlasov code described by Smith (1982b), replacing the circuit used there by that of Figure 4. The boundary condition on the current density  $J_{DL}(t)$  is then given by

$$J_{DL}(t) = \frac{I_s}{\ell_a} - \frac{\phi_{DL}(t)}{\ell_a} \left[ \frac{1}{Z_T(\phi_{DL})} + \frac{1}{R(\phi_{DL})} \right] \quad (10)$$

where  $I_s$  is the constant source current and

$$Z_T = [\alpha/\beta]^{1/4} (Y/\epsilon_1^{1/2}) (V_{e0}/c) (\ell_a/\mu^{1/2}) \phi_{DL}^{1/2} \quad (11)$$

$$R = \left( \frac{\mu}{2} \frac{T_{eo}}{T_{fi}} \right)^{1/2} \frac{(Y \ell_a)^{2/3}}{(\alpha^7 \beta)^{1/8}} \frac{\phi_{DL}^{1/4}}{[1 - \exp(-K_2 Z_K(t))/2]} \quad (12)$$

$\mu = m/M$ ,  $K_2$  is defined in Smith (1986b)  $Y = \omega_{eo}/\Omega_{eo}$ ,  $V_{eo} = \omega_{eo} \lambda_{eo}$ , and all lengths and time scales are normalized to the nominal upstream quantities  $\lambda_{eo}$  and  $\omega_{eo}$ , respectively; also  $\phi_{DL} \rightarrow e\phi_{DL}/T_{eo}$ . The term in [] in equation (10) replaces the physically derived  $I_x$  of equation (8). This term is valid only after the threshold potential  $\phi_*$  has been attained, and so is turned on adiabatically for  $\phi > \phi_*$ . Therefore, the circuit model does not accurately describe the initial dynamics in the linear instability phase of the evolution. In addition, the lumped circuit of Figure 4 cannot represent the distributed nature of the flank charging, and so we cannot construct a circuit topology that allows for inductive fields. Therefore, we cannot model the acceleration of the inflowing (injected) distributions by inductive effects.

For the parameters we use (see below), we estimate that the effect of neglecting inductive effects is small. As for the first limitation, the transient charging mechanism vanishes as  $\partial\phi_{DL}/\partial t \rightarrow 0$ . Thus, we expect the model to be adequate for our present objective of studying time-asymptotic scalings.

We show results for five runs. For all cases, the injected distributions are drifting Maxwellians with drift speeds in the simulation frame of  $U_e = 2 V_{eo}$ ,  $U_i = -0.5 V_{eo}$ . The forms of these distributions are held fixed (up to normalization). The threshold drift parameter  $\beta$  is held equal to 2, and  $M/m = 16$ . Holding  $\ell_a/\lambda_e = 60$ , we use values of  $\alpha = 0.05, 0.02, 0.50$ . Fixing  $\alpha = 0.50$ , we use  $\ell_a/\lambda_e = 20, 40, 60$ . Initialization and other implementations are as described by Smith (1982b).

Figure 5 shows the scaling of  $\phi_{DL}$  with  $\alpha$ , the fundamental parameter of the self-scaling marginal stability model of the MTSI discussed earlier. In the circuit equation (10), the principal effect of  $\alpha$  is contained in the dependence of the impedance  $Z_T$  on the dielectric constant  $\epsilon_\perp$ . In terms of the circuit equation (10), the DL scaling law equation (1) becomes in dimensionless notation

$$\phi_{DL} = G \ell_{DL}^2 J_s \left[ 1 - \frac{\phi_{DL}^{1/2}}{Z_0 J_s} - \frac{\phi_{DL}^{3/4}}{R_0 J_s} \right], \quad (13)$$

where  $Z_T(\phi) = Z_0 \phi^{1/2}$ ,  $R(\phi) = R_0 \phi^{1/4}$ . The RHS (13) has the form of a large factor  $G J_s \ell_{DL}^2$  times a small factor [...], and the upper bound for  $\phi_{DL}$  is obtained from setting [...] = 0. Because  $Z_0 \ll R_0$ , equation (13) implies  $\phi_{DL} \sim Z_0^2$ . In Figure 5 we also plot the dependence of  $Z_0^2$  on  $\alpha$ , which agrees well with the plotted points.

Figure 6 confirms the scaling  $\phi_{DL} \sim \ell_a^2$  found above. Again, this result is contained in equation (13) through the dependence  $\phi_{DL} \sim Z_0^2$  (the results of Fig. 6 are all for  $\alpha = 0.5$ , where  $Z_0 \ll R_0$ ).

Because the speed of light  $c$  is introduced in the impedance, the choice of  $V_{eo}/c$  yields a physical scaling of velocities. Because  $Y = \omega_{eo}/\Omega_{eo}$  is a parameter, we obtain physical values of the length scales for an assumed value of either  $B_0$  or  $n_{eo}$ . All runs discussed here are for  $T_{eo} = T_{io} = 1$  keV, typical of the plasma sheet population (note  $\phi_{DL}$  scales independently of  $T_{eo}$ ). The scaled  $\phi_{DL}$  is then given in kV as shown in the right-hand scale of Figure 6. Similarly, if we adopt a nominal value of  $B_0 = 0.05$  G ( $f_{ce} = 250$  kHz) for the acceleration region, the top scale of Figure 6 gives arc thickness projected into the ionosphere of the order 1 km, which is the correct order of magnitude.



The power flows ( $I\phi$ ) through the various parts of the circuit are shown for one case in Figure 7; for this case  $\phi_{DL} = 42.5$  kV. In the steady state, only 10 percent of the power flows goes through the DL, and about 90 percent goes into charging the flanks. The physical scale on the right shows the power dissipated per 1000 km extent of the arc in the E-W direction. Arcs are generally observed in systems of parallel bands, quasi-periodic in the N-S direction; for the parameters of this example, each DA in such a system would dissipate about  $10^{11}$  W, compared with a typical substorm power of  $\sim 10^{12}$  W.

The scalings in  $\alpha$  and  $\ell_a$  have straightforward physical interpretations. The increase of  $\phi_{DL}$  with  $\alpha$  has two related aspects. First, the efficacy of the anomalous transport mechanism reported in Smith (1986b) increases with  $\alpha$ , which is a measure of the strength of the MTSI. Second, in this self-scaling model the ratio  $R_i(\phi)/\ell_i(\phi) \sim \alpha^{1/2}$ , so that as  $\alpha$  increases, finite-Larmor radius effects lead to decreasing ion drift speed; hence, a higher ratio of electrostatic to kinetic energy is stored in the flank "dielectric" for a given charge. The factor  $\ell_a$  in  $Z_0$  [equation (6)] originates in the current balance ( $I_s = J_s \ell_a$ ), and because the flank is charged from the interior of the arc the charge available increases with  $\ell_a$ . The quadratic scaling  $\phi_{DL} \sim \ell_a^2$  derives from the self-scaling of the transport model because  $\ell_r \sim \phi^{1/2}$ .

#### IV. DISCUSSION

We have shown that basic considerations of DL evolution and stability require anomalous transport processes to divert the uniform upstream current to the flanks of a DA even after the parallel electric field has evolved to a steady state. The transport model we have discussed, albeit highly simplified, yields an estimate [equation (8)] for the arc potential in general accord with observations. Other important consequences of the model are also in accord with satellite and rocket observations of DA's and laboratory DL experiments. These include: (1) the density in a DA is substantially depleted relative to the ambient density (Benson and Calvert, 1979; Alport et al., 1986); and (2) concomitant with the depletion of the arc is that the current is diverted to the flanks, so that the highest current density is at the edges (Bruning, 1983; Burke, 1984).

Besides the simple transport mechanism discussed here, there are many other mechanisms which are probably important in DA's. We are presently investigating models including ion-cyclotron modes.

In terms of the simple circuit model, the potentials, perpendicular length scales, and power flows physically scale to correct orders of magnitude. For the nominal parameters we have chosen, the potential ranges from 5 to 42 kV, while the length scales are consistent with the observational bound of  $\approx 3$  km on the latitudinal scale projected in the ionosphere (Boehm and Mozer, 1981). These quantities scale as  $n_{eo}$  and  $n_{eo}^{-1/2}$ , respectively. We adopted  $B_0 = 0.05$  to correspond to the frequency of peak intensity of the auroral kilometric radiation, and chose  $\omega_{eo}/\Omega_{eo}$  as the marginal limit of strong magnetization ( $\omega_e/\Omega_e = R_e/\lambda_e$ ), which experiments reveal to be a requisite for strong DL formation with Earthward-directed Poynting flux (Smith, 1986a). (Recall that  $n_{eo}$  is the ambient density before DL formation, not that of the evacuated arc.) Thus, our choice of  $\omega_{eo} = \Omega_{eo}$  is an upper bound; smaller values lead to lower potential, larger widths, and lower power flows.

In future publications we shall report on refinements and extensions of the simulation concept, including a model in which the simplified circuit used here is replaced by the transmission-line equations.

*Acknowledgments.* I am grateful to D. P. Chernin, A. T. Drobot, and C. K. Goertz for many stimulating conversations. I also thank J. B. McBride, C. L. Chang, W. Horton, J. D. Huba, A. Mankofsky, E. Ott, J. L. Seftor, and M. Temerin for useful discussions, and A. C. Williams for the invitation to present this work at the Workshop on Double Layers in Astrophysics. This work was supported by NASA contract NASW-3947.

## REFERENCES

- Alport, M. J., S. L. Cartier, and R. L. Merlino, *J. Geophys. Res.*, **91**, 1599-1608 (1986).
- Benson, R. F. and W. Calvert, *Geophys. Res. Lett.*, **6**, 479-482 (1979).
- Boehm, M. H. and F. S. Mozer, *Geophys. Res. Lett.*, **8**, 607-610 (1981).
- Bruning, K., Dissertation, Univ. of Munster, 1983.
- Burke, W. J., in *Magnetospheric Currents*, edited by T. A. Potemra, Amer. Geophys. Union, Washington, D.C., pp. 294-303, 1984.
- Coakley, P. and N. Hershkowitz, *Phys. Fluids*, **22**, 1171-1181 (1979).
- Davidson, R. C. and N. A. Krall, *Nuclear Fusion*, **17**, 1313-1372 (1977).
- Goertz, C. K., *Space Sci. Rev.*, **42**, 499-513 (1985).
- Goertz, C. K., in *Comparative Study of Magnetospheric Systems*, edited by B. M. Pedersen, D. Le Queau, A. Roux, and A. Sant-Marc, CNRS, Toulouse, France, pp. 357-370, 1986.
- Goertz, C. K. and G. Joyce, *Astrophys. Space Sci.*, **32**, 165-173 (1975).
- Gurnett, D. A., *J. Geophys. Res.*, **79**, 4227-4238 (1974).
- Haerendel, G., in *High-Latitude Space Plasma Physics*, edited by B. Hultqvist and T. Hagfors, Plenum, New York, pp. 515-535, 1983.
- Kletzing, C., C. Cattell, F. S. Mozer, S.-I. Akasofu, and K. Makita, *J. Geophys. Res.*, **88**, 4105-4113 (1983).
- McBride, J. B., E. Ott, J. P. Boris, and J. H. Orens, *Phys. Fluids*, **15**, 2367-2383 (1972).
- Smith, R. A., *Physica Scripta*, **25**, 413-415 (1982a).
- Smith, R. A., *Physica Scripta*, **T2**, 238-251 (1982b).
- Smith, R. A., in *Unstable Current Systems and Plasma Instabilities in Astrophysics*, edited by M. R. Kundu and G. D. Holman, Reidel, Dordrecht, pp. 113-123, 1985.
- Smith, R. A., in *Comparative Study of Magnetospheric Systems*, edited by B. M. Pedersen, D. Le Queau, A. Roux, and A. Saint-Marc, CNRS, Toulouse, France, pp. 327-350, 1986a.
- Smith, R. A., *Geophys. Res. Lett.*, submitted, 1986b.
- Smith, R. A., *Geophys. Res. Lett.*, submitted, 1986c.
- Temerin, M., K. Cerny, W. Lotko, and F. S. Mozer, *Phys. Rev. Lett.*, **48**, 1175-1179 (1982).
- Torbert, R. B. and F. S. Mozer, *Geophys. Res. Lett.*, **5**, 135-138 (1978).



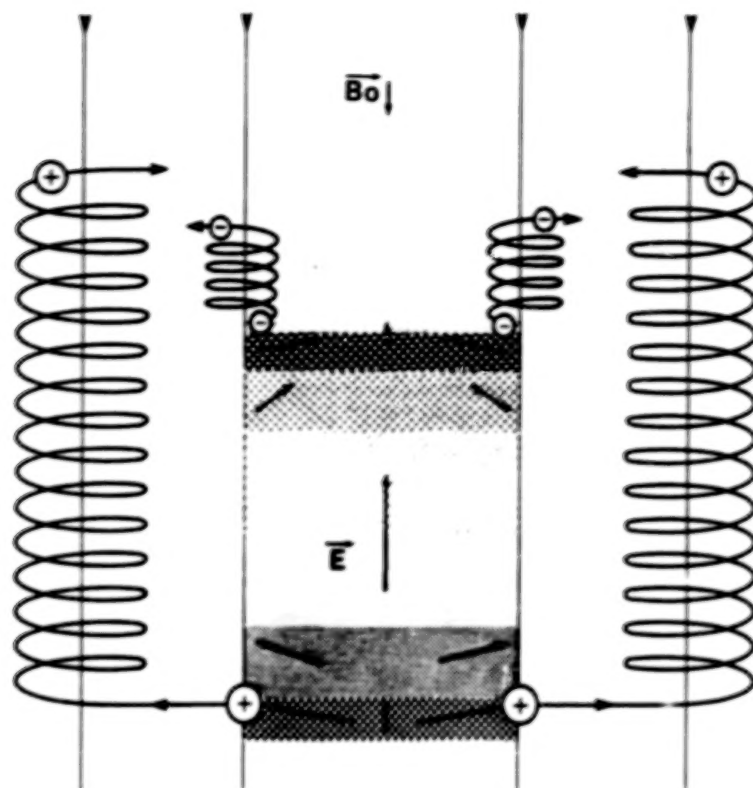


Figure 1. Schematic illustration of initial charging of the DL flanks by expulsion of charge from the localized, rapidly changing non-neutral region (shaded: stippled region  $\rho > 0$ , cross-hatched  $\rho < 0$ ) where onset of current-driven instabilities occurs in the parallel sheet of a kinetic Alfvén wave.

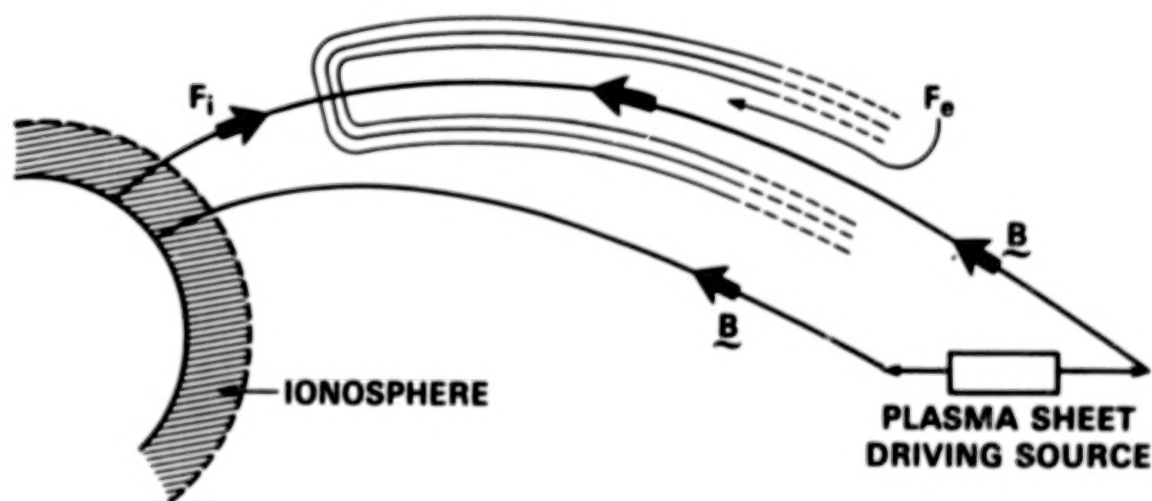


Figure 2. Schematic of the double layer flank spreading along  $\mathbf{B}$  from the double layer toward the generator (here for illustration taken to be in the plasma sheet).

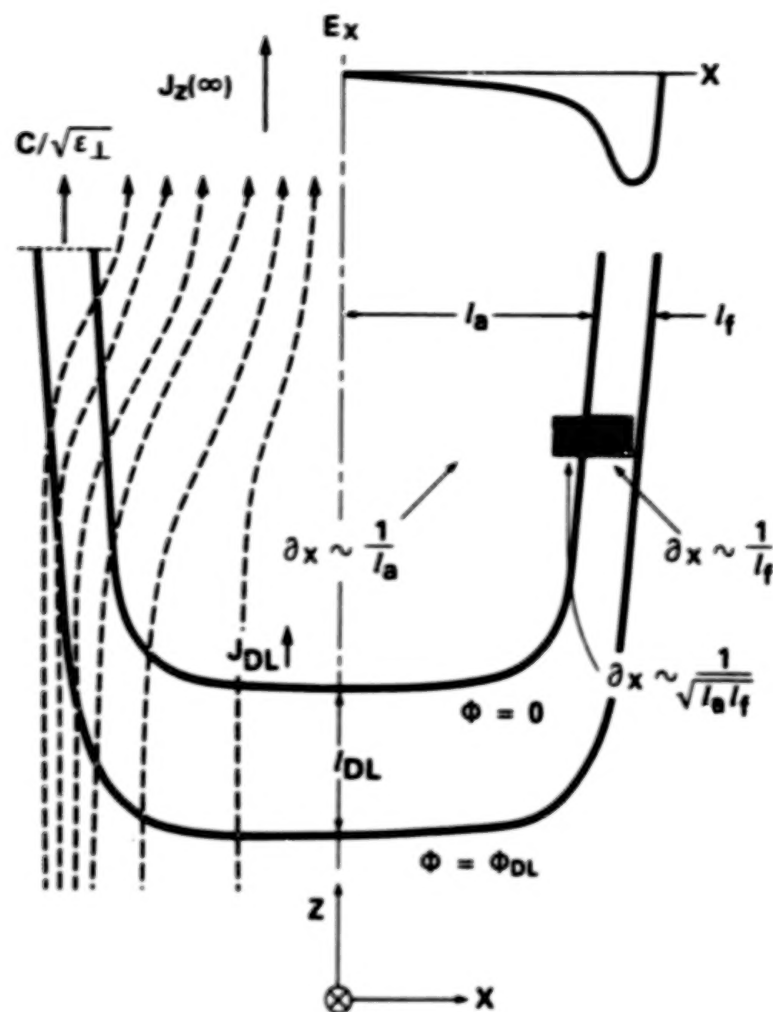


Figure 3. Left side: Schematic of the current diversion in the discrete arc. Right side: Definition of the scale lengths of the arc ( $l_a$ ) and flank ( $l_f$ ) and the associated scale factors which are used in the text to replace perpendicular derivatives. Also shown is a sketch of the inhomogeneous electric field  $E_x$ , which produces relative drift between the electrons and ions owing to finite-Larmor-radius effects, and the definition of the  $xyz$  coordinate system. The magnetic field  $\mathbf{B}_0 = -B_0 \mathbf{e}_z$ .

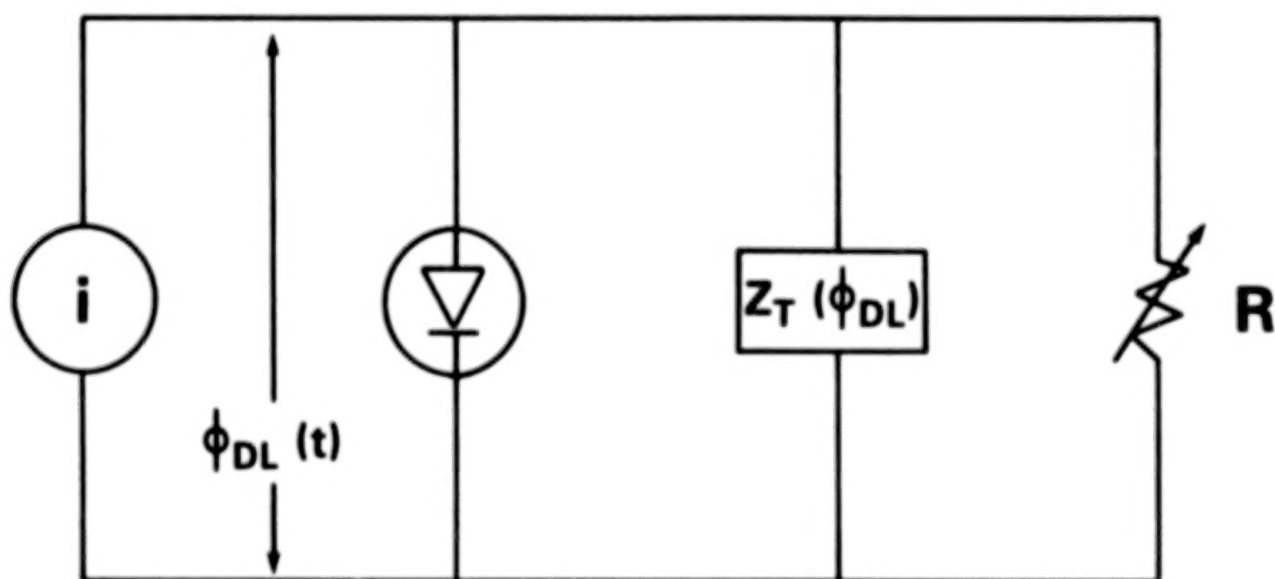


Figure 4. Model circuit used to provide the current density boundary condition in one-dimensional DL simulation.

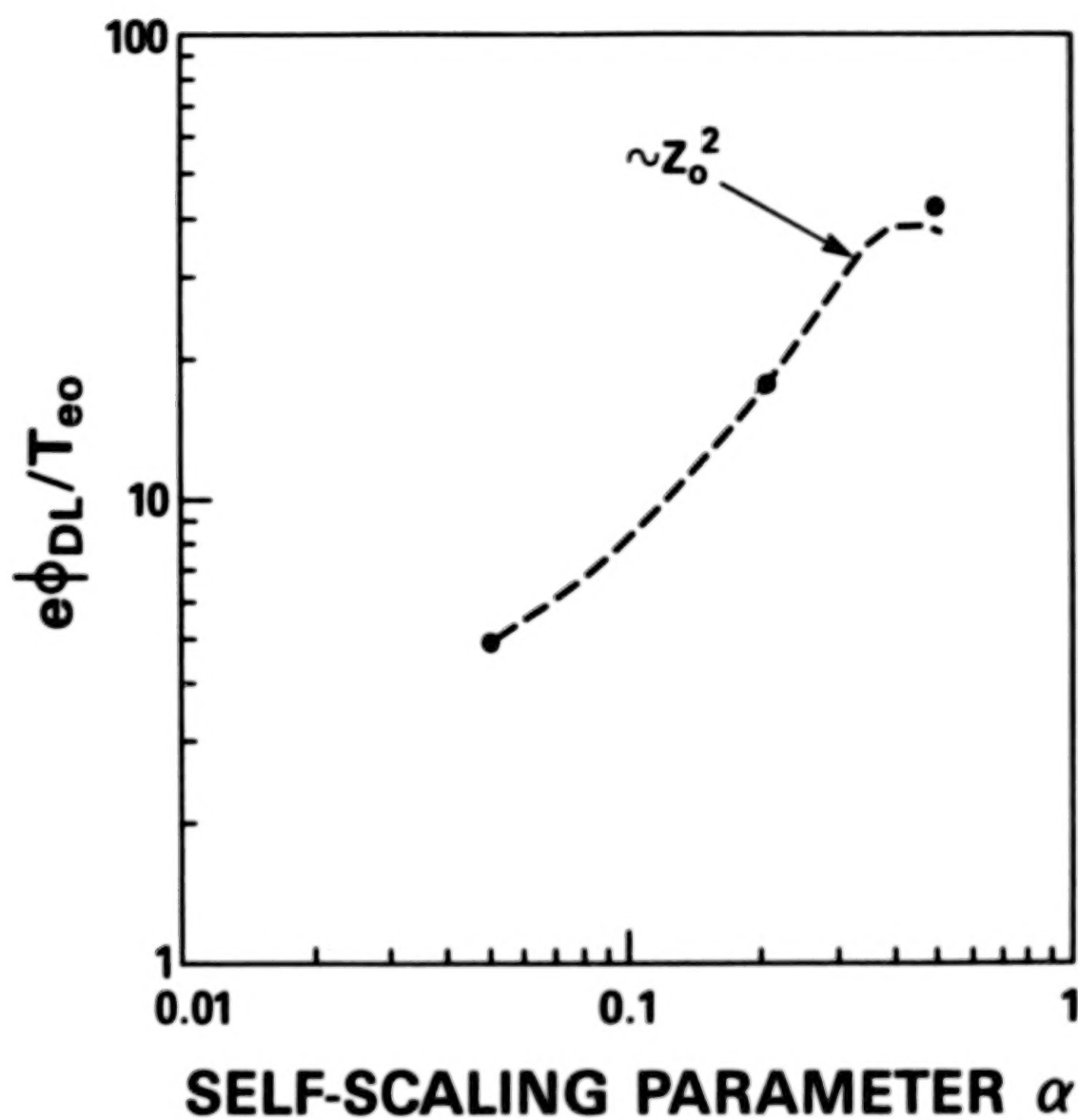


Figure 5. Scaling of the DL potential  $\phi_{DL}$  with the fundamental parameter  $\alpha$  of the anomalous transport mechanism. The dashed curve is arbitrarily normalized to the point at  $\alpha = 0.2$ .

# PROJECTED IONOSPHERIC DIMENSION\* (km); $B_0 = 0.4G$

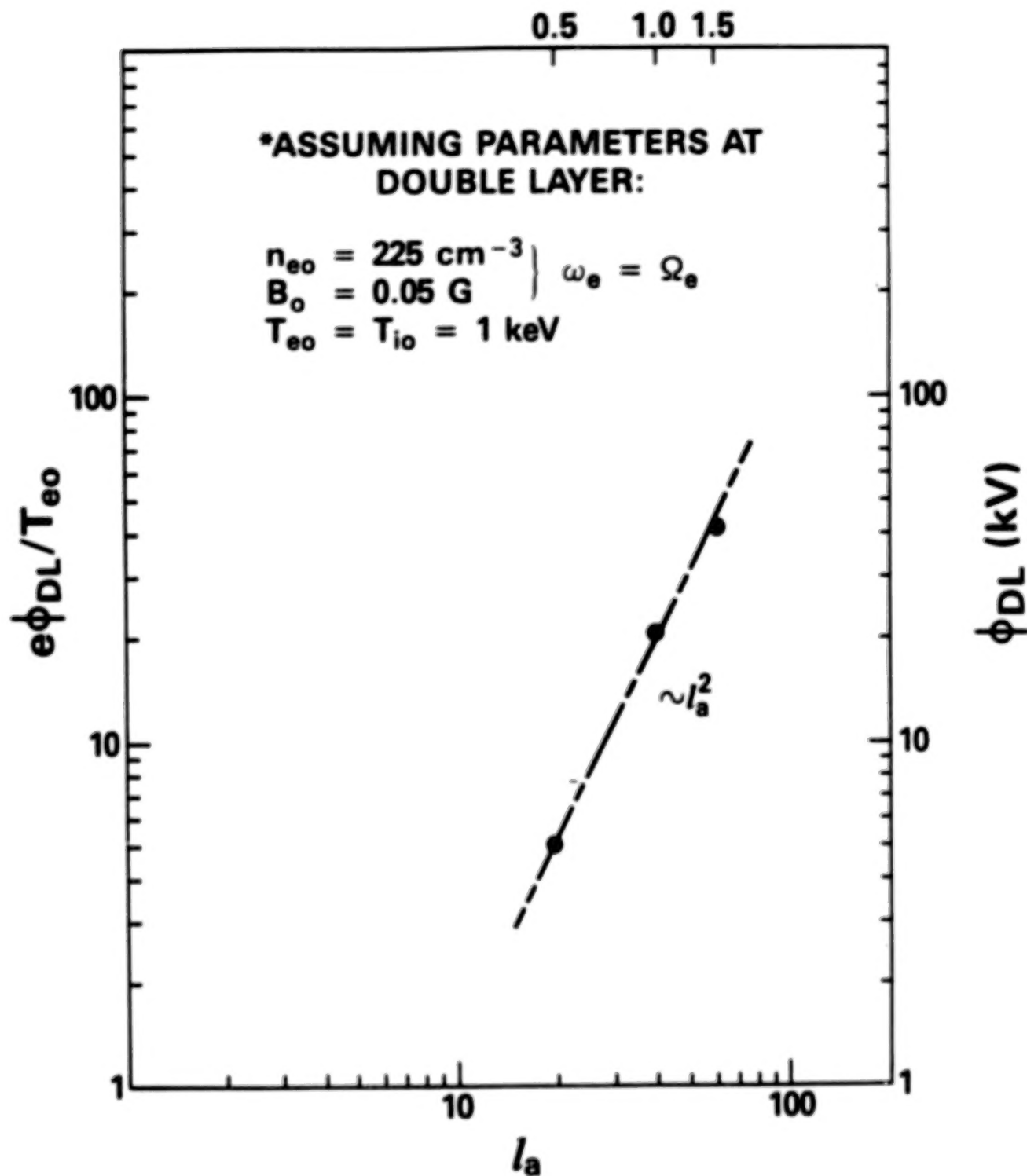


Figure 6. Scaling of  $\phi_{DL}$  with the perpendicular scale width  $l_a$  of the arc model. The bottom and left scales are dimensionless. The right scale shows the potential in kV for assumed  $T_{eo} = 1 \text{ keV}$ ; the top scale shows the arc dimension ( $2l_a$ ) projected into the ionosphere, for the given ambient parameters (before DL formation).

RUN 8606

CIRCUIT POWERS

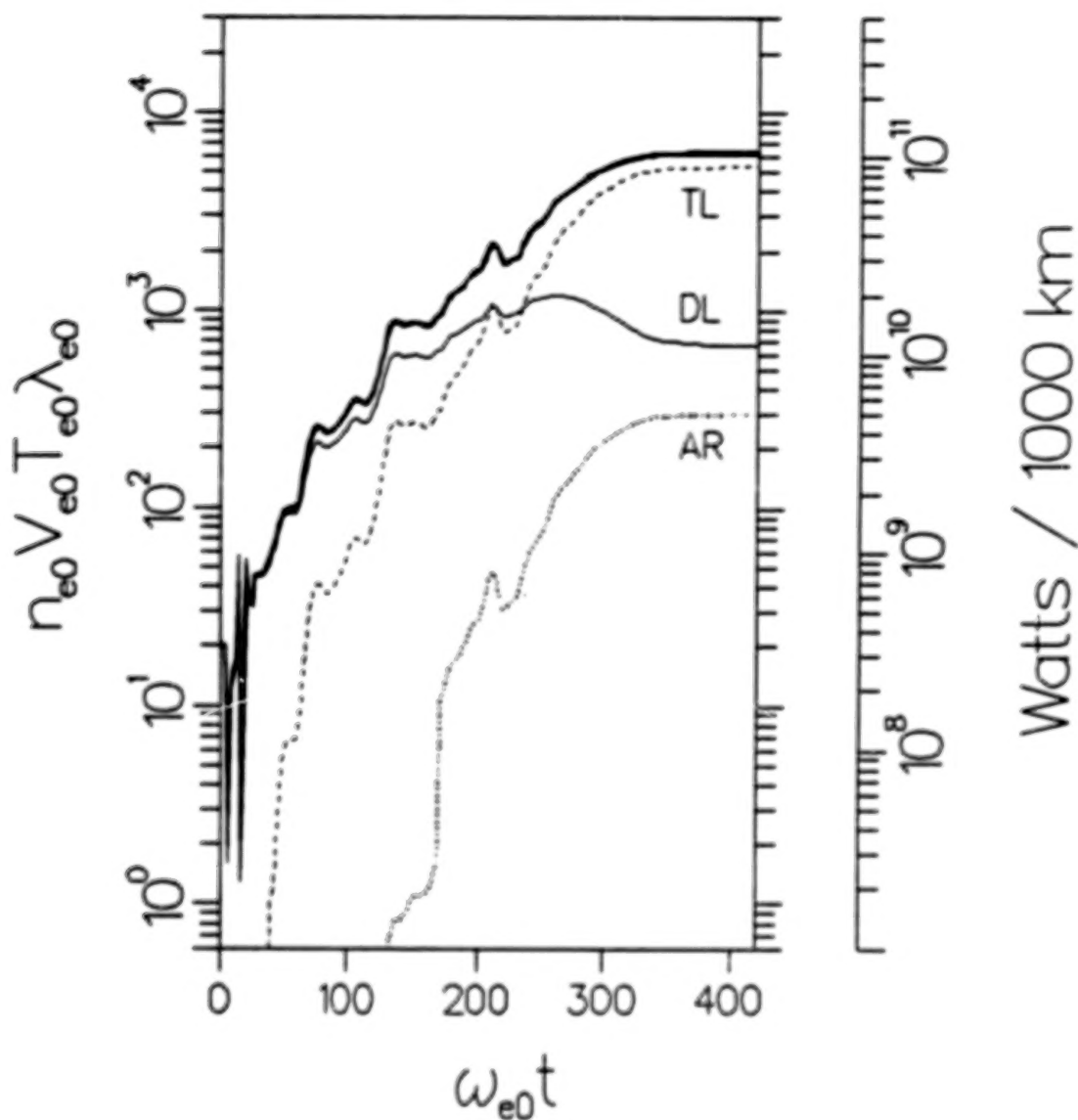


Figure 7. Time history of power flows through the various circuit elements for run 8606 ( $e\phi_{DL}/T_{e0} = 42.5$ ). TL - transmission line (flank) impedance; DL - double layer; AR - anomalous resistivity (leakage) in flank. The right-hand scale shows the physically scaled power for an arc extended 1000 km in the E-W direction.

N87

23326

UNCLAS



## WEAK DOUBLE LAYERS IN THE AURORAL IONOSPHERE

M. K. Hudson, T. L. Crystal, and W. Lotko  
Physics and Astronomy Department  
Dartmouth College  
Hanover, New Hampshire 03755, U.S.A.

and

C. Barnes  
Los Alamos National Laboratory  
Los Alamos, New Mexico 87545, U.S.A.

## ABSTRACT

Previous work on the evolution of weak double layers in a hydrogen plasma has been extended to include  $H^+$  and  $O^+$  with relative drift. It has been shown (Bergmann and Lotko, 1986) that the relative drift between hydrogen and oxygen ions due to a quasi-static parallel electric field gives rise to a strong linear fluid instability which dominates the ion-acoustic mode at the bottom of the auroral acceleration region. This ion-ion instability can modify ion distributions at lower altitudes and the subsequent nonlinear evolution of weak double layers at higher altitudes in the ion-acoustic regime. We have found that ion hole formation can occur for smaller relative electron-ion drifts than seen in previous simulations, due to the hydrogen-oxygen two-stream instability. This results in local modification of the ion distributions in phase space, and a partial filling of the valley between the hydrogen and oxygen peaks, which would be expected at higher altitudes on auroral field lines. It is shown that the observed velocity diffusion does not necessarily preclude ion hole and double layer formation in hydrogen in the ion-acoustic regime. These simulation results are consistent with the experimentally measured persistence of separate hydrogen and oxygen peaks, and the observation of weak double layers above an altitude of 3000 km on auroral field lines.

## 1. INTRODUCTION

Weak double layers with potential jumps comparable to the electron thermal energy have been observed to form in one-dimensional (Sato and Okuda, 1980) and two-dimensional (Barnes et al., 1985) electrostatic particle simulations; the double layer formation is driven by an electron drift relative to ions which is unstable to the ion-acoustic mode but is less than the electron thermal speed. Such weak double layers have been observed in space in the auroral particle acceleration region (Temerin et al., 1982), and in laboratory plasmas (Chan et al., 1984; Sekar and Saxena, 1985; Chan, 1986). Thus far, theoretical efforts at understanding weak double layer formation have focussed on a single ion species, while it is known from space observations that weak double layers occur in regions of upward flowing hydrogen and oxygen of ionospheric origin. A quasi-static parallel electric field has been postulated to explain the observed particle distributions (Chiu and Schulz, 1978; Lyons, 1980). While the existence of such a field will remain a zeroth order assumption in the present paper, we will also examine non-adiabatic modifications of the particle distributions at the bottom of the acceleration region which may affect weak double layer evolution further up the field line, and the stability of the assumed quasi-static field.

We will first briefly review previous work on weak double layer evolution in a hydrogen plasma, and then extend our simulations to include a relative drift between hydrogen, oxygen, and electrons which occurs, for example, in a mirror-supported parallel electric field. Our purpose is to examine the nonlinear effects of the resulting hydrogen-oxygen two-stream instability (Bergmann and Lotko, 1986) on the particle distributions, and consequences for double layer formation further up the field line.

### III. WEAK DOUBLE LAYER FORMATION IN A HYDROGEN PLASMA

Barnes et al. (1985) showed in a series of one- and two-dimensional, bounded and periodic particle simulations that weak double layers with potential jumps comparable to the electron thermal energy form when the system is driven by an electron drift relative to ions which is less than the electron thermal speed, e.g.,  $V_d = 0.5 - 0.7 a_e$ , and an electron to ion temperature ratio  $T_e/T_i \gg 1$ . The electron drift was maintained by injection of electrons from the boundaries at a continuous rate in bounded runs, and by applying a weak electric field uniformly across the system in periodic runs.

Sato and Okuda (1980) first studied the occurrence of weak double layers in a one-dimensional periodic system in which electrons are given an initial drift that subsequently decays. They found that it was necessary to use a long system,  $L > 256 \lambda_D$  (Debye lengths), in order for weak double layers to form in periodic runs. Our subsequent interpretation (Barnes et al., 1985) is that long periodic systems are required to prevent electron recycling from the low to high potential side, which neutralizes the double layer. Electron injection boundary conditions eliminate this problem in bounded simulation runs, and a weak applied electric field acts to impede electron recycling in periodic runs; both of these simulation techniques allow shorter system lengths.

Figure 1 from Barnes et al. (1985) shows the temporal evolution and recurrence of weak double layers in a one-dimensional system with electron injection boundaries. Ion-acoustic turbulence evolves, for  $V_H = 0.5 a_e$  and  $T_e/T_i = 50$ , into a discrete localized pulse which propagates into the system initially at the sound speed. The pulse is characterized by a negative potential dip which amplifies by momentum exchange with reflected electrons (Lotko, 1983; Chanteur et al., 1983); the asymmetric reflection of electrons results in a potential jump downstream. As the negative potential dip grows, it traps ions, slowing down the pulse via mass loading until an effective Bohm criterion for existence of the double layer potential jump is no longer met. The latter requires that ions flow into the high potential side at or near the sound speed (Chen, 1974), achieved here by motion of the pulse in the ion frame. The potential jump then decays and ion holes (Chan, 1986) or ion-acoustic solitons (Sato and Okuda, 1981) propagate away from the high potential side to seed new double layer formation. The decaying ion hole, still apparent in phase space, recoils backward as it moves downward through the ion distribution.

Barnes et al. (1985) examined the persistence of weak double layers in two-dimensional magnetized simulations. Electron injection boundary conditions produce one-dimensional double layers which are roughly uniform across the system in the direction perpendicular to  $\mathbf{B}$ . To examine the transverse scale, a doubly periodic system with a weak electric field imposed uniformly along  $\mathbf{B}$  was employed. The magnitude of the electric field was such that the corresponding potential drop across the system was less than the electron thermal energy, or  $eE_e/T_e = 0.6/160 \lambda_D$ . Figure 2 shows transverse localization of weak double layers for strongly magnetized electrons ( $\omega_{ce}/\omega_{pe} = 3$  is the ratio of electron gyro to plasma frequency). The transverse dimension appears to decrease with increasing magnetic field strength, scaling with  $\sqrt{\lambda_D^2 + \rho_s^2}$ , where  $\lambda_D$  is the Debye length and  $\rho_s$  is the ion gyroradius at the electron temperature. The parallel scale length remains the order of tens of Debye lengths, as in one-dimensionality. Ion-acoustic turbulence becomes homogeneous and does not evolve into localized weak double layers in weakly magnetized ( $\omega_{ce}/\omega_{pe} < 1$ ) periodic systems. One therefore might expect to see such structures in the auroral acceleration region, but not, for example, in the solar wind.

#### IV. ION HOLES IN MULTIPLE ION SPECIES PLASMAS

To the double layer evolution problem we would now like to add the effects of multiple ion species,  $H^+$  and  $O^+$ , with relative drift. This introduces an important complication noted by Bergmann and Lotko (1986). A quasi-static parallel electric field produces a relative drift between ionospheric hydrogen and oxygen ions which have been accelerated through the same potential drop, such that  $V_H/V_O = \sqrt{M_O/M_H} = 4$ . This situation is fluid unstable for parallel propagating modes when the relative  $H^+ - O^+$  drift exceeds a minimum, determined primarily by ion Landau damping, up to a maximum value that is less than about twice the hydrogen sound speed  $C_s = \sqrt{T_e/M_H}$ . This indicates that the ion two-stream instability (for parallel propagating waves) will be confined to the bottom of the acceleration region, since at higher altitudes the relative drift will exceed the upper bound for instability. It is likely, although it has not yet been demonstrated, that obliquely propagating modes may still be unstable for drifts exceeding this upper bound. The growth rate for the ion two-stream instability is larger than that for typical (electron-ion) current-driven instabilities, and one might expect significant modifications of the hydrogen and oxygen distributions to occur. In particular, the unstable ion two-stream waves have phase velocities lying between the hydrogen and oxygen distributions, and one might expect some quasi-linear filling, that is to say, formation of tails on the high and low velocity sides of oxygen and hydrogen, respectively. This quasi-linear filling could, in turn, affect the ion-acoustic instability and double layer evolution at higher altitudes, when ion drifts relative to electrons become a significant fraction of the electron thermal speed, as required for double layer formation in hydrogen plasma simulations. The instability analysis and simulations require knowledge or assumptions about the electron distribution in the region of interest. Bergmann and Lotko (1986) have integrated the electron distribution functions,  $F(v_{\parallel}, v_{\perp})$ , in the Chiu-Schulz (1978) equilibrium model of a mirror-supported electric field to obtain an effective one-dimensional distribution,  $f(v_{\parallel})$ . These electron populations include precipitating magnetospheric electrons, primary and secondary backscattered electrons, and those electrons which are trapped between the magnetic mirror below and retarding electrostatic potential above. At an altitude relevant to the ion two-stream instability, the bulk of ionospheric electrons has been retarded at lower altitudes by the potential drop which produces the relative ion drifts. The sum of the remaining electron populations, shown in Figure 3, is essentially a stationary Maxwellian with a precipitating electron tail. Also shown in the figure is a Maxwellian fit for the first three moments as described by Bergmann and Lotko.

We would like to examine the spatial evolution of the ion distribution functions along the geomagnetic field line at various distances above the bottom of the acceleration region (nominally at an altitude of 2000 km in Chiu and Schulz, 1978), including the ion two-stream unstable regime near the bottom on up to altitudes where the ion drifts become comparable to the electron thermal speed, and where double layers have been observed ( $>3000$  km altitude). Since our computer resources limit the simulation system to lengths less than or the order of 1000 Debye lengths, we examine instead a temporal evolution problem which differs from the spatial evolution problem in at least one respect. In the spatial evolution case, the ratio of the  $H^+ / O^+$  bulk drift velocity is  $\sqrt{M_O/M_H}$ , as oxygen and hydrogen are accelerated to the same energy as a function of potential at a given altitude. In steady state at a fixed altitude there will be a continuous flow of oxygen and hydrogen whose drifts differ by a factor of 1 to 4, respectively, but the hydrogen and oxygen ions passing that altitude at a fixed time will not leave the bottom of the acceleration region simultaneously, since hydrogen flows up the field line faster. This follows from the relation

$$e\phi = 1/2 M_H V_H^2 = 1/2 M_O V_O^2 \quad (1)$$

which holds at any given altitude where the potential is  $e\phi$ . Alternatively, in a simulation system evolving in time with a uniformly applied  $E_{\parallel}$ , the ion velocity varies as



$$V_i = \frac{eE_0 t}{M_i}$$

which results in an  $H^+ - O^+$  velocity of  $M_O/M_H$ , rather than  $(M_O/M_H)^{1/2}$ . Furthermore, depending on the strength of the applied electric field  $E_0$ , the ions may accelerate so rapidly that the upper limit on the relative drift for the ion two-stream instability may be exceeded before nonlinear saturation can occur. In such a case, we would not see the full effects of wave-particle interactions on the ion distributions.

With these caveats in mind, we performed a series of one-dimensional electrostatic simulations using the particle code ES1 (Birdsall and Langdon, 1984), in a periodic system of length  $240 \lambda_D$ , using 16,000 hydrogen and 16,000 oxygen ions and 32,000 electrons. We varied the uniform applied electric field from  $eE_0/T_e = 0, 1.2/240 \lambda_D$  to  $2.4/240 \lambda_D$  and applied it only to the ions in order to simulate the approximately stationary electron Maxwellian (Fig. 3) through which the outflowing ions accelerate. We did initial value runs with  $V_H = V_O = 0$  at  $t = 0$  and runs which were initiated with  $V_H$  and  $V_O$  in the range where the ion two-stream growth rate peaks.

Figure 4 shows the nonlinear evolution of the ion two-stream instability for initial drifts  $V_H = 1.2 C_s$  and  $V_O = 0.3 C_s$  and a uniform applied electric field  $eE_0/T_e = 2.4/240 \lambda_D$ . The electron-to-ion temperature ratio is  $T_e/T_i = 20$  and the mass ratios are  $M_H/M_e = 50$  and  $M_O/M_H = 8$ . The choice of drifts  $V_H/V_O = 4$  is intermediate between the spatial evolution case where  $V_H/V_O = \sqrt{M_O/M_H} = 2\sqrt{2}$  and the temporal evolution case where  $V_H/V_O = M_O/M_H = 8$  for our mass ratio. Variations about this set of parameters are discussed below. One observes the formation of a localized fluctuation in the potential similar to that seen in the previously described (single ion) simulations at a time when the hydrogen drift relative to electrons is  $V_H = 0.2-0.3 a_e$ . This drift is smaller by a factor of 2 than in the single ion runs previously shown. The localized wave is a result of the nonlinear evolution of the ion two-stream instability which occurs at lower relative drifts ( $V_H - V_O$ ) than the current-driven, ion-acoustic instability. The potential pulse is subsonic in the ion frame, and appears to propagate with the ions out the right-hand boundary and re-enter on the left. Periodicity of the system allows one to see that the pulse is continuous from the right through the left boundary of an adjacent frame, since the pulse has not moved much from frame to frame. (The frames are separated in time by  $60 \omega_{pe}^{-1}$ .) A significant localized potential jump  $e\phi/T_e \gtrsim 1$  develops, but does not persist as far downstream as in cases where the relative electron-ion drift is larger (Fig. 11). We therefore hesitate to call this structure a double layer when the system is in the ion two-stream unstable regime, although its features are very similar to those shown in Figure 1, when translated to a frame in which electrons are stationary and ions drift. One sees trapping of hydrogen and oxygen on the sides of the distribution functions corresponding to the phase velocities of the (ion two-stream) unstable waves, namely the low velocity side of hydrogen and the high velocity side of oxygen. It seems appropriate to call this structure an ion hole.

We observed ion hole formation in the ion two-stream unstable regime for a range of parameters summarized in Table 1. The ion two-stream instability was observed over a broader range of parameters (Bergmann and Lotko, 1986) than was ion hole formation, which apparently requires large amplitude waves and occurs only for sufficiently rapid linear instability. Recall that the ion two-stream instability is limited in duration as the electric field accelerates ions into and out of the range of linearly unstable drifts. Ion hole formation did not occur in runs 2-4 until the hydrogen bulk was accelerated to  $0.2-0.3 a_e$ . In run 6, with no applied electric field but the same initial drifts as run 3, ion hole formation was not observed. In run 7, also with no electric field, but with initial drifts in the range produced by the electric field in run 3 at the time ion hole formation was observed, an ion hole forms. Sato and Okuda (1980) saw weak double layer formation in a system  $256 \lambda_D$  long but not in one  $128 \lambda_D$  long. Our system length of  $240 \lambda_D$  is marginally long enough to allow a double layer to form in the absence of an applied electric field before periodic electron cycling neutralizes the evolving double layer space charge. We also did a run (8) using a bounded one-dimensional electrostatic code, PDW1 (Lawson, 1984), with constant particle injection maintained by an external circuit and floating potential at both ends of the system, but with parameters otherwise the same as in run 7. Ion hole formation in runs 7 and 8 is comparable, as shown in Figure 5.

In order to address the temporal evolution question, we performed two runs (9 and 10) with two different values of the applied electric field,  $eE_0/T_e = 1.2, 2.4/240 \lambda_D$ , no initial ion drifts, and periodic boundary conditions. Ion hole formation was evident but weaker for the larger electric field (run 9) than in the initial drift case (e.g., run 3), and absent for the weaker electric field (run 10) when compared at time such that  $C_s < V_H - V_O < 2 C_s$ . Some ion heating occurs in the initial value runs (9 and 10) before the relative drifts are comparable to the initial drift runs, i.e., optimum for ion two-stream instability. In initial value runs the hydrogen and oxygen ion distributions separate more quickly than in the case of spatial evolution, and so spend less time in the range of unstable relative drifts,  $V_H - V_O \lesssim 2 C_s$ . The maximum growth rate of the two ion-stream instability is the order of  $\gamma/\omega_{pe} \sim 10^{-2}$  (Bergmann and Lotko, 1986, Fig. 3) for the  $k$  modes in our simulation system of length  $240 \lambda_D$  and grid size  $0.5 \lambda_D$ . Both initial value (run 9) and initial drift (run 3) cases remain in the range of unstable drifts  $V_H - V_O \sim 1.2-2 C_s$  a number of e-folding times, but there appears to be some difference between initializing the system in the linearly unstable regime and evolving through it. In the auroral problem, one expects spatial evolution and weaker electric fields, discussed below, to separate the drifts more slowly relative to the linear growth time.

The question arises whether ion heating by the ion two-stream instability, evident in Figure 4, will affect double layer evolution at higher altitudes where the ion drift relative to electrons is larger. Figure 6 shows the initial ion and electron distributions for runs 9 and 10. Figure 7 shows the same distributions for run 9 at the time an ion hole is beginning to form, while Figure 8 shows the same distributions at a later time when the hydrogen drift is becoming significant relative to electrons. Figure 9 shows the particle distributions in the weaker electric field case at a time when the drift is the same as Figure 7. We would conclude from this set of figures that there is no major modification of the hydrogen and oxygen distributions by the ion two-stream instability, which is present in runs 9 and 10. There is some heating on the low velocity side of hydrogen and the high velocity side of oxygen, as expected, in the range of unstable ion two-stream phase velocities. Figure 10, a similar plot for run 3 which showed ion hole formation at large trapping amplitudes ( $e\phi/T_e \sim 1$ ), indicates more heating between the hydrogen and oxygen distributions. This plot exhibits distribution functions which are spatially averaged across the whole system, and it is the case that the plateau evident in hydrogen (and oxygen) is due primarily to the spatially localized ion hole evident in Figure 3. It is questionable to call this heating versus localized ion trapping since it is not uniform across the system. It therefore seems reasonable to conclude that in our simulation system the hydrogen and oxygen average distributions are not so greatly modified by the ion two-stream instability as to preclude ion-acoustic instability and double layer formation at larger ion drifts relative to electrons.

#### IV. ION-ACOUSTIC DOUBLE LAYERS IN AN $O^+ - H^+$ PLASMA

As hydrogen and oxygen continue to accelerate up the geomagnetic field line out of the region of ion two-stream instability, hydrogen eventually acquires a drift relative to electrons comparable to the electron thermal speed. If the hydrogen velocity distribution has not been too greatly modified by the ion two-stream instability, as our preceding results indicate, we might expect double layers to evolve from the electron-hydrogen acoustic instability, as described by Barnes et al. (1985), as long as oxygen and hydrogen remain well separated. To test this, we did a series of simulations at large electron drifts ( $0.7-0.9 a_e$ ) in the oxygen frame with hydrogen drifting at  $-0.2 C_s$ . Electron injection boundary conditions were employed as in Barnes et al. (1985), in a system  $512 \lambda_D$  long, containing 8000 ions of each species and 16,000 electrons. More realistic mass ratios,  $M_H/M_e = 1000$  and  $M_O/M_H = 10$ , were used. Oxygen was kept cold relative to electrons,  $T_e/T_O = 100$ , and two cases were examined for hydrogen:  $T_e/T_H = 20$  corresponding to no significant heating of hydrogen by the ion two-stream instability at lower altitudes, and  $T_e/T_H = 2$  where significant heating has occurred. The assumption that electrons are hotter than ions is justified by the altitude where weak double layers have been observed ( $>3000$  km), since the large scale parallel electric field restricts colder electrons to lower altitudes. No electric field was applied in these bounded runs.

Figure 11 shows the hydrogen and oxygen distributions and potential at a time when one and possibly a second double layer are forming with hole(s) evident in hydrogen phase space. Oxygen responds more slowly and appears to play a passive role in the double layer formation, but eventually forms a hole in ion-phase space by the time hydrogen has undergone significant heating and the double layer is disappearing (Fig. 12). In a similar run with  $T_e/T_H = 2$ , a hole does not appear to form in hydrogen but is evident in oxygen at later times. This result is consistent with Schamel's (1982) criterion that ion holes do not form for  $T_e/T_i < 3.5$  (see also Hudson et al., 1983). An oxygen ion hole and weak double layer appear to form when the hydrogen is heated too much to support such a structure. Should the hydrogen be significantly heated and the oxygen remain cool, a hole can still form in oxygen in association with an electron  $-O^+$  drift instability at phase velocities between the electron and  $O^+$  peaks.

## V. APPLICATION TO THE AURORAL REGION

A number of caveats are in order before applying the foregoing simulation results to the auroral particle acceleration region. We have examined separately two regimes: (1) where the two ion-stream instability operates at low relative ion drifts ( $< 2 C_s$ ) produced by a quasi-static parallel electric field near the bottom of the acceleration region, and (2) ion-acoustic double layer formation at higher altitudes where relative electron-ion drifts are larger and the ion distributions will have undergone some heating at lower altitudes. We have restricted our analysis to parallel propagating modes and one-dimensional simulations in the present paper. It is likely that oblique modes will affect the ion distributions. Kaufmann et al. (1986) have examined the stability of hydrogen and oxygen beams measured by the S3-3 and DE 1 satellites and concluded that oblique modes are unstable. It may also be the case that the upper limit on relative drift for the ion two-stream instability is relaxed for oblique modes, since  $\mathbf{k} \cdot (\mathbf{V}_H - \mathbf{V}_O) < 2 C_s$  for larger relative ion drifts when  $\mathbf{k}$  is oblique. The linear instability of oblique modes is under investigation by Bergmann (private communication, 1986). Barnes et al. (1985) showed that ion-acoustic double layers evolve in the presence of oblique (EIC) modes in two-dimensionality with behavior similar to the one-dimensional case. We plan to extend the present multi-ion studies to two-dimensional in the future.

Another qualification to our conclusions is the strength of the electric field used in the initial value simulations. The values of  $eE_0/T_e = 1.2-2.4/240 \lambda_D$  correspond to 5-10 mV/m for  $\lambda_D = 10$  m,  $T_e = 10$  eV, and  $n_e = 10 \text{ cm}^{-3}$ . These are not large parallel electric fields compared with observations in the acceleration region (Temerin, private communication, 1986), but are larger than the mirror-supported fields calculated by Chiu and Schulz (1978) which maximize at  $E_0 < 0.5$  mV/m near the bottom of the acceleration region.

It is somewhat difficult to extrapolate from the temporal evolution approach taken in this paper to the spatial evolution of ion distributions along auroral field lines. Nonetheless, with the neglect of oblique modes and use of somewhat large electric fields, and/or initializing the simulations with unstable drifts, and preheated ions in the ion acoustic regime, we find the following:

1. Ion holes form in the ion two-stream unstable regime at relatively low drifts compared with those required to form ion-acoustic double layers. They occur in systems with and without an applied electric field, but over a narrow range of relative hydrogen-oxygen drifts.
2. The ion two-stream instability does not appear to greatly modify the ion distributions, except locally in the presence of a large amplitude ( $e\phi/T_e \sim 1$ ) ion hole.
3. Double layer evolution should proceed at higher altitudes as previously described in the ion-acoustic regime, with holes forming in hydrogen, and oxygen responding passively.



There are two pieces of experimental evidence supporting our conclusion that hydrogen and oxygen distributions are not so greatly modified at lower altitudes by the ion two-stream instability as to preclude double layer formation at higher altitudes. The first is the set of particle measurements from the S3-3 and DE 1 satellites analyzed by Kaufmann et al. (1986) showing well separated  $H^+$  and  $O^+$  peaks, with a slight filling in between the two. The second is the observation of what have been identified as weak double layers by Temerin et al. (1982), also Temerin and Mozer (1986), at altitudes  $>3000$  km in regions of upward ion flows. These observations indicate that the heating of the ion distributions that occurs at lower altitudes is not as great as the relative acceleration, nor enough to make  $T_e/T_i \sim 1$ , which would preclude ion-acoustic double layer formation.

A number of questions remain to be addressed: Can one design a temporal evolution simulation which better models the spatial evolution problem within the constraints of computer time and memory, e.g., by moving one ion species with an electric field which differs from the other by  $\sqrt{M_H/M_O}$  to mimic the spatial case in an initial value problem? What effects do oblique modes and two-dimensionality introduce in the problem? Is it possible to use weaker electric fields and follow the evolution from the ion two-stream through the ion-acoustic double layer regime. These and other questions remain to be addressed in future work on the evolution of weak double layers in the multi-species auroral plasma.

TABLE 1. ION HOLE FORMATION IN THE ION TWO-STREAM UNSTABLE REGIME

Run	$V_O(0)$ ( $a_e$ )	$V_H(0)$ ( $a_e$ )	$V_H - V_O$ ( $C_s$ )	$eE_0/T_e$	bc	$t$ ( $\omega_{pe}^{-1}$ )	hole
1	0	0.17	1.2	2.4	per	0	no
2	0.035	0.17	0.95	2.4	per	0	yes
3	0.042	0.17	0.91	2.4	per	0	yes
4	0.049	0.17	0.86	2.4	per	0	yes
5	0.06	0.17	0.78	2.4	per	0	no
6	0.042	0.17	0.91	0	per	0	no
7	0.06	0.30	1.7	0	per	0	yes
8	0.06	0.30	1.7	0	bnd	0	yes
9	0	0	0	2.4	per	0	marginal
10	0	0	0	1.2	per	0	no

Note: Units of  $eE_0/T_e$  are  $(240 \lambda_D)^{-1}$ ; bnd and per refer to bounded and periodic boundary conditions (bc).

*Acknowledgments.* This research was supported by NSF grant ATM-8445010, the University of California IGPP Award No. 100, and the U. S. Department of Energy. T. L. Crystal was also supported by a grant from the Andrew Mellon Foundation.

## REFERENCES

- Barnes, C., M. K. Hudson, and W. Lotko, *Phys. Fluids*, 28, 1055 (1985).
- Bergmann, R. A., and W. Lotko, *J. Geophys. Res.*, in press, 1986.
- Birdsall, C. K., and A. B. Langdon, *Plasma Physics via Computer Simulations*, McGraw Hill, New York, 1984.
- Chan, C., these proceedings, 1986.
- Chan, C., M. H. Cho, N. Hershkowitz, and T. Intrator, *Phys. Rev. Lett.*, 52, 1782 (1984).
- Chanteur, G. J., C. Adam, R. Pellat, and A. S. Volokhitin, *Phys. Fluids*, 26, 1584 (1983).
- Chen, F. F., *Introduction to Plasma Physics*, Plenum, New York, 1974.
- Chiu, Y. T., and M. Schulz, *J. Geophys. Res.*, 83, 629 (1978).
- Hudson, M. K., W. Lotko, I. Roth, and E. Witt, *J. Geophys. Res.*, 88, 916 (1983).
- Kaufmann, R. L., G. R. Ludlow, H. L. Collin, W. K. Peterson, and J. L. Burch, *J. Geophys. Res.*, submitted, 1986.
- Lawson, W. S., *PDWI Users Manual*, Memorandum No. UCB/ERL M84/37, University of California, Berkeley, 1984.
- Lotko, W., *Phys. Fluids*, 26, 1771 (1983).
- Lyons, L. R., *J. Geophys. Res.*, 85, 17 (1980).
- Sato, T., and H. Okuda, *Phys. Rev. Lett.*, 44, 740 (1980).
- Sato, T., and H. Okuda, *J. Geophys. Res.*, 86, 3357 (1981).
- Schamel, H., *Symposium on Plasma Double Layers*, Riso (1982).
- Sekar, A. N., and Y. C. Saxena, *Plasma Phys. and Cont. Fusion*, 27, 181 (1985).
- Temerin, M., and F. S. Mozer, these proceedings, 1986.
- Temerin, M., K. Cerny, W. Lotko, and F. S. Mozer, *Phys. Rev. Lett.*, 48, 1175 (1982).

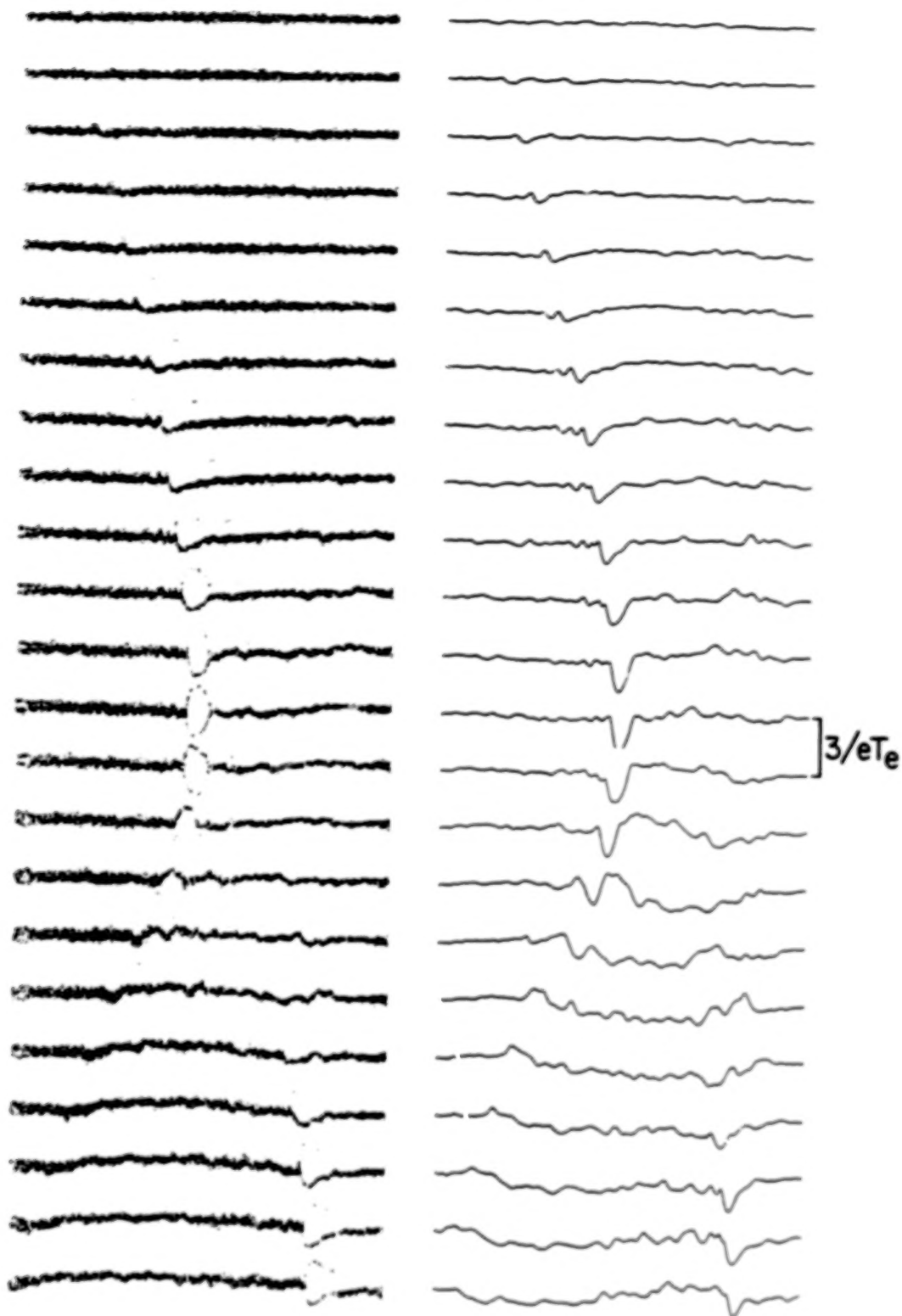


Figure 1. Time series plots of ion-phase space (left) and electrostatic potential (right) for a bounded one-dimensional run with  $M/m = 2000$ ,  $T_e/T_i = 50$ , and  $V_H = 0.5 a_e$ . The snapshots are taken at intervals of  $360 \omega_{pe}^{-1}$  ( $8 \omega_{pi}^{-1}$ ) beginning at  $1080 \omega_{pe}^{-1}$  ( $24 \omega_{pi}^{-1}$ ) (from Barnes et al., 1985).

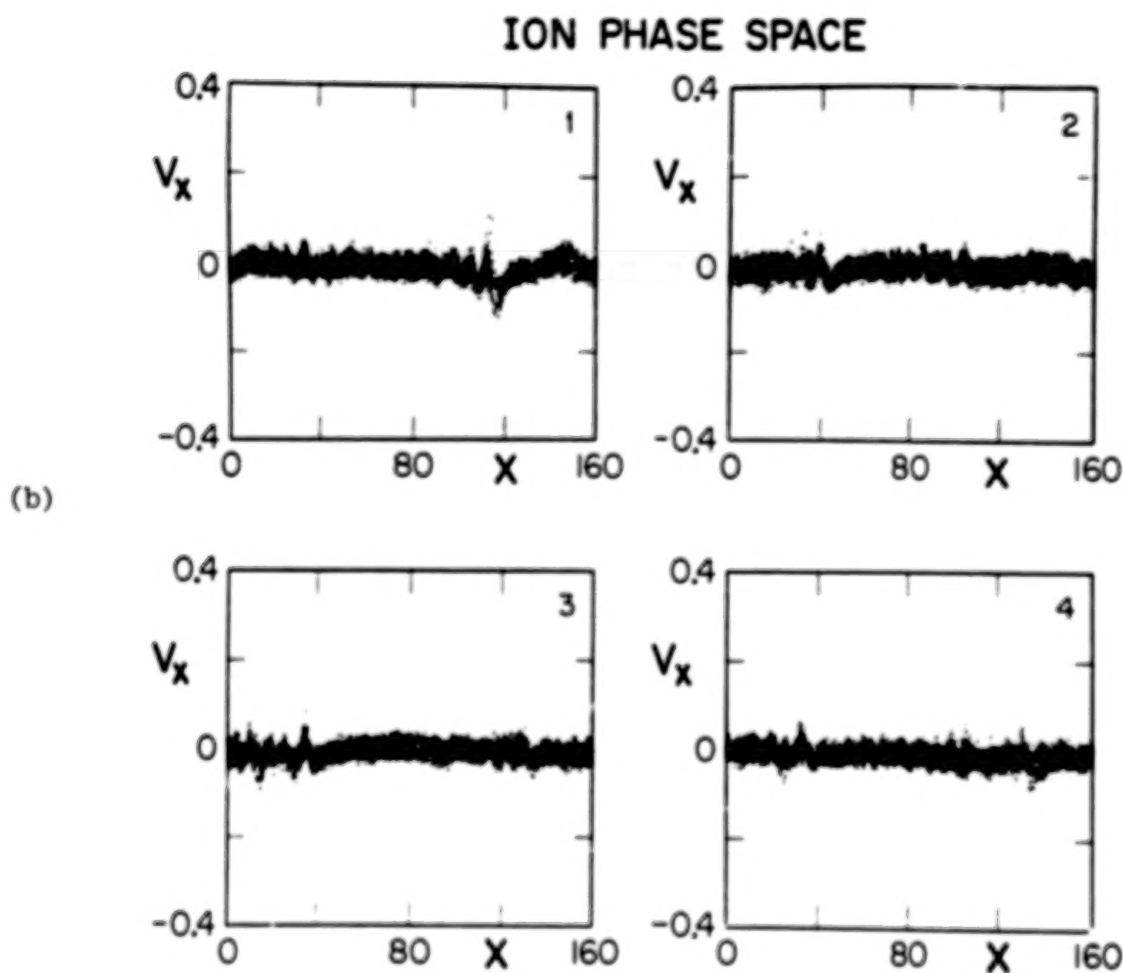
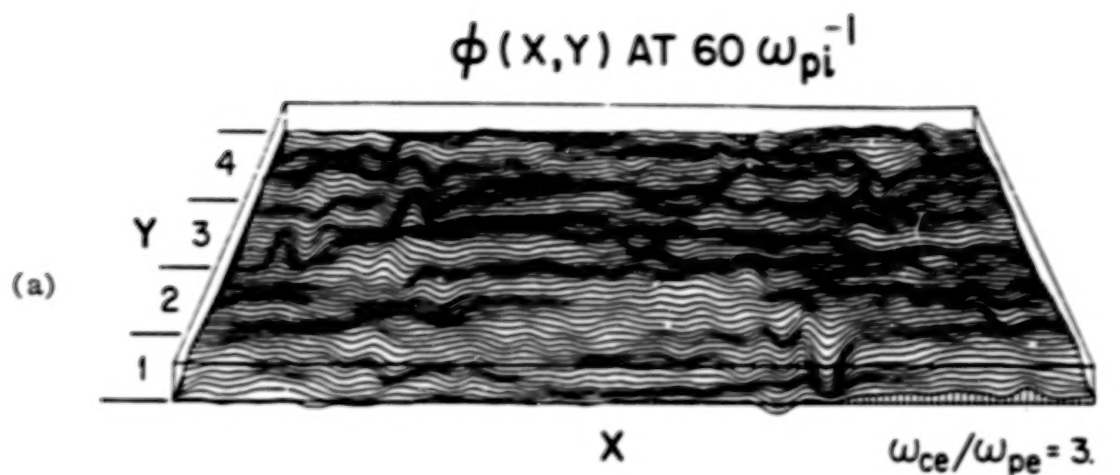


Figure 2. Magnetized doubly periodic system with  $\omega_{ce}/\omega_{pe} = 3$  and a weak uniform applied electric field pointing to the left,  $eE_x/T_e = 0.6/160 \lambda_D$ . (a) Potential profiles are averaged over  $4 \omega_{pi}^{-1}$ ; (b) ion-phase space  $v_x$  versus  $x$  is displayed in each of four bands in  $y$ .  $v_x$  is in units of  $a_e$ . The most prominent double layers are in band 1 at  $x \approx 120 \lambda_D$  and band 3 at  $x \approx 40 \lambda_D$ .

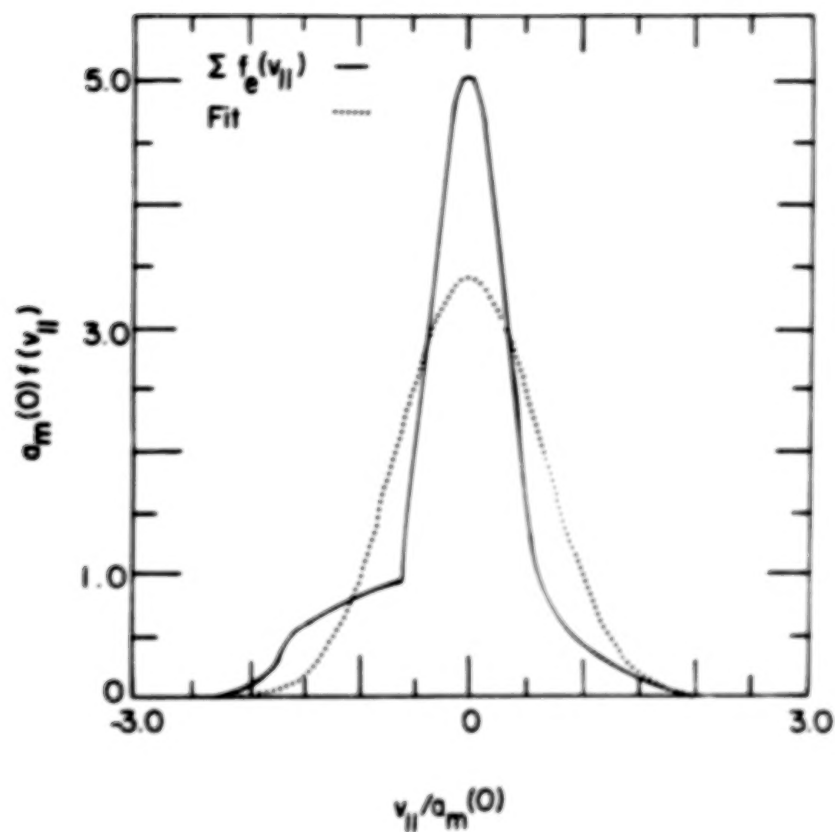


Figure 3. Reduced electron distribution function  $f(V)$  for Chiu and Schulz (1978) Model W, at  $e\phi/T_c = 110$ , where  $T_c$  is the cold ionospheric electron temperature. This represents a sum of contributions from magnetospheric, primary and secondary backscattered and trapped electrons, with ionospheric electrons negligible at this value of the mirror potential measured from zero at an altitude of 2000 km (adapted from Bergmann and Lotko, 1986).

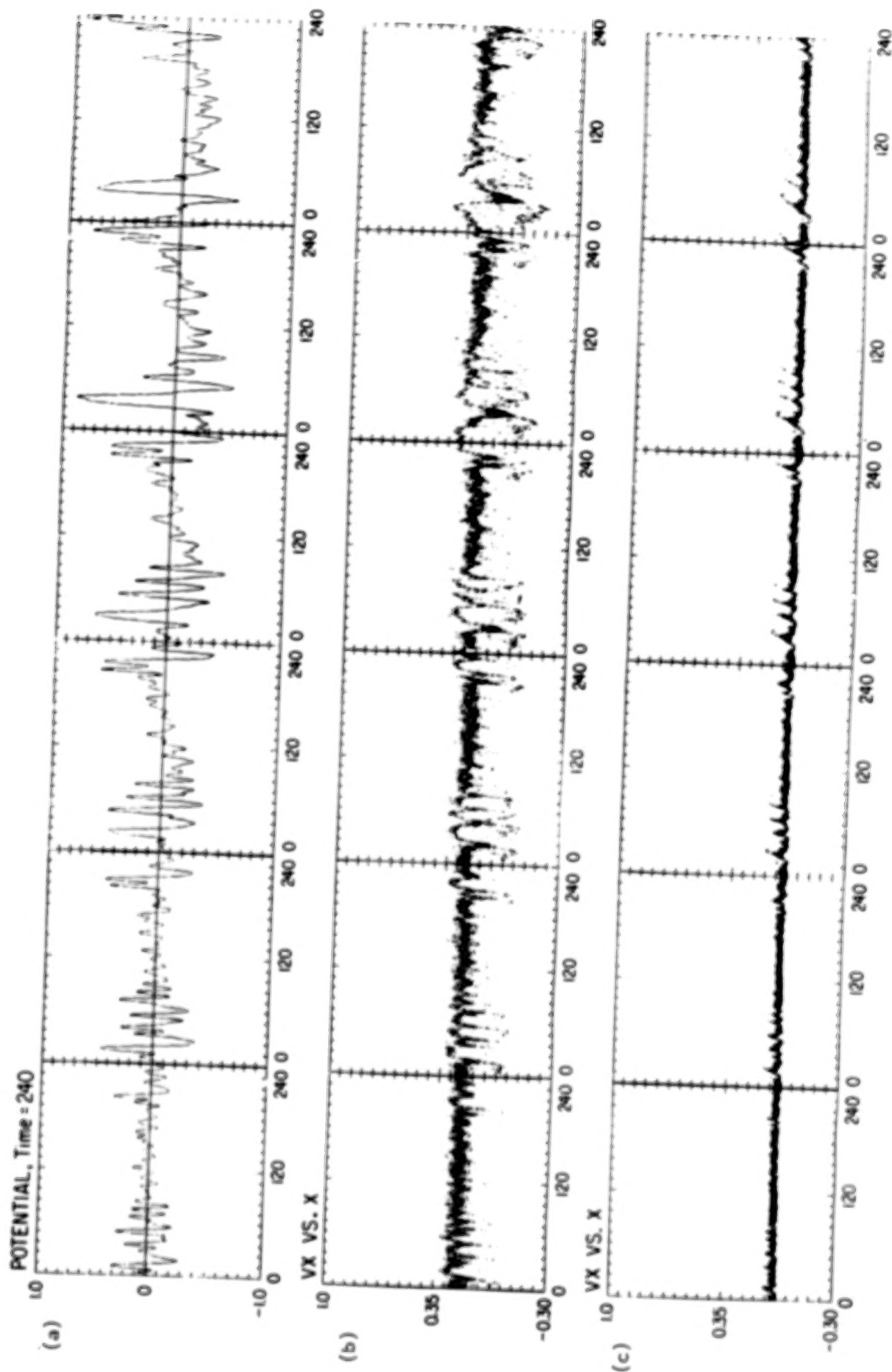


Figure 4. Run 3, Table 1. Time evolution from left to right of (a) the electrostatic potential every  $60 \omega_{pe}^{-1}$  averaged over  $30 \omega_{pe}^{-1}$  from 240-900  $\omega_{pe}^{-1}$ ; (b) corresponding hydrogen; and (c) oxygen phase space. The system is  $240 \lambda_D$  long; timestep  $\omega_{pe} \Delta t = 0.2$  and other parameters are given in the text.



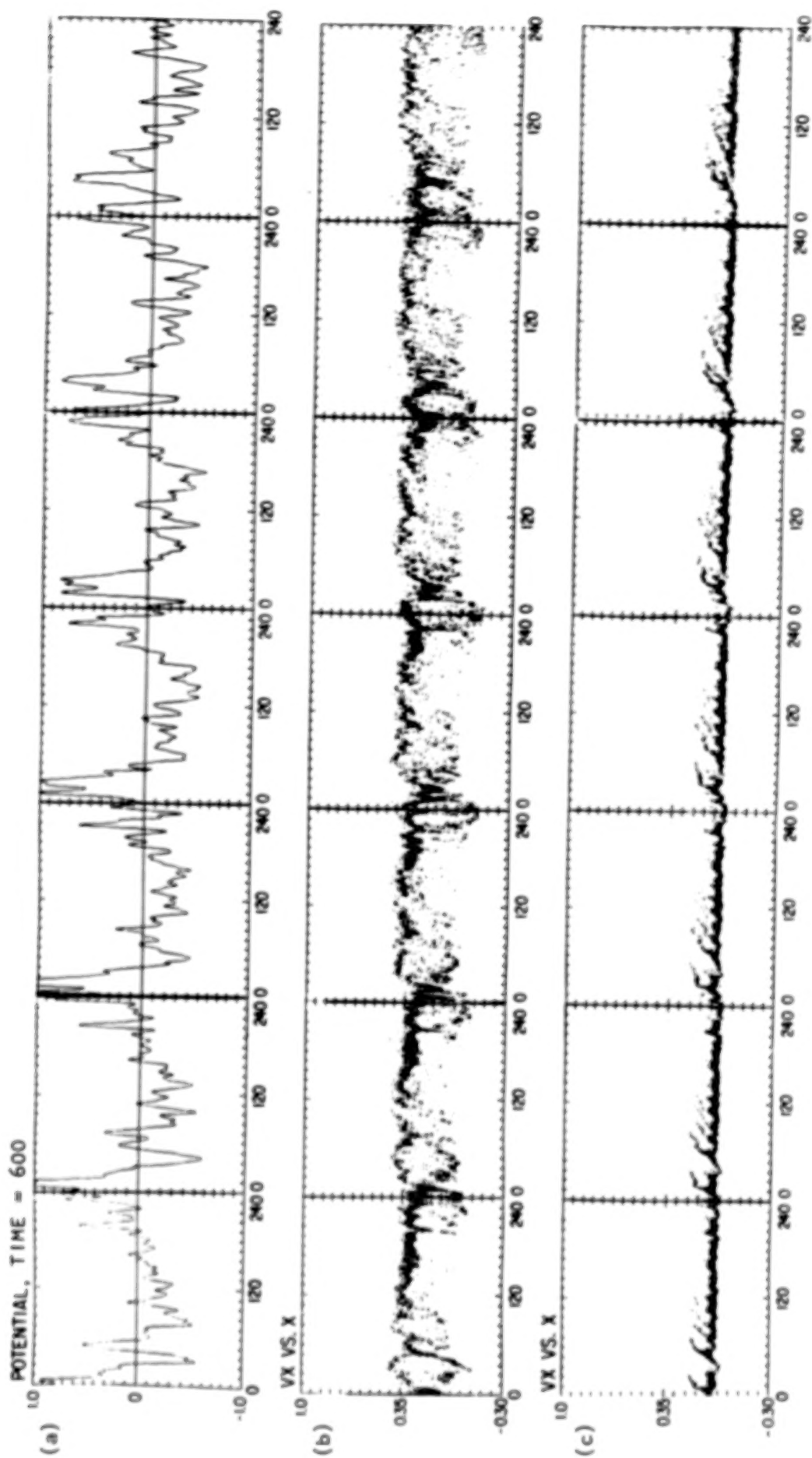


Figure 4. (Concluded)

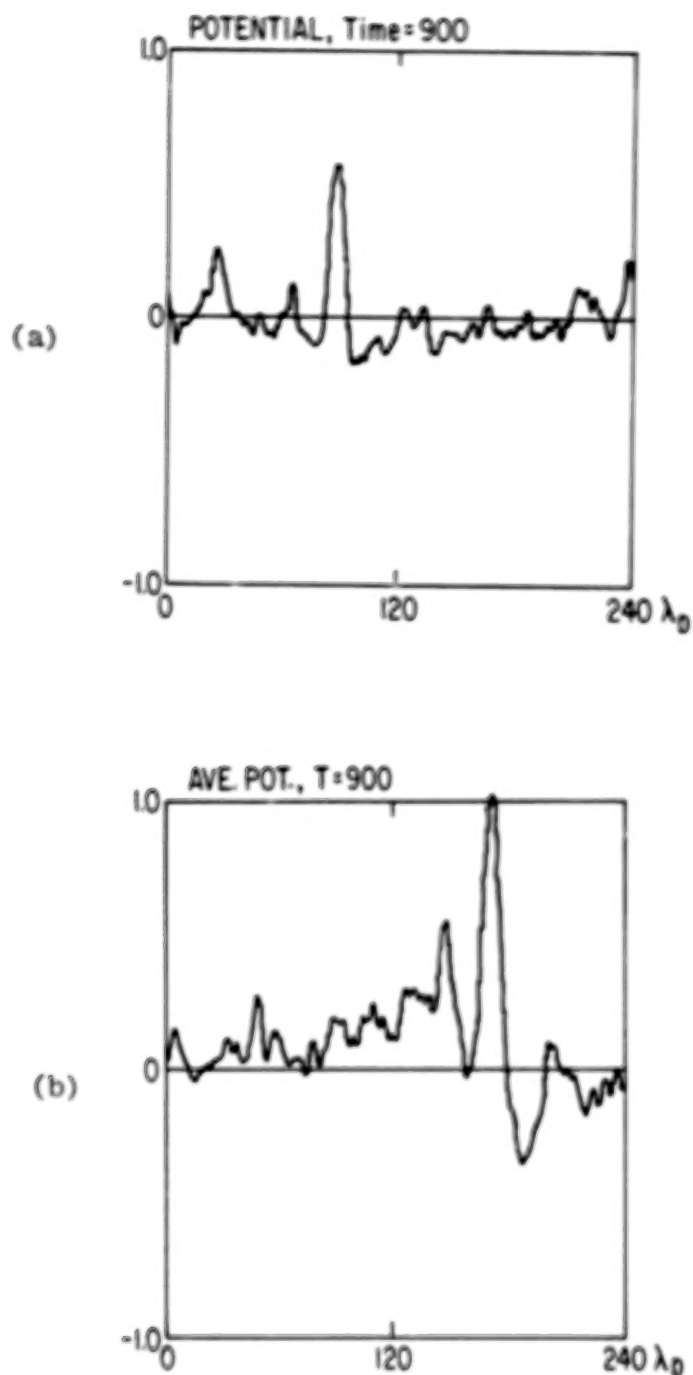


Figure 5. (a) Potential for run 7 at  $\omega_{pe} \Delta t = 900$ ; (b) Potential for run 8 at  $\omega_{pe} \Delta t = 900$ . Parameters in (a) and (b) are the same, except that (a) was periodic, using ES1, and (b) was bounded using PDW1, with particle injection maintained constant as initialized ( $V_H = 0.30$ ,  $V_O = 0.06$ ,  $V_e = 0$  in units of  $a_e$ ) by an external circuit. All potential plots shown are averaged over  $30 \omega_{pe}^{-1}$ .

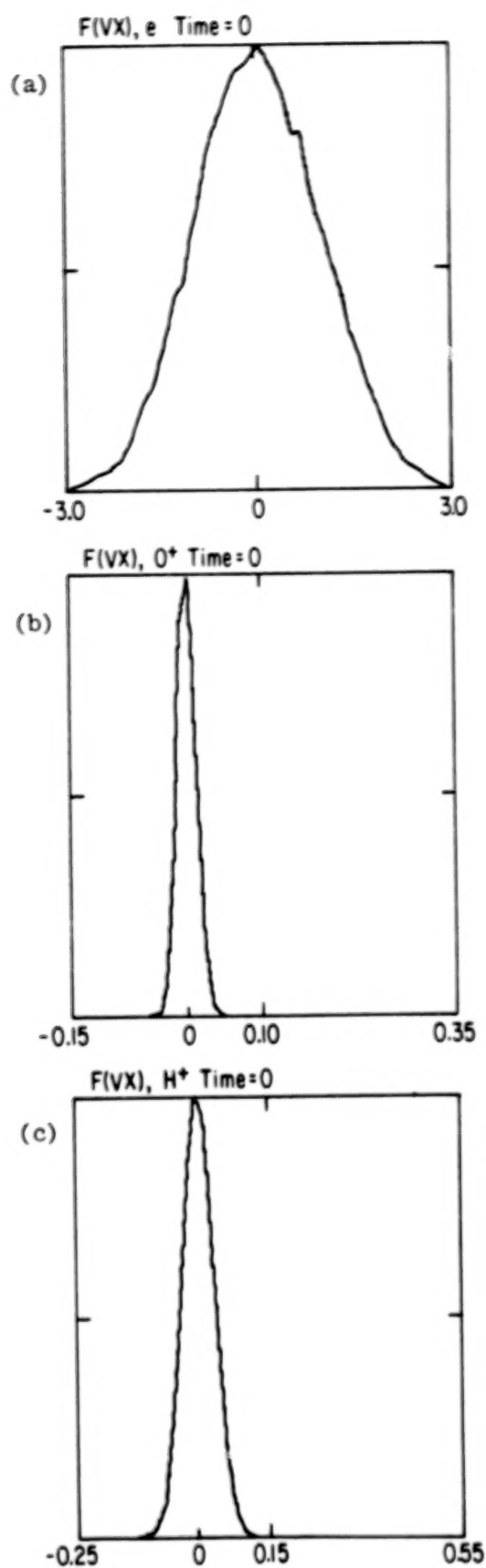


Figure 6. Initial (a) electron, (b) hydrogen, and (c) oxygen distribution functions for runs 9 and 10.

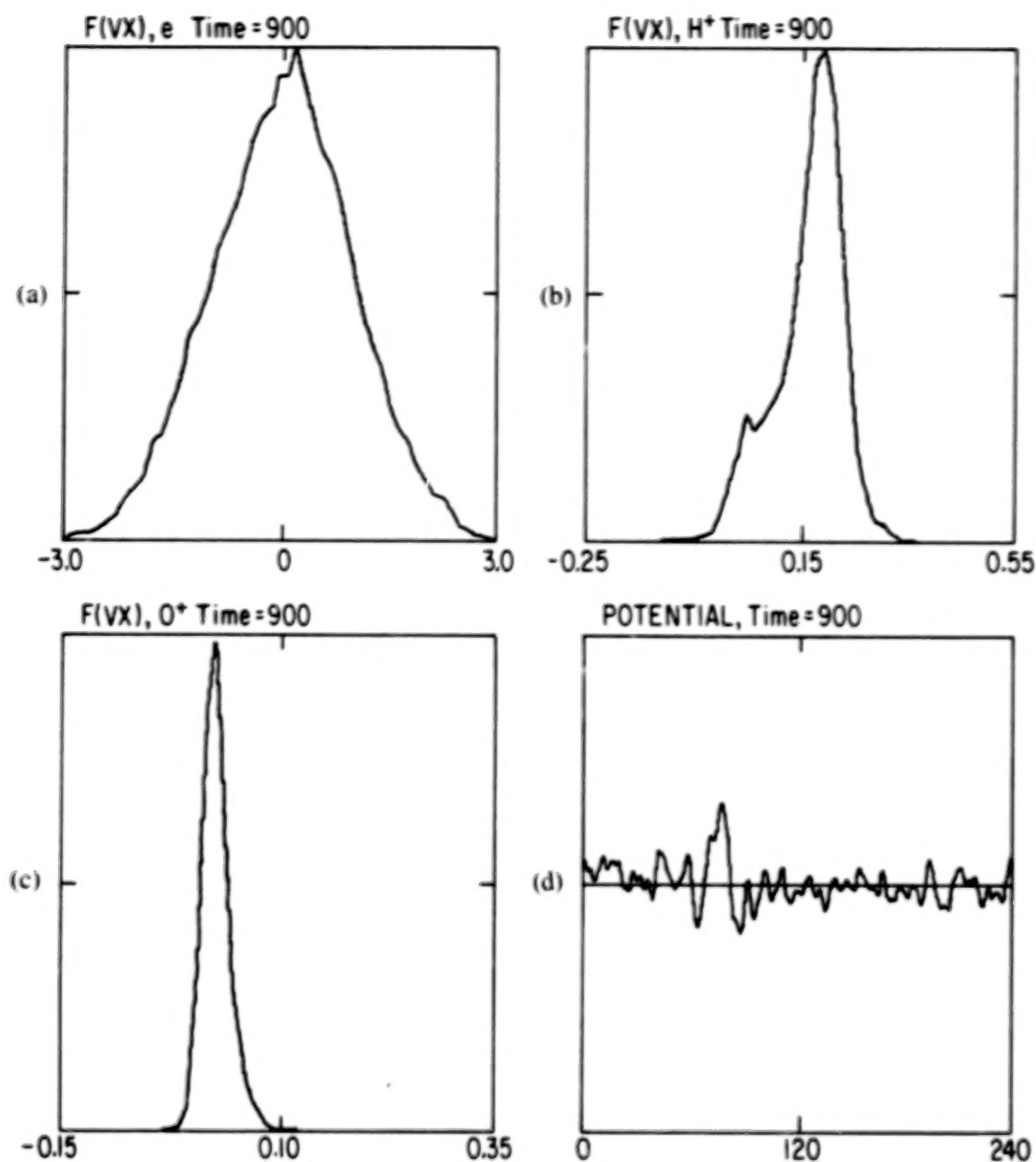


Figure 7. Same plots as Figure 6 for the stronger electric field case  $eE_0/T_e = 2.4/240 \lambda_D$ , at the time an ion hole is beginning to form,  $\omega_{pe} \Delta t = 900$ . The potential averaged over  $30 \omega_{pe}^{-1}$  is also shown in (d).

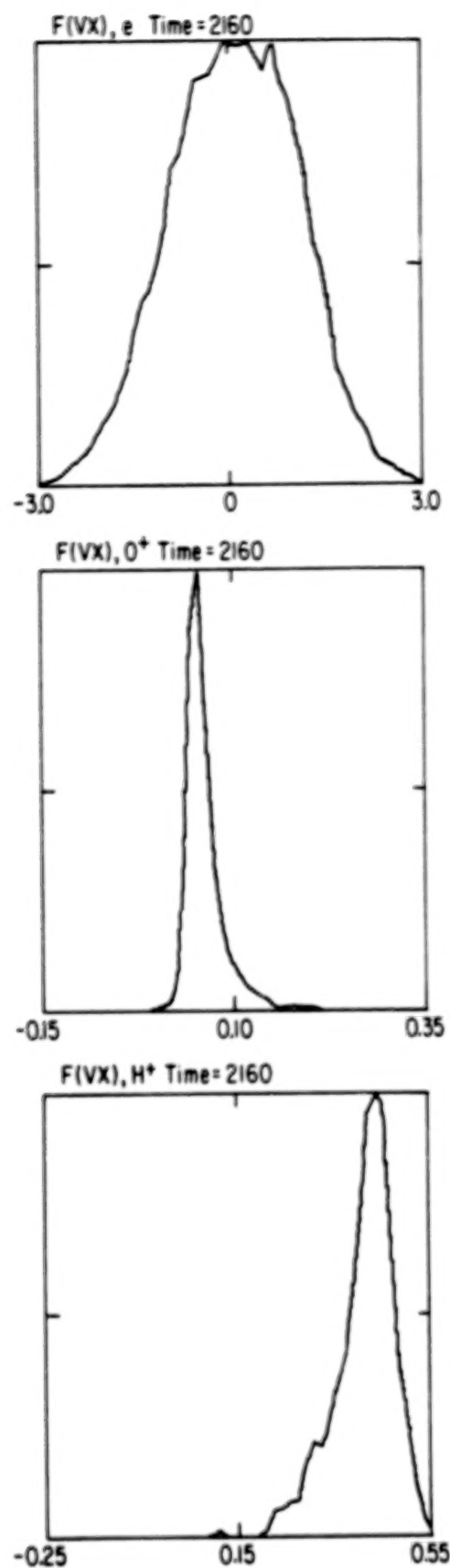


Figure 8. Same plots as Figure 6 for run 9 at  $\omega_{pe} \Delta t = 2160$  when  $V_H = 0.44 a_e$  is becoming comparable to Figure 1.

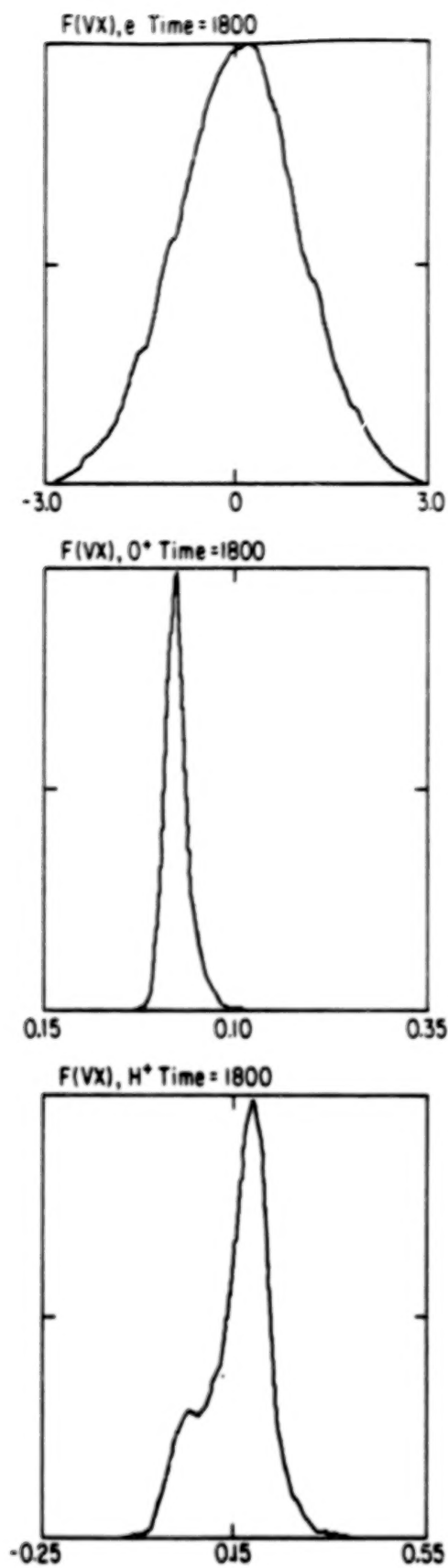


Figure 9. Same plots as Figure 6 for the weaker electric field case, run 10, with  $eE_0/T_e = 1.2/240 \lambda_D$ , at  $\omega_{pe} \Delta t = 1800$ , corresponding to the same amount of ion acceleration as Figure 7.



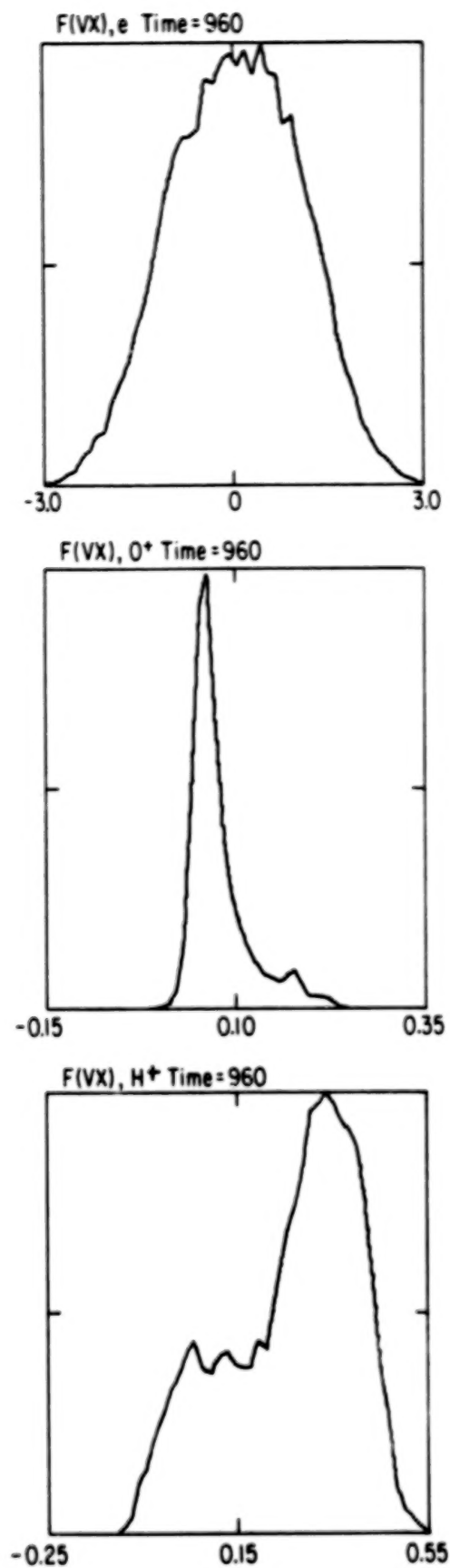


Figure 10. Same plots as Figure 6 for run 3, at the end of the time series shown in Figure 4.

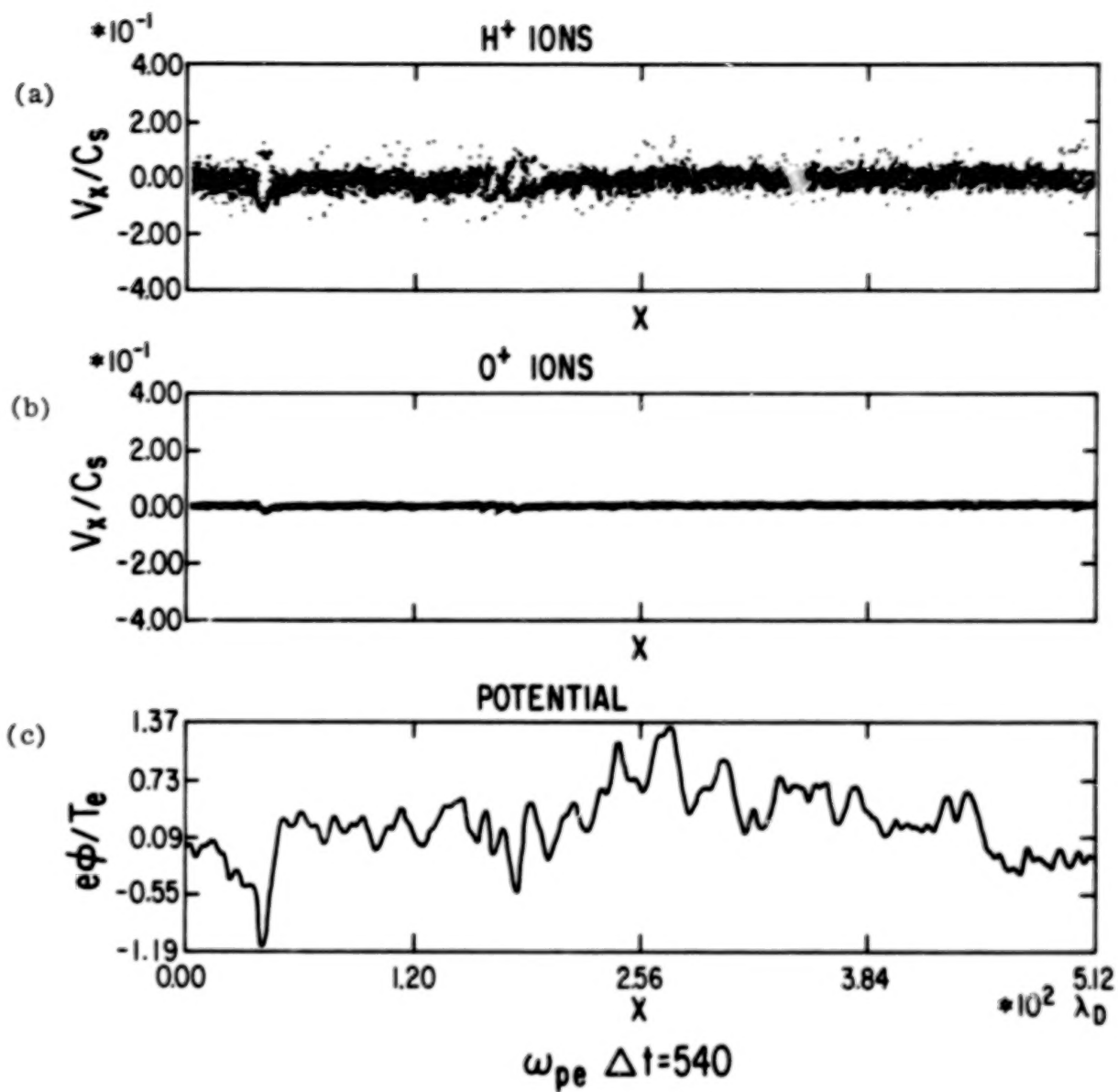


Figure 11. (a) Hydrogen and (b) oxygen distributions, and (c) potential averaged over  $67.5 \omega_{pe}^{-1}$  at  $\omega_{pe} \Delta t = 540$ . One or more double layers are apparent.

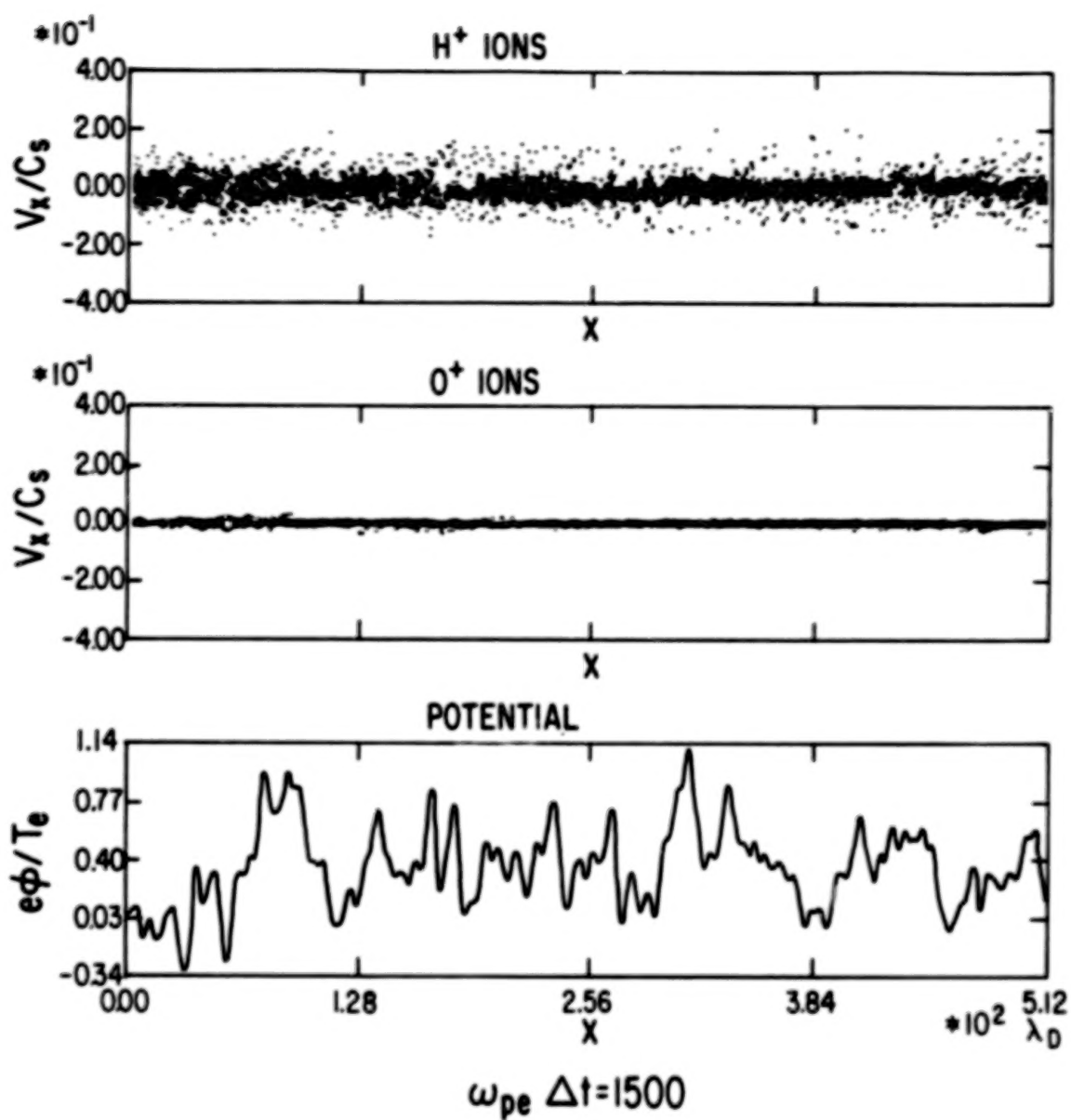


Figure 12. Same as Figure 11 at a later time  $\omega_{pe} \Delta t = 1500$ .

N87

23327

UNCLAS

## PARTICLE SIMULATION OF AURORAL DOUBLE LAYERS

Bruce L. Smith\* and Hideo Okuda  
Princeton Plasma Physics Laboratory  
Princeton, New Jersey 08544, U.S.A.

## ABSTRACT

We report on our work to simulate auroral double layers (DL's) with "realistic" particle-in-cell models. An early model simulated weak DL's formed in a self-consistent circuit but under conditions subject to the ion-acoustic instability. More recent work has focused on strong DL's formed when currentless jets are injected into a dipole magnetic field.

## INTRODUCTION

For several years we have been simulating space plasmas using "realistic" models. These models have included both numerical MHD and particle-in-cell (PIC) codes. Here we discuss two PIC models that simulate auroral double layers (DL's).

An early analysis of DL's was performed by Block (1972). In his model four species of particles, reflecting/passing electrons/ions, were incident upon a strong ( $eV \gg kT$ ) DL. The two fluid equations, an adiabatic equation of state and Poisson's equation, led to two criteria on the drift velocities of ions and electrons incident on the high and low field sides of the DL, respectively. These are called the Bohm criteria in analogy with the similar criterion on ions in a plasma sheath (Bohm, 1949). In Block's model the drifts necessary to sustain the DL result in a net current.

Using these criteria as a recipe, one could easily simulate a DL. Such simulations only required fixed potentials at the boundaries to drive the necessary current or a floating potential (or even periodic boundary conditions) with large enough drifts (i.e., a current) to satisfy the criteria. Although these conditions permit DL's, in auroral regions, where DL's have been observed (Temerin and Mozer, 1984), such conditions may not be present.

Sato and Okuda (1980, 1981) performed a series of simulations with "more realistic" conditions. In one of these simulations they assumed:

1.  $U_{\text{drift } e} < v_{\text{the}}$
2.  $T_e \gg T_i$
3. Floating self-consistent potentials.

This is the range of parameters for ion-acoustic instabilities, but avoids the large relative drifts which may cause the two-stream instability.

Their model was that of the polar region field lines in a self-consistent circuit. Initial conditions included a driving potential and an initial current. The subsequent potential and current were related by a fixed resistance consistent with the initial conditions. One of the results shown in Figure 1 was obtained for  $v_{de}/v_{te} = 0.6$ ,  $M/m = 100$ ,

\* Now at Air Force Office of Scientific Research.

$n\lambda_D = 100$ ,  $w_{pe}\Delta t = 0.2$ . As is apparent, the simulation resulted in multiple weak ( $eV \lesssim kT$ ) DL's about  $1000 \lambda_D$  apart and with scale lengths  $\ell \sim 50 \lambda_D$ . These DL's are unstable and propagate at near the ion-acoustic velocity but recur at a rate such that approximately the same number of DL's are always present.

Hasegawa and Sato (1982) provided the mechanism for such DL's. Basically an ion hole is created which cuts off the electron current. Formation of an adjacent electron hole follows. This yields a DL which decays on the ion time scale.

Other authors have found different ways to relax the constraints imposed by the Bohm criteria. In particular, Kan and Lee (1980) concluded that the condition on the electron velocity was unnecessary if trapped electrons were present. Similarly Perkins and Sun (1981) demonstrated that even currentless DL's could exist. Incidentally, their analysis contrasts with that of Chiu and Schulz (1978) who computed the potential along a mirror magnetic field due to multiple species of ions and electrons using the condition of charge neutrality.

A recent experiment further indicated the possibility for modifying the conditions necessary for creation of DL's. Stenzel et al. (1981) conducted an experiment with a dipole B-field which reflected an incident ion beam. This experiment resulted in strong DL's for varying magnetic field strengths. These, too, were inherently currentless DL's.

The previous investigations compelled us to simulate a flowing neutral plasma injected along a (fully) dipole magnetic field. This model is meant to simulate the storm-generated flow from the reconnection region to the polar auroral regions. Of course, such a flow would cause ions and electrons of the same temperature to have different turning points. As the ions overshoot the electrons, a space charge potential could form and a DL would be present. This model then substantiates a source of energetic electrons for an aurora.

Parameters for the region through which such substorms are supposed to develop are  $n = 10\text{--}1000 \text{ cm}^{-3}$ ,  $B = 10^3\text{--}10^4 \gamma$ , and  $T_e \lesssim T_i \sim 100 \text{ eV}$ . These values yield  $w_{pe} \sim w_{ce} \sim 10^5\text{--}10^6 \text{ rad/s}$  and  $\beta \ll 1$ . In this parameter regime the electrostatic approximation is appropriate (Krall and Trivelpiece, 1973).

## RESULTS

Results for a one-dimensional PIC simulation with  $L/\lambda_D = N_g = 1024$ ,  $M/m = 25$ ,  $w_{pe}\Delta t = 0.25$ , and  $B_{\max}/B_{\min} \approx 25$  are shown. For boundary conditions we chose  $V = 0$  at  $z = 0$  (the "ionosphere") and using symmetry,  $dV/dz = 0$  at  $z = L$  (the "magnetosphere"). Figures 2a-c show the injection of plasma at approximately  $0.8 v_{the}$ . As the plasma drifts into the dipole field, a double layer is evidenced by the acceleration of ions and electrons and by their relative charges at  $L = 600 \lambda_D$  for  $w_{pe}t = 1900$  and  $L = 800 \lambda_D$  for  $w_{pe}t = 2600$ . One notes that the DL is unstable by the modulation (with  $\lambda \sim 25 \lambda_D$ ) and the fact that the DL moves at a velocity  $200 \lambda_D/700/w_{pe} = 2/7 v_{the}$ . This value is on the order of the ion-acoustic velocity.

The f-spectrum for different positions (Fig. 3) shows the presence of a mode at  $w = 0.15\text{--}0.2 w_{pe} \lesssim w_{pi}$  and at  $w = 0.05\text{--}0.1 w_{pe} \ll w_{pi}$ . Similarly the mode structure (Fig. 4) gives wavelengths most strongly peaked at  $\lambda = 0$  and  $\lambda = 60 \lambda_D$ . The data are consistent with a two-stream instability (with  $w \ll w_{pi}$ ). Finally the scale length of the DL is  $kT/eE \sim 50 \lambda_D \gg \lambda_D$ .



In the next panels (Figs. 5 a-d) are shown  $f(v_+)-f(v_-)$  for both electrons and ions at different positions. If there were simply a B-field with no other interaction we would expect a snapshot of the loss cone for such a comparison. Instead the panels clearly show that the electrons accelerate from  $w_{pe1} = 1900$  to  $w_{pe2} = 2800$  as they pass over the DL. Similarly the ions slow down and cool during this same time. (This cooling of ions may allow an ion-acoustic instability.)

In the final panels (Fig. 6) we show the measured energies from the simulation. As can be seen in the first panel, total energy is conserved to within less than 1 percent. One also sees that the ion kinetic energy is converted to electron kinetic energy until the two are approximately equal. Surprisingly, the collective potential energy is a small fraction of the total.

A theory for this model was derived by Serizawa and Sato (unpublished manuscript). Using an adiabatic approximation, their kinetic analysis showed that  $eV \approx KE_i/(1 + T_i/T_e)$  with small variations predicted for mass ratios  $m/M \ll 1$  and mirror ratios  $B_{max}/B_{min} \gg 1$ . A plot of  $eV$  versus  $KE_i$  for varying  $KE_i$  confirms the linear relation between these quantities (Fig. 7).

Similar results for ions and electrons streamed from both ends are obtained.

## CONCLUSION

In conclusion, simulations have been undertaken to model aurorae under realistic conditions. The simulation of ion acoustic DL's in a self-consistent circuit showed multiple DL's with  $eV/kT \leq 1$ . Currentless DL's with  $eV \gg kT$  have been demonstrated. Although not discussed here, these simulations furthered the theory of Fourier transforms for bounded systems and successfully demonstrated the utility of a guiding center code for electrons. Currently two-dimensional codes are being tested to verify the one-dimensional results and to study two-dimensional instability mechanisms.

## REFERENCES

- Block, L. P., *Cosmic Electrodynamics*, 3, 349 (1972).
- Bohm, D., in *The Characteristics of Electrical Discharges in Magnetic Fields*, edited by A. Guthrie and R. K. Wakerling, p. 77, McGraw-Hill, New York, 1949.
- Chiu, Y. T., and M. Schulz, *J. Geophys. Res.*, 83, 629 (1978).
- Hasegawa, A., and T. Sato, *Phys. Fluids*, 25, 632 (1982).
- Kan, J. R., and L. C. Lee, *J. Geophys. Res.*, 85, 788 (1980).
- Krall, N. A., and A. W. Trivelpiece, in *Principles of Plasma Physics*, p. 427, McGraw-Hill, New York, 1973.
- Perkins, F. W., and Y. C. Sun, *Phys. Rev. Lett.*, 46, 115 (1981).
- Sato, T., and H. Okuda, *Phys. Rev. Lett.*, 44, 740 (1980).
- Sato, T., and H. Okuda, *J. Geophys. Res.*, 86, 3357 (1981).
- Serizawa, Y., and T. Sato, unpublished report on "Generation of Large Scale Potential Difference by Currentless Plasma Jets Along the Mirror Field."
- Stenzel, R. L., M. Ooyama, and Y. Nakamura, *Phys. Fluids*, 24, 708 (1981).
- Temerin, M., and F. Mozer, in *Second Symposium on Plasma Double Layers and Related Topics*, edited by R. Schrittwieser and G. Eder, p. 119, University of Innsbruck, 1984.

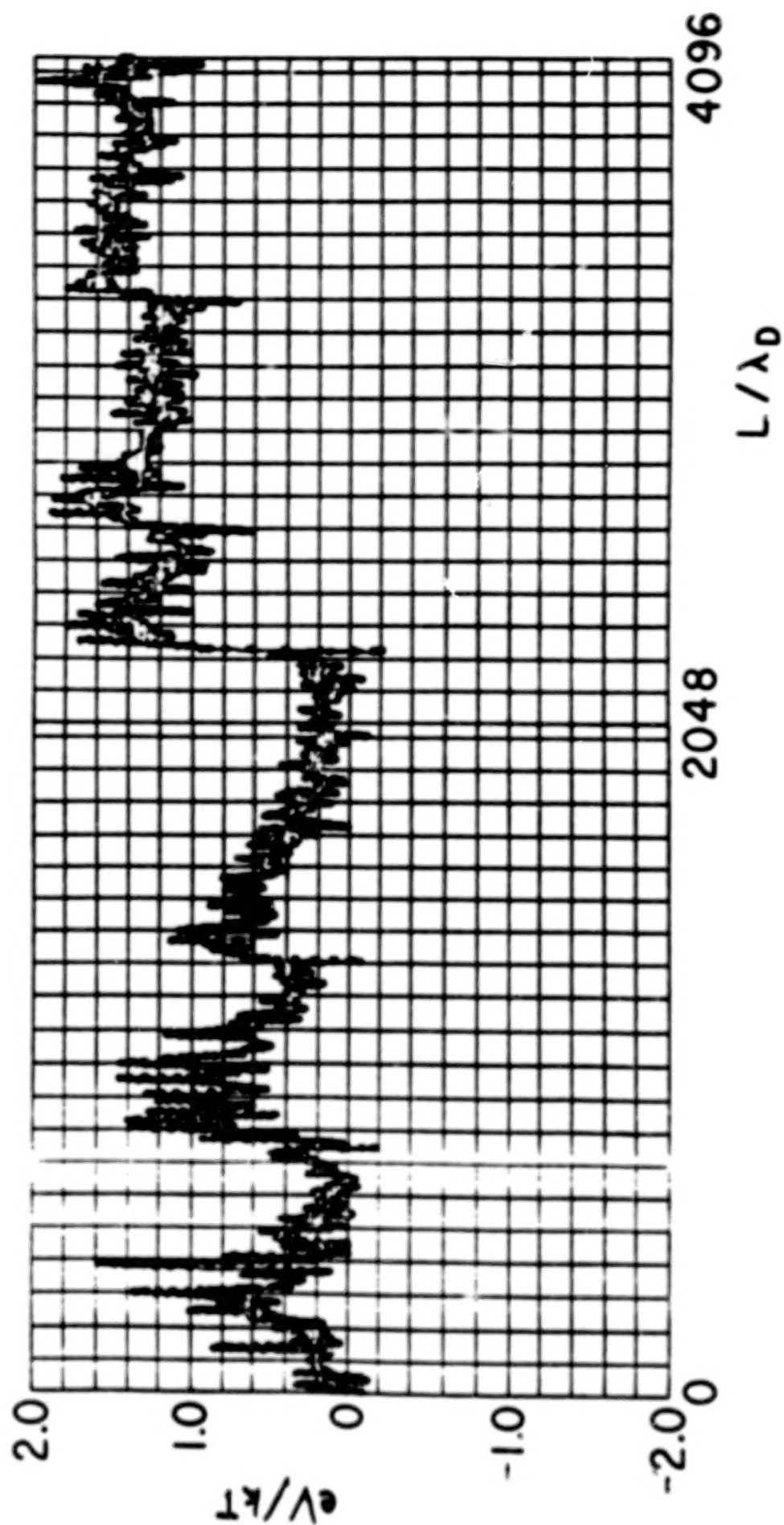


Figure 1. The electric potential as a function of position showing the formation of multiple weak double layers. The simulation results here are due to Sato and Okuda (1980, 1981).

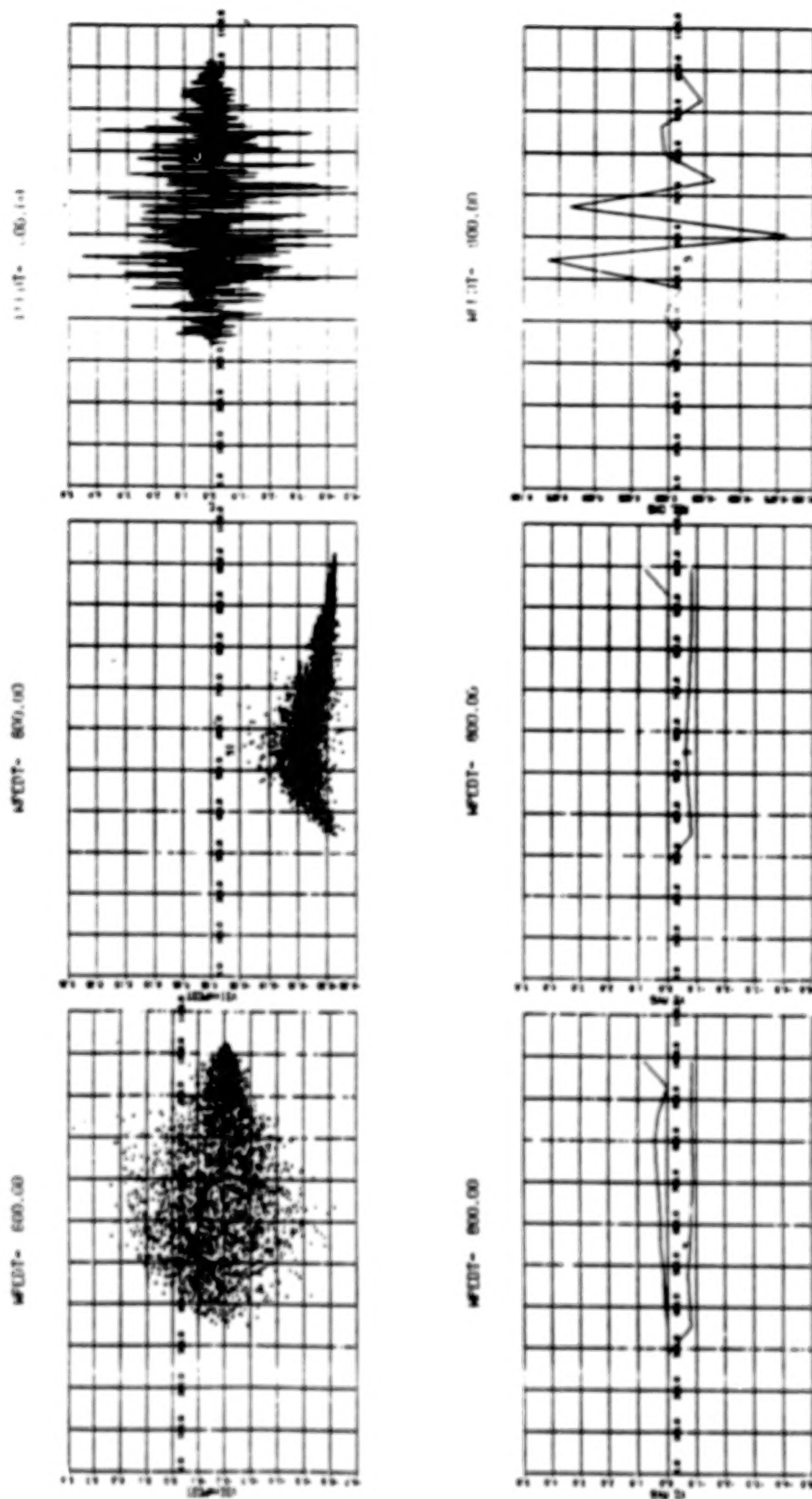


Figure 2. Results for a one-dimensional simulation with  $L/\lambda_0 = N_g = 1024$ ,  $M/m = 25$   
 $B_{max}/B_{min} \approx 25$ , and  $w_{pe}\Delta t$  as indicated by the value of  
 $WPEdT$  in the figures.

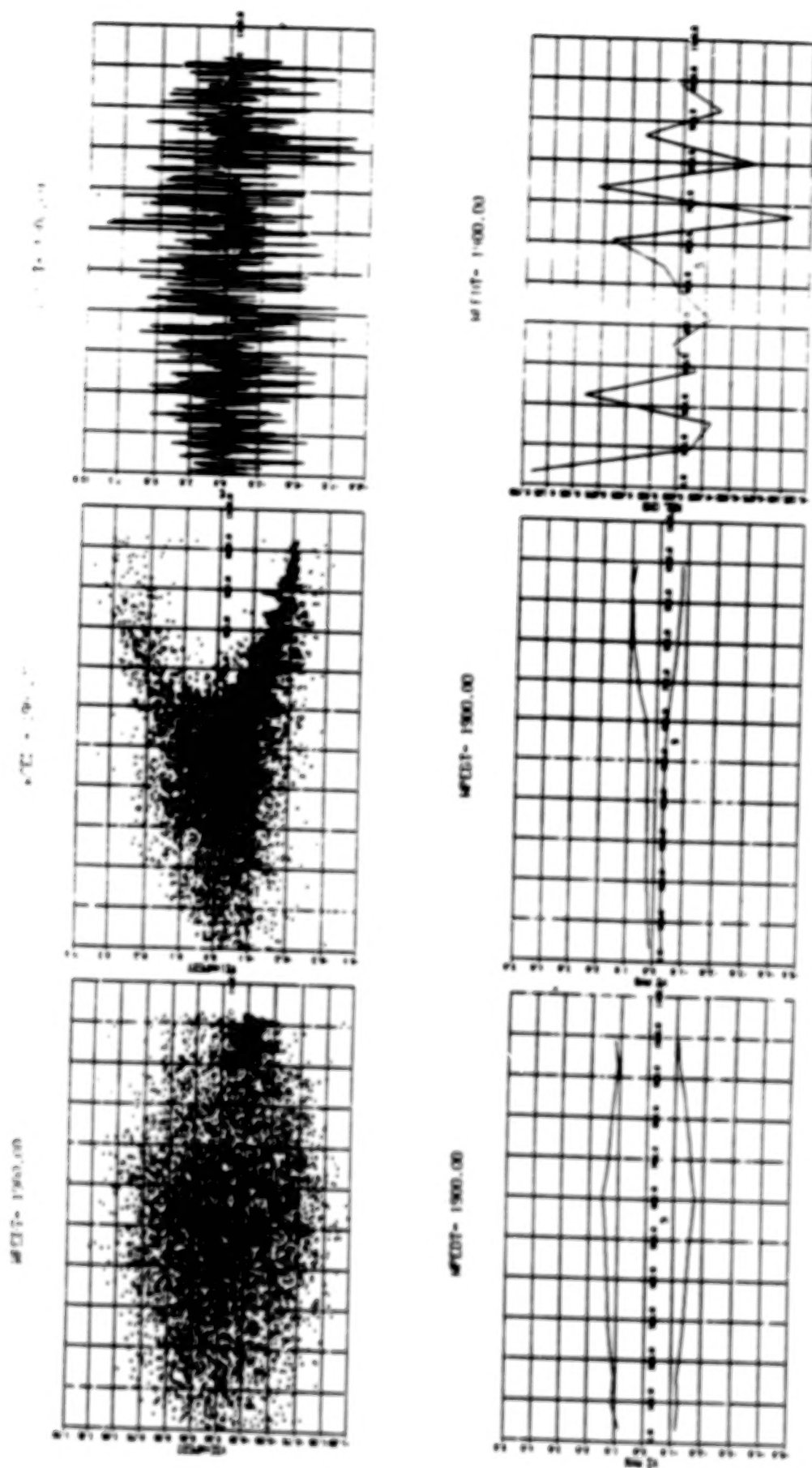


Figure 2. (Continued)

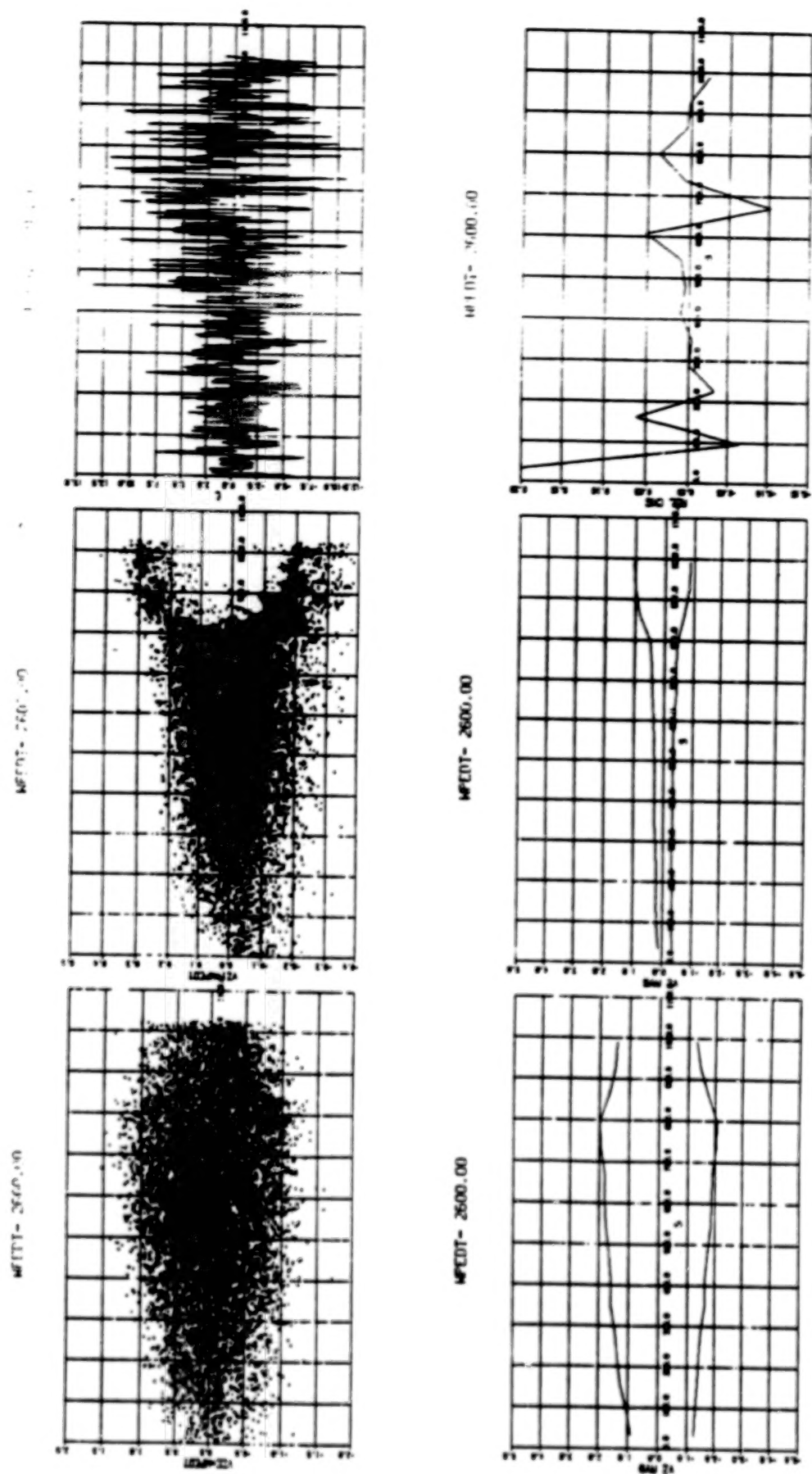


Figure 2. (Concluded)



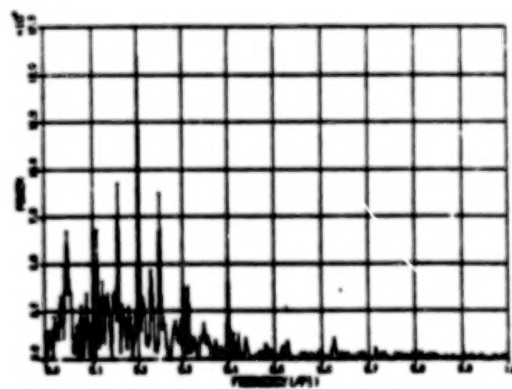
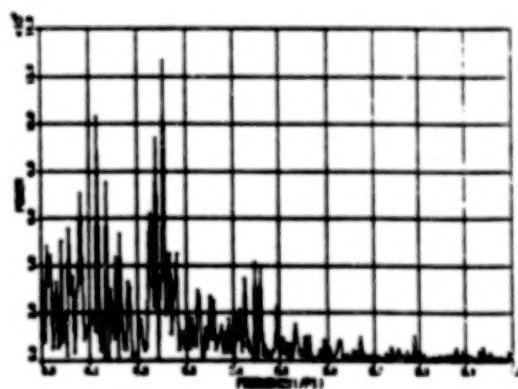
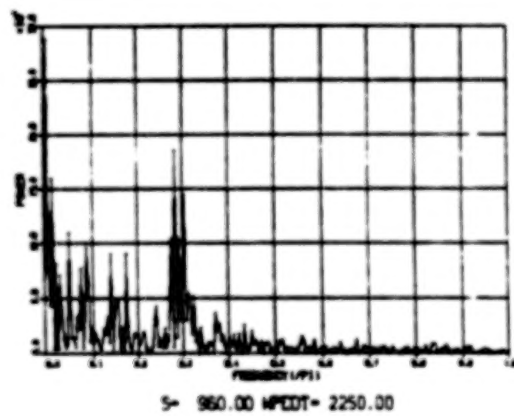
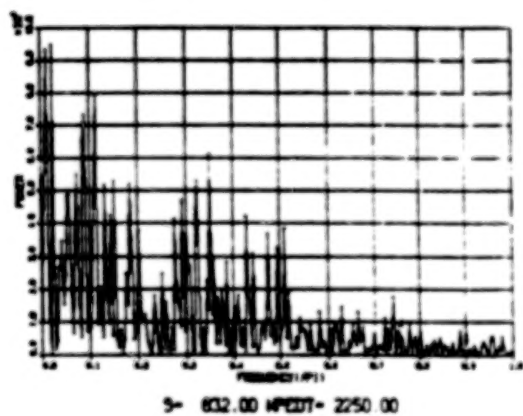
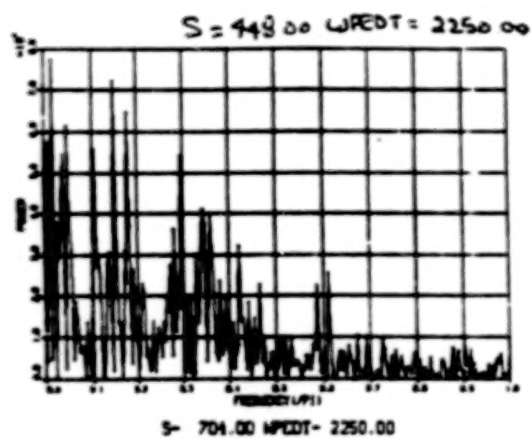
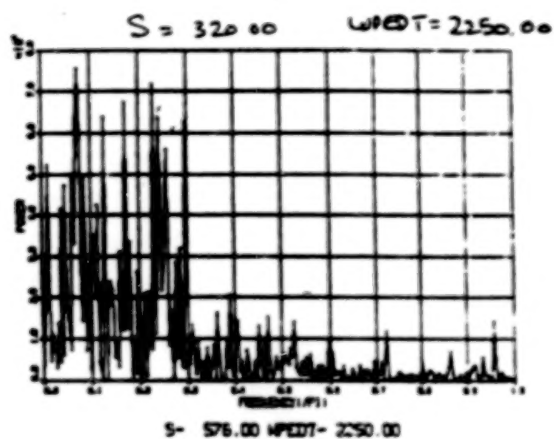
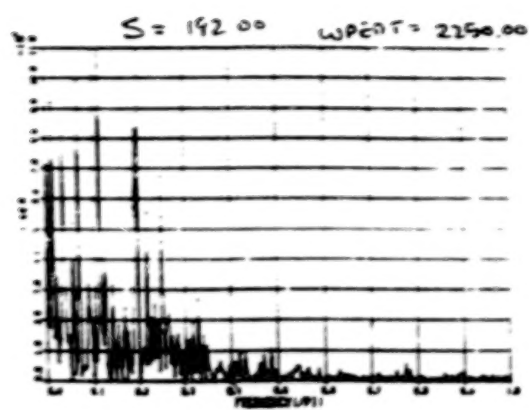
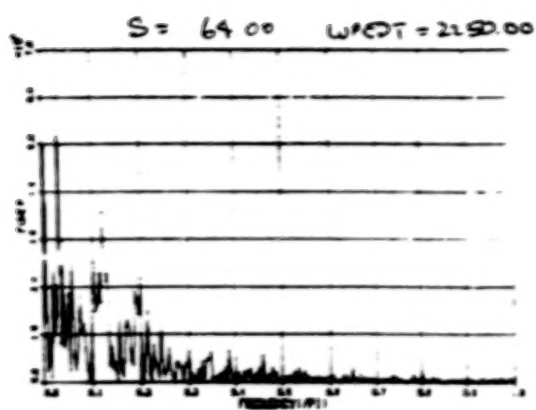


Figure 3. The frequency spectrum for different positions with  $w_{pe}\Delta t = 2250$ .



ORIGINAL PAGE IS  
OF POOR QUALITY

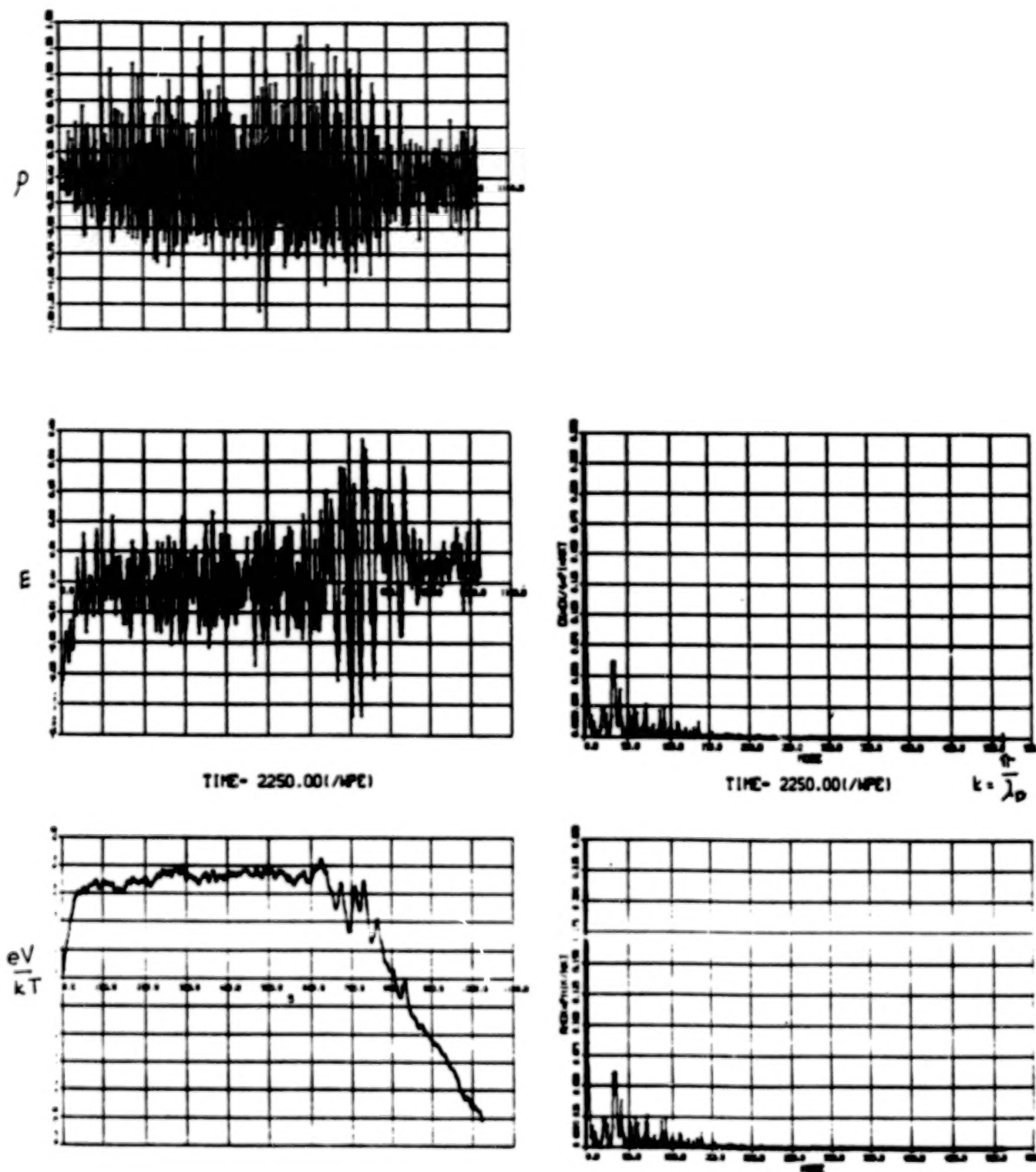
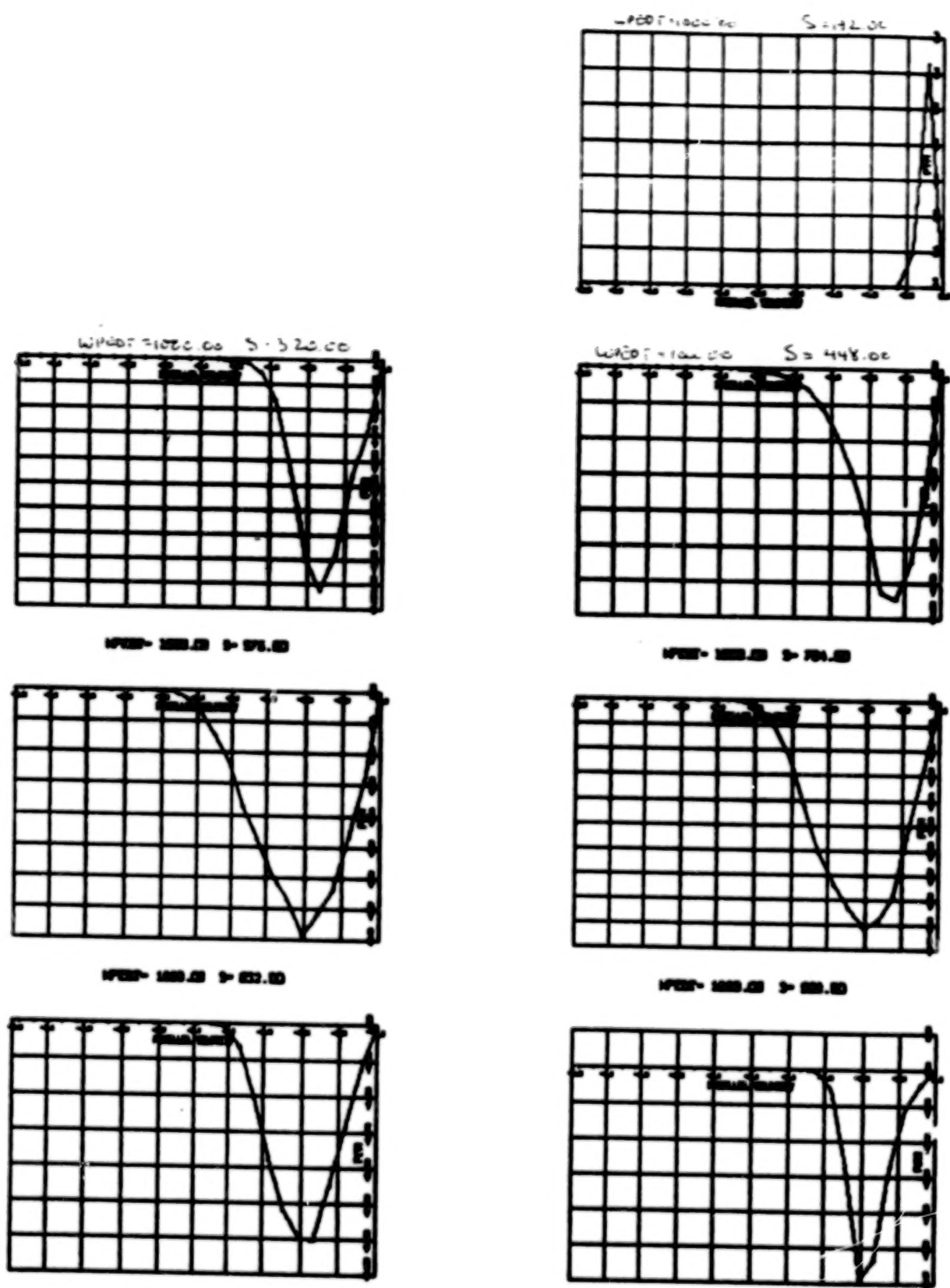


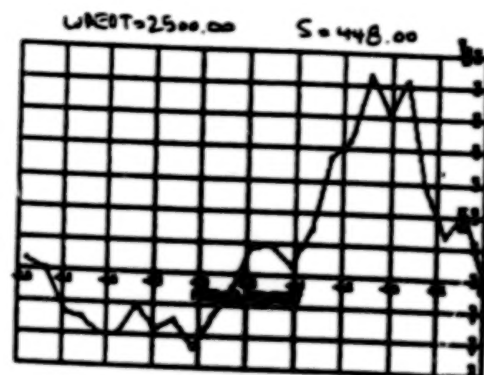
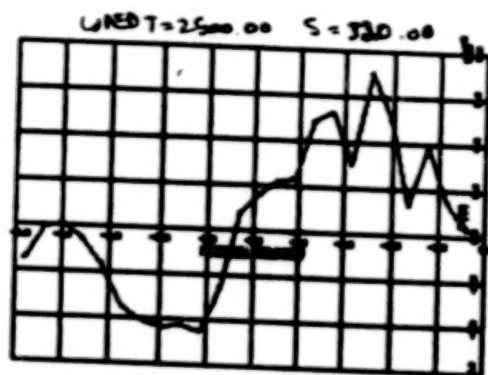
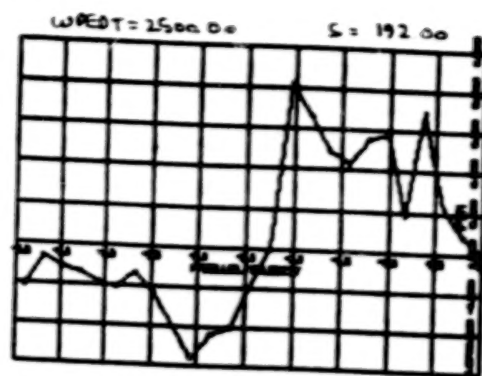
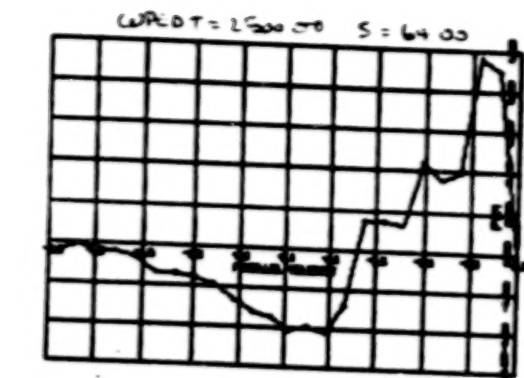
Figure 4. The charge density, electric potential, electric field intensity, and mode structure from the simulations of Figure 3.



(a)

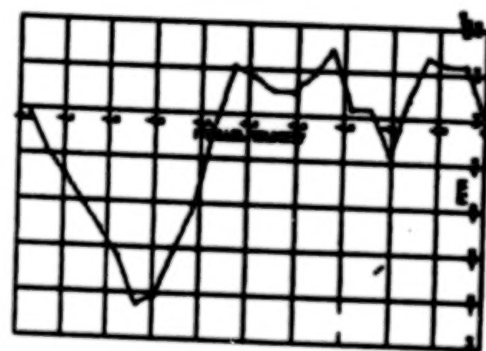
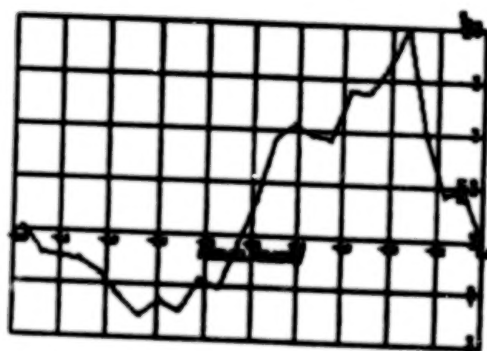
Figure 5. A plot of  $f(v_+) - f(v_-)$  for the electrons and ions at various positions.

ORIGINAL PAGE IS  
OF POOR QUALITY



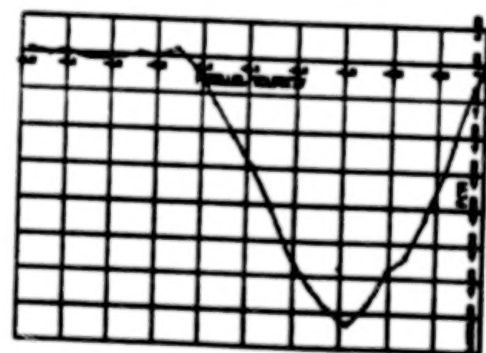
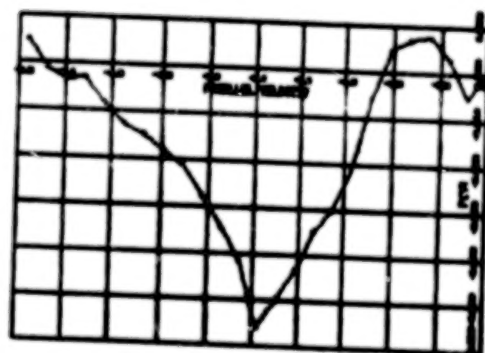
WPEOT = 2500.00 S = 576.00

WPEOT = 2500.00 S = 704.00



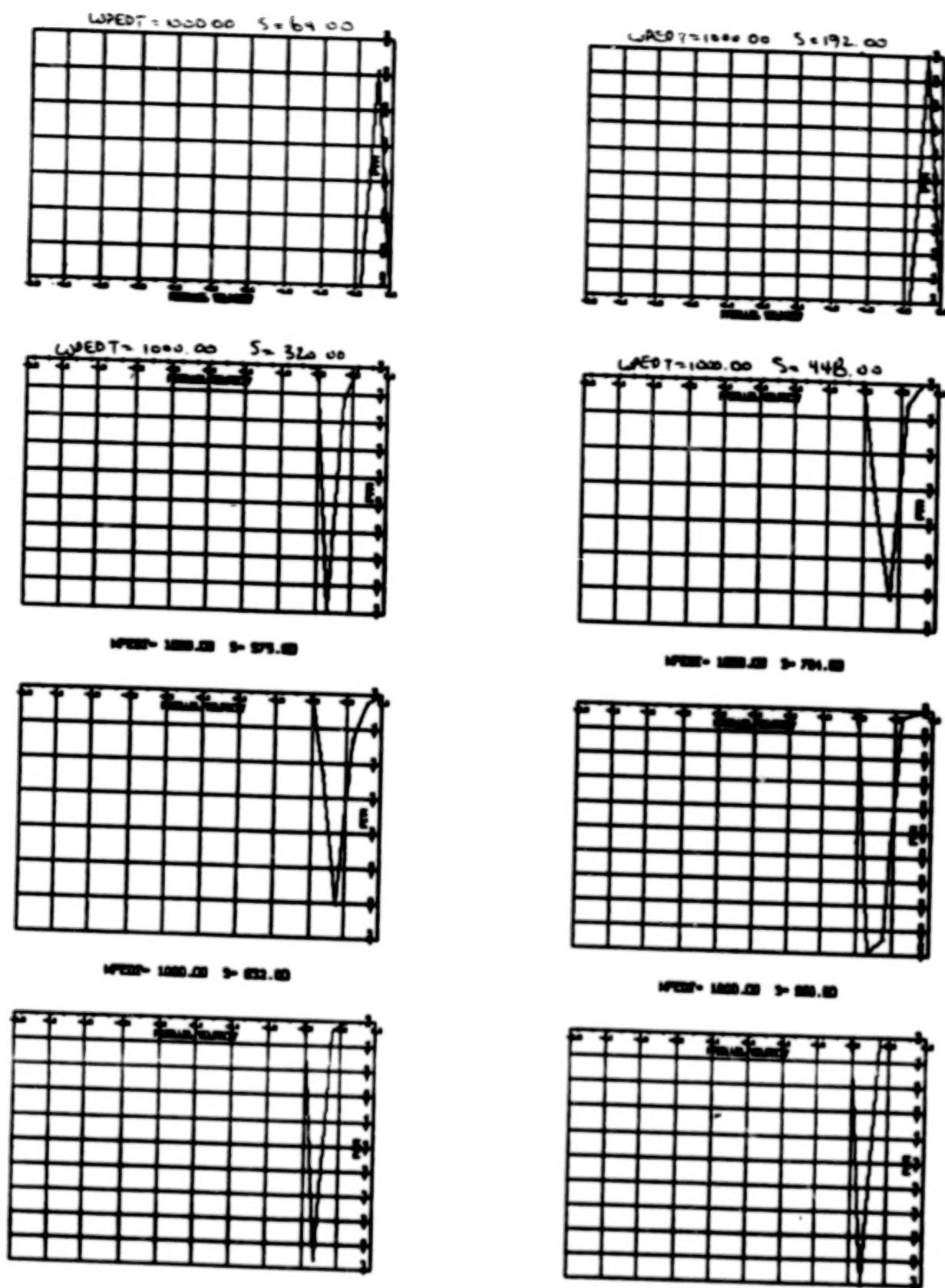
WPEOT = 2500.00 S = 832.00

WPEOT = 2500.00 S = 960.00



(b)

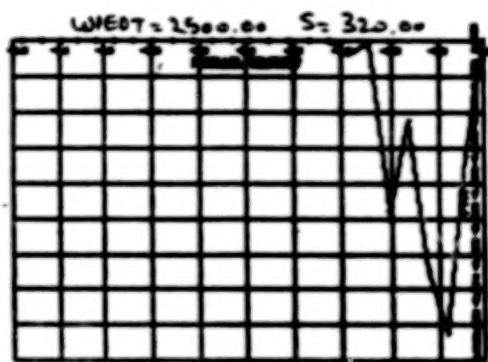
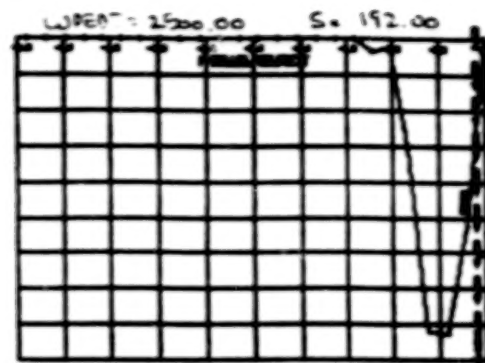
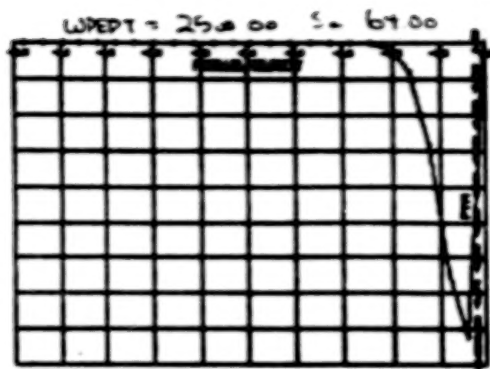
Figure 5. (Continued)



(c)

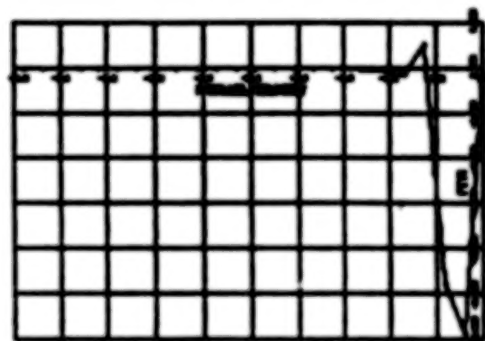
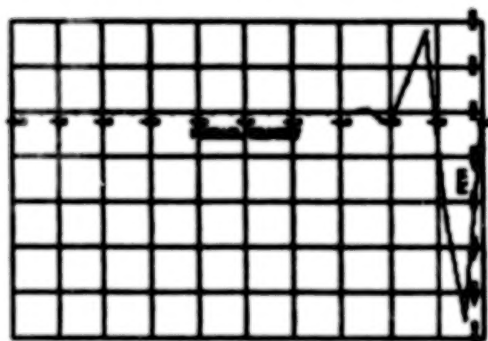
Figure 5. (Continued)

ORIGINAL PAGE IS  
OF POOR QUALITY



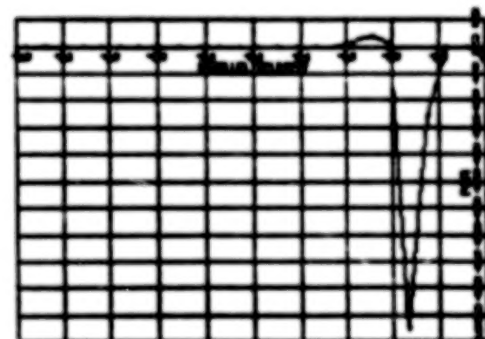
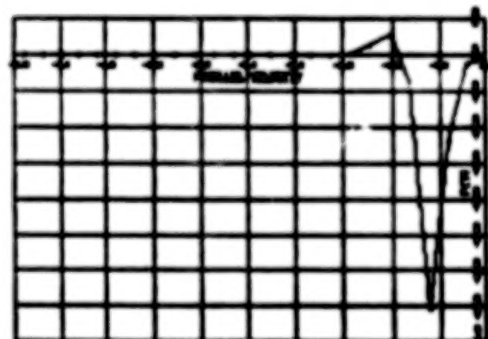
WPEPT = 2500.00 S = 576.00

WPEPT = 2500.00 S = 704.00



WPEPT = 2500.00 S = 832.00

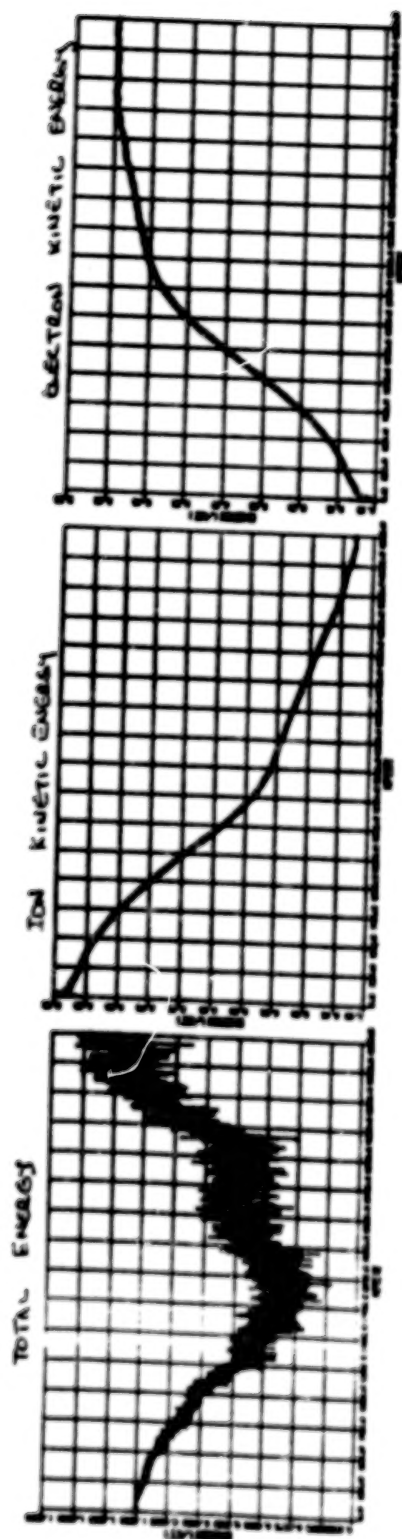
WPEPT = 2500.00 S = 960.00



(d)

Figure 5. (Concluded)





ORIGINAL PLOT  
OF POOR QUALITY

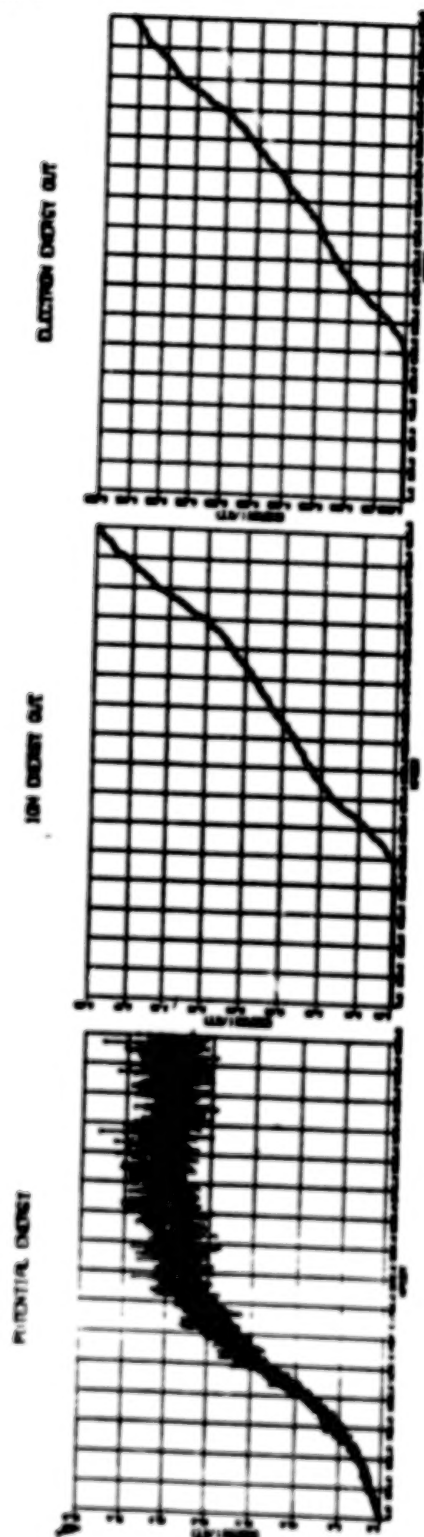


Figure 6. The calculated energies implicit in the simulation results.



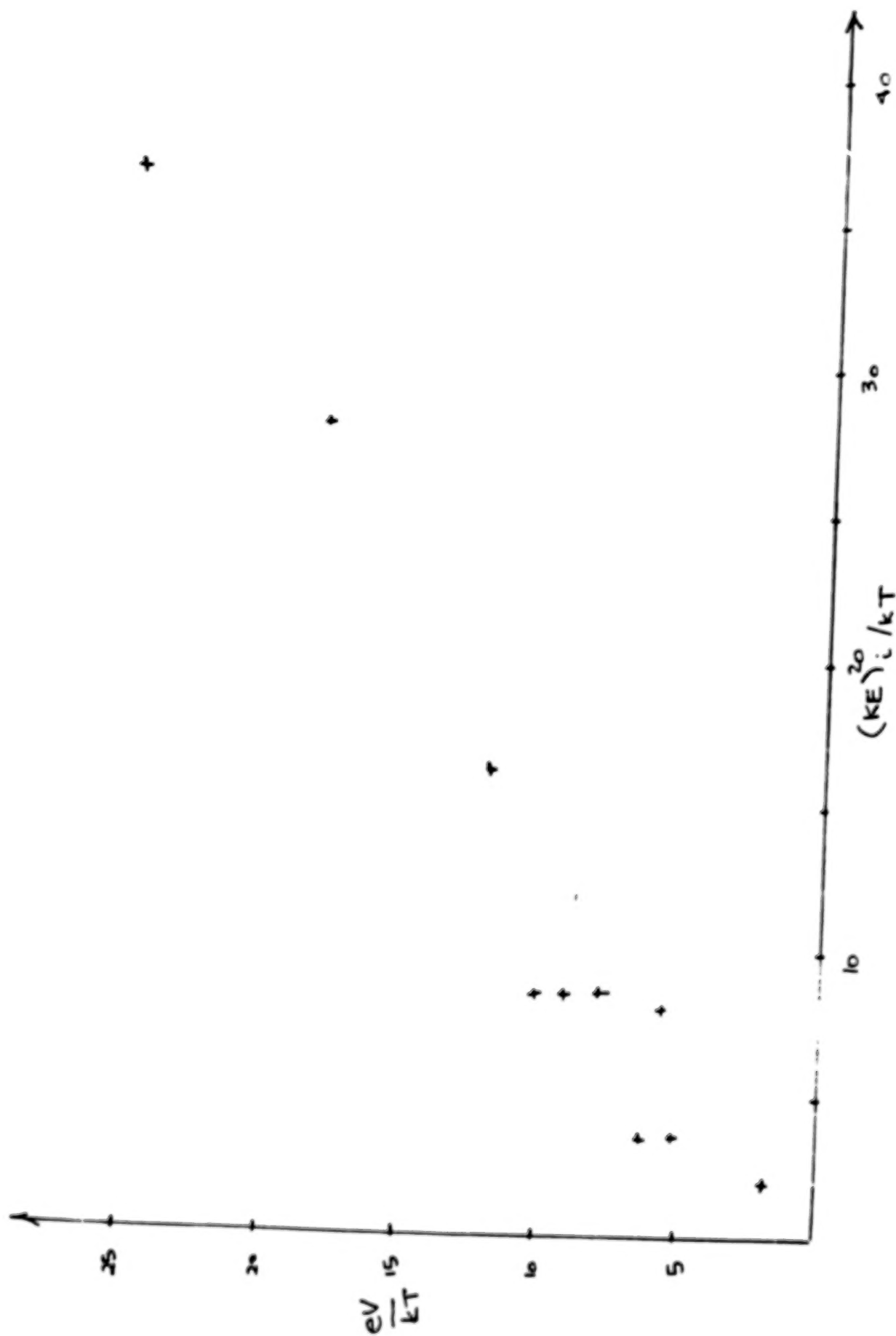


Figure 7. A plot of the double layer potential eV versus the ions kinetic energy.

### **III. SPACE APPLICATIONS**

**PRECEDING PAGE BLANK NOT FILMED**

N87

23328

UNCLAS

# CONDITIONS FOR DOUBLE LAYERS IN THE EARTH'S MAGNETOSPHERE AND PERHAPS IN OTHER ASTROPHYSICAL OBJECTS

L. R. Lyons  
Space Sciences Laboratory, M2-260  
The Aerospace Corporation  
P.O. Box 92957  
Los Angeles, California 90009, U.S.A.

## ABSTRACT

Double layers (i.e., electric fields parallel to  $\mathbf{B}$ ) form along auroral field lines in the Earth's magnetosphere. They form in order to maintain current continuity in the ionosphere in the presence of a magnetospheric electric field  $\mathbf{E}$  with  $\nabla \cdot \mathbf{E} \neq 0$ . Features which govern the formation of the double layers are: (1) the divergence of  $\mathbf{E}$ , (2) the conductivity of the ionosphere, and (3) the current-voltage characteristics of auroral magnetic field lines. Astrophysical situations where  $\nabla \cdot \mathbf{E} \neq 0$  is applied to a conducting plasma similar to the Earth's ionosphere are potential candidates for the formation of double layers. The region with  $\nabla \cdot \mathbf{E} \neq 0$  can be generated within, or along field lines connected to, the conducting plasma. In addition to  $\nabla \cdot \mathbf{E}$ , shear neutral flow in the conducting plasma can also form double layers.

## I. INTRODUCTION

Here I describe the large-scale, electrodynamical phenomena that give rise to the formation of double layers in the Earth's magnetosphere. I point out what I believe are the important features which might be found in association with other astrophysical objects, and which could produce double layers analogous to those associated with the Earth.

In the laboratory, double layers form if one tries to drive a current through a plasma that is greater than that which can be carried by the available charge particles in a plasma. The same situation occurs along auroral magnetic field lines. When the magnetosphere-ionosphere system tries to drive a current with a density greater than can be carried by the plasma available to flow along field lines, a field-aligned potential drop  $V_{\parallel}$  forms. This  $V_{\parallel}$  accelerates electrons toward the atmosphere, and the accelerated electrons form discrete auroral arcs.

In this discussion, I do not distinguish between double layers, where large  $V_{\parallel}$ 's occur across short distances, and smoothly varying potentials, where  $V_{\parallel}$ 's are distributed over large distances along field lines. The overall electrodynamics is the same for both situations.

## II. CONDITIONS FOR DOUBLE LAYERS

Three critical features of the Earth's magnetosphere-ionosphere system are involved in the formation of significant ( $\geq 1$  kV)  $V_{\parallel}$ 's along auroral magnetic field lines. These are listed in Figure 1.

First, it is necessary to drive a current with a non-zero divergence. In the magnetosphere, the large-scale, convection electric  $\mathbf{E}$  has  $\nabla \cdot \mathbf{E} \neq 0$  across auroral field lines. This divergence in  $\mathbf{E}$  maps along field lines to the ionosphere.

Second, the ionosphere has a layer of high conductivity perpendicular to the magnetic field  $\mathbf{B}$ . This conductivity results from collisions between ionospheric particles and the neutral atmospheric particles. Thus, an electric field with  $\nabla \cdot \mathbf{E} \neq 0$  in the ionosphere drives Pedersen (parallel to  $\mathbf{E}$ ) currents  $\mathbf{I}_p$  in the ionosphere with  $\nabla \cdot \mathbf{I}_p \neq 0$ . This divergence in  $\mathbf{I}_p$  must be balanced by field-aligned currents to maintain current continuity in the ionosphere.

Third, if the intensity of the required field-aligned current density  $j_{\parallel}$  exceeds that which can be carried by plasma flowing along field lines with  $V_{\parallel} = 0$ , then a  $V_{\parallel} \neq 0$  must form.

Any astrophysical situation where an electric field drives a current  $\mathbf{I}$  perpendicular to  $\mathbf{B}$ , with  $\nabla \cdot \mathbf{I} \neq 0$ , has the potential for forming  $V_{\parallel}$ 's along  $\mathbf{B}$ . A layer with significant conductivity perpendicular to  $\mathbf{B}$  would be an attractive candidate for having currents with  $\nabla \cdot \mathbf{I} \neq 0$ .

To determine whether a  $V_{\parallel}$  will form, we must evaluate the  $j_{\parallel}$  versus  $V_{\parallel}$  characteristics of magnetic field lines for  $j_{\parallel}$ 's of the magnitude expected from  $\nabla \cdot \mathbf{I}$ . Currents associated with aurora on the Earth typically have  $j_{\parallel} \sim 1$ -10  $\mu\text{A}/\text{m}^2$ . Two particle populations can contribute to this current: the ionospheric plasma moving up along field lines, and magnetospheric plasma (from the plasmasheet) which precipitates into the atmosphere. Only magnetospheric particles within the loss cone contribute to  $j_{\parallel}$ , since particles outside the loss cone mirror above the atmosphere.

Downward  $j_{\parallel}$ 's can result from ionospheric electrons moving upward and from the precipitation of magnetospheric ions. However, ionospheric electrons can generally supply a  $j_{\parallel} > 10 \mu\text{A}/\text{m}^2$  to a downward  $j_{\parallel}$ , so that  $V_{\parallel}$ 's do not generally form for downward  $j_{\parallel}$ 's.

On the other hand, the maximum  $j_{\parallel}$  that can be carried by ionospheric ions is generally  $< 1 \mu\text{A}/\text{m}^2$ . Thus, the precipitation of magnetospheric electrons must be considered for upward  $j_{\parallel}$ 's. For typical parameters of plasmasheet electrons, the maximum  $j_{\parallel}$  that can be supplied by the precipitation of magnetospheric electrons is  $\sim 1 \mu\text{A}/\text{m}^2$  for  $V_{\parallel} = 0$ . However, increasing  $V_{\parallel}$  increases  $j_{\parallel}$  by enhancing the flux of electrons in the loss cone. The relation between  $j_{\parallel}$  and  $V_{\parallel}$  along auroral field lines was obtained by Knight (1973), and is shown in Figure 2.

Figure 2 shows  $j_{\parallel}$  versus  $V_{\parallel}$  for an electron density  $n = 1 \text{ cm}^{-3}$  and an electron thermal energy  $K_{\text{th}} = 1 \text{ keV}$ , values which are reasonable for the plasmasheet. Results for other values of  $n$  and  $K_{\text{th}}$  can be obtained from the normalizations given in the figure. Curves are shown for various values of the ratio between the magnetic field in the ionosphere  $B_i$  and the magnetic field  $B_v$  at the top of the region where significant potential variation exists along field lines. Satellite observations (Gorney et al., 1981) indicate that  $B_i/B_v \approx 30$  is reasonable. Notice from Figure 2 that upward  $j_{\parallel}$ 's  $\sim 1$ -10  $\mu\text{A}/\text{m}^2$  require the existence of  $V_{\parallel}$ 's  $\sim 1$ -10 kV. Such  $V_{\parallel}$ 's are of the magnitude observed over auroras.

Figure 3 illustrates a way in which an  $\mathbf{E}$  with  $\nabla \cdot \mathbf{E} \neq 0$  develops in the Earth's magnetosphere. Both open, polar-cap field lines connected with the interplanetary field and closed, lower latitude field lines are shown. Solar wind flow across the open polar cap field lines forms a dawn-to-dusk electric field across the open field line region, and the electric field changes direction across the boundary between open and closed field lines. The boundary is thus charged as indicated in the figure. Mapping the electric field to the ionosphere gives  $\nabla \cdot \mathbf{I}_p < 0$  and upward  $j_{\parallel}$ 's on the dusk side, and  $\nabla \cdot \mathbf{I}_p > 0$  and downward  $j_{\parallel}$ 's on the dawn side. The magnitude of  $\nabla \cdot \mathbf{I}_p$  gives large enough  $j_{\parallel}$ 's on the dusk side to require a  $V_{\parallel} > 0$ .

Similar situations as shown in Figure 3 should occur in the magnetospheres of other magnetized, solar system planets, and could exist in association with other magnetized, astrophysical objects. Also, regions of  $\nabla \cdot \mathbf{E} \neq 0$  can be formed by plasma sources, such as Io, that move across field lines within a magnetosphere.

Figure 4 shows that the observed change in  $\mathbf{E}$  across the dusk auroral zone can account for the observed magnitude of auroral  $V_{\parallel}$ 's and precipitation intensities. The observations (Gurnett and Frank, 1973) were from a low-altitude satellite. An electric field of 0.12 V/m was observed across the auroral region, and the equation for

current continuity in the ionosphere was solved (Lyons, 1980) for an electric field of magnitude 0.06 V/m on each side of the reversal. The resulting values of  $V_i$  and precipitating electron energy fluxes are shown in Figure 4 as a function of latitudinal distance. These can be seen to compare well in magnitude with values obtained from electron observations on the satellite. The auroral observations in Figure 4 have more structure than that obtained from the simple solution to the current continuity equation. However, this type of structure, which is typical of discrete auroral arcs, can be explained as a result of more detailed structure in the magnetospheric electric field (Lyons, 1981; Chiu et al., 1981).

So far, the discussion here has been under the assumption that the velocity  $V_n$  of neutrals in the conducting layer is zero. Including  $V_n$ ,  $I_p$  may be written as the difference between the electric field drift velocity  $V_E$  and  $V_n$ :

$$I_p = \Sigma_P (-V_E + V_n) \times B$$

where  $\Sigma_P$  is the layer-integrated Pedersen conductivity. Since  $j_{\parallel} = -\nabla \cdot I_p$ , the above relation shows that shears in  $V_n$ , as well as shears in  $V_E$ , can cause field-aligned currents within a conducting layer.

Generally, thermospheric neutral winds in the conducting region of the Earth's ionosphere are not sufficiently large to generate  $V_i$ 's. However, this is not necessarily always the case. Recently, Lyons and Walterscheid (1985) proposed that neutral wind shear can drive waves of aurora (omega bands), with  $V_i > 0$ , that occasionally occur on the poleward boundary of the post-midnight, diffuse aurora. In addition it has been proposed the neutral winds in the photosphere and lower chromosphere of the Sun can generate  $V_i$ 's (e.g., Kan et al., 1983).

### III. SUMMARY

Figure 5 summarizes conditions that might exist in other astrophysical objects and which could lead to the formation of significant  $V_i$ 's in a manner analogous to what occurs in the Earth's auroral zones. A conducting layer carrying current  $I$  perpendicular to  $B$  with  $\nabla \cdot I \neq 0$  will force field-aligned currents. If the required field-aligned current density  $j_{\parallel}$  exceeds the maximum  $j_{\parallel}$  that can be carried along field lines by the available plasma with  $V_i = 0$ , then a  $V_i > 0$  will form.

Two processes can drive Pedersen currents with  $\nabla \cdot I_p \neq 0$  within a collisional, conducting layer. The first is sheared plasma flow (i.e.,  $\nabla \cdot E \neq 0$ ) applied anywhere along the magnetic field lines connected to the conducting layer. In this case, the sheared plasma flow will map along field lines to the conducting layer. The second process is a neutral flow with shear within the conducting layer. Such flow can drive divergent Pedersen currents without an electric field being applied to the system.

*Acknowledgments.* Preparation of this manuscript has benefitted from discussions with M. Schulz and J. F. Fennell. The work was supported in part by NASA grants NAGW-853 and NASW-861 and by the Aerospace Sponsored Research Program.



## REFERENCES

- Chiu, Y. T., A. L. Newman, and J. M. Cornwall, *J. Geophys. Res.*, **86**, 10,029 (1981).  
Gorney, D. J., A. Clarke, D. Croley, J. Fennell, J. Luhmann, and P. Mizera, *J. Geophys. Res.*, **86**, 83 (1981).  
Gurnett, D. A., and L. A. Frank, *J. Geophys. Res.*, **78**, 145 (1973).  
Kan, J. R., S.-I. Akasofu, and L. C. Lee, *Solar Phys.*, **84**, 153 (1983).  
Knight, L., *Planet. Space Sci.*, **21**, 741 (1973).  
Lyons, L. R., *J. Geophys. Res.*, **85**, 17 (1980).  
Lyons, L. R., *J. Geophys. Res.*, **86**, 1 (1981).  
Lyons, L. R., and R. L. Walterscheid, *J. Geophys. Res.*, **90**, 12,321 (1985).

THREE ASPECTS OF MAGNETOSPHERE - IONOSPHERE SYSTEM  
INVOLVED IN FORMATION OF DISCRETE AURORAL ARCS

1. DIVERGENCE OF MAGNETOSPHERIC ELECTRIC FIELD

A. DIVERGENCE REQUIRED TO DRIVE THE ARCS

2. CONDUCTIVITY OF THE IONOSPHERE

A. WITHOUT CONDUCTING IONOSPHERE, THERE WOULD BE NO ARCS

3. CURRENT-VOLTAGE CHARACTERISTICS OF AURORAL FIELD LINES

Figure 1. Critical features of the Earth's magnetosphere-ionosphere system involved in the formation of significant  $V_{II}$ 's.

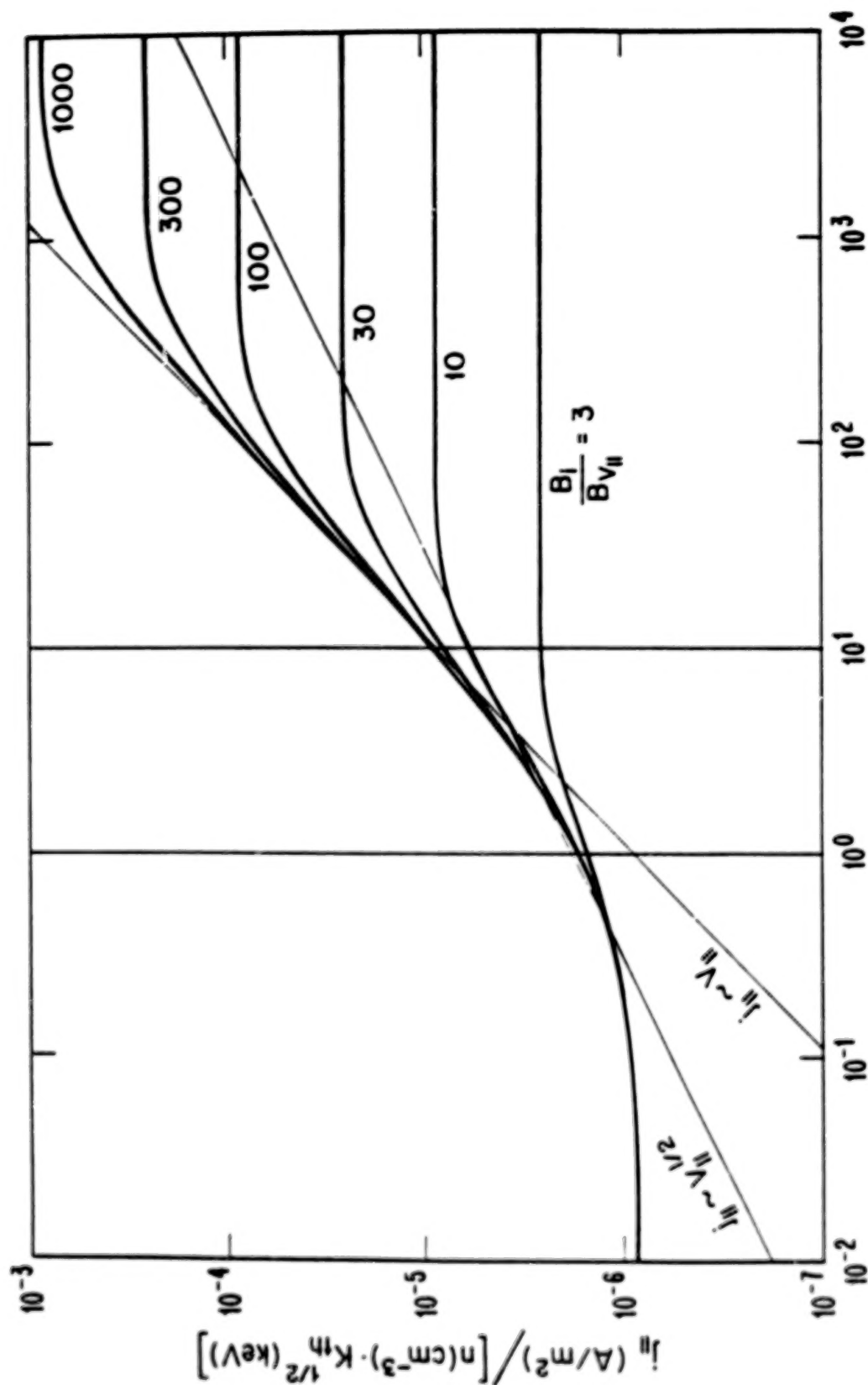


Figure 2. The  $j_{||}$  and  $V_{||}$  relation for uninhibited, single-particle motion along field lines for a high-altitude electron plasma with  $n = 1 \text{ cm}^{-3}$  and  $K_{th} = 1 \text{ keV}$ . Results for other values of  $n$  and  $K_{th}$  can be obtained by multiplying the current densities on the vertical axis by  $n \text{ (cm}^{-3}\text{)}$ ,  $K_{th}^{1/2} \text{ (keV)}$  and the potential differences on the horizontal axis by  $K_{th} \text{ (keV)}$ . Curves are shown for  $B_1/B_v$  from 3 to 1000. Lines for  $j_{||} \sim V_{||}^{1/2}$  and  $V_{||}$  and for  $eV_{||}/K_{th} = 1$  and 10 are shown for reference.

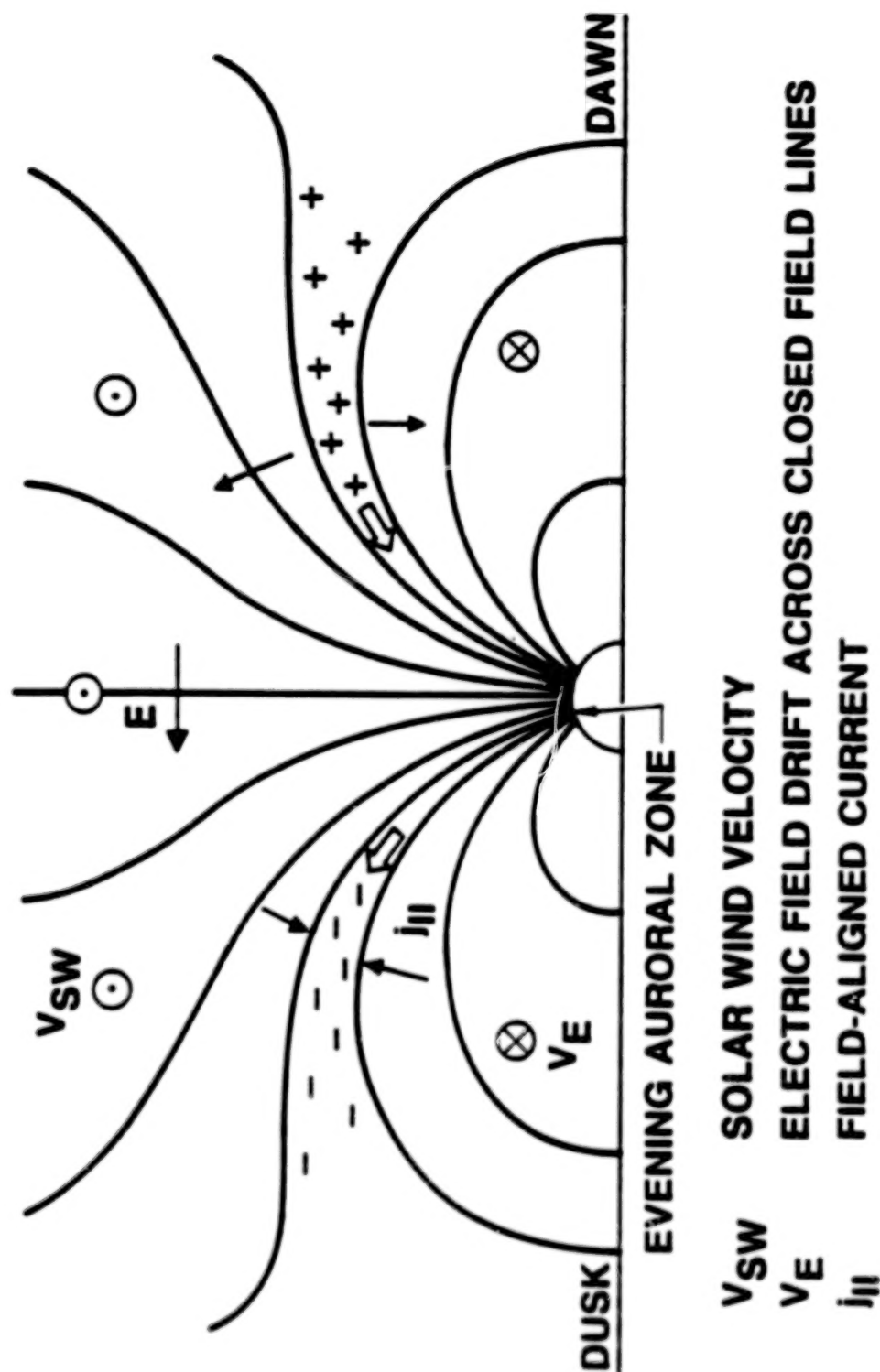


Figure 3. Schematic illustration of generation of  $E$ , with  $\nabla \cdot \mathbf{V} \neq 0$ , by the solar wind flow across the Earth's polar-cap field lines.

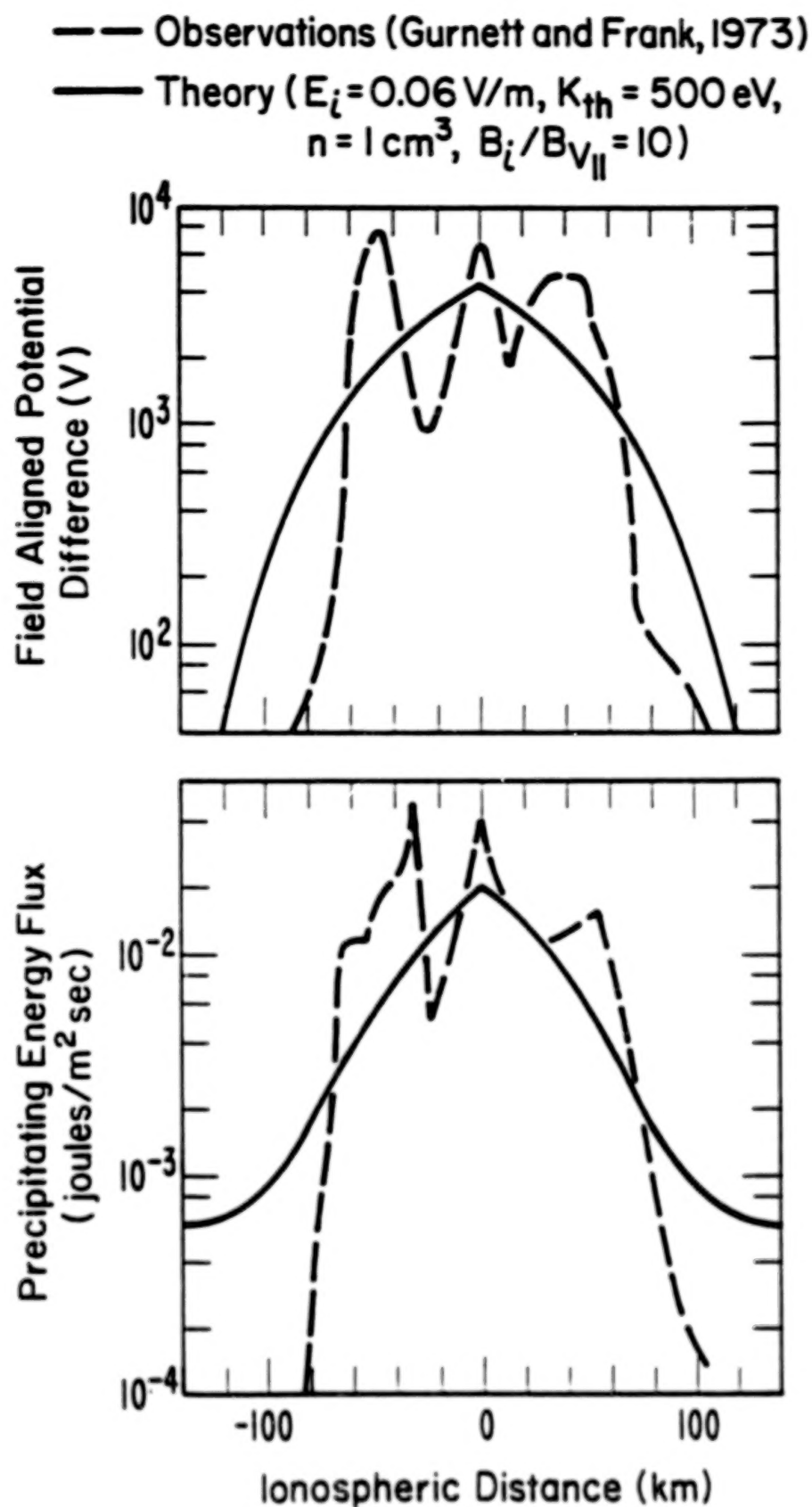
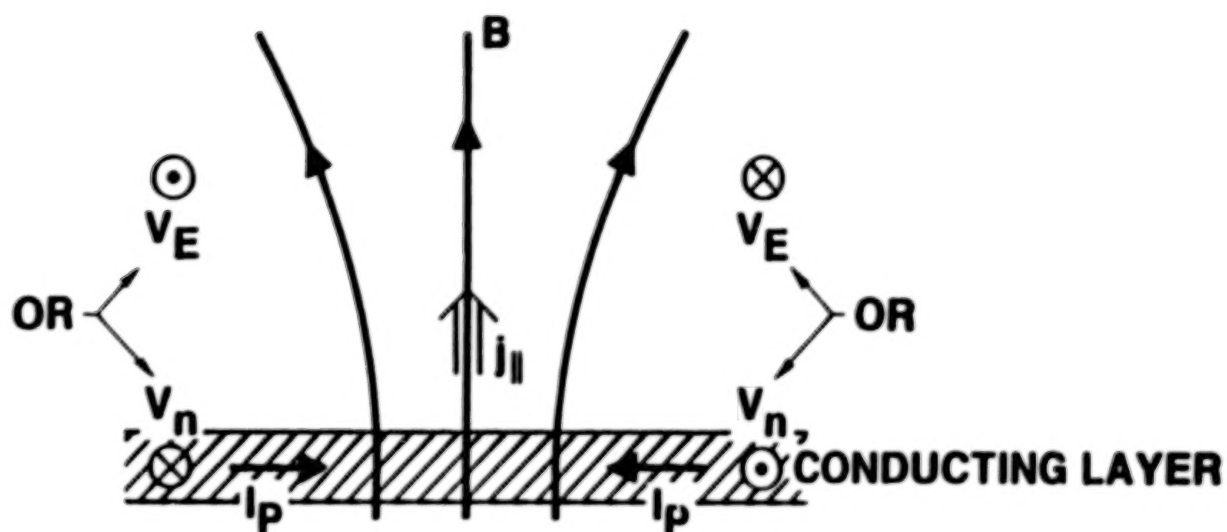


Figure 4. Comparison of the solution to the ionospheric current continuity equation (Lyons, 1980) with observations. The observations (Gurnett and Frank, 1973) were obtained over the auroral zone from a low-altitude satellite near 1800 LT.



- CONVERGING  $I_p$  CAN BE DRIVEN BY:
  1. SHEARED PLASMA FLOW  $v_E$  APPLIED ANYWHERE ALONG  $B$
  2. SHEARED NEUTRAL FLOW  $v_n$  APPLIED IN CONDUCTING LAYER
- IF  $j_{||} > \text{CRITICAL } j_{||}$ , GET  $v_{||}$

Figure 5. Summary of conditions that could lead to the formation of significant  $V_i$ 's in a manner analogous to what occurs in the Earth's auroral zones.



N87

23329

UNCLAS

## SOME ASPECTS OF DOUBLE LAYER FORMATION IN A PLASMA CONSTRAINED BY A MAGNETIC MIRROR

W. Lennartsson  
Lockheed Palo Alto Research Laboratory  
Palo Alto, California 94304, U.S.A.

### ABSTRACT

The discussion of parallel electric fields in the Earth's magnetosphere has undergone a notable shift of emphasis in recent years, away from wave-generated anomalous resistivity toward the more large-scale effects of magnetic confinement of current carrying plasmas. This shift has been inspired in large part by the more extensive data on auroral particle distribution functions that have been made available, data that may often seem consistent with a dissipation-free acceleration of auroral electrons over an extended altitude range.

Efforts to interpret these data have brought new vigor to the concept that a smooth and static electric field can be self-consistently generated by suitable pitch angle anisotropies among the high-altitude particle populations, different for electrons and ions, and that such an electric field is both necessary and sufficient to maintain the plasma in a quasi-neutral steady state. This paper reviews and criticizes certain aspects of this concept, both from a general theoretical standpoint and from the standpoint of what we know about the magnetospheric environment. It is argued that this concept has flaws and that the actual physical problem is considerably more complicated, requiring a more complex electric field, possibly including double layer structures.

### I. INTRODUCTION

Few topics in space plasma physics have been as controversial as that of "parallel electric fields," that is electric fields with a static or quasi-static component aligned along the Earth's magnetic field lines and strong enough to substantially alter the velocity distribution of the charged particles. Much of this controversy has centered on the interpretation of auroral particle data, especially the data on precipitating electrons, and has evolved along with developments in measurement technology (e.g., Swift, 1965; Block, 1967; O'Brien, 1970; Evans, 1974; Lennartsson, 1976; Papadopoulos, 1977; Hudson et al., 1978; Chiu and Schulz, 1978; Goertz, 1979; Lyons et al., 1979; Smith, 1982; and references therein).

Possibly the first truly compelling evidence of parallel electric field was presented by Evans (1974), who was able to account in a rather convincing fashion for the different parts of a typical auroral electron spectrum. The type of data presented by Evans is illustrated in a condensed form in Figure 1, which is taken from a more recent study by Kaufmann and Ludlow (1981). The two principal parts of this spectrum are a virtually isotropic low-energy part, including the central peak and most of the plateau, and a high-energy part on the flanks, which is essentially isotropic in the downward hemisphere (positive  $v_{\parallel}$ ) but strongly reduced in the upward hemisphere (negative  $v_{\parallel}$ ). According to Evans' interpretation, only the high-energy part in the downward hemisphere consists of precipitating primary electrons, accelerated by an upward parallel electric field at higher altitude. Only these primary electrons can contribute to a field-aligned (upward) current at this point in space. The low-energy part consists of back-scattered and energy-degraded primary electrons and of electrons of atmospheric origin, many of which are secondary electrons generated by the impact of primary electrons. All of these low-energy electrons are trapped below the electric field and cannot contribute to the field-aligned current. Any additional contribution must be from upward-moving ions.

As noted by Evans (and by other investigators before him) the primary electrons ("p") on the downward flanks of the distribution typically have a velocity distribution  $f_p$  that is reminiscent of a Maxwell-Boltzmann distribution that has been displaced in energy:

$$f_p(\vec{v}) \approx C \exp[-(m|\vec{v}|^2/2 - U)/kT] \quad (1)$$

where  $C$  is a normalization constant,  $m$  the electron mass,  $kT$  a thermal energy, and the positive quantity  $U$  is independent of  $\vec{v}$  and may be equated to a certain difference in electric potential energy  $eV$ :

$$U = e\Delta V \quad (2)$$

This quantity corresponds to the kinetic energy of the electrons on the downward edge of the plateau in Figure 1 and, by inference, corresponds to primary electrons with zero initial energy (at high altitude).

If the distribution in Figure 1 is integrated in terms of a net field-aligned current density  $i_{\parallel}$ , only the electrons on the flanks make a significant contribution because of the near isotropy at energies smaller than  $U$ . If the distribution of these flank electrons  $f_p$  ("primary electrons") is approximated by (1) at pitch angles  $\alpha \leq \alpha_{\max}$  (where  $\alpha_{\max}$  is slightly larger than  $90^\circ$  in this figure) and approximated by zero at  $\alpha > \alpha_{\max}$ , then the integration of  $-ef_p(\vec{v})v\cos\alpha$  readily yields:

$$i_{\parallel} \approx -eC2\pi(kT/m)^2 \sin^2\alpha_{\max} (1 + U/kT) \quad (3)$$

which is a linear function of  $U$  for constant values of  $C$ ,  $kT$ , and  $\alpha_{\max}$  (the latter corresponding to a local atmospheric "loss cone" angle of  $180^\circ - \alpha_{\max}$ ). Some comparisons of auroral electron spectra with the associated field-aligned currents (inferred from other data) have confirmed that the precipitating primary electrons do in fact account for a large or dominant portion of upward field-aligned currents, and the current density is sometimes fairly well approximated by (3) (Burch et al., 1976; Lyons, 1981; Yeh and Hill, 1981).

Although the right-hand side in (3) can be derived on purely empirical grounds, as an approximation of observed electron fluxes, the same type of expression can also be "predicted" if the primary electrons are assumed to originate at high altitude (a few Earth radii, or more), with an isotropic Maxwell-Boltzmann distribution with a temperature  $T$ , and fall through a static parallel electric field with a total potential difference  $\Delta V = U/e$  (e.g., Knight, 1973; Lemaire and Scherer, 1974; Lennartsson, 1976, 1980; Lyons et al., 1979; Lyons, 1981; Chiu and Schulz, 1978; Chiu and Cornwall, 1980; Stern, 1981). The electric field distribution is not uniquely defined by (3), but to assure the maximum degree of isotropy of the precipitating electrons at low altitude, in accordance with Figure 1, and thus the closest approximation of a linear dependence between  $i_{\parallel}$  and  $\Delta V$ , it is necessary to assume that the electric potential  $V$  varies with the magnetic field strength  $B$  in such a fashion that

$$V(B) - V(B_o) \geq (B - B_o) \Delta V / \Delta B \quad (4)$$

where  $o$  refers to the high-altitude origin of the electrons and  $\Delta B$  refers to the total difference in magnetic field strength between this origin and the low-altitude point of observation (Lennartsson, 1977, 1980). Among the possible solutions of (4) are various double layer configurations, single or multiple.

The fact that (3) can be derived under such simple assumptions and yet give a fair approximation of upward field-aligned currents, at least in some studies, has helped in focusing attention on the subject of magnetic confinement of current carrying plasmas. The theoretical implications of this fact are still obscure, however, and there is no consensus yet on the actual properties of the parallel electric field. This paper reviews a few aspects of this complex problem, including the possible role of double layers.

## II. NATURAL BOUNDARY CONDITIONS

A rather traditional approach to magnetospheric plasma dynamics at non-relativistic energies is to consider adiabatic single-particle motion, assuming that at least the first adiabatic invariant is preserved for both ions and electrons. This approach has proved fruitful in numerous applications but does have intrinsic problems in many others. To illustrate the latter it is assumed that the particle dynamics is dominated by magnetic and electric force fields,  $\vec{B}$  and  $\vec{E}$ , respectively. To save space the symbols  $M$  and  $Q$  are used for the mass and charge, respectively, of either ions or electrons. The first invariant (in MKS units) can thus be expressed as

$$\mu = Mv_g^2/2B \approx \text{constant} \quad , \quad (5)$$

where the gyro velocity  $v_g$  equals  $|\vec{v}_\perp - \vec{E} \times \vec{B}/B^2|$ , apart from a small perturbations velocity  $\vec{v}_\perp'$  defined by:

$$\vec{v}_\perp' = (M/QB^2)(d\vec{E}_\perp/dt + v_g^2(\vec{B} \times \nabla B)/2B + v_\parallel^2 \vec{B} \times (1/B)\vec{B} \cdot \nabla(\vec{B}/B)) \quad , \quad (6)$$

where the time derivative is taken in the frame of reference of the moving particle (e.g., Alfvén and Fälthammar, 1963; Longmire, 1963). This velocity represents the mass and charge dependent part of the gyro center drift, which is added to the common  $\vec{E} \times \vec{B}$  drift. The parallel velocity is likewise defined by

$$M(dv_\parallel/dt)_\parallel \approx QE_\parallel - Mv_g^2(\vec{B} \cdot \nabla B)/2B^2 \quad . \quad (7)$$

The intrinsic problem in these equations lies in the second and third terms on the right-hand side of (6), which have opposite directions for ions and electrons and are generally non-zero in the Earth inhomogeneous magnetosphere. These terms thus translate into electric currents which flow across the magnetic field lines and must be part of closed current loops in a stationary state. Otherwise the assumption in (5) cannot be a valid description of the particle dynamics.

As far as (5) is valid, equations (6) and (7) should provide a valid description of the interaction between the solar wind plasma and the Earth's magnetic field. In this case the currents associated with (6) can, at least in principle, close through the Earth's ionosphere, as indicated schematically in Figure 2. The field-aligned portions of such a current loop may be carried in part by terrestrial particles, but the flow density of these particles is limited by the maximum possible escape rates (e.g., Lemaire and Scherer, 1974). This restriction is less severe for the downward current, since the terrestrial electrons may escape at a higher rate than the ions if allowed to flow freely.

If the demand for upward current exceeds the flow rate of terrestrial ions, the additional contribution must be carried by precipitating solar electrons. The flow density of these electrons is on the other hand limited by the "magnetic mirror" force on the right-hand side of (7), and can only be increased by a parallel electric field. In fact, if these electrons have a Maxwell-Boltzmann distribution with a temperature  $T$  and density  $n$ , the flow density is limited by (3), where  $U = e\Delta V$  and  $C = n\sqrt{kT/(2\pi m)}$  (Lennartsson, 1980). This approach thus leads in a natural fashion to the subject of magnetic confinement. The fact that auroral electrons are observed to have a significantly higher temperature than solar electrons (cf. Fig. 1), may suggest, however, that (5) is not entirely valid.

### III. A "CLASSICAL" APPROACH TO MAGNETIC CONFINEMENT

Since particles with different pitch angles mirror at different locations in an inhomogeneous static magnetic field, the number density  $n$  of these particles is a function of  $B$ , unless the velocity distribution is completely isotropic (according to Liouville's theorem). If the magnetic field strength has a single minimum  $B_0$  and increases monotonically away from this minimum, in at least one direction, then the density  $n$  is known at any  $B > B_0$ , if the distribution function is known at  $B_0$ . This is still true in the presence of a parallel electric field (assuming a one-dimensional geometry), provided the electric field is also time independent:

$$dE/dt = 0 \quad (8)$$

and the electric potential is sufficiently monotonic, for example (Chiu and Schulz, 1978):

$$dV/dB > 0 \quad (9)$$

$$d^2V/dB^2 \leq 0 \quad (10)$$

The last condition is much stronger than (4); it precludes double layer structures and implies that the electron and ion densities are very nearly equal at all points. Under these three conditions, and assuming that (5) holds and the ions are all positive and singly charged, the quasi-neutrality may be expressed in a somewhat "classical" form as:

$$n_e(V, B, f_{e0}) \approx n_i(V, B, f_{i0}) \quad (11)$$

where  $f_{e0}$  and  $f_{i0}$  are the electron and ion distribution functions, respectively, at  $B_0$ . With a careful selection of  $f_{e0}$  and  $f_{i0}$ , this relation will yield a solution for  $V$  in the form  $V = V(B)$  (e.g., Alfvén and Fälthammar, 1963; Persson, 1963, 1966; Block, 1967; Lemaire and Scherer, 1974; Chiu and Schulz, 1978; Stern, 1981). Whether this also yields a self-consistent solution of Poisson's equation is a rather intricate question, however.

A comparatively simple and analytically tractable case is illustrated in Figure 3, which is adapted from the works of Persson (1966) and Block (1967). The shaded areas represent the only populated regions of velocity space. Within these regions the particle distributions are assumed to be isotropic but may have arbitrary functional dependence on the energy and may be different for electrons and ions. The ions are also assumed to have energies



larger than  $e(V_a - V(B))$ , which ensures that no part of the ion energy distribution is entirely excluded from low altitude ( $B \approx B_a$ ). The electron energies are only limited by the acceleration ellipsoid and by the loss hyperboloid. As discussed by Persson and Block, these ion and electron populations can be made to have equal densities everywhere,  $n_i = n_e$ , if and only if:

$$E_i = -(V_a - V_o)/(B_a - B_o)dB/ds \quad (12)$$

where  $s$  is a distance coordinate running along  $\vec{B}$  (downward). The conventional physical interpretation of this case is the following (cf. Persson and Block): Since the ion distribution at  $B = B_o$  includes smaller pitch angles than the electron distribution, the ion density tends to exceed the electron density at  $B > B_o$ , thereby creating an upward electric field that drags the electrons along, modifies the electron and ion distributions, and maintains  $n_i \approx n_e$  at all  $B_o \leq B < B_a$  (and  $n_i = n_e = 0$  at  $B \geq B_a$ ).

Although this case may be considered more of a textbook example than a description of typical magnetospheric conditions, it has generally been thought to illustrate a sound physical principle. However, on closer inspection this physical principle may not seem entirely sound. If the right-hand side in (12) is differentiated once more with respect to  $s$ , assuming the magnetic field is a dipole field, it follows that:

$$dE_i/ds < 0 \quad (13)$$

Hence, the small net charge required to maintain  $n_i \approx n_e$  cannot be provided by the ions. In fact, there is no net positive charge at any location along the magnetic field line where  $n_i > 0$ , and there are no ions to support the electric stress at  $B \geq B_a$ . It can thus be argued that this simple case rather illustrates the difficulty of satisfying all of the conditions in (8)-(11) at the same time.

A much more elaborate and perhaps more realistic case has been presented by Chiu and Schulz (1978) and Chiu and Cornwall (1980). Their case also considers an ion population at high altitude which is isotropic outside of the loss hyperboloids in Figure 3, but the corresponding electron population is required to be anisotropic, with a wider distribution in  $v_{\perp}$  and in  $v_{\parallel}$  (bi-Maxwellian). Their case further includes particles within the loss hyperboloids, some of which have a terrestrial origin, and thus includes a net current. They reach the condition in (11) not by analytical methods alone, but by iterative numerical approximations, and their solution is far too complex to be evaluated here. A few comments with bearing on their case will be made below, however.

#### IV. POSSIBLE ROLE OF DOUBLE LAYERS

The studies of quasi-neutrality in a model magnetic mirror configuration show that it is mathematically possible to satisfy  $n_i \approx n_e$  in a time-independent parallel electric field that extends over large distances and does not contain any double layer structures, provided the particle distribution functions are carefully designed. It is not clear from these studies, however, that such electric fields are realistic, or even physically possible. One argument to that effect was made in the preceding section, applied to a simple case where all particles are trapped by the combined electric and magnetic fields. Other arguments to the same effect may be applied to the more general case where the loss hyperboloids are also populated, and thus a current flows (e.g., Chiu and Schulz, 1978). In that case it can be argued, for instance, that the parallel electric field is made subject to potentially conflicting conditions; on one hand



the model electric field is designed to satisfy  $n_i \approx n_e$  everywhere, based on the entire pitch angle distributions of all particles, while on the other hand the electric field in reality must also be subject to the external condition that the current be of the appropriate magnitude, and the current only involves particles within the loss hyperboloids.

The aforementioned studies, however, do point to an unambiguous condition for the non-existence of electric fields; in order for the parallel electric field to vanish over a large distance along a magnetic flux tube, the pitch angle distributions of ions and electrons, when integrated over all energies, must be identical (cf. Persson, 1963). As a consequence, it may not be possible, given realistic particle distributions, to have the electric field entirely contained within a single stable double layer, or even within multiple double layers. The double layers naturally generate different pitch angle distributions for the ions and the electrons, and these in turn will affect the quasi-neutrality at all other altitudes. In other words, a stable double layer may not be nature's replacement for an extended electric field, but may perhaps be part of it (cf. Stern, 1981). Such a configuration cannot be modeled, however, if the condition in (10) is part of the assumptions.

A possibly fundamental shortcoming of the classical approach to magnetic confinement is its disallowance of temporal variations in the electric field, including rapid and small-scale fluctuations. The assumption in (8) is needed to make a tractable problem, but may not be supported by data. Close scrutiny of Figure 1, for example, fails to produce the sharp boundaries of Figure 3 (with  $B \approx B_0$ ). This and other published illustrations of auroral electron spectra have in fact a rather blurred appearance, suggesting that the electrons have traversed a "turbulent" electric field. Numerous reports of intense plasma wave turbulence at various altitudes along auroral magnetic field lines (e.g., Fredricks et al., 1973; Gurnett and Frank, 1977; Mozer et al., 1980; and references therein) lend additional support to that kind of interpretation.

Allowing the electric field to have temporal fluctuations of a small scale size may render an untractable computational problem, but provides for a more realistic description of the collective behavior of the particles. From a qualitative point of view this may also seem to make the magnetic mirror a more favorable environment for the formation of double layers, as illustrated schematically in Figure 4. This figure assumes that the increase in kinetic energy of individual electrons is not a unique function of location in space, but varies somewhat randomly about an average increase, due to temporal fluctuations in the electric field. Only the average increase is a function of location and has the sharp boundaries in velocity space. An electron that has a kinetic energy slightly inside of the acceleration boundary when passing point P, either on the way down or after mirroring in the magnetic field below, is likely to be trapped by the average electric field on the way up, thereby adding to the local concentration of negative charge (during part of its oscillation), at the expense of the negative charge at higher altitude. This in turn further widens the acceleration boundary in the transverse direction, enabling electrons with a larger perpendicular energy to be trapped as well. Electrons inside the acceleration boundary may be removed again after a slight increase in the energy, but the net diffusion is assumed inward as long as the density of particles is higher on the outside. A conceivable end result may be some form of double layer, thin enough to harbor a significant charge imbalance in a stable fashion (cf. Lennartsson, 1980).

Whether trapping of electrons between magnetic and electric mirror points will produce a stable double layer, or merely add to the plasma turbulence, cannot be decided from this simplistic exercise alone. A redistribution of the electric field from higher to lower altitude carries with it a redistribution of the ion density as well, and that is not considered. It is worth noting, however, that the shape and size of the electron acceleration boundary depends on the angle of the double layer, and is the smallest for a double layer with the electric field nearly perpendicular to  $\vec{B}$ . In that case the boundary may be almost circular (cf. Figure 3 with  $B \gg B_0$ ), and can trap the fewest number of electrons. This kind of structure is perhaps the most likely to materialize and is, in fact, reminiscent of the "electrostatic shocks" commonly observed in the auroral regions (e.g., Mozer et al., 1977; see also Swift, 1979; Lennartsson, 1980; Borovsky and Joyce, 1983). It also has a favorable geometry for satisfying (4), thus producing a large electron current.

*Acknowledgment.* This work was supported by the National Science Foundation under grant ATM-8317710 and the Lockheed Independent Research Program.

## REFERENCES

- Alfvén, H., and C.-G. Fälthammar, *Cosmical Electrodynamics, Fundamental Principles*, Clarendon Press, Oxford, 1963.
- Block, L. P., *Space Sci. Rev.*, 7, 198 (1967).
- Burch, J. L., W. Lennartsson, W. B. Hanson, R. A. Heelis, J. H. Hoffman, and R. A. Hoffman, *J. Geophys. Res.*, 81, 3886 (1976).
- Borovsky, J. E., and G. Joyce, *J. Geophys. Res.*, 88, 3116 (1983).
- Chiu, Y. T., and M. Schulz, *J. Geophys. Res.*, 83, 629 (1978).
- Chiu, Y. T., and J. M. Cornwall, *J. Geophys. Res.*, 85, 543 (1980).
- Evans, D. S., *J. Geophys. Res.*, 79, 2853 (1974).
- Fredricks, R. W., F. L. Scarf, and C. T. Russell, *J. Geophys. Res.*, 78, 2133 (1973).
- Goertz, C. K., *Rev. Geophys. Space Phys.*, 17, 418 (1979).
- Gurnett, D. A., and L. A. Frank, *J. Geophys. Res.*, 82, 1031 (1977).
- Hudson, M. K., R. L. Lysak, and F. S. Mozer, *Geophys. Res. Lett.*, 5, 143 (1978).
- Kaufmann, R. L., and G. R. Ludlow, *J. Geophys. Res.*, 86, 7577 (1981).
- Knight, S., *Planet. Space Sci.*, 21, 741 (1973).
- Lemaire, J., and M. Scherer, *Planet. Space Sci.*, 22, 1485 (1974).
- Lennartsson, W., *J. Geophys. Res.*, 81, 5583 (1976).
- Lennartsson, W., *Astrophys. Space Sci.*, 51, 461 (1977).
- Lennartsson, W., *Planet. Space Sci.*, 28, 135 (1980).
- Longmire, C. L., *Elementary Plasma Physics*, John Wiley and Sons, Inc., New York, London, 1963.
- Lyons, L. R., D. S. Evans, and R. Lundin, *J. Geophys. Res.*, 84, 457 (1979).
- Lyons, L. R., *J. Geophys. Res.*, 86, 1 (1981).
- Mozer, F. S., M. K. Hudson, R. B. Torbert, B. Parady, and J. Yatteau, *Phys. Rev. Lett.*, 38, 292 (1977).
- Mozer, F. S., C. A. Cattell, M. K. Hudson, R. L. Lysak, M. Temerin, and R. B. Torbert, *Space Sci. Rev.*, 27, 155 (1980).
- O'Brien, B. J., *Planet. Space Sci.*, 18, 1821 (1970).
- Papadopoulos, K., *Rev. Geophys. Space Phys.*, 15, 113 (1977).
- Persson, H., *Phys. Fluids*, 6, 1756 (1963).
- Persson, H., *Phys. Fluids*, 9, 1090 (1966).
- Smith, R. A., *Physica Scripta*, 25, 413 (1982).
- Stern, D. P., *J. Geophys. Res.*, 86, 5839 (1981).
- Swift, D. W., *J. Geophys. Res.*, 70, 3061 (1965).
- Swift, D. W., *J. Geophys. Res.*, 84, 6427 (1979).
- Yeh, H.-C., and T. W. Hill, *J. Geophys. Res.*, 86, 6706 (1981).

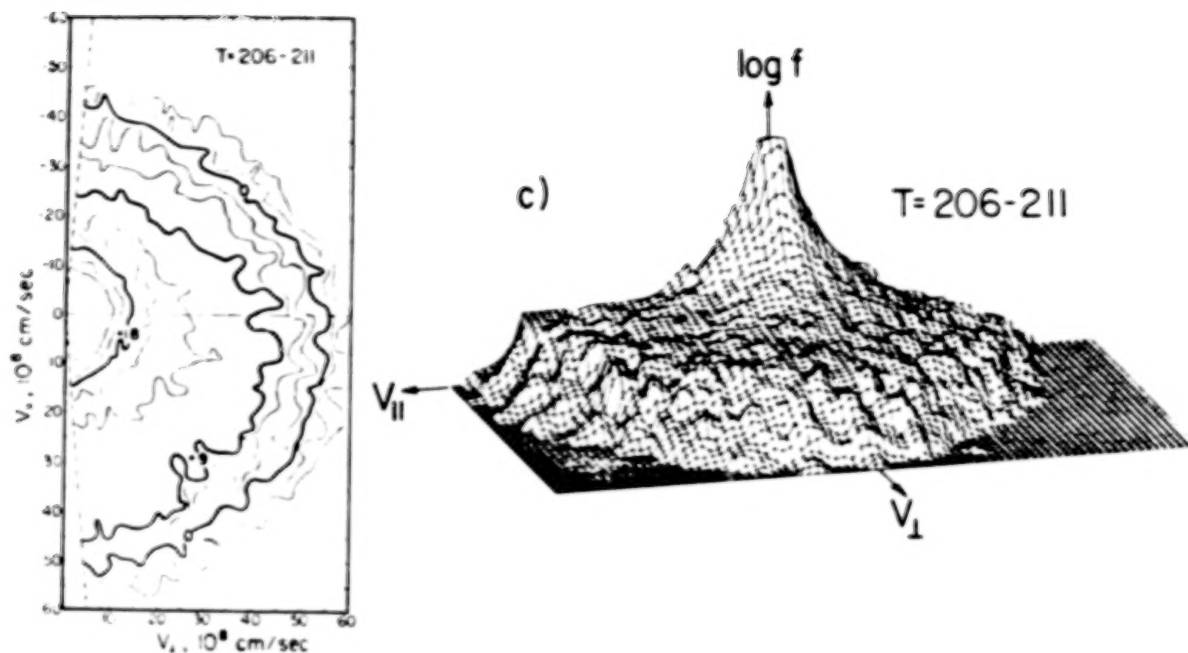


Figure 1. Contour and three-dimensional plot of auroral electron distribution function, in the energy range 25eV to 15 keV, measured from a rocket at about 240 km altitude. Downgoing electrons have positive  $v_z$ . Curves of constant  $f(\vec{v})$  on the contour plot are labeled by the common logarithm of  $f(\vec{v})$  in  $s^3/km^6$ . This distribution is typical of electrons producing discrete auroral arcs (from Kaufmann and Ludlow, 1981).

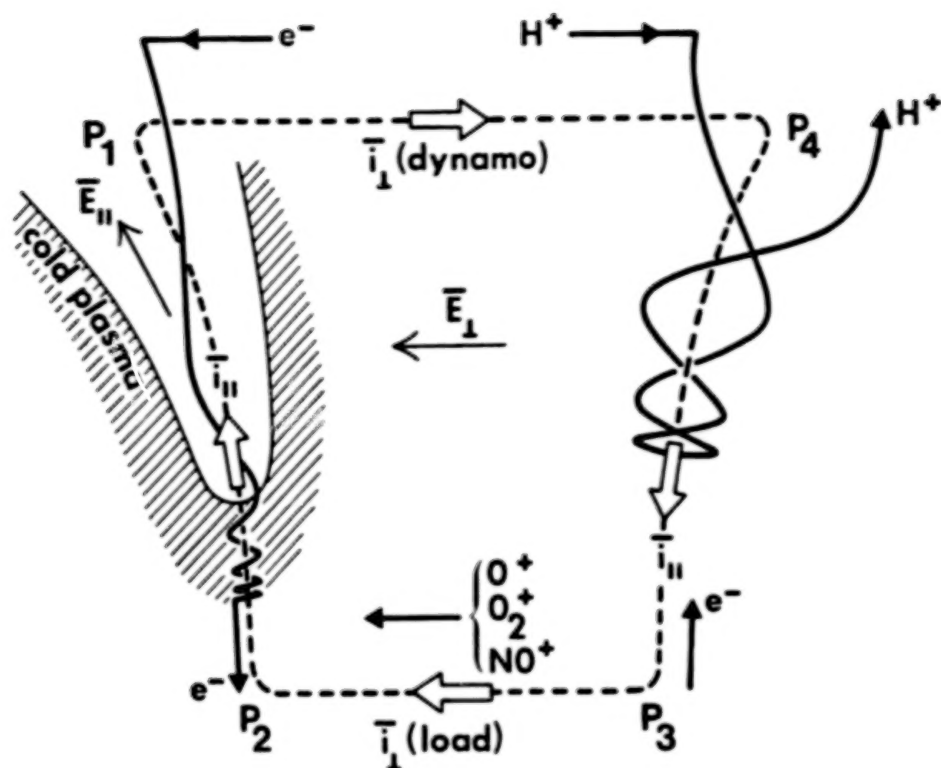


Figure 2. Schematic magnetosphere-ionosphere current system. The dynamo current  $P_1 - P_4$  is assumed to be caused by the differential drift of hot protons and electrons. The downward parallel current  $P_4 - P_3$  may be carried mainly by escaping ionospheric electrons, while the upward parallel current  $P_2 - P_1$  is carried to a large extent by downflowing hot electrons. Point  $P_2$  is at a high positive potential with respect to point  $P_1$ , which enables the downflowing electrons to overcome the magnetic mirror. The current  $P_3 - P_2$  is a Pedersen current (from Lennartsson, 1976).

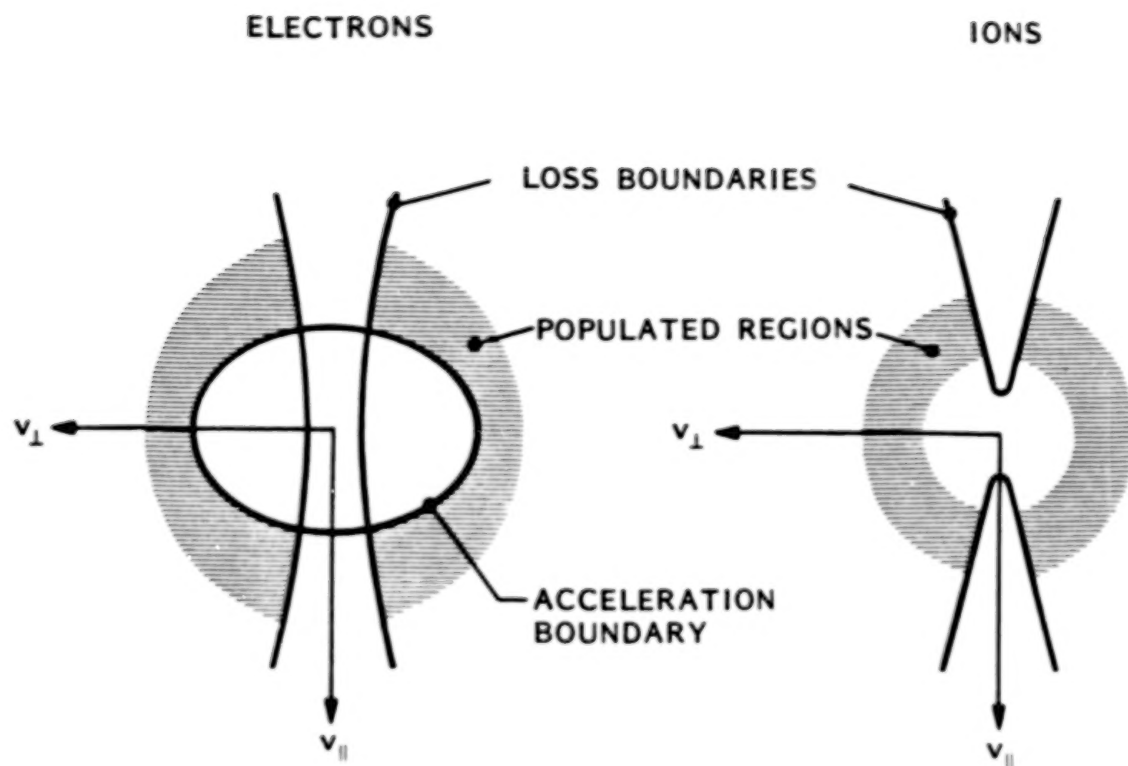


Figure 3. Hypothetical case of plasma confinement by a magnetic mirror in the presence of a parallel electric field, directed away from the magnetic mirror (upward). Only the shaded regions are assumed populated (see text). The loss boundaries (hyperboloids) are defined by  $(B_a/B - 1)v_{\perp}^2 - v_{\parallel}^2 = 2H(V_a - V)$ , where the subscript a refers to atmospheric (loss) altitude and  $H = e/m_e$  for electrons and  $H = -e/m_i$  for ions. The acceleration boundary (ellipsoid) is defined by  $(1 - B_o/B)v_{\perp}^2 + v_{\parallel}^2 = 2(e/m_e)(V - V_o)$ , where the subscript o refers to a high altitude ( $B_o < B$ ) (adapted from Persson, 1966).

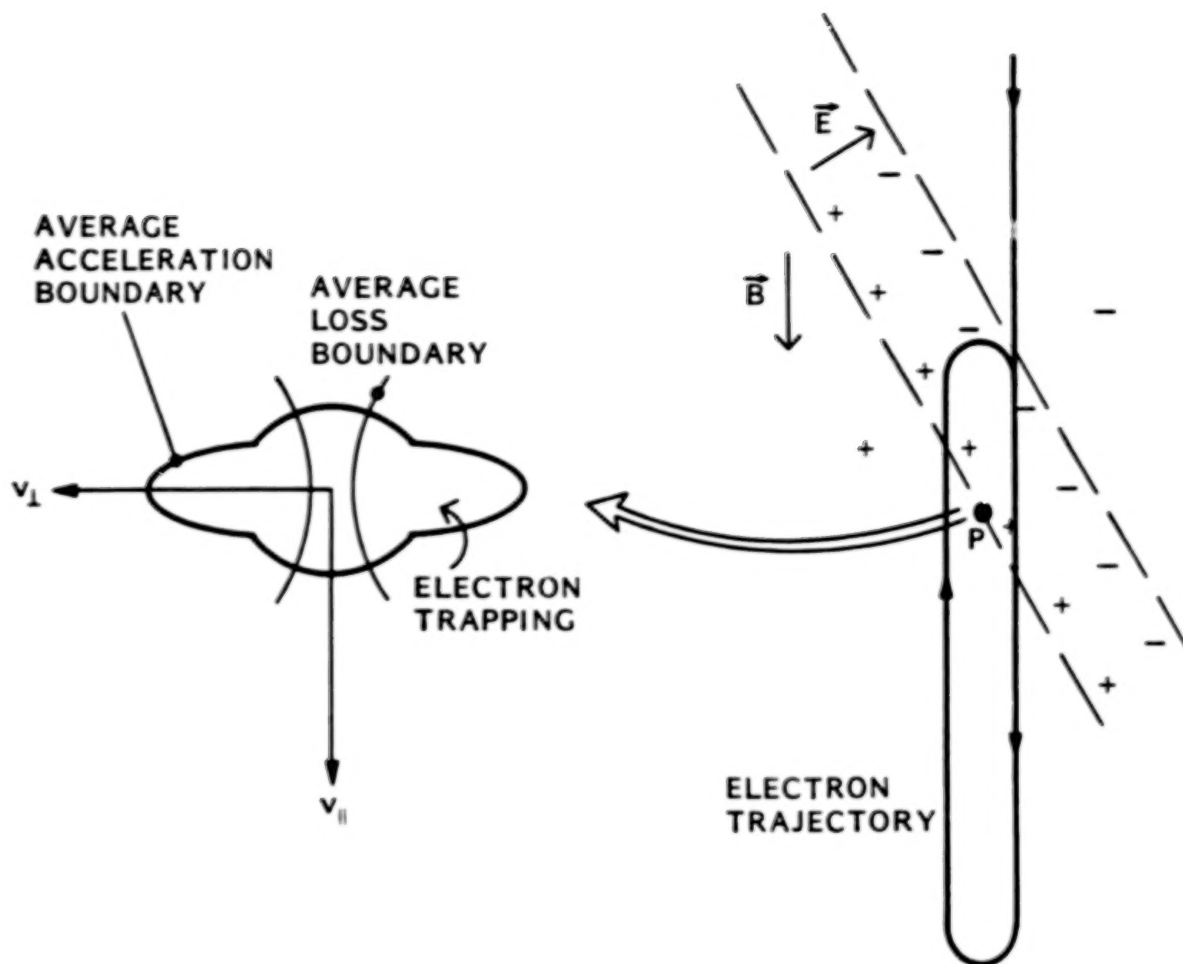


Figure 4. Hypothetical case of electron trapping by a locally enhanced electric field (right panel), associated with diffusion in velocity space (left panel). The diffusion is assumed to result from small-scale fluctuations in the electric field. The acceleration boundary at point P refers to an average acceleration and is the combined effect of the weak electric field at higher altitudes and the stronger field nearby (see text) (adapted from Lennartsson, 1980).



N87

23330

UNCLAS

**ELECTRIC POTENTIAL DISTRIBUTIONS AT THE INTERFACE  
BETWEEN PLASMASHEET CLOUDS**

D. S. Evans  
NOAA/SEL  
325 Broadway  
Boulder, Colorado 80303, U.S.A.

and

M. Roth and J. Lemaire  
Institut d'Aéronomie Spatiale de Belgique  
3 av. Circulaire  
B-1180 Bruxelles, Belgium

**ABSTRACT**

At the interface between two plasma clouds with different densities, temperatures, and/or bulk velocities, there are large charge separation electric fields which can be modeled in the framework of a collisionless theory for tangential discontinuities (see Lemaire and Burlaga, 1976; Roth, 1980; Botticher et al., 1983).

Two different classes of layers have been identified: the first one corresponds to (stable) ion layers which are thicker than one ion Larmor radius; the second one corresponds to (unstable) electron layers which are only a few electron Larmor radii thick.

We suggest that these thin electron layers with large electric potential gradients (up to 400 mV/m) are the regions where large-amplitude electrostatic waves are spontaneously generated. These waves scatter the pitch angles of the ambient plasmasheet electron into the atmospheric loss cone. The unstable electron layers can therefore be considered as the seat of strong pitch angle scattering for the primary auroral electrons.

**I. INTRODUCTION**

Lyons and Evans (1984) found direct evidence from coordinated auroral and magnetospheric particle observations that discrete auroral arcs are located along geomagnetic field lines mapping in plasmasheet regions where significant spatial gradients in the magnetospheric particles velocity distribution are observed.

These observations as well as earlier theoretical calculations by Lemaire and Burlaga (1976) and Roth (1976, 1978, 1979, 1980) have motivated the present application of kinetic plasma theory to thin layers separating a hot plasmasheet cloud from a cooler background or another cloud which is populated with ions and electrons of different densities and temperatures. However, we do not simulate the magnetic field reversal region in the neutral sheet of the magnetotail.

We briefly recall the basic features of the kinetic model as well as the boundary conditions in the next section. The numerical results are presented in Section III; the discussion of this solution is given in the last section with the conclusions.

## II. FORMULATION OF THE MODEL AND BOUNDARY CONDITIONS

The kinetic model used below is an extension of that proposed by Sestero (1964) to describe collisionless plasma sheaths in the laboratory. Although the plasmashield is rarely in a stationary state, we assume that its structure does not change significantly over the characteristic period of time required for an Alfvén wave to traverse the transition layer.

Furthermore, it is assumed that the radius of curvature of the plasma sheath is much larger than its characteristic thickness, which is of the order of a few ion gyroradii. Under these circumstances the plasma layer can be considered as planar. Every physical quantity depends then on one space coordinate only, say  $x$ .

Since in general the magnetic field direction at the interface between plasmashield diamagnetic irregularities does not vary by more than  $10^\circ$  or  $20^\circ$ , we consider that the direction of  $\mathbf{B}$ , does not change nor reverse across the transition layer, but that  $\mathbf{B}$  remains always parallel to the  $z$ -axis. The partial electric current densities ( $j^{+/-}$ ) of the ions (+) and electrons (-) are then necessarily parallel to the  $y$ -axis. The electric field (as spatial gradient of the potential  $\phi$ ) is in the  $x$ -direction. Indeed we assume that, in a frame of reference fixed with respect to the plasma layer, there is no mass flow across nor toward the surface of discontinuity ( $v_x = 0$ ).

In our kinetic model the ions and electrons from the left-hand side (i.e., side 1) have velocity distributions ( $f_1^{+/-}$ ) which tend to an isotropic Maxwellian at  $x = -\infty$ . The zero-order moment (i.e., the density:  $n_1^{+/-}$ ) of these distribution functions tends to an asymptotic density  $N_1 = N_1^- = 0.5 \text{ cm}^{-3}$ , at  $x = -\infty$ . The temperature of the ions and electrons  $\theta_1^{+/-}$  from side 1 is determined by the second-order moments of  $f_1^{+/-}$ . When  $x$  tends to  $-\infty$ ,  $\theta_1^{+/-}(x)$  tends to  $T_1^{+/-} = 1.2 \text{ keV}$ , and  $\theta_1^-(x)$  tends to  $T_1^- = 2.5 \text{ keV}$ .

When  $x$  varies from  $-\infty$  to  $+\infty$  we expect  $n_1^{+/-}$  to decrease to zero, and the velocity distributions  $f_1^{+/-}$  to become depleted in the domain of the velocity space which is not accessible to the particles from side 1, i.e., for those particles with the smallest velocities and therefore the smallest gyroradii.

In absence of Coulomb collisions and wave-particle interactions, these velocity distributions are solutions to the collisionless Boltzmann-Vlasov equation. Any function of the constants of motion is then a solution. Following Sestero (1964) we choose for  $f_1^{+/-}$  truncated distributions which tend to isotropic Maxwellians at  $x = -\infty$ , where  $n_1^{+/-}$  and  $\theta_1^{+/-}$  tend to the above given values for the densities and temperatures ( $N_1^{+/-}$  and  $T_1^{+/-}$ ), respectively.

When  $x$  tends to  $+\infty$  the domains of the velocity space where  $f_1^{+/-}$  differs from zero become vanishingly small;  $n_1^{+/-}$  decreases then asymptotically to zero, as expected, because a smaller and smaller fraction of ions and electrons from side 1 has large enough gyroradius to penetrate deep into region 2 on the opposite side of the transition layer. For details see Roth et al. (1986).

Region 2 is populated with electrons and ions of a different origin, i.e., with different temperature distributions  $\theta_2^{+/-}(x)$  and different density distributions  $n_2^{+/-}(x)$ . In our numerical calculation we have taken the following boundary conditions:  $\theta_2^{+/-}(\infty) = T_2^{+/-}$  with  $T_2^{+/-} = 3 \text{ keV}$  and  $T_2^- = 0.8 \text{ keV}$ ;  $n_2^{+/-}(\infty) = N_2^{+/-} = 0$ ,  $15 \text{ cm}^{-3}$  and  $n_2^{+/-}(-\infty) = 0$ .

The velocity distributions  $f_2^{+/-}$  of the ions and electrons originating from region 2 can again be any function of the constants of motion. As above, truncated Maxwellian velocity distributions are adopted. They tend to isotropic Maxwellians at  $x = +\infty$ , with densities and temperatures, respectively, equal to  $N_2^{+/-}$  and  $T_2^{+/-}$ . When  $x$  tends to  $-\infty$ ,  $f_2^{+/-} \neq 0$  only for a decreasing number of particles from side 2 which has large enough velocities (and gyroradii) to penetrate deep inside region 1.

Note that the asymptotic behavior of the plasma distribution depends only on the asymptotic form of  $f_{1,2}^{+/-}$  when  $x$  goes to  $\pm\infty$ . The form of  $f_{1,2}^{+/-}$  for any other  $x$  in between is responsible for the shape of the transition profiles. Thus, the state of the plasma at one end of the transition region (or at both ends in our case) does not uniquely determine the plasma and field variation within the transition. This results from the collisionless and adiabatic nature of the interaction between the plasma particles. In a collision-dominated plasma when irreversible processes are important, this would not, however, be the case; the transition profile is then uniquely determined by the boundary conditions.

The moments of  $f_{1,2}^{+/-}$  are integrals over the domain of velocity space where  $f_{1,2}^{+/-}$  is not equal to zero. The densities  $n_{1,2}^{+/-}(x)$  are the zero-order moments of  $f_{1,2}^{+/-}$ ; the partial current densities ( $j_{1,2}^{+/-} = eZ^{+/-} n_{1,2}^{+/-} \cdot v_{1,2}^{+/-}$ ) are first-order moments, etc. These moments are analytical expressions depending on  $x$  through the electric potential  $\phi(x)$  and the magnetic vector potential  $a(x)$ . Indeed, both  $\phi(x)$  and  $a(x)$  appear explicitly in the constants of motion and consequently in  $f_{1,2}^{+/-}$ . The analytic expressions for  $n_{1,2}^{+/-}$  and  $j_{1,2}^{+/-}$  are similar to those derived by Sestero (1964, 1966). They are given in the more detailed article by Roth et al. (1986).

The electric potential  $\phi(x)$  must satisfy Poisson's equation. However, in non-relativistic plasmas, where the thermal velocity of the ions and electrons is much smaller than the speed of light, Sestero (1966) has shown that a satisfactory first approximation for  $\phi(x)$  is obtained by solving, iteratively, the charge-neutral approximation of Poisson's equation, i.e.,

$$n_1^+ + n_2^+ = n_1^- + n_2^- \quad (1)$$

Once  $\phi(x)$  has been determined for all  $x$ , the charge separation electric field,  $E(x)$ , can also be evaluated as  $-d\phi/dx$ . Finally, the Laplacian of  $\phi(x)$  (i.e.,  $d^2\phi/dx^2$ ) can be calculated to estimate the value of the electric charge density  $e(n^+ - n^-)$  associated with  $\phi(x)$ . It is shown, a posteriori, that the actual charge separation relative density  $(n^+ - n^-)/n^+$  is indeed a small quantity throughout the whole plasma sheath; i.e., that (1) is a valid first approximation and substitute for Poisson's equation.

In the next section we present numerical results corresponding to a solution of equation (1) for which the electric potential  $\phi_1$  at  $x = -\infty$  is equal to  $\phi_2$  at  $x = +\infty$ . A wider family of solutions for which  $\phi_2 - \phi_1 = 0$  is discussed in Roth et al. (1986).

The partial current densities ( $j_{1,2}^{+/-}$ ) carried by the ions and electrons drifting in the electric field  $E(x)$  and magnetic fields  $B(x)$  are also analytical expressions of  $\phi(x)$  and  $a(x)$ . The currents produce diamagnetic effects which determine the variation of  $a(x)$  and consequently of  $B_z(x)$ , the  $z$ -component of curl  $a$ . The vector potential  $a(x)$  is solution of Maxwell's equations:

$$B_z = da/dx \text{ and } dB_z/dx = -\mu_0(j_1^+ + j_2^+ - j_1^- - j_2^-) \quad (2)$$

The standard predictor-corrector Hamming method for numerical integration of equation (2) can be used to obtain the value of  $a(x)$  for all  $x$ , across the diamagnetic plasma layer (Ralston and Wilf, 1965). Since the magnetic field does not change direction,  $a(x)$  is an increasing function of  $x$ ; it varies from  $a = -\infty$  at  $x = -\infty$  to  $a = +\infty$  at  $x = +\infty$ .

### III. NUMERICAL RESULTS

Figures 1a and 1b show the distributions of  $n_{1,2}^{+/-}$ , the partial ion and electron density distributions as a function of  $x$ . The upper horizontal scale represents  $x$  in kilometers. The lower scale of the left-hand panels corresponds to  $x$  in units of proton gyroradii. The  $x$ 's in the lower scale of the right-hand panels are expressed in electron gyroradii. Note in the left-hand side panels the smooth variation of the densities over distances of 2-3 ion Larmor gyroradii, i.e., 500-800 km. In the middle of this broad transition region near  $x = 0$ , there is a much sharper transition where all densities change significantly over distances of 2-3 electron Larmor gyroradii, i.e., 6-9 km (see enlargement in the right-hand side panels).

Panels c1 and c2 in Figure 1 show the total ion density,  $n^+ = n_1^+ = n_2^+$ , which according to the charge neutral equation (1), is equal to the total electron density  $n^- = n_1^- + n_2^-$ .

Panels d1 and d2 illustrate how  $\theta^{+/-}$ , the total ion and electron temperatures vary in the transition region:  $\theta^{+/-} = (n_1^{+/-} \theta_1^{+/-} + n_2^{+/-} \theta_2^{+/-}) / (n_1^{+/-} + n_2^{+/-})$ . Note again the broader scale of variation in the left-hand side panels and the much sharper decrease of  $\theta^-$  near  $x = 0$ , illustrated in the right-hand side panel.

The distribution of the magnetic field  $B_z(x)$  is shown in panels e1 and e2. The magnetic field intensity is equal to 40 nT at  $x = -\infty$ ; this is a typical value of  $B$  in the plasmasheet chosen as boundary condition on side 1 at  $x = -\infty$ . The value of  $B_z(x)$  increases to 66.4 nT at  $x = +\infty$  with an enhanced variation near  $x = 0$  due to the diamagnetic current contributed by the electrons in the thin electron sheath. It could be shown that the sum of the magnetic pressure and kinetic pressure is precisely a constant throughout the plasma layer.

The electric potential distribution shown in panels f1 and f2 is a continuous function of  $x$ . The potential difference between  $x = -\infty$  and  $x = +\infty$  is equal to zero in the case considered. But similar continuous solutions have been obtained for positive and negative values of  $\phi_2 - \phi_1$  of the order of  $\pm k T_{1,2}^{+/-} / e$  (see Roth et al. 1986). The gradient of the electric potential has a different direction in the electron layer near  $x = 0$  than on both sides in the proton layer. This is also illustrated in the next panels (g1 and g2) showing the electric field intensity which is perpendicular to the surface of the plasma layer:  $E_x$  has a large negative value of -220 mV/m in the middle of the thin electron layer. This charge separation electric field accelerates the hotter and more numerous electrons from side 1 toward region 2. On both sides of the electron layer  $E_x$  has smaller positive values, not exceeding 2.5 mV/m. This electric field tends to accelerate the hotter and more numerous protons of side 1 toward the cooler and less dense region 2.

The relative electric space charge density deduced from  $d^2\phi/dx^2$  is given in panels h1 and h2. It can be seen that  $|n^+ - n^-|/n^+$  is smaller than 2 percent within the electron layer; it is smaller than  $3 \times 10^{-6}$  in the ion layer. This confirms a posteriori that charge-neutrality is satisfied to a very good approximation. This confirms also that the solution of equation (1) gives a satisfactory approximation  $\phi(x)$  for the electric potential distribution throughout the whole transition.

The average bulk speed of the protons and electrons is given in kilometers per second in the panels i1 and i2:  $V^{+/-} = (n_1^{+/-} V_1^{+/-} + n_2^{+/-} V_2^{+/-}) / (n_1^{+/-} + n_2^{+/-})$ . In the left-hand panel note the large ion jet velocity of more than 500 km/s.  $V^+$  is parallel to the plasma layer and perpendicular to the magnetic field direction. These large ion jets (or ion beams) are spread over a distance of several hundred kilometers. Even more surprising is the narrow jet sheath of electrons with a velocity of the order of 10,000 km/s near  $x = 0$  (see panel i2). These bulk speeds result from the acceleration of charges by the inhomogeneous electric field  $E(x)$  and from their deflection in opposite direction by the non-uniform magnetic field  $B(x)$ .



Panels j1 and j2 give the value of  $A = (V^+ - V^-)/U^+$  across the plasma layer;  $U^+$  is the average thermal ion speed. When  $A$  is larger than unity, the plasma is unstable. Indeed  $A = 1$  corresponds to the threshold for the modified two-stream instability (McBride et al., 1972) also called the lower-hybrid drift instability. It can be seen that in the ionic layer, outside the thin electron layer,  $A < 1$ ; therefore, the parts of the plasma layer on both sides of the electron layer are stable, at least with respect to the modified two-stream instability. However, the thin electron sheath near  $x = 0$  is highly unstable and consequently is a potential source for large-amplitude electrostatic waves. These waves can then interact with the electrons, change their pitch angles, and fill the atmospheric loss cone.

As a result of wave-particle interactions, the initially anisotropic (truncated) electron velocity distribution becomes more isotropic until  $A$  is equal to or lower than unity: the instability is then quenched. However, as long as the velocity distributions of the electrons have not become isotropic everywhere between  $x = -\infty$  and  $x = +\infty$ , unstable electron layers will form and generate electrostatic noise.

#### IV. DISCUSSION AND CONCLUSIONS

The results of the stationary kinetic model illustrated in this paper indicate a number of features pertinent to the study of plasma layers which are associated with discrete auroral arcs.

1. First of all, for the boundary conditions considered (i.e., different densities and temperatures of the electrons and ions on both sides of the plasma layer), the electric potential  $\phi(x)$  is not constant, although  $\phi(-\infty)$  and  $\phi(+\infty)$  are imposed to be equal to zero at  $x = \pm\infty$ . This indicates that a plasma layer like that studied by Harris (1962) and Alpers (1969), where it is assumed that  $\phi(x) = 0$ , is by no means a unique nor a general solution.

2. The characteristic scales of variation of the plasma and field variables are the average ion Larmor radius for the broadest structure and the average electron Larmor radius for the thinner embedded electron sheath. If the wider scale of variation is typically 500-800 km in the equatorial plane of the magnetosphere at  $L = 10$ , its extent projected in the ionosphere is 30 times smaller, i.e., 15-30 km. This corresponds almost to the extent of inverted-V regions near discrete auroral arcs. It corresponds also to the region over which auroral field-aligned potential differences vary significantly.

3. Superimposed on these broad regions of potential variation are often much narrower ones (only a few hundred meters in extent) where sharp potential gradients are observed. We suggest that these thin regions with large electric field intensities are associated with electron layers in the magnetosphere like that found in our kinetic model calculation. The minimum thickness of these electron layers is 5-9 km in the plasmasheet. One can imagine velocity distributions for which there are several electron sheaths embedded in one broader ion structure. The thickness of 5-9 km is a minimum one; indeed electron sheaths are unstable with respect to the modified two-stream instability or lower-hybrid drift instability. Therefore, pitch angle scattering or diffusion of the electrons as a result of wave-particle interactions within these regions eventually tend to make the electron velocity distribution more isotropic. As a consequence the electron sheath tends to broaden and eventually to disappear when the velocity distribution of electrons has become isotropic within the plasma cloud and in the ambient background plasma.

4. Although in our one-dimensional model there is no proper atmospheric loss cone for the plasmasheet electrons, one can easily imagine that for a three-dimensional plasma layer in the magnetosphere the modified two-stream instability can similarly be a source for pitch angle scattering of the electrons and for filling of the atmospheric loss cone. To aliment this source of auroral electron precipitation it is necessary, however, to maintain the electron sheath unstable for the whole lifetime of the discrete auroral arc. Therefore, the plasma layer must constantly be reforming for instance by convection of the plasma cloud "surfing" earthward in the ambient plasmasheet background.



5. The peak value of  $\sim 200$  mV/m for the electric field intensity obtained in our kinetic model calculation is probably excessive. Indeed, the wave-particle diffusion mechanism mentioned above, will smooth irreversibly any too large electric potential gradient. Furthermore, such large perpendicular magnetospheric electric fields (EMF), when mapped down at ionospheric altitudes, must drive very large Pedersen and Hall electric currents through the resistive ionosphere. The Joule dissipation of these currents increases the local plasma temperature. But the local ionization density is then enhanced not only by the increased plasma temperature but also by primary auroral electron bombardment. All these effects concur to enhance the local electric conductivity and to short-circuit the ionospheric load. The large potential gradients applied across the magnetospheric plasma sheath are then discharged as the ionospheric resistance becomes vanishingly small. Magnetospheric potential differences (EMF) perpendicular to magnetic field lines then become field-aligned potential differences accelerating auroral electrons downward along auroral arc magnetic field lines.

6. Ion beams streaming earthward and/or tailward are typical features in the plasmasheet boundary layer adjacent to the tail lobe. These ion beams are observed from high energies of tens of keV to low energies of tens of eV (Lui et al., 1983). Occasionally, these ion beams are found within the plasma sheet proper, near its outer boundary where irregular magnetic field intensities are generally observed. Sugiura et al. (1970) have interpreted these irregular B-field variations as being diamagnetic signatures of spatial plasma clouds for which  $\beta$  is of the order of unity or larger (see also Meng and Mihalov, 1972). Both the ion beam streaming and the change in the magnetic field intensities are inherent in the kinetic model illustrated in Figure 1. It is suggested that ion beam streaming observed at the outer edge of the plasmasheet results from the electric field acceleration and magnetic field deflection of charge particles in plasma layers separating a hot plasma cloud and the cooler ambient plasmasheet or two adjacent diamagnetic plasma clouds of different densities, different temperatures, and different magnetizations, as in our kinetic model.

7. Changing boundary conditions at  $x = \pm \infty$  ( $N_{1,2}^{\pm \infty}$ ,  $T_{1,2}^{\pm \infty}$ ) and the choice of the velocity distributions  $f_{1,2}^{\pm \infty}$ , one can generate a wide variety of different plasma and field distributions within the plasma layer. The plasma layer shown in Figure 1 is only an illustrative example for a magnetospheric EMF source. From this case study one can deduce orders of magnitudes for maximum electric potential gradients (i.e., charge separation electric field), as well as for the maximum velocity of ion beams or jets expected in such plasma layers. By adjusting these boundary conditions and by adequately choosing  $f_{1,2}^{\pm \infty}$ , it is likely that such kinetic model calculations will be able to simulate a variety of detailed plasma and field measurements across plasma layers or boundaries when available from instruments with high enough time resolution.

The temperature  $\theta(x)$  and density  $n(x)$  of each plasma species vary across the potential layer separating the hot plasmasheet cloud at  $x = -\infty$  from the cooler background magnetotail plasma at  $x = +\infty$ . The layers considered here [for different values of  $\phi_2 - \phi_1 = \phi(+\infty)$ ] have boundary conditions listed in Table 1.  $B_{sh}$  denotes the value of the magnetic field at  $x = -\infty$ , i.e., deeply inside the plasmasheet cloud. The lower indices sh and t refer to the plasmasheet cloud and background magnetotail particles, respectively, while the upper indices (-) and (+) refer to electrons and protons, respectively. The following notations are assumed:  $n_{sh}^{+(-)}(-\infty) = N_{sh}^{+(-)}$ ;  $\theta_{sh}^{+(-)}(-\infty) = T_{sh}^{+(-)}$ ;  $n_t^{+(-)}(+\infty) = N_t^{+(-)}$ ;  $\theta_t^{+(-)}(+\infty) = T_t^{+(-)}$ .

The plasma boundary conditions given in Table 1 correspond to two interpenetrated hydrogen plasmas with different characteristics. Therefore,  $n_{sh}^{+(-)}(+\infty) = 0$  and  $n_t^{+(-)}(-\infty) = 0$ .

TABLE 1. BOUNDARY CONDITIONS

$N_{sh}^-$ cm <sup>-3</sup>	$T_{sh}^-$ keV	$N_{sh}^+$ cm <sup>-3</sup>	$T_{sh}^+$ keV	$N_t^-$ cm <sup>-3</sup>	$T_t^-$ keV	$N_t^+$ cm <sup>-3</sup>	$T_t^+$ keV	$B_{sh}$ nT
0.5	2.5	0.5	12	0.15	0.8	0.15	3	40

## REFERENCES

- Alpers, W., *Astrophys. Space Sci.*, **5**, 425-537 (1969).
- Botticher, W., H. Wank, and E. Schulz-Gulde (editors), *Proceedings of International Conference on Phenomena in Ionized Gases*, Dusseldorf, August 29-September 2, 1983, pp. 139-147, 1983.
- Harris, E. G., *Nuovo Cimento*, **23**, 115-121 (1962).
- Lemaire, J., and L. F. Burlaga, *Astrophys. Space Sci.*, **45**, 303-325 (1976).
- Lui, A. T. Y., T. E. Eastman, D. J. Williams, and L. A. Frank, Preprint APL/JHU 83-22, 1983.
- Lyons, L. R., and D. S. Evans, *J. Geophys. Res.*, **89**, 2395-2400 (1984).
- McBride, J. E., E. Ott, J. P. Boris, and J. H. Orens, *Phys. Fluids*, **15**, 2367-2383 (1972).
- Meng, C. I., and J. D. Mihalov, *J. Geophys. Res.*, **77**, 4661-4669 (1972).
- Ralston, A., and H. S. Wilf, *Méthodes Mathématiques Pour Calculateurs Arithmétiques*, Dunod, Paris, 482 pp., 1965.
- Roth, M., *J. Atmos. Terr. Phys.*, **38**, 1065-1070 (1976).
- Roth, M., *J. Atmos. Terr. Phys.*, **40**, 323-329 (1978).
- Roth, M., in *Proceedings of Magnetospheric Boundary Layers Conference, Alpbach, 11-15 June 1979*, ESA SP-148, edited by B. Battrock and J. Mort, pp. 295-309, ESTEC, Noordwijk, The Netherlands, 1979.
- Roth, M., Ph.D. Thesis, ULB, Brussels, 1980; *Aeronomica Acta A*, **221** (1980) (also *Académie Royale de Belgique, Mémoire de la Classe des Sciences*, Collection in 8° - 2e série, T XLIV - Fascicule 7 et dernier, 1984).
- Roth, M., D. S. Evans, and J. Lemaire, *J. Geophys. Res.*, submitted, 1986.
- Sestero, A., *Phys. Fluids*, **7**, 44-51 (1964).
- Sestero, A., *Phys. Fluids*, **9**, 2006-2013 (1966).
- Sugiura, M., T. L. Skillman, B. G. Ledley, and J. P. Heppner, in *Particles and Fields in the Magnetosphere*, edited by B. M. McCormac, pp. 165-170, D. Reidel Publishing Company, Hingham, Massachusetts, 1970.

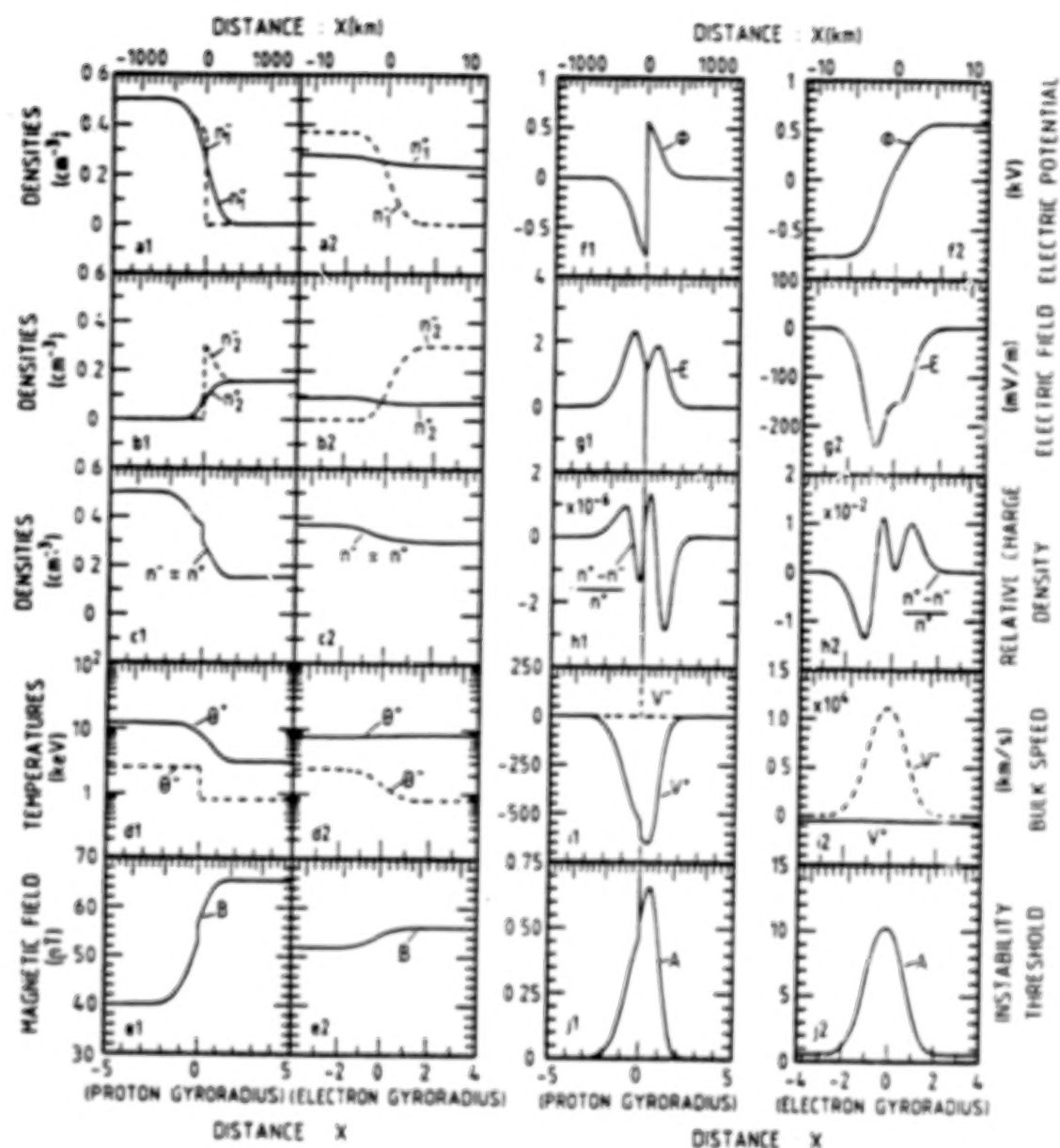


Figure 1. Plasma and field distributions across a plasma layer with boundary conditions typical in the plasmasheet.  $\phi(x)$  and  $B(x)$  are the electric potential and magnetic field intensity, respectively:  $\phi$  varies from  $\phi(-\infty) = 0$  to  $\phi(+\infty) = 0$  (see panels f1 and f2); the gradient of  $\phi$  determines the charge separation electric field  $E$  which is normal to the surface of the plasma layer (see panels g1 and g2); the relative electric space charge density remains small (see panels h1 and h2); the proton (+) and electron (-) densities  $n_{1,2}^{\pm}$  from side 1 (i.e.,  $x = -\infty$ ) and from side 2 (i.e.,  $x = +\infty$ ) vary across the layer from  $n_1^+ = 0.5 \text{ cm}^{-3}$ ,  $n_2^+ = 0$  at  $x = -\infty$  to  $n_1^+ = 0$ ,  $n_2^+ = 0.15 \text{ cm}^{-3}$  at  $x = +\infty$  (see panels a1, a2, b1, b2, c1, c2); the proton (+) and electron (-) temperatures  $\theta^{\pm}$  vary from  $\theta_1^+ = 12 \text{ keV}$ ,  $\theta_1^- = 2.5 \text{ keV}$  at  $x = -\infty$  to  $\theta_2^+ = 3 \text{ keV}$ ,  $\theta_2^- = 0.8 \text{ keV}$  at  $x = +\infty$  (see panels d1 and d2); the proton (+) and electron (-) bulk velocities  $V^{\pm}$  have large peak values in the middle of the composite plasma layer (see panels i1 and i2). Note the very thin electron layer embedded near  $x = 0$  within the broader ion layer extending over 4 average ion Larmor gyroradii (see lower scales of left-hand side panels). Expanded views of the narrow electron layer (only 3 or 4 average electron Larmor gyroradii in extent) are shown in the right-hand side panels. The distance  $x$  across the planar surface of interface is also shown in kilometers by the upper scales. The thin electron layer is unstable with respect to the modified two-stream instability. Indeed the instability threshold  $A$  (see panel j2) exceeds unity in this narrow region where extremely large (and unstable) E-fields are generated.

N87  
23331  
UNCLAS

## DOUBLE LAYERS ABOVE THE AURORA

M. Temerin and F. S. Mozer

Space Sciences Laboratory and Physics Department  
University of California, Berkeley, California 94720, U.S.A.

## ABSTRACT

Two different kinds of double layers have been found in association with auroral precipitation. One of these is the so-called "electrostatic shock," which is oriented at an oblique angle to the magnetic field in such a way that the perpendicular electric field is much larger than the parallel electric field. This type of double layer is often found at the edges of regions of upflowing ion beams and the direction of the electric field in the shock points toward the ion beam. The potential drop through the shock can be several kV and is comparable to the total potential needed to produce auroral acceleration. Instabilities associated with the shock may generate obliquely propagating Alfvén waves, which may accelerate electrons to produce flickering aurora. The flickering aurora provides evidence that the electrostatic shock may have large temporal fluctuations.

The other kind of double layer is the small-amplitude double layer found in regions of upward flowing ion beams, often in association with electrostatic ion cyclotron waves. The parallel and perpendicular electric fields in these structures are comparable in magnitude. The associated potentials are a few eV, which is substantially less than the energy of the measured particles. However, since many such double layers are found in regions of upward flowing ion beams, the combined potential drop through a set of these double layers can be substantial.

Some important questions concerning double layers and their relation to parallel electric fields in the aurora are:

1. What is the relation between small-amplitude double layers and electrostatic shocks?
2. What is the relation between electrostatic shocks and discrete arcs?
3. Are there strong double layers in the aurora?
4. What is the relation between ion conics and electrostatic shocks?
5. What are the parallel electric field magnitudes on auroral field lines?
6. Are there large parallel electric fields in the return current region?
7. How important are the dynamic properties of the parallel electric field on auroral field lines?

Here are some answers:

1. What is the relation between small-amplitude double layers and electrostatic shocks?

Small-amplitude double layers and electrostatic shocks are distinctly different phenomena. Electrostatic shocks are large, greater than about 100 mV/m, mostly perpendicular electric fields that vary discontinuously when measured at the 0.125 s resolution of the dc electric field detector on the S3-3 satellite below 8000 km altitude (Mozer et al., 1977, 1980) (see Fig. 1 for examples). Small-amplitude double layers are several mV/m, mostly



parallel electric fields lasting for a few milliseconds as measured by the S3-3 satellite (Temerin et al., 1982; Mozer and Temerin, 1983; Temerin and Mozer, 1984a,b) (Fig. 2). Electrostatic shocks occur in both upward and downward current regions (Cattell et al., 1979) in association with both upflowing ion beams and ion conics (Redsun et al., 1985) (Figs. 3 and 4). The electrostatic shocks associated with upflowing ion beams typically occur at the edges of energetic ( $>1$  keV) upflowing ion beams (Temerin et al., 1981; Bennett et al., 1983; Temerin and Mozer, 1984a; Redsun et al., 1985), and the potential drop through the electrostatic shock corresponds fairly well to the energy of the upflowing ion beam. Small-amplitude double layers, on the other hand, occur within regions of less energetic upflowing ion beams, and the potential drop through many small double layers may correspond to the total potential drop along the field line. It is often difficult to determine on the basis of the S3-3 wave data whether small-amplitude double layers occur in more energetic ion beams because of detector saturation problems associated with the large-amplitude wave turbulence that occurs in the more energetic events.

## 2. What is the relation between electrostatic shocks and discrete arcs?

It has previously been argued that electrostatic shocks are associated with discrete arcs (Torbert and Mozer, 1978; Kletzing et al., 1983). It is clear from the data that, as described in 1 above, some electrostatic shocks are associated with upflowing ion beams and inverted-V events. Other electrostatic shocks are associated with conics and counterstreaming and field-aligned electron events (Temerin and Mozer, 1984a). These latter electrostatic shocks would then not be associated with discrete arcs. It should be noted that upflowing ion beams and inverted-V electron events associated with electrostatic shocks have the  $\sim 10$  km to over 200 km latitudinal width normally associated with inverted-V electron events (Lin and Hoffman, 1979a; Redsun et al., 1985). This is typically larger than the latitudinal width of the electrostatic shock and implies that the electrostatic shock makes an oblique angle with respect to the magnetic field over part of its altitudinal extent.

## 3. Are there strong double layers in the aurora?

Whether there are strong double layers in the aurora depends to some extent on one's definition of a strong double layer. If by a strong double layer one means a potential drop the order of a significant fraction of the total auroral zone potential drop over a few Debye lengths, then the parallel electric field should be in excess of 1 V/m. Boehm and Mozer (1981) searched the S3-3 electric field data and found no convincing parallel electric fields greater than 250 mV/m in association with inverted-V events. They concluded that strong double layers are not associated with inverted-V events but could be associated with narrow discrete auroral arcs since the statistics were not good enough to rule out strong double layers if they were confined to narrow regions. This begs the question of whether there is any qualitative difference between narrow discrete arcs and inverted-V electron events with respect to the auroral potential structure. The problem of narrow discrete arc scales was raised by Maggs and Davis (1968) who reported that discrete arcs had scales down to 70 m. It has become popular to contrast such scales with inverted-V scales which are known to be much larger. However, the observation of 70 m scales was made by image orthicon television cameras that tend to emphasize small contrasts (Davis, 1978). Rocket observations indicate that typically the smallest gradients in the downward auroral electron energy flux are an order of magnitude larger (D. Evans, private communication). One should also keep in mind that inverted-V scales can be quite small. Lin and Hoffman (1979a), using AE-D data, reported that the largest number of inverted-V events had scales close to the minimum resolution of  $0.2^\circ$  or about 20 km in the ionosphere. The smallest paired electrostatic shock structure, which includes the region of smaller electric field between the large electric fields of the paired shock, and the smallest resolvable inverted-V structure on S3-3 map to about 5 km in the ionosphere (e.g., the first paired shock structure in orbit 209 in Fig. 1). In addition, one should keep in mind that smaller scale structures, such as field-aligned electron fluxes at the edges of inverted-V events (Arnoldy et al., 1985; McFadden et al., 1986) and field-aligned electron structures within inverted-V events, do not seem to correspond to larger overall potential as measured by the monoenergetic peak in the electron distribution function (Lin and Hoffman, 1979b). Thus, it seems consistent to regard narrow discrete arcs as narrow inverted-V events with the smallest scale structure within the arc as either due to relatively small changes in the field-aligned potential or enhanced field-aligned electron fluxes not directly related to changes in the potential. If this is the case, it could be that there are no strong double layers associated with the aurora. More data are needed to answer the question definitively.



#### 4. What is the relation between ion conic and electrostatic shocks?

It has been proposed that electrostatic shocks produce ion conics (Yang and Kan, 1983; Greenspan, 1984; Borovsky, 1984). Figures 3 and 4 show that many electrostatic shocks are indeed associated with ion conics. However, the idea that electrostatic shocks produce conics does not explain the clear distinction between electrostatic shocks associated with ion beams and electrostatic shocks associated with ion conics, nor does it explain the production of conics in regions where there are no electrostatic shocks. Even in regions where there are electrostatic shocks, the conic occurs in a much broader region than the electrostatic shock. Models for the generation of ion conics by electrostatic shocks show that the thickness of the electrostatic shock and the angle it makes with the magnetic field determine the relative perpendicular and parallel acceleration. One would then expect a continuous transition between conics and ion beams. In fact there is almost always at S3-3 altitudes ( $<8000$  km) a clear distinction between ion beams and ion conics, and, except for some general heating of the ion distribution, ion beams are consistent with acceleration purely parallel to the magnetic field while ion conics are consistent with acceleration purely perpendicular to the magnetic field. As mentioned previously, energetic ion beams are clearly associated with electrostatic shock. This implies that electrostatic shocks associated with ion beams are quasi-static on the ion transit time scale but that electrostatic shocks associated with ion conics are not. A more correct model of ion conic acceleration in regions of electrostatic shocks would need to take account of the fluctuations in the electric field and the general electric field turbulence in the region surrounding the electrostatic shocks. In regions of ion conics "electrostatic shocks" are not necessarily electrostatic (Temerin and Mozer, 1984a).

#### 5. What are the parallel electric field magnitudes on auroral field lines?

The parallel electric field can be measured directly or inferred from particle measurements. Measurements of ion beams and electron loss cones indicate that potential drops of 10 kV or larger can sometimes occur below the S3-3 satellite at altitudes of 6000 to 8000 km. Since the upward pointing electric field region has never been observed on S3-3 to extend below 3000 km and is usually limited to above 5000 km, the average parallel electric field in an inverted-V acceleration region must at least sometimes be the order of 5 to 10 mV/m and the maximum parallel electric field should be substantially larger since it is not likely that the electric field is uniform throughout the region. Direct measurements in electrostatic shocks indicate parallel electric fields up to about 100 mV/m (Mozer et al., 1980; Mozer, 1980). However, in most cases, the parallel electric field is less than 25 mV/m even in electrostatic shocks associated with upward flowing ion beams (Temerin and Mozer, 1984a).

#### 6. Are there large parallel electric fields in the return current region?

There are also large potential drops in the return current region. The electric field points down, which is in the direction to accelerate ions into the ionosphere and electrons into the magnetosphere. Some of the best evidence for downward pointing electric fields is shown in Figure 5, which displays some recent rocket data, courtesy of C. Carlson, J. McFadden, and M. Boehm. At 760 s into the flight, there was an almost complete dropout in the energetic electrons correlated with an enhancement in the precipitating ions flux over a narrow energy range at energies between 5 and 10 keV. At the same time, the eastward component of the magnetometer was consistent with a downward field-aligned current. These data imply a potential drop in the return current region in excess of 5 kV. Large downward electric fields can also be inferred from the observations of black aurora (Davis, 1978). Black aurora appear as narrow streaks of dark sky in regions of otherwise diffuse illumination. Broader regions of weaker parallel electric fields can be inferred from the S3-3 and DE 1 observations of upward flowing field-aligned electrons. One would expect that the narrow regions of downward pointing electric fields would correspond to paired electrostatic shocks with the electric fields in the paired shock pointing away from the region of parallel acceleration. Examples of such events are, however, comparatively rare in the S3-3 data.

7. How important are the dynamic properties of the parallel electric field on auroral field lines?

On the ion transit time scale the fluctuating portion of the parallel electric field must be several times larger than the dc portion. This is clear from the parallel velocity distribution of the upflowing ion beam. Typically, there is observable flux in an ion beam at energies four times larger than the energy of the maximum flux. This implies that in the frame of reference moving with the energetic ion the electric field is four times larger than the average field. These fields may be provided by the small-amplitude double layers and the parallel electric field components of the electrostatic ion cyclotron waves that are associated with the upflowing ion beams.

Another interesting dynamic property of auroral acceleration is flickering aurora. Recent data and theoretical models (Temerin et al., 1986) show that an obliquely propagating ion cyclotron wave, which may be produced by an oscillating double layer or oscillating parallel electric field, can produce the oscillating field-aligned electron flux in the flickering aurora.

*Acknowledgments.* The work was supported by the Office of Naval Research under contract N00014-81-C-0006.

## REFERENCES

- Arnoldy, R. L., T. E. Moore, and L. H. Cahill, Jr., *J. Geophys. Res.*, **90**, 8445 (1985).  
Bennett, E. L., M. Temerin, and F. S. Mozer, *J. Geophys. Res.*, **88**, 7107 (1983).  
Boehm, M. H., and F. S. Mozer, *Geophys. Res. Lett.*, **8**, 607 (1981).  
Borovsky, J. E., *J. Geophys. Res.*, **89**, 2251 (1984).  
Cattell, C. A., R. L. Lysak, R. B. Torbert, and F. S. Mozer, *Geophys. Res. Lett.*, **6**, 621 (1979).  
Davis, T. N., *Space Sci. Rev.*, **22**, 77 (1978).  
Greenspan, M. E., *J. Geophys. Res.*, **89**, 2842 (1984).  
Kletzing, C., C. Cattell, F. S. Mozer, S.-I. Akasofu, and K. Makita, *J. Geophys. Res.*, **84**, 4105 (1983).  
Lin, C. S., and R. A. Hoffman, *J. Geophys. Res.*, **84**, 1514 (1979a).  
Lin, C. S., and R. A. Hoffman, *J. Geophys. Res.*, **84**, 6547 (1979b).  
Maggs, J. E., and T. N. Davis, *Planet. Space Sci.*, **16**, 205 (1968).  
McFadden, J. P., C. W. Carlson, and M. H. Boehm, *J. Geophys. Res.*, **91**, 1723 (1986).  
Mozer, F. S., *Geophys. Res. Lett.*, **7**, 1097 (1980).  
Mozer, F. S., and M. Temerin, in *High-Latitude Space Plasma Physics*, edited by B. Hultqvist and T. Hagfors, Plenum, New York, 1983.  
Mozer, F. S., C. W. Carlson, M. K. Hudson, R. B. Torbert, B. Parady, J. Yatteau, and M. C. Kelley, *Phys. Rev. Lett.*, **38**, 292 (1977).  
Mozer, F. S., C. A. Cattell, R. L. Lysak, M. K. Hudson, M. Temerin, and R. B. Torbert, *Space Sci. Rev.*, **27**, 15 (1980).  
Redsun, M. S., M. Temerin, and F. S. Mozer, *J. Geophys. Res.*, **90**, 9615 (1985).  
Temerin, M., and F. S. Mozer, *Proc. Indian Acad. Sci.*, **93**, 227 (1984a).  
Temerin, M., and F. S. Mozer, in *Second Symposium on Plasma Double Layers and Related Topics*, edited by R. Schrittwieser and G. Eder, University of Innsbruck, 1984b.  
Temerin, M., M. H. Boehm, and F. S. Mozer, *Geophys. Res. Lett.*, **8**, 799 (1981).  
Temerin, M., K. Cerny, W. Lotko, and F. S. Mozer, *Phys. Rev. Lett.*, **48**, 1175 (1982).  
Temerin, M., J. McFadden, M. Boehm, and C. W. Carlson, *J. Geophys. Res.*, in press, 1986.  
Torbert, R. B., and F. S. Mozer, *Geophys. Res. Lett.*, **5**, 135 (1978).  
Yang, W. H., and J. R. Kan, *J. Geophys. Res.*, **88**, 465 (1983).

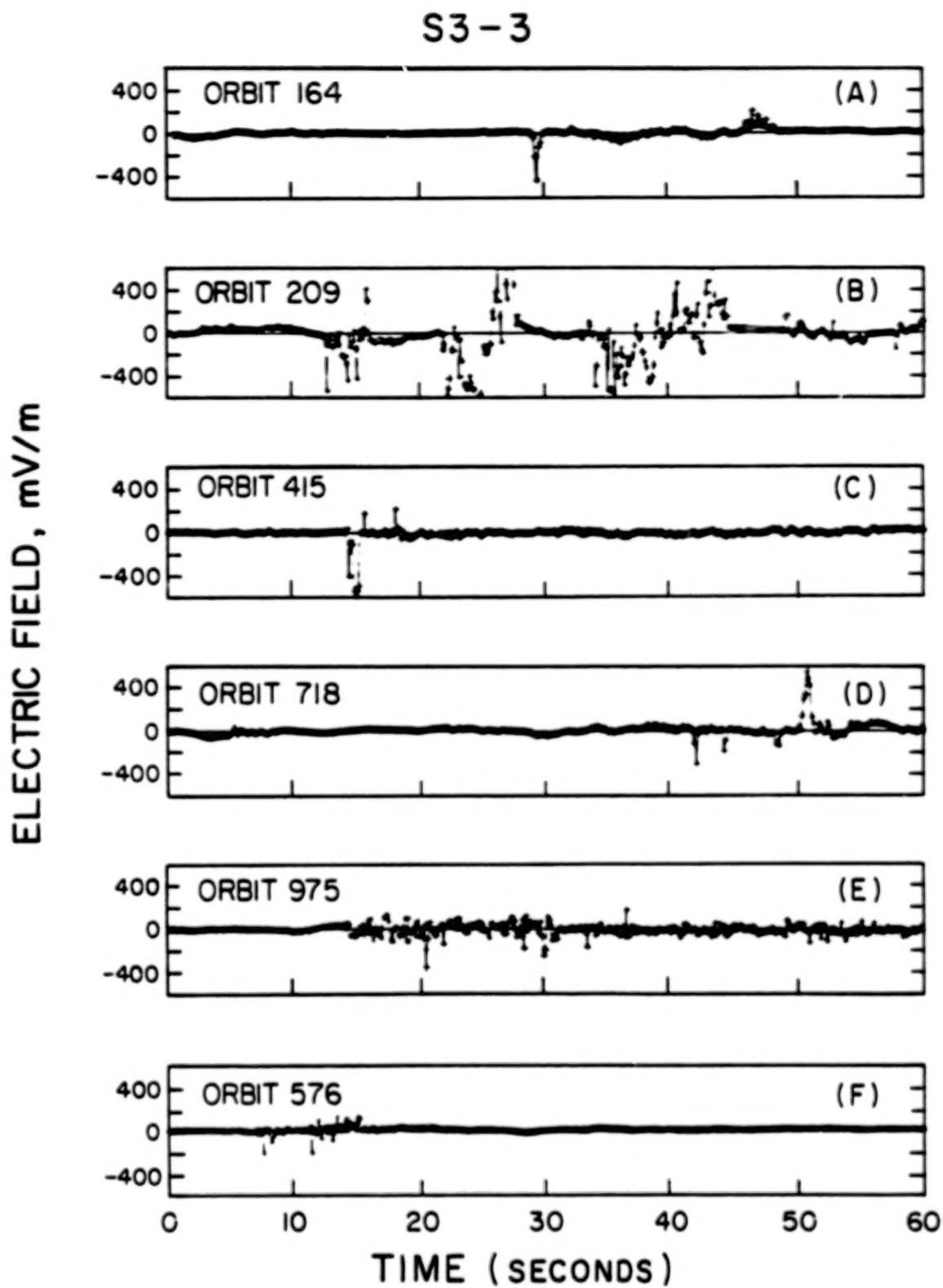


Figure 1. Examples of electrostatic shocks measured by the S3-3 satellite at altitudes below 8000 km.

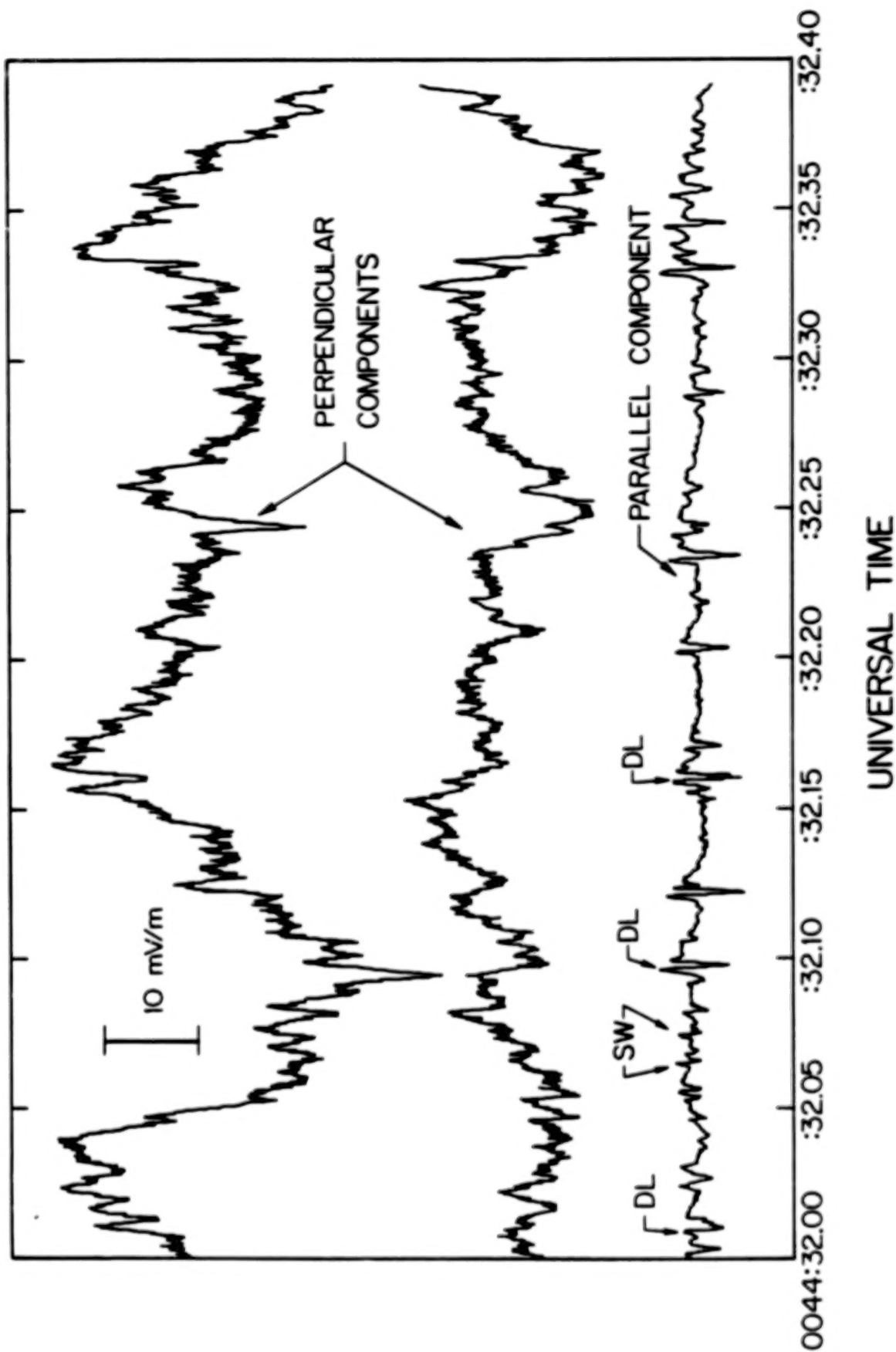


Figure 2. Examples of small-amplitude double layers measured by the S3-3 satellite. The noteworthy aspect of small-amplitude double layers is the significant parallel electric field (from Temerin et al., 1982).

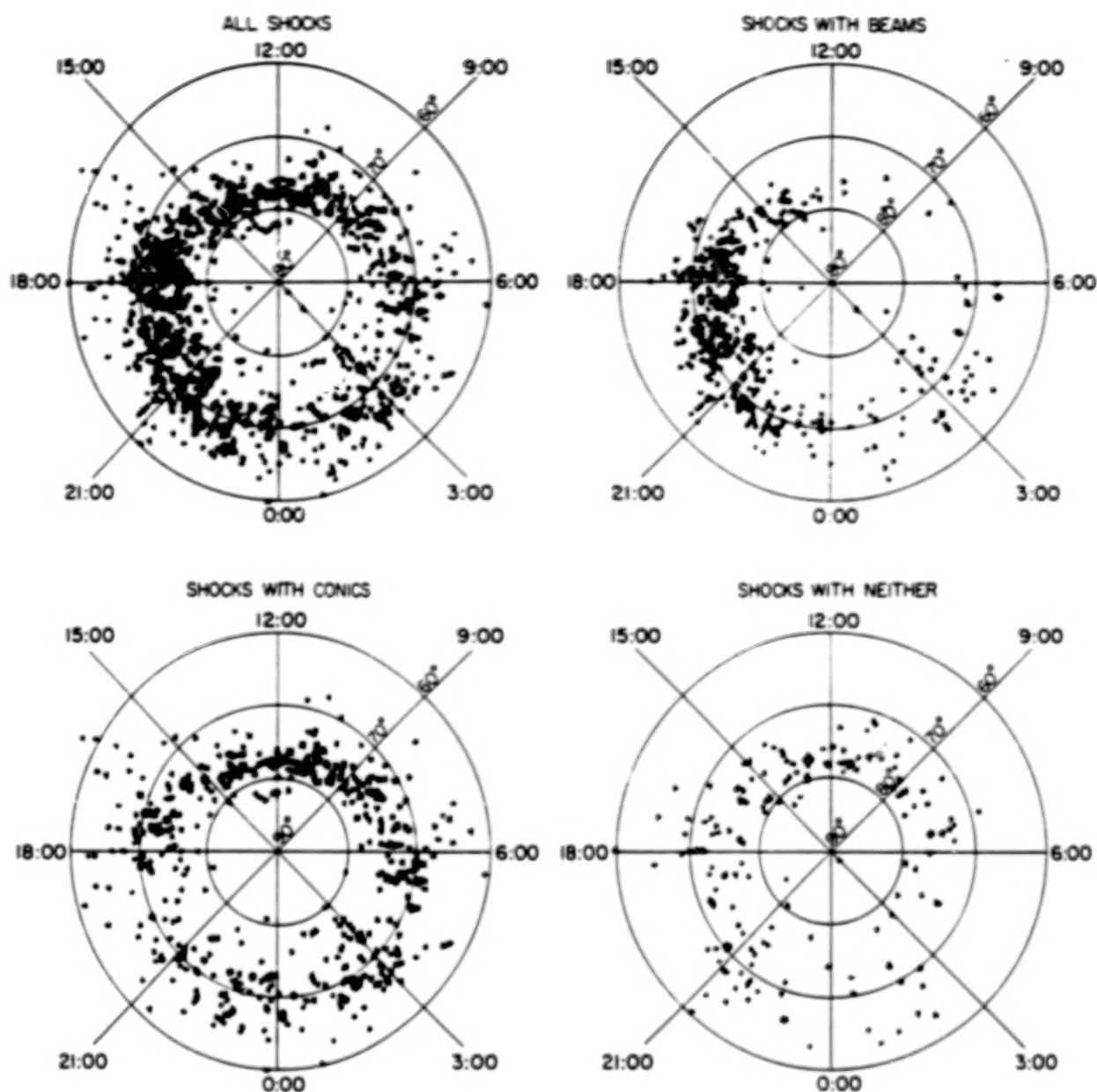


Figure 3. The distribution of electrostatic shocks as a function of invariant latitude and magnetic local time (from Redsun et al., 1985).



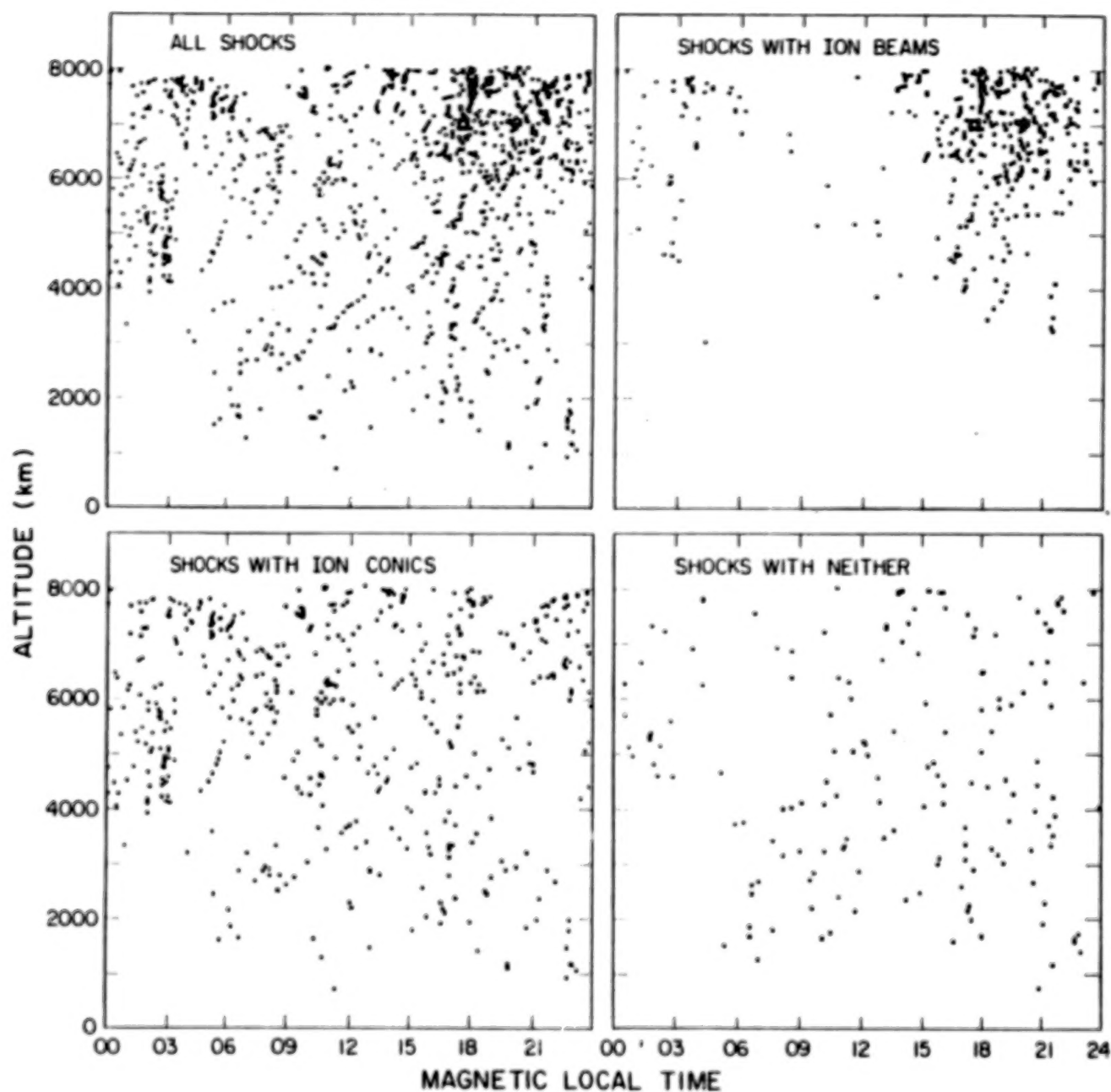


Figure 4. The distribution of electrostatic shocks as a function of altitude and magnetic local time (from Redsun et al., 1985).



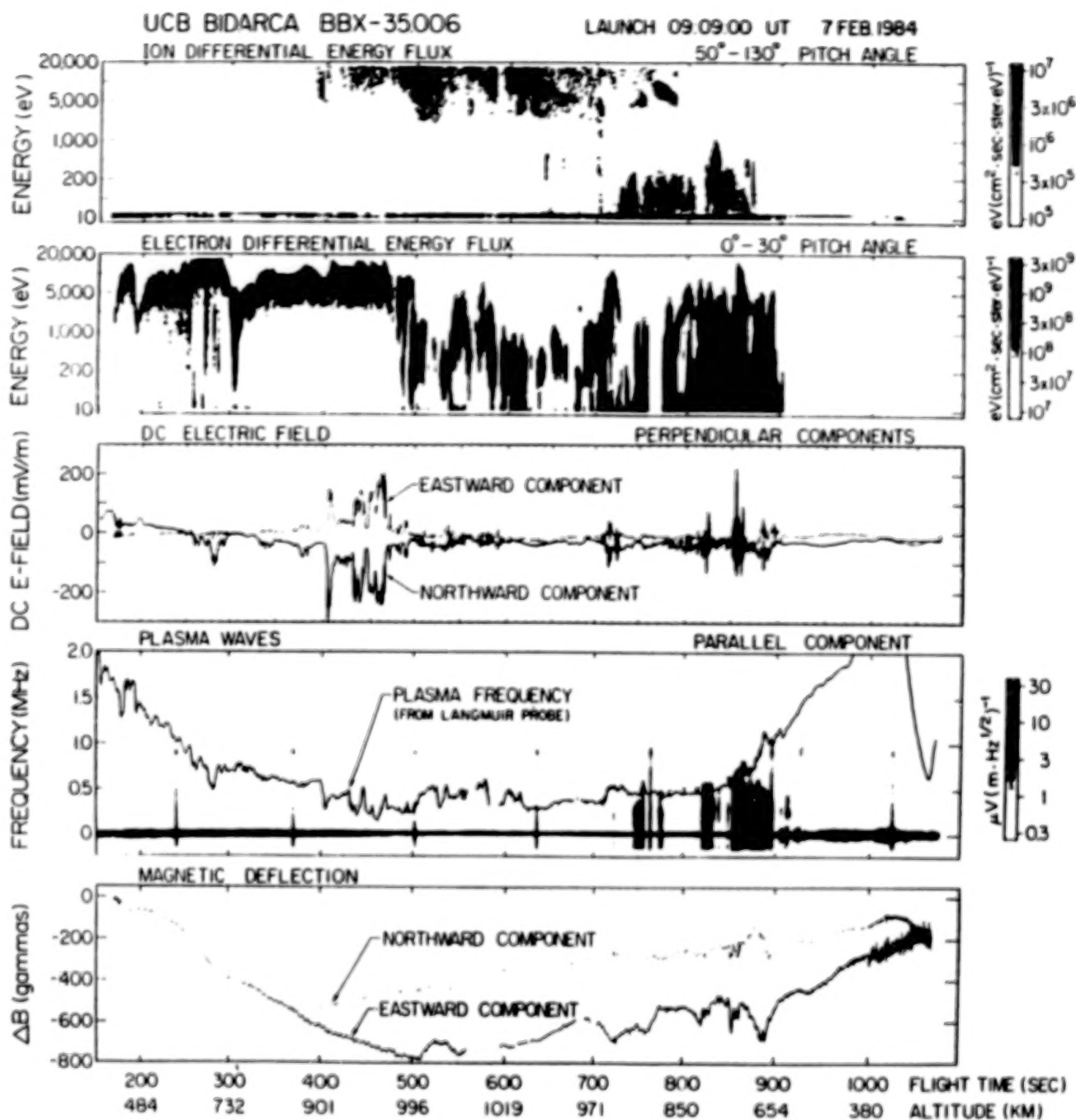


Figure 5. Recent rocket data. Example of anticorrelation of electron and ion fluxes can be seen at 760 s flight time. (Data courtesy of C. Carlson, J. McFadden and M. Boehm.)

N87

23332

UNCLAS

## BEAMED EMISSION FROM GAMMA-RAY BURST SOURCES

R. Epstein

Los Alamos National Laboratory

Los Alamos, New Mexico 87545, U.S.A.

Gamma-ray bursts are intense fluxes of radiation in the 100 keV to several MeV energy range which typically persist for between a fraction of a second and several seconds. The observed spectral shapes of these bursts suggest that the radiation is emitted as highly collimated beams emanating from neutron stars. This inference is based on the lack of significant gamma-gamma absorption (which indicates that photon paths do not cross at large angles) and by the dirth of x-ray energy photons (which are produced when gamma rays interact with stellar surfaces). The gamma-ray beams may be a consequence of particle acceleration in double layers in neutron star magnetospheres.

N87

23333

UNCLAS

**DOUBLE LAYERS AND PLASMA-WAVE RESISTIVITY IN EXTRAGALACTIC JETS:  
CAVITY FORMATION AND RADIO-WAVE EMISSION**

Joseph E. Borovsky  
Space Plasma Physics Group  
Los Alamos National Laboratory  
Los Alamos New Mexico 87545, U.S.A.

**ABSTRACT**

For estimated values of the currents carried by extragalactic jets, current-driven electrostatic-wave- and electromagnetic-wave-produced resistivities do not occur. Strong plasma double layers, however, may exist within self-maintained density cavities, the relativistic double-layer-emitted electron, and ion beams driving plasma-wave resistivities in the low- and high-potential plasma adjacent to the double layers. The double-layer-emitted electron beams may also emit polarized radio waves via a collective bremsstrahlung process mediated by electrostatic two-stream instabilities.

**I. INTRODUCTION**

Extragalactic jets are collimated radio-luminous plasmas that are thought to be supersonic outflows from the nuclei of elliptical galaxies, the jet plasma traveling long distances through the intergalactic medium before being stopped (Begelman et al., 1984). Often, the length of a jet is much larger than the size of its parent galaxy.

The internal plasma pressures of some extragalactic jets are thought to exceed the plasma pressures in the external media. This has led to the hypothesis that these jet plasmas are radially confined via electric-current pinching, the electrical current flowing axially through the column of jet plasmas (Alfvén, 1977, 1978; Benford, 1978), as depicted in Figure 1. The hypothesis that jets carry currents is also supported by electrodynamic models of jet-plasma acceleration (Lovelace, 1976). The presence of currents opens the important possibility that large amounts of energy are being transported down the jets via electrical processes. If electrical currents are in fact present, then electric fields are also expected to be present.

In this report, a model of the electric field that may reside within an extragalactic jet is described. The model involves a plasma double layer or a multiple of plasma double layers in series, each one residing within a density cavity that is created by the action of the double-layer-emitted particle beams.

In section II, the properties of extragalactic jets are reviewed and the Coulomb-collision resistivities and the plasma-wave resistivities within the jets are discussed. In Section III, the double layer model is described. In Section IV, some consequences of the double layer model are discussed, including radio-wave emission from the double-layer-emitted electron beams via a collective bremsstrahlung process, and in Section V, some double layer topics that need further research are pointed out.

PRECEDING PAGE BLANK NOT FILMED

## II. COLLISIONAL AND PLASMA-WAVE RESISTIVITIES IN JETS

Subject to great uncertainties, extragalactic jets and the plasmas within them have the following properties (Begelman et al., 1984). The lengths of the jets vary from  $L \sim 10^4$  Pc to  $L \sim 10^6$  Pc, where  $1 \text{ Pc} = 3.1 \times 10^{18} \text{ cm}$ , and the radii of the jets vary from  $r \sim 10^2$  Pc close to the galactic centers to  $r \sim 10^3$  Pc further out; typical diameters of galaxies are  $10^4$  to  $10^5$  Pc. The jet plasma is believed to be of low density,  $n \sim 10^{-6} - 10^{-4} \text{ cm}^{-3}$  and warm  $T_e \sim T_i \sim 10^5 \text{ K}$ , with an additional population of relativistic synchrotron-emitting electrons. The luminosity of the jet plasma is non-uniform, implying higher densities of relativistic electrons and/or stronger magnetic fields in localized hot spots. Estimates of the magnetic field strength yield  $B \sim 10^{-5} - 10^{-4}$  gauss. For a few jets that reside in the centers of clusters of galaxies, the ambient plasma is detectable via its x-ray bremsstrahlung, and pressure estimates for these ambient media can be obtained. In some of these instances, the pressures of the jet plasmas are believed to exceed the pressures of the ambient plasmas, and z-pinching of the jets by electrical currents may be acting to confine the jets. Estimates of the total amount of current needed to z-pinch the jets are  $I \sim 10^{17} - 10^{18} \text{ Amp}$ , implying current densities  $j \sim 10^{-23} - 10^{-21} \text{ Amp/m}^2$ . If these currents are carried by drifts between the ion and electron distributions, then typical drift velocities are  $10^{-5} - 10^{-2} \text{ cm/s}$ .

These jet plasmas are very nearly collisionless; for a plasma with  $n = 10^{-4} \text{ cm}^{-3}$  and  $T = 10^5 \text{ K}$ , the Coulomb-collision conductivity is  $\sigma_{||} \approx 1.8 \times 10^{13} \text{ s}^{-1}$ . For a current density  $j_{||} = 1.0 \times 10^{-21} \text{ Amp m}^{-2}$ , the electric field along the jet required to drive the current is  $E_{||} = 4.9 \times 10^{-7} \text{ V/cm}$ . For a jet  $10^5 \text{ Pc}$  in length, this amounts to a total potential drop  $\Delta\phi$  of a mere  $1.5 \times 10^{-3} \text{ V}$ . By almost all standards, the jet is a perfect conductor.

Electrostatic plasma-wave instabilities that are driven by relative drifts between Maxwellian ions and electrons require an electron-ion relative drift velocity  $v_o$  that is comparable to  $v_{te}$  (Papadopoulos, 1977). As mentioned above, the relative drift within an extragalactic jet is typically  $v_o \sim 10^{-5} - 10^{-2} \text{ cm/s}$ . This drift speed is orders of magnitude lower than the electron thermal velocity. Thus, electrostatic microinstabilities driven by electron-ion relative drifts will not provide electrical resistivities in current-carrying extragalactic jets.

Neither will electromagnetic plasma-wave instabilities that are driven by relative drifts between Maxwellian ions and electrons produce resistivity in extragalactic jets. For a uniform-current-density z-pinch jet in equilibrium, no electromagnetic waves with wavelengths shorter than the jet diameter are unstable (Borovsky, 1986). Hence, no resistivity can be produced.

Note that since anomalous-resistivity processes might not occur in the jet plasma, the jet plasmas might be truly ohmic, at least for the current densities envisioned to z-pinch the jets.

## III. THE DOUBLE LAYER MODEL

Some of the properties of strong plasma double layers are as follows (Michelsen and Rasmussen, 1982; Schrittwieser and Eder, 1984). The thicknesses of double layers are  $\Delta L \sim 10^1 - 10^5 \lambda_D$ , the double layers being thicker if the potential jump  $\Delta\phi$  across them is greater. The current density within and near the double layer is independent of the local electric field strength; therefore, the plasma containing the double layer is non-ohmic. Ions that drift into the high potential edge of the double layer are accelerated to form a fast, cold beam in the low potential plasma, and electrons that drift into the low potential edge of the double layer are accelerated to form a fast, cold beam in the high potential plasma. The efficiency of turning electrical energy into the kinetic energy of high-energy particles in the double layer is 100 percent. These beams drive space charge waves in the adjacent plasmas (Borovsky and Joyce, 1983), the electron beam drives Langmuir waves and electrostatic electron-cyclotron waves in the high potential plasma, and the ion beam drives ion-acoustic and electrostatic and ion-cyclotron waves in the low potential plasma. If the double layer has a large enough potential drop  $\Delta\phi$ , then Langmuir waves and electrostatic electron-cyclotron waves will also be driven by the ion beam in the low potential plasma.



Double layers are also characterized by Bohm criteria at their high and low potential edges. For steady-state double layers, these criteria require the ion-inflow drift velocity to exceed  $C_s$  and the electron-inflow drift velocity to exceed  $v_{te}$ . As was the case for electrostatic plasma-wave instabilities, these required inflow velocities imply large current densities. However, the Bohm criteria may be satisfied without large current densities if a density cavity is formed by the action of the double-layer-emitted beams. When the potential drop  $\Delta\phi$  of a double layer is large enough to produce highly relativistic electron beams, the growth length for two-stream electrostatic waves in the high potential plasma is

$$\lambda_{\text{growth}}/\lambda_{De} = 2.1 \times 10^{-3} T_e^{4/3} (e\Delta\phi/k_B T) ,$$

and if the potential jump is large enough to produce a highly relativistic ion beam, then the growth length for high-frequency electrostatic plasma waves in the low potential plasma is

$$\lambda_{\text{growth}}/\lambda_{De} = 4.8 \times 10^{-5} T_e^{4/3} (e\Delta\phi/k_B T)$$

(Borovsky, 1986). Because the phase and group velocities of the growing waves are in the direction of the beams, these waves will propagate away from the double layer, leaving regions of calm plasma near the double layer. Beyond these calm regions, however, plasma waves will be present with very large amplitudes (Fig. 2). In the fields of waves on either side of the double layer, the effective collision frequency may approach  $\omega_{pe}$ . Since the mobilities of charged particles in these regions are small, they require long periods of time to transit to the double layer; accordingly, their number densities are high within these regions. When a particle leaks out of one of these turbulent regions and passes into a calm region near the double layer, it drifts without scattering; this drift being at the thermal velocity, the number density is low (see Fig. 3, top and middle). Thus, the double layer produces electron and ion beams which create two regions of plasma turbulence removed from the double layer itself, these regions acting to keep the plasma density high away from the double layer and creating a cavity around the double layer. It is in this density-cavity region that the Bohm criteria for the double layer can be met; these high drift velocities do not produce high current densities because they occur only in regions where the particle density is low. The current density is conserved throughout the region (Fig. 3, bottom). This cavity production can also be described as the outwardly directed double-layer-emitted beams driving plasma waves that transfer the beam momentum to the ambient plasma, pushing open a cavity and maintaining it with beam pressure.

In order for current to be driven through the regions of electrostatic turbulence near the double layer, resistive electric fields will arise, adding to the potential of the double layer. Note that in this model the anomalous resistivity regions are required, not for their resistive potential drops, but for the reduction of the particle mobility that they cause.

A laboratory example of a double-layer-driven cavity is contained in Figures 9 and 10 of Guyot and Hollenstein (1983), reproduced here as Figure 4. In the first panel of Figure 4, the double layer is clearly visible at  $x \approx 50$  cm. Note also that there is a region of resistive potential drop in the high potential plasma adjacent to the double layer. In the second panel, a density cavity around the double layer is visible. In the bottom panel, the electron drift speed is seen to increase within the cavity. Electrostatic turbulence is detected on both sides of the double layer. Another example of a cavity formed around a laboratory double layer appears in Figure 3 of Sato et al. (1981).

Multiple double layers may occur in a series, each double layer surrounded by regions of beam-driven turbulence that maintains density cavities. The double layers must be separated by distances large enough for their emitted electron and ion beams to thermalize, the thermalized beam particles constituting plasma sources between the double layers.

#### IV. CONSEQUENCES OF THE MODEL

If they are of relativistic energies, the double-layer-produced beams of electrons will undoubtedly emit synchrotron radiation, making the high potential plasmas near double layers radio luminous. More important, however, the relativistic electron beams will rapidly emit polarized radio waves via a collective-bremsstrahlung process (Kato et al., 1983). The electron-electron two-stream instability that produces the electrostatic waves in the high potential plasma causes the beam electrons to bunch up and the background-plasma electrons to bunch up. The beam electrons are accelerated by random electric fields as they pass through the charge-bunched background plasma, causing them to emit electromagnetic radiation. Because the beam electrons are charge-bunched, they emit coherently. Thus, this emission is like a collective bremsstrahlung, with charge clumps in the beam radiating as they scatter off charge clumps in the background plasma. As observed in the laboratory, the electron beams emit electromagnetic waves with frequencies of approximately  $\gamma^2\omega_{pe}$  (Kato et al., 1983), where  $\gamma$  is the relativistic factor of the beam.

It is reasonable to anticipate that a radio hot spot would be associated with a double layer or a series of double layers within a jet, since most of the energy dissipated by the double layer appears as an energetic electron beam that is capable of radiating. Further, if multiple double layers are separated by distances great enough, then the individual radio striations in the jet might be resolvable.

A model that proves to be very similar to this model was developed by Langmuir (1929) to describe the current flows in partially ionized gases. In that model, the inflow of plasma to a double layer was described as an ambipolar diffusion down density gradients. A similar approach may be taken in the present model, with only a change in the nature of the diffusion coefficient.

The double layers envisioned here have many features in common with auroral zone double layers (Shawhan, 1978; Borovsky, 1984). Auroral double layers accelerate electrons to energies of 1–10 keV, the electrons following the terrestrial magnetic field lines to the upper atmosphere where they produce visible auroral arcs. The auroral double layers also accelerate ions upward where they are believed to drive the large-amplitude electrostatic ion-cyclotron waves. The energetic beam electrons are believed to drive Langmuir and electrostatic electron-cyclotron waves, and are also believed to drive collective radio emissions (Anderson, 1983).

#### V. FUTURE RESEARCH IN DOUBLE LAYERS

There are many topics that must be researched before the double layer model discussed in Sections III and IV is complete.

Two topics important to this model are relativistic double layers and double layers in finite- $\beta$  plasmas, the stability and dynamics of both types of double layers having yet to be examined. For relativistic double layers, stability factors may favor particular values for the potential jump, such as  $e\Delta\phi = m_e c^2$  or  $e\Delta\phi = m_i c^2$ . For finite- $\beta$  double layers, beam-driven electromagnetic-wave turbulence may provide another cavity-forming mechanism. Laboratory diagnostics will be difficult to construct for relativistic double layers, and very large plasma chambers will be required to magnetize the particles for finite- $\beta$  double layer experiments.

Another important topic is the dynamics of multiple double layers. In most laboratory devices, the system potential drops are limited to the ionization potentials of the gases used, and the ions are Coulomb-collisional. To investigate multiple double layers via computer simulation, very large numerical systems must be used to resolve the large-scale phenomena (beam thermalization), the small-scale phenomena (double layers), the fast time scales (Langmuir waves), and the slow time scales (beam evolution). A further goal would be to understand the pre-sheaths at the edges of the double layers. Unfortunately for the theoretical approach, pre-sheaths in collisionless plasmas probably involve electric field fluctuations, and, unfortunately for laboratory experiments, these weak electric field structures are very difficult to observe.

In order to understand the inflow of plasma through the regions of electrostatic turbulence, diffusive flows driven by density gradients and fluctuating electric fields need to be studied.

The spatial evolution of double-layer-emitted electron beams is also a topic for future study. Since these electrons scatter and lose energy as they travel, there will be a spatial dependence of the collective bremsstrahlung spectra. A knowledge of this spectral evolution matched against the spectra of radio hot spots will provide a direct test for the presence of double layer energy dissipation within jets.

*Acknowledgments.* The author wishes to thank Dan Baker, Jack Burns, Jean Eilek, Rich Epstein, Steve Fuselier, Peter Gary, Michelle Thomsen, and Terry Whelan for their assistance. This work was supported by the NASA Solar-Terrestrial Theory Program and by the U.S. Department of Energy.

## REFERENCES

- Alfvén, H., *Rev. Geophys. Space Phys.*, **15**, 271 (1977).  
Alfvén, H., *Astrophys. Space Sci.*, **54**, 279 (1978).  
Anderson, R. R., *Rev. Geophys. Space Phys.*, **21**, 474 (1983).  
Begelman, M. C., R. D. Blandford, and M. J. Rees, *Rev. Mod. Phys.*, **56**, 255 (1984).  
Benford, G., *Mon. Not. Roy. Astron. Soc.*, **183**, 29 (1978).  
Borovsky, J. E., *J. Geophys. Res.*, **89**, 2251 (1984).  
Borovsky, J. E., *Astrophys. J.*, in press, 1986.  
Borovsky, J. E., and G. Joyce, *J. Plasma Phys.*, **29**, 45 (1983).  
Guyot, M., and G. Hollenstein, *Phys. Fluids*, **26**, 1596 (1983).  
Kato, K. G., G. Benford, and D. Tzach, *Phys. Fluids*, **26**, 3636 (1983).  
Langmuir, I., *Phys. Rev.*, **33**, 954 (1929).  
Lovelace, R. V. E., *Nature*, **262**, 649 (1976).  
Michelsen, P., and J. J. Rasmussen (editors), *First Symposium on Plasma Double Layers*, Riso National Laboratory, Denmark, Document Riso-R-472, 1982.  
Papadopoulos, K., *Rev. Geophys. Space Phys.*, **15**, 113 (1977).  
Sato, N., R. Hatakeyama, S. Iizuka, T. Mieno, K. Saeki, J. J. Rasmussen, and P. Michelsen, *Phys. Rev. Lett.*, **46**, 1330 (1981).  
Schrittwieser, R., and G. Eder (editors), *Second Symposium on Plasma Double Layers and Related Topics*, University of Innsbruck, 1984.  
Shawhan, S. D., C.-G. Fälthammar, and L. P. Block, *J. Geophys. Res.*, **83**, 1049 (1978).

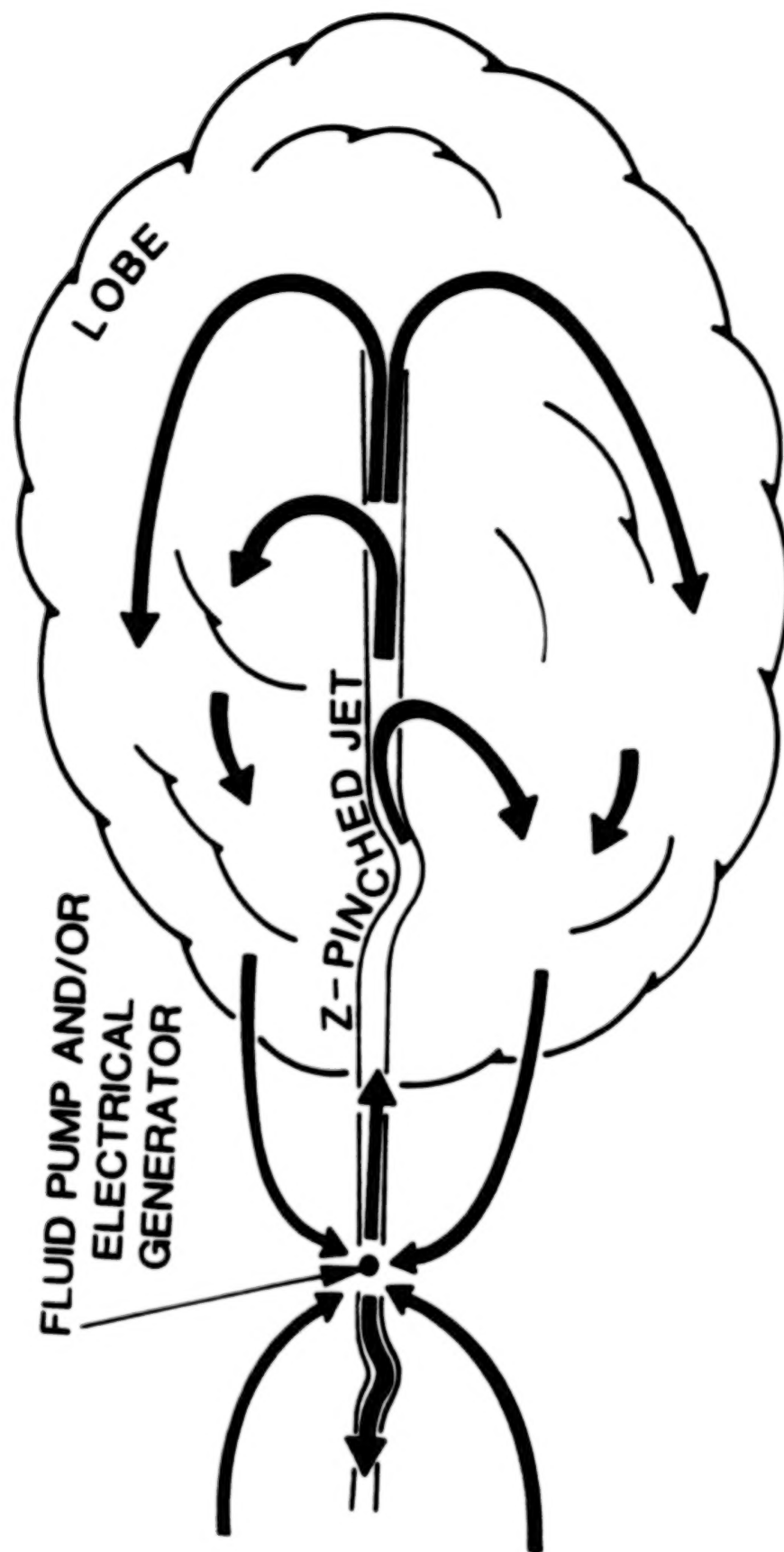


Figure 1. Schematic of an extragalactic jet carrying current within a collimated jet plasma.

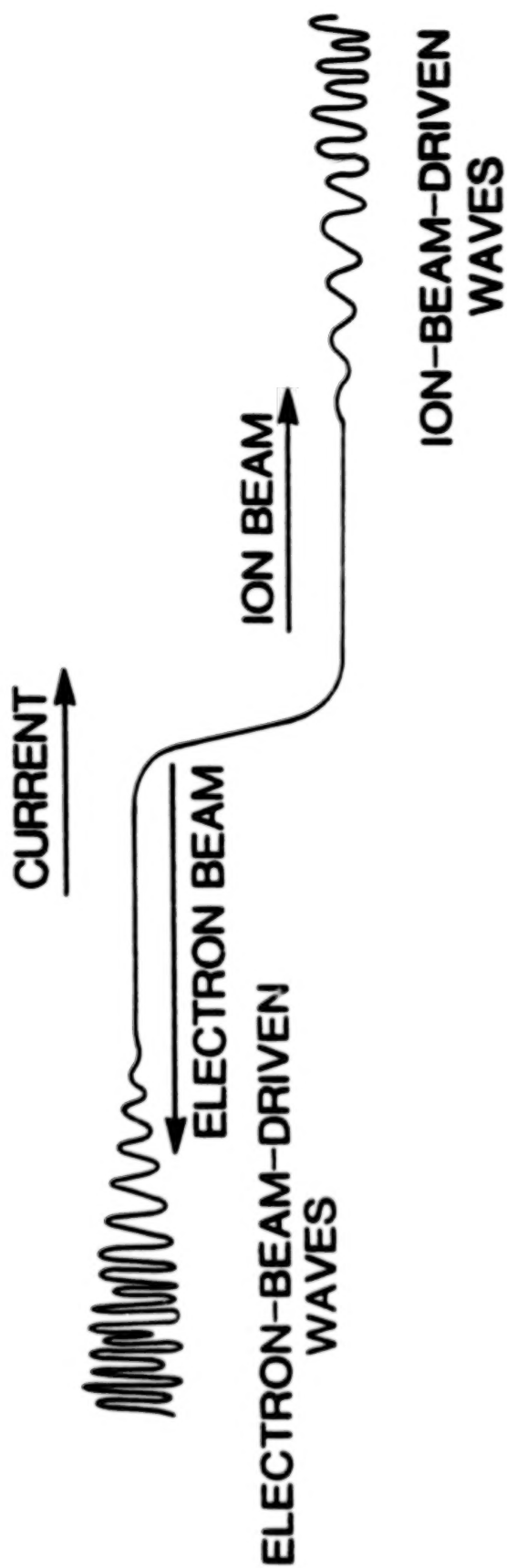


Figure 2. Schematic of a plasma double layer and the waves that the double-layer-emitted electron and ion beams produce.



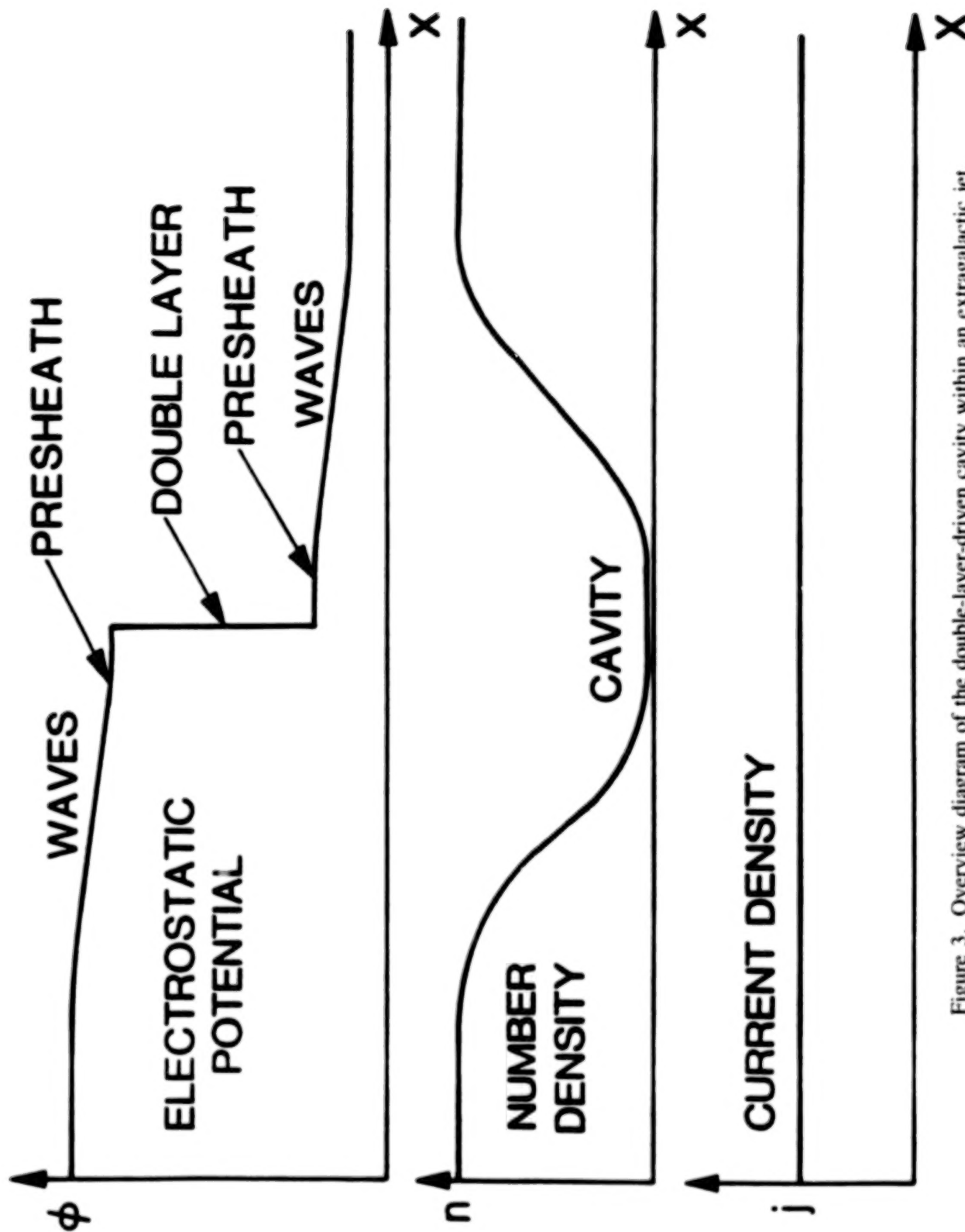


Figure 3. Overview diagram of the double-layer-driven cavity within an extragalactic jet. In the top panel the electrostatic potential is depicted, in the middle panel the particle density is depicted, and in the bottom panel the current density is depicted, all as functions of the distance along the jet.



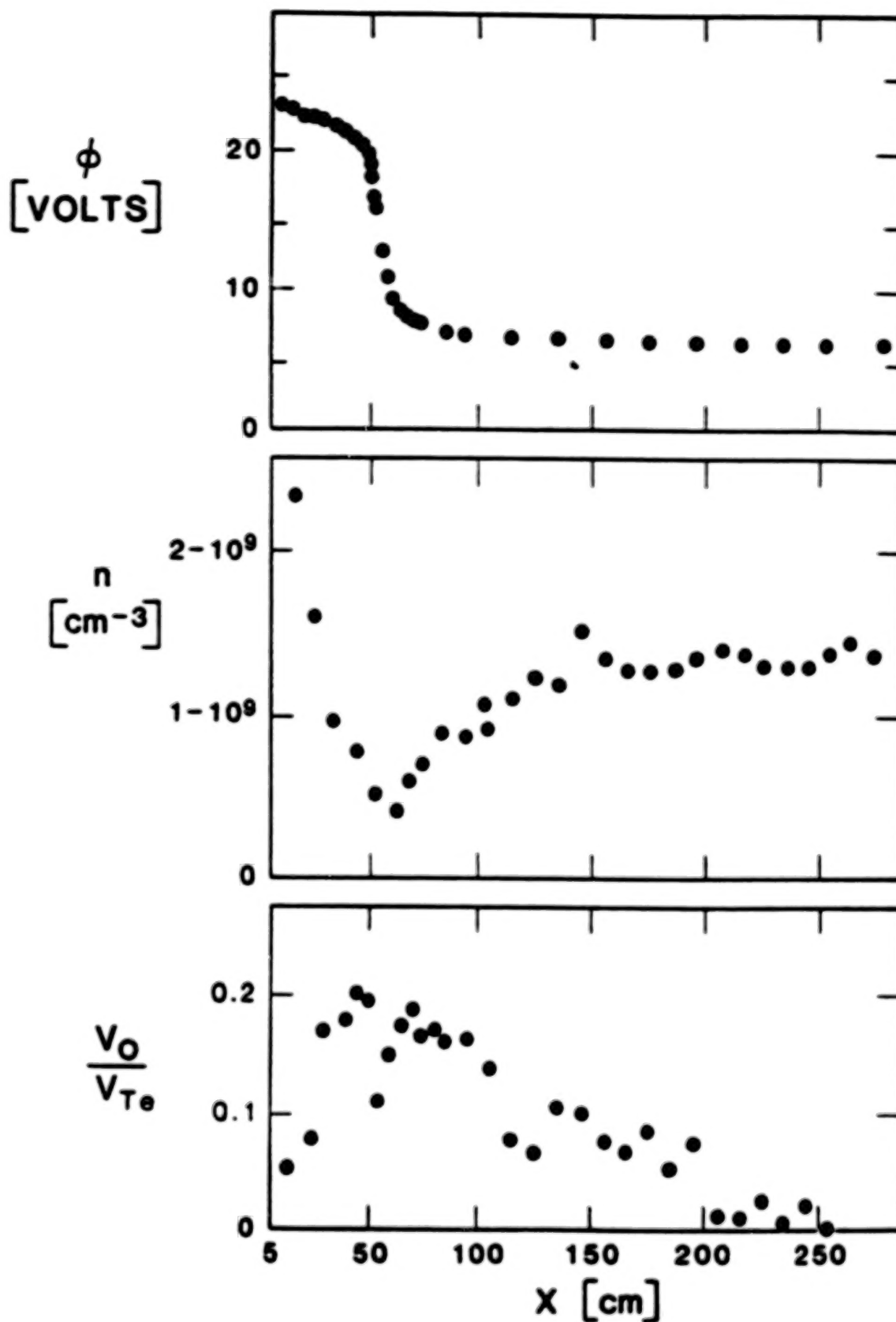


Figure 4. After Figures 9 and 10 of Guyot and Hollenstein (1983), the experimentally measured electrostatic potential  $\phi$ , the number density  $n$ , and the electron drift velocity  $v_0$  are plotted as functions of distance in the top, middle, and bottom panels, respectively.

N87

23334

UNCLAS

**ACCRETION ONTO NEUTRON STARS WITH THE PRESENCE  
OF A DOUBLE LAYER**

A. C. Williams, M. C. Weisskopf, R. F. Elsner, and W. Darbro  
Space Science Laboratory  
NASA Marshall Space Flight Center  
Huntsville, Alabama 35812 U.S.A.

and

P. G. Sutherland  
Department of Physics, McMaster University  
Hamilton, Ontario L8S4M1, Canada

It is known, from laboratory experiments, that double layers will form in plasmas, usually in the presence of an electric current. In this paper we argue that a double layer may be present in the accretion column of a neutron star in a binary system. We suggest that the double layer may be the predominant deceleration mechanism for the accreting ions, especially for sources with x-ray luminosities of less than about  $10^{37}$  erg s<sup>-1</sup>. Previous models have involved either a collisionless shock or an assumed gradual deceleration of the accreting ions to thermalize the energy of the infalling matter.

N87

23335

UNCLAS

# THE FORMATION OF A DOUBLE LAYER LEADING TO THE CRITICAL VELOCITY PHENOMENON

A. C. Williams  
Space Science Laboratory  
NASA Marshall Space Flight Center  
Huntsville, Alabama 35812, U.S.A.

## ABSTRACT

The formation of a double layer is proposed as the mechanism which produces the critical velocity phenomenon. We examine this hypothesis, qualitatively, and find that the double layer can be a very efficient mechanism for transferring the kinetic energy of the neutral gas into the kinetic energy of electrons which, in turn, will ionize the neutral gas if the critical velocity has been reached or exceeded.

## I. INTRODUCTION

In a study of the mass distribution of secondary bodies in the solar system, Alfvén (1954) noted that these bodies were arranged in discrete bands surrounding the central object. The particular location of the band in which each body appeared was found to be dependent upon the chemical composition of the dominant elements of the body. To explain this band structure, Alfvén proposed that a strong coupling suddenly occurs between a neutral gas and a magnetized plasma whenever their relative velocity reaches the critical velocity,  $v_{crit}$ , given by

$$v_{crit} = (2eV_i/m_n)^{1/2} \quad (1)$$

Here,  $V_i$  is the ionization potential of the neutral gas and  $m_n$  is the mass of one of the neutral particles. The proposed interaction has to have the effect of prohibiting the relative velocity from exceeding this critical velocity in order to explain the band structure.

In the rest frame of the plasma, equation (1) implies that when the kinetic energy of the neutral particles is equal to the ionization potential, a strong coupling occurs between the neutral gas and the plasma. Such a coupling would be expected if, for example, the gas suddenly begins to be ionized at this relative velocity. Then the magnetic field, which is threading the plasma, will interact strongly with the newly formed ions and electrons. However, ionization is not expected to become prominent when the relative velocity is equal to the critical velocity because the cross section for ionization due to binary collisions between neutral particles and plasma ions is essentially zero for the energy transfer needed at this relative velocity (assuming negligible random kinetic energy). For equal mass particles the maximum energy transfer is one-half the kinetic energy. Furthermore, the energy of electrons with a velocity equal to the critical velocity is orders of magnitude smaller than the ionization energy.

Hence, traditional classical plasma physics seems to be unable to explain why an enhanced interaction should occur between a neutral gas and a magnetized plasma when the relative velocity reaches the critical value. However, laboratory experiments have verified the critical velocity phenomenon and the validity of equation (1) (see Danielsson, 1973, and Raadu, 1981, for reviews). Subsequently, theories have been proposed to explain the

experiments (see Sherman, 1973, and Raadu, 1978, for reviews). The present theoretical situation, nevertheless, is that there is no one theory that satisfactorily explains the phenomenon over the wide range of parameters (magnetic field, density of the gas, etc.) that have been demonstrated in the laboratory. Hence, the general consensus has been that different physical processes occur, depending upon the parameters, to give the one result – the critical velocity phenomenon.

In this paper, however, a simple mechanism is proposed to explain the critical velocity phenomenon. This mechanism appears to be applicable over the entire range of experimental parameters examined to date. This mechanism invokes the formation of a double layer. Double layers form in a plasma, usually when a current exceeding a certain threshold value is passed through the plasma (see Block, 1978, for a review).

## II. THE FORMATION OF A DOUBLE LAYER

On a macroscopic level, a double layer can be defined as a local discontinuity surface in a plasma; but, microscopically, it consists of two equal but oppositely charged space-charge layers. The electric field within the double layer is very strong, but it is essentially zero outside this region. The spatial extent of the double layer is roughly of the order of the Debye length, although experimental results have shown that the double layer can be as thick as 1000 Debye lengths (Chan et al., 1984; Sato and Okuda, 1981). The electric potential for the type of double layer that we will be considering (the strong double layer) is monotonic and has the general form as that shown in Figure 1.

The double layer, once formed, separates the plasma into two sections with a potential difference across them. Years of laboratory research on the formation and stability of double layers have revealed that they form easily either by utilizing density gradients or by introducing a potential difference across the plasma (or across a segment of the plasma by inserting a charged electrode), or by some other method. Regardless of how the double layer is formed, the determining factor as to whether it will remain depends upon the distribution functions of the various types of charged particles that will be accelerated, decelerated, or reflected by the double layer.

To understand why a double layer should be expected to form when a neutral gas is incident upon a magnetized plasma, consider Figure 2. Here, the neutral gas is incident from the left. The magnetic field of the plasma, for simplicity, is assumed to be uniform, and in order to simulate the experimental situations where the critical velocity phenomenon has been observed, the magnetic field is taken to be almost perpendicular to the incoming neutral beam velocity vector. Even before the velocity of the neutral atoms reaches the critical velocity, a limited amount of ionization will naturally take place due mainly to impact and charge exchange collisions. Suppose that an atom is ionized at point O in Figure 2. The electron and ion will then be influenced by the magnetic field which is threading the plasma. Because of differences in magnetic moments, the ions will penetrate more deeply into the plasma than the electrons; i.e., both will spiral about the field lines but the ions with much large radii. This will result in a charge separation in the plasma which, in turn, will force the plasma to react in order to maintain charge neutrality. We expect the plasma to respond through the formation of a double layer, just as in the laboratory. The potential difference across the double layer will be essentially the kinetic energy of the newly formed ions since it is these ions that must be stopped in order to maintain charge neutrality. These ions, though, will have approximately the same energy as the original neutral atoms. Hence, the potential energy of the double layer is expected to be equal to the kinetic energy of the neutral gas.

This scenario also dictates the length scale of the double layer. It must have a width which is intermediate between the electron and the ion gyro radius. This is precisely the scale length associated with the leaky ionization fronts which have been observed in the experimental investigations of the critical velocity phenomenon (see e.g. Petelski, 1981).



The double layer will decelerate the newly formed ions. It will also accelerate the newly formed electrons as well as any electrons of the background plasma which drift into the double layer region. On the high potential side of the double layer, then, there will be some energetic electrons moving anti-parallel to the magnetic field. These electrons will be available for ionizing more neutral atoms through impact collisions. This process, in turn, will tend to establish a second double layer. This process could then be repeated and result in a series of double layers in the plasma. However, as mentioned previously, the charged particle distributions determine whether the double layers are stable. Although it may be possible that the conditions are favorable for the formation of several double layers, we speculate these double layers dissipate after they are formed. In this case, we have the equivalent to a single double layer moving through the plasma. Moving double layers are observed to occur in laboratory plasmas when the particle fluxes do not satisfy what is referred to as the Langmuir condition for a stable double layer (Block, 1978). In the laboratory, these moving double layers propagate to the end of the physical system confining the plasma where they disappear, and a new double layer appears at the opposite end.

The process described above may take place whenever a neutral gas beam is incident upon a magnetized plasma, regardless of the relative velocity of the beam. Laboratory experiments, as well as theoretical considerations, indicate that the thermal speed of the plasma particles makes the formation of a double layer possible. However, when the relative velocity becomes equal to the critical velocity, the picture we have presented leads to the conclusion that predicts a strong interaction should occur. This follows from the fact that the potential energy difference across the double layer and, hence, the energy of the accelerated electrons, is equal to the kinetic energy of the neutral atoms. When this energy is equal to the ionization energy of the atoms, the electrons will then have precisely the amount of energy needed to ionize the atoms. Consequently, when the relative velocity is equal to, or higher than, the critical velocity, the effect of the moving double layer (or a stationary double layer if appropriate) is to establish an ionization front which ionizes the neutral beam. This explains the observed connection between the critical velocity and ionization. This also implies that energetic electrons will be produced with velocity vectors directed anti-parallel to the magnetic field. This conclusion, in turn, is consistent with laboratory studies of the critical velocity phenomenon (see e.g. Danielsson and Brenning, 1975).

### III. THE ORIENTATION OF THE MAGNETIC FIELD

In all of the laboratory experiments that have studied the critical velocity phenomena, the magnetic field has been more or less perpendicular to the velocity vector of the incoming neutral beam. In our explanation of the critical velocity phenomenon, we must require that the angle between the two vectors is not precisely  $90^\circ$ . This requirement is necessary in order to have both a component of the electron's velocity parallel to the magnetic field line and also traverse through the double layer region. In Figure 3, this departure from  $90^\circ$  is given by the angle  $\delta$ . To examine the minimum value that  $\delta$  may have, we consider the experimental arrangement of Danielsson and Brenning (1975). The effective physical confines of the plasma region in this experiment was  $5 \text{ cm} \times 5 \text{ cm}$ . Therefore the length (along an equipotential surface) of the double layer was 5 cm. The width of the double layer, of course, can be no more than 5 cm, but its value will be determined mainly by the electron and ion gyro radii. The width,  $a$ , of the double layer satisfies the condition

$$r_e \ll a \ll r_i \quad (2)$$

where  $r_e$  and  $r_i$  are the corresponding gyro radii of the electrons and ions. The exact value of  $a$ , of course, depends upon the particle densities. For the Danielsson and Brenning experiment, typical parameters were  $B = 0.18 \text{ T}$  and  $v = 400 \text{ km/s}$ , resulting in  $r_e = 13 \text{ } \mu\text{m}$  and  $r_i = 10 \text{ cm}$ . Hence, the width of the double layer,  $a$ , was of the order of 1 mm. For this value of  $a$ , Figure 3 implies that the minimum value of  $\delta$  is  $1.2^\circ$ , which is hardly a stringent requirement. Hence, it can be concluded that the magnetic field vector can be essentially perpendicular to the relative velocity vector within our model.

#### IV. COMPARISON WITH OTHER THEORIES

Some theorists have examined the consequences of building up space charge by the trapping of electrons by the magnetic field. In particular, Piel et al. (1980) proposed the formation of a sheath similar to the double layer, but they considered only the  $\mathbf{E} \times \mathbf{B}$  drift motion in the sheath. They considered the possibility that the drift motion would lead to a modified two-stream instability which, in turn, would heat the electrons. This would then provide a feedback mechanism to produce the ionization, and thus explain the critical velocity phenomenon. As is the case with essentially all of the theoretical models, this particular approach explains a subset of the experimental observations of the phenomenon, but it fails in other cases (see e.g. Haerendel, 1982).

Lehnert (1967) analytically examined the potential structure that could form consistent with the Vlasov and Poisson equations. Assuming that collisions are negligible over scale lengths, of the order of the ions gyro radius, and a potential gradient in the plasma, he found that an oscillatory-type potential structure could be supported. The spatial extent of each cycle in the potential, naturally, turned out to be comparable to the gyro radius of the ions. The formation mechanism for this charge separation, however, requires that the electric field within the sheath be directed in the same direction as the velocity vector of the incoming neutral beam. This is precisely in the opposite direction of the field of the double layer in our picture. Because of the direction of the electric field in Lehnert's model, it is difficult for him to utilize it to energize the electrons. He, thus, relies on collisions to accomplish this (Danielsson and Brenning, 1975). Nevertheless, if the particle distributions in the plasma are such that a series of double layers would be stable, then the potential structure of the present model would be similar to Lehnert's model except for the oppositely directed electric field. The electric field of the present model is properly oriented for direct electron acceleration.

Varma (1978) also examined a possible consequence of charge separation upon the ionization of a marginal amount of the neutral gas. However, his analysis was directed mainly at explaining the direct interaction experiments (Danielsson, 1970, 1973; Danielsson and Brenning, 1975). Since these experiments provided evidence for electron acceleration parallel to the magnetic field, Varma suggested that a density gradient in the direction parallel to the magnetic field, due to the finite size of the experimental apparatus, would cause a potential well to form which could accelerate the electrons in the required direction. Again, this is a theoretical model which is very dependent upon the experimental parameters. Hence, it does not explain the general critical velocity phenomenon.

#### V. SUMMARY

In this paper, we have proposed that the formation of a double layer leads to the critical velocity phenomenon. The role of the double layer is to transfer the energy of the neutral particles to electrons which, in turn, ionize the neutral particles when the critical velocity is reached or exceeded. This mechanism is expected to operate under a wide variety of conditions as has been verified by double layer observations in the laboratory.

Although we have only described the model qualitatively here, it is evident that such a mechanism is a viable candidate for explaining the critical velocity phenomenon. It remains for future work to carry out computer simulation studies to investigate the formation and stability of double layers under the conditions where the critical velocity phenomenon has been observed.

*Acknowledgments.* I would like to thank H. Alfvén for a very fruitful discussion which led to looking at this solution to the critical velocity phenomenon. I also wish to express my indebtedness to N. Brenning and M. Raadu of Stockholm for providing some very helpful comments on an earlier version of this paper. M. C. Weisskopf also provided helpful suggestions which are reflected in the final version of the paper.

## REFERENCES

- Alfvén, H., *On the Origin of the Solar System*, Oxford University Press, Oxford, 1954.
- Block, L. P., *Ap. Space Sci.*, 55, 59 (1978).
- Chan, C., M. H. Cho, N. Hershkowitz, and T. Intrator, *Phys. Rev. Lett.*, 52, 1782 (1984).
- Danielsson, L., *Phys. Fluids*, 13, 2288 (1970).
- Danielsson, L., *Ap. Space Sci.*, 24, 459 (1973).
- Danielsson, L., and N. Brenning, *Phys. Fluids*, 18, 661 (1975).
- Haerendel, G., *Z. Naturforsch.*, 371, 728 (1982).
- Lehnert, B., *Phys. Fluids*, 10, 2216 (1967).
- Petelski, E. F., in *Relations Between Laboratory and Space Plasmas*, p. 23, D. Reidel, Dordrecht, 1981.
- Piel, A., E. Möbius, and G. Himmel, *Ap. Space Sci.*, 72, 211 (1980).
- Raadu, M. A., *Ap. Space Sci.*, 55, 125 (1978).
- Raadu, M. A., in *Relations Between Laboratory and Space Plasmas*, p. 13, D. Reidel, Dordrecht, 1981.
- Sato, T., and H. Okuda, *J. Geophys. Res.*, 86, 3357 (1981).
- Sherman, J. C., *Ap. Space Sci.*, 24, 487 (1973).
- Varma, R. K., *Ap. Space Sci.*, 55, 113 (1978).

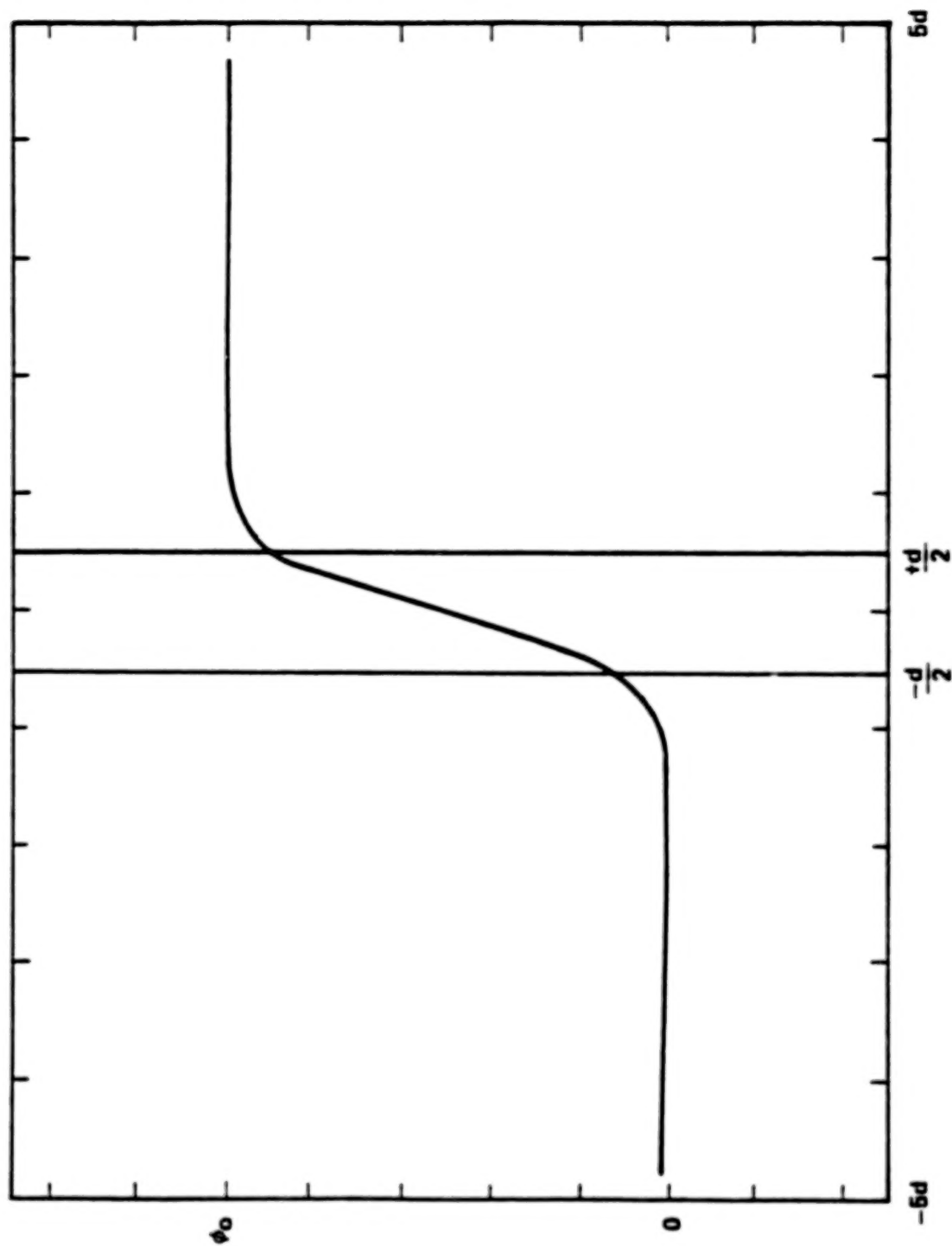


Figure 1. The general shape of the electric potential of a strong double layer as a function of position. The strength of the double layer is  $\phi_0$ , and its effective width is  $d$ .

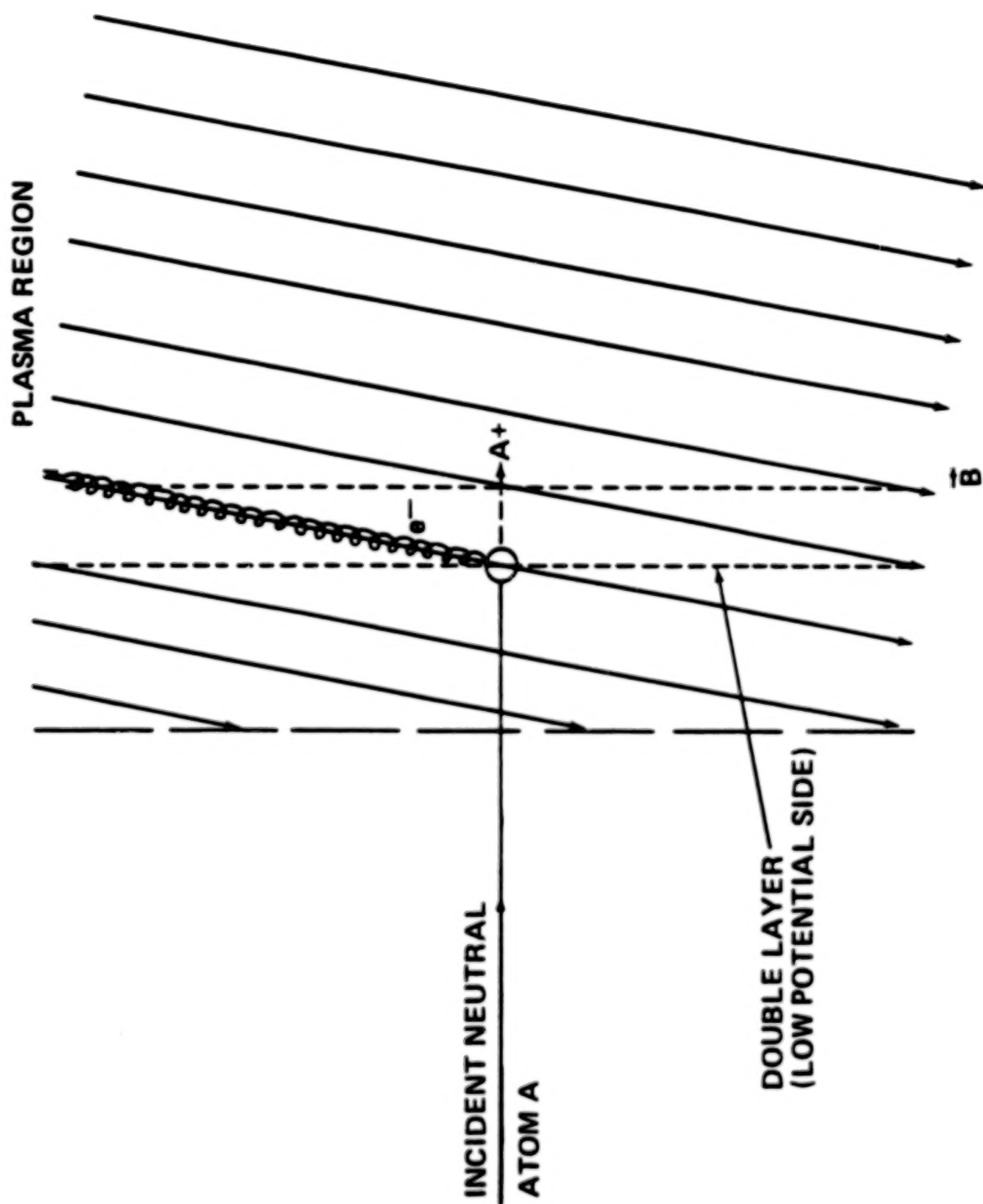


Figure 2. The interaction of a neutral gas beam with a magnetized plasma.

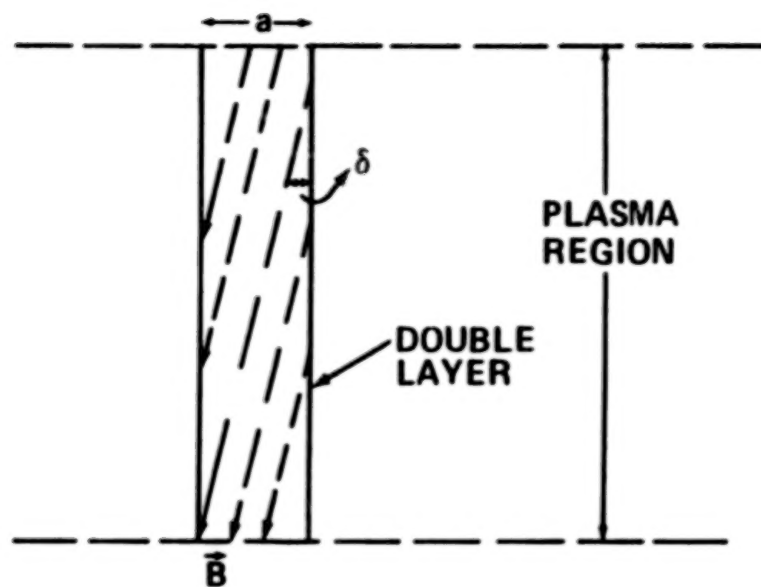


Figure 3. The orientation of the magnetic field vector of the plasma with respect to the equipotential surfaces of the double layer.



## RECOMMENDATIONS

One noteworthy outcome of the symposium was the adoption of a circuit symbol for the double layer. This symbol was proposed by H. Alfvén, and the participants agreed to adopt it and use it in future papers dealing with double layers. The symbol is shown in Figure 1. An example of a circuit with a double layer is the prominence-solar flare circuit where an exploding double layer is assumed to be responsible for the flare. Such a circuit was presented at the symposium by Alfvén and is shown in Figure 2.

Although it is possible to have a plasma double layer without a net current, many applications will have a net current. In these applications the "L" in the double layer symbol would be most appropriately oriented so as to show the direction of the current. This is illustrated in Figure 3.

Since the double layer will accelerate and decelerate particles depending upon their charge and direction of travel, power will be delivered to, as well as taken from, charged particles passing through it. The net power delivered to the charged particles passing through the double layer is the equation

$$P = I\Delta V$$

where  $I$  is the net current and  $\Delta V$  is the potential difference across the double layer. In the case of no net current, the double layer simply serves as an energy transfer mechanism. It transfers energy from one species of charged particles to another. Applications of this type of double layer were discussed in the symposium by Williams.

It is hoped that researchers in this field, as well as all who refer to the double layer, will join with the participants of the symposium in adopting the double layer symbol in Figure 1 in all future references.

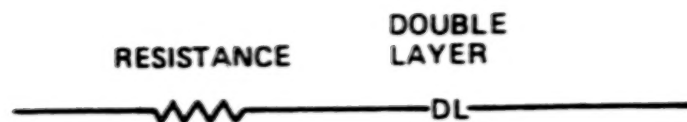


Figure 1. A diagram showing the adopted electrical symbol for the double layer when represented in a circuit.

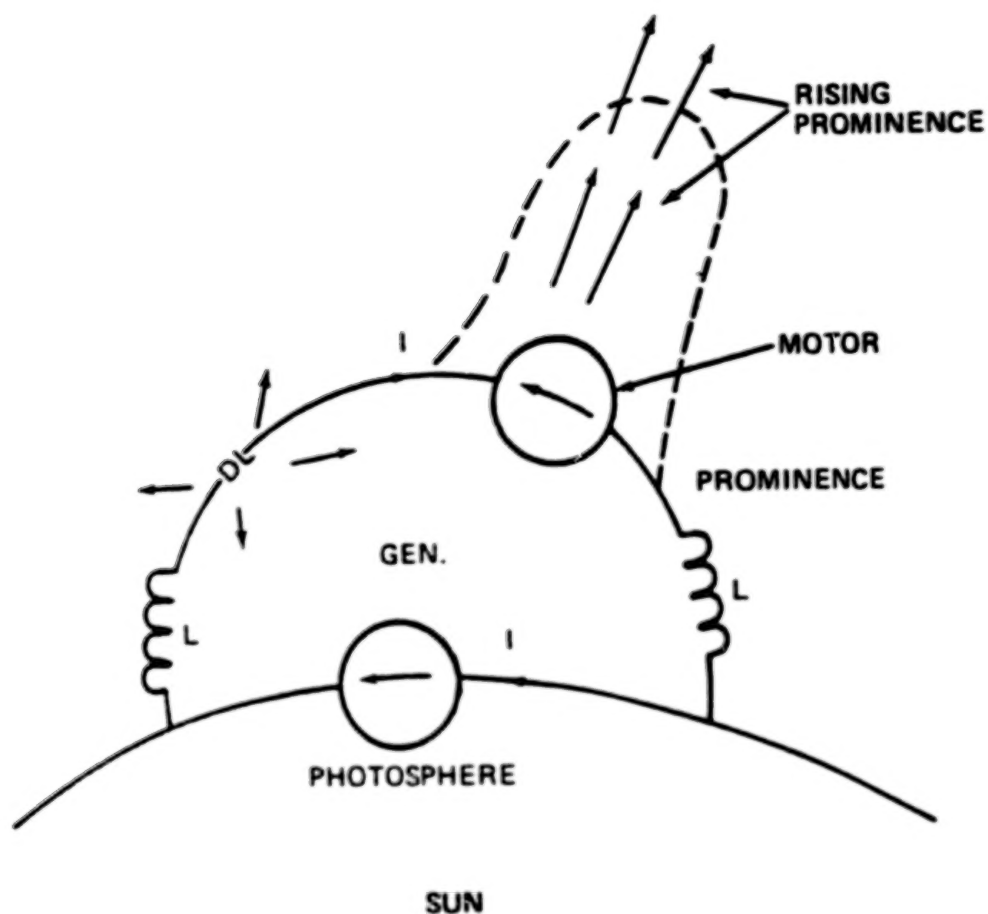


Figure 2. An example of an astrophysical circuit where a double layer plays a role - the solar prominence/flare circuit.

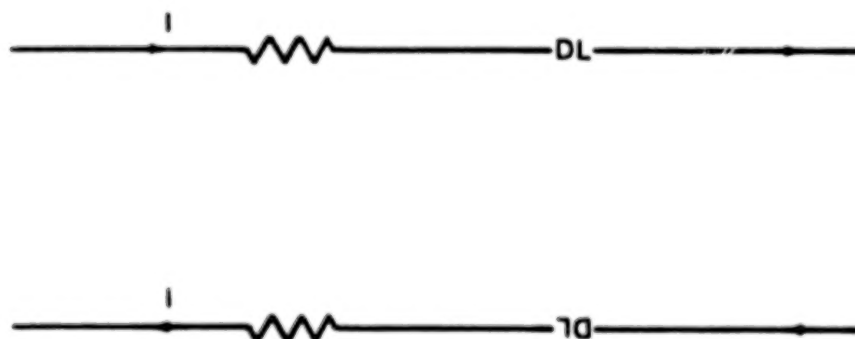


Figure 3. A diagram showing how the double layer symbol can indicate the direction of the current.

1. REPORT NO. NASA CP-2469		2. GOVERNMENT ACCESSION NO.		3. RECIPIENT'S CATALOG NO.	
4. TITLE AND SUBTITLE  Double Layers in Astrophysics				5. REPORT DATE May 1987	
				6. PERFORMING ORGANIZATION CODE ES65/ES01	
7. AUTHOR(S) Alton C. Williams and Tauna W. Moorehead, Editors				8. PERFORMING ORGANIZATION REPORT #	
9. PERFORMING ORGANIZATION NAME AND ADDRESS  George C. Marshall Space Flight Center Marshall Space Flight Center, Alabama 35812				10. WORK UNIT NO. M-560	
				11. CONTRACT OR GRANT NO.	
12. SPONSORING AGENCY NAME AND ADDRESS  National Aeronautics and Space Administration Washington, D.C. 20546				13. TYPE OF REPORT & PERIOD COVERED  Conference Publication	
				14. SPONSORING AGENCY CODE	
15. SUPPLEMENTARY NOTES  Sponsored, in part, by the Universities Space Research Association, Washington, D.C.					
16. ABSTRACT  This report contains results of a workshop held on March 17-19, 1986, at the Space Science Laboratory of NASA/Marshall Space Flight Center, Huntsville, Alabama. The contents of this report are divided as follows:  <ul style="list-style-type: none"> <li>o Double Layers in the Laboratory</li> <li>o Theory and Simulation of Double Layers</li> <li>o Space Applications</li> </ul>					
17. KEY WORDS  Double Layers, X-Ray Astrophysics, Gamma Ray Astronomy, Magnetospheric Physics			18. DISTRIBUTION STATEMENT  Unclassified—Unlimited  Subject Category 88		
19. SECURITY CLASSIF. (of this report)  Unclassified		20. SECURITY CLASSIF. (of this page)  Unclassified		21. NO. OF PAGES  339	
				22. PRICE  A15	

**END  
DATE  
FILMED**

AUG 5 1987